EMLA-2022-BF158-02-001

September 29, 2022

Mr. Rick Shean
Bureau Chief
Hazardous Waste Bureau
New Mexico Environment Department
2905 Rodeo Park Drive East, Building 1
Santa Fe, NM 87505-6313

Subject: Submittal of the Fate and Transport Modeling and Risk Assessment Report for
RDX Contamination in Deep Groundwater, Revision 1

Dear Mr. Shean:

Enclosed please find two hard copies with electronic files of the "Fate and Transport Modeling and
Risk Assessment Report for RDX Contamination in Deep Groundwater, Revision 1." Submittal of this
report fulfills fiscal year 2022 Milestone #10 of Appendix B of the 2016 Compliance Order on Consent.
The report includes a comprehensive present-day risk assessment and predictions for future fate and
transport of RDX (Royal Demolition Explosive) in deep groundwater. Enclosure 1 includes an electronic
copy of a redline strikeout version of the report that incorporates all changes made in response to
discussions held in seven pre-submission meetings with the New Mexico Environment Department and
the U.S. Environmental Protection Agency on April 8, 2021, April 29, 2021, November 18, 2021,
December 8, 2021, January 10, 2022, January 21, 2022, and February 24, 2022.

The overall conclusions of this risk assessment are that there is no current, potential, or
reasonably foreseeable future unacceptable risk to human life, either
1. associated with RDX contamination in the regional aquifer or
2 due to land use controls restricting installation of potable water wells in the perched-
   intermediate groundwater, from drinking groundwater originating from this aquifer.

The U.S. Department of Energy Environmental Management Los Alamos Field Office (EM-LA) and
Newport News Nuclear BWXT-Los Alamos, LLC (N3B) recommend continuation of long-term
groundwater monitoring to monitor the plume and ensure protection of human health. EM-LA and N3B
will collaborate with NMED to determine when groundwater conditions have the potential to cause an
unacceptable risk to human health and the necessary response actions to be taken.

If you have any questions, please contact Joseph Sena at (505) 551-2964 (joseph.sena@em-la.doe.gov) or Cheryl Rodriguez at (505) 414-0450 (cheryl.rodriguez@em.doe.gov).

Sincerely,

ARTURO DURAN

Digitally signed by ARTURO DURAN
Date: 2022.09.29 07:18:08 -06'00'

Arturo Q. Duran
Compliance and Permitting Manager
U.S. Department of Energy
Environmental Management
Los Alamos Field Office

Enclosure(s): Two hard copies with electronic files (including a redline strikeout version):

1. Fate and Transport Modeling and Risk Assessment Report for RDX Contamination in Deep Groundwater, Revision 1 (EM2022-0581)

cc (letter with CD/DVD enclosure[s]):
Laurie King, EPA Region 6, Dallas, TX
Scott Ellinger, EPA Region 6, Dallas, TX
Raymond Martinez, San Ildefonso Pueblo, NM
Dino Chavarria, Santa Clara Pueblo, NM
Steve Yanicak, NMED-DOE-OB
Chris Catechis, NMED-RPD
Patrick McGuire, N3B
Cheryl Rodriguez, EM-LA
emla.docs@em.doe.gov
n3brecords@em-la.doe.gov
Public Reading Room (EPRR)
PRS Website

CC (letter emailed without enclosures):
Jennifer Payne, LANL
Stephen Hoffman, NA-LA
William Alexander, N3B
Ryan Flynn, N3B
Kim Lebak, N3B
Joseph Legare, N3B
Dana Lindsay, N3B

Pamela Maestas, N3B
Christian Maupin, N3B
Robert McFarlane, N3B
Bruce Robinson, N3B
Troy Thomson, N3B
M. Lee Bishop, EM-LA
John Evans, EM-LA
Michael Mikolanis, EM-LA
David Nickless, EM-LA
Hai Shen, EM-LA

Fate and Transport Modeling and Risk Assessment Report for RDX Contamination in Deep Groundwater Revision 1

N3B Los Alamos

Fate and Transport Modeling and Risk Assessment Report for RDX Contamination in Deep Groundwater Revision 1

September 2022

Responsible program director:

Joseph Sena	*[signature]*	Director, Water Program Oversight	Water Program	9/22/22
Printed Name	Signature	Title	Organization	Date

Responsible N3B representative:

Troy Thomson	*[signature]*	Program Manager	N3B Environmental Remediation Program	9/22/22
Printed Name	Signature	Title	Organization	Date

Responsible DOE EM-LA representative:

Arturo Q. Duran	ARTURO DURAN Digitally signed by ARTURO DURAN Date: 2022.09.29 07:19:00 -06'00'	Compliance and Permitting Manager	Office of Quality and Regulatory Compliance	
Printed Name	Signature	Title	Organization	Date

EXECUTIVE SUMMARY

This revision to the May 2020 risk assessment and fate and transport model report for Royal Demolition Explosive (RDX) contamination in deep groundwater at Los Alamos National Laboratory (LANL or the Laboratory) fulfills a requirement of the 2016 Compliance Order on Consent (Consent Order) Appendix B fiscal year 2022 milestones and targets. In December 2021 the New Mexico Environment Department (NMED) issued the fiscal year 2022 Consent Order Appendix B milestones that included Milestone 10, described as "Revision 1 to the report submitted to NMED in May 2020. The revision incorporates updates to the risk assessment and fate and transport model that reflect discussions and draft comments received from NMED. Appendix B Milestone 10 is described as a report that will present a fate and transport evaluation and risk assessment for RDX in deep groundwater (i.e., perched-intermediate groundwater and the regional aquifer).

Operations and standard industrial practices at LANL mesa-top facilities between 1951 and 1996 led to the release of RDX to the facilities' process water outfall, adjacent and underlying soils, and alluvial sediments and surface water in Cañon de Valle (where the treated water was discharged). Two remedial actions (between 2000 and 2010) removed much of this surficial and near-surface RDX. However, recharge from precipitation has carried RDX down to the perched-intermediate zone and ultimately to the regional aquifer. Groundwater monitoring data indicate that RDX concentrations exceed the New Mexico tap water screening level (9.66 µg/L) in some wells in the southwestern portion of LANL.

This risk assessment report revision has been prepared to evaluate potential risks associated with exposure to RDX in groundwater and to determine the probability that RDX might encroach on water-supply wells at some time in the future. A calibrated probabilistic fate and transport model, developed to support this risk assessment report, provides long-term predictions of the spatial extent and associated concentrations of RDX in the regional aquifer.

This report integrates applicable information from groundwater-related investigations and modeling and addresses potential groundwater-related risks by evaluation of the following assessment scenarios:

- Scenario 1: Evaluating risk to human health under current conditions, where land-use control restricting potable groundwater wells is exercised by LANL within the facility's administrative boundary. The evaluation of Scenario 1, which takes into account the location of water-supply wells with respect to the impacted groundwater bodies and the extent of contamination within the impacted groundwater bodies, leads to the conclusion that there is no present-day risk to human health from groundwater contamination, either within or outside of LANL administrative boundaries.

- Scenario 2: Performing a screening-level groundwater risk assessment for RDX and all other detected constituents under present-day and potential future baseline conditions. This screening-level assessment indicates that concentrations of chemicals detected in perched-intermediate groundwater warrant institutional controls to eliminate the possibility of the use of impacted groundwater for consumption now and in the foreseeable future.

- Scenario 3: Evaluating future plume expansion in the regional aquifer, as predicted by the fate and transport model using the estimated mass of RDX above the aquifer, focusing on the probability that RDX will reach and impact existing water-supply wells. The fate and transport model indicates that by year 2200 there is effectively no probability that RDX groundwater concentrations at the tap water screening level (9.66 µg/L) will reach the three nearest water-supply wells. The median concentrations that do arrive at water-supply wells fall below 0.25 ppb, and the middle 50% of simulations fall below 0.5 ppb, suggesting that if RDX were ever to reach these wells it would likely be below current analytical detection limits.

CONTENTS

Figures

Tables

Appendices

1.0   INTRODUCTION

This risk assessment and fate and transport model report (hereafter, risk assessment report) for dissolved phase Royal Demolition Explosive (RDX) contamination in a portion of deep groundwater at Los Alamos National Laboratory (LANL or the Laboratory) Technical Area 16 (TA-16) fulfills the requirements of the 2016 Compliance Order on Consent (Consent Order) Appendix B milestones and targets for fiscal years (FYs) 2020 and 2022. FY 2020 Appendix B Milestone 7 required a report that presents a fate and transport evaluation and risk assessment for RDX in deep groundwater, and the report was submitted to the New Mexico Environment Department (NMED) on May 29, 2020 (N3B 2020, 700925). NMED issued comments to the U.S. Department of Energy (DOE) Environmental Management-Los Alamos Field Office (EM-LA) on November 25, 2020 (Krambis 2020, 701140) and directed EM-LA to submit a revised report addressing the comments. On March 1, 2021, EM-LA provided NMED with responses to each NMED comment (Maupin 2021, 701363) and a series of technical team meetings was held to discuss these comment responses. The meeting dates and summaries of the meeting topics are listed below.

- April 8, 2021 – meeting to discuss risk assessment report comment responses on model setup, information presented during a July 15, 2020, presentation on site hydrology, development of exposure point concentration, model validation, model distribution development, and the model grid

- April 29, 2021 – meeting to discuss risk assessment report comment responses on model validation, hydraulic conductivity distribution development, use of particle tracking, model run time, future water use, inclusion of public water supply well pumping, vertical gradients, site stratigraphy, model domain size, point of compliance

- November 18, 2021 – Technical Team meeting to discuss risk assessment report comment responses on what data to use, use of sensitivity analysis, site horizontal gradient, aquifer test methods and hydraulic conductivity distribution, and public water-supply wells in the model

- December 8, 2021 – Technical Team meeting to discuss modeling overview

- January 10, 2022 – Technical Team meeting to discuss aquifer test methods; these affect the use of the hydraulic conductivity distributions used in the model.

- January 27, 2022 – Technical Team meeting to discuss NMED's risk assessment report comment concerning water-supply well (PM well) pumping and present hydraulic analyses quantifying any "hinge effect" and any impact of water-supply pumping on lateral and vertical gradients at the site

- February 24, 2022 – Technical Team meeting to discuss risk assessment report Scenario 2

In December 2021 NMED issued the FY 2022 Consent Order appendix milestones that included Milestone 10, described as "Revision 1 to the report submitted to NMED in May 2020. The revision incorporates updates to the risk assessment and groundwater model that reflects discussions and draft comments received from NMED."

Deep groundwater in this report refers to both the perched-intermediate zone beneath TA-16 and the underlying regional aquifer.

The geographic setting of LANL is on the Pajarito Plateau, which consists of fingerlike mesas separated by canyons. The Pajarito Plateau is bounded by the Jemez Mountains to the west and the Rio Grande to the east. Groundwater migrates generally from west to east but with some local perturbations due to the manner in which the alluvial fans that form the groundwater-bearing unit's matrix were deposited and due to northeast-trending faults and fractures that cut across the RDX primary source and the infiltration zone at Cañon de Valle.

The original sources of the RDX at LANL are mesa-top facilities and an outfall to Cañon de Valle, which were active from 1951 to 1996. Standard industrial practices at the time led to the release of RDX to the facilities' process water outfall, adjacent and underlying soils, and alluvial sediments and surface water in Cañon de Valle (where the treated water was discharged). Two remedial actions (between 2000 and 2010) removed much of this surficial and near-surface RDX (N3B 2019, 700561).

RDX is present in a localized perched-intermediate groundwater zone above the regional aquifer and in a portion of the regional aquifer in the southwestern portion of LANL. Groundwater monitoring data indicate that RDX concentrations exceed the New Mexico tap water screening level (9.66 μg/L) in some wells.

The Consent Order provides a process to follow when a sample result shows a compound's concentration exceeds a screening level. Section IX.C of the Consent Order states

> …the corrective action process employs both screening levels and cleanup levels. Screening levels are contaminant concentrations that indicate the potential for unacceptable risk. If contaminants are present at concentrations above screening levels, it does not necessarily indicate that cleanup is required, but it does indicate that additional risk evaluation is needed to determine the potential need for cleanup. Cleanup levels are the contaminant concentrations that indicate when cleanup objectives are met. The need for cleanup is triggered by potential unacceptable risk and not by exceedance of screening levels.

Further, Section IX.F of the Consent Order states "NMED's tap water screening levels shall be used as groundwater screening levels for protection of human health if groundwater is a current or reasonably foreseeable source of drinking water."

The scope of this risk assessment focuses on the potential exposures to deep groundwater contaminants. Screening of potential health risks pertaining to residual contamination in surface and near-surface soil and sediment, alluvial groundwater, springs, and shallow groundwater in areas overlying deep groundwater is presented in separate reports, including the "Phase III RFI Report for Solid Waste Management Unit 16-021(c)-99" (LANL 2003, 077965), "Investigation Report for Water Canyon/ Cañon de Valle" (LANL 2011, 207069), and the "Supplemental Investigation Report for S-Site Aggregate Area, Revision 1" (N3B 2019, 700414).

Information on radioactive materials and radionuclides, including the results of sampling and analysis of radioactive constituents, is voluntarily provided to NMED in accordance with DOE policy.

The remaining parts of section 1 introduce the purpose and objective of this report and the regulatory context. Section 2 presents the conceptual site model (CSM). Sections 3, 4, and 5 describe the assessments performed and results for Scenarios 1, 2, and 3, respectively. Section 6 presents conclusions and recommendations. References and map data sources are found in section 7. The report appendices include Acronyms and Abbreviations, Metric Conversion Table, and Data Qualifier Definitions (Appendix A), Data Preparation Protocol, Time Plots, Box Plots, and ProUCL Files for Chemicals of Potential Concern (Appendix B), Probabilistic Groundwater Modeling of the Royal Demotion Explosive Plume at Los Alamos National Laboratory to Support Risk Assessment (Appendix C and Appendix D), and Perched-Intermediate Groundwater Database Query (Appendix E, on CD included with this document).

1.1   Report Purpose and Objectives

The objective of this risk assessment report revision is to address NMED's comments on the May 2020 report and to present a comprehensive description of the potential risks to human health related to contamination in perched-intermediate and regional groundwater at TA-16. Achieving this objective involved revising the RDX fate and transport model and evaluating potential risks under three assessment scenarios related to present-day and potential future site conditions:

- Scenario 1: Present-day conditions within and outside LANL boundaries, including LANL land-use controls

- Scenario 2: Present-day conditions within and outside LANL boundaries, excluding LANL land-use controls

- Scenario 3: Potential future conditions at the existing water-supply wells in the regional aquifer

The Scenario 1 assessment considered the present-day spatial extent of groundwater contamination in deep groundwater in reference to the location of LANL administrative boundaries. Scenario 1 assessed current conditions and the potential for complete present-day exposure pathways for contaminants in perched-intermediate groundwater and the regional aquifer.

The Scenario 2 screening-level risk assessment evaluated potential human health risks under present-day conditions in the absence of land use controls. This assessment used groundwater risk-based screening levels published by NMED and the U.S. Environmental Protection Agency (EPA) to evaluate potential risks to a hypothetical future resident who might have a domestic water-supply well drawing groundwater from an impacted groundwater body.

Scenario 3 applies the results of RDX fate and transport modeling in the regional aquifer to evaluate the probability that RDX could reach and impact regional aquifer water-supply wells at some time approximately within the next 180 yr.

1.2   Regulatory Context

NMED issued the Consent Order to DOE pursuant to Section 74-4-10 of the New Mexico Hazardous Waste Act. The Consent Order was also issued under Section 74-9-36.D of the New Mexico Solid Waste Act and 20.9.9.14 New Mexico Administrative Code (NMAC) for the limited purpose of addressing the corrective action activities, including requirements, concerning groundwater contaminants listed at 20.6.2.3103 NMAC, toxic pollutants listed at 20.6.2.7.T(2) NMAC, and explosive compounds as defined in this report.

The Consent Order provides the process by which investigation and remediation of contamination from legacy waste management activities at the Laboratory occurs. The Consent Order both guides and governs the ongoing cleanup of legacy waste at the Laboratory through a campaign-based approach and the annual planning process. The annual planning process allows for revisions to cleanup campaigns based on actual work progress, changed conditions, and funding, with the DOE Environmental Management Los Alamos Field Office (EM-LA) updating the milestones and targets listed in the Consent Order Appendix B Milestones and Targets table.

EM-LA proposed to use the annual planning process described in Section VIII.C of the Consent Order to discuss and establish a new target date for the final corrective measures evaluation (CME) report based upon the recommendations in the "Investigation Report for Royal Demolition Explosive in Deep Groundwater," (hereafter, DGIR) (N3B 2019, 700561). EM-LA proposed to delay the CME report target in

Appendix B so that a fate and transport model and risk assessment report, consistent with the Consent Order process, could be prepared and submitted to NMED. During the 2018 annual planning process, the Appendix B milestone table showed a CME being submitted in August 2020. During the 2019 planning process, the fate and transport model and risk assessment report for deep groundwater submission date was set as May 29, 2020, and a target date for the CME was set at December 18, 2020. After submission of FY 2020 Consent Order Milestone 7 in May 2020 and receipt of NMED's comments in November 2020, a series of technical team meetings discussing EM-LA's response to NMED's comments took place (see section 1.0). During these meetings the fate and transport modeling and risk assessment report revision submission date was set as September 30, 2022, and a CME target date was set as September 30, 2024.

1.2.1 Applicable Regulations and Guidance for Human Health Risk Assessment

The primary guidance applied for the methodology employed in the human health risk assessment is NMED's soil screening guidance for human health risk assessment (NMED 2019, 700550). Risk-based groundwater screening levels are provided in this guidance for the purpose of supporting soil screening for the leaching-to-groundwater pathway. These groundwater screening levels are applied in this risk assessment. NMED (2019, 700550) also describes relevant methodology for conducting a screening-level risk assessment that, although published for the purpose of soil screening, can be applied to groundwater risk assessment.

Groundwater concentrations are also evaluated in the context of applicable regulatory standards for groundwater, specifically New Mexico Water Quality Control Commission standards (20 6.2.3103 NMAC Parts A and B) and EPA maximum contaminant levels (MCLs), which can be found at https://www.nrc.gov/docs/ML1307/ML13078A040.pdf.

2.0 CONCEPTUAL SITE MODEL

2.1 Site Description

RDX impacts on groundwater are associated with operations at TA-16, which is located in the southwestern corner of the Laboratory and covers 2410 acres (3.8 mi^2). Figure 2.1-1 shows the boundary of TA-16 within the Laboratory. Bandelier National Monument borders TA-16 along NM 4 to the south. The Santa Fe National Forest, along NM 501, borders TA-16 to the west. To the north and east, TA-16 is bordered by TA-08, TA-09, TA-11, TA-14, TA-15, TA-37, and TA-49. TA-16 is fenced and posted along NM 4. Water Canyon, a 200-ft-deep ravine with steep walls, separates NM 4 from active sites at TA-16. Cañon de Valle forms the northern border of TA-16.

Building 16-260, located on the north side of TA-16 (Figure 2.1-2), has been used for processing and machining high explosives (HE) since 1951. Water is used to machine HE, which is slightly water soluble. Effluent from machining operations contains dissolved HE and may contain entrained HE cuttings. At building 16-260, effluent treatment consists of routing the water to 13 settling sumps to recover any entrained HE cuttings. From 1951 to 1996, the water from these sumps was discharged to the 260 Outfall (Figure 2.1-2) that drained into Cañon de Valle. In 1994, outfall discharge volumes were measured at several million gallons per year. The discharge volumes were probably greater during the 1950s when HE production output from building 260 was substantially greater than it was in the 1990s (LANL 1994, 076858).

In the past, barium was a constituent of certain HE formulations and inert components and was present in the outfall effluent from building 16-260. The HE machining building (16-260) and associated sumps, drainlines, and troughs discharged effluent into the 260 Outfall drainage channel. The 260 Outfall drainage channel consisted of a settling pond and an upper and lower drainage channel that extends from the 260 Outfall downgradient to the confluence of the drainage and Cañon de Valle. The former approximately 50-ft-long × 20-ft-wide settling pond was located within the upper drainage channel, approximately 45 ft below the 260 Outfall. The drainage channel runs approximately 600 ft northeast from the 260 Outfall to the bottom of Cañon de Valle. Historically, HE-containing water from the outfall entered the former settling pond and drained into the 260 Outfall drainage channel. Current management of this waste stream includes pumping the sumps and treating the water at the TA-16 HE wastewater treatment plant.

2.2   Conceptual Exposure Model of Current and Future Land Use

Current and future land use at TA-16, according to the Laboratory's 25-year site plan for 2013 to 2037 (LANL 2012, 601095), is designated as HE research, development, testing, assembly, and production, in addition to weapons engineering tritium research. Most areas within TA-16 are active sites for the Weapons Engineering Technology Division of the Laboratory. As described in the site plan, construction of new facilities is planned during this 25-year period. As shown in Figure 2.1-2, many roads and utilities are present at the site.

In addition, on Laboratory property there are institutional controls and safeguards that govern access and land use at TA-16. Security controls prevent unknowing entry and minimize the possibility for unauthorized entry of persons or livestock onto TA-16, thus ensuring no unauthorized land use, including installation of a water-supply well. There are also requirements for land transfer. Land transfer protocols govern any transfer of property from DOE to another entity. These land transfer protocols require a notice to NMED when DOE intends to transfer property.

2.2.1   Potentially Complete Human Exposure Pathways

The assessment of potential risks related to domestic use of groundwater was evaluated employing the exposure model associated with NMED tap water screening levels (NMED 2019, 700550; inputs to soil screening for the leaching-to-groundwater pathway). This exposure model is consistent with the model used by EPA for calculation of residential tap water regional screening levels. The exposure pathways addressed in the NMED and EPA tap water screening levels include

1. ingestion of drinking water,

2. dermal absorption from water while bathing, and

3. inhalation of volatile chemicals released from water into indoor air.

It is important to recognize the implications of the assumed duration of exposure used in the calculation of these tap water screening levels. For chemicals with screening levels based on the assessment endpoint of cancer risk, such as RDX, this is a 26-yr exposure duration. The tap water exposure concentration that is associated with these screening levels is the average concentration across a 26-yr period. This is true regardless of what value from a data set is used to represent the exposure concentration. This is discussed in relation to the Scenario 2 risk screening for baseline conditions in section 4 of this report.

One other potentially complete exposure pathway related to tap water is ingestion of produce products contaminated through irrigation of crops with impacted tap water and of livestock products contaminated through livestock ingesting impacted tap water. As discussed below, the potential contribution of

exposures from food-ingestion pathways is expected to be small for organic chemicals dissolved in tap water relative to the pathways that are addressed in the NMED and EPA tap water exposure models. Therefore, these pathways are not included in the risk-based groundwater criteria used in this risk assessment report.

2.2.2 Bioaccumulation Considerations for Organic Chemicals in Plant Tissues

Plant and animal uptake and retention of organic chemicals is related to the lipophilicity of such chemicals, as well as their resistance to metabolism once they are absorbed into plant or animal tissues. NMED guidance for ecological risk assessment (NMED 2017, 602274, Equation 11) describes how plant concentrations of organic chemicals can be estimated based on a chemical's octanol-water partition coefficient (K_{ow}), within a range of K_{ow} between approximately 1 and 10 (Travis and Arms 1988, 059108). Concentrations of more soluble organic chemicals in plants are predicted to be greater than those of less soluble chemicals. However, man-made organic chemicals are not expected to become concentrated in plant tissues because, unlike essential nutrients and certain endogenous organic molecules, such chemicals are not actively transported across the cell membranes of plants. Therefore, human intake of organic chemicals from direct ingestion of contaminated water is always likely to be far greater than from ingestion of produce irrigated with contaminated water.

2.2.3 Bioaccumulation Considerations for Organic Chemicals in Animal Tissues

Bioaccumulation of certain organic chemicals in lipid-rich animal tissues can be of concern. Organic chemicals that are known to bioaccumulate in animal tissues, such as polychlorinated biphenyls (PCBs), dioxins-furans, and certain organochlorine pesticides, generally share the physical properties of being largely insoluble in water and also resistant to metabolism. Appendix D of NMED's soil screening guidance for human health risk assessments (NMED 2019, 700550) discusses PCBs as an example of a persistent environmental pollutant that possesses these properties. Because of their low solubility, and tendency to adsorb onto soils and sediments, such chemicals are not typically encountered in groundwater. RDX has a generally low to negligible water solubility at 59.7 mg/L at 25°C. RDX is not very lipid soluble, and therefore has a low potential for bioaccumulation in aquatic species (https://www.atsdr.cdc.gov/toxprofiles/tp78-c6.pdf). RDX is not expected to bioaccumulate in livestock through ingestion of contaminated water.

2.3 Conceptual Site Model of Contaminant Occurrence and Transport

This section presents a summary of the conceptual site model as it pertains to assessing risk to human health. Additional details on the perched-intermediate groundwater system and the regional aquifer can be found in the DGIR (N3B 2019, 700561).

Based on data collected from previous investigations showing the spatial distribution of HE constituents in the Cañon de Valle watershed, the 260 Outfall was the most significant source for releases of HE (and in particular, RDX) at TA-16 (N3B 2019, 700561).

The direction of groundwater flow in the perched-intermediate groundwater zones is predominantly from west to east (Figure 2.3-1). As shown in Figure 2.3-2, the regional groundwater table beneath the Pajarito Plateau has a generally east-sloping gradient that extends from an elevation of approximately 6600 ft at the Pajarito fault to approximately 5500 ft at the Rio Grande, over a distance of approximately 9.3 mi.

The vertical transport pathway for RDX found in perched-intermediate groundwater zones in the lower vadose zone and in the regional aquifer is downward percolation of canyon-floor infiltration through the upper vadose zone. Infiltration through the vadose zone is expected to be predominantly vertical and

controlled by gravity as modified by the hydrogeological properties of the various stratigraphic units. Hydraulic properties of stratigraphic and structural features (e.g., laterally discontinuous silt layers, faults) appear to be locally significant. Significant vertical anisotropy occurs because of the layered nature of the stratigraphic units, and horizontal hydraulic conductivities within stratigraphic units are significantly greater than vertical hydraulic conductivities across bedding within and between units. As a result, downward percolating moisture is likely to be diverted laterally at capillary barriers associated with bedding contacts in the stratigraphic sequence.

Two main horizons (or zones) of perched-intermediate groundwater occur in the lower vadose zone as a result of perching on less permeable strata. These perched-intermediate zones are characterized by complex, lateral-discontinuous pathways for the transport of RDX in the vadose zone via "stair-stepping" that likely follows dips of beds within the geologic units. Both perched-intermediate zones contain RDX at concentrations greater than the 9.66-µg/L NMED tap water screening level. RDX concentrations are greater in the upper perched-intermediate zone than the lower perched-intermediate zone, and perched-intermediate RDX concentrations are greater than those observed in the regional aquifer (N3B 2019, 700561). Concentrations of RDX that exceed 100 µg/L have been measured in the upper perched-intermediate zone in intermediate wells CdV-16-2(i)r and CdV-16-4ip.

The estimated mass of RDX in both the upper and lower perched-intermediate zones combined is estimated to be between 263 kg and 1478 kg (N3B 2019, 700561). The approximate boundaries of the upper perched-intermediate groundwater zone, and the approximate area where RDX concentrations exceed the NMED tap water screening level, are shown in Figure 2.3-1.

The regional groundwater system is a complex heterogeneous system that consists of a shallow, predominantly unconfined zone and a deep, predominantly confined zone. Vertical hydraulic stratification in the regional aquifer is indicated by pronounced vertical differences in hydraulic heads in multiscreen wells and a lack of vertical propagation of pumping drawdown caused by pumping tests and pumping of municipal water-supply wells. There are no clearly defined laterally continuous aquitards or confining layers that provide hydraulic separation between the shallow and deep zones of the regional aquifer. The vertical hydraulic separation is likely caused by pronounced vertical aquifer anisotropy caused by the complex depositional layering of the Puye Formation, with the lateral permeability substantially higher than the vertical permeability.

The regional groundwater zone contains between 35 and 415 kg of RDX according to inventory performed in 2017 (LANL 2018, 602963).

3.0   ASSESSMENT SCENARIO 1: EVALUATION OF CURRENT CONDITIONS

The objective of Scenario 1 is to evaluate potential risks from dissolved phase RDX in deep groundwater under present-day conditions, which includes institutional controls exercised by LANL within its administrative boundaries. These controls prohibit and prevent the drilling, installation, and operation of potable groundwater wells within or in the vicinity of the area of impacted groundwater.

As shown in Figure 2.3-1, the approximate present-day spatial extent of RDX above the NMED tap water screening level in upper perched-intermediate groundwater is primarily within TA-16, with some extension into adjacent regions of TA-09 and TA-14. However, the extent of RDX within upper perched-intermediate groundwater is wholly contained within LANL administrative boundaries (Figure 2.1-1). As indicated in the water table contours in Figure 2.3-1, and discussed in section 2.3, the predominant direction of groundwater migration of perched-intermediate groundwater is from west to east. This west-to-east migration direction is also characteristic of the regional aquifer (Figure 2.3-2).

The estimated extent of RDX in the regional aquifer is depicted in Figure 2.3-3. The approximate area of RDX deep groundwater concentrations shown in Figure 2.3-3 is indicated by the cluster of monitoring wells (R-25, R-63, R-68, R-69, R-47, and R-18) in and around Cañon de Valle. A comparison of the spatial extent of RDX in the regional aquifer with that of RDX in upper perched-intermediate groundwater shows that RDX concentrations in the regional aquifer extend farther to the north-northeast. However, the extent of RDX in the regional aquifer is about 3 mi from the nearest LANL administrative boundary. Figure 2.3-2 shows the location of LANL administrative boundaries, along with the location of downgradient regional aquifer municipal supply wells PM-2, PM-4, and PM-5.

In summary, the factors that support a conclusion that there is no potential current human exposure to site-related groundwater contamination are the following:

- No water-supply wells exist in impacted perched-intermediate groundwater. Therefore, there are no present-day exposures to contaminants in the perched-intermediate zone.

- The current boundaries of the dissolved-phase RDX in the regional aquifer above the NMED tap water screening levels are at least 3 mi from the nearest existing water-supply well. Therefore, there are no present-day exposures to RDX via this pathway.

- The extent of detectable concentrations of RDX in the perched-intermediate groundwater zone and the regional aquifer are entirely within the LANL administrative boundary. In addition, the entire extent of the perched-intermediate zone is within that boundary. No exposures are taking place because of migration off-site.

4.0   ASSESSMENT SCENARIO 2: EVALUATION OF RISK UNDER BASELINE CONDITIONS

This section presents a screening-level groundwater risk assessment for all detected constituents under an assumption that no land use controls are exercised and that no engineering controls or future remediation takes place to mitigate groundwater concentrations of possible contaminants. The assessment evaluates potential risks using data from monitoring wells. As discussed in section 4.5, risks are assessed separately for each of the nine monitoring wells evaluated in the risk assessment, since any future exposure would pertain to groundwater pumped from a single, hypothetical, domestic well at a particular location.

4.1   Identification of Wells for the Screening-Level Risk Assessment

As discussed in section 2.3, contaminants related to releases from TA-16 migrate vertically through the vadose zone to reach deep groundwater. Observed contaminant concentrations are higher in perched-intermediate groundwater than in the regional aquifer. The screening assessment protectively assumes that a hypothetical future well is screened in the perched-intermediate zone, where contaminant concentrations are highest.

As discussed in the DGIR (N3B 2019, 700561), groundwater monitoring at TA-16 and in downgradient areas is conducted under an annual interim facility-wide groundwater monitoring plan. Groundwater monitoring wells where sampling of perched-intermediate groundwater is performed are identified in Table 3.1-2 of the DGIR. Wells with screens in the perched-intermediate zone used to support the RDX vadose zone model (discussed in Appendix D section D-3.2) were also reviewed to support identification of wells and well screens for this screening-level risk assessment. Other candidate wells were identified by review of maps and figures published in the DGIR and discussion with subject matter experts at LANL. The initial list of candidate wells and well screens is shown in Table 4.1-1.

Well R-25c is a dry well; therefore, no usable analytical data for perched-intermediate groundwater exist for this well.

Three of the wells shown in Table 4.1-1 (16-26644, R-26 PZ-2, and MSC-16-02665) are screened in fractures in shallow tuff bedrock at a depth below ground surface (bgs) of between approximately 94 and 180 ft. Data from these wells were not used in this assessment because the occurrence of only localized and limited groundwater in shallow bedrock is inconsistent with the water production requirements of a domestic supply well. As noted below, MSC-16-02665 in particular is screened in a zone of bedrock that is only intermittently saturated.

Section 3.2.2.1 of the DGIR (N3B 2019, 700561) describes the characteristics of these shallow bedrock wells:

> Most shallow boreholes (<200 ft) drilled on TA-16 mesas are dry; however, three wells, 16-260E-02712, MSC-16-02665, and 90LP-SE-16-02669, are intermittently saturated and one well, 16-26644, is perennially saturated (Figure 3.2-2). The spotty distribution of groundwater associated with the springs and shallow boreholes supports the interpretation that the shallow bedrock perched-groundwater occurs as ribbons of saturation that are stratigraphically controlled.

R-26 PZ-2 is a shallow borehole (<200 ft) completed in the Tshirege Member tuff. Analytical data for well R-26 PZ-2 are related to water sampled during piezometer tests. Since this well was not constructed as a monitoring well for collection of decision-level data, results from the piezometer tests are considered screening-level data and are therefore not used in this risk assessment. Section 3.1.2 of the DGIR (N3B 2019, 700561) notes that water from well 16-26644 is chemically similar to the surface system comprising the Cañon de Valle springs and base flows.

Drilling activities in 2000 caused screen 1 and screen 2 of well R-25 to become plugged with concrete/ stainless-steel shavings. The presence of the stainless-steel shavings in screens 1 and 2 have led to some stainless-steel corrosion and nonrepresentativeness of data collected from those screens. The Westbay sampling system used in well R-25 does not allow purging of the well before sampling, and therefore the corroding metal resulted in anomalously large values reported for several analytes. Therefore, samples from these screened intervals have not been included in the data set used for this risk assessment.

A subset of the wells shown in Table 4.1-1 has been identified as representative of groundwater background conditions. These wells are identified in Table 3.2-2 of "Groundwater Background Investigation Report, Revision 5" (LANL 2016, 601920) and include PCI-2, R-26 (screen 1), R-27(i), and R-47(i). Analytical data from these wells are used to support identification of chemicals of potential concern (COPCs) in the perched-intermediate wells evaluated in this assessment.

The final list of site characterization and background wells is shown in Table 4.1-2. Note that, per discussion in section 4.2, well CdV-R-37-2 is not included in this list because of the lack of usable analytical data. Additionally, note that there is only a single sample, obtained in 2019, available from well R-63(i). Although results from a single sample are inadequate to characterize groundwater concentrations for this well, these data have been included in the assessment to provide a potential indication of chemical and radionuclide groundwater concentrations in this well.

4.2 Data Retrieval and Preparation

The perched-intermediate well list discussed in section 4.1 was used to query data in LANL's Environmental Information Management (EIM) database. In EIM, the view V_LANL_REPORT_CHEM_SWTS was used to query the data for the well list. The results of this query were downloaded on March 6, 2020.

The final data set, with Data Removal field flags and the associated Data Removal Reason field defined, is provided in Appendix E (on CD included with this document).

The following provides an overview of the data filters applied to the EIM data query for this risk assessment: (1) sample purpose = regular (REG), (2) sample type = water (W) or groundwater (WG), (3) best value flag = YES, and (4) sample usage code = investigation (INV) or blank. No data related to screening samples, well testing or development samples, tracer study samples, or quality control samples were included in the data set. A complete description of the data filters applied, as well as the selected analytical method in cases where the same analyte was measured by multiple methods for the same sample, is provided in Appendix B.

After the data preparation filters described above were applied, no usable groundwater data were identified in well CdV-R-37-2. Therefore, this well is not included in this risk assessment.

The following logic was applied with regard to handling of data qualifiers:

- Do not use data if qualifier = R (rejected).

- If qualifier contains a U, data are used and result is considered not detected.

- For all other qualifiers, data are used and considered detected.

4.2.1 Data Filters Related to Evaluation of Temporal Trends

Evaluation of temporal trends was performed by review of plots that show patterns of constituent concentrations over time. Some data collected very early within a time series may not be representative because of an initial period of stabilization of newly constructed wells or because of changes in the nature and extent of the plume over time. Because the intention of the risk assessment evaluation is to evaluate current and potential future groundwater conditions, the data plots were reviewed to identify early sample results that are not representative of current conditions for either of the reasons above. Temporal plots of the data reviewed to identify time trends are provided in Appendix B, Attachment B-1 (Time Plots for Data Trimming, on CD included with this document).

The plots for inorganic chemicals and radionuclides were reviewed to support development of the data set used to perform statistical tests comparing site and background groundwater concentrations (see section 4.3). Based on this review, the following inorganic chemical data were removed from the data set:

1. Inorganic chemical results for samples collected before 2010 in well CdV-16-2(i)r were removed. Review of the temporal plots showed anomalously high values for several inorganic chemicals, including aluminum, barium, copper, iron, lead, magnesium, potassium, sodium, uranium, vanadium, and zinc.

2. Inorganic chemical results for samples collected before 2003 in well R-19 were removed. Review of the temporal plots showed anomalously high values for several inorganic chemicals in these early samples, including barium, copper, iron, manganese, nitrate-nitrite as nitrogen, potassium, strontium, and zinc.

3. Inorganic chemical results for samples collected before 2003 in well R-25 were removed. Review of the temporal plots showed anomalously high values for several inorganic chemicals in these early samples, including barium, calcium, chromium, iron, manganese, potassium, selenium, thallium, uranium, and vanadium.

A summary of the analytical data in both site wells and background wells (see Table 4.1-2) applied in the risk assessment to identify COPCs is provided in Table 4.2-1. This data summary is presented for each analyte and well combination and includes the number of samples; number of detected values; and the minimum, maximum, median, and mean of the detected values and nondetections.

Removal of the early inorganic chemical results from wells CdV-16-2(i)r, R-19, and R-25 leaves adequate data to characterize current groundwater concentrations of these analytes. The data set for inorganic chemicals in well CdV-16-2(i)r is from 2006 through 2019, the data set for inorganic chemicals in well R-19 begins in 2000 and ends in 2019, and the data set for inorganic chemicals in well R-25 begins in 2000 and ends in 2016. There are many more-recent sampling events in these wells to characterize concentrations of inorganic chemicals that are more representative of current conditions.

Review of the temporal plots for well R-25b showed anomalously high values for molybdenum, uranium, and zinc in samples collected before 2010. However, no samples were systematically removed from well R-25b because the number of potentially impacted inorganic chemicals in early samples appears limited relative to wells CdV-16-2(i)r, R-19, and R-25.

Temporal plots of organic COPCs were also reviewed to determine whether additional trimming of the data set could be warranted at some wells. Although there is some indication of possible trends for certain organic chemicals, these trends are noisy and uncertain. For example, concentrations of RDX appear to be declining over time at wells CdV-9-1(i), CdV-16-4ip, and R-25b but appear to be increasing at well CdV-16-2(i)r. The potential for possible temporal trends to influence the results of the risk assessment screening is discussed in the uncertainty analysis in section 4.6.3. In particular, the impact of excluding early inorganic chemical results from wells CdV-16-2(i)r, R-19, and R-25 is evaluated.

The relatively large short-term variability observed for some analytes in wells CdV-16-4ip and R-25 is likely related to the fact that data from two well screens at different depths were aggregated for these wells.

4.2.1.1 Temporal Trend Analysis for RDX

Temporal trend analysis for RDX was performed in this screening assessment because RDX is present at concentrations exceeding the New Mexico tap water screening level of 9.66 µg/L in 5 of the 9 perched-intermediate groundwater monitoring wells including CdV-16-1(i), CdV-16-2(i)r, CdV-16-4ip, CdV-9-1(i), and R-25. As noted above, inspection of time-series plots indicates that concentrations of RDX appear to be declining over time at wells CdV-9-1(i) and CdV-16-4ip but appear to be increasing at well CdV-16-2(i)r. Time trend analysis was conducted for RDX to support a determination of whether to calculate a 95% upper confidence limit (UCL) with the data from these wells.

Three statistical methods were selected for the RDX time trend analyses. These methods are ordinary least squares regression (OLS), the Mann-Kendall trend test (M-K), and the Theil-Sen trend test (T-S). These three methods were selected for the following reasons:

1. They provide a combination of parametric and non-parametric methods of trend analysis.

2. All three tests are relatively robust and viewing the collective results provides a measure of confidence in assessing whether there is an increasing or decreasing concentration trend.

3. These are the trend tests currently available within EPA's ProUCL software (EPA 2022, 702275).

The M-K test provides an estimate of whether a trend is "increasing," "decreasing," or "uncertain" whereas the OLS and T-S tests provide linear estimates of trend based on a 95% confidence level. To normalize the results of the three tests, an assignment of increasing, decreasing, or uncertain trend is given based on the 95% confidence interval of the trend line for OLS and T-S and the 95% confidence level for the M-K test. The outcome of these tests is provided below:

Well	Number of Samples	Number of Detections	OLS trend	T-S trend	M-K trend
CdV-16-1(i)	31	31	Increasing	Increasing	Inconclusive
CdV-16-2(i)r	33	32	Increasing	Increasing	Increasing
CDV-16-4ip (S1 + S2)*	29	29	Inconclusive	Decreasing	Inconclusive
CDV-9-1(i) (S1)	17	17	Decreasing	Decreasing	Decreasing
R-25 (S3 and S4)	20	18	Increasing	Increasing	Increasing

* S = Screened interval.

All three trend tests, or two of the three tests in the case of CdV-16-1(i), indicate increasing RDX concentrations over time at wells CdV-16-1(i), CdV-16-2(i)r, and R-25. A 95% UCL is not calculated for these wells where concentrations are increasing because a statistic based on the available time series of data may underestimate average concentrations in the future. Instead, the maximum detected value is used as the exposure point concentration (EPC) at wells CdV-16-1(i), CdV-16-2(i)r, and R-25, and uncertainty in future RDX concentrations is discussed in section 4.6.3.

4.3   Data Evaluation and Identification of COPCs

COPCs were identified for each monitoring well, because local aquifer concentrations are applicable to exposure from water pumped from a single, hypothetical, domestic well. Unlike in soil assessments, where a receptor is assumed to roam at random across an exposure unit, the exposure source in a groundwater risk assessment is the groundwater that is pumped at the location where a well is drilled.

Organic chemicals detected in one or more samples at a monitoring well are evaluated directly in the screening assessment presented in section 4.6 of this report. Sometimes this resulted in organic COPCs being evaluated in the assessment even though concentrations may not be representative of current groundwater conditions. For example, several noncarcinogenic polycyclic aromatic hydrocarbons were identified in a single, early sample at well R-19. Although these results are not representative of more recent groundwater samples, they were included in the risk screening to demonstrate that the measured concentrations are, in any case, of negligible toxicological concern.

For inorganic chemicals and radionuclides, where there are commonly background levels of naturally occurring analytes in groundwater, statistical tests and data visualization plots are used to identify analytes present at concentrations exceeding background levels. The data visualization plots are provided for organic chemicals as well, to facilitate data review.

Box-and whisker plots (box plots) were constructed to facilitate comparisons of the site and background data for each analyte. The box plots divide the data into four sections, each containing 25% of the data. The length of the central box indicates the spread of the central 50% of the data, while the length of the whiskers shows the breadth of the tails of the distribution. Potential outliers are those data that lie beyond the whiskers, which extend to 1.5 times the interquartile range (75th percentile minus the 25th percentile) from either end of the central box. The box plot also demonstrates the shape of the data in the following manner. If the upper box and whisker are approximately the same length as the lower box and whisker, then the data are distributed symmetrically. If the upper box and whisker are longer than the lower box and whisker, then the data are right-skewed. If the upper box and whisker are shorter than the lower box and whisker, then the data are left-skewed. Box plots for all analytes are provided in Appendix B, Attachment B-2 (on CD included with this document).

As discussed in section 4.2.1, temporal data plots were constructed to allow visualization of potential patterns of increasing or decreasing concentrations over time. These plots are useful in conjunction with box plots for determining when potential outliers were measured during the sampling period. As noted above, the temporal data plots were reviewed to identify where early sampling results for one or more analytes are very different from the more-recent results in a monitoring well. Inclusion of analytical data that are clearly not representative of current conditions is inappropriate because the intention of the risk assessment evaluation is to evaluate current and potential future groundwater conditions. A set of temporal data plots for the final data set used in this screening-level risk assessment, subsequent to the trimming of early sample results for inorganic chemicals in some wells as discussed in section 4.2.1, is provided in Appendix B, Attachment B-3 (Time Plot Final Data Set, on CD included with this document). Hence, the box plots in Appendix B, Attachment B-2 and temporal data plots in Appendix B, Attachment B-3 both reflect the final data set used in the screening assessment.

Statistical background comparisons were conducted for all inorganic chemicals and radionuclides. The null hypothesis of each of the four chosen statistical tests is that site and background concentrations are of the same source. Analyte concentrations were considered to be potentially above background concentrations if any of the statistical tests failed this hypothesis test, using a p-value of 0.05. The box plots and temporal data plots were also reviewed in conjunction with the results of the statistical tests to identify COPCs. Additionally, the range of the data were sometimes compared with risk-based criteria and regulatory standards to support decisions on COPC identification. Complete results from the statistical background comparisons, with notes describing information taken from review of the box plots and temporal plots, are presented in Table 4.3-1.

The Student's t-test and the Gehan test (Gehan 1965, 055611; Gilbert and Simpson 1992, 054952) were used to compare the mean and the median of the distributions of metals concentrations at the site and background wells, respectively. The quantile and the slippage tests were used to compare the upper tails of the distributions relative to background. A more detailed description of these four tests is provided in section B-2.0 of Appendix B.

The final list of COPCs for each site well, including detected organic chemicals and inorganic chemicals and radionuclides present at concentrations above background levels, is shown in Table 4.3-2.

4.4   Identification of Risk-Based Screening Criteria and Regulatory Standards

A domestic water-supply well is assumed to exist in the impacted perched-intermediate groundwater zone for the Scenario 2 risk assessment. This assumption indicates that residential land use is the limiting (most protective) potential future exposure scenario. Under residential land use assumptions, both children and adults are evaluated, where children are considered to be potentially more sensitive to adverse effects than adults. Also, relative to an industrial or commercial scenario, individual daily consumption rates are likely to be greater under residential land use assumptions where individuals may be at home for the majority of their waking hours.

NMED tap water screening levels, described in Section 2.4 of NMED's soil screening guidance (NMED 2019, 700550) are used as inputs to soil screening for the leaching-to-groundwater pathway discussed in that guidance. In this assessment, these screening levels were preferentially used to evaluate potential health risks related to groundwater exposure in a residence. Section IX.F of the Consent Order states "NMED's tap water screening levels shall be used as groundwater screening levels for protection of human health if groundwater is a current or reasonably foreseeable source of drinking water."

If tap water screening levels are not included in NMED's soil screening guidance (NMED 2019, 700550) for one or more chemicals, EPA regional screening levels (RSLs) for tap water were applied. This hierarchy of sources is consistent with Section 1.1 of NMED's soil screening guidance (NMED 2019, 700550), and in accordance with that guidance, RSLs based on a carcinogenic endpoint were adjusted to the NMED 1×10^{-5} risk threshold, since RSLs for carcinogenic effects are derived using a risk threshold of 1×10^{-6}. As noted in section 2.2.1 of this report, the same exposure pathways are addressed in both NMED and EPA tap water screening criteria. EPA tap water RSLs are the values published in November 2019 at https://www.epa.gov/risk/regional-screening-levels-rsls-generic-tables.

For radionuclides, EPA's preliminary remediation goal (PRG) calculator was used to calculate tap water ingestion PRGs using a target risk of 1×10^{-5}. For consistency with the chemical screening criteria, potential exposures to radionuclides in groundwater were evaluated for both tap water ingestion and inhalation of gas-phase radionuclides. As discussed in section 2.2.1, ingestion of garden produce was not included in the PRGs developed for this screening. Default PRG calculator inputs for the tap water ingestion and inhalation pathways for the residential scenario were used to calculate radionuclide PRGs.

Radionuclide PRGs were calculated with the PRG calculator option "Does not assume secular equilibrium, provide results for progeny throughout chain (with decay)." For long-lived radionuclides, such as uranium-234, uranium-235, and uranium-238, secular equilibrium within the uranium or actinium decay chains requires many millennia. Such an assumption of secular equilibrium is inconsistent with the assumed release and transport of specific radionuclides that are being evaluated as possible COPCs related to LANL operations. However, secular equilibrium with short-lived progeny (i.e., half-life < approximately 1 yr) is accounted for in developing radionuclide PRGs. The contributions of short-lived progeny to PRG for a parent radionuclide are included in the parent radionuclide's PRG. The method of adding the contribution of short-lived progeny to the PRG of a parent radionuclide is by the inverse sum of reciprocals. For a parent radionuclide, X_parent, and short-lived progeny, X_progeny, the calculation proceeds as

$$X\_total = 1 / ((1 / X\_parent) + (1 / X\_progeny)) \qquad \textbf{Equation 1}$$

NMED and EPA risk-based screening criteria for chemical COPCs for both cancer and noncancer endpoints, and for radionuclide PRGs, are provided in Table 4.4-1.

Groundwater concentrations of COPCs are also compared with regulatory standards, specifically, New Mexico groundwater protection standards (NMAC 20.6.2.3103, Parts A and B) and EPA National Primary Drinking Water Regulations tap water MCLs. These regulatory standards for COPCs are provided in Table 4.4-2.

4.5 Identification of Exposure Point Concentrations

In principle, estimates of average groundwater concentrations at assessment locations over the time periods pertaining to noncancer health effects of RDX (6 yr) and carcinogenic effects of RDX (26 yr) are of interest. As stated in section 2.2.1, regardless of what statistic is used to represent the EPC (even when using maxima), the characteristics of the exposure model are such that the EPC represents an average concentration in groundwater pumped from the well during the entire exposure duration. For assessment of exposure to tap water from a domestic water well, average aquifer concentrations across a well screen length are the appropriate basis for estimating EPCs because of the physical characteristics of the perched-intermediate zone described in section 2.3 that limit the volume and rate at which groundwater can be pumped.

The distance between perched-intermediate groundwater wells where RDX concentrations exceed the New Mexico tap water screening level of 9.66 µg/L is many hundreds of feet. To avoid inappropriate averaging of groundwater concentrations over such distances, a separate set of COPCs and associated EPCs was developed for each individual monitoring well. EPCs for the screening assessment are estimated using the protocol described in NMED's soil screening guidance (NMED 2019, 700550), which suggests estimating risks using both maxima and averages. As an initial estimation, average groundwater concentrations over a residential exposure period are represented by the maximum detected concentration at a well. Secondly, for COPCs where there are a sufficient number of samples and detections to support estimation of a 95% UCL at a well, the 95% UCL is also used to represent groundwater EPCs in the cumulative risk screening for perched-intermediate groundwater.

Calculation of UCLs of the mean concentrations was done using statistical methods that are available in the EPA ProUCL 5.2.0 software (EPA 2022, 702275). Consistent with the ProUCL v5.1 Technical Guide (EPA 2015, 601724), and NMED soil screening guidance (NMED 2019, 700550), a minimum of eight samples and five detections in a data set were required to calculate UCLs. ProUCL documentation strongly recommends against using the maximum detected concentration for the EPC when there are a sufficient number of samples and number of detections to calculate a UCL. However, consistent with the recommendations of NMED's soil screening guidance (NMED 2019, 700550), EPCs were also represented by the maximum detected concentration when a 95% UCL was calculated.

To prepare the data set for calculating 95% UCLs, COPC nondetection data were first imputed to a value equal to one-half of the associated detection limit. This approach was chosen because of concerns that the Kaplan-Meier method (often applied in the ProUCL software) for imputing values for nondetection data can sometimes produce artificially low estimates of 95% UCLs, particularly when there is a wide range of nondetection values such as occurs for some analytes in this data set. The Kaplan-Meier imputation method substitutes a nondetection with the next lowest detected value except it uses the detection limit for the nondetection when there is no lower-valued detection. When there is a large gap between nondetections and the next lowest detected value, this can result in underestimation of the mean, and hence of the UCL of the mean. Data that span many years often suffer from this type of effect, because detection limits have usually decreased over time. Investigation of these data revealed that this was the case for too many of the chemicals to allow reliance on UCL methods that included the Kaplan-Meier imputation approach. Consequently, the substitution approach of using half the detection limit was chosen so that UCLs, and hence risk, would not be underestimated.

The data set with nondetection results assigned a value of one-half of the detection limit was then used in ProUCL to calculate 95% UCLs for each COPC. Specifically, the 95% Student's t-test UCL (*t*-UCL) and the 95% bias-corrected and accelerated (BCA) bootstrap UCL were chosen from the ProUCL output to represent the 95% UCL. For each COPC and well combination, the larger of these two UCLs was protectively used as the 95% UCL. Additionally, if the selected 95% UCL was ever greater than the highest detected value, the maximum detected concentration was used as the EPC instead.

The *t*-UCL and BCA bootstrap methods were selected for estimating 95% UCLs because of their general robustness. If the data come from an underlying normal distribution, then the *t*-UCL is appropriate. If the data are sufficiently skewed, then the BCA bootstrap method is likely to provide a more realistic estimate of a 95% UCL. The methodology described here was chosen because ProUCL's suggested 95% UCL is sometimes unrealistic in cases where small sample size results in low power for ProUCL's goodness-of-fit tests. Because small sample sizes result in low statistical power to determine that a data set does not belong to a statistical distribution, ProUCL may select a parametric 95% UCL when there is little evidence that the data follow an underlying distribution.

A set of box plots for individual COPCs showing the mean and 95% UCL in relation to the site well data are provided in Appendix B, Attachment B-4 (Box Plots with 95% UCL Line, on CD included with this document) to support review of the reasonableness of the 95% UCL estimates. Note that nondetection results in the Appendix B, Attachment B-4 plots are shown as one-half of the sample analytical detection limit to represent the value used in the calculation of the 95% UCL. Input and output data files for ProUCL calculations are provided in Appendix B, Attachment B-5 (on CD included with this document).

Table 4.5-1 summarizes minimum detected value, maximum detected value, mean, 95% UCL concentrations, and the selected EPC for all site wells and COPCs.

4.6   Screening-Level Risk Assessment Results

4.6.1   Assessment of Cancer Risk and Chemical Hazard

The screening-level risk assessment evaluated the ratios of groundwater EPCs and risk-based groundwater concentrations. Screening for COPCs, performed on a per-well basis, included (1) incremental lifetime cancer risk (cancer risk) and noncancer hazard quotient (HQ) assessment endpoints for chemicals and (2) cancer risk for radionuclides.

As discussed in section 4.5, the risk-based screening follows the general protocol described in NMED's soil screening guidance (NMED 2019, 700550). First, maximum detected concentrations are compared with screening criteria, and a sum-of-ratios is calculated for cancer and noncancer endpoints. Next, for analytes and wells where data support estimation of a 95% UCL, the 95% UCL is also used to represent groundwater EPCs in the cumulative risk screening for the perched-intermediate zone.

For both cancer risk and HQ, the water concentration at each well (initially the maximum detected value, and then the EPC estimated as described in section 4.5) was divided by the tap water screening value, and these ratios were summed for each assessment endpoint. For cancer risk, the resulting ratios were multiplied by 1×10^{-5} to express the sum-of-ratios as the equivalent cancer risk. The HQ sum-of-ratios, referred to as a hazard index (HI), does not require this adjustment because the target HQ is 1.

Table 4.6-1 displays the cumulative risk-screening summary results for chemicals and radionuclides in perched-intermediate groundwater for the nine groundwater monitoring wells evaluated in the risk assessment screening. Cancer risks calculated using maximum detected COPC concentrations as well as EPCs exceeded the 1×10^{-5} risk threshold in all wells excepting CdV-37-1(i), R-19, and R-63(i). The

highest cancer risk calculated using EPCs (1×10^{-4}) was at monitoring wells CdV-16-4ip and CdV-16-2(i)r. Cancer risk results calculated using EPCs for the remaining wells with risk above the threshold were between 3×10^{-5} and 6×10^{-5}. HIs exceed the threshold value of 1 at monitoring wells CdV-16-4ip, CdV-16-2(i)r, and R-25. Cancer risks described in this paragraph were almost entirely related to chemical COPCs; the contribution of radionuclide COPCs to cancer risks above the 1×10^{-5} risk threshold was negligible.

Tables 4.6-2 through 4.6-10 display the full cumulative risk screening results for chemicals by well, showing the individual contribution of all chemical COPCs to the cancer risk sum and HI. With the exception of well R-25b, RDX was the dominant contributor to cancer risks above the threshold of 1×10^{-5} at all monitoring wells. RDX was also the dominant contributor to HI values at or above 1 in monitoring wells CdV-16-4ip and CdV-16-2(i)r, but at well R-25 cobalt was the major contributor. Table 4.6-11 indicates the major contributors to cancer risk and HI results above thresholds at each monitoring well, with EPCs used to represent groundwater concentrations.

RDX is clearly the most significant contributor to cancer risk values above the threshold of 1×10^{-5}. The sole exception is well R-25b, where 3 halogenated volatile organic compounds (VOCs) contribute 90% of the total cancer risk of 6×10^{-5}. These 3 VOCs were each detected in the same 2 of the 11 groundwater samples that compose the R-25b data set. These samples were the last 2 samples acquired from well R-25b, where the last sample was obtained in 2017. The similar VOC bromoform was also detected in these samples, although it is a negligible contributor to calculated health effects. These 4 VOCs were not detected in any of the other 8 site wells.

RDX is also the major contributor to HI values in two of the three wells with HI results above the threshold of 1, contributing 69% and 77% respectively at wells CdV-16-4ip and CdV-16-2(i)r. Monitoring well R-25 is the exception, where cobalt contributes 76% of the HI value of 4.

Table 4.6-12 displays the full cumulative risk-screening results for radionuclide COPCs, which consist of tritium, uranium-234, and uranium-238. Relative to chemical cancer risks, radionuclide COPCs were negligible contributors to cancer risks above the 1×10^{-5} risk threshold. Cancer risk results for radionuclides, calculated using EPCs to represent groundwater concentrations, were below the 1×10^{-5} risk threshold and ranged from 6×10^{-7} to 6×10^{-6}. Most of the radionuclide cancer risk was contributed by tritium when this analyte was a COPC in a monitoring well.

4.6.2   Comparison of EPCs with Regulatory Standards

Table 4.6-13 presents a comparison of maximum detected values and EPCs with regulatory standards (20.6.2.3103 NMAC and EPA MCLs) . The only exceedance of an 20.6.2.3103 NMAC Part A human health standard was for the COPC nitrate-nitrite as nitrogen in well CdV-9-1(i). The EPC of 1300 µg/L exceeded the Part A standard of 1000 µg/L, as well as the primary MCL standard, which is also 1000 µg/L.

There were three occurrences of an EPC at a monitoring well exceeding a secondary MCL, where secondary MCLs are guidelines related to possible cosmetic or aesthetic effects. The iron EPC of 330 µg/L at CdV-16-1(i) exceeded the secondary MCL of 300 µg/L. Also, the aluminum secondary MCL of 50 to 200 µg/L was exceeded at wells R-25 (600 µg/L) and R-25b (360 µg/L).

4.6.3   Uncertainty Analysis

The assessment presented in this report is specifically a screening-level evaluation of potential risks related to consumption of groundwater in the vicinity of TA-16. As a screening assessment, it is proper that the assessment include protective assumptions intended to ensure that potential risks are not

inadvertently overlooked. This is important because it implies that the tabulated risk estimates are intentionally biased high. In this context, a tabulated residential cancer risk estimate of 1×10^{-5} should not be interpreted to indicate that this level of potential risk is likely or anticipated. Rather, it signifies that one can conclude with reasonable assurance that potential cancer risks would not exceed 1×10^{-5} should a residence be sited in the area and obtain domestic water from impacted groundwater.

The major uncertainties and biases in the risk assessment screening results are discussed below.

1. The representativeness of EPCs for characterizing average COPC concentrations in the volume of groundwater that would be pumped from a domestic well during the assumed residential exposure period

   A potentially important aspect of this topic is (1) the application of the ProUCL approach to avoid computing a 95% UCL when there are fewer than 5 detected values and (2) the application of NMED guidance (NMED 2019, 700550) to represent the EPC as the maximum value under these circumstances. For RDX, where detection frequency is generally high in the impacted wells, a 95% UCL was calculated unless trend analyses indicated increasing concentrations with time [CdV-16-1(i), CdV-16-2(i)r, and R-25]. In these three wells, the average RDX groundwater concentration for an entire 26-yr exposure duration is represented by a single data point, which is the maximum detected value. However, as shown in the RDX time-series plot in Appendix B, Attachment B-1 (Time Plots for Data Trimming, on CD included with this document), the maximum detected RDX concentrations in these three wells occur several years before the last sample date. This indicates a relatively high degree of temporal variability in RDX well concentrations over time, where the maximum value does not necessarily occur in the last few samples of a monitoring well data set even when there is an overall increasing trend in concentrations. Review of the RDX concentration time-series plots for CdV-16-1(i), CdV-16-2(i)r, and R-25 in Attachment B-1 suggests that the maximum detected concentration is likely a protective estimate of concentrations in these wells in the future.

   Maximum detected values were also used as EPCs for risk drivers at well R-25b, where 3 halogenated VOCs that were detected in only 2 of the 11 groundwater samples available for well R-25b contribute 90% of the total cancer risk of 6×10^{-5}. As shown in Table 4.5-1, the maximum concentrations of chlorodibromomethane, bromodichloromethane, and chloroform were approximately 3 to 5 times larger than the average value across all 11 samples.

   Cobalt contributes 76% to an HI of 4 at well R-25. As shown in the cobalt time-series plot in Appendix B, Attachment B-1 (Time Plots for Data Trimming, on CD included with this document), the last two groundwater sample maximum detected concentrations (19.7 µg/L in July 2015 and 12.2 µg/L in December 2016) are much higher than all other detected values since 2001 (less than 2 µg/L.) The maximum detected concentration of 19.7 µg/L was used as the EPC for the R-25 data set. The representativeness of the maximum detected concentration of 19.7 µg/L for current and future groundwater conditions in the vicinity of well R-25 is uncertain. However, the collocated intermediate well R-25b does not show similar cobalt concentrations, with the only detection in the period between 2010 and the last sampling date of August 2019 being 2.95 µg/L in March 2019. Given that cobalt concentrations measured at R-25b from 2010 through 2019 do not corroborate the two high values observed in 2015 and 2016 at well R-25, it is likely that the chemical hazard attributed to cobalt at well R-25 based on the maximum detected concentration of 19.7 µg/L is biased high.

2. The influence of removing inorganic chemical data from early samples collected at wells CdV-16-2(i)r, R-19, and R-25

   As discussed in section 4.2.1, review of time-trend plots provided in Appendix B, Attachment B-1 (Time Plots for Data Trimming, on CD included with this document), early groundwater samples from wells CdV-16-2(i)r, R-19, and R-25 contained anomalously high values for a number of metals such as aluminum, barium, copper, iron, magnesium, potassium, uranium, vanadium, and zinc. These early results likely reflect perturbed groundwater conditions during a period of stabilization of the newly constructed wells. A review of the early inorganic chemical data from these wells indicates that the only instance where a detected concentration exceeds a primary drinking water standard is in well CdV-16-2(i)r, where lead was measured at 15.7 µg/L in a sample from May 2007 (the New Mexico and EPA primary drinking water standard for lead is 15 µg/L). Among the 32 samples in the CdV-16-2(i)r trimmed data set, collected in the period of 2010 to 2019, lead was detected in only four samples at a maximum concentration of 2.08 µg/L. This review indicates that uncertainty in the judgment to remove early inorganic chemical data from the data sets of wells CdV-16-2(i)r, R-19, and R-25 likely has little impact on the results of the screening risk assessment.

3. Whether the perched-intermediate groundwater zone has adequate transmissivity to support a domestic well, which commonly requires that at least a few gallons per minute be produced in a pump test

   To mitigate this uncertainty in wells R-25 and CdV-16-4ip, the data from both screened intervals from which perched-intermediate groundwater were available were combined. As noted in section 2.3, the heterogeneity and limited areal extent of the paleo channels where groundwater flow is dominant presents significant challenges to effectively removing water at a rate required for a domestic well. Ultimately, if an attempted well were to be insufficiently productive in the perched-intermediate groundwater zone, it is likely the driller would continue to drill and obtain water from the regional aquifer. The use of perched-intermediate groundwater data is a protective assumption since concentrations or RDX (the main risk-driver) are lower in the regional aquifer.

4. The likelihood that a single-residence well would be financially feasible

   This uncertainty could potentially be evaluated by review of existing well information in New Mexico, but within the context of this screening assessment, this is, like the assumption of adequate water production from the perched-intermediate zone, a protective assumption required to conduct the screening assessment.

5. The uncertainty in the dose-response information for key risk-drivers

   Ingestion of RDX, and associated cancer risk, is the main contributor to screening assessment results above the NMED threshold of 1×10^{-5}. EPA's "Guidelines for Carcinogen Risk Assessment" (https://www.epa.gov/risk/guidelines-carcinogen-risk-assessment) describes five recommended standard descriptors of the weight of evidence of a chemicals' carcinogenicity: (1) carcinogenic to humans, (2) likely to be carcinogenic to humans, (3) suggestive evidence of carcinogenic potential, (4) inadequate information to assess carcinogenic potential, and (5) not likely to be carcinogenic to humans. RDX has been assigned the third descriptor, suggestive evidence of carcinogenic potential, which indicates the weight of evidence from animal studies is suggestive of carcinogenicity, and a concern for potential carcinogenic effects in humans exists, but the data are judged to be insufficient for supporting a stronger conclusion. The oral slope factor used to calculate the NMED and EPA tap water criteria is based on a 2-yr dietary study in mice, which included 4 dose groups and a control group, and 85 mice per sex per group. The oral slope factor was derived from increased incidence of hepatocellular adenomas or carcinomas

and alveolar/bronchiolar adenomas or carcinomas in female mice. Details of this study can be found in EPA's toxicological review for RDX, available online through the Integrated Risk Information System (IRIS) database at https://cfpub.epa.gov/ncea/iris/iris_documents/documents/toxreviews/0313tr.pdf.

6. The residential exposure assumptions applied in the NMED and EPA tap water screening criteria

   The main protective biases applied in these exposure models are that for a hypothetical individual, most or all of water consumption will occur at home and the individual will reside in the home from birth for an exposure period of 26 yr. The exposure period of 26 yr corresponds to the 90th percentile of the key population mobility study described in EPA's "Exposure Factors Handbook" (EPA 2011, 208374). From the same study, the average length of time that an individual resides at a residence is 12 yr. Since cancer risk scales linearly with the duration of exposure, the degree of protective bias associated with that specific exposure assumption is a bit more than twofold.

4.7   Screening Assessment Conclusions

Concentrations of chemicals in perched-intermediate groundwater necessitate that institutional controls be maintained to eliminate the possibility of contaminated groundwater being accessed for consumption in the foreseeable future. This conclusion is based on a screening-level assessment that indicates potential cancer risks exceed NMED's cancer risk threshold of 1×10^{-5} at six of the nine monitoring wells evaluated in this assessment. RDX is the most significant contributor to cancer risk and HI values above NMED's regulatory thresholds of 1×10^{-5} and 1, respectively. However, NMED's cancer risk threshold of 1×10^{-5} is at the midpoint of the risk management range of 1×10^{-6} to 1×10^{-4} that EPA has used to evaluate cancer risk across the country as described in the "National Oil and Hazardous Substances Pollution Contingency Plan" (40 Code of Federal Regulations 300.430) The HI for non-cancer risk was exceeded at three of the wells: CdV-16-2(i)r (HI = 2), CdV-16-4ip (HI = 2), and R-25 (HI = 4). As discussed in section 4.6.3, the calculated HI for well R-25 is likely to be unrealistically high. While there is evidence of a slight potential risk for non-cancer effects from domestic use of perched-intermediate zone groundwater, the cancer risk endpoint is the larger concern.

5.0   ASSESSMENT SCENARIO 3: EVALUATION OF FUTURE CONDITIONS AT EXISTING WATER-SUPPLY WELLS

The objective of Scenario 3 is to evaluate the probability that RDX could reach any of the downgradient regional aquifer water-supply wells PM-2, PM-4, or PM-5, at some time in the future. The model was run until the year 2200. Evaluation of Scenario 3 applies the results of RDX fate and transport modeling in the regional aquifer, which is summarized in Appendix C and discussed in detail in Appendix D of this report. No risk assessment calculations related to modeled RDX concentrations at future times and locations are included in this evaluation because Scenario 3 evaluates the migration of RDX in the regional aquifer and the potential that it could reach the water supply wells.

As discussed in Appendix C, fate and transport modeling of RDX in the regional aquifer was conducted using a probabilistic RDX regional aquifer model (RRM) to predict regional aquifer concentrations over space and time. The CSM, assumptions, model structures, input parameterization, model discretization, RDX source fluxes, and all other details of the RRM construction, operation, and results are summarized in Appendix C, with additional supporting detail in Appendix D. The model was calibrated with measured RDX groundwater concentrations over time, up to December 2019; trends in concentrations; drawdown responses to municipal water-supply well pumping; hydraulic heads in the regional aquifer wells; and

hydraulic gradients. The objective of the calibration work is to develop a model that matches the observed pattern of RDX concentrations in monitoring wells through the present day, accounting for uncertainty, thus providing a measure of assurance in predicted future concentrations at those locations and in downgradient areas where monitoring data are unavailable. The RRM calibration is effective at matching all targets listed above. Additional confidence in the model is developed through validation using data sets that were not used as targets in the calibration. The model was validated against data collected between the end of 2019 and present day, hydraulic gradients distal to the plume (close gradients were used as targets), and conceptual information. Appendix C discusses results of the calibration and validation, with extensive plots demonstrating goodness of fit and providing confidence in the predictive ability of the RRM to represent explicit estimates of hydraulic head and RDX concentration (spatially and temporally), with associated measures of uncertainty, at all modeled points within the spatial domain of the model and within the time period of modeling (until the year 2200).

The RRM was run through the year 2200, or about 180 yr beyond the time of the last data used for model calibration. The multi-decadal timeframe was selected to bound a reasonably foreseeable future time period during which these wells might be used and capture the period during which the estimated RDX mass available for leaching to the regional aquifer has been exhausted. The probability of RDX reaching each of the water-supply wells is shown in Figure 5.1-1 and is discussed in section C-3.3 of Appendix C. In Figure 5.1-1, the black line represents the median predicted concentration of RDX (which is effectively 0 at PM-2 and PM-5 and reaches a maximum of 0.25 ppb, below the approximate RDX detection limit of 0.33 ppb, at PM-4). The dark shading shows the most likely output of the model runs (the middle 50% of the simulations), and the light grey shading shows the middle 95% of the runs. Full plume maps through time are provided in Appendix C.

The Appendix C plume maps show that RDX is not likely to occur at levels above the detection limit at any of the regional aquifer water-supply wells and is 95% likely to remain at concentrations below 2 ppb at these locations. The RRM indicates that by year 2200 there is a 42% probability that concentrations above 0.33 ppb (the approximate detection limit) could reach one of the three nearest water-supply wells and that there is a 10% probability that concentrations exceeding 1 ppb could reach one of these wells. However, there is very little probability of exceeding 2 ppb at any water-supply well, a concentration well below the NMED tap water screening level of 9.66 µg/L.

The RRM assumes continuous recharge and flux of RDX to the regional aquifer from the vadose zone until the mass of RDX in the vadose is exhausted. In 30% of the simulations, RDX mass is not exhausted and is continuously added to the regional aquifer throughout the simulation (until 2200), whereas in 70% of simulations the mass is exhausted before the end of the simulation period. As discussed in the total mass distribution development (Appendix C section C-2.3 and Appendix D section D-4.13), after all inventory above the regional aquifer is exhausted, RDX concentrations must necessarily decrease within the regional aquifer. At water-supply wells, results show mitigating RDX concentrations through natural attenuation and that the small flux of RDX that arrives in some predictive simulations begins to get smaller because inventory has been exhausted upgradient in 70% of simulations by the year 2200, which suggests that modeling further in the future will only reduce the plume footprint further.

As discussed and shown in Appendix C, plots of the RDX plume (see in particular Figures C-3.3-5 through C-3.3-7) indicate that the modeled rate of plume expansion is slow and that RDX concentrations gradually dilute as the plume expands in the regional aquifer. Based on the model results, there is effectively no probability that the RDX plume (concentrations at or above the NMED tap water screening level of 9.66 µg/L) will reach downgradient water-supply wells PM-2, PM-4, and PM-5 during the modeling period (Figure 5.1-1).

6.0   CONCLUSIONS AND RECOMMENDATIONS

This risk assessment report has been prepared to evaluate potential risks associated with exposure to RDX in groundwater and to determine the probability of RDX arrival and impacts on existing water-supply wells at some time in the future. A calibrated probabilistic fate and transport model (Appendix C), developed to support this risk assessment report, provides long-term predictions of the spatial extent and associated concentrations of RDX in the regional aquifer.

This report integrates applicable information from groundwater-related investigations and modeling and addresses potential groundwater-related risks by evaluation of the following assessment scenarios:

- Scenario 1: Evaluating risk to human health under current conditions, where land use control restricting potable groundwater wells is exercised by LANL within the facility's administrative boundary

- Scenario 2: Performing a screening-level groundwater risk assessment for RDX and all other detected constituents under present-day and potential future baseline conditions

- Scenario 3: Evaluating future plume expansion in the regional aquifer, as predicted by the fate and transport model, focusing on the probability that RDX will reach and impact existing water-supply wells

The principal conclusions of this risk assessment report with respect to the three assessment scenarios follow:

- Assessment Scenario 1 Conclusions: There is no present-day risk to human health from groundwater contamination, either within or outside of LANL administrative boundaries, for the following reasons:

    - ❖ No water-supply wells exist in the impacted perched-intermediate groundwater body. Therefore, there are no present-day exposures to RDX in perched-intermediate groundwater.

    - ❖ RDX in the regional aquifer is approximately 3 mi from nearest existing water-supply wells. Therefore, there are no present-day exposures to contaminants in the regional aquifer.

    - ❖ The extent of RDX in both perched-intermediate groundwater and the regional aquifer is currently within LANL administrative boundaries. Additionally, the downgradient extent of the perched-intermediate groundwater zone is well within these LANL boundaries, so near-term migration to locations outside of the LANL boundary is not considered feasible.

- Assessment Scenario 2 Conclusions: The screening-level assessment indicates that at six of the wells evaluated, potential risks exceed NMED's risk threshold, with RDX being the most significant contributor to these risks. Based on these results, concentrations of chemicals detected in perched-intermediate groundwater warrant institutional controls to eliminate the possibility of the use of contaminated groundwater for consumption now and in the foreseeable future.

- Assessment Scenario 3 Conclusions: The RRM indicates that by year 2200 the plume could expand downgradient and that there is a 42% probability that concentrations above 0.33 ppb (the approximate detection limit) could reach one of the three nearest water-supply wells. However, there is effectively no probability of RDX exceeding 2 ppb at any well, a groundwater concentration nearly 5 times lower than the New Mexico tap water screening level (9.66 µg/L).

The overall conclusions of this risk assessment are that there is no current, potential, or reasonably foreseeable future unacceptable risk to human health, either associated with RDX contamination in the regional aquifer or based on land use controls restricting potable groundwater wells, from drinking groundwater from the perched-intermediate groundwater. As stated in Section IX.C of the Consent Order, "If Contaminants are present at concentrations above screening levels, it does not necessarily indicate that cleanup is required, but it does indicate that additional risk evaluation is needed to determine the potential need for cleanup. Cleanup levels are the Contaminant concentrations that indicate when cleanup objectives are met. The need for cleanup is triggered by potential unacceptable risk and not by exceedance of screening levels." Consistent with Section IX.C of the Consent Order, the results of this risk assessment report constitute an input to determine the potential need for cleanup. Given the results of this risk assessment, EM-LA and Newport News Nuclear BWXT-Los Alamos, LLC (N3B) recommend continuation of long-term groundwater monitoring for the protection of human health and to monitor fate and transport of the plume compared with the modeling results. EM-LA and N3B will collaborate with NMED to determine the potential need for cleanup, which would be triggered by groundwater conditions that pose potential unacceptable risk to human health.

7.0   REFERENCES AND MAP DATA SOURCES

7.1   References

The following reference list includes documents cited in this report. Parenthetical information following each reference provides the author(s), publication date, and ERID, ESHID, or EMID. ERIDs were assigned by the Laboratory's Associate Directorate for Environmental Management (IDs through 599999); ESHIDs were assigned by the Laboratory's Associate Directorate for Environment, Safety, and Health (IDs 600000 through 699999); and EMIDs are assigned by N3B (IDs 700000 and above)

EPA (U.S. Environmental Protection Agency), September 2011. "Exposure Factors Handbook: 2011 Edition," EPA/600/R-09/052F, Office of Research and Development, Washington, D.C. (EPA 2011, 208374)

EPA (U.S. Environmental Protection Agency), October 2015. "ProUCL Version 5.1.002 Technical Guide," Statistical Software for Environmental Applications for Data Sets with and without Nondetect Observations, EPA/600/R-07/041, Office of Research and Development, Washington, D.C. (EPA 2015, 601724)

EPA (U.S. Environmental Protection Agency), June 2022. "ProUCL Version 5.2.0 User Guide," Statistical Software for Environmental Applications for Data Sets with and without Nondetect Observations, EPA/600/B-22/087, Office of Research and Development, Washington, D.C. (EPA 2022, 702275)

Gehan, E.A., June 1965. "A Generalized Wilcoxon Test for Comparing Arbitrarily Singly-Censored Samples," *Biometrika,* Vol. 52, No. 1 and 2, pp. 203–223. (Gehan 1965, 055611)

Gilbert, R.O., and J.C. Simpson, December 1992. "Statistical Methods for Evaluating the Attainment of Cleanup Standards, Volume 3: Reference-Based Standards for Soils and Solid Media," document prepared for the U.S. Environmental Protection Agency, Pacific Northwest Laboratory, Richland, Washington. (Gilbert and Simpson 1992, 054952)

Krambis, C., November 25, 2020. Draft Comments on the 5/29/2020 submittal to NMED concerning the RDX Risk Assessment and Fate and Transport Modelling Report. E-mail message to E. Day (N3B), P. McGuire (N3B), B. Robinson (N3B), C. Rodriguez (EM-LA), and A. Duran (EM-LA) from C. Krambis (NMED), Santa Fe, New Mexico. (Krambis 2020, 701140)

LANL (Los Alamos National Laboratory), May 9, 1994. "Process Flow Reductions from Waste Minimization for Value Engineering Study," Los Alamos National Laboratory, Los Alamos, New Mexico. (LANL 1994, 076858)

LANL (Los Alamos National Laboratory), September 2003. "Phase III RFI Report for Solid Waste Management Unit 16-021(c)-99," Los Alamos National Laboratory document LA-UR-03-5248, Los Alamos, New Mexico. (LANL 2003, 077965)

LANL (Los Alamos National Laboratory), September 2011. "Investigation Report for Water Canyon/ Cañon de Valle," Los Alamos National Laboratory document LA-UR-11-5478, Los Alamos, New Mexico. (LANL 2011, 207069)

LANL (Los Alamos National Laboratory), July 12, 2012. "Twenty-Five Year Site Plan, FY2013 - FY2037," Los Alamos National Laboratory document LA-UR-12-22913, Los Alamos, New Mexico. (LANL 2012, 601095)

LANL (Los Alamos National Laboratory), October 27, 2016. "Groundwater Background Investigation Report, Revision 5," Los Alamos National Laboratory document LA-UR-16-27907, Los Alamos, New Mexico. (LANL 2016, 601920)

LANL (Los Alamos National Laboratory), March 2018. "Compendium of Technical Reports Related to the Deep Groundwater Investigation for the RDX Project at Los Alamos National Laboratory," Los Alamos National Laboratory document LA-UR-18-21326, Los Alamos, New Mexico. (LANL 2018, 602963)

Maupin, C., March 1, 2021. RE: NMED Draft Comments on the Investigation Report for Royal Demolition Explosive in Deep Groundwater. E-mail message to C. Krambis (NMED) from C. Maupin (N3B), Los Alamos, New Mexico. (Maupin 2021, 701363)

N3B (Newport News Nuclear BWXT-Los Alamos, LLC), April 2019. "Supplemental Investigation Report for S-Site Aggregate Area, Revision 1," Newport News Nuclear BWXT-Los Alamos, LLC, document EM2019-0048, Los Alamos, New Mexico. (N3B 2019, 700414)

N3B (Newport News Nuclear BWXT-Los Alamos, LLC), August 2019. "Investigation Report for Royal Demolition Explosive in Deep Groundwater," Newport News Nuclear BWXT-Los Alamos, LLC, document EM2019-0235, Los Alamos, New Mexico. (N3B 2019, 700561)

N3B (Newport News Nuclear BWXT-Los Alamos, LLC), May 2020. "Fate and Transport Modeling and Risk Assessment Report for RDX Contamination in Deep Groundwater," Newport News Nuclear BWXT-Los Alamos, LLC, document EM2020-0135, Los Alamos, New Mexico. (N3B 2020, 700925)

NMED (New Mexico Environment Department), March 2017. "Risk Assessment Guidance for Site Investigations and Remediation, Volume 2, Soil Screening Guidance for Ecological Risk Assessments," Hazardous Waste Bureau and Ground Water Quality Bureau, Santa Fe, New Mexico. (NMED 2017, 602274)

NMED (New Mexico Environment Department), June 19, 2019. "Risk Assessment Guidance for Site Investigations and Remediation, Volume 1, Soil Screening Guidance for Human Health Risk Assessments," February 2019 (Revision 2, 6/19/19), Hazardous Waste Bureau and Ground Water Quality Bureau, Santa Fe, New Mexico. (NMED 2019, 700550)

Travis, C.C., and A.D. Arms, 1988. "Bioconcentration of Organics in Beef, Milk, and Vegetation," *Environmental Science & Technology,* Vol. 22, No. 3, pp. 271-274. (Travis and Arms 1988, 059108)

7.2   Map Data Sources

Monitoring well and spring point features; Former LANL ER-DB Database pull; 02 February 2004; As published 02 February 2004.

Infiltration area outline; Los Alamos National Laboratory, ER-ES, As published, project folder 11-0015; \\172.30.0.10\n3b-shares\GIS Data and Projects\11-Projects\11-0057\gdb\gdb_11-057.mdb\infiltration_lines_buffer; 2012.

SWMU or AOC; Los Alamos National Laboratory, Site Planning & Project Initiation Group, Infrastructure Planning Office; September 2007; As published 13 August 2010.

Structures; Los Alamos National Laboratory, KSL Site Support Services, Planning, Locating and Mapping Section; 06 January 2004; As published 29 November 2010.

Contours, 100, 20-ft interval; Los Alamos National Laboratory, Site Planning & Project Initiation Group, Infrastructure Planning Office; September 2007; As published 13 August 2010.

Paved Road; Los Alamos National Laboratory, FWO Site Support Services, Planning, Locating and Mapping Section; 06 January 2004; As published 29 November 2010.

Unpaved Road; Los Alamos National Laboratory, ER-ES, As published, GIS projects folder; \\slip\GIS\Projects\14-Projects\14-0062\project_data.gdb; digitized_site_features; digitized_road; 2017.

Drainage Channel; Los Alamos National Laboratory, ER-ES, As published, GIS projects folder; \\slip\GIS\Projects\11-Projects\11-0108\\gdb\gdb_11-0108_generic.mdb; drainage; 2017.

Watersheds; Los Alamos National Laboratory, ENV Environmental Remediation and Surveillance Program; EP2006-0942; 1:2,500 Scale Data; 27 October 2006
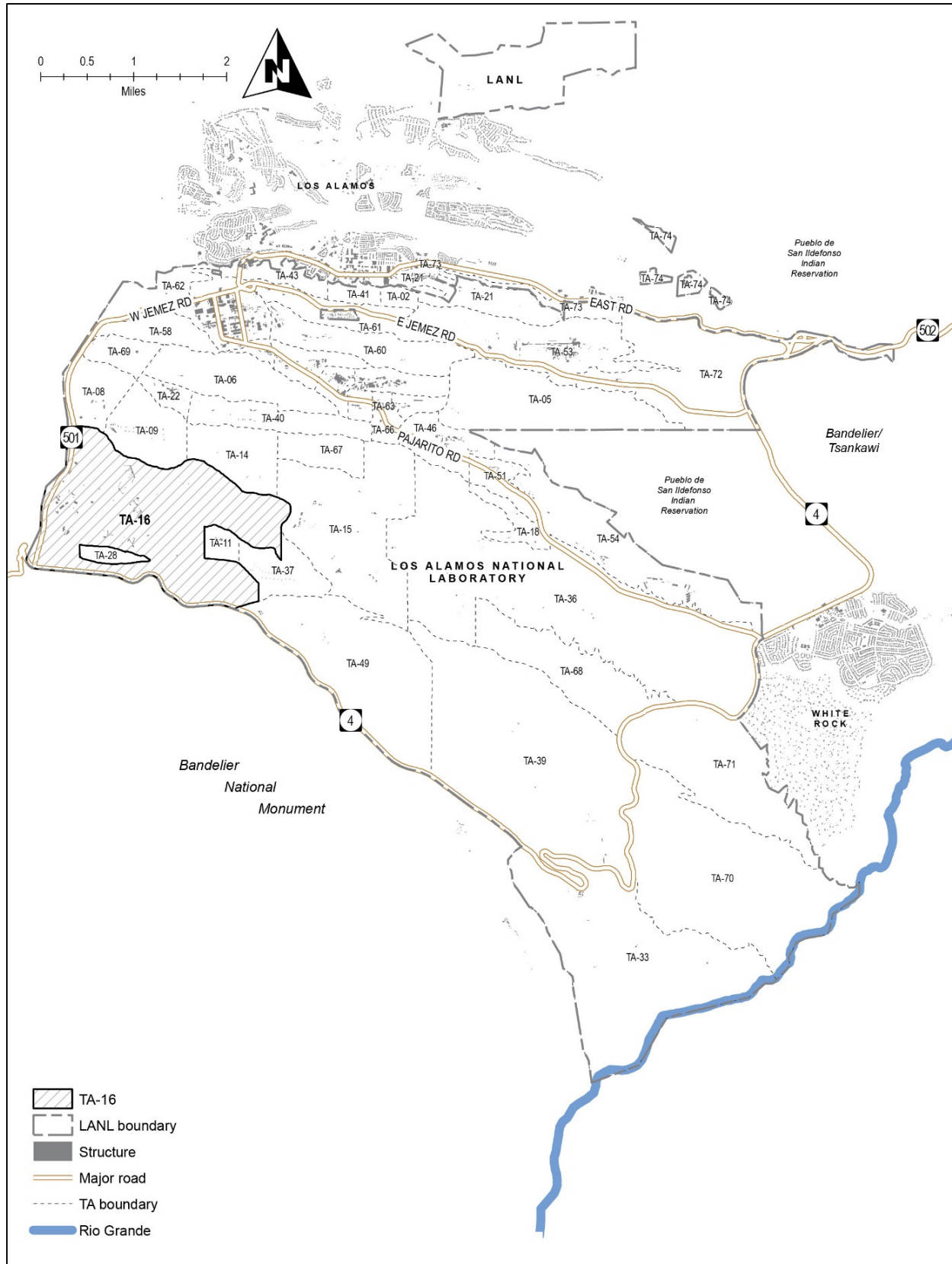
Figure 2.1-1   Location of TA-16 within the LANL boundary
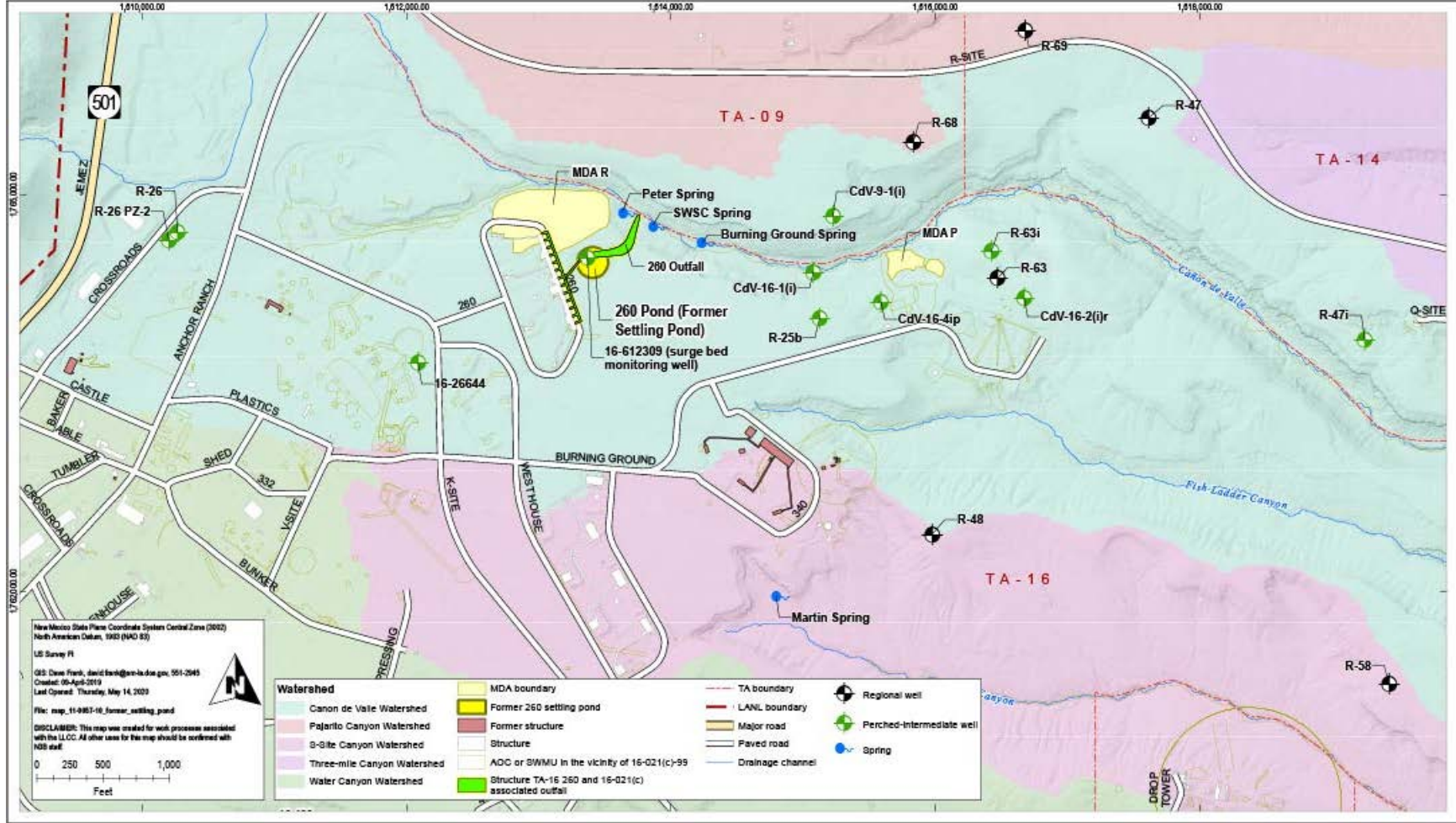
Figure 2.1-2   TA-16 site map
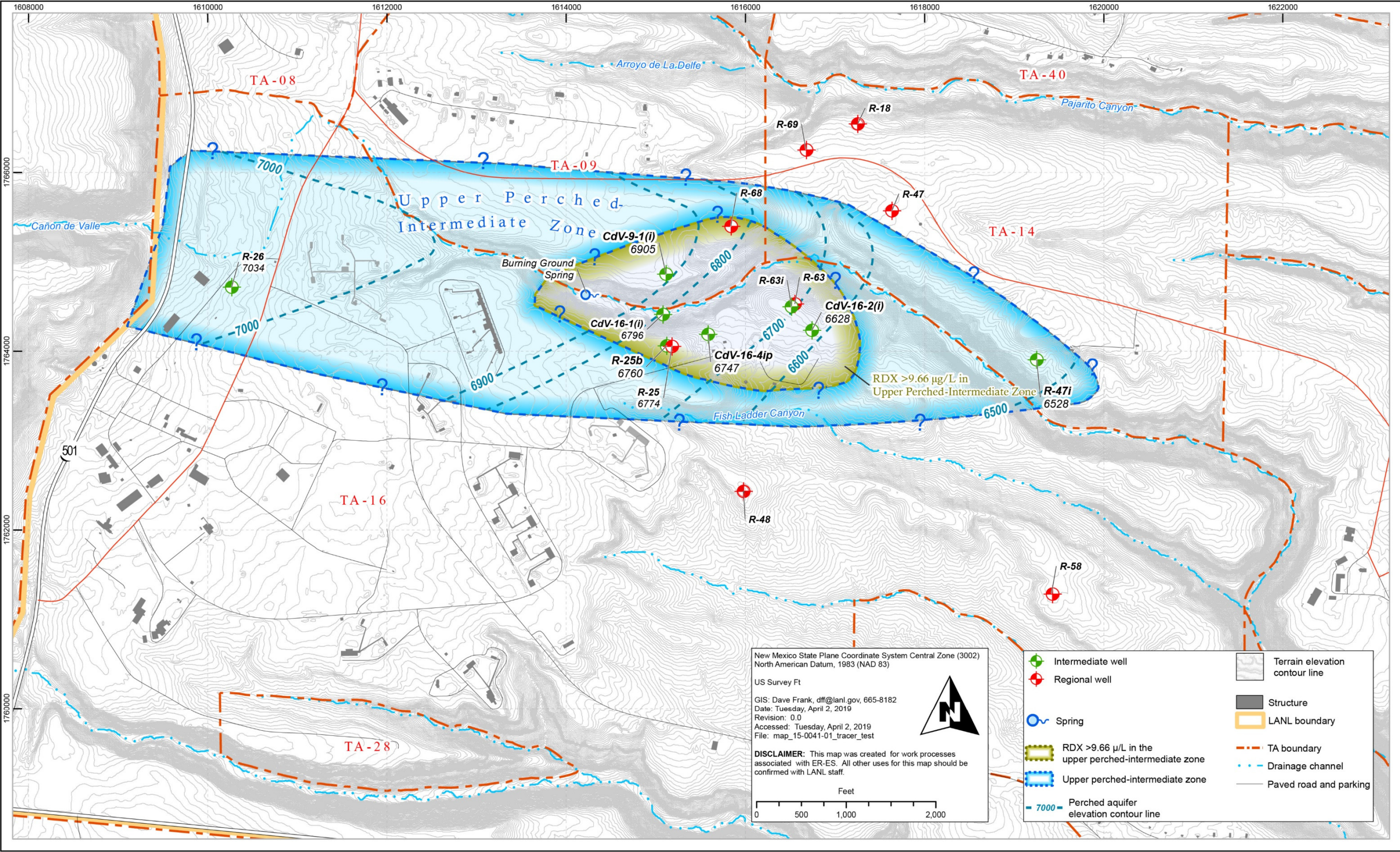
Figure 2.3-1   Spatial extent of the upper perched-intermediate groundwater zone and associated RDX concentrations above the NMED tap water screening criterion
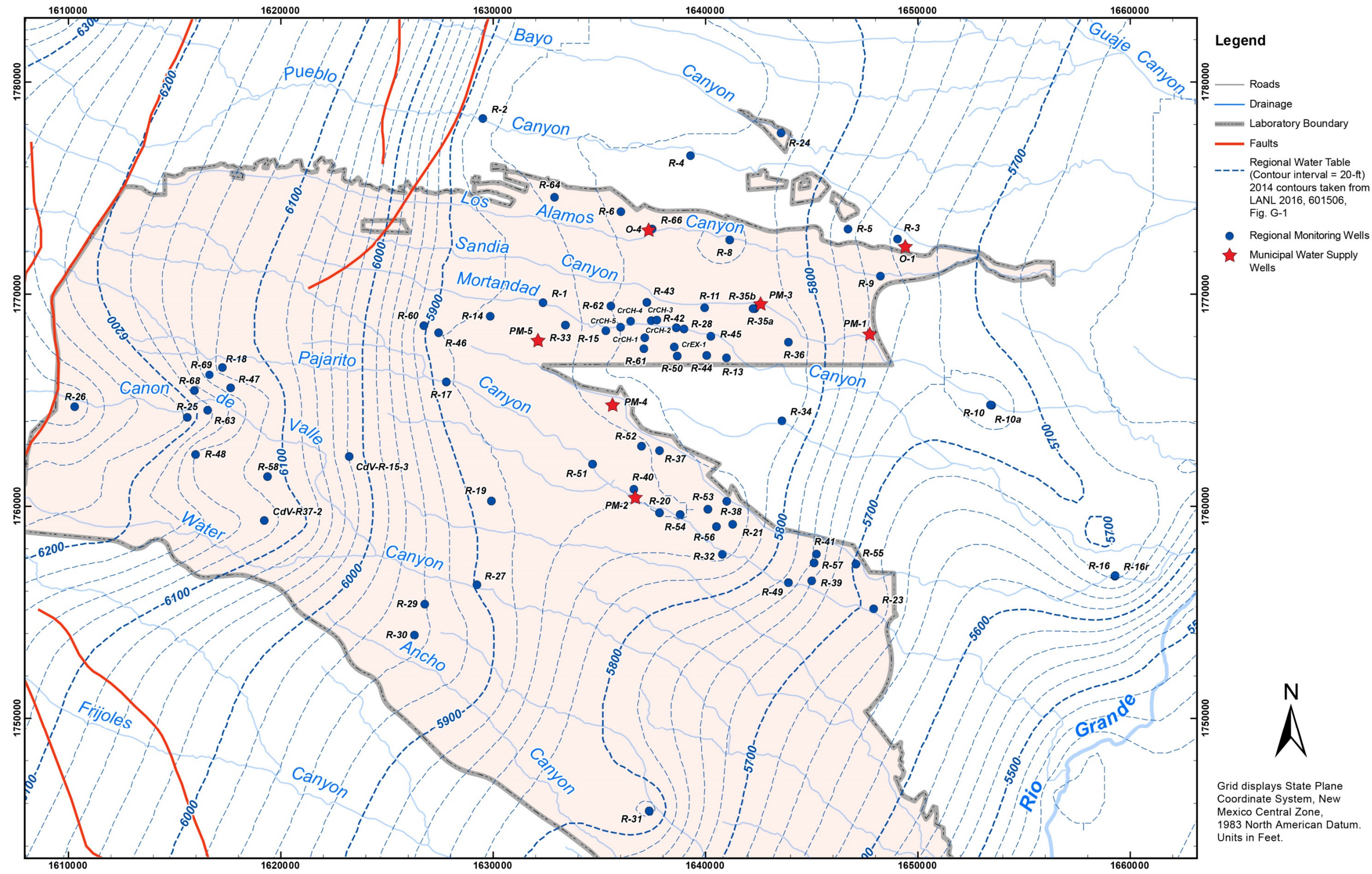
Figure 2.3-2   Location of LANL administrative boundary and municipal supply wells in the regional aquifer relative to TA-16 monitoring wells
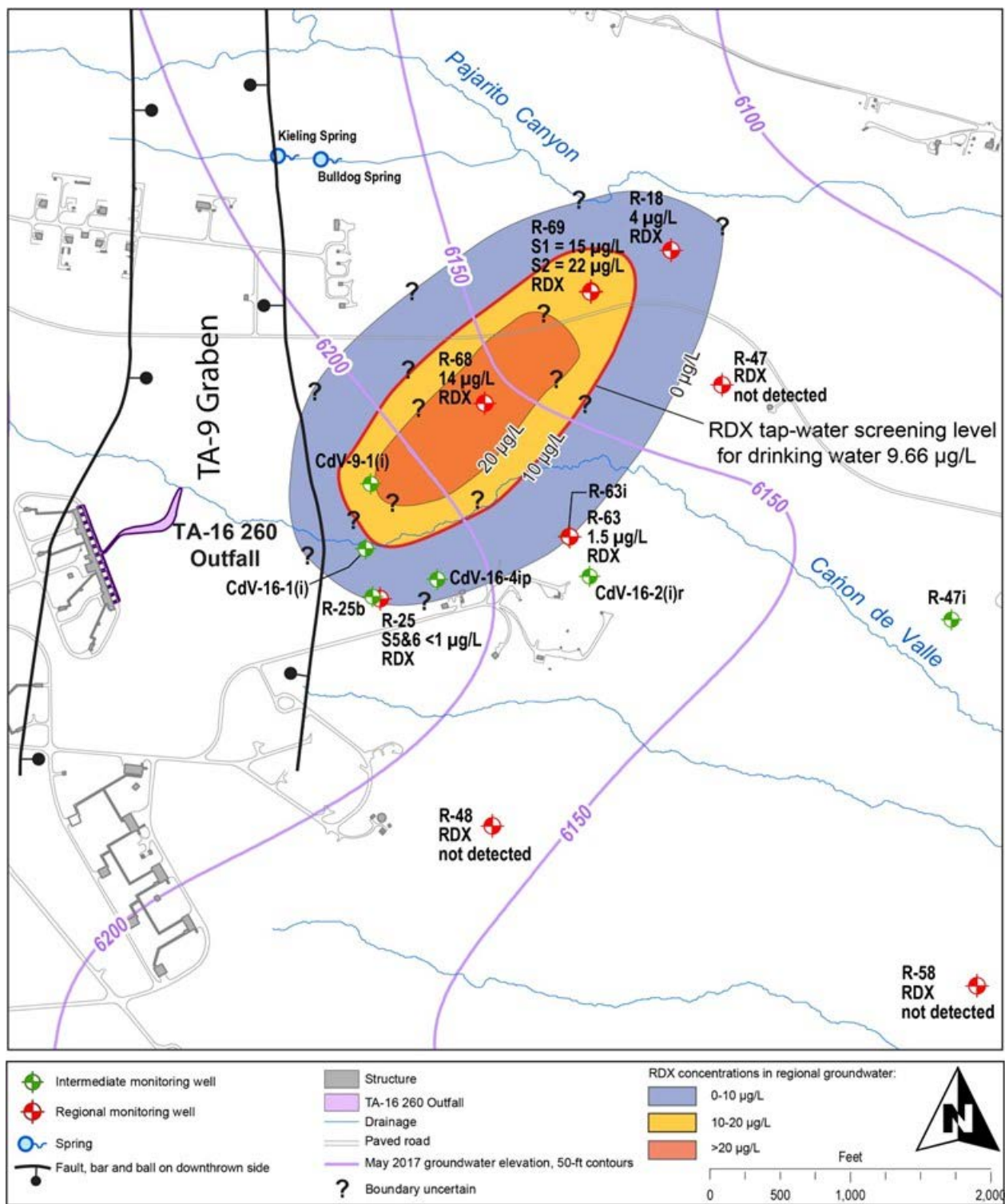
Figure 2.3-3   Approximate extent of RDX in the regional aquifer
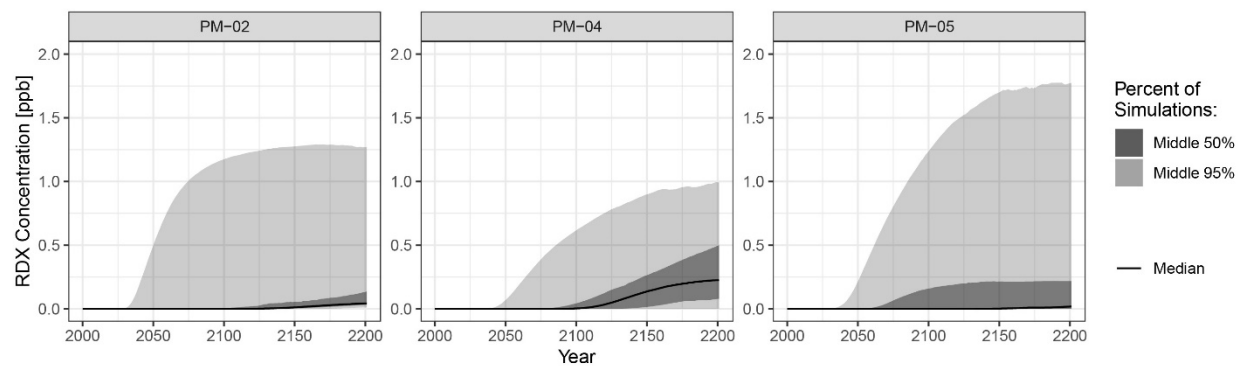
Notes: The black line represents the median predicted concentration of RDX. The dark shading shows the most likely 50% of runs, and the light grey shading shows 95% of runs.

Figure 5.1-1   Predictive summary of results at county supply wells nearest to the RDX plume

Table 4.1-1
Initial List of Perched-Intermediate Wells Considered for the Risk Assessment

Location ID	Northing	Easting	Hydrostratigraphic Unit	Geologic Unit	Top of Screen (ft bgs)	Bottom of Screen (ft bgs)	Number of Water Level Data Points Available	Used In DGIR	Used In Vadose Zone Model
16-26644	1763721.08	1612085.66	Intermediate Perched	Qbt 3	129.0	144.0	7507	Yes	No
CdV-16-1(i)	1764415.20	1615078.20	Intermediate Perched	Qbo	624.0	634.0	9106	Yes	Yes
CdV-16-2(i)r	1764219.40	1616673.24	Intermediate Perched	Tpf	850.0	859.7	8556	Yes	Yes
CdV-16-4ip S1*	1764195.74	1615587.07	Intermediate Perched	Tpf	815.6	879.2	6374	Yes	Yes
CdV-16-4ip S2	1764195.74	1615587.07	Intermediate	Tpf	1110.0	1141.1	1	Yes	No
CdV-37-1(i)	1757798.61	1624592.30	Intermediate Perched	Tpf	632.0	652.5	8411	Yes	No
CdV-9-1(i) S1	1764875.09	1615113.20	Intermediate Perched	Tpf	937.4	992.4	5446	Yes	Yes
R-25 S1	1764060.50	1615178.42	Intermediate	Qbo	737.6	758.4	10,129	Yes	Yes
R-25 S2	1764060.50	1615178.42	Intermediate	Tpf	882.6	893.4	10,127	Yes	Yes
R-25 S3	1764060.50	1615178.42	Intermediate	Tpf	1054.6	1064.6	8893	Yes	Yes
R-25 S4	1764060.50	1615178.42	Intermediate	Tpf	1184.6	1194.6	10,137	Yes	Yes
R-25b	1764074.70	1615125.60	Intermediate Perched	Qbo	750.0	770.8	8795	Yes	Yes
R-26 PZ-2	1764660.61	1610201.96	Intermediate	Qbt3	150.0	180.0	8531	Yes	Yes
R-26 S1	1764721.12	1610267.23	Intermediate Perched	Qct	651.8	669.9	8826	Yes	Yes
R-27(i)	1756302.42	1629129.03	Intermediate	Tpf	619.0	629.0	7422	Yes	No
R-47(i)	1763907.91	1619250.01	Intermediate Perched	Tpf	840.0	860.6	7543	Yes	Yes
R-63(i)	1764507.14	1616520.27	Intermediate Perched	Tpf	1122.5	1189.0	7166	Yes	Yes
CdV-R-37-2 S1	1759327.28	1619218.96	Intermediate	Tpf	914.4	939.5	363	No	No
R-19 S1	1760252.10	1629918.40	Intermediate Perched	Qbog	827.2	843.6	841	No	No
R-19 S2	1760252.10	1629918.40	Intermediate Perched	Tp	893.3	909.6	6698	No	No
R-25c	1764083.07	1615073.72	Intermediate Perched	Tpf	1039.6	1060.0	16	No	No
MSC-16-02665	1762530.55	1614427.59	Intermediate Perched	Qbt 3	93.5	123.5	0	No	No
PCI-2	1765872.63	1627648.27	Intermediate Perched	Tpf	512.0	522.0	10,757	No	No

* S = Screen.

Table 4.1-2
Final List of Perched-Intermediate Wells Used in the Risk Assessment

Well Name	Site Well or Background Well[a]	Screen Depth (ft)
CdV-16-1(i)	Site	624–634
CdV-16-2(i)r	Site	850–860
CdV-16-4ip (S1 + S2)[b]	Site	816–880; 1110–1141
CdV-37-1(i)	Site	632–653
CdV-9-1(i) (S1)	Site	937–992
PCI-2	Background	512–522
R-19 (S2)[c]	Site	893–910
R-25 (S3 and S4)[d]	Site	1055–1065; 1185–1195
R-25b	Site	750–771
R-26 S1	Background	652–670
R-27(i)	Background	619–629
R-47(i)	Background	840–861
R-63(i)	Site	1123–1189

[a] Background wells are identified in "Groundwater Background Investigation Report, Rev. 5" (LANL 2016, 601920).

[b] S = Screen.

[c] No usable data were identified in the first well screened interval.

[d] Damage to well screens 1 and 2 compromised more recent data; see section 4.1.

Table 4.2-1
Analytical Data Summary for Site and Background Wells

Parameter Name	Parameter Code	Well	Analytical Method	Analytical Method Category[a]	Geological Unit Code[a]	No. Samples	No. Detects	Unit	Mean Detect	Median Detect	Min Detect	Max Detect	Mean ND[b]	Median ND	Min ND	Max ND
1,5-naphthalenedisulfonic acid	1655-29-4	CdV-16-1(i)	SW-846:8330	HEXP[c]	Qbo	1	1	µg/L	20,714	20,714	20,714	20,714	—[d]	—	—	—
Acenaphthene	83-32-9	CdV-16-1(i)	SW-846:8270C, SW-846:8270D, SW-846:8270DGCMS_SIM, SW-846:8310	SVOC[e]	Qbo	9	0	µg/L	—	—	—	—	0.70133333	0.962	0.104	1.11
Acenaphthylene	208-96-8	CdV-16-1(i)	SW-846:8270C, SW-846:8270D, SW-846:8270DGCMS_SIM, SW-846:8310	SVOC	Qbo	9	0	µg/L	—	—	—	—	0.70133333	0.962	0.104	1.11
Acetone	67-64-1	CdV-16-1(i)	SW-846:8260B	VOC[f]	Qbo	23	1	µg/L	1.84	1.84	1.84	1.84	9.64090909	10	1.5	63.5
Acidity or alkalinity of a solution	pH	CdV-16-1(i)	EPA:150.1	General Chemistry	Qbo	25	25	SU	7.2576	7.13	6.96	8.4	—	—	—	—
Alkalinity-CO3	ALK-CO3	CdV-16-1(i)	EPA:310.1	General Chemistry	Qbo	26	0	µg/L	—	—	—	—	1431.73077	1000	725	4000
Alkalinity-CO3+HCO3	ALK-CO3+HCO3	CdV-16-1(i)	EPA:310.1	General Chemistry	Qbo	28	28	µg/L	61,967.107	59,100	54,700	79,579	—	—	—	—
Alkalinity-HCO3	ALK-HCO3	CdV-16-1(i)	EPA:310.1	General Chemistry	Qbo	1	1	µg/L	54,600	54,600	54,600	54,600	—	—	—	—
Aluminum	Al	CdV-16-1(i)	EPA:200.7, SW-846:6010B, SW 846:6010C	Inorganic	Qbo	41	1	µg/L	69	69	69	69	139.03	200	1	200
Amino-2,6-dinitrotoluene[4-]	19406-51-0	CdV-16-1(i)	SW-846:8321A_MOD, SW-846:8330B, SW-846:8321A(M)	LCMS/MS[g] High Explosives, LCMS/MS Perchlorate	Qbo	30	29	µg/L	0.1891379	0.184	0.134	0.292	0.325	0.325	0.325	0.325
Amino-4,6-dinitrotoluene[2-]	35572-78-2	CdV-16-1(i)	SW-846:8321A_MOD, SW_846:8330B, SW-846:8321A(M)	LCMS/MS High Explosives, LCMS/MS Perchlorate	Qbo	29	19	µg/L	0.1215737	0.114	0.0841	0.193	0.18051	0.17145	0.0816	0.325
Ammonia as nitrogen	NH3-N	CdV-16-1(i)	EPA:350.1	General Chemistry	Qbo	25	10	µg/L	95.02	35.15	24.8	353	44.1933333	44	10	150
Anthracene	120-12-7	CdV-16-1(i)	SW-846:8270C, SW-846:8270D, SW-846:8270DGCMS_SIM, SW-846:8310	SVOC	Qbo	9	0	µg/L	—	—	—	—	0.70133333	0.962	0.104	1.11
Antimony	Sb	CdV-16-1(i)	EPA:200.8, SW-846:6020	Inorganic	Qbo	41	0	µg/L	—	—	—	—	1.90243902	2	0.5	3
Arsenic	As	CdV-16-1(i)	EPA:200.8, SW-846:6010B, SW-846:6020	Inorganic	Qbo	41	6	µg/L	2.118845	2.32	0.3431	3.02	4.77142857	5	1.5	6
Barium	Ba	CdV-16-1(i)	EPA:200.7, SW-846:6010B, SW-846:6010C	Inorganic	Qbo	41	41	µg/L	16.558317	16.5	14.7	17.9	—	—	—	—
Benzo(g,h,i)perylene	191-24-2	CdV-16-1(i)	SW-846:8270C, SW-846:8270D, SW-846:8270DGCMS_SIM, SW-846:8310	SVOC	Qbo	8	0	µg/L	—	—	—	—	0.611375	0.653	0.051	1.11
Benzoic acid	65-85-0	CdV-16-1(i)	SW-846:8270C, SW-846:8270D	SVOC	Qbo	8	0	µg/L	—	—	—	—	16.44	20.45	6.12	22.2
Beryllium	Be	CdV-16-1(i)	EPA:200.8, SW-846:6010B, SW-846:6010C, SW-846:6020	Inorganic	Qbo	41	5	µg/L	0.168	0.17	0.15	0.2	3.64166667	5	0.1	5
Bis(2-ethylhexyl)phthalate	117-81-7	CdV-16-1(i)	SW-846:8270C, SW-846:8270D	SVOC	Qbo	9	2	µg/L	3.695	3.695	3	4.39	8.65428571	10.3	3.06	11.1
Boron	B	CdV-16-1(i)	EPA:200.7, SW-846:6010B, SW-846:6010C	Inorganic	Qbo	41	41	µg/L	60.754171	60.7	29.521	78.9	—	—	—	—
Bromide	Br(-1)	CdV-16-1(i)	EPA:300.0	General Chemistry	Qbo	29	20	µg/L	86.8045	86.1	44.987	117	152.666667	200	41	200
Bromodichloromethane	75-27-4	CdV-16-1(i)	SW-846:8260B	VOC	Qbo	23	0	µg/L	—	—	—	—	0.87826087	1	0.3	1
Bromoform	75-25-2	CdV-16-1(i)	SW-846:8260B	VOC	Qbo	23	0	µg/L	—	—	—	—	0.87826087	1	0.3	1
Butanone[2-]	78-93-3	CdV-16-1(i)	SW-846:8260B	VOC	Qbo	23	1	µg/L	11.6	11.6	11.6	11.6	4.36363636	5	1.5	5
Cadmium	Cd	CdV-16-1(i)	EPA:200.8, SW-846:6020	Inorganic	Qbo	41	0	µg/L	—	—	—	—	0.66878049	1	0.1	1
Calcium	Ca	CdV-16-1(i)	EPA:200.7, SW-846:6010B, SW-846:6010C	Inorganic	Qbo	41	41	µg/L	13,251.171	13,200	11,300	14,700	—	—	—	—

Table 4.2-1 (continued)

Parameter Name	Parameter Code	Well	Analytical Method	Analytical Method Category[a]	Geological Unit Code[a]	No. Samples	No. Detects	Unit	Mean Detect	Median Detect	Min Detect	Max Detect	Mean ND	Median ND	Min ND	Max ND
Carbon disulfide	75-15-0	CdV-16-1(i)	SW-846:8260B	VOC	Qbo	23	0	µg/L	—	—	—	—	4.39130435	5	1.5	5
Chloride	Cl(-1)	CdV-16-1(i)	EPA:300.0	General Chemistry	Qbo	28	28	µg/L	7936.7143	7335	5780	22378	—	—	—	—
Chlorobenzene	108-90-7	CdV-16-1(i)	SW-846:8260B	VOC	Qbo	23	0	µg/L	—	—	—	—	0.87826087	1	0.3	1
Chlorodibromomethane	124-48-1	CdV-16-1(i)	SW-846:8260B	VOC	Qbo	23	0	µg/L	—	—	—	—	0.87826087	1	0.3	1
Chloroform	67-66-3	CdV-16-1(i)	SW-846:8260B	VOC	Qbo	23	0	µg/L	—	—	—	—	0.87826087	1	0.3	1
Chloromethane	74-87-3	CdV-16-1(i)	SW-846:8260B	VOC	Qbo	23	0	µg/L	—	—	—	—	0.87826087	1	0.3	1
Chromium	Cr	CdV-16-1(i)	EPA:200.8, SW-846:6010B, SW-846:6020	Inorganic	Qbo	41	11	µg/L	2.6472727	2.5	1.2	4.48	6.00833333	6.5	1	10
Cobalt	Co	CdV-16-1(i)	EPA:200.8, SW-846:6010B, SW-846:6010C	Inorganic	Qbo	41	1	µg/L	1.13	1.13	1.13	1.13	3.3	5	1	5
Copper	Cu	CdV-16-1(i)	EPA:200.8, SW-846:6010B, SW-846:6010C	Inorganic	Qbo	41	39	µg/L	13.177513	10.8	3.7	63.2	6.28	6.28	3	9.56
Cyanide (total)	CN (Total)	CdV-16-1(i)	EPA:335.3, EPA:335.4	Inorganic	Qbo	16	0	µg/L	—	—	—	—	3.94875	5	1.5	5
DNX[h]	DNX	CdV-16-1(i)	SW-846:8321A_MOD, SW-846:8330B, SW-846:8330RDX	LCMS/MS High Explosives	Qbo	21	19	µg/L	0.1786316	0.148	0.106	0.452	0.5	0.5	0.5	0.5
Fluoranthene	206-44-0	CdV-16-1(i)	SW-846:8270C, SW-846:8270D, SW-846:8270DGCMS_SIM, SW-846:8310	SVOC	Qbo	9	0	µg/L	—	—	—	—	0.65033333	0.962	0.051	1.11
Fluoride	F(-1)	CdV-16-1(i)	EPA:300.0	General Chemistry	Qbo	28	23	µg/L	116.63957	105	42.8	402.51	59.2	33	30	100
Gross alpha	GrossA	CdV-16-1(i)	EPA:900	RAD[j]	Qbo	7	2	pCi/L	2.765	2.765	1.38	4.15	1.1584	1.06	-1.27	2.67
Gross beta	GrossB	CdV-16-1(i)	EPA:900	RAD	Qbo	7	5	pCi/L	3.158	3.32	2.47	3.63	1.905	1.905	1.34	2.47
Gross gamma	GrossG	CdV-16-1(i)	EPA:901.1	RAD	Qbo	3	0	pCi/L	—	—	—	—	48.81	58.1	0.73	87.6
Hardness	Hardness	CdV-16-1(i)	SM:A2340B	Inorganic	Qbo	34	34	µg/L	55,785.294	55,800	46,800	62,400	—	—	—	—
Heptachlor	76-44-8	CdV-16-1(i)	SW-846:8081A	PESTPCB[j]	Qbo	2	1	µg/L	0.0165	0.0165	0.0165	0.0165	0.022	0.022	0.022	0.022
Hexachlorobutadiene	87-68-3	CdV-16-1(i)	SW-846:8260B	VOC	Qbo	20	0	µg/L	—	—	—	—	0.86	1	0.3	1
HMX[k]	2691-41-0	CdV-16-1(i)	SW-846:8321A_MOD, SW-846:8330B, SW-846:8321A(M)	LCMS/MS High Explosives, LCMS/MS Perchlorate	Qbo	30	30	µg/L	1.7153333	1.66	1.21	2.53	—	—	—	—
Iron	Fe	CdV-16-1(i)	EPA:200.7, SW-846:6010B, SW-846:6010C	Inorganic	Qbo	41	11	µg/L	364.82727	48.6	29.4	2750	75.46	100	10	100
Lead	Pb	CdV-16-1(i)	EPA:200.8, SW-846:6020	Inorganic	Qbo	41	5	µg/L	3.038414	0.72	0.2591	12.7	1.45833333	2	0.5	2
Lithium	Li	CdV-16-1(i)	EPA:200.7	Inorganic	Qbo	1	1	µg/L	5.8417	5.8417	5.8417	5.8417	—	—	—	—
Magnesium	Mg	CdV-16-1(i)	EPA:200.7, SW-846:6010B, SW-846:6010C	Inorganic	Qbo	41	41	µg/L	5534.2049	5560	4500	6210	—	—	—	—
Manganese	Mn	CdV-16-1(i)	EPA:200.7, SW-846:6010B, SW-846:6010C, SW-846:6020	Inorganic	Qbo	41	29	µg/L	5.0124207	3.8	2.2	13.6	6	6	2	10
Mercury	Hg	CdV-16-1(i)	EPA:200.8, EPA:245.2, SW-846:7470A	Inorganic	Qbo	52	1	µg/L	0.071	0.071	0.071	0.071	0.14572549	0.2	0.03	0.2
Methyl tert-butyl ether	1634-04-4	CdV-16-1(i)	SW-846:8260B	VOC	Qbo	18	16	µg/L	1.202875	1.16	0.966	1.48	1.195	1.195	1	1.39
Methyl-2-pentanone[4-]	108-10-1	CdV-16-1(i)	SW-846:8260B	VOC	Qbo	23	0	µg/L	—	—	—	—	4.39130435	5	1.5	5
Methylene chloride	75-09-2	CdV-16-1(i)	SW-846:8260B	VOC	Qbo	23	0	µg/L	—	—	—	—	6.83478261	10	1	10
MNX[l]	MNX	CdV-16-1(i)	SW-846:8321A_MOD, SW-846:8330B, SW-846:8330RDX	LCMS/MS High Explosives	Qbo	21	19	µg/L	0.2971579	0.3	0.141	0.391	0.5	0.5	0.5	0.5
Molybdenum	Mo	CdV-16-1(i)	EPA:200.8, SW-846:6010B, SW-846:6020	Inorganic	Qbo	41	31	µg/L	1.5570645	1.1	0.535	3.6	1.5186	1.065	0.631	3.3
Nickel	Ni	CdV-16-1(i)	EPA:200.8, SW-846:6010B, SW-846:6020	Inorganic	Qbo	41	41	µg/L	4.9947976	4.45	1.69	13.2	—	—	—	—
Nitrate	NO3	CdV-16-1(i)	EPA:300.0	General Chemistry	Qbo	1	1	µg/L	3927.1	3927.1	3927.1	3927.1	—	—	—	—

Table 4.2-1 (continued)

Parameter Name	Parameter Code	Well	Analytical Method	Analytical Method Category[a]	Geological Unit Code[a]	No. Samples	No. Detects	Unit	Mean Detect	Median Detect	Min Detect	Max Detect	Mean ND	Median ND	Min ND	Max ND
Nitrate-nitrite as nitrogen	NO3+NO2-N	CdV-16-1(i)	EPA:353.1, EPA:353.2	General Chemistry	Qbo	27	27	µg/L	844.7037	880	510	1090	—	—	—	—
Nitrotoluene[2-]	88-72-2	CdV-16-1(i)	SW-846:8321A_MOD, SW-846:8330B, SW-846:8321A(M)	LCMS/MS High Explosives, LCMS/MS Perchlorate	Qbo	29	0	µg/L	—	—	—	—	0.24397241	0.272	0.0837	0.325
Oxygen-18/oxygen-16 ratio from nitrate	O18O16-NO3	CdV-16-1(i)	Generic:Oxygen Isotope Ratio	General Chemistry	Qbo	1	1	permil	-0.28189	-0.2819	-0.2819	-0.2819	—	—	—	—
Perchlorate	ClO4	CdV-16-1(i)	SW-846:6850, SW846 6850 Modified	LCMS/MS Perchlorate	Qbo	27	27	µg/L	0.5188519	0.521	0.461	0.577	—	—	—	—
Perfluorooctanoic acid	335-67-1	CdV-16-1(i)	EPA:537M	LCMS/MS PFAS[m]	Qbo	1	1	µg/L	0.00115	0.0012	0.0012	0.0012	—	—	—	—
Phenanthrene	85-01-8	CdV-16-1(i)	SW-846:8270C, SW-846:8270D, SW-846:8270DGCMS_SIM, SW-846:8310	SVOC	Qbo	9	0	µg/L	—	—	—	—	0.70133333	0.962	0.104	1.11
Potassium	K	CdV-16-1(i)	EPA:200.7, SW-846:6010B, SW-846:6010C	Inorganic	Qbo	41	41	µg/L	2387.6098	2400	1722	2700	—	—	—	—
Pyrene	129-00-0	CdV-16-1(i)	SW-846:8270C, SW-846:8270D, SW-846:8270DGCMS_SIM, SW-846:8310	SVOC	Qbo	9	0	µg/L	—	—	—	—	0.65033333	0.962	0.051	1.11
Radium-226	Ra-226	CdV-16-1(i)	EPA:903.1	RAD	Qbo	2	0	pCi/L	—	—	—	—	0.304	0.304	0.255	0.353
Radium-228	Ra-228	CdV-16-1(i)	EPA:904	RAD	Qbo	2	0	pCi/L	—	—	—	—	0.314	0.314	0.251	0.377
RDX	121-82-4	CdV-16-1(i)	SW-846:8330, SW-846:8321A_MOD, SW-846:8330B, SW-846:8321A(M)	HEXP, LCMS/MS High Explosives, LCMS/MS Perchlorate	Qbo	31	31	µg/L	28.570968	28.1	22.2	37.4	—	—	—	—
Selenium	Se	CdV-16-1(i)	EPA:200.8, SW-846:6010B, SW-846:6020	Inorganic	Qbo	41	0	µg/L	—	—	—	—	4.31707317	5	1	6
Silicon dioxide	SiO2	CdV-16-1(i)	EPA:200.7, SW-846:6010B, SW-846:6010C	Inorganic	Qbo	31	31	µg/L	58,063	57,600	52,800	63,200	—	—	—	—
Silver	Ag	CdV-16-1(i)	EPA:200.8, SW-846:6010B, SW-846:6020	Inorganic	Qbo	41	0	µg/L	—	—	—	—	0.81463415	1	0.2	1
Sodium	Na	CdV-16-1(i)	EPA:200.7, SW-846:6010B, SW-846:6010C	Inorganic	Qbo	41	41	µg/L	12353.463	12000	10300	23600	—	—	—	—
Strontium	Sr	CdV-16-1(i)	EPA:200.7, SW-846:6010B, SW-846:6010C	Inorganic	Qbo	41	41	µg/L	94.587244	94.5	76.1	110	—	—	—	—
Styrene	100-42-5	CdV-16-1(i)	SW-846:8260B	VOC	Qbo	23	0	µg/L	—	—	—	—	0.87826087	1	0.3	1
Sulfate	SO4(-2)	CdV-16-1(i)	EPA:300.0	General Chemistry	Qbo	28	28	µg/L	9839.5357	9635	8670	12,500	—	—	—	—
Temperature	TEMP	CdV-16-1(i)	EPA:170.0	VOC	Qbo	13	13	deg C	2.9230769	3	1	4	—	—	—	—
Tetrachloroethene	127-18-4	CdV-16-1(i)	SW-846:8260B	VOC	Qbo	23	21	µg/L	1.0935238	1.11	0.79	1.49	1.245	1.245	1	1.49
Thallium	Tl	CdV-16-1(i)	EPA:200.8, SW-846:6020	Inorganic	Qbo	41	6	µg/L	0.5341667	0.4875	0.41	0.74	1.23868571	1	0.3	2
Tin	Sn	CdV-16-1(i)	EPA:200.8, SW-846:6010B, SW-846:6010C	Inorganic	Qbo	35	1	µg/L	10	10	10	10	12.5294118	10	1	100
TNX[n]	TNX	CdV-16-1(i)	SW-846:8321A_MOD, SW-846:8330B, SW-846:8330RDX	LCMS/MS High Explosives	Qbo	21	19	µg/L	0.2303158	0.226	0.163	0.362	0.5	0.5	0.5	0.5
Toluene	108-88-3	CdV-16-1(i)	SW-846:8260B	VOC	Qbo	23	9	µg/L	17.166444	3.04	0.268	119	0.8	1	0.3	1
Total dissolved solids	TDS	CdV-16-1(i)	EPA:160.1	General Chemistry	Qbo	24	24	µg/L	151845.83	148,500	94,300	194,000	—	—	—	—
Total Kjeldahl nitrogen	TKN	CdV-16-1(i)	EPA:351.2	General Chemistry	Qbo	23	9	µg/L	197.34444	138	36	520	76.0357143	100	10	100
Total organic carbon	TOC	CdV-16-1(i)	SW-846:9060	General Chemistry	Qbo	23	22	µg/L	1897.3636	1050	639	16,900	1040	1040	1040	1040
Total phosphate as phosphorus	PO4-P	CdV-16-1(i)	EPA:365.4	General Chemistry	Qbo	27	14	µg/L	50.1	42.7	22.8	107	56.6769231	52	24	88.4
Trichlorobenzene[1,2,3-]	87-61-6	CdV-16-1(i)	SW-846:8260B	VOC	Qbo	20	0	µg/L	—	—	—	—	0.86	1	0.3	1
Trichloroethene	79-01-6	CdV-16-1(i)	SW-846:8260B	VOC	Qbo	23	0	µg/L	—	—	—	—	0.87826087	1	0.3	1

Table 4.2-1 (continued)

Parameter Name	Parameter Code	Well	Analytical Method	Analytical Method Category[a]	Geological Unit Code[a]	No. Samples	No. Detects	Unit	Mean Detect	Median Detect	Min Detect	Max Detect	Mean ND	Median ND	Min ND	Max ND
Trinitrobenzene[1,3,5-]	99-35-4	CdV-16-1(i)	SW-846:8321A_MOD, SW-846:8330B, SW-846:8321A(M)	LCMS/MS High Explosives, LCMS/MS Perchlorate	Qbo	29	0	µg/L	—	—	—	—	0.24345517	0.272	0.0816	0.325
Trinitrotoluene[2,4,6-]	118-96-7	CdV-16-1(i)	SW-846:8321A_MOD, SW-846:8330B, SW-846:8321A(M)	LCMS/MS High Explosives, LCMS/MS Perchlorate	Qbo	29	0	µg/L	—	—	—	—	0.24345517	0.272	0.0816	0.325
Tritium	H-3	CdV-16-1(i)	Generic:LLEE, Generic:Low_Level_Tritium	RAD	Qbo	8	8	pCi/L	55.3415	63.595	26.645	68.264	—	—	—	—
Uranium	U	CdV-16-1(i)	EPA:200.8, SW-846:6020	Inorganic	Qbo	41	40	µg/L	0.443151	0.435	0.3	0.62	0.359	0.359	0.359	0.359
Uranium-234	U-234	CdV-16-1(i)	HASL-300:ISOU	RAD	Qbo	8	8	pCi/L	0.397625	0.4045	0.293	0.462	—	—	—	—
Uranium-235/236	U-235/236	CdV-16-1(i)	HASL-300:ISOU	RAD	Qbo	8	0	pCi/L	—	—	—	—	0.021035	0.015	-0.0147	0.0855
Uranium-238	U-238	CdV-16-1(i)	HASL-300:ISOU	RAD	Qbo	8	8	pCi/L	0.17175	0.1475	0.112	0.28	—	—	—	—
Vanadium	V	CdV-16-1(i)	EPA:200.8, SW-846:6010B, SW-846:6010C	Inorganic	Qbo	41	37	µg/L	2.6780838	2.6	1.5	4.73	2.85	3.05	1.2	4.1
Zinc	Zn	CdV-16-1(i)	EPA:200.7, SW-846:6010B, SW-846:6010C	Inorganic	Qbo	41	36	µg/L	23.897417	24	4.9	70.7	10.47	12.3	5.48	14.7
Acenaphthene	83-32-9	CdV-16-2(i)r	SW-846:8270C, SW-846:8270D, SW-846:8270DGCMS_SIM, SW-846:8310	SVOC	Tpf	10	0	µg/L	—	—	—	—	0.7811	1.035	0.105	1.12
Acenaphthylene	208-96-8	CdV-16-2(i)r	SW-846:8270C, SW-846:8270D, SW-846:8270DGCMS_SIM, SW-846:8310	SVOC	Tpf	10	0	µg/L	—	—	—	—	0.7811	1.035	0.105	1.12
Acetone	67-64-1	CdV-16-2(i)r	SW-846:8260B	VOC	Tpf	23	1	µg/L	7.81	7.81	7.81	7.81	7.05272727	10	1.5	10
Acidity or Alkalinity of a solution	pH	CdV-16-2(i)r	EPA:150.1	General Chemistry	Tpf	19	19	SU	7.4094737	7.35	7.11	7.85	—	—	—	—
Alkalinity-CO3	ALK-CO3	CdV-16-2(i)r	EPA:310.1	General Chemistry	Tpf	19	0	µg/L	—	—	—	—	1486.84211	1000	1000	4000
Alkalinity-CO3+HCO3	ALK-CO3+HCO3	CdV-16-2(i)r	EPA:310.1	General Chemistry	Tpf	19	19	µg/L	51342.105	51,400	44,800	55,800	—	—	—	—
Aluminum	Al	CdV-16-2(i)r	SW-846:6010B, SW-846:6010C	Inorganic	Tpf	24	2	µg/L	197	197	165	229	170	200	68	200
Amino-2,6-dinitrotoluene[4-]	19406-51-0	CdV-16-2(i)r	SW-846:8321A_MOD, SW-846:8330B	LCMS/MS High Explosives	Tpf	33	20	µg/L	0.12414	0.121	0.0958	0.166	0.29855385	0.325	0.0842	0.325
Amino-4,6-dinitrotoluene[2-]	35572-78-2	CdV-16-2(i)r	SW-846:8321A_MOD, SW-846:8330B	LCMS/MS High Explosives	Tpf	32	1	µg/L	0.182	0.182	0.182	0.182	0.2243	0.263	0.0816	0.325
Ammonia as nitrogen	NH3-N	CdV-16-2(i)r	EPA:350.1	General Chemistry	Tpf	19	13	µg/L	70.961538	43.5	22	234	72.0333333	57.4	32	154
Anthracene	120-12-7	CdV-16-2(i)r	SW-846:8270C, SW-846:8270D, SW-846:8270DGCMS_SIM, SW-846:8310	SVOC	Tpf	10	0	µg/L	—	—	—	—	0.7811	1.035	0.105	1.12
Antimony	Sb	CdV-16-2(i)r	SW-846:6020	Inorganic	Tpf	24	0	µg/L	—	—	—	—	2.58333333	3	1	3
Arsenic	As	CdV-16-2(i)r	SW-846:6020	Inorganic	Tpf	24	4	µg/L	2.6475	2.285	2.12	3.9	4.6385	5	2	5
Barium	Ba	CdV-16-2(i)r	SW-846:6010B, SW-846:6010C	Inorganic	Tpf	24	24	µg/L	2.5175	2.42	1.95	3.55	—	—	—	—
Benzo(g,h,i)perylene	191-24-2	CdV-16-2(i)r	SW-846:8270C, SW-846:8270D, SW-846:8270DGCMS_SIM, SW-846:8310	SVOC	Tpf	9	0	µg/L	—	—	—	—	0.64973333	1.03	0.0505	1.12
Benzoic acid	65-85-0	CdV-16-2(i)r	SW-846:8270C, SW-846:8270D	SVOC	Tpf	9	0	µg/L	—	—	—	—	17.9444444	20.8	6	21.7
Beryllium	Be	CdV-16-2(i)r	SW-846:6010B, SW-846:6010C	Inorganic	Tpf	24	0	µg/L	—	—	—	—	4.16666667	5	1	5
Bis(2-ethylhexyl)phthalate	117-81-7	CdV-16-2(i)r	SW-846:8270C, SW-846:8270D	SVOC	Tpf	10	0	µg/L	—	—	—	—	9.28	10.45	3	11.2
Boron	B	CdV-16-2(i)r	SW-846:6010B, SW-846:6010C	Inorganic	Tpf	24	21	µg/L	26.97619	27.5	17.7	37.5	38.3333333	50	15	50
Bromide	Br(-1)	CdV-16-2(i)r	EPA:300.0	General Chemistry	Tpf	19	4	µg/L	75.15	76.05	69.1	79.4	164.533333	200	67	200

Table 4.2-1 (continued)

Parameter Name	Parameter Code	Well	Analytical Method	Analytical Method Category[a]	Geological Unit Code[a]	No. Samples	No. Detects	Unit	Mean Detect	Median Detect	Min Detect	Max Detect	Mean ND	Median ND	Min ND	Max ND
Bromodichloromethane	75-27-4	CdV-16-2(i)r	SW-846:8260B	VOC	Tpf	23	0	µg/L	—	—	—	—	0.84782609	1	0.3	1
Bromoform	75-25-2	CdV-16-2(i)r	SW-846:8260B	VOC	Tpf	23	0	µg/L	—	—	—	—	0.84782609	1	0.3	1
Butanone[2-]	78-93-3	CdV-16-2(i)r	SW-846:8260B	VOC	Tpf	23	1	µg/L	11.7	11.7	11.7	11.7	4.20454545	5	1.5	5
Cadmium	Cd	CdV-16-2(i)r	SW-846:6020	Inorganic	Tpf	24	0	µg/L	—	—	—	—	0.85416667	1	0.3	1
Calcium	Ca	CdV-16-2(i)r	SW-846:6010B, SW-846:6010C	Inorganic	Tpf	24	24	µg/L	9817.9167	9875	8510	11,100	—	—	—	—
Carbon disulfide	75-15-0	CdV-16-2(i)r	SW-846:8260B	VOC	Tpf	23	0	µg/L	—	—	—	—	4.23913043	5	1.5	5
Chloride	Cl(-1)	CdV-16-2(i)r	EPA:300.0	General Chemistry	Tpf	19	19	µg/L	2823.6842	3020	1950	3280	—	—	—	—
Chlorobenzene	108-90-7	CdV-16-2(i)r	SW-846:8260B	VOC	Tpf	23	0	µg/L	—	—	—	—	0.84782609	1	0.3	1
Chlorodibromomethane	124-48-1	CdV-16-2(i)r	SW-846:8260B	VOC	Tpf	23	0	µg/L	—	—	—	—	0.84782609	1	0.3	1
Chloroform	67-66-3	CdV-16-2(i)r	SW-846:8260B	VOC	Tpf	23	0	µg/L	—	—	—	—	0.84782609	1	0.3	1
Chloromethane	74-87-3	CdV-16-2(i)r	SW-846:8260B	VOC	Tpf	23	1	µg/L	2.7	2.7	2.7	2.7	0.84090909	1	0.3	1
Chromium	Cr	CdV-16-2(i)r	SW-846:6020	Inorganic	Tpf	24	3	µg/L	2.6833333	2.66	2.5	2.89	8.33333333	10	3	10
Cobalt	Co	CdV-16-2(i)r	SW-846:6010B, SW-846:6010C	Inorganic	Tpf	24	0	µg/L	—	—	—	—	4.16666667	5	1	5
Copper	Cu	CdV-16-2(i)r	SW-846:6010B, SW-846:6010C	Inorganic	Tpf	24	8	µg/L	4.94	4.395	3.14	9.4	8.25	10	3	10
Cyanide (total)	CN (Total)	CdV-16-2(i)r	EPA:335.4	Inorganic	Tpf	15	0	µg/L	—	—	—	—	3.89	5	1.67	5
DNX	DNX	CdV-16-2(i)r	SW-846:8321A_MOD, SW-846:8330B, SW-846:8330RDX	LCMS/MS High Explosives	Tpf	26	20	µg/L	0.20135	0.176	0.081	0.385	0.3657	0.5	0.0842	0.5
Fluoranthene	206-44-0	CdV-16-2(i)r	SW-846:8270C, SW-846:8270D, SW-846:8270DGCMS_SIM, SW-846:8310	SVOC	Tpf	10	0	µg/L	—	—	—	—	0.68876	1.035	0.0505	1.12
Fluoride	F(-1)	CdV-16-2(i)r	EPA:300.0	General Chemistry	Tpf	19	19	µg/L	148.19474	142	75.6	248	—	—	—	—
Gross alpha	GrossA	CdV-16-2(i)r	EPA:900	RAD	Tpf	8	0	pCi/L	—	—	—	—	0.956	1.435	-0.565	2.08
Gross beta	GrossB	CdV-16-2(i)r	EPA:900	RAD	Tpf	8	0	pCi/L	—	—	—	—	1.00895913	1.045	0.00067	1.74
Gross gamma	GrossG	CdV-16-2(i)r	EPA:901.1	RAD	Tpf	5	0	pCi/L	—	—	—	—	82.03	84.8	8.55	142
Hardness	Hardness	CdV-16-2(i)r	SM:A2340B	Inorganic	Tpf	24	24	µg/L	34,762.5	35,100	30,400	38,800	—	—	—	—
Heptachlor	76-44-8	CdV-16-2(i)r	SW-846:8081A	PESTPCB	Tpf	2	0	µg/L	—	—	—	—	0.02295	0.02295	0.0206	0.0253
Hexachlorobutadiene	87-68-3	CdV-16-2(i)r	SW-846:8260B	VOC	Tpf	22	0	µg/L	—	—	—	—	0.84090909	1	0.3	1
HMX	2691-41-0	CdV-16-2(i)r	SW-846:8321A_MOD, SW-846:8330B	LCMS/MS High Explosives	Tpf	33	32	µg/L	0.8444063	0.925	0.155	1.98	0.0842	0.0842	0.0842	0.0842
Iron	Fe	CdV-16-2(i)r	SW-846:6010B, SW-846:6010C	Inorganic	Tpf	24	3	µg/L	128.83333	156	54.5	176	86.6666667	100	30	100
Lead	Pb	CdV-16-2(i)r	SW-846:6020	Inorganic	Tpf	24	2	µg/L	0.64	0.64	0.569	0.711	1.65909091	2	0.5	2
Magnesium	Mg	CdV-16-2(i)r	SW-846:6010B, SW-846:6010C	Inorganic	Tpf	24	24	µg/L	2490	2540	2180	2840	—	—	—	—
Manganese	Mn	CdV-16-2(i)r	SW-846:6010B, SW-846:6010C	Inorganic	Tpf	24	3	µg/L	6.63	4.85	2.24	12.8	8.0952381	10	2	10
Mercury	Hg	CdV-16-2(i)r	EPA:245.2	Inorganic	Tpf	38	0	µg/L	—	—	—	—	0.165	0.2	0.067	0.2
Methyl tert-butyl ether	1634-04-4	CdV-16-2(i)r	SW-846:8260B	VOC	Tpf	19	16	µg/L	0.47875	0.475	0.31	0.64	0.76666667	1	0.3	1
Methyl-2-pentanone[4-]	108-10-1	CdV-16-2(i)r	SW-846:8260B	VOC	Tpf	23	1	µg/L	5.35	5.35	5.35	5.35	4.20454545	5	1.5	5
Methylene chloride	75-09-2	CdV-16-2(i)r	SW-846:8260B	VOC	Tpf	23	0	µg/L	—	—	—	—	6.82869565	10	1	10
MNX	MNX	CdV-16-2(i)r	SW-846:8321A_MOD, SW-846:8330B, SW-846:8330RDX	LCMS/MS High Explosives	Tpf	26	23	µg/L	0.4212609	0.449	0.16	0.667	0.2814	0.26	0.0842	0.5
Molybdenum	Mo	CdV-16-2(i)r	SW-846:6020	Inorganic	Tpf	24	21	µg/L	1.0073333	0.971	0.84	1.38	1.004	0.933	0.819	1.26

Table 4.2-1 (continued)

Parameter Name	Parameter Code	Well	Analytical Method	Analytical Method Category[a]	Geological Unit Code[a]	No. Samples	No. Detects	Unit	Mean Detect	Median Detect	Min Detect	Max Detect	Mean ND	Median ND	Min ND	Max ND
Nickel	Ni	CdV-16-2(i)r	SW-846:6020	Inorganic	Tpf	24	10	µg/L	0.8824	0.687	0.52	1.8	1.43342857	1.93	0.6	2
Nitrate-nitrite as nitrogen	NO3+NO2-N	CdV-16-2(i)r	EPA:353.2	General Chemistry	Tpf	19	19	µg/L	626.68421	607	498	763	—	—	—	—
Nitrotoluene[2-]	88-72-2	CdV-16-2(i)r	SW-846:8321A_MOD, SW-846:8330B	LCMS/MS High Explosives	Tpf	32	0	µg/L	—	—	—	—	0.22810313	0.263	0.0837	0.325
Oxygen-18/oxygen-16 ratio from nitrate	O18O16-NO3	CdV-16-2(i)r	Generic:Oxygen Isotope Ratio	General Chemistry	Tpf	2	2	permil	3.68095	3.681	2.0179	5.344	—	—	—	—
Perchlorate	ClO4	CdV-16-2(i)r	SW-846:6850	LCMS/MS Perchlorate	Tpf	19	19	µg/L	0.3121053	0.314	0.242	0.385	—	—	—	—
Perfluorooctanoic acid	335-67-1	CdV-16-2(i)r	EPA:537M	LCMS/MS PFAS	Tpf	1	1	µg/L	0.0108	0.0108	0.0108	0.0108	—	—	—	—
Phenanthrene	85-01-8	CdV-16-2(i)r	SW-846:8270C, SW-846:8270D, SW-846:8270DGCMS_SIM, SW-846:8310	SVOC	Tpf	10	0	µg/L	—	—	—	—	0.7722	1.0005	0.105	1.12
Potassium	K	CdV-16-2(i)r	SW-846:6010B, SW-846:6010C	Inorganic	Tpf	24	22	µg/L	303	304	204	543	332.5	332.5	324	341
Pyrene	129-00-0	CdV-16-2(i)r	SW-846:8270C, SW-846:8270D, SW-846:8270DGCMS_SIM, SW-846:8310	SVOC	Tpf	10	0	µg/L	—	—	—	—	0.68876	1.035	0.0505	1.12
Radium-226	Ra-226	CdV-16-2(i)r	EPA:903.1	RAD	Tpf	1	0	pCi/L	—	—	—	—	0.285	0.285	0.285	0.285
Radium-228	Ra-228	CdV-16-2(i)r	EPA:904	RAD	Tpf	1	0	pCi/L	—	—	—	—	-0.0291	-0.0291	-0.0291	-0.0291
RDX	121-82-4	CdV-16-2(i)r	SW-846:8321A_MOD, SW-846:8330B	LCMS/MS High Explosives	Tpf	33	32	µg/L	83.091875	89.2	1.34	128	46.1	46.1	46.1	46.1
Selenium	Se	CdV-16-2(i)r	SW-846:6020	Inorganic	Tpf	24	0	µg/L	—	—	—	—	4.375	5	2	5
Silicon dioxide	SiO2	CdV-16-2(i)r	SW-846:6010B, SW-846:6010C	Inorganic	Tpf	19	19	µg/L	60,831.579	61,400	53,300	63,800	—	—	—	—
Silver	Ag	CdV-16-2(i)r	SW-846:6020	Inorganic	Tpf	24	0	µg/L	—	—	—	—	0.85416667	1	0.3	1
Sodium	Na	CdV-16-2(i)r	SW-846:6010B, SW-846:6010C	Inorganic	Tpf	24	24	µg/L	12,550	12,600	10,900	13,300	—	—	—	—
Strontium	Sr	CdV-16-2(i)r	SW-846:6010B, SW-846:6010C	Inorganic	Tpf	24	24	µg/L	61.845833	62.5	56.1	67.8	—	—	—	—
Styrene	100-42-5	CdV-16-2(i)r	SW-846:8260B	VOC	Tpf	23	0	µg/L	—	—	—	—	0.84782609	1	0.3	1
Sulfate	SO4(-2)	CdV-16-2(i)r	EPA:300.0	General Chemistry	Tpf	19	19	µg/L	4217.3684	4310	3190	5000	—	—	—	—
Temperature	TEMP	CdV-16-2(i)r	EPA:170.0	VOC	Tpf	16	16	deg C	2.3125	2	1	4	—	—	—	—
Tetrachloroethene	127-18-4	CdV-16-2(i)r	SW-846:8260B	VOC	Tpf	23	22	µg/L	0.5580909	0.53	0.289	0.92	1	1	1	1
Thallium	Tl	CdV-16-2(i)r	SW-846:6020	Inorganic	Tpf	24	0	µg/L	—	—	—	—	1.58333333	2	0.6	2
Tin	Sn	CdV-16-2(i)r	SW-846:6010B, SW-846:6010C	Inorganic	Tpf	24	2	µg/L	5.42	5.42	2.93	7.91	15.9090909	10	2.5	50
TNX	TNX	CdV-16-2(i)r	SW-846:8321A_MOD, SW-846:8330B, SW-846:8330RDX	LCMS/MS High Explosives	Tpf	26	19	µg/L	0.1348632	0.134	0.0887	0.193	0.38488571	0.5	0.0842	0.5
Toluene	108-88-3	CdV-16-2(i)r	SW-846:8260B	VOC	Tpf	23	15	µg/L	3.0840667	1.81	0.321	12	0.65	0.65	0.3	1
Total dissolved solids	TDS	CdV-16-2(i)r	EPA:160.1	General Chemistry	Tpf	19	19	µg/L	119,694.74	120,000	62,900	161,000	—	—	—	—
Total Kjeldahl nitrogen	TKN	CdV-16-2(i)r	EPA:351.2	General Chemistry	Tpf	17	4	µg/L	232.575	164.5	36.3	565	77.2846154	100	33	100
Total organic carbon	TOC	CdV-16-2(i)r	SW-846:9060	General Chemistry	Tpf	17	16	µg/L	575.1875	587.5	354	919	674	674	674	674
Total phosphate as phosphorus	PO4-P	CdV-16-2(i)r	EPA:365.4	General Chemistry	Tpf	19	7	µg/L	100.91429	80.8	21.1	278	58.4583333	47.1	30.7	155
Trichlorobenzene[1,2,3-]	87-61-6	CdV-16-2(i)r	SW-846:8260B	VOC	Tpf	21	0	µg/L	—	—	—	—	0.83333333	1	0.3	1
Trichloroethene	79-01-6	CdV-16-2(i)r	SW-846:8260B	VOC	Tpf	23	14	µg/L	0.3923571	0.37	0.293	0.57	0.84444444	1	0.3	1
Trinitrobenzene[1,3,5-]	99-35-4	CdV-16-2(i)r	SW-846:8321A_MOD, SW-846:8330B	LCMS/MS High Explosives	Tpf	32	10	µg/L	0.11405	0.1026	0.0856	0.16	0.23607727	0.266	0.0825	0.325

Table 4.2-1 (continued)

Parameter Name	Parameter Code	Well	Analytical Method	Analytical Method Category[a]	Geological Unit Code[a]	No. Samples	No. Detects	Unit	Mean Detect	Median Detect	Min Detect	Max Detect	Mean ND	Median ND	Min ND	Max ND
Trinitrotoluene[2,4,6-]	118-96-7	CdV-16-2(i)r	SW-846:8321A_MOD, SW-846:8330B	LCMS/MS High Explosives	Tpf	32	0	µg/L	—	—	—	—	0.22744688	0.263	0.0816	0.325
Tritium	H-3	CdV-16-2(i)r	EPA:906.0, Generic:LLEE, Generic:Low_Level_Tritium	RAD	Tpf	11	9	pCi/L	7.2240222	7.567	4.993	8.4686	52.95	52.95	35.3	70.6
Uranium	U	CdV-16-2(i)r	SW-846:6020	Inorganic	Tpf	24	21	µg/L	0.2889524	0.283	0.214	0.394	0.30333333	0.302	0.25	0.358
Uranium-234	U-234	CdV-16-2(i)r	HASL-300:ISOU	RAD	Tpf	9	8	pCi/L	0.213	0.1995	0.139	0.348	0.244	0.244	0.244	0.244
Uranium-235/236	U-235/236	CdV-16-2(i)r	HASL-300:ISOU	RAD	Tpf	9	0	pCi/L	—	—	—	—	0.02570111	0.013	0.00389	0.106
Uranium-238	U-238	CdV-16-2(i)r	HASL-300:ISOU	RAD	Tpf	9	9	pCi/L	0.1136333	0.0975	0.0714	0.203	—	—	—	—
Vanadium	V	CdV-16-2(i)r	SW-846:6010B, SW-846:6010C	Inorganic	Tpf	24	13	µg/L	1.2615385	1.23	1.01	1.66	4.27272727	5	1	5
Zinc	Zn	CdV-16-2(i)r	SW-846:6010B, SW-846:6010C	Inorganic	Tpf	24	24	µg/L	17.299583	15.65	9.19	33.3	—	—	—	—
Acenaphthene	83-32-9	CDV-16-4ip	SW-846:8270C, SW-846:8270D, SW-846:8270DGCMS_SIM, SW-846:8310	SVOC	Tpf	13	0	µg/L	—	—	—	—	0.82807692	1	0.101	1.15
Acenaphthylene	208-96-8	CDV-16-4ip	SW-846:8270C, SW-846:8270D, SW-846:8270DGCMS_SIM, SW-846:8310	SVOC	Tpf	13	0	µg/L	—	—	—	—	0.82807692	1	0.101	1.15
Acetone	67-64-1	CDV-16-4ip	SW-846:8260B	VOC	Tpf	20	2	µg/L	39.6	39.6	10.5	68.7	7.53611111	10	1.5	10
Acidity or alkalinity of a solution	pH	CDV-16-4ip	EPA:150.1	General Chemistry	Tpf	28	28	SU	7.4428571	7.45	7.08	7.67	—	—	—	—
Alkalinity-CO3	ALK-CO3	CDV-16-4ip	EPA:310.1	General Chemistry	Tpf	28	0	µg/L	—	—	—	—	1534.82143	1000	725	4000
Alkalinity-CO3+HCO3	ALK-CO3+HCO3	CDV-16-4ip	EPA:310.1	General Chemistry	Tpf	28	28	µg/L	49,157.143	49,900	43,700	52,100	—	—	—	—
Aluminum	Al	CDV-16-4ip	SW-846:6010B, SW-846:6010C	Inorganic	Tpf	28	0	µg/L	—	—	—	—	171.714286	200	68	200
Amino-2,6-dinitrotoluene[4-]	19406-51-0	CDV-16-4ip	SW-846:8321A_MOD, SW-846:8330B	LCMS/MS High Explosives	Tpf	29	28	µg/L	1.9696429	1.87	1.47	2.67	0.27	0.27	0.27	0.27
Amino-4,6-dinitrotoluene[2-]	35572-78-2	CDV-16-4ip	SW-846:8321A_MOD, SW-846:8330B	LCMS/MS High Explosives	Tpf	28	0	µg/L	—	—	—	—	0.20116786	0.259	0.0816	0.284
Ammonia as nitrogen	NH3-N	CDV-16-4ip	EPA:350.1	General Chemistry	Tpf	28	12	µg/L	77.541667	49.1	24.3	194	59.84375	52.2	17	143
Anthracene	120-12-7	CDV-16-4ip	SW-846:8270C, SW-846:8270D, SW-846:8270DGCMS_SIM, SW-846:8310	SVOC	Tpf	13	0	µg/L	—	—	—	—	0.82807692	1	0.101	1.15
Antimony	Sb	CDV-16-4ip	SW-846:6020	Inorganic	Tpf	28	0	µg/L	—	—	—	—	2.57142857	3	1	3
Arsenic	As	CDV-16-4ip	SW-846:6020	Inorganic	Tpf	28	4	µg/L	2.3775	2.39	1.87	2.86	4.6125	5	1.7	5
Barium	Ba	CDV-16-4ip	SW-846:6010B, SW-846:6010C	Inorganic	Tpf	28	27	µg/L	4.0192593	3.14	2.2	8.56	3.74	3.74	3.74	3.74
Benzo(g,h,i)perylene	191-24-2	CDV-16-4ip	SW-846:8270C, SW-846:8270D, SW-846:8270DGCMS_SIM, SW-846:8310	SVOC	Tpf	13	0	µg/L	—	—	—	—	0.75600769	1	0.0515	1.15
Benzoic acid	65-85-0	CDV-16-4ip	SW-846:8270C, SW-846:8270D	SVOC	Tpf	13	0	µg/L	—	—	—	—	18.7423077	20	6.25	23
Beryllium	Be	CDV-16-4ip	SW-846:6010B, SW-846:6010C	Inorganic	Tpf	28	0	µg/L	—	—	—	—	4.14285714	5	1	5
Bis(2-ethylhexyl)phthalate	117-81-7	CDV-16-4ip	SW-846:8270C, SW-846:8270D	SVOC	Tpf	13	0	µg/L	—	—	—	—	9.37	10	3.13	11.5
Boron	B	CDV-16-4ip	SW-846:6010B, SW-846:6010C	Inorganic	Tpf	28	27	µg/L	65.392593	63.7	15.1	115	50	50	50	50
Bromide	Br(-1)	CDV-16-4ip	EPA:300.0	General Chemistry	Tpf	28	11	µg/L	80.690909	79.3	72	96.9	160.882353	200	67	200
Bromodichloromethane	75-27-4	CDV-16-4ip	SW-846:8260B	VOC	Tpf	20	0	µg/L	—	—	—	—	0.825	1	0.3	1
Bromoform	75-25-2	CDV-16-4ip	SW-846:8260B	VOC	Tpf	20	0	µg/L	—	—	—	—	0.825	1	0.3	1
Butanone[2-]	78-93-3	CDV-16-4ip	SW-846:8260B	VOC	Tpf	20	0	µg/L	—	—	—	—	4.125	5	1.5	5
Cadmium	Cd	CDV-16-4ip	SW-846:6020	Inorganic	Tpf	28	0	µg/L	—	—	—	—	0.84321429	1	0.11	1

Table 4.2-1 (continued)

Parameter Name	Parameter Code	Well	Analytical Method	Analytical Method Category[a]	Geological Unit Code[a]	No. Samples	No. Detects	Unit	Mean Detect	Median Detect	Min Detect	Max Detect	Mean ND	Median ND	Min ND	Max ND
Calcium	Ca	CDV-16-4ip	SW-846:6010B, SW-846:6010C	Inorganic	Tpf	28	28	µg/L	10,565	10,700	9470	11,600	—	—	—	—
Carbon disulfide	75-15-0	CDV-16-4ip	SW-846:8260B	VOC	Tpf	20	0	µg/L	—	—	—	—	4.125	5	1.5	5
Chloride	Cl(-1)	CDV-16-4ip	EPA:300.0	General Chemistry	Tpf	28	28	µg/L	3388.5714	3500	1500	4150	—	—	—	—
Chlorobenzene	108-90-7	CDV-16-4ip	SW-846:8260B	VOC	Tpf	20	0	µg/L	—	—	—	—	0.825	1	0.3	1
Chlorodibromomethane	124-48-1	CDV-16-4ip	SW-846:8260B	VOC	Tpf	20	0	µg/L	—	—	—	—	0.825	1	0.3	1
Chloroform	67-66-3	CDV-16-4ip	SW-846:8260B	VOC	Tpf	20	0	µg/L	—	—	—	—	0.825	1	0.3	1
Chloromethane	74-87-3	CDV-16-4ip	SW-846:8260B	VOC	Tpf	20	0	µg/L	—	—	—	—	0.825	1	0.3	1
Chromium	Cr	CDV-16-4ip	SW-846:6020	Inorganic	Tpf	28	4	µg/L	2.5325	2.53	2.34	2.73	8.20833333	10	2	10
Cobalt	Co	CDV-16-4ip	SW-846:6010B, SW-846:6010C	Inorganic	Tpf	28	0	µg/L	—	—	—	—	4.14285714	5	1	5
Copper	Cu	CDV-16-4ip	SW-846:6010B, SW-846:6010C	Inorganic	Tpf	28	0	µg/L	—	—	—	—	8.5	10	3	10
Cyanide (total)	CN (Total)	CDV-16-4ip	EPA:335.4	Inorganic	Tpf	17	0	µg/L	—	—	—	—	3.82470588	5	1.67	5
DNX	DNX	CDV-16-4ip	SW-846:8321A_MOD, SW-846:8330B, SW-846:8330RDX	LCMS/MS High Explosives	Tpf	24	24	µg/L	0.3058333	0.284	0.202	0.578	—	—	—	—
Fluoranthene	206-44-0	CDV-16-4ip	SW-846:8270C, SW-846:8270D, SW-846:8270DGCMS_SIM, SW-846:8310	SVOC	Tpf	13	0	µg/L	—	—	—	—	0.75600769	1	0.0515	1.15
Fluoride	F(-1)	CDV-16-4ip	EPA:300.0	General Chemistry	Tpf	28	28	µg/L	108.73929	99.5	49.9	282	—	—	—	—
Gross alpha	GrossA	CDV-16-4ip	EPA:900	RAD	Tpf	5	0	pCi/L	—	—	—	—	0.9284	0.842	0.465	1.62
Gross beta	GrossB	CDV-16-4ip	EPA:900	RAD	Tpf	5	0	pCi/L	—	—	—	—	0.8278	0.937	-0.149	1.48
Hardness	Hardness	CDV-16-4ip	SM:A2340B	Inorganic	Tpf	28	28	µg/L	39,082.143	39,150	35,400	43,500	—	—	—	—
Hexachlorobutadiene	87-68-3	CDV-16-4ip	SW-846:8260B	VOC	Tpf	20	0	µg/L	—	—	—	—	0.825	1	0.3	1
HMX	2691-41-0	CDV-16-4ip	SW-846:8321A_MOD, SW-846:8330B	LCMS/MS High Explosives	Tpf	29	29	µg/L	9.0641379	9.17	6.33	11.8	—	—	—	—
Iron	Fe	CDV-16-4ip	SW-846:6010B, SW-846:6010C	Inorganic	Tpf	28	2	µg/L	69.45	69.45	33.9	105	86.5384615	100	30	100
Lead	Pb	CDV-16-4ip	SW-846:6020	Inorganic	Tpf	28	0	µg/L	—	—	—	—	1.67857143	2	0.5	2
Magnesium	Mg	CDV-16-4ip	SW-846:6010B, SW-846:6010C	Inorganic	Tpf	28	28	µg/L	3091.0714	3065	2800	3540	—	—	—	—
Manganese	Mn	CDV-16-4ip	SW-846:6010B, SW-846:6010C	Inorganic	Tpf	28	5	µg/L	8.88	6.87	2.34	14.6	7.91304348	10	2	10
Mercury	Hg	CDV-16-4ip	EPA:245.2	Inorganic	Tpf	45	0	µg/L	—	—	—	—	0.20453333	0.2	0.067	2
Methyl tert-butyl ether	1634-04-4	CDV-16-4ip	SW-846:8260B	VOC	Tpf	20	18	µg/L	0.5855556	0.6	0.32	0.8	0.65	0.65	0.3	1
Methyl-2-pentanone[4-]	108-10-1	CDV-16-4ip	SW-846:8260B	VOC	Tpf	20	0	µg/L	—	—	—	—	4.125	5	1.5	5
Methylene chloride	75-09-2	CDV-16-4ip	SW-846:8260B	VOC	Tpf	20	0	µg/L	—	—	—	—	7.75	10	1	10
MNX	MNX	CDV-16-4ip	SW-846:8321A_MOD, SW-846:8330B, SW-846:8330RDX	LCMS/MS High Explosives	Tpf	24	24	µg/L	0.5874167	0.6005	0.273	0.92	—	—	—	—
Molybdenum	Mo	CDV-16-4ip	SW-846:6020	Inorganic	Tpf	28	20	µg/L	0.5855	0.5765	0.514	0.734	0.617375	0.6075	0.546	0.686
Nickel	Ni	CDV-16-4ip	SW-846:6020	Inorganic	Tpf	28	17	µg/L	0.7288824	0.693	0.526	1.19	1.26372727	1.15	0.6	2
Nitrate-nitrite as nitrogen	NO3+NO2-N	CDV-16-4ip	EPA:353.2	General Chemistry	Tpf	28	28	µg/L	868.71429	882.5	433	1120	—	—	—	—
Nitrotoluene[2-]	88-72-2	CDV-16-4ip	SW-846:8321A_MOD, SW-846:8330B	LCMS/MS High Explosives	Tpf	28	0	µg/L	—	—	—	—	0.201925	0.259	0.0837	0.284
Oxygen-18/oxygen-16 ratio from nitrate	O18O16-NO3	CDV-16-4ip	Generic:Oxygen Isotope Ratio	General Chemistry	Tpf	2	2	permil	8.19985	8.1999	5.3747	11.025	—	—	—	—

Table 4.2-1 (continued)

Parameter Name	Parameter Code	Well	Analytical Method	Analytical Method Category[a]	Geological Unit Code[a]	No. Samples	No. Detects	Unit	Mean Detect	Median Detect	Min Detect	Max Detect	Mean ND	Median ND	Min ND	Max ND
Perchlorate	ClO4	CDV-16-4ip	SW-846:6850	LCMS/MS Perchlorate	Tpf	28	28	µg/L	0.35375	0.359	0.246	0.397	—	—	—	—
Perfluorooctanoic acid	335-67-1	CDV-16-4ip	EPA:537M	LCMS/MS PFAS	Tpf	1	1	µg/L	0.0117	0.0117	0.0117	0.0117	—	—	—	—
Phenanthrene	85-01-8	CDV-16-4ip	SW-846:8270C, SW-846:8270D, SW-846:8270DGCMS_SIM, SW-846:8310	SVOC	Tpf	13	0	µg/L	—	—	—	—	0.82807692	1	0.101	1.15
Potassium	K	CDV-16-4ip	SW-846:6010B, SW-846:6010C	Inorganic	Tpf	28	28	µg/L	961.60714	960.5	554	1320	—	—	—	—
Pyrene	129-00-0	CDV-16-4ip	SW-846:8270C, SW-846:8270D, SW-846:8270DGCMS_SIM, SW-846:8310	SVOC	Tpf	13	0	µg/L	—	—	—	—	0.75600769	1	0.0515	1.15
RDX	121-82-4	CDV-16-4ip	SW-846:8321A_MOD, SW-846:8330B	LCMS/MS High Explosives	Tpf	29	29	µg/L	132.24138	131	104	177	—	—	—	—
Selenium	Se	CDV-16-4ip	SW-846:6020	Inorganic	Tpf	28	0	µg/L	—	—	—	—	4.33928571	5	1.5	5
Silicon dioxide	SiO2	CDV-16-4ip	SW-846:6010B, SW-846:6010C	Inorganic	Tpf	28	28	µg/L	60,271.429	59,800	55,500	67,100	—	—	—	—
Silver	Ag	CDV-16-4ip	SW-846:6020	Inorganic	Tpf	28	0	µg/L	—	—	—	—	0.84642857	1	0.2	1
Sodium	Na	CDV-16-4ip	SW-846:6010B, SW-846:6010C	Inorganic	Tpf	28	28	µg/L	10,034.643	9970	8480	12,700	—	—	—	—
Strontium	Sr	CDV-16-4ip	SW-846:6010B, SW-846:6010C	Inorganic	Tpf	28	28	µg/L	61.45	61.3	55.7	71.9	—	—	—	—
Styrene	100-42-5	CDV-16-4ip	SW-846:8260B	VOC	Tpf	20	0	µg/L	—	—	—	—	0.825	1	0.3	1
Sulfate	SO4(-2)	CDV-16-4ip	EPA:300.0	General Chemistry	Tpf	28	28	µg/L	3693.2143	3680	2410	5660	—	—	—	—
Temperature	TEMP	CDV-16-4ip	EPA:170.0	VOC	Tpf	16	16	deg C	2.375	2	1	4	—	—	—	—
Tetrachloroethene	127-18-4	CDV-16-4ip	SW-846:8260B	VOC	Tpf	20	20	µg/L	0.9145	0.92	0.73	1.12	—	—	—	—
Thallium	Tl	CDV-16-4ip	SW-846:6020	Inorganic	Tpf	28	0	µg/L	—	—	—	—	1.5875	2	0.45	2
Tin	Sn	CDV-16-4ip	SW-846:6010B, SW-846:6010C	Inorganic	Tpf	28	1	µg/L	8.06	8.06	8.06	8.06	15.462963	10	2.5	100
TNX	TNX	CDV-16-4ip	SW-846:8321A_MOD, SW-846:8330B, SW-846:8330RDX	LCMS/MS High Explosives	Tpf	24	24	µg/L	0.2610833	0.228	0.129	1.1	—	—	—	—
Toluene	108-88-3	CDV-16-4ip	SW-846:8260B	VOC	Tpf	20	0	µg/L	—	—	—	—	0.825	1	0.3	1
Total dissolved solids	TDS	CDV-16-4ip	EPA:160.1	General Chemistry	Tpf	28	28	µg/L	117,489.29	120,500	42,900	156,000	—	—	—	—
Total Kjeldahl nitrogen	TKN	CDV-16-4ip	EPA:351.2	General Chemistry	Tpf	23	9	µg/L	134.41111	132	46.3	266	81.8714286	100	33	100
Total organic carbon	TOC	CDV-16-4ip	SW-846:9060	General Chemistry	Tpf	23	22	µg/L	698.63636	666.5	401	1110	530	530	530	530
Total phosphate as phosphorus	PO4-P	CDV-16-4ip	EPA:365.4	General Chemistry	Tpf	28	14	µg/L	49.735714	42.8	22.5	91.8	56.0357143	50	38.9	95.4
Trichlorobenzene[1,2,3-]	87-61-6	CDV-16-4ip	SW-846:8260B	VOC	Tpf	20	1	µg/L	0.9	0.9	0.9	0.9	0.81578947	1	0.3	1
Trichloroethene	79-01-6	CDV-16-4ip	SW-846:8260B	VOC	Tpf	20	20	µg/L	0.6435	0.645	0.45	0.79	—	—	—	—
Trinitrobenzene[1,3,5-]	99-35-4	CDV-16-4ip	SW-846:8321A_MOD, SW-846:8330B	LCMS/MS High Explosives	Tpf	28	12	µg/L	0.1156583	0.1175	0.0867	0.158	0.2096625	0.2625	0.0833	0.284
Trinitrotoluene[2,4,6-]	118-96-7	CDV-16-4ip	SW-846:8321A_MOD, SW-846:8330B	LCMS/MS High Explosives	Tpf	28	0	µg/L	—	—	—	—	0.20116786	0.259	0.0816	0.284
Tritium	H-3	CDV-16-4ip	Generic:Low_Level_Tritium	RAD	Tpf	7	7	pCi/L	13.724571	10.401	8.407	33.114	—	—	—	—
Uranium	U	CDV-16-4ip	SW-846:6020	Inorganic	Tpf	28	27	µg/L	0.4844074	0.476	0.36	0.705	0.412	0.412	0.412	0.412
Uranium-234	U-234	CDV-16-4ip	HASL-300:ISOU	RAD	Tpf	5	5	pCi/L	0.2814	0.278	0.239	0.346	—	—	—	—
Uranium-235/236	U-235/236	CDV-16-4ip	HASL-300:ISOU	RAD	Tpf	5	0	pCi/L	—	—	—	—	0.02661	0.0199	0.00805	0.0695
Uranium-238	U-238	CDV-16-4ip	HASL-300:ISOU	RAD	Tpf	5	5	pCi/L	0.1712	0.175	0.141	0.197	—	—	—	—

Table 4.2-1 (continued)

Parameter Name	Parameter Code	Well	Analytical Method	Analytical Method Category[a]	Geological Unit Code[a]	No. Samples	No. Detects	Unit	Mean Detect	Median Detect	Min Detect	Max Detect	Mean ND	Median ND	Min ND	Max ND
Vanadium	V	CDV-16-4ip	SW-846:6010B, SW-846:6010C	Inorganic	Tpf	28	28	µg/L	2.4971429	2.475	1.52	3.45	—	—	—	—
Zinc	Zn	CDV-16-4ip	SW-846:6010B, SW-846:6010C	Inorganic	Tpf	28	4	µg/L	7.93	7.65	4.02	12.4	8.36083333	10	3.3	10
Acenaphthene	83-32-9	CDV-37-1(i)	SW-846:8270C, SW-846:8270D, SW-846:8270DGCMS_SIM, SW-846:8310	SVOC	Tpf	5	0	µg/L	—	—	—	—	0.4932	0.521	0.103	1
Acenaphthylene	208-96-8	CDV-37-1(i)	SW-846:8270C, SW-846:8270D, SW-846:8270DGCMS_SIM, SW-846:8310	SVOC	Tpf	5	0	µg/L	—	—	—	—	0.4932	0.521	0.103	1
Acetone	67-64-1	CDV-37-1(i)	SW-846:8260B	VOC	Tpf	11	2	µg/L	3.44	3.44	2.47	4.41	6.22888889	10	1.5	10
Acidity or alkalinity of a solution	pH	CDV-37-1(i)	EPA:150.1	General Chemistry	Tpf	17	17	SU	7.4670588	7.44	7.15	7.82	—	—	—	—
Alkalinity-CO3	ALK-CO3	CDV-37-1(i)	EPA:310.1	General Chemistry	Tpf	17	0	µg/L	—	—	—	—	1367.64706	1000	1000	4000
Alkalinity-CO3+HCO3	ALK-CO3+HCO3	CDV-37-1(i)	EPA:310.1	General Chemistry	Tpf	17	17	µg/L	54,670.588	53,800	51,500	65,400	—	—	—	—
Aluminum	Al	CDV-37-1(i)	SW-846:6010B, SW-846:6010C	Inorganic	Tpf	17	2	µg/L	138	138	116	160	164.8	200	68	200
Amino-2,6-dinitrotoluene[4-]	19406-51-0	CDV-37-1(i)	SW-846:8321A_MOD, SW-846:8330B	LCMS/MS High Explosives	Tpf	11	0	µg/L	—	—	—	—	0.19171818	0.259	0.0842	0.325
Amino-4,6-dinitrotoluene[2-]	35572-78-2	CDV-37-1(i)	SW-846:8321A_MOD, SW-846:8330B	LCMS/MS High Explosives	Tpf	11	0	µg/L	—	—	—	—	0.19171818	0.259	0.0842	0.325
Ammonia as nitrogen	NH3-N	CDV-37-1(i)	EPA:350.1	General Chemistry	Tpf	17	8	µg/L	47.75	35.25	16.7	94	43.8111111	44	17	91.4
Anthracene	120-12-7	CDV-37-1(i)	SW-846:8270C, SW-846:8270D, SW-846:8270DGCMS_SIM, SW-846:8310	SVOC	Tpf	5	0	µg/L	—	—	—	—	0.4932	0.521	0.103	1
Antimony	Sb	CDV-37-1(i)	SW-846:6020	Inorganic	Tpf	17	4	µg/L	0.7695	0.7365	0.575	1.03	2.07476923	3	0.972	3
Arsenic	As	CDV-37-1(i)	SW-846:6020	Inorganic	Tpf	17	2	µg/L	2.705	2.705	2.61	2.8	4.26	5	2	5.9
Barium	Ba	CDV-37-1(i)	SW-846:6010B, SW-846:6010C	Inorganic	Tpf	17	17	µg/L	9.6288235	7.88	6.44	18.6	—	—	—	—
Benzo(g,h,i)perylene	191-24-2	CDV-37-1(i)	SW-846:8270C, SW-846:8270D, SW-846:8270DGCMS_SIM, SW-846:8310	SVOC	Tpf	5	0	µg/L	—	—	—	—	0.30474	0.103	0.0521	1
Benzoic Acid	65-85-0	CDV-37-1(i)	SW-846:8270C, SW-846:8270D	SVOC	Tpf	5	0	µg/L	—	—	—	—	15.384	20	6.32	20.4
Beryllium	Be	CDV-37-1(i)	SW-846:6010B, SW-846:6010C	Inorganic	Tpf	17	0	µg/L	—	—	—	—	3.82352941	5	1	5
Bis(2-ethylhexyl)phthalate	117-81-7	CDV-37-1(i)	SW-846:8270C, SW-846:8270D	SVOC	Tpf	5	0	µg/L	—	—	—	—	7.692	10	3.16	10.2
Boron	B	CDV-37-1(i)	SW-846:6010B, SW-846:6010C	Inorganic	Tpf	17	1	µg/L	17.4	17.4	17.4	17.4	39.0625	50	15	50
Bromide	Br(-1)	CDV-37-1(i)	EPA:300.0	General Chemistry	Tpf	17	0	µg/L	—	—	—	—	160.882353	200	67	200
Bromodichloromethane	75-27-4	CDV-37-1(i)	SW-846:8260B	VOC	Tpf	11	0	µg/L	—	—	—	—	0.68181818	1	0.3	1
Bromoform	75-25-2	CDV-37-1(i)	SW-846:8260B	VOC	Tpf	11	0	µg/L	—	—	—	—	0.68181818	1	0.3	1
Butanone[2-]	78-93-3	CDV-37-1(i)	SW-846:8260B	VOC	Tpf	11	0	µg/L	—	—	—	—	3.40909091	5	1.5	5
Cadmium	Cd	CDV-37-1(i)	SW-846:6020	Inorganic	Tpf	17	0	µg/L	—	—	—	—	0.79411765	1	0.3	1
Calcium	Ca	CDV-37-1(i)	SW-846:6010B, SW-846:6010C	Inorganic	Tpf	17	17	µg/L	9383.5294	9370	8590	10,200	—	—	—	—
Carbon Disulfide	75-15-0	CDV-37-1(i)	SW-846:8260B	VOC	Tpf	11	0	µg/L	—	—	—	—	3.40909091	5	1.5	5
Chloride	Cl(-1)	CDV-37-1(i)	EPA:300.0	General Chemistry	Tpf	17	17	µg/L	1271.7647	1220	1140	1720	—	—	—	—
Chlorobenzene	108-90-7	CDV-37-1(i)	SW-846:8260B	VOC	Tpf	11	0	µg/L	—	—	—	—	0.68181818	1	0.3	1
Chlorodibromomethane	124-48-1	CDV-37-1(i)	SW-846:8260B	VOC	Tpf	11	0	µg/L	—	—	—	—	0.68181818	1	0.3	1
Chloroform	67-66-3	CDV-37-1(i)	SW-846:8260B	VOC	Tpf	11	0	µg/L	—	—	—	—	0.68181818	1	0.3	1
Chloromethane	74-87-3	CDV-37-1(i)	SW-846:8260B	VOC	Tpf	11	0	µg/L	—	—	—	—	0.68181818	1	0.3	1

Table 4.2-1 (continued)

Parameter Name	Parameter Code	Well	Analytical Method	Analytical Method Category[a]	Geological Unit Code[a]	No. Samples	No. Detects	Unit	Mean Detect	Median Detect	Min Detect	Max Detect	Mean ND	Median ND	Min ND	Max ND
Chromium	Cr	CDV-37-1(i)	SW-846:6020	Inorganic	Tpf	17	1	µg/L	3.36	3.36	3.36	3.36	7.51875	10	3	10
Cobalt	Co	CDV-37-1(i)	SW-846:6010B, SW-846:6010C	Inorganic	Tpf	17	1	µg/L	1.12	1.12	1.12	1.12	3.75	5	1	5
Copper	Cu	CDV-37-1(i)	SW-846:6010B, SW-846:6010C	Inorganic	Tpf	17	0	µg/L	—	—	—	—	7.94117647	10	3	10
Cyanide (total)	CN (Total)	CDV-37-1(i)	EPA:335.4	Inorganic	Tpf	9	0	µg/L	—	—	—	—	3.15	1.67	1.67	5
DNX	DNX	CDV-37-1(i)	SW-846:8321A_MOD, SW-846:8330B, SW-846:8330RDX	LCMS/MS High Explosives	Tpf	10	0	µg/L	—	—	—	—	0.20249	0.1773	0.0842	0.5
Fluoranthene	206-44-0	CDV-37-1(i)	SW-846:8270C, SW-846:8270D, SW-846:8270DGCMS_SIM, SW-846:8310	SVOC	Tpf	5	0	µg/L	—	—	—	—	0.30474	0.103	0.0521	1
Fluoride	F(-1)	CDV-37-1(i)	EPA:300.0	General Chemistry	Tpf	17	17	µg/L	153.21176	144	78.6	312	—	—	—	—
Gross alpha	GrossA	CDV-37-1(i)	EPA:900	RAD	Tpf	4	0	pCi/L	—	—	—	—	-0.0968	-0.0836	-1.67	1.45
Gross beta	GrossB	CDV-37-1(i)	EPA:900	RAD	Tpf	4	1	pCi/L	5.24	5.24	5.24	5.24	0.39433333	0.158	-0.855	1.88
Hardness	Hardness	CDV-37-1(i)	SM:A2340B	Inorganic	Tpf	17	17	µg/L	32,894.118	32,700	30,300	36,000	—	—	—	—
Hexachlorobutadiene	87-68-3	CDV-37-1(i)	SW-846:8260B	VOC	Tpf	11	0	µg/L	—	—	—	—	0.68181818	1	0.3	1
HMX	2691-41-0	CDV-37-1(i)	SW-846:8321A_MOD, SW-846:8330B	LCMS/MS High Explosives	Tpf	11	0	µg/L	—	—	—	—	0.19171818	0.259	0.0842	0.325
Iron	Fe	CDV-37-1(i)	SW-846:6010B, SW-846:6010C	Inorganic	Tpf	17	5	µg/L	46.98	47.7	31	62.9	67.05	77.3	30	100
Lead	Pb	CDV-37-1(i)	SW-846:6020	Inorganic	Tpf	17	0	µg/L	—	—	—	—	1.55882353	2	0.5	2
Magnesium	Mg	CDV-37-1(i)	SW-846:6010B, SW-846:6010C	Inorganic	Tpf	17	17	µg/L	2297.0588	2290	2130	2570	—	—	—	—
Manganese	Mn	CDV-37-1(i)	SW-846:6010B, SW-846:6010C	Inorganic	Tpf	17	12	µg/L	10.159167	7.35	2.17	22.8	2	2	2	2
Mercury	Hg	CDV-37-1(i)	EPA:245.2	Inorganic	Tpf	26	0	µg/L	—	—	—	—	0.14884615	0.2	0.067	0.2
Methyl tert-butyl ether	1634-04-4	CDV-37-1(i)	SW-846:8260B	VOC	Tpf	11	0	µg/L	—	—	—	—	0.68181818	1	0.3	1
Methyl-2-pentanone[4-]	108-10-1	CDV-37-1(i)	SW-846:8260B	VOC	Tpf	11	0	µg/L	—	—	—	—	3.40909091	5	1.5	5
Methylene chloride	75-09-2	CDV-37-1(i)	SW-846:8260B	VOC	Tpf	11	0	µg/L	—	—	—	—	5.90909091	10	1	10
MNX	MNX	CDV-37-1(i)	SW-846:8321A_MOD, SW-846:8330B, SW-846:8330RDX	LCMS/MS High Explosives	Tpf	10	0	µg/L	—	—	—	—	0.20249	0.1773	0.0842	0.5
Molybdenum	Mo	CDV-37-1(i)	SW-846:6020	Inorganic	Tpf	17	15	µg/L	1.2908667	1.11	0.993	2.14	1.365	1.365	1.04	1.69
Nickel	Ni	CDV-37-1(i)	SW-846:6020	Inorganic	Tpf	17	17	µg/L	3.6258824	2.83	1.41	7.07	—	—	—	—
Nitrate-nitrite as nitrogen	NO3+NO2-N	CDV-37-1(i)	EPA:353.2	General Chemistry	Tpf	17	16	µg/L	134.84375	117	27.4	255	250	250	250	250
Nitrotoluene[2-]	88-72-2	CDV-37-1(i)	SW-846:8321A_MOD, SW-846:8330B	LCMS/MS High Explosives	Tpf	11	0	µg/L	—	—	—	—	0.1927	0.259	0.0863	0.325
Perchlorate	ClO4	CDV-37-1(i)	SW-846:6850	LCMS/MS Perchlorate	Tpf	16	16	µg/L	0.134625	0.127	0.108	0.257	—	—	—	—
Phenanthrene	85-01-8	CDV-37-1(i)	SW-846:8270C, SW-846:8270D, SW-846:8270DGCMS_SIM, SW-846:8310	SVOC	Tpf	5	0	µg/L	—	—	—	—	0.4932	0.521	0.103	1
Potassium	K	CDV-37-1(i)	SW-846:6010B, SW-846:6010C	Inorganic	Tpf	17	17	µg/L	509.17647	513	323	736	—	—	—	—
Pyrene	129-00-0	CDV-37-1(i)	SW-846:8270C, SW-846:8270D, SW-846:8270DGCMS_SIM, SW-846:8310	SVOC	Tpf	5	0	µg/L	—	—	—	—	0.30474	0.103	0.0521	1
Radium-226	Ra-226	CDV-37-1(i)	EPA:903.1	RAD	Tpf	1	0	pCi/L	—	—	—	—	0.0379	0.0379	0.0379	0.0379
Radium-228	Ra-228	CDV-37-1(i)	EPA:904	RAD	Tpf	1	1	pCi/L	2.66	2.66	2.66	2.66	—	—	—	—
RDX	121-82-4	CDV-37-1(i)	SW-846:8321A_MOD, SW-846:8330B	LCMS/MS High Explosives	Tpf	11	0	µg/L	—	—	—	—	0.19171818	0.259	0.0842	0.325

Table 4.2-1 (continued)

Parameter Name	Parameter Code	Well	Analytical Method	Analytical Method Category[a]	Geological Unit Code[a]	No. Samples	No. Detects	Unit	Mean Detect	Median Detect	Min Detect	Max Detect	Mean ND	Median ND	Min ND	Max ND
Selenium	Se	CDV-37-1(i)	SW-846:6020	Inorganic	Tpf	17	0	µg/L	—	—	—	—	4.11764706	5	2	5
Silicon dioxide	SiO2	CDV-37-1(i)	SW-846:6010B, SW-846:6010C	Inorganic	Tpf	17	17	µg/L	61,629.412	62,200	57,100	64,500	—	—	—	—
Silver	Ag	CDV-37-1(i)	SW-846:6020	Inorganic	Tpf	17	0	µg/L	—	—	—	—	0.79411765	1	0.3	1
Sodium	Na	CDV-37-1(i)	SW-846:6010B, SW-846:6010C	Inorganic	Tpf	17	17	µg/L	11,568.824	10,600	9480	15,100	—	—	—	—
Strontium	Sr	CDV-37-1(i)	SW-846:6010B, SW-846:6010C	Inorganic	Tpf	17	17	µg/L	48.6	49.2	45.6	51	—	—	—	—
Styrene	100-42-5	CDV-37-1(i)	SW-846:8260B	VOC	Tpf	11	0	µg/L	—	—	—	—	0.68181818	1	0.3	1
Sulfate	SO4(-2)	CDV-37-1(i)	EPA:300.0	General Chemistry	Tpf	17	17	µg/L	2505.2941	2050	1430	5130	—	—	—	—
Temperature	TEMP	CDV-37-1(i)	EPA:170.0	VOC	Tpf	10	10	deg C	2.6	2	2	4	—	—	—	—
Tetrachloroethene	127-18-4	CDV-37-1(i)	SW-846:8260B	VOC	Tpf	11	0	µg/L	—	—	—	—	0.68181818	1	0.3	1
Thallium	Tl	CDV-37-1(i)	SW-846:6020	Inorganic	Tpf	17	0	µg/L	—	—	—	—	1.31323529	1	0.325	2
Tin	Sn	CDV-37-1(i)	SW-846:6010B, SW-846:6010C	Inorganic	Tpf	17	0	µg/L	—	—	—	—	14.8529412	10	2.5	50
TNX	TNX	CDV-37-1(i)	SW-846:8321A_MOD, SW-846:8330B, SW-846:8330RDX	LCMS/MS High Explosives	Tpf	10	0	µg/L	—	—	—	—	0.20249	0.1773	0.0842	0.5
Toluene	108-88-3	CDV-37-1(i)	SW-846:8260B	VOC	Tpf	11	0	µg/L	—	—	—	—	0.68181818	1	0.3	1
Total dissolved solids	TDS	CDV-37-1(i)	EPA:160.1	General Chemistry	Tpf	17	17	µg/L	117,864.71	121,000	84,300	157,000	—	—	—	—
Total Kjeldahl nitrogen	TKN	CDV-37-1(i)	EPA:351.2	General Chemistry	Tpf	11	1	µg/L	61.6	61.6	61.6	61.6	77.36	89.8	33	162
Total organic carbon	TOC	CDV-37-1(i)	SW-846:9060	General Chemistry	Tpf	11	11	µg/L	697.63636	648	346	1160	—	—	—	—
Total phosphate as phosphorus	PO4-P	CDV-37-1(i)	EPA:365.4	General Chemistry	Tpf	17	4	µg/L	101.225	90.9	25.1	198	50.5615385	50	28	87
Trichlorobenzene[1,2,3-]	87-61-6	CDV-37-1(i)	SW-846:8260B	VOC	Tpf	11	0	µg/L	—	—	—	—	0.68181818	1	0.3	1
Trichloroethene	79-01-6	CDV-37-1(i)	SW-846:8260B	VOC	Tpf	11	0	µg/L	—	—	—	—	0.68181818	1	0.3	1
Trinitrobenzene[1,3,5-]	99-35-4	CDV-37-1(i)	SW-846:8321A_MOD, SW-846:8330B	LCMS/MS High Explosives	Tpf	11	0	µg/L	—	—	—	—	0.19171818	0.259	0.0842	0.325
Trinitrotoluene[2,4,6-]	118-96-7	CDV-37-1(i)	SW-846:8321A_MOD, SW-846:8330B	LCMS/MS High Explosives	Tpf	11	0	µg/L	—	—	—	—	0.19171818	0.259	0.0842	0.325
Tritium	H-3	CDV-37-1(i)	Generic:Low_Level_Tritium	RAD	Tpf	6	0	pCi/L	—	—	—	—	-0.0293333	0.022	-1.539	1.126
Uranium	U	CDV-37-1(i)	SW-846:6020	Inorganic	Tpf	17	16	µg/L	0.443	0.425	0.293	0.623	0.2	0.2	0.2	0.2
Uranium-234	U-234	CDV-37-1(i)	HASL-300:ISOU	RAD	Tpf	4	4	pCi/L	0.26375	0.265	0.243	0.282	—	—	—	—
Uranium-235/236	U-235/236	CDV-37-1(i)	HASL-300:ISOU	RAD	Tpf	4	0	pCi/L	—	—	—	—	0.0169725	0.0184	0.00569	0.0254
Uranium-238	U-238	CDV-37-1(i)	HASL-300:ISOU	RAD	Tpf	4	3	pCi/L	0.1586667	0.156	0.152	0.168	0.0763	0.0763	0.0763	0.0763
Vanadium	V	CDV-37-1(i)	SW-846:6010B, SW-846:6010C	Inorganic	Tpf	17	5	µg/L	1.534	1.49	1.26	1.79	3.33	4.105	1	5
Zinc	Zn	CDV-37-1(i)	SW-846:6010B, SW-846:6010C	Inorganic	Tpf	17	15	µg/L	11.643333	10.3	3.61	30.7	6.65	6.65	3.3	10
Acenaphthene	83-32-9	CDV-9-1(i)	SW-846:8270D, SW-846:8270DGCMS_SIM	SVOC	Tpf	9	0	µg/L	—	—	—	—	0.66011111	1	0.1	1.08
Acenaphthylene	208-96-8	CDV-9-1(i)	SW-846:8270D, SW-846:8270DGCMS_SIM	SVOC	Tpf	9	0	µg/L	—	—	—	—	0.66011111	1	0.1	1.08
Acetone	67-64-1	CDV-9-1(i)	SW-846:8260B	VOC	Tpf	12	2	µg/L	10.545	10.545	2.59	18.5	6.6	10	1.5	10
Acidity or alkalinity of a solution	pH	CDV-9-1(i)	EPA:150.1	General Chemistry	Tpf	12	12	SU	7.4575	7.38	7.23	7.83	—	—	—	—
Alkalinity-CO3	ALK-CO3	CDV-9-1(i)	EPA:310.1	General Chemistry	Tpf	12	0	µg/L	—	—	—	—	2020.83333	1450	1000	4000
Alkalinity-CO3+HCO3	ALK-CO3+HCO3	CDV-9-1(i)	EPA:310.1	General Chemistry	Tpf	12	12	µg/L	63,600	64,100	57,600	66,800	—	—	—	—

Table 4.2-1 (continued)

Parameter Name	Parameter Code	Well	Analytical Method	Analytical Method Category[a]	Geological Unit Code[a]	No. Samples	No. Detects	Unit	Mean Detect	Median Detect	Min Detect	Max Detect	Mean ND	Median ND	Min ND	Max ND
Aluminum	Al	CDV-9-1(i)	SW-846:6010C	Inorganic	Tpf	12	1	µg/L	189	189	189	189	140	200	68	200
Amino-2,6-dinitrotoluene[4-]	19406-51-0	CDV-9-1(i)	SW-846:8321A_MOD, SW-846:8330B	LCMS/MS High Explosives	Tpf	17	17	µg/L	0.3519412	0.306	0.199	0.769	—	—	—	—
Amino-4,6-dinitrotoluene[2-]	35572-78-2	CDV-9-1(i)	SW-846:8321A_MOD, SW-846:8330B	LCMS/MS High Explosives	Tpf	17	17	µg/L	0.3428824	0.34	0.29	0.47	—	—	—	—
Ammonia as nitrogen	NH3-N	CDV-9-1(i)	EPA:350.1	General Chemistry	Tpf	12	4	µg/L	49.85	51.4	33.4	63.2	92.5875	90.3	57.4	149
Anthracene	120-12-7	CDV-9-1(i)	SW-846:8270D, SW-846:8270DGCMS_SIM	SVOC	Tpf	9	0	µg/L	—	—	—	—	0.66011111	1	0.1	1.08
Antimony	Sb	CDV-9-1(i)	SW-846:6020	Inorganic	Tpf	12	0	µg/L	—	—	—	—	2.16666667	3	1	3
Arsenic	As	CDV-9-1(i)	SW-846:6020	Inorganic	Tpf	12	4	µg/L	2.26	2.125	2.01	2.78	3.865	5	1.92	5
Barium	Ba	CDV-9-1(i)	SW-846:6010C	Inorganic	Tpf	12	12	µg/L	4.9283333	4.98	2.94	7.07	—	—	—	—
Benzo(g,h,i)perylene	191-24-2	CDV-9-1(i)	SW-846:8270D, SW-846:8270DGCMS_SIM	SVOC	Tpf	9	0	µg/L	—	—	—	—	0.66011111	1	0.1	1.08
Benzoic acid	65-85-0	CDV-9-1(i)	SW-846:8270D	SVOC	Tpf	9	0	µg/L	—	—	—	—	15.0133333	20	6	21.5
Beryllium	Be	CDV-9-1(i)	SW-846:6010C	Inorganic	Tpf	12	0	µg/L	—	—	—	—	3.33333333	5	1	5
Bis(2-ethylhexyl)phthalate	117-81-7	CDV-9-1(i)	SW-846:8270D	SVOC	Tpf	9	0	µg/L	—	—	—	—	7.51222222	10	3	10.8
Boron	B	CDV-9-1(i)	SW-846:6010C	Inorganic	Tpf	12	10	µg/L	35.08	31.75	27.5	52.4	15	15	15	15
Bromide	Br(-1)	CDV-9-1(i)	EPA:300.0	General Chemistry	Tpf	12	11	µg/L	501.80909	164	74.5	2440	67	67	67	67
Bromodichloromethane	75-27-4	CDV-9-1(i)	SW-846:8260B	VOC	Tpf	12	0	µg/L	—	—	—	—	0.70833333	1	0.3	1
Bromoform	75-25-2	CDV-9-1(i)	SW-846:8260B	VOC	Tpf	12	0	µg/L	—	—	—	—	0.70833333	1	0.3	1
Butanone[2-]	78-93-3	CDV-9-1(i)	SW-846:8260B	VOC	Tpf	12	1	µg/L	4.35	4.35	4.35	4.35	3.40909091	5	1.5	5
Cadmium	Cd	CDV-9-1(i)	SW-846:6020	Inorganic	Tpf	12	0	µg/L	—	—	—	—	0.70833333	1	0.3	1
Calcium	Ca	CDV-9-1(i)	SW-846:6010C	Inorganic	Tpf	12	12	µg/L	13,489.167	13,950	8070	16,700	—	—	—	—
Carbon disulfide	75-15-0	CDV-9-1(i)	SW-846:8260B	VOC	Tpf	12	1	µg/L	1.5	1.5	1.5	1.5	3.40909091	5	1.5	5
Chloride	Cl(-1)	CDV-9-1(i)	EPA:300.0	General Chemistry	Tpf	12	12	µg/L	17,348.333	12,650	9130	66,500	—	—	—	—
Chlorobenzene	108-90-7	CDV-9-1(i)	SW-846:8260B	VOC	Tpf	12	0	µg/L	—	—	—	—	0.70833333	1	0.3	1
Chlorodibromomethane	124-48-1	CDV-9-1(i)	SW-846:8260B	VOC	Tpf	12	0	µg/L	—	—	—	—	0.70833333	1	0.3	1
Chloroform	67-66-3	CDV-9-1(i)	SW-846:8260B	VOC	Tpf	12	0	µg/L	—	—	—	—	0.70833333	1	0.3	1
Chloromethane	74-87-3	CDV-9-1(i)	SW-846:8260B	VOC	Tpf	12	0	µg/L	—	—	—	—	0.70833333	1	0.3	1
Chromium	Cr	CDV-9-1(i)	SW-846:6020	Inorganic	Tpf	12	2	µg/L	2.17	2.17	2.16	2.18	6.5	6.5	3	10
Cobalt	Co	CDV-9-1(i)	SW-846:6010C	Inorganic	Tpf	12	0	µg/L	—	—	—	—	3.38166667	5	1	5
Copper	Cu	CDV-9-1(i)	SW-846:6010C	Inorganic	Tpf	12	0	µg/L	—	—	—	—	7.08333333	10	3	10
Cyanide (total)	CN (Total)	CDV-9-1(i)	EPA:335.4	Inorganic	Tpf	12	0	µg/L	—	—	—	—	3.6125	5	1.67	5
DNX	DNX	CDV-9-1(i)	SW-846:8321A_MOD, SW-846:8330B	LCMS/MS High Explosives	Tpf	17	4	µg/L	0.11855	0.103	0.0892	0.179	0.15392308	0.087	0.0821	0.272
Fluoranthene	206-44-0	CDV-9-1(i)	SW-846:8270D, SW-846:8270DGCMS_SIM	SVOC	Tpf	9	0	µg/L	—	—	—	—	0.66011111	1	0.1	1.08
Fluoride	F(-1)	CDV-9-1(i)	EPA:300.0	General Chemistry	Tpf	12	12	µg/L	122.475	107	78.2	239	—	—	—	—
Gross alpha	GrossA	CDV-9-1(i)	EPA:900	RAD	Tpf	4	1	pCi/L	2.01	2.01	2.01	2.01	1.244	0.945	0.927	1.86
Gross beta	GrossB	CDV-9-1(i)	EPA:900	RAD	Tpf	4	1	pCi/L	2.83	2.83	2.83	2.83	0.68466667	0.875	-0.021	1.2
Hardness	Hardness	CDV-9-1(i)	SM:A2340B	Inorganic	Tpf	12	12	µg/L	51,416.667	53,500	31,700	62,900	—	—	—	—
Hexachlorobutadiene	87-68-3	CDV-9-1(i)	SW-846:8260B	VOC	Tpf	12	0	µg/L	—	—	—	—	0.7125	1	0.3	1

Table 4.2-1 (continued)

Parameter Name	Parameter Code	Well	Analytical Method	Analytical Method Category[a]	Geological Unit Code[a]	No. Samples	No. Detects	Unit	Mean Detect	Median Detect	Min Detect	Max Detect	Mean ND	Median ND	Min ND	Max ND
HMX	2691-41-0	CDV-9-1(i)	SW-846:8321A_MOD, SW-846:8330B	LCMS/MS High Explosives	Tpf	17	17	µg/L	1.4786471	1.3	0.728	3.46	—	—	—	—
Iron	Fe	CDV-9-1(i)	SW-846:6010C	Inorganic	Tpf	12	2	µg/L	88.4	88.4	50.8	126	65	65	30	100
Lead	Pb	CDV-9-1(i)	SW-846:6020	Inorganic	Tpf	12	0	µg/L	—	—	—	—	1.375	2	0.5	2
Magnesium	Mg	CDV-9-1(i)	SW-846:6010C	Inorganic	Tpf	12	12	µg/L	4368.3333	4550	2820	5130	—	—	—	—
Manganese	Mn	CDV-9-1(i)	SW-846:6010C	Inorganic	Tpf	12	4	µg/L	4.9325	4.22	2.79	8.5	5	2	2	10
Mercury	Hg	CDV-9-1(i)	EPA:245.2	Inorganic	Tpf	24	0	µg/L	—	—	—	—	0.14458333	0.2	0.067	0.2
Methyl tert-butyl ether	1634-04-4	CDV-9-1(i)	SW-846:8260B	VOC	Tpf	12	11	µg/L	0.81	0.82	0.36	1.24	0.3	0.3	0.3	0.3
Methyl-2-pentanone[4-]	108-10-1	CDV-9-1(i)	SW-846:8260B	VOC	Tpf	12	0	µg/L	—	—	—	—	3.54166667	5	1.5	5
Methylene chloride	75-09-2	CDV-9-1(i)	SW-846:8260B	VOC	Tpf	12	0	µg/L	—	—	—	—	5.54833333	5.755	1	10
MNX	MNX	CDV-9-1(i)	SW-846:8321A_MOD, SW-846:8330B	LCMS/MS High Explosives	Tpf	17	14	µg/L	0.1700857	0.1465	0.0852	0.414	0.08573333	0.086	0.0842	0.087
Molybdenum	Mo	CDV-9-1(i)	SW-846:6020	Inorganic	Tpf	12	12	µg/L	1.15	0.948	0.844	2.23	—	—	—	—
Nickel	Ni	CDV-9-1(i)	SW-846:6020	Inorganic	Tpf	12	8	µg/L	0.756125	0.69	0.547	1.17	0.95	0.6	0.6	2
Nitrate-nitrite as nitrogen	NO3+NO2-N	CDV-9-1(i)	EPA:353.2	General Chemistry	Tpf	12	12	µg/L	1133.0833	1080	945	1650	—	—	—	—
Nitrotoluene[2-]	88-72-2	CDV-9-1(i)	SW-846:8321A_MOD, SW-846:8330B	LCMS/MS High Explosives	Tpf	17	2	µg/L	0.10755	0.1076	0.0941	0.121	0.14530667	0.0882	0.0841	0.272
Oxygen-18/oxygen-16 ratio from Nitrate	O18O16-NO3	CDV-9-1(i)	Generic:Oxygen Isotope Ratio	General Chemistry	Tpf	2	2	permil	3.8822	3.8822	3.775	3.9894	—	—	—	—
Perchlorate	ClO4	CDV-9-1(i)	SW-846:6850	LCMS/MS Perchlorate	Tpf	12	12	µg/L	0.4519167	0.4365	0.404	0.532	—	—	—	—
Perfluorooctanoic acid	335-67-1	CDV-9-1(i)	EPA:537M	LCMS/MS PFAS	Tpf	1	1	µg/L	0.00217	0.0022	0.0022	0.0022	—	—	—	—
Phenanthrene	85-01-8	CDV-9-1(i)	SW-846:8270D, SW-846:8270DGCMS_SIM	SVOC	Tpf	9	0	µg/L	—	—	—	—	0.66011111	1	0.1	1.08
Potassium	K	CDV-9-1(i)	SW-846:6010C	Inorganic	Tpf	12	12	µg/L	1755.8333	1835	1020	2220	—	—	—	—
Pyrene	129-00-0	CDV-9-1(i)	SW-846:8270D, SW-846:8270DGCMS_SIM	SVOC	Tpf	9	0	µg/L	—	—	—	—	0.66011111	1	0.1	1.08
RDX	121-82-4	CDV-9-1(i)	SW-846:8321A_MOD, SW-846:8330B	LCMS/MS High Explosives	Tpf	17	17	µg/L	19.742941	18.1	8.03	37.3	—	—	—	—
Selenium	Se	CDV-9-1(i)	SW-846:6020	Inorganic	Tpf	12	1	µg/L	3.76	3.76	3.76	3.76	3.63636364	5	2	5
Silicon dioxide	SiO2	CDV-9-1(i)	SW-846:6010C	Inorganic	Tpf	12	12	µg/L	47,483.333	46,950	44,300	51,400	—	—	—	—
Silver	Ag	CDV-9-1(i)	SW-846:6020	Inorganic	Tpf	12	0	µg/L	—	—	—	—	0.70833333	1	0.3	1
Sodium	Na	CDV-9-1(i)	SW-846:6010C	Inorganic	Tpf	12	12	µg/L	17,633.333	17,200	13,200	23,800	—	—	—	—
Strontium	Sr	CDV-9-1(i)	SW-846:6010C	Inorganic	Tpf	12	12	µg/L	82.058333	86.5	47.7	104	—	—	—	—
Styrene	100-42-5	CDV-9-1(i)	SW-846:8260B	VOC	Tpf	12	0	µg/L	—	—	—	—	0.70833333	1	0.3	1
Sulfate	SO4(-2)	CDV-9-1(i)	EPA:300.0	General Chemistry	Tpf	12	12	µg/L	7625.8333	7525	6470	9490	—	—	—	—
Temperature	TEMP	CDV-9-1(i)	EPA:170.0	VOC	Tpf	18	18	deg C	2.7611111	3	1	5	—	—	—	—
Tetrachloroethene	127-18-4	CDV-9-1(i)	SW-846:8260B	VOC	Tpf	12	12	µg/L	1.0816667	1.065	0.87	1.35	—	—	—	—
Thallium	Tl	CDV-9-1(i)	SW-846:6020	Inorganic	Tpf	12	0	µg/L	—	—	—	—	1.41666667	2	0.6	2
Tin	Sn	CDV-9-1(i)	SW-846:6010C	Inorganic	Tpf	12	1	µg/L	3.18	3.18	3.18	3.18	7.41818182	10	2.5	10
TNX	TNX	CDV-9-1(i)	SW-846:8321A_MOD, SW-846:8330B	LCMS/MS High Explosives	Tpf	16	5	µg/L	0.16986	0.126	0.0863	0.35	0.11863636	0.086	0.0821	0.272

Table 4.2-1 (continued)

Parameter Name	Parameter Code	Well	Analytical Method	Analytical Method Category[a]	Geological Unit Code[a]	No. Samples	No. Detects	Unit	Mean Detect	Median Detect	Min Detect	Max Detect	Mean ND	Median ND	Min ND	Max ND
Toluene	108-88-3	CDV-9-1(i)	SW-846:8260B	VOC	Tpf	12	1	µg/L	0.85	0.85	0.85	0.85	0.68181818	1	0.3	1
Total dissolved solids	TDS	CDV-9-1(i)	EPA:160.1	General Chemistry	Tpf	12	12	µg/L	13,3916.67	130,500	117,000	166,000	—	—	—	—
Total Kjeldahl nitrogen	TKN	CDV-9-1(i)	EPA:351.2	General Chemistry	Tpf	12	3	µg/L	97.033333	112	37.1	142	95.8444444	100	33	169
Total organic carbon	TOC	CDV-9-1(i)	SW-846:9060	General Chemistry	Tpf	12	11	µg/L	1147.2727	1030	534	2300	1010	1010	1010	1010
Total Phosphate as phosphorus	PO4-P	CDV-9-1(i)	EPA:365.4	General Chemistry	Tpf	12	6	µg/L	56.716667	54.9	30.5	99.2	56.7333333	52.6	40.4	93.9
Trichlorobenzene[1,2,3-]	87-61-6	CDV-9-1(i)	SW-846:8260B	VOC	Tpf	12	0	µg/L	—	—	—	—	0.70833333	1	0.3	1
Trichloroethene	79-01-6	CDV-9-1(i)	SW-846:8260B	VOC	Tpf	12	12	µg/L	0.5083333	0.505	0.31	0.74	—	—	—	—
Trinitrobenzene[1,3,5-]	99-35-4	CDV-9-1(i)	SW-846:8321A_MOD, SW-846:8330B	LCMS/MS High Explosives	Tpf	17	0	µg/L	—	—	—	—	0.15855882	0.087	0.0821	0.272
Trinitrotoluene[2,4,6-]	118-96-7	CDV-9-1(i)	SW-846:8321A_MOD, SW-846:8330B	LCMS/MS High Explosives	Tpf	17	6	µg/L	0.1235833	0.1063	0.0897	0.209	0.18189091	0.254	0.0825	0.272
Tritium	H-3	CDV-9-1(i)	Generic:Low_Level_Tritium	RAD	Tpf	6	6	pCi/L	14.295167	15.592	7.472	16.423	—	—	—	—
Uranium	U	CDV-9-1(i)	SW-846:6020	Inorganic	Tpf	12	11	µg/L	0.7576364	0.739	0.526	0.967	0.624	0.624	0.624	0.624
Uranium-234	U-234	CDV-9-1(i)	HASL-300:ISOU	RAD	Tpf	4	4	pCi/L	0.56575	0.5445	0.49	0.684	—	—	—	—
Uranium-235/236	U-235/236	CDV-9-1(i)	HASL-300:ISOU	RAD	Tpf	4	0	pCi/L	—	—	—	—	0.0346	0.0344	0.0255	0.0441
Uranium-238	U-238	CDV-9-1(i)	HASL-300:ISOU	RAD	Tpf	4	4	pCi/L	0.32675	0.3245	0.252	0.406	—	—	—	—
Vanadium	V	CDV-9-1(i)	SW-846:6010C	Inorganic	Tpf	12	12	µg/L	1.8083333	1.79	1.11	2.71	—	—	—	—
Zinc	Zn	CDV-9-1(i)	SW-846:6010C	Inorganic	Tpf	12	7	µg/L	5.1857143	4.77	3.49	7.83	10	10	10	10
Acenaphthene	83-32-9	PCI-2	SW-846:8270C, SW-846:8270D, SW-846:8270DGCMS_SIM, SW-846:8310	SVOC	Tpf	14	0	µg/L	—	—	—	—	0.57207143	0.5075	0.1	1
Acenaphthylene	208-96-8	PCI-2	SW-846:8270C, SW-846:8270D, SW_846:8270DGCMS_SIM, SW-846:8310	SVOC	Tpf	14	0	µg/L	—	—	—	—	0.57207143	0.5075	0.1	1
Acetone	67-64-1	PCI-2	SW-846:8260B	VOC	Tpf	14	1	µg/L	2.99	2.99	2.99	2.99	7.38461538	10	1.5	10
Acidity or Alkalinity of a solution	pH	PCI-2	EPA:150.1	General Chemistry	Tpf	23	23	SU	7.5552174	7.53	7.2	7.86	—	—	—	—
Alkalinity-CO3	ALK-CO3	PCI-2	EPA:310.1	General Chemistry	Tpf	23	0	µg/L	—	—	—	—	1358.69565	1000	1000	4000
Alkalinity-CO3+HCO3	ALK-CO3+HCO3	PCI-2	EPA:310.1	General Chemistry	Tpf	23	23	µg/L	51,139.13	51,600	44,000	55,000	—	—	—	—
Aluminum	Al	PCI-2	SW-846:6010B, SW-846:6010C	Inorganic	Tpf	22	0	µg/L	—	—	—	—	176.681818	200	68	215
Amino-2,6-dinitrotoluene[4-]	19406-51-0	PCI-2	SW-846:8321A_MOD, SW-846:8330B	LCMS/MS High Explosives	Tpf	11	0	µg/L	—	—	—	—	0.19828182	0.265	0.0851	0.278
Amino-4,6-dinitrotoluene[2-]	35572-78-2	PCI-2	SW-846:8321A_MOD, SW-846:8330B	LCMS/MS High Explosives	Tpf	11	0	µg/L	—	—	—	—	0.19828182	0.265	0.0851	0.278
Ammonia as nitrogen	NH3-N	PCI-2	EPA:350.1	General Chemistry	Tpf	22	8	µg/L	66.025	60.3	18.2	127	40.8142857	48.4	17	50
Anthracene	120-12-7	PCI-2	SW-846:8270C, SW-846:8270D, SW-846:8270DGCMS_SIM, SW-846:8310	SVOC	Tpf	14	0	µg/L	—	—	—	—	0.57207143	0.5075	0.1	1
Antimony	Sb	PCI-2	SW-846:6020, SW-846:6020B	Inorganic	Tpf	22	0	µg/L	—	—	—	—	2.5	3	1	3
Arsenic	As	PCI-2	SW-846:6020, SW-846:6020B	Inorganic	Tpf	22	5	µg/L	2.454	2.4	1.96	3.04	4.64705882	5	2	5
Barium	Ba	PCI-2	SW-846:6010B, SW-846:6010C	Inorganic	Tpf	22	22	µg/L	5.4286364	4.25	3.3	19.8	—	—	—	—
Benzo(g,h,i)perylene	191-24-2	PCI-2	SW-846:8270C, SW-846:8270D, SW-846:8270DGCMS_SIM, SW-846:8310	SVOC	Tpf	14	1	µg/L	0.0301	0.0301	0.0301	0.0301	0.5365	0.309	0.0515	1

Table 4.2-1 (continued)

Parameter Name	Parameter Code	Well	Analytical Method	Analytical Method Category[a]	Geological Unit Code[a]	No. Samples	No. Detects	Unit	Mean Detect	Median Detect	Min Detect	Max Detect	Mean ND	Median ND	Min ND	Max ND
Benzoic acid	65-85-0	PCI-2	SW-846:8270C, SW-846:8270D	SVOC	Tpf	14	0	µg/L	—	—	—	—	13.4757143	13	6	21.1
Beryllium	Be	PCI-2	SW-846:6010B, SW-846:6010C	Inorganic	Tpf	22	0	µg/L	—	—	—	—	4.09090909	5	1	5
Bis(2-ethylhexyl)phthalate	117-81-7	PCI-2	SW-846:8270C, SW-846:8270D	SVOC	Tpf	14	0	µg/L	—	—	—	—	5.94835714	6.5	0.3	10.5
Boron	B	PCI-2	SW-846:6010B, SW-846:6010C	Inorganic	Tpf	22	1	µg/L	16.9	16.9	16.9	16.9	41.6666667	50	15	50
Bromide	Br(-1)	PCI-2	EPA:300.0	General Chemistry	Tpf	23	0	µg/L	—	—	—	—	171.086957	200	67	200
Bromodichloromethane	75-27-4	PCI-2	SW-846:8260B	VOC	Tpf	14	0	µg/L	—	—	—	—	0.75	1	0.3	1
Bromoform	75-25-2	PCI-2	SW-846:8260B	VOC	Tpf	14	0	µg/L	—	—	—	—	0.75	1	0.3	1
Butanone[2-]	78-93-3	PCI-2	SW-846:8260B	VOC	Tpf	14	0	µg/L	—	—	—	—	3.75	5	1.5	5
Cadmium	Cd	PCI-2	SW-846:6020, SW-846:6020B	Inorganic	Tpf	22	0	µg/L	—	—	—	—	0.84090909	1	0.3	1
Calcium	Ca	PCI-2	SW-846:6010B, SW-846:6010C	Inorganic	Tpf	22	22	µg/L	8790.4545	8890	8060	9450	—	—	—	—
Carbon Disulfide	75-15-0	PCI-2	SW-846:8260B	VOC	Tpf	14	0	µg/L	—	—	—	—	3.75	5	1.5	5
Chloride	Cl(-1)	PCI-2	EPA:300.0	General Chemistry	Tpf	23	23	µg/L	1390.4783	1420	341	1690	—	—	—	—
Chlorobenzene	108-90-7	PCI-2	SW-846:8260B	VOC	Tpf	14	0	µg/L	—	—	—	—	0.75	1	0.3	1
Chlorodibromomethane	124-48-1	PCI-2	SW-846:8260B	VOC	Tpf	14	0	µg/L	—	—	—	—	0.75	1	0.3	1
Chloroform	67-66-3	PCI-2	SW-846:8260B	VOC	Tpf	14	0	µg/L	—	—	—	—	0.75	1	0.3	1
Chloromethane	74-87-3	PCI-2	SW-846:8260B	VOC	Tpf	14	0	µg/L	—	—	—	—	0.75	1	0.3	1
Chromium	Cr	PCI-2	SW-846:6020, SW-846:6020B	Inorganic	Tpf	22	0	µg/L	—	—	—	—	7.64318182	10	3	10
Cobalt	Co	PCI-2	SW-846:6010B, SW-846:6010C	Inorganic	Tpf	22	1	µg/L	1.99	1.99	1.99	1.99	4.04761905	5	1	5
Copper	Cu	PCI-2	SW-846:6010B, SW-846:6010C	Inorganic	Tpf	22	0	µg/L	—	—	—	—	8.40909091	10	3	10
Cyanide (total)	CN (Total)	PCI-2	EPA:335.3, EPA:335.4	Inorganic	Tpf	14	0	µg/L	—	—	—	—	3.81071429	5	1.67	5
DNX	DNX	PCI-2	SW-846:8321A_MOD	LCMS/MS High Explosives	Tpf	2	0	µg/L	—	—	—	—	0.2665	0.2665	0.266	0.267
Fluoranthene	206-44-0	PCI-2	SW-846:8270C, SW-846:8270D, SW-846:8270DGCMS_SIM, SW-846:8310	SVOC	Tpf	14	0	µg/L	—	—	—	—	0.50225714	0.3085	0.0515	1
Fluoride	F(-1)	PCI-2	EPA:300.0	General Chemistry	Tpf	23	23	µg/L	186.00435	181	91.1	379	—	—	—	—
Gross alpha	GrossA	PCI-2	EPA:900	RAD	Tpf	10	0	pCi/L	—	—	—	—	0.47422	0.4645	-1.33	1.96
Gross beta	GrossB	PCI-2	EPA:900	RAD	Tpf	10	1	pCi/L	8.05	8.05	8.05	8.05	0.91784444	0.693	-0.29	2.28
Gross gamma	GrossG	PCI-2	EPA:901.1	RAD	Tpf	2	0	pCi/L	—	—	—	—	22.3	22.3	21.9	22.7
Hardness	Hardness	PCI-2	SM:A2340B	Inorganic	Tpf	22	22	µg/L	31,013.636	31,300	29,300	33,200	—	—	—	—
Hexachlorobutadiene	87-68-3	PCI-2	SW-846:8260B	VOC	Tpf	14	0	µg/L	—	—	—	—	0.75	1	0.3	1
HMX	2691-41-0	PCI-2	SW-846:8321A_MOD, SW-846:8330B	LCMS/MS High Explosives	Tpf	11	0	µg/L	—	—	—	—	0.19828182	0.265	0.0851	0.278
Iron	Fe	PCI-2	SW-846:6010B, SW-846:6010C	Inorganic	Tpf	22	2	µg/L	45.4	45.4	33.2	57.6	85.79	100	30	100
Lead	Pb	PCI-2	SW-846:6020, SW-846:6020B	Inorganic	Tpf	22	0	µg/L	—	—	—	—	1.65909091	2	0.5	2
Magnesium	Mg	PCI-2	SW-846:6010B, SW-846:6010C	Inorganic	Tpf	22	22	µg/L	2203.6364	2225	2010	2370	—	—	—	—
Manganese	Mn	PCI-2	SW-846:6010B, SW-846:6010C	Inorganic	Tpf	22	6	µg/L	6.22	4.87	2.09	11.5	7.5	10	2	10
Mercury	Hg	PCI-2	EPA:245.2, SW-846:7470A	Inorganic	Tpf	34	0	µg/L	—	—	—	—	0.16182353	0.2	0.067	0.2
Methyl tert-butyl ether	1634-04-4	PCI-2	SW-846:8260B	VOC	Tpf	14	0	µg/L	—	—	—	—	0.75	1	0.3	1
Methyl-2-pentanone[4-]	108-10-1	PCI-2	SW-846:8260B	VOC	Tpf	14	0	µg/L	—	—	—	—	3.75	5	1.5	5

Table 4.2-1 (continued)

Parameter Name	Parameter Code	Well	Analytical Method	Analytical Method Category[a]	Geological Unit Code[a]	No. Samples	No. Detects	Unit	Mean Detect	Median Detect	Min Detect	Max Detect	Mean ND	Median ND	Min ND	Max ND
Methylene chloride	75-09-2	PCI-2	SW-846:8260B	VOC	Tpf	14	0	µg/L	—	—	—	—	6.79642857	10	1	10
MNX	MNX	PCI-2	SW-846:8321A_MOD	LCMS/MS High Explosives	Tpf	2	0	µg/L	—	—	—	—	0.2665	0.2665	0.266	0.267
Molybdenum	Mo	PCI-2	SW-846:6020, SW-846:6020B	Inorganic	Tpf	22	21	µg/L	1.007381	1.03	0.829	1.2	1.3	1.3	1.3	1.3
Nickel	Ni	PCI-2	SW-846:6020, SW-846:6020B	Inorganic	Tpf	22	10	µg/L	0.8044	0.6835	0.502	1.8	1.43408333	2	0.6	2
Nitrate-nitrite as nitrogen	NO3+NO2-N	PCI-2	EPA:353.2	General Chemistry	Tpf	22	21	µg/L	121.04762	117	67	178	50	50	50	50
Nitrotoluene[2-]	88-72-2	PCI-2	SW-846:8321A_MOD, SW-846:8330B	LCMS/MS High Explosives	Tpf	11	0	µg/L	—	—	—	—	0.19905455	0.265	0.0872	0.278
Perchlorate	ClO4	PCI-2	SW-846:6850	LCMS/MS Perchlorate	Tpf	22	22	µg/L	0.1756818	0.1765	0.145	0.202	—	—	—	—
Perfluorooctanoic acid	335-67-1	PCI-2	EPA:537M	LCMS/MS PFAS	Tpf	1	0	µg/L	—	—	—	—	0.000643	0.00064	0.00064	0.00064
Phenanthrene	85-01-8	PCI-2	SW-846:8270C, SW-846:8270D, SW-846:8270DGCMS_SIM, SW-846:8310	SVOC	Tpf	14	0	µg/L	—	—	—	—	0.57207143	0.5075	0.1	1
Potassium	K	PCI-2	SW-846:6010B, SW-846:6010C	Inorganic	Tpf	22	22	µg/L	312.68182	314.5	165	444	—	—	—	—
Pyrene	129-00-0	PCI-2	SW-846:8270C, SW-846:8270D, SW-846:8270DGCMS_SIM, SW-846:8310	SVOC	Tpf	14	0	µg/L	—	—	—	—	0.50225714	0.3085	0.0515	1
RDX	121-82-4	PCI-2	SW-846:8321A_MOD, SW-846:8330B	LCMS/MS High Explosives	Tpf	11	0	µg/L	—	—	—	—	0.19828182	0.265	0.0851	0.278
Selenium	Se	PCI-2	SW-846:6020, SW-846:6020B	Inorganic	Tpf	22	0	µg/L	—	—	—	—	4.13909091	5	1.06	5
Silicon dioxide	SiO2	PCI-2	SW-846:6010B, SW-846:6010C	Inorganic	Tpf	23	23	µg/L	69,234.783	69,100	61,000	76,500	—	—	—	—
Silver	Ag	PCI-2	SW-846:6020, SW-846:6020B	Inorganic	Tpf	22	1	µg/L	0.108	0.108	0.108	0.108	0.83333333	1	0.3	1
Sodium	Na	PCI-2	SW-846:6010B, SW-846:6010C	Inorganic	Tpf	22	22	µg/L	11,713.636	11,500	10,700	14,000	—	—	—	—
Strontium	Sr	PCI-2	SW-846:6010B, SW-846:6010C	Inorganic	Tpf	22	22	µg/L	48.368182	48.1	44.4	67.8	—	—	—	—
Styrene	100-42-5	PCI-2	SW-846:8260B	VOC	Tpf	14	0	µg/L	—	—	—	—	0.75	1	0.3	1
Sulfate	SO4(-2)	PCI-2	EPA:300.0	General Chemistry	Tpf	23	22	µg/L	1617.5455	1680	576	1790	1670	1670	1670	1670
Temperature	TEMP	PCI-2	EPA:170.0	VOC	Tpf	12	12	deg C	2.5	2	2	4	—	—	—	—
Tetrachloroethene	127-18-4	PCI-2	SW-846:8260B	VOC	Tpf	14	0	µg/L	—	—	—	—	0.75	1	0.3	1
Thallium	Tl	PCI-2	SW-846:6020, SW-846:6020B	Inorganic	Tpf	22	1	µg/L	0.354	0.354	0.354	0.354	1.34909524	1	0.331	2
Tin	Sn	PCI-2	SW-846:6010B, SW-846:6010C	Inorganic	Tpf	22	0	µg/L	—	—	—	—	16.0227273	10	2.5	100
TNX	TNX	PCI-2	SW-846:8321A_MOD	LCMS/MS High Explosives	Tpf	2	0	µg/L	—	—	—	—	0.2665	0.2665	0.266	0.267
Toluene	108-88-3	PCI-2	SW-846:8260B	VOC	Tpf	14	0	µg/L	—	—	—	—	0.75	1	0.3	1
Total dissolved solids	TDS	PCI-2	EPA:160.1	General Chemistry	Tpf	23	23	µg/L	114,304.35	120,000	67,100	134,000	—	—	—	—
Total Kjeldahl nitrogen	TKN	PCI-2	EPA:351.2	General Chemistry	Tpf	15	3	µg/L	119.93333	106	49.8	204	77.6666667	100	33	100
Total organic carbon	TOC	PCI-2	SW-846:9060, SW-846:9060A	General Chemistry	Tpf	15	9	µg/L	467.33333	454	337	852	698.333333	765	330	1000
Total phosphate as phosphorus	PO4-P	PCI-2	EPA:365.4	General Chemistry	Tpf	23	4	µg/L	79.7	43.65	27.5	204	42.6736842	49	20	84.2
Trichlorobenzene[1,2,3-]	87-61-6	PCI-2	SW-846:8260B	VOC	Tpf	14	0	µg/L	—	—	—	—	0.75	1	0.3	1
Trichloroethene	79-01-6	PCI-2	SW-846:8260B	VOC	Tpf	14	0	µg/L	—	—	—	—	0.75	1	0.3	1
Trinitrobenzene[1,3,5-]	99-35-4	PCI-2	SW-846:8321A_MOD, SW-846:8330B	LCMS/MS High Explosives	Tpf	11	0	µg/L	—	—	—	—	0.19828182	0.265	0.0851	0.278

Table 4.2-1 (continued)

Parameter Name	Parameter Code	Well	Analytical Method	Analytical Method Category[a]	Geological Unit Code[a]	No. Samples	No. Detects	Unit	Mean Detect	Median Detect	Min Detect	Max Detect	Mean ND	Median ND	Min ND	Max ND
Trinitrotoluene[2,4,6-]	118-96-7	PCI-2	SW-846:8321A_MOD, SW-846:8330B	LCMS/MS High Explosives	Tpf	11	0	µg/L	—	—	—	—	0.19828182	0.265	0.0851	0.278
Tritium	H-3	PCI-2	Generic:Low_Level_Tritium	RAD	Tpf	5	0	pCi/L	—	—	—	—	-0.8984	0.694	-8.284	1.82
Uranium	U	PCI-2	SW-846:6020, SW-846:6020B	Inorganic	Tpf	22	19	µg/L	0.3432105	0.334	0.285	0.576	0.33066667	0.332	0.309	0.351
Uranium-234	U-234	PCI-2	HASL-300:ISOU	RAD	Tpf	10	10	pCi/L	0.2198	0.2215	0.144	0.288	—	—	—	—
Uranium-235/236	U-235/236	PCI-2	HASL-300:ISOU	RAD	Tpf	10	1	pCi/L	0.0547	0.0547	0.0547	0.0547	0.01407556	0.0105	0	0.0578
Uranium-238	U-238	PCI-2	HASL-300:ISOU	RAD	Tpf	10	9	pCi/L	0.1222333	0.124	0.0921	0.161	0.0816	0.0816	0.0816	0.0816
Vanadium	V	PCI-2	SW-846:6010B, SW-846:6010C	Inorganic	Tpf	22	20	µg/L	1.4305	1.42	1.14	1.78	4.135	4.135	3.27	5
Zinc	Zn	PCI-2	SW-846:6010B, SW-846:6010C	Inorganic	Tpf	22	7	µg/L	4.3328571	4.25	2.6	5.45	9.10666667	10	3.3	10
Acenaphthene	83-32-9	R-19	SW-846:8270, SW-846:8270C, SW-846:8270D, SW-846:8310	SVOC	Tp	8	1	µg/L	0.18	0.18	0.18	0.18	5.05671429	1	0.315	11
Acenaphthylene	208-96-8	R-19	SW-846:8270, SW-846:8270C, SW-846:8270D, SW-846:8310	SVOC	Tp	8	1	µg/L	0.16	0.16	0.16	0.16	5.05671429	1	0.315	11
Acetone	67-64-1	R-19	SW-846:8260, SW-846:8260B	VOC	Tp	9	1	µg/L	3.1	3.1	3.1	3.1	15.91375	10	2.31	30
Acidity or alkalinity of a solution	pH	R-19	EPA:150.1	General Chemistry	Tp	17	17	SU	8.1505882	8.32	6.23	8.79	—	—	—	—
Alkalinity-CO3	ALK-CO3	R-19	EPA:310.1	General Chemistry	Tp	17	7	µg/L	2634.2857	2120	1070	5230	1135	1000	1000	1450
Alkalinity-CO3+HCO3	ALK-CO3+HCO3	R-19	EPA:310.1	General Chemistry	Tp	17	17	µg/L	73,600	74,300	68,300	80,200	—	—	—	—
Alkalinity-HCO3	ALK-HCO3	R-19	EPA:310.1	General Chemistry	Tp	2	2	µg/L	67,900	67,900	67,200	68,600	—	—	—	—
Aluminum	Al	R-19	SW-846:6010B, SW-846:6010C	Inorganic	Tp	21	1	µg/L	217	217	217	217	176.9	200	68	200
Amino-2,6-dinitrotoluene[4-]	19406-51-0	R-19	SW-846:8330, SW-846:8321A_MOD, SW-846:8330B, SW-846:8321A(M)	HEXP, LCMS/MS High Explosives, LCMS/MS Perchlorate	Tp	14	0	µg/L	—	—	—	—	0.21904286	0.258	0.0846	0.325
Amino-4,6-dinitrotoluene[2-]	35572-78-2	R-19	SW-846:8330, SW-846:8321A_MOD, SW-846:8330B, SW-846:8321A(M)	HEXP, LCMS/MS High Explosives, LCMS/MS Perchlorate	Tp	14	0	µg/L	—	—	—	—	0.23068571	0.2785	0.0846	0.325
Ammonia as nitrogen	NH3-N	R-19	EPA:350.1	General Chemistry	Tp	15	5	µg/L	42.88	39	31.7	58	49.45	50	24	80
Anthracene	120-12-7	R-19	SW-846:8270, SW-846:8270C, SW-846:8270D, SW-846:8310	SVOC	Tp	8	1	µg/L	0.2	0.2	0.2	0.2	5.05671429	1	0.315	11
Antimony	Sb	R-19	SW-846:6020	Inorganic	Tp	22	0	µg/L	—	—	—	—	2.11636364	2	0.28	3
Arsenic	As	R-19	SW-846:6010B, SW-846:6020	Inorganic	Tp	22	1	µg/L	2.14	2.14	2.14	2.14	4.53238095	5	2	6
Barium	Ba	R-19	SW-846:6010B, SW-846:6010C	Inorganic	Tp	22	22	µg/L	25.090909	25	22.4	28.2	—	—	—	—
Benzo(g,h,i)perylene	191-24-2	R-19	SW-846:8270, SW-846:8270C, SW-846:8270D, SW-846:8310	SVOC	Tp	8	0	µg/L	—	—	—	—	4.4529	1.1	0.0526	11
Benzoic acid	65-85-0	R-19	SW-846:8270, SW-846:8270C, SW-846:8270D	SVOC	Tp	6	0	µg/L	—	—	—	—	35.8683333	38.75	6.31	56
Beryllium	Be	R-19	SW-846:6010B, SW-846:6010C	Inorganic	Tp	22	0	µg/L	—	—	—	—	4.01436364	5	0.158	5
Bis(2-ethylhexyl)phthalate	117-81-7	R-19	SW-846:8270, SW-846:8270C, SW-846:8270D	SVOC	Tp	6	2	µg/L	0.39	0.39	0.17	0.61	8.675	11	1.7	11
Bismuth-214	Bi-214	R-19	EPA:901.1, Generic:Gamma Spec.	RAD	Tp	4	0	pCi/L	—	—	—	—	4.5875	4.175	3	7
Boron	B	R-19	SW-846:6010B, SW-846:6010C	Inorganic	Tp	22	11	µg/L	16.027273	15.2	12.7	20.9	50	50	50	50
Bromide	Br(-1)	R-19	EPA:300.0	General Chemistry	Tp	15	0	µg/L	—	—	—	—	180.533333	200	41	200

Table 4.2-1 (continued)

Parameter Name	Parameter Code	Well	Analytical Method	Analytical Method Category[a]	Geological Unit Code[a]	No. Samples	No. Detects	Unit	Mean Detect	Median Detect	Min Detect	Max Detect	Mean ND	Median ND	Min ND	Max ND
Bromodichloromethane	75-27-4	R-19	SW-846:8260, SW-846:8260B	VOC	Tp	9	0	µg/L	—	—	—	—	2.25555556	1	0.3	5
Bromoform	75-25-2	R-19	SW-846:8260, SW-846:8260B	VOC	Tp	9	0	µg/L	—	—	—	—	2.25555556	1	0.3	5
Butanone[2-]	78-93-3	R-19	SW-846:8260, SW-846:8260B	VOC	Tp	9	0	µg/L	—	—	—	—	9.61111111	5	1.5	20
Cadmium	Cd	R-19	SW-846:6020	Inorganic	Tp	22	1	µg/L	0.156	0.156	0.156	0.156	0.78952381	1	0.04	1
Calcium	Ca	R-19	SW-846:6010B, SW-846:6010C	Inorganic	Tp	22	22	µg/L	16,390.909	16,500	14,600	17,700	—	—	—	—
Carbon Disulfide	75-15-0	R-19	SW-846:8260, SW-846:8260B	VOC	Tp	9	0	µg/L	—	—	—	—	4.61111111	5	1.5	5
Chloride	Cl(-1)	R-19	EPA:300.0	General Chemistry	Tp	17	17	µg/L	2759.4118	2720	2420	3120	—	—	—	—
Chlorobenzene	108-90-7	R-19	SW-846:8260, SW-846:8260B	VOC	Tp	9	0	µg/L	—	—	—	—	2.25555556	1	0.3	5
Chlorodibromomethane	124-48-1	R-19	SW-846:8260, SW-846:8260B	VOC	Tp	9	0	µg/L	—	—	—	—	2.25555556	1	0.3	5
Chloroform	67-66-3	R-19	SW-846:8260, SW-846:8260B	VOC	Tp	9	0	µg/L	—	—	—	—	2.25555556	1	0.3	5
Chloromethane	74-87-3	R-19	SW-846:8260, SW-846:8260B	VOC	Tp	9	0	µg/L	—	—	—	—	3.92222222	1	0.3	10
Chromium	Cr	R-19	SW-846:6010B, SW-846:6020	Inorganic	Tp	22	14	µg/L	6.1335714	3.01	1.5	46.6	6.4975	7.49	1	10
Cobalt	Co	R-19	SW-846:6010B, SW-846:6010C	Inorganic	Tp	22	1	µg/L	1.04	1.04	1.04	1.04	4.00390476	5	0.541	5
Copper	Cu	R-19	SW-846:6010B, SW-846:6010C	Inorganic	Tp	22	0	µg/L	—	—	—	—	8.35909091	10	1.39	10
Cyanide (total)	CN (Total)	R-19	SW-846:9012A, EPA:335.3, EPA:335.4	General Chemistry, Inorganic	Tp	6	0	µg/L	—	—	—	—	2.935	2.11	1.67	5
DNX	DNX	R-19	SW-846:8321A_MOD, SW-846:8330RDX	LCMS/MS High Explosives	Tp	5	0	µg/L	—	—	—	—	0.42	0.5	0.291	0.5
Fluoranthene	206-44-0	R-19	SW-846:8270, SW-846:8270C, SW-846:8270D, SW-846:8310	SVOC	Tp	8	1	µg/L	0.19	0.19	0.19	0.19	4.9176	1	0.0526	11
Fluoride	F(-1)	R-19	EPA:300.0	General Chemistry	Tp	17	17	µg/L	571.11765	565	409	849	—	—	—	—
Gross alpha	GrossA	R-19	EPA:900, Generic:GrossAB	RAD	Tp	16	3	pCi/L	5.6466667	3.73	3.51	9.7	0.77515385	0.53	-0.119	2.28
Gross beta	GrossB	R-19	EPA:900, Generic:GrossAB	RAD	Tp	16	3	pCi/L	2.86	3.26	1.79	3.53	0.748	0.645	-0.368	2.44
Gross gamma	GrossG	R-19	EPA:901.1, Generic:Gross Gamma	RAD	Tp	13	1	pCi/L	132	132	132	132	33.9733333	20	7.62	108
Hardness	Hardness	R-19	EPA:200.7, SM:A2340B	Inorganic	Tp	22	22	µg/L	52,740.909	53,200	47,600	56,800	—	—	—	—
Heptachlor	76-44-8	R-19	SW-846:8080, SW-846:8081	PESTPCB	Tp	4	0	µg/L	—	—	—	—	0.0465	0.0545	0.021	0.056
Hexachlorobutadiene	87-68-3	R-19	SW-846:8260, SW-846:8260B	VOC	Tp	8	0	µg/L	—	—	—	—	2.4125	1	0.3	5
HMX	2691-41-0	R-19	SW-846:8330, SW-846:8321A_MOD, SW-846:8330B, SW-846:8321A(M)	HEXP, LCMS/MS High Explosives, LCMS/MS Perchlorate	Tp	14	0	µg/L	—	—	—	—	0.27261429	0.2785	0.0846	1
Iron	Fe	R-19	SW-846:6010B, SW-846:6010C	Inorganic	Tp	22	5	µg/L	79.06	26	25	281	87.9411765	100	12.6	100
Lead	Pb	R-19	SW-846:6020	Inorganic	Tp	22	0	µg/L	—	—	—	—	1.61818182	2	0.05	2
Magnesium	Mg	R-19	SW-846:6010B, SW-846:6010C	Inorganic	Tp	22	22	µg/L	2867.2727	2900	2510	3120	—	—	—	—
Manganese	Mn	R-19	SW-846:6010B, SW-846:6010C	Inorganic	Tp	22	4	µg/L	3.7775	3.03	2.25	6.8	8.16055556	10	1	10
Mercury	Hg	R-19	EPA:245.1, EPA:245.2	Inorganic	Tp	25	0	µg/L	—	—	—	—	0.165136	0.2	0.0472	0.2
Methyl tert-butyl ether	1634-04-4	R-19	SW-846:8260B	VOC	Tp	4	0	µg/L	—	—	—	—	0.825	1	0.3	1
Methyl-2-pentanone[4-]	108-10-1	R-19	SW-846:8260, SW-846:8260B	VOC	Tp	9	0	µg/L	—	—	—	—	9.61111111	5	1.5	20
Methylene chloride	75-09-2	R-19	SW-846:8260, SW-846:8260B	VOC	Tp	9	0	µg/L	—	—	—	—	5.94222222	5	1.38	10

Table 4.2-1 (continued)

Parameter Name	Parameter Code	Well	Analytical Method	Analytical Method Category[a]	Geological Unit Code[a]	No. Samples	No. Detects	Unit	Mean Detect	Median Detect	Min Detect	Max Detect	Mean ND	Median ND	Min ND	Max ND
MNX	MNX	R-19	SW-846:8321A_MOD, SW-846:8330RDX	LCMS/MS High Explosives	Tp	4	0	µg/L	—	—	—	—	0.4	0.4045	0.291	0.5
Molybdenum	Mo	R-19	SW-846:6010B, SW-846:6020	Inorganic	Tp	22	19	µg/L	1.6542105	1.35	1.12	6.2	1.68333333	1.51	1.43	2.11
Nickel	Ni	R-19	SW-846:6010B, SW-846:6020	Inorganic	Tp	22	11	µg/L	3.3546364	0.745	0.51	28.6	1.79027273	2	0.5	2.92
Nitrate-nitrite as nitrogen	NO3+NO2-N	R-19	EPA:353.1, EPA:353.2	General Chemistry	Tp	17	17	µg/L	356.11765	360	128	496	—	—	—	—
Nitrotoluene[2-]	88-72-2	R-19	SW-846:8330, SW-846:8321A_MOD, SW-846:8330B, SW-846:8321A(M)	HEXP, LCMS/MS High Explosives, LCMS/MS Perchlorate	Tp	14	0	µg/L	—	—	—	—	0.27276429	0.2785	0.0867	1
Perchlorate	ClO4	R-19	EPA:314.0, SW-846:6850, SW846 6850 Modified	General Chemistry, LCMS/MS Perchlorate	Tp	17	16	µg/L	0.340125	0.3405	0.299	0.381	4	4	4	4
Phenanthrene	85-01-8	R-19	SW-846:8270, SW-846:8270C, SW-846:8270D, SW-846:8310	SVOC	Tp	8	1	µg/L	0.24	0.24	0.24	0.24	5.05671429	1	0.315	11
Potassium	K	R-19	SW-846:6010B, SW-846:6010C	Inorganic	Tp	22	22	µg/L	1005.2273	1005	897	1060	—	—	—	—
Pyrene	129-00-0	R-19	SW-846:8270, SW-846:8270C, SW-846:8270D, SW-846:8310	SVOC	Tp	8	1	µg/L	0.19	0.19	0.19	0.19	4.9176	1	0.0526	11
Radium-226	Ra-226	R-19	EPA:903.1	RAD	Tp	1	0	pCi/L	—	—	—	—	0.0884	0.0884	0.0884	0.0884
Radium-228	Ra-228	R-19	EPA:901.1	RAD	Tp	1	0	pCi/L	—	—	—	—	3.79	3.79	3.79	3.79
RDX	121-82-4	R-19	SW-846:8330, SW-846:8321A_MOD, SW-846:8330B, SW-846:8321A(M)	HEXP, LCMS/MS High Explosives, LCMS/MS Perchlorate	Tp	14	1	µg/L	0.098	0.098	0.098	0.098	0.21666154	0.266	0.0846	0.325
Selenium	Se	R-19	SW-846:6010B, SW-846:6020	Inorganic	Tp	22	1	µg/L	2.8	2.8	2.8	2.8	4.52952381	5	2	5
Silicon dioxide	SiO2	R-19	SW-846:6010B, SW-846:6010C	Inorganic	Tp	18	18	µg/L	70,777.778	71,200	64,800	74,700	—	—	—	—
Silver	Ag	R-19	SW-846:6010B, SW-846:6020	Inorganic	Tp	22	0	µg/L	—	—	—	—	0.88045455	1	0.2	1
Sodium	Na	R-19	SW-846:6010B, SW-846:6010C	Inorganic	Tp	22	22	µg/L	14463.636	14,550	13,100	15,300	—	—	—	—
Strontium	Sr	R-19	SW-846:6010B, SW-846:6010C	Inorganic	Tp	22	22	µg/L	70.309091	70.85	56.6	77.2	—	—	—	—
Styrene	100-42-5	R-19	SW-846:8260, SW-846:8260B	VOC	Tp	9	0	µg/L	—	—	—	—	2.25555556	1	0.3	5
Sulfate	SO4(-2)	R-19	EPA:300.0	General Chemistry	Tp	17	17	µg/L	3226.4706	3270	2570	3560	—	—	—	—
Suspended sediment concentration	SSC	R-19	EPA:160.2	General Chemistry	Tp	1	0	µg/L	—	—	—	—	2000	2000	2000	2000
Temperature	TEMP	R-19	EPA:170.0	VOC	Tp	2	2	deg C	2	2	2	2	—	—	—	—
Tetrachloroethene	127-18-4	R-19	SW-846:8260, SW-846:8260B	VOC	Tp	9	0	µg/L	—	—	—	—	2.25555556	1	0.3	5
Thallium	Tl	R-19	SW-846:6020	Inorganic	Tp	22	2	µg/L	0.407	0.407	0.294	0.52	1.0663	1	0.066	2
Tin	Sn	R-19	SW-846:6010B, SW-846:6010C	Inorganic	Tp	22	0	µg/L	—	—	—	—	21.5463636	10	2.5	100
TNX	TNX	R-19	SW-846:8321A_MOD, SW-846:8330RDX	LCMS/MS High Explosives	Tp	5	0	µg/L	—	—	—	—	0.42	0.5	0.291	0.5
Toluene	108-88-3	R-19	SW-846:8260, SW-846:8260B	VOC	Tp	9	1	µg/L	0.54	0.54	0.54	0.54	2.4125	1	0.3	5
Total dissolved solids	TDS	R-19	EPA:160.1	General Chemistry	Tp	17	17	µg/L	152,294.12	151,000	145,000	164,000	—	—	—	—
Total Kjeldahl nitrogen	TKN	R-19	EPA:351.2	General Chemistry	Tp	8	1	µg/L	324	324	324	324	90.4285714	100	33	100
Total organic carbon	TOC	R-19	SW-846:9060	General Chemistry	Tp	7	6	µg/L	504.5	420	304	924	240	240	240	240

Table 4.2-1 (continued)

Parameter Name	Parameter Code	Well	Analytical Method	Analytical Method Category[a]	Geological Unit Code[a]	No. Samples	No. Detects	Unit	Mean Detect	Median Detect	Min Detect	Max Detect	Mean ND	Median ND	Min ND	Max ND
Total phosphate as phosphorus	PO4-P	R-19	EPA:365.4	General Chemistry	Tp	17	8	µg/L	86.1	79.75	51	139	63.5444444	64	48.9	81
Total suspended solids	TSS	R-19	EPA:160.2	General Chemistry	Tp	2	0	µg/L	—	—	—	—	1132	1132	734	1530
Trichlorobenzene[1,2,3-]	87-61-6	R-19	SW-846:8260, SW-846:8260B	VOC	Tp	7	0	µg/L	—	—	—	—	2.61428571	1	0.3	5
Trichloroethene	79-01-6	R-19	SW-846:8260, SW-846:8260B	VOC	Tp	9	0	µg/L	—	—	—	—	2.25555556	1	0.3	5
Trinitrobenzene[1,3,5-]	99-35-4	R-19	SW-846:8330, SW-846:8321A_MOD, SW-846:8330B, SW-846:8321A(M)	HEXP, LCMS/MS High Explosives, LCMS/MS Perchlorate	Tp	14	0	µg/L	—	—	—	—	0.2314	0.2785	0.0846	0.325
Trinitrotoluene[2,4,6-]	118-96-7	R-19	SW-846:8330, SW-846:8321A_MOD, SW-846:8330B, SW-846:8321A(M)	HEXP, LCMS/MS High Explosives, LCMS/MS Perchlorate	Tp	14	0	µg/L	—	—	—	—	0.21904286	0.258	0.0846	0.325
Tritium	H-3	R-19	EPA:906.0, Generic:LLEE, Generic:Low_Level_Tritium, Generic:Tritium	RAD	Tp	14	0	pCi/L	—	—	—	—	-5.3084143	0.0966	-158	80.5
Uranium	U	R-19	SW-846:6020	Inorganic	Tp	22	22	µg/L	0.2773182	0.2785	0.214	0.344	—	—	—	—
Uranium-234	U-234	R-19	Generic:Alpha-Spec, HASL-300:ISOU	RAD	Tp	19	19	pCi/L	0.2625263	0.256	0.192	0.332	—	—	—	—
Uranium-235/236	U-235/236	R-19	Generic:Alpha-Spec, HASL-300:ISOU	RAD	Tp	19	1	pCi/L	0.041	0.041	0.041	0.041	0.014425	0.00656	-0.0175	0.0929
Uranium-238	U-238	R-19	Generic:Alpha-Spec, HASL-300:ISOU	RAD	Tp	19	17	pCi/L	0.1134882	0.114	0.0786	0.171	0.0665	0.0665	0.0498	0.0832
Vanadium	V	R-19	SW-846:6010B, SW-846:6010C	Inorganic	Tp	22	20	µg/L	2.0715	1.945	1.2	3.1	2.43	2.43	2.18	2.68
Zinc	Zn	R-19	SW-846:6010B, SW-846:6010C	Inorganic	Tp	21	15	µg/L	9.164	5.73	3	44.4	10.49	10	7.64	17.2
Acenaphthene	83-32-9	R-25	SW-846:8270, SW-846:8270C	SVOC	Tpf	5	0	µg/L	—	—	—	—	1.058	1.06	1	1.1
Acenaphthylene	208-96-8	R-25	SW-846:8270, SW-846:8270C	SVOC	Tpf	5	0	µg/L	—	—	—	—	1.058	1.06	1	1.1
Acetone	67-64-1	R-25	SW-846:8260, SW-846:8260B	VOC	Tpf	18	2	µg/L	2.705	2.705	2.01	3.4	13.75	10	5	30
Acidity or alkalinity of a solution	pH	R-25	EPA:150.1	General Chemistry	Tpf	16	16	SU	7.518125	7.19	6.58	11.8	—	—	—	—
Alkalinity-CO3	ALK-CO3	R-25	EPA:310.1	General Chemistry	Tpf	16	1	µg/L	38,100	38,100	38,100	38,100	1223.33333	1000	725	4000
Alkalinity-CO3+HCO3	ALK-CO3+HCO3	R-25	EPA:310.1	General Chemistry	Tpf	16	16	µg/L	81600	68,000	59,400	286,000	—	—	—	—
Alkalinity-HCO3	ALK-HCO3	R-25	EPA:310.1	General Chemistry	Tpf	1	1	µg/L	75300	75,300	75,300	75,300	—	—	—	—
Aluminum	Al	R-25	SW-846:6010B, SW-846:6010C	Inorganic	Tpf	24	4	µg/L	235.75	131.5	76	604	173.6	200	68	200
Amino-2,6-dinitrotoluene[4-]	19406-51-0	R-25	SW-846:8330, SW-846:8321A_MOD, SW-846:8321A(M)	HEXP, LCMS/MS High Explosives, LCMS/MS Perchlorate	Tpf	20	2	µg/L	0.4945	0.4945	0.389	0.6	0.29916667	0.3045	0.1	1.04
Amino-4,6-dinitrotoluene[2-]	35572-78-2	R-25	SW-846:8330, SW-846:8321A_MOD, SW-846:8321A(M)	HEXP, LCMS/MS High Explosives, LCMS/MS Perchlorate	Tpf	20	4	µg/L	0.2635	0.1555	0.093	0.65	0.31	0.3045	0.1	1.04
Ammonia as nitrogen	NH3-N	R-25	EPA:350.1	General Chemistry	Tpf	16	8	µg/L	626.1	218.5	20	2660	44.475	40	10	106
Anthracene	120-12-7	R-25	SW-846:8270, SW-846:8270C	SVOC	Tpf	5	0	µg/L	—	—	—	—	1.058	1.06	1	1.1
Antimony	Sb	R-25	SW-846:6020	Inorganic	Tpf	24	1	µg/L	0.67	0.67	0.67	0.67	2.09913043	3	0.28	3
Arsenic	As	R-25	SW-846:6020, SW-846:6010B	Inorganic	Tpf	24	2	µg/L	2.295	2.295	1.7	2.89	4.32909091	5	1.5	6

Table 4.2-1 (continued)

Parameter Name	Parameter Code	Well	Analytical Method	Analytical Method Category[a]	Geological Unit Code[a]	No. Samples	No. Detects	Unit	Mean Detect	Median Detect	Min Detect	Max Detect	Mean ND	Median ND	Min ND	Max ND
Barium	Ba	R-25	SW-846:6010B, SW-846:6010C	Inorganic	Tpf	24	24	µg/L	21.708333	20.3	18.7	40.4	—	—	—	—
Benzo(g,h,i)perylene	191-24-2	R-25	SW-846:8270, SW-846:8270C	SVOC	Tpf	5	0	µg/L	—	—	—	—	1.058	1.06	1	1.1
Benzoic Acid	65-85-0	R-25	SW-846:8270, SW-846:8270C	SVOC	Tpf	4	0	µg/L	—	—	—	—	21.4	21.4	20.6	22.2
Beryllium	Be	R-25	SW-846:6010B, SW-846:6010C	Inorganic	Tpf	23	0	µg/L	—	—	—	—	3.95652174	5	1	5
Bis(2-ethylhexyl)phthalate	117-81-7	R-25	SW-846:8270, SW-846:8270C	SVOC	Tpf	5	0	µg/L	—	—	—	—	8.74	10.3	1.8	10.8
Bismuth-214	Bi-214	R-25	Generic:Gamma Spec.	RAD	Tpf	2	0	pCi/L	—	—	—	—	27.5	27.5	25	30
Boron	B	R-25	SW-846:6010B, SW-846:6010C	Inorganic	Tpf	24	24	µg/L	29.15	27.7	12.3	61.6	—	—	—	—
Bromide	Br(-1)	R-25	EPA:300.0	General Chemistry	Tpf	15	11	µg/L	103.50909	101	72	154	133	133	66	200
Bromodichloromethane	75-27-4	R-25	SW-846:8260, SW-846:8260B	VOC	Tpf	18	0	µg/L	—	—	—	—	1.88888889	1	1	5
Bromoform	75-25-2	R-25	SW-846:8260, SW-846:8260B	VOC	Tpf	18	0	µg/L	—	—	—	—	1.88888889	1	1	5
Butanone[2-]	78-93-3	R-25	SW-846:8260, SW-846:8260B	VOC	Tpf	18	0	µg/L	—	—	—	—	8.33333333	5	5	20
Cadmium	Cd	R-25	SW-846:6020	Inorganic	Tpf	24	0	µg/L	—	—	—	—	0.735	1	0.04	1
Calcium	Ca	R-25	SW-846:6010B, SW-846:6010C	Inorganic	Tpf	24	24	µg/L	34,870.833	24,250	18,600	106,000	—	—	—	—
Carbon disulfide	75-15-0	R-25	SW-846:8260, SW-846:8260B	VOC	Tpf	18	1	µg/L	1.36	1.36	1.36	1.36	5	5	5	5
Chloride	Cl(-1)	R-25	EPA:300.0	General Chemistry	Tpf	16	16	µg/L	8541.25	8075	6330	11,500	—	—	—	—
Chlorobenzene	108-90-7	R-25	SW-846:8260, SW-846:8260B	VOC	Tpf	18	3	µg/L	1.3066667	0.89	0.73	2.3	1.26666667	1	1	5
Chlorodibromomethane	124-48-1	R-25	SW-846:8260, SW-846:8260B	VOC	Tpf	18	0	µg/L	—	—	—	—	1.88888889	1	1	5
Chloroform	67-66-3	R-25	SW-846:8260, SW-846:8260B	VOC	Tpf	18	0	µg/L	—	—	—	—	1.88888889	1	1	5
Chloromethane	74-87-3	R-25	SW-846:8260, SW-846:8260B	VOC	Tpf	18	0	µg/L	—	—	—	—	3	1	1	10
Chromium	Cr	R-25	SW-846:6020, SW-846:6010B	Inorganic	Tpf	24	5	µg/L	3.546	4	2.04	4.6	7.35421053	10	1	10.7
Cobalt	Co	R-25	SW-846:6010B, SW-846:6010C	Inorganic	Tpf	24	4	µg/L	8.5875	6.735	1.18	19.7	3.70705	5	0.541	5
Copper	Cu	R-25	SW-846:6010B, SW-846:6010C	Inorganic	Tpf	23	2	µg/L	3.555	3.555	2.66	4.45	8.33333333	10	3	10
Cyanide (total)	CN (Total)	R-25	SW-846:9012A, EPA:335.3, EPA:335.4	General Chemistry, Inorganic	Tpf	8	1	µg/L	-1.47	-1.47	-1.47	-1.47	3.03142857	1.72	1.5	5
DNX	DNX	R-25	SW-846:8321A_MOD, SW-846:8330RDX	LCMS/MS High Explosives	Tpf	11	6	µg/L	0.1403333	0.1395	0.101	0.18	0.3766	0.5	0.11	0.5
Fluoranthene	206-44-0	R-25	SW-846:8270, SW-846:8270C	SVOC	Tpf	5	0	µg/L	—	—	—	—	1.058	1.06	1	1.1
Fluoride	F(-1)	R-25	EPA:300.0	General Chemistry	Tpf	16	14	µg/L	126.37857	111	67.9	277	44.15	44.15	33	55.3
Gross alpha	GrossA	R-25	EPA:900, Generic:GrossAB	RAD	Tpf	7	1	pCi/L	3.09	3.09	3.09	3.09	0.919	1.13	0.22	1.6
Gross beta	GrossB	R-25	EPA:900, Generic:GrossAB	RAD	Tpf	8	0	pCi/L	—	—	—	—	0.9251875	1.2	0.0316	1.7
Gross gamma	GrossG	R-25	EPA:901.1, Generic:Gross Gamma	RAD	Tpf	9	2	pCi/L	168.5	168.5	153	184	65.4257143	75.2	6.35	113
Hardness	Hardness	R-25	SM:A2340B, EPA:200.7	Inorganic	Tpf	24	24	µg/L	106,279.17	81,600	66,000	285,000	—	—	—	—
Heptachlor	76-44-8	R-25	SW-846:8081A	PESTPCB	Tpf	2	0	µg/L	—	—	—	—	0.02085	0.02085	0.02	0.0217
Hexachlorobutadiene	87-68-3	R-25	SW-846:8260, SW-846:8260B	VOC	Tpf	17	0	µg/L	—	—	—	—	1.94117647	1	1	5
HMX	2691-41-0	R-25	SW-846:8330, SW-846:8321A_MOD, SW-846:8321A(M)	HEXP, LCMS/MS High Explosives, LCMS/MS Perchlorate	Tpf	20	7	µg/L	1.0585714	0.134	0.115	4.9	0.36676923	0.325	0.08	1.04
Iron	Fe	R-25	SW-846:6010B, SW-846:6010C	Inorganic	Tpf	24	13	µg/L	157.93846	153	32.3	524	77.5363636	100	18	168

Table 4.2-1 (continued)

Parameter Name	Parameter Code	Well	Analytical Method	Analytical Method Category[a]	Geological Unit Code[a]	No. Samples	No. Detects	Unit	Mean Detect	Median Detect	Min Detect	Max Detect	Mean ND	Median ND	Min ND	Max ND
Lead	Pb	R-25	SW-846:6020	Inorganic	Tpf	24	1	µg/L	0.336	0.336	0.336	0.336	1.60869565	2	0.5	2
Magnesium	Mg	R-25	SW-846:6010B, SW-846:6010C	Inorganic	Tpf	24	23	µg/L	4865.2174	4970	3660	5610	300	300	300	300
Manganese	Mn	R-25	SW-846:6010B, SW-846:6010C	Inorganic	Tpf	24	20	µg/L	18.5145	9.215	2	52.7	10	10	10	10
Mercury	Hg	R-25	EPA:245.2, EPA:245.1	Inorganic	Tpf	26	0	µg/L	—	—	—	—	0.22758462	0.2	0.0472	2
Methyl tert-butyl ether	1634-04-4	R-25	SW-846:8260B	VOC	Tpf	9	9	µg/L	1.1044444	1.09	0.94	1.31	—	—	—	—
Methyl-2-pentanone[4-]	108-10-1	R-25	SW-846:8260, SW-846:8260B	VOC	Tpf	18	0	µg/L	—	—	—	—	8.33333333	5	5	20
Methylene chloride	75-09-2	R-25	SW-846:8260, SW-846:8260B	VOC	Tpf	18	1	µg/L	0.85	0.85	0.85	0.85	6.72352941	5.8	1.1	10
MNX	MNX	R-25	SW-846:8321A_MOD, SW-846:8330RDX	LCMS/MS High Explosives	Tpf	11	10	µg/L	0.2203	0.197	0.13	0.42	0.5	0.5	0.5	0.5
Molybdenum	Mo	R-25	SW-846:6020, SW-846:6010B	Inorganic	Tpf	24	9	µg/L	1.2185556	0.414	0.294	7.4	1.20706667	0.623	0.39	2.5
Nickel	Ni	R-25	SW-846:6020, SW-846:6010B	Inorganic	Tpf	24	21	µg/L	3.3219048	2.71	0.75	11	2.00333333	1.96	1.4	2.65
Nitrate-nitrite as nitrogen	NO3+NO2-N	R-25	EPA:353.2, EPA:353.1	General Chemistry	Tpf	16	12	µg/L	677.125	763.5	58.5	1230	91.5	53	10	250
Nitrotoluene[2-]	88-72-2	R-25	SW-846:8330, SW-846:8321A_MOD, SW-846:8321A(M)	HEXP, LCMS/MS High Explosives, LCMS/MS Perchlorate	Tpf	20	2	µg/L	0.602	0.602	0.104	1.1	0.39072222	0.325	0.1	1.04
Perchlorate	ClO4	R-25	SW-846:6850, EPA:314.0, SW846 6850 Modified	LCMS/MS Perchlorate, General Chemistry	Tpf	15	13	µg/L	0.3514077	0.452	0.0521	0.53	2.1	2.1	0.2	4
Phenanthrene	85-01-8	R-25	SW-846:8270, SW-846:8270C	SVOC	Tpf	4	0	µg/L	—	—	—	—	1.065	1.08	1	1.1
Potassium	K	R-25	SW-846:6010B, SW-846:6010C	Inorganic	Tpf	24	24	µg/L	1095.9583	701	401	10300	—	—	—	—
Pyrene	129-00-0	R-25	SW-846:8270, SW-846:8270C	SVOC	Tpf	5	0	µg/L	—	—	—	—	1.058	1.06	1	1.1
RDX	121-82-4	R-25	SW-846:8330, SW-846:8321A_MOD, SW-846:8321A(M)	HEXP, LCMS/MS High Explosives, LCMS/MS Perchlorate	Tpf	20	18	µg/L	14.17	14.75	1.9	26.7	7.95	7.95	3.4	12.5
Selenium	Se	R-25	SW-846:6020, SW-846:6010B	Inorganic	Tpf	24	0	µg/L	—	—	—	—	4.28375	5	2.5	5
Silicon dioxide	SiO2	R-25	SW-846:6010B, SW-846:6010C	Inorganic	Tpf	17	17	µg/L	51,464.706	53,900	12,500	56,700	—	—	—	—
Silver	Ag	R-25	SW-846:6020, SW-846:6010B	Inorganic	Tpf	24	1	µg/L	0.87	0.87	0.87	0.87	0.81891304	1	0.2	1
Sodium	Na	R-25	SW-846:6010B, SW-846:6010C	Inorganic	Tpf	24	24	µg/L	9452.0833	9505	5680	19600	—	—	—	—
Strontium	Sr	R-25	SW-846:6010B, SW-846:6010C	Inorganic	Tpf	24	24	µg/L	139.67083	115	96.9	366	—	—	—	—
Styrene	100-42-5	R-25	SW-846:8260, SW-846:8260B	VOC	Tpf	18	1	µg/L	1	1	1	1	1.70588235	1	1	5
Sulfate	SO4(-2)	R-25	EPA:300.0	General Chemistry	Tpf	16	16	µg/L	30,841.25	19,800	9310	207,000	—	—	—	—
Suspended sediment Concentration	SSC	R-25	EPA:160.2	General Chemistry	Tpf	1	1	µg/L	8000	8000	8000	8000	—	—	—	—
Tetrachloroethene	127-18-4	R-25	SW-846:8260, SW-846:8260B	VOC	Tpf	18	11	µg/L	0.7654545	0.83	0.31	1.21	3.28571429	5	1	5
Thallium	Tl	R-25	SW-846:6020	Inorganic	Tpf	24	2	µg/L	0.53	0.53	0.41	0.65	1.19659091	1	0.02	2
Tin	Sn	R-25	SW-846:6010B, SW-846:6010C	Inorganic	Tpf	24	1	µg/L	2.51	2.51	2.51	2.51	22.5330435	10	2.5	100
TNX	TNX	R-25	SW-846:8321A_MOD, SW-846:8330RDX	LCMS/MS High Explosives	Tpf	11	8	µg/L	0.1475	0.1395	0.12	0.2	0.362	0.5	0.086	0.5
Toluene	108-88-3	R-25	SW-846:8260, SW-846:8260B	VOC	Tpf	17	5	µg/L	4.128	0.94	0.24	15	0.98416667	1	0.81	1

Table 4.2-1 (continued)

Parameter Name	Parameter Code	Well	Analytical Method	Analytical Method Category[a]	Geological Unit Code[a]	No. Samples	No. Detects	Unit	Mean Detect	Median Detect	Min Detect	Max Detect	Mean ND	Median ND	Min ND	Max ND
Total dissolved solids	TDS	R-25	EPA:160.1	General Chemistry	Tpf	16	16	µg/L	188,812.5	160,500	117,000	459,000	—	—	—	—
Total Kjeldahl nitrogen	TKN	R-25	EPA:351.2	General Chemistry	Tpf	12	5	µg/L	111.04	105	13	189	89.8571429	100	29	100
Total organic carbon	TOC	R-25	SW-846:9060	General Chemistry	Tpf	10	9	µg/L	1227.5556	928	617	3040	330	330	330	330
Total phosphate as phosphorus	PO4-P	R-25	EPA:365.4	General Chemistry	Tpf	16	11	µg/L	401.31818	122	35	3350	123.92	128	75.6	174
Total suspended solids	TSS	R-25	EPA:160.2	General Chemistry	Tpf	1	1	µg/L	2400	2400	2400	2400	—	—	—	—
Trichlorobenzene[1,2,3-]	87-61-6	R-25	SW-846:8260, SW-846:8260B	VOC	Tpf	15	0	µg/L	—	—	—	—	2.06666667	1	1	5
Trichloroethene	79-01-6	R-25	SW-846:8260, SW-846:8260B	VOC	Tpf	18	12	µg/L	0.60375	0.615	0.31	0.9	3.66666667	5	1	5
Trinitrobenzene[1,3,5-]	99-35-4	R-25	SW-846:8330, SW-846:8321A_MOD, SW-846:8321A(M)	HEXP, LCMS/MS High Explosives, LCMS/MS Perchlorate	Tpf	20	1	µg/L	0.315	0.315	0.315	0.315	0.29763158	0.284	0.1	1.04
Trinitrotoluene[2,4,6-]	118-96-7	R-25	SW-846:8330, SW-846:8321A_MOD, SW-846:8321A(M)	HEXP, LCMS/MS High Explosives, LCMS/MS Perchlorate	Tpf	20	1	µg/L	0.36	0.36	0.36	0.36	0.29763158	0.284	0.1	1.04
Tritium	H-3	R-25	Generic:Tritium, EPA:906.0, Generic:LLEE, Generic:Low_Level_Tritium, Generic:LSC	RAD	Tpf	11	10	pCi/L	38.42104	34.293	30.654	67.942	0	0	0	0
Uranium	U	R-25	SW-846:6020	Inorganic	Tpf	24	23	µg/L	0.5863478	0.614	0.127	0.812	0.2	0.2	0.2	0.2
Uranium-234	U-234	R-25	HASL-300:ISOU	RAD	Tpf	15	13	pCi/L	0.4541538	0.4	0.315	0.733	0.11015	0.11015	0.0213	0.199
Uranium-235/236	U-235/236	R-25	HASL-300:ISOU	RAD	Tpf	15	0	pCi/L	—	—	—	—	0.022762	0.022	0.00296	0.0545
Uranium-238	U-238	R-25	HASL-300:ISOU	RAD	Tpf	15	14	pCi/L	0.2772143	0.225	0.15	0.47	0.00776	0.00776	0.00776	0.00776
Vanadium	V	R-25	SW-846:6010B, SW-846:6010C	Inorganic	Tpf	24	7	µg/L	2.1542857	1.2	1.01	7.7	3.90588235	5	1	5
Zinc	Zn	R-25	SW-846:6010B, SW-846:6010C	Inorganic	Tpf	24	19	µg/L	8.2105263	7.4	2.4	20.1	8.994	9.27	7.8	10
Acenaphthene	83-32-9	R-25b	SW-846:8270C, SW-846:8270DGCMS_SIM, SW-846:8310	SVOC	Qbo	4	0	µg/L	—	—	—	—	0.55875	0.5075	0.1	1.12
Acenaphthylene	208-96-8	R-25b	SW-846:8270C, SW-846:8270DGCMS_SIM, SW-846:8310	SVOC	Qbo	4	0	µg/L	—	—	—	—	0.55875	0.5075	0.1	1.12
Acetone	67-64-1	R-25b	SW-846:8260B	VOC	Qbo	11	0	µg/L	—	—	—	—	9.63181818	10	5.95	10
Acidity or alkalinity of a solution	pH	R-25b	EPA:150.1	General Chemistry	Qbo	18	18	SU	7.6711111	7.71	7.23	7.91	—	—	—	—
Alkalinity-CO3	ALK-CO3	R-25b	EPA:310.1	General Chemistry	Qbo	18	0	µg/L	—	—	—	—	1277.77778	1000	1000	4000
Alkalinity-CO3+HCO3	ALK-CO3+HCO3	R-25b	EPA:310.1	General Chemistry	Qbo	18	18	µg/L	72,988.889	66,900	54,600	123,000	—	—	—	—
Aluminum	Al	R-25b	SW-846:6010B, SW-846:6010C	Inorganic	Qbo	19	8	µg/L	400.875	274.5	111	1010	200	200	200	200
Amino-2,6-dinitrotoluene[4-]	19406-51-0	R-25b	SW-846:8321A_MOD	LCMS/MS High Explosives	Qbo	11	2	µg/L	0.143	0.143	0.117	0.169	0.266	0.266	0.255	0.275
Amino-4,6-dinitrotoluene[2-]	35572-78-2	R-25b	SW-846:8321A_MOD	LCMS/MS High Explosives	Qbo	11	1	µg/L	0.165	0.165	0.165	0.165	0.2778	0.2675	0.255	0.325
Ammonia as nitrogen	NH3-N	R-25b	EPA:350.1	General Chemistry	Qbo	18	9	µg/L	74.722222	75.9	17.8	172	43.6666667	48.2	31	50
Anthracene	120-12-7	R-25b	SW-846:8270C, SW-846:8270DGCMS_SIM, SW-846:8310	SVOC	Qbo	4	0	µg/L	—	—	—	—	0.55875	0.5075	0.1	1.12
Antimony	Sb	R-25b	SW-846:6020	Inorganic	Qbo	19	1	µg/L	1.26	1.26	1.26	1.26	2.94444444	3	2	3

Table 4.2-1 (continued)

Parameter Name	Parameter Code	Well	Analytical Method	Analytical Method Category[a]	Geological Unit Code[a]	No. Samples	No. Detects	Unit	Mean Detect	Median Detect	Min Detect	Max Detect	Mean ND	Median ND	Min ND	Max ND
Arsenic	As	R-25b	SW-846:6020	Inorganic	Qbo	19	11	µg/L	3.4554545	3.39	1.94	5.37	5	5	5	5
Barium	Ba	R-25b	SW-846:6010B, SW-846:6010C	Inorganic	Qbo	19	18	µg/L	17.062222	12.45	8.41	40.6	14.8	14.8	14.8	14.8
Benzo(g,h,i)perylene	191-24-2	R-25b	SW-846:8270C, SW-846:8270DGCMS_SIM, SW-846:8310	SVOC	Qbo	4	0	µg/L	—	—	—	—	0.330375	0.0755	0.0505	1.12
Benzoic Acid	65-85-0	R-25b	SW-846:8270C, SW-846:8270D	SVOC	Qbo	4	0	µg/L	—	—	—	—	18.525	20.4	10.8	22.5
Beryllium	Be	R-25b	SW-846:6010B, SW-846:6010C	Inorganic	Qbo	19	0	µg/L	—	—	—	—	5	5	5	5
Bis(2-ethylhexyl)phthalate	117-81-7	R-25b	SW-846:8270C, SW-846:8270D	SVOC	Qbo	4	0	µg/L	—	—	—	—	9.245	10.2	5.38	11.2
Boron	B	R-25b	SW-846:6010B, SW-846:6010C	Inorganic	Qbo	19	12	µg/L	23.483333	20.7	15.5	51.4	46.6714286	50	26.7	50
Bromide	Br(-1)	R-25b	EPA:300.0	General Chemistry	Qbo	18	2	µg/L	73	73	71.4	74.6	200	200	200	200
Bromodichloromethane	75-27-4	R-25b	SW-846:8260B	VOC	Qbo	11	2	µg/L	1.63	1.63	1.08	2.18	1	1	1	1
Bromoform	75-25-2	R-25b	SW-846:8260B	VOC	Qbo	11	2	µg/L	1.255	1.255	0.72	1.79	1	1	1	1
Butanone[2-]	78-93-3	R-25b	SW-846:8260B	VOC	Qbo	11	0	µg/L	—	—	—	—	5	5	5	5
Cadmium	Cd	R-25b	SW-846:6020	Inorganic	Qbo	19	0	µg/L	—	—	—	—	1	1	1	1
Calcium	Ca	R-25b	SW-846:6010B, SW-846:6010C	Inorganic	Qbo	19	19	µg/L	11,548.947	11,700	6240	14,900	—	—	—	—
Carbon disulfide	75-15-0	R-25b	SW-846:8260B	VOC	Qbo	11	0	µg/L	—	—	—	—	5	5	5	5
Chloride	Cl(-1)	R-25b	EPA:300.0	General Chemistry	Qbo	18	18	µg/L	2531.1111	2085	1770	4850	—	—	—	—
Chlorobenzene	108-90-7	R-25b	SW-846:8260B	VOC	Qbo	11	0	µg/L	—	—	—	—	1	1	1	1
Chlorodibromomethane	124-48-1	R-25b	SW-846:8260B	VOC	Qbo	11	2	µg/L	2.255	2.255	1.47	3.04	1	1	1	1
Chloroform	67-66-3	R-25b	SW-846:8260B	VOC	Qbo	11	2	µg/L	2.855	2.855	1.62	4.09	1	1	1	1
Chloromethane	74-87-3	R-25b	SW-846:8260B	VOC	Qbo	11	0	µg/L	—	—	—	—	1	1	1	1
Chromium	Cr	R-25b	SW-846:6020	Inorganic	Qbo	19	6	µg/L	3.7016667	3.675	1.7	5.34	9.55384615	10	4.2	10
Cobalt	Co	R-25b	SW-846:6010B, SW-846:6010C	Inorganic	Qbo	19	2	µg/L	3.815	3.815	2.2	5.43	5	5	5	5
Copper	Cu	R-25b	SW-846:6010B, SW-846:6010C	Inorganic	Qbo	19	7	µg/L	8.6957143	7.47	3.99	15.9	10	10	10	10
Cyanide (total)	CN (Total)	R-25b	EPA:335.3, EPA:335.4	Inorganic	Qbo	10	0	µg/L	—	—	—	—	5	5	5	5
DNX	DNX	R-25b	SW-846:8321A_MOD, SW-846:8330RDX	LCMS/MS High Explosives	Qbo	9	0	µg/L	—	—	—	—	0.318	0.266	0.255	0.5
Fluoranthene	206-44-0	R-25b	SW-846:8270C, SW-846:8270DGCMS_SIM, SW-846:8310	SVOC	Qbo	4	0	µg/L	—	—	—	—	0.330375	0.0755	0.0505	1.12
Fluoride	F(-1)	R-25b	EPA:300.0	General Chemistry	Qbo	18	18	µg/L	130.86111	129.5	54.8	226	—	—	—	—
Gross alpha	GrossA	R-25b	EPA:900	RAD	Qbo	3	1	pCi/L	3.92	3.92	3.92	3.92	0.69825	0.69825	-0.0235	1.42
Gross beta	GrossB	R-25b	EPA:900	RAD	Qbo	3	3	pCi/L	2.96	3.68	1.42	3.78	—	—	—	—
Gross gamma	GrossG	R-25b	EPA:901.1	RAD	Qbo	2	0	pCi/L	—	—	—	—	31.8	31.8	25.8	37.8
Hardness	Hardness	R-25b	SM:A2340B	Inorganic	Qbo	19	19	µg/L	44,163.158	45,200	24,800	52,300	—	—	—	—
Hexachlorobutadiene	87-68-3	R-25b	SW-846:8260B	VOC	Qbo	11	0	µg/L	—	—	—	—	1	1	1	1
HMX	2691-41-0	R-25b	SW-846:8321A_MOD	LCMS/MS High Explosives	Qbo	12	9	µg/L	0.3321111	0.271	0.155	0.656	0.26666667	0.266	0.265	0.269
Iron	Fe	R-25b	SW-846:6010B, SW-846:6010C	Inorganic	Qbo	19	10	µg/L	214.27	143	32.5	600	94.1222222	100	47.1	100
Lead	Pb	R-25b	SW-846:6020	Inorganic	Qbo	19	5	µg/L	1.1822	0.819	0.512	2.25	2	2	2	2
Magnesium	Mg	R-25b	SW-846:6010B, SW-846:6010C	Inorganic	Qbo	19	19	µg/L	3722.6316	3750	2230	4400	—	—	—	—

Table 4.2-1 (continued)

Parameter Name	Parameter Code	Well	Analytical Method	Analytical Method Category[a]	Geological Unit Code[a]	No. Samples	No. Detects	Unit	Mean Detect	Median Detect	Min Detect	Max Detect	Mean ND	Median ND	Min ND	Max ND
Manganese	Mn	R-25b	SW-846:6010B, SW-846:6010C	Inorganic	Qbo	19	10	µg/L	37.551	24.3	4.3	102	10	10	10	10
Mercury	Hg	R-25b	EPA:245.2	Inorganic	Qbo	26	0	µg/L	—	—	—	—	0.2	0.2	0.2	0.2
Methyl tert-butyl ether	1634-04-4	R-25b	SW-846:8260B	VOC	Qbo	11	0	µg/L	—	—	—	—	1	1	1	1
Methyl-2-pentanone[4-]	108-10-1	R-25b	SW-846:8260B	VOC	Qbo	11	0	µg/L	—	—	—	—	5	5	5	5
Methylene chloride	75-09-2	R-25b	SW-846:8260B	VOC	Qbo	11	0	µg/L	—	—	—	—	10	10	10	10
MNX	MNX	R-25b	SW-846:8321A_MOD, SW-846:8330RDX	LCMS/MS High Explosives	Qbo	9	0	µg/L	—	—	—	—	0.318	0.266	0.255	0.5
Molybdenum	Mo	R-25b	SW-846:6020	Inorganic	Qbo	19	18	µg/L	9.3607222	4.115	0.62	40.3	0.965	0.965	0.965	0.965
Nickel	Ni	R-25b	SW-846:6020	Inorganic	Qbo	19	15	µg/L	2.3094667	2.13	0.627	5.6	1.79	2	1.16	2
Nitrate-nitrite as nitrogen	NO3+NO2-N	R-25b	EPA:353.2	General Chemistry	Qbo	18	17	µg/L	538.95882	597	41.3	930	715	715	715	715
Nitrotoluene[2-]	88-72-2	R-25b	SW-846:8321A_MOD	LCMS/MS High Explosives	Qbo	11	0	µg/L	—	—	—	—	0.27672727	0.266	0.255	0.325
Perchlorate	ClO4	R-25b	SW-846:6850	LCMS/MS Perchlorate	Qbo	16	16	µg/L	0.2810625	0.289	0.208	0.313	—	—	—	—
Phenanthrene	85-01-8	R-25b	SW-846:8270C, SW-846:8270DGCMS_SIM, SW-846:8310	SVOC	Qbo	4	0	µg/L	—	—	—	—	0.55875	0.5075	0.1	1.12
Potassium	K	R-25b	SW-846:6010B, SW-846:6010C	Inorganic	Qbo	19	19	µg/L	1893.6842	1420	1180	4220	—	—	—	—
Pyrene	129-00-0	R-25b	SW-846:8270C, SW-846:8270DGCMS_SIM, SW-846:8310	SVOC	Qbo	4	0	µg/L	—	—	—	—	0.330375	0.0755	0.0505	1.12
Radium-226	Ra-226	R-25b	EPA:903.1	RAD	Qbo	1	1	pCi/L	1.27	1.27	1.27	1.27	—	—	—	—
Radium-228	Ra-228	R-25b	EPA:904	RAD	Qbo	1	1	pCi/L	0.879	0.879	0.879	0.879	—	—	—	—
RDX	121-82-4	R-25b	SW-846:8321A_MOD	LCMS/MS High Explosives	Qbo	12	12	µg/L	3.5201667	3.36	0.144	8.49	—	—	—	—
Selenium	Se	R-25b	SW-846:6020	Inorganic	Qbo	19	0	µg/L	—	—	—	—	5	5	5	5
Silicon dioxide	SiO2	R-25b	SW-846:6010B, SW-846:6010C	Inorganic	Qbo	18	18	µg/L	57,422.222	56,200	49,300	69,800	—	—	—	—
Silver	Ag	R-25b	SW-846:6020	Inorganic	Qbo	19	0	µg/L	—	—	—	—	1	1	1	1
Sodium	Na	R-25b	SW-846:6010B, SW-846:6010C	Inorganic	Qbo	19	19	µg/L	47,714.211	14,100	8710	246,000	—	—	—	—
Strontium	Sr	R-25b	SW-846:6010B, SW-846:6010C	Inorganic	Qbo	19	19	µg/L	73.457895	72.2	50.8	91.9	—	—	—	—
Styrene	100-42-5	R-25b	SW-846:8260B	VOC	Qbo	11	0	µg/L	—	—	—	—	1	1	1	1
Sulfate	SO4(-2)	R-25b	EPA:300.0	General Chemistry	Qbo	18	18	µg/L	7283.3333	4615	2250	21000	—	—	—	—
Tetrachloroethene	127-18-4	R-25b	SW-846:8260B	VOC	Qbo	11	3	µg/L	0.3433333	0.33	0.32	0.38	1	1	1	1
Thallium	Tl	R-25b	SW-846:6020	Inorganic	Qbo	19	0	µg/L	—	—	—	—	1.66968421	2	0.724	2
Tin	Sn	R-25b	SW-846:6010B, SW-846:6010C	Inorganic	Qbo	19	3	µg/L	6.2566667	4.46	3.91	10.4	17.5	10	10	50
TNX	TNX	R-25b	SW-846:8321A_MOD, SW-846:8330RDX	LCMS/MS High Explosives	Qbo	9	0	µg/L	—	—	—	—	0.318	0.266	0.255	0.5
Toluene	108-88-3	R-25b	SW-846:8260B	VOC	Qbo	11	0	µg/L	—	—	—	—	1	1	1	1
Total dissolved solids	TDS	R-25b	EPA:160.1	General Chemistry	Qbo	18	18	µg/L	373,150	124,500	32,900	2E+06	—	—	—	—
Total Kjeldahl nitrogen	TKN	R-25b	EPA:351.2	General Chemistry	Qbo	12	4	µg/L	193.85	139	89.4	408	119.25	100	100	254
Total organic carbon	TOC	R-25b	SW-846:9060	General Chemistry	Qbo	12	12	µg/L	145,859.08	861.5	505	693,000	—	—	—	—

Table 4.2-1 (continued)

Parameter Name	Parameter Code	Well	Analytical Method	Analytical Method Category[a]	Geological Unit Code[a]	No. Samples	No. Detects	Unit	Mean Detect	Median Detect	Min Detect	Max Detect	Mean ND	Median ND	Min ND	Max ND
Total phosphate as phosphorus	PO4-P	R-25b	EPA:365.4	General Chemistry	Qbo	18	13	µg/L	139.94615	119	19.5	531	97.36	106	50	143
Trichlorobenzene[1,2,3-]	87-61-6	R-25b	SW-846:8260B	VOC	Qbo	11	0	µg/L	—	—	—	—	1	1	1	1
Trichloroethene	79-01-6	R-25b	SW-846:8260B	VOC	Qbo	11	0	µg/L	—	—	—	—	1	1	1	1
Trinitrobenzene[1,3,5-]	99-35-4	R-25b	SW-846:8321A_MOD	LCMS/MS High Explosives	Qbo	11	0	µg/L	—	—	—	—	0.27672727	0.266	0.255	0.325
Trinitrotoluene[2,4,6-]	118-96-7	R-25b	SW-846:8321A_MOD	LCMS/MS High Explosives	Qbo	11	0	µg/L	—	—	—	—	0.27672727	0.266	0.255	0.325
Tritium	H-3	R-25b	Generic:Low_Level_Tritium	RAD	Qbo	1	0	pCi/L	—	—	—	—	1.289	1.289	1.289	1.289
Uranium	U	R-25b	SW-846:6020	Inorganic	Qbo	19	19	µg/L	1.1376842	1.11	0.264	3.12	—	—	—	—
Uranium-234	U-234	R-25b	HASL-300:ISOU	RAD	Qbo	4	4	pCi/L	1.10425	1.22	0.207	1.77	—	—	—	—
Uranium-235/236	U-235/236	R-25b	HASL-300:ISOU	RAD	Qbo	4	1	pCi/L	0.0615	0.0615	0.0615	0.0615	0.01793333	0.014	0.0118	0.028
Uranium-238	U-238	R-25b	HASL-300:ISOU	RAD	Qbo	4	4	pCi/L	0.3875	0.433	0.13	0.554	—	—	—	—
Vanadium	V	R-25b	SW-846:6010B, SW-846:6010C	Inorganic	Qbo	19	19	µg/L	3.0047368	2.8	2	6.41	—	—	—	—
Zinc	Zn	R-25b	SW-846:6010B, SW-846:6010C	Inorganic	Qbo	19	18	µg/L	110.92222	29	7.5	1420	10	10	10	10
Acenaphthene	83-32-9	R-26	SW-846:8270C, SW-846:8270D, SW-846:8270DGCMS_SIM, SW-846:8310	SVOC	Qct	14	0	µg/L	—	—	—	—	0.88428571	1.04	0.1	1.2
Acenaphthylene	208-96-8	R-26	SW-846:8270C, SW-846:8270D, SW-846:8270DGCMS_SIM, SW-846:8310	SVOC	Qct	14	0	µg/L	—	—	—	—	0.88428571	1.04	0.1	1.2
Acetone	67-64-1	R-26	SW-846:8260B	VOC	Qct	23	2	µg/L	9.645	9.645	4.79	14.5	6.18952381	5	1.5	10
Acidity or alkalinity of a solution	pH	R-26	EPA:150.1	General Chemistry	Qct	24	24	SU	7.7279167	7.725	7.33	7.96	—	—	—	—
Alkalinity-CO3	ALK-CO3	R-26	EPA:310.1	General Chemistry	Qct	25	0	µg/L	—	—	—	—	1224	1000	725	4000
Alkalinity-CO3+HCO3	ALK-CO3+HCO3	R-26	EPA:310.1	General Chemistry	Qct	27	27	µg/L	48,874.074	47,300	43,200	94,500	—	—	—	—
Alkalinity-HCO3	ALK-HCO3	R-26	EPA:310.1	General Chemistry	Qct	1	1	µg/L	47,600	47,600	47,600	47,600	—	—	—	—
Aluminum	Al	R-26	SW-846:6010B, SW-846:6010C	Inorganic	Qct	38	0	µg/L	—	—	—	—	134	134	68	200
Amino-2,6-dinitrotoluene[4-]	19406-51-0	R-26	SW-846:8330, SW-846:8321A_MOD, SW-846:8330B	HEXP, LCMS/MS High Explosives	Qct	23	0	µg/L	—	—	—	—	0.31073043	0.273	0.0833	1
Amino-4,6-dinitrotoluene[2-]	35572-78-2	R-26	SW-846:8330, SW-846:8321A_MOD, SW-846:8330B	HEXP, LCMS/MS High Explosives	Qct	23	0	µg/L	—	—	—	—	0.31073043	0.273	0.0833	1
Ammonia as nitrogen	NH3-N	R-26	EPA:350.1	General Chemistry	Qct	25	8	µg/L	49.1625	37	18.5	115	60.4529412	50	10	250
Anthracene	120-12-7	R-26	SW-846:8270C, SW-846:8270D, SW-846:8270DGCMS_SIM, SW-846:8310	SVOC	Qct	14	0	µg/L	—	—	—	—	0.88428571	1.04	0.1	1.2
Antimony	Sb	R-26	SW-846:6020	Inorganic	Qct	38	0	µg/L	—	—	—	—	1.68421053	1.5	0.5	3
Arsenic	As	R-26	SW-846:6010B, SW-846:6020	Inorganic	Qct	38	8	µg/L	2.44	2.39	1.7	3.48	4.46666667	5	1.5	6
Barium	Ba	R-26	SW-846:6010B, SW-846:6010C	Inorganic	Qct	38	37	µg/L	7.7756757	7.7	6.39	10	9.45	9.45	9.45	9.45
Benzo(g,h,i)perylene	191-24-2	R-26	SW-846:8270C, SW-846:8270D, SW-846:8270DGCMS_SIM, SW-846:8310	SVOC	Qct	14	0	µg/L	—	—	—	—	0.8155	1.04	0.0521	1.2
Benzoic acid	65-85-0	R-26	SW-846:8270C, SW-846:8270D	SVOC	Qct	13	1	µg/L	14.6	14.6	14.6	14.6	19.6583333	21.5	6	24.1
Beryllium	Be	R-26	SW-846:6010B, SW-846:6010C, SW-846:6020	Inorganic	Qct	38	0	µg/L	—	—	—	—	2.85789474	3	0.1	5
Bis(2-ethylhexyl)phthalate	117-81-7	R-26	SW-846:8270C, SW-846:8270D	SVOC	Qct	13	0	µg/L	—	—	—	—	9.19153846	10.2	3	12

Table 4.2-1 (continued)

Parameter Name	Parameter Code	Well	Analytical Method	Analytical Method Category[a]	Geological Unit Code[a]	No. Samples	No. Detects	Unit	Mean Detect	Median Detect	Min Detect	Max Detect	Mean ND	Median ND	Min ND	Max ND
Bismuth-214	Bi-214	R-26	EPA:901.1	RAD	Qct	3	1	pCi/L	13.8	13.8	13.8	13.8	4.67	4.67	3.41	5.93
Boron	B	R-26	SW-846:6010B, SW-846:6010C	Inorganic	Qct	38	1	µg/L	13.3	13.3	13.3	13.3	30.1351351	15	10	50
Bromide	Br(-1)	R-26	EPA:300.0	General Chemistry	Qct	27	2	µg/L	74.25	74.25	70.2	78.3	131.88	200	41	200
Bromodichloromethane	75-27-4	R-26	SW-846:8260B	VOC	Qct	24	0	µg/L	—	—	—	—	0.85416667	1	0.3	1
Bromoform	75-25-2	R-26	SW-846:8260B	VOC	Qct	24	0	µg/L	—	—	—	—	0.85416667	1	0.3	1
Butanone[2-]	78-93-3	R-26	SW-846:8260B	VOC	Qct	24	0	µg/L	—	—	—	—	4.27083333	5	1.5	5
Cadmium	Cd	R-26	SW-846:6020	Inorganic	Qct	38	1	µg/L	0.18	0.18	0.18	0.18	0.56540541	0.3	0.1	1
Calcium	Ca	R-26	SW-846:6010B, SW-846:6010C	Inorganic	Qct	38	38	µg/L	7576.0526	7520	7150	8600	—	—	—	—
Carbon disulfide	75-15-0	R-26	SW-846:8260B	VOC	Qct	24	0	µg/L	—	—	—	—	4.27083333	5	1.5	5
Chloride	Cl(-1)	R-26	EPA:300.0	General Chemistry	Qct	27	27	µg/L	1172.5926	1180	1060	1250	—	—	—	—
Chlorobenzene	108-90-7	R-26	SW-846:8260B	VOC	Qct	24	0	µg/L	—	—	—	—	0.85416667	1	0.3	1
Chlorodibromomethane	124-48-1	R-26	SW-846:8260B	VOC	Qct	24	0	µg/L	—	—	—	—	0.85416667	1	0.3	1
Chloroform	67-66-3	R-26	SW-846:8260B	VOC	Qct	24	0	µg/L	—	—	—	—	0.85416667	1	0.3	1
Chloromethane	74-87-3	R-26	SW-846:8260B	VOC	Qct	24	1	µg/L	0.36	0.36	0.36	0.36	0.84782609	1	0.3	1
Chromium	Cr	R-26	SW-846:6010B, SW-846:6020	Inorganic	Qct	38	20	µg/L	4.311	2.76	1.6	25.1	5.63111111	3.88	1	10
Cobalt	Co	R-26	SW-846:6010B, SW-846:6010C	Inorganic	Qct	38	1	µg/L	1.1	1.1	1.1	1.1	3.05405405	5	1	5
Copper	Cu	R-26	SW-846:6010B, SW-846:6010C	Inorganic	Qct	34	0	µg/L	—	—	—	—	6.91176471	10	3	10
Cyanide (total)	CN (Total)	R-26	SW-846:9012A, EPA:335.3, EPA:335.4	General Chemistry, Inorganic	Qct	22	2	µg/L	4.94	4.94	3.97	5.91	2.944	2.265	1.5	5
DNX	DNX	R-26	SW-846:8321A_MOD, SW-846:8330B, SW-846:8330RDX	LCMS/MS High Explosives	Qct	17	0	µg/L	—	—	—	—	0.32107647	0.273	0.0833	0.5
Fluoranthene	206-44-0	R-26	SW-846:8270C, SW-846:8270D, SW-846:8270DGCMS_SIM, SW-846:8310	SVOC	Qct	14	0	µg/L	—	—	—	—	0.8155	1.04	0.0521	1.2
Fluoride	F(-1)	R-26	EPA:300.0	General Chemistry	Qct	27	25	µg/L	121.884	114	38.7	273	97.5	97.5	30	165
Gross alpha	GrossA	R-26	EPA:900	RAD	Qct	10	0	pCi/L	—	—	—	—	0.08996	0.2043	-1.35	1.56
Gross beta	GrossB	R-26	EPA:900	RAD	Qct	10	6	pCi/L	3.14	3.255	1.96	3.85	1.17025	0.9465	0.218	2.57
Gross gamma	GrossG	R-26	EPA:901.1	RAD	Qct	6	0	pCi/L	—	—	—	—	64.9166667	68.65	14	101
Hardness	Hardness	R-26	SM:A2340B	Inorganic	Qct	32	32	µg/L	31,009.375	30,950	28,900	34,800	—	—	—	—
Heptachlor	76-44-8	R-26	SW-846:8081A	PESTPCB	Qct	6	0	µg/L	—	—	—	—	0.02171667	0.0222	0.02	0.0232
Hexachlorobutadiene	87-68-3	R-26	SW-846:8260B	VOC	Qct	21	0	µg/L	—	—	—	—	0.83333333	1	0.3	1
HMX	2691-41-0	R-26	SW-846:8330, SW-846:8321A_MOD, SW-846:8330B	HEXP, LCMS/MS High Explosives	Qct	23	0	µg/L	—	—	—	—	0.31073043	0.273	0.0833	1
Iron	Fe	R-26	SW-846:6010B, SW-846:6010C	Inorganic	Qct	38	6	µg/L	53.333333	45.3	24.8	109	64.1875	65	18	211
Lead	Pb	R-26	SW-846:6020	Inorganic	Qct	38	0	µg/L	—	—	—	—	1.25	1.25	0.5	2
Magnesium	Mg	R-26	SW-846:6010B, SW-846:6010C	Inorganic	Qct	38	38	µg/L	2907.8947	2905	2660	3240	—	—	—	—
Manganese	Mn	R-26	SW-846:6010B, SW-846:6010C, SW-846:6020	Inorganic	Qct	38	8	µg/L	2.695	2.53	1.2	4.86	5.658	2.37	1	10
Mercury	Hg	R-26	EPA:245.2, SW-846:7470A	Inorganic	Qct	48	0	µg/L	—	—	—	—	0.13291667	0.185	0.03	0.2
Methyl tert-butyl ether	1634-04-4	R-26	SW-846:8260B	VOC	Qct	19	0	µg/L	—	—	—	—	0.81578947	1	0.3	1
Methyl-2-pentanone[4-]	108-10-1	R-26	SW-846:8260B	VOC	Qct	24	0	µg/L	—	—	—	—	4.27083333	5	1.5	5

Table 4.2-1 (continued)

Parameter Name	Parameter Code	Well	Analytical Method	Analytical Method Category[a]	Geological Unit Code[a]	No. Samples	No. Detects	Unit	Mean Detect	Median Detect	Min Detect	Max Detect	Mean ND	Median ND	Min ND	Max ND
Methylene chloride	75-09-2	R-26	SW-846:8260B	VOC	Qct	24	0	µg/L	—	—	—	—	6.34208333	5	1	10
MNX	MNX	R-26	SW-846:8321A_MOD, SW-846:8330B, SW-846:8330RDX	LCMS/MS High Explosives	Qct	16	0	µg/L	—	—	—	—	0.30989375	0.271	0.0833	0.5
Molybdenum	Mo	R-26	SW-846:6010B, SW-846:6020	Inorganic	Qct	38	28	µg/L	0.9941786	0.962	0.78	1.4	1.804	2	0.99	2
Nickel	Ni	R-26	SW-846:6010B, SW-846:6020	Inorganic	Qct	38	17	µg/L	2.5021765	1.48	0.654	14.9	1.2447619	1.1	0.5	2.35
Nitrate-nitrite as nitrogen	NO3+NO2-N	R-26	EPA:353.1, EPA:353.2	General Chemistry	Qct	30	30	µg/L	344.12333	365	77.7	459	—	—	—	—
Nitrotoluene[2-]	88-72-2	R-26	SW-846:8330, SW-846:8321A_MOD, SW-846:8330B	HEXP, LCMS/MS High Explosives	Qct	23	0	µg/L	—	—	—	—	0.31119565	0.273	0.0854	1
Perchlorate	ClO4	R-26	SW-846:6850, SW846 6850 Modified	LCMS/MS Perchlorate	Qct	26	26	µg/L	0.2310385	0.2325	0.204	0.254	—	—	—	—
Phenanthrene	85-01-8	R-26	SW-846:8270C, SW-846:8270D, SW-846:8270DGCMS_SIM, SW-846:8310	SVOC	Qct	13	0	µg/L	—	—	—	—	0.86846154	1.02	0.1	1.2
Potassium	K	R-26	SW-846:6010B, SW-846:6010C	Inorganic	Qct	38	38	µg/L	2195.2632	2170	2050	2450	—	—	—	—
Pyrene	129-00-0	R-26	SW-846:8270C, SW-846:8270D, SW-846:8270DGCMS_SIM, SW-846:8310	SVOC	Qct	14	0	µg/L	—	—	—	—	0.8155	1.04	0.0521	1.2
Radium-226	Ra-226	R-26	EPA:901.1, EPA:903.1	RAD	Qct	6	1	pCi/L	0.373	0.373	0.373	0.373	2	0.274	0.152	5.93
Radium-228	Ra-228	R-26	EPA:904	RAD	Qct	4	2	pCi/L	1.023	1.023	0.646	1.4	0.4725	0.4725	0.384	0.561
RDX	121-82-4	R-26	SW-846:8330, SW-846:8321A_MOD, SW-846:8330B	HEXP, LCMS/MS High Explosives	Qct	23	0	µg/L	—	—	—	—	0.31073043	0.273	0.0833	1
Selenium	Se	R-26	SW-846:6010B, SW-846:6020	Inorganic	Qct	38	0	µg/L	—	—	—	—	4.15789474	5	1	6
Silicon dioxide	SiO2	R-26	SW-846:6010B, SW-846:6010C	Inorganic	Qct	30	30	µg/L	57,176.667	57,300	52,100	61,100	—	—	—	—
Silver	Ag	R-26	SW-846:6010B, SW-846:6020	Inorganic	Qct	38	0	µg/L	—	—	—	—	0.73947368	1	0.2	1
Sodium	Na	R-26	SW-846:6010B, SW-846:6010C	Inorganic	Qct	38	38	µg/L	8456.0526	8445	7910	9120	—	—	—	—
Strontium	Sr	R-26	SW-846:6010B, SW-846:6010C	Inorganic	Qct	38	38	µg/L	45.007895	45	41.6	49	—	—	—	—
Styrene	100-42-5	R-26	SW-846:8260B	VOC	Qct	24	0	µg/L	—	—	—	—	0.85416667	1	0.3	1
Sulfate	SO4(-2)	R-26	EPA:300.0	General Chemistry	Qct	27	26	µg/L	1189.1923	1200	799	1420	1210	1210	1210	1210
Suspended sediment concentration	SSC	R-26	EPA:160.2	General Chemistry	Qct	1	0	µg/L	—	—	—	—	4750	4750	4750	4750
Temperature	TEMP	R-26	EPA:170.0	VOC	Qct	10	10	deg C	2.4	2	2	3	—	—	—	—
Tetrachloroethene	127-18-4	R-26	SW-846:8260B	VOC	Qct	24	0	µg/L	—	—	—	—	0.85416667	1	0.3	1
Thallium	Tl	R-26	SW-846:6020	Inorganic	Qct	38	2	µg/L	0.405	0.405	0.4	0.41	1.00127778	0.6	0.3	2
Tin	Sn	R-26	SW-846:6010B, SW-846:6010C	Inorganic	Qct	32	1	µg/L	4.71	4.71	4.71	4.71	10.7258065	10	2.5	50
TNX	TNX	R-26	SW-846:8321A_MOD, SW-846:8330B, SW-846:8330RDX	LCMS/MS High Explosives	Qct	17	0	µg/L	—	—	—	—	0.32107647	0.273	0.0833	0.5
Toluene	108-88-3	R-26	SW-846:8260B	VOC	Qct	24	4	µg/L	0.73	0.86	0.31	0.89	0.825	1	0.3	1
Total dissolved solids	TDS	R-26	EPA:160.1	General Chemistry	Qct	24	23	µg/L	94,539.13	97,000	62,900	126,000	108,000	108,000	108,000	108000
Total Kjeldahl nitrogen	TKN	R-26	EPA:351.2	General Chemistry	Qct	31	8	µg/L	202.175	54	24	656	81.3608696	76.4	10	500
Total organic carbon	TOC	R-26	SW-846:9060	General Chemistry	Qct	23	13	µg/L	512.23077	436	206	1120	598.7	481.5	132	1000
Total phosphate as phosphorus	PO4-P	R-26	EPA:365.4	General Chemistry	Qct	30	12	µg/L	72.2	70.6	38.8	111	47.8666667	49.55	10	98.9
Trichlorobenzene[1,2,3-]	87-61-6	R-26	SW-846:8260B	VOC	Qct	21	0	µg/L	—	—	—	—	0.83333333	1	0.3	1

Table 4.2-1 (continued)

Parameter Name	Parameter Code	Well	Analytical Method	Analytical Method Category[a]	Geological Unit Code[a]	No. Samples	No. Detects	Unit	Mean Detect	Median Detect	Min Detect	Max Detect	Mean ND	Median ND	Min ND	Max ND
Trichloroethene	79-01-6	R-26	SW-846:8260B	VOC	Qct	24	0	µg/L	—	—	—	—	0.85416667	1	0.3	1
Trinitrobenzene[1,3,5-]	99-35-4	R-26	SW-846:8330, SW-846:8321A_MOD, SW-846:8330B	HEXP, LCMS/MS High Explosives	Qct	23	0	µg/L	—	—	—	—	0.31073043	0.273	0.0833	1
Trinitrotoluene[2,4,6-]	118-96-7	R-26	SW-846:8330, SW-846:8321A_MOD, SW-846:8330B	HEXP, LCMS/MS High Explosives	Qct	23	0	µg/L	—	—	—	—	0.31073043	0.273	0.0833	1
Tritium	H-3	R-26	Generic:LLEE, Generic:Low_Level_Tritium	RAD	Qct	13	0	pCi/L	—	—	—	—	0.13623077	0.1288	-1.328	1.35
Uranium	U	R-26	SW-846:6020	Inorganic	Qct	38	36	µg/L	0.33275	0.328	0.282	0.607	0.317	0.317	0.304	0.33
Uranium-234	U-234	R-26	HASL-300:ISOU	RAD	Qct	14	14	pCi/L	0.212	0.206	0.142	0.257	—	—	—	—
Uranium-235/236	U-235/236	R-26	HASL-300:ISOU	RAD	Qct	14	0	pCi/L	—	—	—	—	0.01760643	0.01565	-0.0082	0.05
Uranium-238	U-238	R-26	HASL-300:ISOU	RAD	Qct	14	14	pCi/L	0.1225857	0.1215	0.0853	0.175	—	—	—	—
Vanadium	V	R-26	SW-846:6010B, SW-846:6010C	Inorganic	Qct	38	38	µg/L	8.3910526	8.355	7.35	9.68	—	—	—	—
Zinc	Zn	R-26	SW-846:6010B, SW-846:6010C	Inorganic	Qct	38	28	µg/L	8.5882143	9.04	2.31	19.6	4.395	3.3	2	10
Acenaphthene	83-32-9	R-27i	SW-846:8270C, SW-846:8270D, SW-846:8270DGCMS_SIM, SW-846:8310	SVOC	Tpf	8	0	µg/L	—	—	—	—	0.610625	0.5265	0.103	1.08
Acenaphthylene	208-96-8	R-27i	SW-846:8270C, SW-846:8270D, SW-846:8270DGCMS_SIM, SW-846:8310	SVOC	Tpf	8	0	µg/L	—	—	—	—	0.610625	0.5265	0.103	1.08
Acetone	67-64-1	R-27i	SW-846:8260B	VOC	Tpf	8	0	µg/L	—	—	—	—	7.875	10	1.5	10
Acidity or alkalinity of a solution	pH	R-27i	EPA:150.1	General Chemistry	Tpf	14	14	SU	7.4257143	7.38	7.29	7.81	—	—	—	—
Alkalinity-CO3	ALK-CO3	R-27i	EPA:310.1	General Chemistry	Tpf	14	0	µg/L	—	—	—	—	1350	1000	1000	4000
Alkalinity-CO3+HCO3	ALK-CO3+HCO3	R-27i	EPA:310.1	General Chemistry	Tpf	14	14	µg/L	54,735.714	50,000	47,100	125,000	—	—	—	—
Aluminum	Al	R-27i	SW-846:6010B, SW-846:6010C	Inorganic	Tpf	14	0	µg/L	—	—	—	—	181.142857	200	68	200
Amino-2,6-dinitrotoluene[4-]	19406-51-0	R-27i	SW-846:8321A_MOD	LCMS/MS High Explosives	Tpf	5	0	µg/L	—	—	—	—	0.2652	0.263	0.258	0.279
Amino-4,6-dinitrotoluene[2-]	35572-78-2	R-27i	SW-846:8321A_MOD	LCMS/MS High Explosives	Tpf	5	0	µg/L	—	—	—	—	0.2652	0.263	0.258	0.279
Ammonia as nitrogen	NH3-N	R-27i	EPA:350.1	General Chemistry	Tpf	14	0	µg/L	—	—	—	—	41.1571429	48.4	17	88
Anthracene	120-12-7	R-27i	SW-846:8270C, SW-846:8270D, SW-846:8270DGCMS_SIM, SW-846:8310	SVOC	Tpf	8	0	µg/L	—	—	—	—	0.610625	0.5265	0.103	1.08
Antimony	Sb	R-27i	SW-846:6020	Inorganic	Tpf	14	0	µg/L	—	—	—	—	2.71428571	3	1	3
Arsenic	As	R-27i	SW-846:6020	Inorganic	Tpf	14	1	µg/L	1.73	1.73	1.73	1.73	4.64769231	5	2	7.72
Barium	Ba	R-27i	SW-846:6010B, SW-846:6010C	Inorganic	Tpf	14	14	µg/L	10.064286	9.605	8.97	13.7	—	—	—	—
Benzo(g,h,i)perylene	191-24-2	R-27i	SW-846:8270C, SW-846:8270D, SW-846:8270DGCMS_SIM, SW-846:8310	SVOC	Tpf	8	0	µg/L	—	—	—	—	0.4921625	0.3145	0.0521	1.08
Benzoic Acid	65-85-0	R-27i	SW-846:8270C, SW-846:8270D	SVOC	Tpf	8	0	µg/L	—	—	—	—	15.79625	20.2	6.25	21.5
Beryllium	Be	R-27i	SW-846:6010B, SW-846:6010C	Inorganic	Tpf	14	0	µg/L	—	—	—	—	4.42857143	5	1	5
Bis(2-ethylhexyl)phthalate	117-81-7	R-27i	SW-846:8270C, SW-846:8270D	SVOC	Tpf	8	0	µg/L	—	—	—	—	7.191125	10.1	0.313	10.8
Boron	B	R-27i	SW-846:6010B, SW-846:6010C	Inorganic	Tpf	14	0	µg/L	—	—	—	—	45	50	15	50
Bromide	Br(-1)	R-27i	EPA:300.0	General Chemistry	Tpf	14	0	µg/L	—	—	—	—	181	200	67	200
Bromodichloromethane	75-27-4	R-27i	SW-846:8260B	VOC	Tpf	8	0	µg/L	—	—	—	—	0.825	1	0.3	1
Bromoform	75-25-2	R-27i	SW-846:8260B	VOC	Tpf	8	0	µg/L	—	—	—	—	0.825	1	0.3	1

Table 4.2-1 (continued)

Parameter Name	Parameter Code	Well	Analytical Method	Analytical Method Category[a]	Geological Unit Code[a]	No. Samples	No. Detects	Unit	Mean Detect	Median Detect	Min Detect	Max Detect	Mean ND	Median ND	Min ND	Max ND
Butanone[2-]	78-93-3	R-27i	SW-846:8260B	VOC	Tpf	8	0	µg/L	—	—	—	—	4.125	5	1.5	5
Cadmium	Cd	R-27i	SW-846:6020	Inorganic	Tpf	14	0	µg/L	—	—	—	—	0.9	1	0.3	1
Calcium	Ca	R-27i	SW-846:6010B, SW-846:6010C	Inorganic	Tpf	14	14	µg/L	8612.1429	8625	8080	9150	—	—	—	—
Carbon disulfide	75-15-0	R-27i	SW-846:8260B	VOC	Tpf	8	0	µg/L	—	—	—	—	4.125	5	1.5	5
Chloride	Cl(-1)	R-27i	EPA:300.0	General Chemistry	Tpf	14	14	µg/L	1352.1429	1335	1220	1790	—	—	—	—
Chlorobenzene	108-90-7	R-27i	SW-846:8260B	VOC	Tpf	8	0	µg/L	—	—	—	—	0.825	1	0.3	1
Chlorodibromomethane	124-48-1	R-27i	SW-846:8260B	VOC	Tpf	8	0	µg/L	—	—	—	—	0.825	1	0.3	1
Chloroform	67-66-3	R-27i	SW-846:8260B	VOC	Tpf	8	0	µg/L	—	—	—	—	0.825	1	0.3	1
Chloromethane	74-87-3	R-27i	SW-846:8260B	VOC	Tpf	8	0	µg/L	—	—	—	—	0.825	1	0.3	1
Chromium	Cr	R-27i	SW-846:6020	Inorganic	Tpf	14	2	µg/L	2.1	2.1	2.07	2.13	8.83333333	10	3	10
Cobalt	Co	R-27i	SW-846:6010B, SW-846:6010C	Inorganic	Tpf	14	0	µg/L	—	—	—	—	4.42857143	5	1	5
Copper	Cu	R-27i	SW-846:6010B, SW-846:6010C	Inorganic	Tpf	14	0	µg/L	—	—	—	—	9	10	3	10
Cyanide (total)	CN (Total)	R-27i	EPA:335.4	Inorganic	Tpf	6	0	µg/L	—	—	—	—	3.89	5	1.67	5
DNX	DNX	R-27i	SW-846:8321A_MOD, SW-846:8330RDX	LCMS/MS High Explosives	Tpf	3	0	µg/L	—	—	—	—	0.342	0.266	0.26	0.5
Fluoranthene	206-44-0	R-27i	SW-846:8270C, SW-846:8270D, SW-846:8270DGCMS_SIM, SW-846:8310	SVOC	Tpf	8	0	µg/L	—	—	—	—	0.4921625	0.3145	0.0521	1.08
Fluoride	F(-1)	R-27i	EPA:300.0	General Chemistry	Tpf	14	14	µg/L	177.07143	169	141	219	—	—	—	—
Gross alpha	GrossA	R-27i	EPA:900	RAD	Tpf	8	0	pCi/L	—	—	—	—	0.2475	0.284	-0.658	1.12
Gross beta	GrossB	R-27i	EPA:900	RAD	Tpf	8	1	pCi/L	4.02	4.02	4.02	4.02	0.95857143	0.713	0.426	2
Hardness	Hardness	R-27i	SM:A2340B	Inorganic	Tpf	14	14	µg/L	31,671.429	31,600	29,700	33,300	—	—	—	—
Hexachlorobutadiene	87-68-3	R-27i	SW-846:8260B	VOC	Tpf	8	1	µg/L	0.37	0.37	0.37	0.37	0.8	1	0.3	1
HMX	2691-41-0	R-27i	SW-846:8321A_MOD	LCMS/MS High Explosives	Tpf	5	0	µg/L	—	—	—	—	0.2652	0.263	0.258	0.279
Iron	Fe	R-27i	SW-846:6010B, SW-846:6010C	Inorganic	Tpf	14	0	µg/L	—	—	—	—	85.2714286	100	30	100
Lead	Pb	R-27i	SW-846:6020	Inorganic	Tpf	14	0	µg/L	—	—	—	—	1.78571429	2	0.5	2
Magnesium	Mg	R-27i	SW-846:6010B, SW-846:6010C	Inorganic	Tpf	14	14	µg/L	2469.2857	2475	2290	2640	—	—	—	—
Manganese	Mn	R-27i	SW-846:6010B, SW-846:6010C	Inorganic	Tpf	14	5	µg/L	4.788	2.98	2.06	10.6	8.22222222	10	2	10
Mercury	Hg	R-27i	EPA:245.2	Inorganic	Tpf	20	0	µg/L	—	—	—	—	0.1734	0.2	0.067	0.2
Methyl tert-butyl ether	1634-04-4	R-27i	SW-846:8260B	VOC	Tpf	8	0	µg/L	—	—	—	—	0.825	1	0.3	1
Methyl-2-pentanone[4-]	108-10-1	R-27i	SW-846:8260B	VOC	Tpf	8	0	µg/L	—	—	—	—	4.125	5	1.5	5
Methylene chloride	75-09-2	R-27i	SW-846:8260B	VOC	Tpf	8	0	µg/L	—	—	—	—	7.75	10	1	10
MNX	MNX	R-27i	SW-846:8321A_MOD, SW-846:8330RDX	LCMS/MS High Explosives	Tpf	3	0	µg/L	—	—	—	—	0.342	0.266	0.26	0.5
Molybdenum	Mo	R-27i	SW-846:6020	Inorganic	Tpf	14	13	µg/L	1.6053846	1.59	1.42	1.91	1.65	1.65	1.65	1.65
Nickel	Ni	R-27i	SW-846:6020	Inorganic	Tpf	14	7	µg/L	0.7214286	0.749	0.55	0.875	1.27557143	1.09	0.6	2
Nitrate-nitrite as nitrogen	NO3+NO2-N	R-27i	EPA:353.2	General Chemistry	Tpf	14	11	µg/L	121.04545	99.7	58	377	163.333333	190	50	250
Nitrotoluene[2-]	88-72-2	R-27i	SW-846:8321A_MOD	LCMS/MS High Explosives	Tpf	5	0	µg/L	—	—	—	—	0.2652	0.263	0.258	0.279

Table 4.2-1 (continued)

Parameter Name	Parameter Code	Well	Analytical Method	Analytical Method Category[a]	Geological Unit Code[a]	No. Samples	No. Detects	Unit	Mean Detect	Median Detect	Min Detect	Max Detect	Mean ND	Median ND	Min ND	Max ND
Perchlorate	ClO4	R-27i	SW-846:6850	LCMS/MS Perchlorate	Tpf	13	13	µg/L	0.1199	0.12	0.0957	0.134	—	—	—	—
Phenanthrene	85-01-8	R-27i	SW-846:8270C, SW-846:8270D, SW-846:8270DGCMS_SIM, SW-846:8310	SVOC	Tpf	8	0	µg/L	—	—	—	—	0.610625	0.5265	0.103	1.08
Potassium	K	R-27i	SW-846:6010B, SW-846:6010C	Inorganic	Tpf	14	14	µg/L	861.85714	898	673	981	—	—	—	—
Pyrene	129-00-0	R-27i	SW-846:8270C, SW-846:8270D, SW-846:8270DGCMS_SIM, SW-846:8310	SVOC	Tpf	8	0	µg/L	—	—	—	—	0.4921625	0.3145	0.0521	1.08
RDX	121-82-4	R-27i	SW-846:8321A_MOD	LCMS/MS High Explosives	Tpf	5	0	µg/L	—	—	—	—	0.2652	0.263	0.258	0.279
Selenium	Se	R-27i	SW-846:6020	Inorganic	Tpf	14	0	µg/L	—	—	—	—	4.57142857	5	2	5
Silicon dioxide	SiO2	R-27i	SW-846:6010B, SW-846:6010C	Inorganic	Tpf	14	14	µg/L	68,292.857	68,250	63,900	71,100	—	—	—	—
Silver	Ag	R-27i	SW-846:6020	Inorganic	Tpf	14	0	µg/L	—	—	—	—	0.9	1	0.3	1
Sodium	Na	R-27i	SW-846:6010B, SW-846:6010C	Inorganic	Tpf	14	14	µg/L	9880	9835	9450	10,600	—	—	—	—
Strontium	Sr	R-27i	SW-846:6010B, SW-846:6010C	Inorganic	Tpf	14	14	µg/L	46.85	46.65	44.9	49.9	—	—	—	—
Styrene	100-42-5	R-27i	SW-846:8260B	VOC	Tpf	8	0	µg/L	—	—	—	—	0.825	1	0.3	1
Sulfate	SO4(-2)	R-27i	EPA:300.0	General Chemistry	Tpf	14	14	µg/L	1865.7143	1855	1370	2770	—	—	—	—
Temperature	TEMP	R-27i	EPA:170.0	VOC	Tpf	4	4	deg C	2	2	2	2	—	—	—	—
Tetrachloroethene	127-18-4	R-27i	SW-846:8260B	VOC	Tpf	8	0	µg/L	—	—	—	—	0.825	1	0.3	1
Thallium	Tl	R-27i	SW-846:6020	Inorganic	Tpf	14	1	µg/L	0.354	0.354	0.354	0.354	1.55384615	2	0.6	2
Tin	Sn	R-27i	SW-846:6010B, SW-846:6010C	Inorganic	Tpf	14	0	µg/L	—	—	—	—	17.5	10	2.5	50
TNX	TNX	R-27i	SW-846:8321A_MOD, SW-846:8330RDX	LCMS/MS High Explosives	Tpf	3	0	µg/L	—	—	—	—	0.342	0.266	0.26	0.5
Toluene	108-88-3	R-27i	SW-846:8260B	VOC	Tpf	8	0	µg/L	—	—	—	—	0.825	1	0.3	1
Total dissolved solids	TDS	R-27i	EPA:160.1	General Chemistry	Tpf	14	14	µg/L	122,064.29	119,500	82,900	157,000	—	—	—	—
Total Kjeldahl nitrogen	TKN	R-27i	EPA:351.2	General Chemistry	Tpf	8	1	µg/L	527	527	527	527	199.385714	100	33	500
Total organic carbon	TOC	R-27i	SW-846:9060	General Chemistry	Tpf	8	6	µg/L	491.5	438.5	330	780	665	665	330	1000
Total phosphate as phosphorus	PO4-P	R-27i	EPA:365.4	General Chemistry	Tpf	14	3	µg/L	128.76667	150	39.3	197	45.2909091	50	20	70
Trichlorobenzene[1,2,3-]	87-61-6	R-27i	SW-846:8260B	VOC	Tpf	8	1	µg/L	0.31	0.31	0.31	0.31	0.8	1	0.3	1
Trichloroethene	79-01-6	R-27i	SW-846:8260B	VOC	Tpf	8	0	µg/L	—	—	—	—	0.825	1	0.3	1
Trinitrobenzene[1,3,5-]	99-35-4	R-27i	SW-846:8321A_MOD	LCMS/MS High Explosives	Tpf	5	0	µg/L	—	—	—	—	0.2652	0.263	0.258	0.279
Trinitrotoluene[2,4,6-]	118-96-7	R-27i	SW-846:8321A_MOD	LCMS/MS High Explosives	Tpf	5	0	µg/L	—	—	—	—	0.2652	0.263	0.258	0.279
Tritium	H-3	R-27i	Generic:Low_Level_Tritium	RAD	Tpf	8	0	pCi/L	—	—	—	—	0.213375	0.2705	-0.594	1.128
Uranium	U	R-27i	SW-846:6020	Inorganic	Tpf	14	11	µg/L	0.2632727	0.263	0.24	0.294	0.27066667	0.265	0.25	0.297
Uranium-234	U-234	R-27i	HASL-300:ISOU	RAD	Tpf	8	8	pCi/L	0.19625	0.203	0.139	0.257	—	—	—	—
Uranium-235/236	U-235/236	R-27i	HASL-300:ISOU	RAD	Tpf	8	1	pCi/L	0.0553	0.0553	0.0553	0.0553	0.01674143	0.0131	0.00723	0.044
Uranium-238	U-238	R-27i	HASL-300:ISOU	RAD	Tpf	8	8	pCi/L	0.10755	0.1035	0.0827	0.138	—	—	—	—
Vanadium	V	R-27i	SW-846:6010B, SW-846:6010C	Inorganic	Tpf	14	11	µg/L	1.7590909	1.63	1.33	2.45	5	5	5	5

Table 4.2-1 (continued)

Parameter Name	Parameter Code	Well	Analytical Method	Analytical Method Category[a]	Geological Unit Code[a]	No. Samples	No. Detects	Unit	Mean Detect	Median Detect	Min Detect	Max Detect	Mean ND	Median ND	Min ND	Max ND
Zinc	Zn	R-27i	SW-846:6010B, SW-846:6010C	Inorganic	Tpf	14	5	µg/L	5.43	5.01	4.27	7.68	9.25555556	10	3.3	10
Acenaphthene	83-32-9	R-47i	SW-846:8270C, SW-846:8270D, SW-846:8310	SVOC	Tpf	5	0	µg/L	—	—	—	—	0.6942	0.532	0.309	1.09
Acenaphthylene	208-96-8	R-47i	SW-846:8270C, SW-846:8270D, SW-846:8310	SVOC	Tpf	5	0	µg/L	—	—	—	—	0.6942	0.532	0.309	1.09
Acetone	67-64-1	R-47i	SW-846:8260B	VOC	Tpf	12	0	µg/L	—	—	—	—	6.45833333	10	1.5	10
Acidity or alkalinity of a solution	pH	R-47i	EPA:150.1	General Chemistry	Tpf	20	20	SU	7.5825	7.555	7.29	7.97	—	—	—	—
Alkalinity-CO3	ALK-CO3	R-47i	EPA:310.1	General Chemistry	Tpf	20	0	µg/L	—	—	—	—	1712.5	1000	1000	4000
Alkalinity-CO3+HCO3	ALK-CO3+HCO3	R-47i	EPA:310.1	General Chemistry	Tpf	20	20	µg/L	57,875	57,900	50,500	70,900	—	—	—	—
Aluminum	Al	R-47i	SW-846:6010B, SW-846:6010C	Inorganic	Tpf	21	3	µg/L	143.36667	143	73.1	214	163.333333	200	68	200
Amino-2,6-dinitrotoluene[4-]	19406-51-0	R-47i	SW-846:8321A_MOD, SW-846:8330B	LCMS/MS High Explosives	Tpf	18	0	µg/L	—	—	—	—	0.18311111	0.1725	0.0808	0.325
Amino-4,6-dinitrotoluene[2-]	35572-78-2	R-47i	SW-846:8321A_MOD, SW-846:8330B	LCMS/MS High Explosives	Tpf	18	0	µg/L	—	—	—	—	0.18311111	0.1725	0.0808	0.325
Ammonia as nitrogen	NH3-N	R-47i	EPA:350.1	General Chemistry	Tpf	20	9	µg/L	46.888889	45	24.2	84.8	52.2545455	50	17	134
Anthracene	120-12-7	R-47i	SW-846:8270C, SW-846:8270D, SW-846:8310	SVOC	Tpf	5	0	µg/L	—	—	—	—	0.6942	0.532	0.309	1.09
Antimony	Sb	R-47i	SW-846:6020	Inorganic	Tpf	21	2	µg/L	0.546	0.546	0.541	0.551	2.47368421	3	1	3
Arsenic	As	R-47i	SW-846:6020	Inorganic	Tpf	21	5	µg/L	2.444	2.56	1.92	2.83	4.319375	5	2	7.57
Barium	Ba	R-47i	SW-846:6010B, SW-846:6010C	Inorganic	Tpf	21	21	µg/L	6.4809524	6.02	3.67	13.1	—	—	—	—
Benzo(g,h,i)perylene	191-24-2	R-47i	SW-846:8270C, SW-846:8270D, SW-846:8310	SVOC	Tpf	5	0	µg/L	—	—	—	—	0.50664	0.309	0.051	1.09
Benzoic acid	65-85-0	R-47i	SW-846:8270C, SW-846:8270D	SVOC	Tpf	5	1	µg/L	32.6	32.6	32.6	32.6	17.4475	20.95	6.19	21.7
Beryllium	Be	R-47i	SW-846:6010B, SW-846:6010C	Inorganic	Tpf	21	0	µg/L	—	—	—	—	4.04761905	5	1	5
Bis(2-ethylhexyl)phthalate	117-81-7	R-47i	SW-846:8270C, SW-846:8270D	SVOC	Tpf	5	0	µg/L	—	—	—	—	8.978	10.3	3.09	10.9
Boron	B	R-47i	SW-846:6010B, SW-846:6010C	Inorganic	Tpf	21	9	µg/L	18.3	18.1	15.6	22.4	38.3333333	50	15	50
Bromide	Br(-1)	R-47i	EPA:300.0	General Chemistry	Tpf	20	3	µg/L	72.866667	72.1	70.8	75.7	160.882353	200	67	200
Bromodichloromethane	75-27-4	R-47i	SW-846:8260B	VOC	Tpf	12	0	µg/L	—	—	—	—	0.70833333	1	0.3	1
Bromoform	75-25-2	R-47i	SW-846:8260B	VOC	Tpf	12	0	µg/L	—	—	—	—	0.70833333	1	0.3	1
Butanone[2-]	78-93-3	R-47i	SW-846:8260B	VOC	Tpf	12	0	µg/L	—	—	—	—	3.54166667	5	1.5	5
Cadmium	Cd	R-47i	SW-846:6020	Inorganic	Tpf	21	0	µg/L	—	—	—	—	0.83333333	1	0.3	1
Calcium	Ca	R-47i	SW-846:6010B, SW-846:6010C	Inorganic	Tpf	21	21	µg/L	10,057.143	9990	9120	109,00	—	—	—	—
Carbon disulfide	75-15-0	R-47i	SW-846:8260B	VOC	Tpf	12	0	µg/L	—	—	—	—	3.54166667	5	1.5	5
Chloride	Cl(-1)	R-47i	EPA:300.0	General Chemistry	Tpf	20	20	µg/L	2507.5	2370	1870	3970	—	—	—	—
Chlorobenzene	108-90-7	R-47i	SW-846:8260B	VOC	Tpf	12	0	µg/L	—	—	—	—	0.70833333	1	0.3	1
Chlorodibromomethane	124-48-1	R-47i	SW-846:8260B	VOC	Tpf	12	0	µg/L	—	—	—	—	0.70833333	1	0.3	1
Chloroform	67-66-3	R-47i	SW-846:8260B	VOC	Tpf	12	0	µg/L	—	—	—	—	0.70833333	1	0.3	1
Chloromethane	74-87-3	R-47i	SW-846:8260B	VOC	Tpf	12	0	µg/L	—	—	—	—	0.70833333	1	0.3	1
Chromium	Cr	R-47i	SW-846:6020	Inorganic	Tpf	21	8	µg/L	3.5775	2.8	2.01	8.22	7.30769231	10	3	10
Cobalt	Co	R-47i	SW-846:6010B, SW-846:6010C	Inorganic	Tpf	21	0	µg/L	—	—	—	—	4.04761905	5	1	5
Copper	Cu	R-47i	SW-846:6010B, SW-846:6010C	Inorganic	Tpf	21	1	µg/L	4.19	4.19	4.19	4.19	8.25	10	3	10
Cyanide (total)	CN (Total)	R-47i	EPA:335.4	Inorganic	Tpf	12	0	µg/L	—	—	—	—	3.6125	5	1.67	5

Table 4.2-1 (continued)

Parameter Name	Parameter Code	Well	Analytical Method	Analytical Method Category[a]	Geological Unit Code[a]	No. Samples	No. Detects	Unit	Mean Detect	Median Detect	Min Detect	Max Detect	Mean ND	Median ND	Min ND	Max ND
DNX	DNX	R-47i	SW-846:8321A_MOD, SW-846:8330B, SW-846:8330RDX	LCMS/MS High Explosives	Tpf	17	0	µg/L	—	—	—	—	0.19929412	0.087	0.0808	0.5
Fluoranthene	206-44-0	R-47i	SW-846:8270C, SW-846:8270D, SW-846:8310	SVOC	Tpf	5	0	µg/L	—	—	—	—	0.50664	0.309	0.051	1.09
Fluoride	F(-1)	R-47i	EPA:300.0	General Chemistry	Tpf	20	20	µg/L	146.345	140	79.3	310	—	—	—	—
Gross alpha	GrossA	R-47i	EPA:900	RAD	Tpf	4	1	pCi/L	11.4	11.4	11.4	11.4	0.522	0.691	-0.505	1.38
Gross beta	GrossB	R-47i	EPA:900	RAD	Tpf	4	1	pCi/L	13.7	13.7	13.7	13.7	0.71166667	0.809	0.365	0.961
Gross gamma	GrossG	R-47i	EPA:901.1	RAD	Tpf	1	0	pCi/L	—	—	—	—	271	271	271	271
Hardness	Hardness	R-47i	SM:A2340B	Inorganic	Tpf	21	21	µg/L	35,138.095	34,800	32,300	38,400	—	—	—	—
Heptachlor	76-44-8	R-47i	SW-846:8081A	PESTPCB	Tpf	1	0	µg/L	—	—	—	—	0.0204	0.0204	0.0204	0.0204
Hexachlorobutadiene	87-68-3	R-47i	SW-846:8260B	VOC	Tpf	12	0	µg/L	—	—	—	—	0.70833333	1	0.3	1
HMX	2691-41-0	R-47i	SW-846:8321A_MOD, SW-846:8330B	LCMS/MS High Explosives	Tpf	18	0	µg/L	—	—	—	—	0.18311111	0.1725	0.0808	0.325
Iron	Fe	R-47i	SW-846:6010B, SW-846:6010C	Inorganic	Tpf	21	5	µg/L	129.42	55.6	41.6	359	78.125	100	30	100
Lead	Pb	R-47i	SW-846:6020	Inorganic	Tpf	21	2	µg/L	0.578	0.578	0.571	0.585	1.60526316	2	0.5	2
Magnesium	Mg	R-47i	SW-846:6010B, SW-846:6010C	Inorganic	Tpf	21	21	µg/L	2431.9048	2410	2310	2720	—	—	—	—
Manganese	Mn	R-47i	SW-846:6010B, SW-846:6010C	Inorganic	Tpf	21	7	µg/L	33.707143	24.4	3.3	95.2	7.14285714	10	2	10
Mercury	Hg	R-47i	EPA:245.2	Inorganic	Tpf	32	0	µg/L	—	—	—	—	0.1584375	0.2	0.067	0.2
Methyl tert-butyl ether	1634-04-4	R-47i	SW-846:8260B	VOC	Tpf	12	0	µg/L	—	—	—	—	0.70833333	1	0.3	1
Methyl-2-pentanone[4-]	108-10-1	R-47i	SW-846:8260B	VOC	Tpf	12	0	µg/L	—	—	—	—	3.54166667	5	1.5	5
Methylene chloride	75-09-2	R-47i	SW-846:8260B	VOC	Tpf	12	0	µg/L	—	—	—	—	6.25	10	1	10
MNX	MNX	R-47i	SW-846:8321A_MOD, SW-846:8330B, SW-846:8330RDX	LCMS/MS High Explosives	Tpf	17	0	µg/L	—	—	—	—	0.19929412	0.087	0.0808	0.5
Molybdenum	Mo	R-47i	SW-846:6020	Inorganic	Tpf	21	20	µg/L	2.6795	2.04	1.27	8.16	1.45	1.45	1.45	1.45
Nickel	Ni	R-47i	SW-846:6020	Inorganic	Tpf	21	16	µg/L	1.668875	1.185	0.574	4.93	1.006	0.6	0.6	2
Nitrate-nitrite as nitrogen	NO3+NO2-N	R-47i	EPA:353.2	General Chemistry	Tpf	20	20	µg/L	381.45	408.5	130	489	—	—	—	—
Nitrotoluene[2-]	88-72-2	R-47i	SW-846:8321A_MOD, SW-846:8330B	LCMS/MS High Explosives	Tpf	18	0	µg/L	—	—	—	—	0.18417222	0.17355	0.0828	0.325
Oxygen-18/Oxygen-16 Ratio from Nitrate	O18O16-NO3	R-47i	Generic:Oxygen Isotope Ratio	General Chemistry	Tpf	2	2	permil	0.36645	0.3665	-1.2922	2.0251	—	—	—	—
Perchlorate	ClO4	R-47i	SW-846:6850	LCMS/MS Perchlorate	Tpf	19	19	µg/L	0.2495263	0.25	0.222	0.286	—	—	—	—
Perfluorooctanoic acid	335-67-1	R-47i	EPA:537M	LCMS/MS PFAS	Tpf	1	0	µg/L	—	—	—	—	0.000728	0.00073	0.00073	0.00073
Phenanthrene	85-01-8	R-47i	SW-846:8270C, SW-846:8270D, SW-846:8310	SVOC	Tpf	5	0	µg/L	—	—	—	—	0.6942	0.532	0.309	1.09
Potassium	K	R-47i	SW-846:6010B, SW-846:6010C	Inorganic	Tpf	21	20	µg/L	483.7	415	347	882	568	568	568	568
Pyrene	129-00-0	R-47i	SW-846:8270C, SW-846:8270D, SW-846:8310	SVOC	Tpf	5	0	µg/L	—	—	—	—	0.50664	0.309	0.051	1.09
Radium-226	Ra-226	R-47i	EPA:903.1	RAD	Tpf	1	1	pCi/L	4.86	4.86	4.86	4.86	—	—	—	—
Radium-228	Ra-228	R-47i	EPA:904	RAD	Tpf	1	0	pCi/L	—	—	—	—	0.0894	0.0894	0.0894	0.0894
RDX	121-82-4	R-47i	SW-846:8321A_MOD, SW-846:8330B	LCMS/MS High Explosives	Tpf	18	0	µg/L	—	—	—	—	0.18311111	0.1725	0.0808	0.325
Selenium	Se	R-47i	SW-846:6020	Inorganic	Tpf	21	1	µg/L	2.77	2.77	2.77	2.77	4.0765	5	1.53	5

Table 4.2-1 (continued)

Parameter Name	Parameter Code	Well	Analytical Method	Analytical Method Category[a]	Geological Unit Code[a]	No. Samples	No. Detects	Unit	Mean Detect	Median Detect	Min Detect	Max Detect	Mean ND	Median ND	Min ND	Max ND
Silicon dioxide	SiO2	R-47i	SW-846:6010B, SW-846:6010C	Inorganic	Tpf	20	20	µg/L	58,810	58,850	54,900	62,500	—	—	—	—
Silver	Ag	R-47i	SW-846:6020	Inorganic	Tpf	21	0	µg/L	—	—	—	—	0.83333333	1	0.3	1
Sodium	Na	R-47i	SW-846:6010B, SW-846:6010C	Inorganic	Tpf	21	21	µg/L	15,866.667	14,800	11,700	30,300	—	—	—	—
Strontium	Sr	R-47i	SW-846:6010B, SW-846:6010C	Inorganic	Tpf	21	21	µg/L	53.12381	52.4	46	66	—	—	—	—
Styrene	100-42-5	R-47i	SW-846:8260B	VOC	Tpf	12	0	µg/L	—	—	—	—	0.70833333	1	0.3	1
Sulfate	SO4(-2)	R-47i	EPA:300.0	General Chemistry	Tpf	20	20	µg/L	6545	4975	3440	18,500	—	—	—	—
Temperature	TEMP	R-47i	EPA:170.0	VOC	Tpf	16	16	deg C	2.5625	2	2	4	—	—	—	—
Tetrachloroethene	127-18-4	R-47i	SW-846:8260B	VOC	Tpf	12	0	µg/L	—	—	—	—	0.70833333	1	0.3	1
Thallium	Tl	R-47i	SW-846:6020	Inorganic	Tpf	21	0	µg/L	—	—	—	—	1.42857143	2	0.6	2
Tin	Sn	R-47i	SW-846:6010B, SW-846:6010C	Inorganic	Tpf	21	2	µg/L	5.235	5.235	3.09	7.38	12.6315789	10	2.5	50
TNX	TNX	R-47i	SW-846:8321A_MOD, SW-846:8330B, SW-846:8330RDX	LCMS/MS High Explosives	Tpf	17	0	µg/L	—	—	—	—	0.19929412	0.087	0.0808	0.5
Toluene	108-88-3	R-47i	SW-846:8260B	VOC	Tpf	12	0	µg/L	—	—	—	—	0.70833333	1	0.3	1
Total dissolved solids	TDS	R-47i	EPA:160.1	General Chemistry	Tpf	20	20	µg/L	122,255	126,000	81,400	151,000	—	—	—	—
Total Kjeldahl nitrogen	TKN	R-47i	EPA:351.2	General Chemistry	Tpf	14	5	µg/L	138.42	106	39.7	309	73.8666667	100	33	100
Total organic carbon	TOC	R-47i	SW-846:9060	General Chemistry	Tpf	14	14	µg/L	2648.2143	2590	429	4960	—	—	—	—
Total phosphate as phosphorus	PO4-P	R-47i	EPA:365.4	General Chemistry	Tpf	20	9	µg/L	66.122222	46.3	26.9	150	51.3	50	27.1	95.6
Trichlorobenzene[1,2,3-]	87-61-6	R-47i	SW-846:8260B	VOC	Tpf	12	0	µg/L	—	—	—	—	0.70833333	1	0.3	1
Trichloroethene	79-01-6	R-47i	SW-846:8260B	VOC	Tpf	12	0	µg/L	—	—	—	—	0.72166667	1	0.3	1
Trinitrobenzene[1,3,5-]	99-35-4	R-47i	SW-846:8321A_MOD, SW-846:8330B	LCMS/MS High Explosives	Tpf	18	0	µg/L	—	—	—	—	0.18311111	0.1725	0.0808	0.325
Trinitrotoluene[2,4,6-]	118-96-7	R-47i	SW-846:8321A_MOD, SW-846:8330B	LCMS/MS High Explosives	Tpf	18	0	µg/L	—	—	—	—	0.18311111	0.1725	0.0808	0.325
Tritium	H-3	R-47i	Generic:Low_Level_Tritium	RAD	Tpf	6	1	pCi/L	2.484	2.484	2.484	2.484	0.52884	0.5152	-0.232	1.689
Uranium	U	R-47i	SW-846:6020	Inorganic	Tpf	21	21	µg/L	0.4266667	0.34	0.219	0.774	—	—	—	—
Uranium-234	U-234	R-47i	HASL-300:ISOU	RAD	Tpf	4	4	pCi/L	0.38625	0.3895	0.303	0.463	—	—	—	—
Uranium-235/236	U-235/236	R-47i	HASL-300:ISOU	RAD	Tpf	4	0	pCi/L	—	—	—	—	0.0244425	0.01455	0.00897	0.0597
Uranium-238	U-238	R-47i	HASL-300:ISOU	RAD	Tpf	4	3	pCi/L	0.16	0.158	0.158	0.164	0.0694	0.0694	0.0694	0.0694
Vanadium	V	R-47i	SW-846:6010B, SW-846:6010C	Inorganic	Tpf	21	15	µg/L	1.3966667	1.36	1.02	2.08	3.98	5	1	5
Zinc	Zn	R-47i	SW-846:6010B, SW-846:6010C	Inorganic	Tpf	21	7	µg/L	7.0671429	4.95	3.53	12	8.56428571	10	3.3	10
Acetone	67-64-1	R-63i	SW-846:8260B	VOC	Tpf	1	1	µg/L	1.92	1.92	1.92	1.92	—	—	—	—
Acidity or alkalinity of a solution	pH	R-63i	EPA:150.1	General Chemistry	Tpf	1	1	SU	9.31	9.31	9.31	9.31	—	—	—	—
Alkalinity-CO3	ALK-CO3	R-63i	EPA:310.1	General Chemistry	Tpf	1	1	µg/L	37,000	37,000	37,000	37,000	—	—	—	—
Alkalinity-CO3+HCO3	ALK-CO3+HCO3	R-63i	EPA:310.1	General Chemistry	Tpf	1	1	µg/L	89,000	89,000	89,000	89,000	—	—	—	—
Aluminum	Al	R-63i	SW-846:6010C	Inorganic	Tpf	1	0	µg/L	—	—	—	—	68	68	68	68
Amino-2,6-dinitrotoluene[4-]	19406-51-0	R-63i	SW-846:8330B	LCMS/MS High Explosives	Tpf	1	0	µg/L	—	—	—	—	0.0908	0.0908	0.0908	0.0908

Table 4.2-1 (continued)

Parameter Name	Parameter Code	Well	Analytical Method	Analytical Method Category[a]	Geological Unit Code[a]	No. Samples	No. Detects	Unit	Mean Detect	Median Detect	Min Detect	Max Detect	Mean ND	Median ND	Min ND	Max ND
Amino-4,6-dinitrotoluene[2-]	35572-78-2	R-63i	SW-846:8330B	LCMS/MS High Explosives	Tpf	1	0	µg/L	—	—	—	—	0.0908	0.0908	0.0908	0.0908
Ammonia as nitrogen	NH3-N	R-63i	EPA:350.1	General Chemistry	Tpf	1	1	µg/L	48.6	48.6	48.6	48.6	—	—	—	—
Antimony	Sb	R-63i	SW-846:6020	Inorganic	Tpf	1	0	µg/L	—	—	—	—	1	1	1	1
Arsenic	As	R-63i	SW-846:6020	Inorganic	Tpf	1	1	µg/L	3.03	3.03	3.03	3.03	—	—	—	—
Barium	Ba	R-63i	SW-846:6010C	Inorganic	Tpf	1	1	µg/L	10.9	10.9	10.9	10.9	—	—	—	—
Beryllium	Be	R-63i	SW-846:6010C	Inorganic	Tpf	1	0	µg/L	—	—	—	—	1	1	1	1
Boron	B	R-63i	SW-846:6010C	Inorganic	Tpf	1	0	µg/L	—	—	—	—	15	15	15	15
Bromide	Br(-1)	R-63i	EPA:300.0	General Chemistry	Tpf	1	0	µg/L	—	—	—	—	67	67	67	67
Bromodichloromethane	75-27-4	R-63i	SW-846:8260B	VOC	Tpf	1	0	µg/L	—	—	—	—	0.3	0.3	0.3	0.3
Bromoform	75-25-2	R-63i	SW-846:8260B	VOC	Tpf	1	0	µg/L	—	—	—	—	0.3	0.3	0.3	0.3
Butanone[2-]	78-93-3	R-63i	SW-846:8260B	VOC	Tpf	1	0	µg/L	—	—	—	—	1.5	1.5	1.5	1.5
Cadmium	Cd	R-63i	SW-846:6020	Inorganic	Tpf	1	0	µg/L	—	—	—	—	0.3	0.3	0.3	0.3
Calcium	Ca	R-63i	SW-846:6010C	Inorganic	Tpf	1	1	µg/L	12,900	12,900	12,900	12,900	—	—	—	—
Carbon Disulfide	75-15-0	R-63i	SW-846:8260B	VOC	Tpf	1	0	µg/L	—	—	—	—	1.5	1.5	1.5	1.5
Chloride	Cl(-1)	R-63i	EPA:300.0	General Chemistry	Tpf	1	1	µg/L	1790	1790	1790	1790	—	—	—	—
Chlorobenzene	108-90-7	R-63i	SW-846:8260B	VOC	Tpf	1	0	µg/L	—	—	—	—	0.3	0.3	0.3	0.3
Chlorodibromomethane	124-48-1	R-63i	SW-846:8260B	VOC	Tpf	1	0	µg/L	—	—	—	—	0.3	0.3	0.3	0.3
Chloroform	67-66-3	R-63i	SW-846:8260B	VOC	Tpf	1	0	µg/L	—	—	—	—	0.3	0.3	0.3	0.3
Chloromethane	74-87-3	R-63i	SW-846:8260B	VOC	Tpf	1	0	µg/L	—	—	—	—	0.3	0.3	0.3	0.3
Chromium	Cr	R-63i	SW-846:6020	Inorganic	Tpf	1	0	µg/L	—	—	—	—	3	3	3	3
Cobalt	Co	R-63i	SW-846:6010C	Inorganic	Tpf	1	0	µg/L	—	—	—	—	1	1	1	1
Copper	Cu	R-63i	SW-846:6010C	Inorganic	Tpf	1	0	µg/L	—	—	—	—	3	3	3	3
Cyanide (total)	CN (Total)	R-63i	EPA:335.4	Inorganic	Tpf	1	0	µg/L	—	—	—	—	1.67	1.67	1.67	1.67
DNX	DNX	R-63i	SW-846:8330B	LCMS/MS High Explosives	Tpf	1	0	µg/L	—	—	—	—	0.0908	0.0908	0.0908	0.0908
Fluoride	F(-1)	R-63i	EPA:300.0	General Chemistry	Tpf	1	1	µg/L	270	270	270	270	—	—	—	—
Hardness	Hardness	R-63i	SM:A2340B	Inorganic	Tpf	1	1	µg/L	46,700	46,700	46,700	46,700	—	—	—	—
Hexachlorobutadiene	87-68-3	R-63i	SW-846:8260B	VOC	Tpf	1	0	µg/L	—	—	—	—	0.3	0.3	0.3	0.3
HMX	2691-41-0	R-63i	SW-846:8330B	LCMS/MS High Explosives	Tpf	1	0	µg/L	—	—	—	—	0.0908	0.0908	0.0908	0.0908
Iron	Fe	R-63i	SW-846:6010C	Inorganic	Tpf	1	1	µg/L	37.3	37.3	37.3	37.3	—	—	—	—
Lead	Pb	R-63i	SW-846:6020	Inorganic	Tpf	1	0	µg/L	—	—	—	—	0.5	0.5	0.5	0.5
Magnesium	Mg	R-63i	SW-846:6010C	Inorganic	Tpf	1	1	µg/L	3530	3530	3530	3530	—	—	—	—
Manganese	Mn	R-63i	SW-846:6010C	Inorganic	Tpf	1	1	µg/L	5.67	5.67	5.67	5.67	—	—	—	—
Mercury	Hg	R-63i	EPA:245.2	Inorganic	Tpf	2	0	µg/L	—	—	—	—	0.067	0.067	0.067	0.067
Methyl tert-butyl ether	1634-04-4	R-63i	SW-846:8260B	VOC	Tpf	1	0	µg/L	—	—	—	—	0.3	0.3	0.3	0.3
Methyl-2-pentanone[4-]	108-10-1	R-63i	SW-846:8260B	VOC	Tpf	1	0	µg/L	—	—	—	—	1.5	1.5	1.5	1.5
Methylene chloride	75-09-2	R-63i	SW-846:8260B	VOC	Tpf	1	1	µg/L	1.42	1.42	1.42	1.42	—	—	—	—

Table 4.2-1 (continued)

Parameter Name	Parameter Code	Well	Analytical Method	Analytical Method Category[a]	Geological Unit Code[a]	No. Samples	No. Detects	Unit	Mean Detect	Median Detect	Min Detect	Max Detect	Mean ND	Median ND	Min ND	Max ND
MNX	MNX	R-63i	SW-846:8330B	LCMS/MS High Explosives	Tpf	1	0	µg/L	—	—	—	—	0.0908	0.0908	0.0908	0.0908
Molybdenum	Mo	R-63i	SW-846:6020	Inorganic	Tpf	1	1	µg/L	2.39	2.39	2.39	2.39	—	—	—	—
Nickel	Ni	R-63i	SW-846:6020	Inorganic	Tpf	1	1	µg/L	0.75	0.75	0.75	0.75	—	—	—	—
Nitrate-nitrite as nitrogen	NO3+NO2-N	R-63i	EPA:353.2	General Chemistry	Tpf	1	1	µg/L	561	561	561	561	—	—	—	—
Nitrotoluene[2-]	88-72-2	R-63i	SW-846:8330B	LCMS/MS High Explosives	Tpf	1	0	µg/L	—	—	—	—	0.093	0.093	0.093	0.093
Perchlorate	ClO4	R-63i	SW-846:6850	LCMS/MS Perchlorate	Tpf	1	1	µg/L	0.223	0.223	0.223	0.223	—	—	—	—
Potassium	K	R-63i	SW-846:6010C	Inorganic	Tpf	1	1	µg/L	1250	1250	1250	1250	—	—	—	—
RDX	121-82-4	R-63i	SW-846:8330B	LCMS/MS High Explosives	Tpf	1	1	µg/L	0.31	0.31	0.31	0.31	—	—	—	—
Selenium	Se	R-63i	SW-846:6020	Inorganic	Tpf	1	0	µg/L	—	—	—	—	2	2	2	2
Silicon dioxide	SiO2	R-63i	SW-846:6010C	Inorganic	Tpf	1	1	µg/L	53,000	53,000	53,000	53,000	—	—	—	—
Silver	Ag	R-63i	SW-846:6020	Inorganic	Tpf	1	0	µg/L	—	—	—	—	0.3	0.3	0.3	0.3
Sodium	Na	R-63i	SW-846:6010C	Inorganic	Tpf	1	1	µg/L	22,000	22,000	22,000	22,000	—	—	—	—
Strontium	Sr	R-63i	SW-846:6010C	Inorganic	Tpf	1	1	µg/L	66.3	66.3	66.3	66.3	—	—	—	—
Styrene	100-42-5	R-63i	SW-846:8260B	VOC	Tpf	1	0	µg/L	—	—	—	—	0.3	0.3	0.3	0.3
Sulfate	SO4(-2)	R-63i	EPA:300.0	General Chemistry	Tpf	1	1	µg/L	3730	3730	3730	3730	—	—	—	—
Temperature	TEMP	R-63i	EPA:170.0	VOC	Tpf	2	2	deg C	2	2	2	2	—	—	—	—
Tetrachloroethene	127-18-4	R-63i	SW-846:8260B	VOC	Tpf	1	0	µg/L	—	—	—	—	0.3	0.3	0.3	0.3
Thallium	Tl	R-63i	SW-846:6020	Inorganic	Tpf	1	0	µg/L	—	—	—	—	0.6	0.6	0.6	0.6
Tin	Sn	R-63i	SW-846:6010C	Inorganic	Tpf	1	0	µg/L	—	—	—	—	2.5	2.5	2.5	2.5
TNX	TNX	R-63i	SW-846:8330B	LCMS/MS High Explosives	Tpf	1	0	µg/L	—	—	—	—	0.0908	0.0908	0.0908	0.0908
Toluene	108-88-3	R-63i	SW-846:8260B	VOC	Tpf	1	0	µg/L	—	—	—	—	0.3	0.3	0.3	0.3
Total dissolved solids	TDS	R-63i	EPA:160.1	General Chemistry	Tpf	1	1	µg/L	124,000	124,000	124,000	124,000	—	—	—	—
Total Kjeldahl nitrogen	TKN	R-63i	EPA:351.2	General Chemistry	Tpf	1	1	µg/L	94.2	94.2	94.2	94.2	—	—	—	—
Total organic carbon	TOC	R-63i	SW-846:9060	General Chemistry	Tpf	1	1	µg/L	823	823	823	823	—	—	—	—
Total phosphate as phosphorus	PO4-P	R-63i	EPA:365.4	General Chemistry	Tpf	1	1	µg/L	100	100	100	100	—	—	—	—
Trichlorobenzene[1,2,3-]	87-61-6	R-63i	SW-846:8260B	VOC	Tpf	1	0	µg/L	—	—	—	—	0.3	0.3	0.3	0.3
Trichloroethene	79-01-6	R-63i	SW-846:8260B	VOC	Tpf	1	0	µg/L	—	—	—	—	0.3	0.3	0.3	0.3

Table 4.2-1 (continued)

Parameter Name	Parameter Code	Well	Analytical Method	Analytical Method Category[a]	Geological Unit Code[a]	No. Samples	No. Detects	Unit	Mean Detect	Median Detect	Min Detect	Max Detect	Mean ND	Median ND	Min ND	Max ND
Trinitrobenzene[1,3,5-]	99-35-4	R-63i	SW-846:8330B	LCMS/MS High Explosives	Tpf	1	0	µg/L	—	—	—	—	0.0908	0.0908	0.0908	0.0908
Trinitrotoluene[2,4,6-]	118-96-7	R-63i	SW-846:8330B	LCMS/MS High Explosives	Tpf	1	0	µg/L	—	—	—	—	0.0908	0.0908	0.0908	0.0908
Uranium	U	R-63i	SW-846:6020	Inorganic	Tpf	1	1	µg/L	0.943	0.943	0.943	0.943	—	—	—	—
Vanadium	V	R-63i	SW-846:6010C	Inorganic	Tpf	1	1	µg/L	1.41	1.41	1.41	1.41	—	—	—	—
Zinc	Zn	R-63i	SW-846:6010C	Inorganic	Tpf	1	0	µg/L	—	—	—	—	6.32	6.32	6.32	6.32

Note: This table summarizes the analytical data used to identify COPCs and calculate EPCs for the risk assessment.

[a] These fields concatenate entries from all samples for the analyte and well combination.

[b] ND = Nondetection,

[c] HEXP = High explosives.

[d] — = Not applicable.

[e] SVOC = Semivolatile organic compound.

[f] VOC = Volatile organic compound.

[g] LCMS/MS = Liquid chromatography mass spectrometry/mass spectrometry.

[h] DNX = Hexahydro-1,3-dinitro-5-nitro-1,3,5-triazine.

[I] RAD = Radionuclides.

[j] PESTPCB = Pesticides/PCBs.

[k] HMX = Her Majesty's Explosive.

[l] MNX = Hexahydro-1-nitroso-3,5-dinitro-1,3,5-triazine.

[m] PFAS = Per- and polyfluoroalkyl substances.

[n] TNX = 2,4,6-trinitroxylene.

Table 4.3-1
Statistical Background Comparison Test Results and Identification of COPCs for Inorganic Chemicals and Radionuclides

Analyte	Two-Sample t-test	Gehan Test	Quantile Test (0.75)	Quantile Test (0.90)	Slippage Test	Notes on Stat Tests	COPC Identification Notes
Aluminum	0.00677	0.1768	0.06279	0.06279	0.03655		Identified as a COPC in R-25 and R-25b. Statistical test results without these wells are 0.28, 0.46, 0.54, 0.54, and 0.37.
Ammonia as nitrogen	0.01484	0.0176	0.04016	0.01008	0.001298		Not a COPC. Ammonia is not recognized as a potential health hazard by EPA or NMED.
Antimony	0.2593	0.3275	1	1	0.05832		
Arsenic	0.2078	0.2681	0.7854	0.6305	0.06389		
Barium	1.425e-15	1.016e-05	4.97e-14	3.196e-06	5.98e-09		Plots show elevated concentrations in a number of wells. Identified as a COPC in all wells where there are one or more detections for simplicity since max concentrations for all wells are far below screening levels.
Beryllium	0.1423	0.1323	1	1	—[a]	Slippage: No detects in background	
Boron	1.606e-24	5.603e-06	8.873e-15	3.196e-06	6.142e-21		Plots show the range of detects in most wells are above the range of background well detects. Identified as a COPC in all wells where there are one or more detections for simplicity since max concentrations for all wells are far below screening levels.
Bromide	0.02459	0.7058	0.1729	0.1729	9.655e-08		Not a COPC. No toxicity data or regulatory criteria.
Cadmium	0.1518	0.1494	1	1	1		

Table 4.3-1 (continued)

Analyte	Two-Sample t-test	Gehan Test	Quantile Test (0.75)	Quantile Test (0.90)	Slippage Test	Notes on Stat Tests	COPC Identification Notes
Calcium	1.076e-11	0	8.546e-16	3.196e-06	7.587e-30		Essential nutrient per Section 5.2 of NMED 2019, 700550.
Cesium	NC[b]	NC	NC	NC	NC	All:less than 2 observations in site or background	
Chloride	1.529e-12	0	3.721e-14	1.646e-05	3.721e-14		Essential nutrient per Section 5.2 of NMED 2019, 700550. Maximum below NMAC and MCL standard of 250 mg/L.
Chromium	0.4566	0.2772	0.7225	0.8736	0.6643		
Cobalt	0.07145	0.2144	0.2916	0.2916	0.1703		Identified as a COPC in R-25. Statistical test results without this well are 0.20, 0.21, 0.60, 0.60, and 0.33.
Copper	1.129e-06	0.0446	1.799e-05	1.799e-05	9.774e-09		An early outlier result exists in CdV-16-1(i). Identified as a COPC in two wells (CdV-16-1(i) and R-25b based on review of plots. Statistical test results w/o these wells are 0.23, 0.50, 1, 1 and 0.067.
Cyanide (total)	0.5005	0.2027	1	1	1		
Fluoride	0.07989	0.9921	0.9193	0.009958	0.0002975		Identified as a COPC in R-19. Statistical test results without these wells are 1, 1, 1, 0.80, and 0.62.
Hardness	1.651e-15	0	7.833e-15	1.603e-05	4.737e-35		A measure that's analogous to calcium and magnesium.
Iron	0.01249	0.01946	0.006069	0.002832	0.1271		An early outlier result exists in CdV-16-1(i). In later years, the box plot shows potentially elevated concentrations in at least three other wells [R-19, CdV-16-2(i)r, and R-25b]. Identified as a COPC in all wells where there are one or more detections for simplicity since max concentrations other than the single outlier are far below screening levels.
Lead	0.06189	0.1798	0.4405	0.4405	0.02382		Not identified as a COPC. A single outlier result from 2005 exists in CdV-16-1(i), but all subsequent detections in this well are below the nominal detection limit. The slippage test result without this value is 0.088. Both stat tests and review of plots indicate no differences between site and background wells subsequent to the early outlier result in CdV-16-1(i).
Lithium	NC	NC	NC	NC	NC	All:less than 2 observations in site or background	
Magnesium	4.182e-28	0	8.546e-16	3.196e-06	1.989e-23		No toxicity data or regulatory criteria. Essential nutrient per Section 5.2 of NMED 2019, 700550.
Manganese	0.08557	0.05722	0.1559	0.03501	0.4405		Plots show potentially elevated in wells R-25 and R-25b. Identified as a COPC these wells. Statistical test results w/o R-25 and R-25b are 0.80, 0.37, 0.76, 0.76, 1.
Mercury	0.03332	0.1307	0.1268	0.1268	—	Slippage: No detects in background	Not a COPC. The box plot shows detects all within the range of NDs[c], with a few outlier ND values, and max detect < screening level.
Molybdenum	0.1015	0.9996	0.9935	0.3093	0.1271		
Nickel	1.484e-06	3.965e-06	1.953e-07	0.0005081	0.6643		Outlier result in R-19. Plots show potentially elevated results in R-25, CdV-16-1(i), and CdV-37-1(i). Identified as a COPC in all wells where there are one or more detections for simplicity since max concentrations in wells near background levels are far below screening levels.
Nitrate	NC	NC	NC	NC	NC	All:less than 2 observations in site or background	
Nitrate-nitrite as nitrogen	8.044e-28	0	1.72e-14	1.254e-05	3.36e-30		Plots show potentially elevated concentrations in most wells. Identified as a COPC in all wells where there are one or more detections for simplicity since max concentrations in wells near background levels are far below screening levels.
Nitrite	NC	NC	NC	NC	NC	All:less than 2 observations in site or background	
Perchlorate	5.113e-16	0	1.537e-13	3.01e-05	2.901e-35		Plots show potentially elevated concentrations in most wells. Identified as a COPC in all wells where there are one or more detections for simplicity since max concentrations in wells near background levels are far below screening levels.
Potassium	0.1286	0.01878	0.8563	5.823e-05	0.0004759		No toxicity data or regulatory criteria. Essential nutrient per Section 5.2 of NMED 2019, 700550.
Selenium	0.1856	0.2766	0.7384	0.7384	0.3634		
Silver	0.1307	0.2011	1	1	0.5		
Sodium	0.007582	2.603e-07	0.004634	0.6305	0.1271		No toxicity data or regulatory criteria. Essential nutrient per Section 5.2 of NMED 2019, 700550.

Table 4.3-1 (continued)

Analyte	Two-Sample t-test	Gehan Test	Quantile Test (0.75)	Quantile Test (0.90)	Slippage Test	Notes on Stat Tests	COPC Identification Notes
Strontium	5.632e-27	0	8.546e-16	3.196e-06	5.281e-26		Plots show potentially elevated concentrations in most wells. Identified as a COPC in all wells where there are one or more detections for simplicity since max concentrations in wells near background levels are far below screening levels.
Sulfate	5.996e-05	0	8.895e-08	0.009958	0.007698		An early outlier result exists in R-25. Plots show potentially elevated concentrations in most wells. Identified as a COPC in all wells for simplicity since max concentrations in wells near background levels are far below the NMAC and MCL standards.
Thallium	0.08002	0.07917	1	1	0.0212		Not a COPC. Although slippage is <0.05, the box plot shows that the detects are all well within the range of NDs and the plots are identical in form.
Tin	0.1409	0.1614	0.1996	0.4039	0.1752		
Titanium	NC	NC	NC	NC	NC	All:less than 2 observations in site or background	
Total organic carbon	0.04275	0.006923	0.2934	0.9586	0.1854		No toxicity data or regulatory criteria; organic (carbon-containing) compounds with potential toxicity are assessed individually.
Total phosphate as phosphorus	0.04075	0.00138	0.02212	0.05863	0.1659		No toxicity data or regulatory criteria. Essential nutrient per Section 5.2 of NMED 2019, 700550.
Uranium	2.023e-09	2.163e-09	1.135e-06	0.0005081	0.0004759		Plots show elevated concentrations in many wells. Identified as a COPC in all wells where there are one or more detections for simplicity since max concentrations for all wells are far below screening levels and regulatory standards.
Vanadium	1	0.991	1	1	1		
Zinc	0.01911	6.37e-08	1.717e-07	3.012e-06	3.984e-08		An early outlier result exists in R-25b. Plots show elevated concentrations in many wells. Identified as a COPC in all wells where there are one or more detections for simplicity since max concentrations for all wells are far below screening levels.
Actinium-228	NC	NC	NC	NC	NC	All:less than 2 observations in site or background	
Americium-241	0.1356	0.2214	1	1	—	Slippage: No detects in background	
Antimony-124	NC	NC	NC	NC	NC	All:less than 2 observations in site or background	
Antimony-125	NC	NC	NC	NC	NC	All:less than 2 observations in site or background	
Barium-133	NC	NC	NC	NC	NC	All:less than 2 observations in site or background	
Barium-140	NC	NC	NC	NC	NC	All:less than 2 observations in site or background	
Beryllium-7	NC	NC	NC	NC	NC	All:less than 2 observations in site or background	
Bismuth-211	0.2979	0.2819	1	1	—	Slippage: No detects in background	
Bismuth-212	NC	NC	NC	NC	NC	All:less than 2 observations in site or background	
Bismuth-214	0.5036	0.3981	1	1	1		
Cadmium-109	NC	NC	NC	NC	NC	All:less than 2 observations in site or background	
Cerium-139	0.9023	0.9495	1	1	—	Slippage: No detects in background	
Cerium-141	NC	NC	NC	NC	NC	All:less than 2 observations in site or background	

Table 4.3-1 (continued)

Analyte	Two-Sample t-test	Gehan Test	Quantile Test (0.75)	Quantile Test (0.90)	Slippage Test	Notes on Stat Tests	COPC Identification Notes
Cerium-144	NC	NC	NC	NC	NC	All:less than 2 observations in site or background	
Cesium-134	0.8086	0.8492	1	1	—	Slippage: No detects in background	
Cesium-137	0.6788	0.667	1	1	—	Slippage: No detects in background	
Chromium-51	NC	NC	NC	NC	NC	All:less than 2 observations in site or background	
Cobalt-57	NC	NC	NC	NC	NC	All:less than 2 observations in site or background	
Cobalt-60	0.4916	0.2539	1	1	—	Slippage: No detects in background	
Europium-152	0.6387	0.6019	1	1	—	Slippage: No detects in background	
Europium-154	NC	NC	NC	NC	NC	All:less than 2 observations in site or background	
Europium-155	NC	NC	NC	NC	NC	All:less than 2 observations in site or background	
Gross alpha	0.1507	0.00114	0.01388	0.08397	1		Plots show potentially elevated concentrations in R-19, R-25, and R-25b. Identified as a COPC in all wells where there are one or more detections for simplicity since max concentrations are below the NMAC and MCL standards.
Gross alpha/beta	NC	NC	NC	NC	NC	All:less than 2 observations in site or background	
Gross beta	0.8897	0.7497	0.7657	0.8088	1		
Gross gamma	0.5336	0.7252	0.7006	0.7959	—	Slippage: No detects in background	
Iodine-129	NC	NC	NC	NC	NC	All:less than 2 observations in site or background	
Iron-59	NC	NC	NC	NC	NC	All:less than 2 observations in site or background	
Lanthanum-140	NC	NC	NC	NC	NC	All:less than 2 observations in site or background	
Lead-211	NC	NC	NC	NC	NC	All:less than 2 observations in site or background	
Lead-212	0.6652	0.6972	1	1	—	Slippage: No detects in background	
Lead-214	0.9323	0.7807	1	1	—	Slippage: No detects in background	
Manganese-54	NC	NC	NC	NC	NC	All:less than 2 observations in site or background	
Mercury-203	0.8226	0.9101	1	1	—	Slippage: No detects in background	
Neptunium-237	0.2593	0.6122	1	1	—	Slippage: No detects in background	
Neptunium-239	NC	NC	NC	NC	NC	All:less than 2 observations in site or background	
Niobium-95	NC	NC	NC	NC	NC	All:less than 2 observations in site or background	
Plutonium-238	0.2931	0.1632	1	1	—	Slippage: No detects in background	
Plutonium-239/240	0.4126	0.1273	1	1	—	Slippage: No detects in background	
Potassium-40	0.4463	0.7409	1	1	—	Slippage: No detects in background	

Table 4.3-1 (continued)

Analyte	Two-Sample t-test	Gehan Test	Quantile Test (0.75)	Quantile Test (0.90)	Slippage Test	Notes on Stat Tests	COPC Identification Notes
Protactinium-231	NC	NC	NC	NC	NC	All:less than 2 observations in site or background	
Protactinium-233	NC	NC	NC	NC	NC	All:less than 2 observations in site or background	
Protactinium-234m	NC	NC	NC	NC	NC	All:less than 2 observations in site or background	
Radium-223	NC	NC	NC	NC	NC	All:less than 2 observations in site or background	
Radium-224	NC	NC	NC	NC	NC	All:less than 2 observations in site or background	
Radium-226	0.9235	0.9007	0.8776	0.7308	1		
Radium-228	0.2056	0.4276	0.5758	0.5455	0.5		
Radon-219	NC	NC	NC	NC	NC	All:less than 2 observations in site or background	
Rhodium-106	NC	NC	NC	NC	NC	All:less than 2 observations in site or background	
Ruthenium-103	NC	NC	NC	NC	NC	All:less than 2 observations in site or background	
Ruthenium-106	0.2074	0.5	1	1	—	Slippage: No detects in background	
Selenium-75	NC	NC	NC	NC	NC	All:less than 2 observations in site or background	
Sodium-22	0.998	0.9953	1	1	—	Slippage: No detects in background	
Strontium-85	0.5204	0.3274	1	1	—	Slippage: No detects in background	
Strontium-90	0.5913	0.684	1	1	—	Slippage: No detects in background	
Technetium-99	NC	NC	NC	NC	NC	All:less than 2 observations in site or background	
Thallium-208	0.7404	0.5	1	1	—	Slippage: No detects in background	
Thorium-227	0.4523	0.5	1	1	—	Slippage: No detects in background	
Thorium-228	NC	NC	NC	NC	NC	All:less than 2 observations in site or background	
Thorium-230	NC	NC	NC	NC	NC	All:less than 2 observations in site or background	
Thorium-231	NC	NC	NC	NC	NC	All:less than 2 observations in site or background	
Thorium-232	NC	NC	NC	NC	NC	All:less than 2 observations in site or background	
Thorium-234	0.6429	0.6023	1	1	—	Slippage: No detects in background	
Tin-113	0.5732	0.348	1	1	—	Slippage: No detects in background	
Tritium	2.585e-07	4.416e-07	9.603e-06	0.01343	3.671e-11		Plots show concentrations are elevated in many wells. Identified as a COPC in all wells where there are one or more detections for simplicity since max concentrations for all wells are far below screening levels and regulatory standard.
Uranium-234	5.831e-05	2.309e-06	0.0004643	0.006873	0.004213		Plots show concentrations are potentially elevated in many wells. Identified as a COPC in all wells where there are one or more detections for simplicity since max concentrations in wells near background levels are far below screening levels.

Table 4.3-1 (continued)

Analyte	Two-Sample t-test	Gehan Test	Quantile Test (0.75)	Quantile Test (0.90)	Slippage Test	Notes on Stat Tests	COPC Identification Notes
Uranium-235	0.5749	0.8531	1	1	—	Slippage: No detects in background	
Uranium-235/236	0.4232	0.267	0.868	0.7697	0.6531		
Uranium-238	2.108e-05	0.001743	4.419e-05	0.006873	6.483e-06		Plots show concentrations are potentially elevated in many wells. Identified as a COPC in all wells where there are one or more detections for simplicity since max concentrations in wells near background levels are far below SLs.
Yttrium-88	0.1939	0.3274	1	1	—	Slippage: No detects in background	
Zinc-65	NC	NC	NC	NC	NC	All:less than 2 observations in site or background	
Zirconium-95	NC	NC	NC	NC	NC	All:less than 2 observations in site or background	

Note: Yellow shading indicates a p-value for the statistical test below the significance threshold of 0.05 (meaning there is less than a 1 in 20 probability that site well concentrations are not larger than background well concentrations.)

[a] — = Not applicable.

[b] NC = Not calculated.

[c] ND = Nondetection.

Table 4.3-2
Final List of COPCs, by Site Well

COPC	CdV-16-1(i)	CdV-16-2(i)r	CdV-16-4ip	CdV-37-1(i)	CdV-9-1(i)	R-19	R-25	R-25b	R-63i
Aluminum	No	No	No	No	No	No	Yes	Yes	No
Barium	Yes	Yes	Yes	Yes	Yes	Yes	Yes	Yes	Yes
Boron	Yes	Yes	Yes	Yes	Yes	Yes	Yes	Yes	No
Cobalt	No	No	No	No	No	No	Yes	No	No
Copper	Yes	No	No	No	No	No	No	Yes	No
Fluoride	No	No	No	No	No	Yes	No	No	No
Iron	Yes	Yes	Yes	Yes	Yes	Yes	Yes	Yes	Yes
Manganese	Yes	No	No	No	No	No	Yes	Yes	No
Nickel	Yes	Nickel	Nickel	Nickel	Nickel	Nickel	Nickel	Nickel	Nickel
Nitrate-nitrite as nitrogen	Yes	Yes	Yes	Yes	Yes	Yes	Yes	Yes	Yes
Perchlorate	Yes	Yes	Yes	Yes	Yes	Yes	Yes	Yes	Yes
Strontium	Yes	Yes	Yes	Yes	Yes	Yes	Yes	Yes	Yes
Sulfate	Yes	Yes	Yes	Yes	Yes	Yes	Yes	Yes	Yes
Uranium	Yes	Yes	Yes	Yes	Yes	Yes	Yes	Yes	Yes
Zinc	Yes	Yes	Yes	Yes	Yes	Yes	Yes	Yes	No
Gross alpha	Yes	No	No	No	Yes	Yes	Yes	Yes	No
Tritium	Yes	Yes	Yes	No	Yes	No	Yes	No	No
Uranium-234	Yes	Yes	Yes	Yes	Yes	Yes	Yes	Yes	No
Uranium-238	Yes	Yes	Yes	Yes	Yes	Yes	Yes	Yes	No

Table 4.3-2 (continued)

COPC	CdV-16-1(i)	CdV-16-2(i)r	CdV-16-4ip	CdV-37-1(i)	CdV-9-1(i)	R-19	R-25	R-25b	R-63i
Naphthalenedisulfonic acid[1,5-]	Yes	No	No	No	No	No	No	No	No
Acetone	Yes	Yes	Yes	Yes	Yes	Yes	Yes	No	Yes
Amino-2,6-dinitrotoluene[4-]	Yes	Yes	Yes	No	Yes	No	Yes	Yes	No
Amino-4,6-dinitrotoluene[2-]	Yes	Yes	No	No	Yes	No	Yes	Yes	No
Anthracene	No	No	No	No	No	Yes	No	No	No
Bis(2-ethylhexyl)phthalate	Yes	No	No	No	No	Yes	No	No	No
Bromodichloromethane	No	No	No	No	No	No	No	Yes	No
Bromoform	No	No	No	No	No	No	No	Yes	No
Butanone[2-]	Yes	Yes	No	No	Yes	No	No	No	No
Carbon disulfide	No	No	No	No	Yes	No	Yes	No	No
Chlorobenzene	No	No	No	No	No	No	Yes	No	No
Chlorodibromomethane	No	No	No	No	No	No	No	Yes	No
Chloroform	No	No	No	No	No	No	No	Yes	No
Chloromethane	No	Yes	No	No	No	No	No	No	No
DNX[a]	No	Yes	Yes	No	Yes	No	Yes	No	No
Fluoranthene	No	No	No	No	No	Yes	No	No	No
Heptachlor	Yes	No	No	No	No	No	No	No	No
HMX[b]	Yes	Yes	Yes	No	Yes	No	Yes	Yes	No
Methyl tert-butyl ether	Yes	Yes	Yes	No	Yes	No	Yes	No	No
Methyl-2-pentanone[4-]	No	Yes	No	No	No	No	No	No	No
Methylene chloride	No	No	No	No	No	No	Yes	No	Yes
MNX[c]	Yes	Yes	Yes	No	Yes	No	Yes	No	No
Nitrotoluene[2-]	No	No	No	No	Yes	No	Yes	No	No
Perfluorooctanoic acid	Yes	Yes	Yes	No	Yes	No	No	No	No
Phenanthrene	No	No	No	No	No	Yes	No	No	No
Pyrene	No	No	No	No	No	Yes	No	No	No
RDX	Yes	Yes	Yes	No	Yes	Yes	Yes	Yes	Yes
Styrene	No	No	No	No	No	No	Yes	No	No
Tetrachloroethene	Yes	Yes	Yes	No	Yes	No	Yes	Yes	No
TNX[d]	Yes	Yes	Yes	No	Yes	No	Yes	No	No
Toluene	Yes	Yes	No	No	Yes	Yes	Yes	No	No
Trichlorobenzene[1,2,3-]	No	No	Yes	No	No	No	No	No	No
Trichloroethene	No	Yes	Yes	No	Yes	No	Yes	No	No
Trinitrobenzene[1,3,5-]	No	Yes	Yes	No	No	No	Yes	No	No
Trinitrotoluene[2,4,6-]	No	No	No	No	Yes	No	Yes	No	No

[a] DNX = Hexahydro-1,3-dinitro-5-nitro-1,3,5-triazine.

[b] HMX = Her Majesty's Explosive.

[c] MNX = Hexahydro-1-nitroso-3,5-dinitro-1,3,5-triazine.

[d] TNX = 2,4,6-trinitroxylene.

Table 4.4-1
NMED and EPA Risk-Based Tap Water Screening Criteria

COPC	CAS[a] Identifier (or Parameter Code)	NMED SL[b]; Noncarcinogenic µg/L	NMED SL; Carcinogenic µg/L	EPA RSL[c]; Noncarcinogenic µg/L	EPA RSL; Carcinogenic µg/L	EPA PRG[d] pCi/L	Notes
Aluminum	7429-90-5	1.99E+04	NA[e]	20,000	NA	—[f]	
Barium	7440-39-3	3.28E+03	NA	3800	NA	—	
Boron	7440-42-8	3.95E+03	NA	4000	NA	—	
Cobalt	7440-48-4	5.98E+00	NA	6	NA	—	
Copper	7440-50-8	7.90E+02	NA	800	NA	—	
Fluoride	16984-48-8	1.18E+03	NA	800	NA	—	
Iron	7439-89-6	1.38E+04	NA	14,000	NA	—	
Manganese	7439-96-5	2.02E+03	NA	430	NA	—	EPA value for manganese as "manganese (non-diet)"
Nickel	7440-02-0	3.72E+02	NA	390	NA	—	EPA value for nickel as "nickel soluble salts"
Nitrate-nitrite as nitrogen	E701177	1.68E+04	NA	NA	NA	—	
Perchlorate	14797-73-0	1.38E+01	NA	14	NA	—	
Strontium	7440-24-6	1.18E+04	NA	12,000	NA	—	
Sulfate	14996-02-2	NL[g]	NL	NL	NL	—	
Uranium	7440-61-1	5.92E+01	NA	4	NA	—	
Zinc	7440-66-6	5.96E+03	NA	6000	NA	—	
Tritium	10028-17-8	NA	NA	NA	NA	1.45E+02	
Uranium-234	7440-61-1	NA	NA	NA	NA	7.39E+00	
Uranium-238	7440-61-1	NA	NA	NA	NA	5.86E+00	
Naphthalenedisulfonic acid[1,5-]	1655-29-4	NL	NL	NL	NL	—	
Acetone	67-64-1	1.41E+04	NA	1.40E+04	NA	—	
Amino-2,6-dinitrotoluene[4-]	19406-51-0	NL	NL	39	NA	—	
Amino-4,6-dinitrotoluene[2-]	35572-78-2	NL	NL	39	NA	—	
Anthracene	120-12-7	1.72E+03	NA	1800	NA	—	
Bis(2-ethylhexyl)phthalate	117-81-7	4.01E+02	5.56E+01	400	56	—	
Bromodichloromethane	75-27-4	3.77E+02	1.34E+00	380	1.3	—	
Bromoform	75-25-2	3.76E+02	3.29E+01	380	33	—	
Butanone[2-]	78-93-3	5.56E+03	NA	5600	NA	—	Synonym: methyl ethyl ketone (MEK)
Carbon disulfide	75-15-0	8.10E+02	NA	810	NA	—	
Chlorobenzene	108-90-7	7.76E+01	NA	78	NA	—	
Chlorodibromomethane	124-48-1	3.78E+02	1.68E+00	380	8.7	—	Synonym: dibromochloromethane
Chloroform	67-66-3	9.72E+01	2.29E+00	97	2.2	—	
Chloromethane	74-87-3	1.88E+02	2.03E+01	190	NA	—	
DNX[h]	DNX	7.96E+01	9.66E+00	80	9.7	—	An RDX degradation product; RDX used as a toxicity surrogate.
Fluoranthene	206-44-0	8.02E+02	NA	800	NA	—	
Heptachlor	76-44-8	2.72E+00	2.21E-02	1.3	0.014	—	
HMX[i]	2691-41-0	1.00E+03	NA	1000	NA	—	

Table 4.4-1 (continued)

COPC	CAS[a] Identifier (or Parameter Code)	NMED SL[b]; Noncarcinogenic μg/L	NMED SL; Carcinogenic μg/L	EPA RSL[c]; Noncarcinogenic μg/L	EPA RSL; Carcinogenic μg/L	EPA PRG[d] pCi/L	Notes
Methyl tert-butyl ether	1634-04-4	6.26E+03	NA	6300	140	—	
Methyl-2-pentanone[4-]	108-10-1	1.24E+03	NA	6300	NA	—	Synonym: methyl isobutyl ketone (MIBK)
Methylene chloride	75-09-2	1.06E+02	1.18E+02	110	110	—	Synonym: dichloromethane
MNX[j]	MNX	7.96E+01	9.66E+00	80	9.7	—	An RDX degradation product; RDX used as a toxicity surrogate.
Nitrotoluene[2-]	88-72-2	1.61E+01	3.14E+00	16	3.1	—	
Perfluorooctanoic acid	335-67-1	7.00E-02	NA	NL	NL	—	
Phenanthrene	85-01-8	1.70E+02	NA	NL	NL	—	
Pyrene	129-00-0	1.17E+02	NA	120	NA	—	
RDX	121-82-4	7.96E+01	9.66E+00	80	9.7	—	
Styrene	100-42-5	1.21E+03	NA	1200	NA	—	
Tetrachloroethene	127-18-4	4.03E+01	1.13E+02	41	110	—	
TNX[k]	TNX	7.96E+01	9.66E+00	80	9.7	—	An RDX degradation product; RDX used as a toxicity surrogate.
Toluene	108-88-3	1.09E+03	NA	1100	NA	—	
Trichlorobenzene[1,2,3-]	87-61-6	NL	NL	7	NA	—	
Trichloroethene	79-01-6	2.82E+00	2.59E+00	2.8	4.9	—	
Trinitrobenzene[1,3,5-]	99-35-4	NL	NL	590	NA	—	
Trinitrotoluene[2,4,6-]	118-96-7	9.80E+00	2.53E+01	9.8	25	—	

[a] CAS = Chemical Abstracts Service.

[b] NMED SL = Tap water screening level (NMED 2019, 700550).

[c] EPA RSL = Tap water regional screening level https://www.epa.gov/risk/regional-screening-levels-rsls-generic-tables.

[d] EPA PRG = Calculated tap water preliminary remediation goal.

[e] NA = Not available; no toxicity criteria published for this chemical.

[f] — = Not applicable; EPA preliminary remediation goals apply to radionuclides.

[g] NL = Not listed; this chemical is not listed in the reference.

[h] DNX = Hexahydro-1,3-dinitro-5-nitro-1,3,5-triazine.

[i] HMX = Her Majesty's Explosive.

[j] MNX = Hexahydro-1-nitroso-3,5-dinitro-1,3,5-triazine.

[k] TNX = 2,4,6-trinitroxylene.

Table 4.4-2
NMED Groundwater Standards and EPA Tap Water Maximum Contaminant Levels

COPC	CAS[a] Identifier (or Parameter Code)	NMAC; Part A	NMAC; Part B	Primary MCL or TT[b]	Secondary MCL
Aluminum	7429-90-5	NA[c]	NA	NA	50
Barium	7440-39-3	2000	NA	2000	NA
Boron	7440-42-8	NA	NA	NA	NA
Cobalt	7440-48-4	NA	NA	NA	NA
Copper	7440-50-8	NA	1000	1300	1000
Fluoride	16984-48-8	1600	NA	4000	2000
Iron	7439-89-6	NA	1000	NA	300
Manganese	7439-96-5	NA	200	NA	50
Nickel	7440-02-0	NA	NA	NA	NA
Nitrate-nitrite as nitrogen[d]	E701177	1000	NA	1000	NA
Perchlorate	14797-73-0	NA	NA	NA	NA
Strontium	7440-24-6	NA	NA	NA	NA
Sulfate	14996-02-2	NA	600,000	NA	250,000
Uranium	7440-61-1	30	NA	30	NA
Zinc	7440-66-6	NA	10,000	NA	5000
Naphthalenedisulfonic acid[1,5-]	1655-29-4	NA	NA	NA	NA
Acetone	67-64-1	NA	NA	NA	NA
Amino-2,6-dinitrotoluene[4-]	19406-51-0	NA	NA	NA	NA
Amino-4,6-dinitrotoluene[2-]	35572-78-2	NA	NA	NA	NA
Anthracene	120-12-7	NA	NA	NA	NA
Bis(2-ethylhexyl)phthalate	117-81-7	NA	NA	400	NA
Bromodichloromethane	75-27-4	NA	NA	NA	NA
Bromoform	75-25-2	NA	NA	NA	NA
Butanone[2-]	78-93-3	NA	NA	NA	NA
Carbon disulfide	75-15-0	NA	NA	NA	NA
Chlorobenzene	108-90-7	NA	NA	100	NA
Chlorodibromomethane	124-48-1	NA	NA	NA	NA
Chloroform	67-66-3	100	NA	NA	NA
Chloromethane	74-87-3	NA	NA	NA	NA
DNX[e]	DNX	NA	NA	NA	NA
Fluoranthene	206-44-0	NA	NA	NA	NA
Heptachlor	76-44-8	NA	NA	0.4	NA
HMX[f]	2691-41-0	NA	NA	NA	NA
Methyl tert-butyl ether	1634-04-4	NA	100	NA	NA
Methyl-2-pentanone[4-]	108-10-1	NA	NA	NA	NA
Methylene chloride	75-09-2	5	NA	5	NA
MNX[g]	MNX	NA	NA	NA	NA

Table 4.4-2 (continued)

COPC	CAS[a] Identifier (or Parameter Code)	NMAC; Part A	NMAC; Part B	Primary MCL or TT[b]	Secondary MCL
Nitrotoluene[2-]	88-72-2	NA	NA	NA	NA
Perfluorooctanoic acid	335-67-1	NA	NA	NA	NA
Phenanthrene	85-01-8	NA	NA	NA	NA
Pyrene	129-00-0	NA	NA	NA	NA
RDX	121-82-4	NA	NA	NA	NA
Styrene	100-42-5	100	NA	100	NA
Tetrachloroethene	127-18-4	5	NA	5	NA
TNX[h]	TNX	NA	NA	NA	NA
Toluene	108-88-3	1000	NA	1000	NA
Trichlorobenzene[1,2,3-]	87-61-6	NA	NA	NA	NA
Trichloroethene	79-01-6	5	NA	5	NA
Trinitrobenzene[1,3,5-]	99-35-4	NA	NA	NA	NA
Trinitrotoluene[2,4,6-]	118-96-7	NA	NA	NA	NA
Gross alpha (pCi/L)	GROSSA	NA	NA	15	NA
Tritium (pCi/L)	10028-17-8	NA	NA	20,000[i]	NA

Note: Units are in µg/L unless otherwise noted.

[a] CAS = Chemical Abstracts Service.

[b] TT = Treatment technique.

[c] NA = Not available; no standard published for this chemical.

[d] Nitrate-nitrite as nitrogen protectively represented as nitrite (NO_2 as N) from 20.6.2 NMAC.

[e] DNX = Hexahydro-1,3-dinitro-5-nitro-1,3,5-triazine.

[f] HMX = Her Majesty's Explosive.

[g] MNX = Hexahydro-1-nitroso-3,5-dinitro-1,3,5-triazine.

[h] TNX = 2,4,6-trinitroxylene.

[i] The tritium MCL of 20,000 pCi/L is equivalent to 4-mrem/year MCL for beta and photon emitters.

Table 4.5-1
Groundwater Exposure Point Concentrations

COPC Name	Site Well	Category	No. of Analyses[a]	No. of Detects[b]	Min Detect (µg/L)	Max Detect (µg/L)	Mean Concentration[c] (µg/L)	EPC[d] (µg/L)	EPC Method[e]
Naphthalenedisulfonic acid[1,5-]	CdV-16-1(i)	Organic	1	1	20,714	20,714	20,714	20,714	Max detected concentration
Acetone	CdV-16-1(i)	Organic	23	1	1.84	1.84	4.690869565	1.84	Max detected concentration
Amino-2,6-dinitrotoluene[4-]	CdV-16-1(i)	Organic	30	29	0.134	0.292	0.18825	0.198	95% Student's-t UCL
Amino-4,6-dinitrotoluene[2-]	CdV-16-1(i)	Organic	29	19	0.0841	0.193	0.110774138	0.124	95% Student's-t UCL
Barium	CdV-16-1(i)	Inorganic	41	41	14.7	17.9	16.55831707	16.73	95% Student's-t UCL
Bis(2-ethylhexyl)phthalate	CdV-16-1(i)	Organic	9	2	3	4.39	4.186666667	4.39	Max detected concentration
Boron	CdV-16-1(i)	Inorganic	41	41	29.521	78.9	60.75417073	63.46	95% Student's-t UCL
Butanone[2-]	CdV-16-1(i)	Organic	23	1	11.6	11.6	2.591304348	11.6	Max detected concentration
Copper	CdV-16-1(i)	Inorganic	41	39	3.7	63.2	12.68787805	16.21	95% BCA Bootstrap UCL
DNX[f]	CdV-16-1(i)	Organic	21	19	0.106	0.452	0.185428571	0.227	95% BCA Bootstrap UCL
Gross alpha	CdV-16-1(i)	Rad	7	2	1.38	4.15	1.203714286	4.15	Max detected concentration
Heptachlor	CdV-16-1(i)	Organic	2	1	0.0165	0.0165	0.01375	0.0165	Max detected concentration
HMX[g]	CdV-16-1(i)	Organic	30	30	1.21	2.53	1.715333333	1.828	95% BCA Bootstrap UCL
Iron	CdV-16-1(i)	Inorganic	41	11	29.4	2750	125.4878049	334.2	95% BCA Bootstrap UCL
Manganese	CdV-16-1(i)	Inorganic	41	29	2.2	13.6	4.423419512	5.331	95% BCA Bootstrap UCL
Methyl tert-butyl ether	CdV-16-1(i)	Organic	18	16	0.966	1.48	1.135611111	1.235	95% Student's-t UCL
MNX[h]	CdV-16-1(i)	Organic	21	19	0.141	0.391	0.292666667	0.314	95% Student's-t UCL
Nickel	CdV-16-1(i)	Inorganic	41	41	1.69	13.2	4.994797561	5.687	95% BCA Bootstrap UCL
Nitrate-nitrite as nitrogen	CdV-16-1(i)	Inorganic	27	27	510	1090	844.7037037	894.7	95% Student's-t UCL
Perchlorate	CdV-16-1(i)	Inorganic	27	27	0.461	0.577	0.518851852	0.528	95% Student's-t UCL
Perfluorooctanoic acid	CdV-16-1(i)	Organic	1	1	0.00115	0.00115	0.00115	0.0012	Max detected concentration
RDX	CdV-16-1(i)	Organic	31	31	22.2	37.4	28.57096774	37.4	Max detected concentration[j]
Strontium	CdV-16-1(i)	Inorganic	41	41	76.1	110	94.5872439	95.79	95% Student's-t UCL

Table 4.5-1 (continued)

COPC Name	Site Well	Category	No. of Analyses[a]	No. of Detects[b]	Min Detect (µg/L)	Max Detect (µg/L)	Mean Concentration[c] (µg/L)	EPC[d] (µg/L)	EPC Method[e]
Sulfate	CdV-16-1(i)	Inorganic	28	28	8670	12,500	9839.535714	10,215	95% BCA Bootstrap UCL
Tetrachloroethene	CdV-16-1(i)	Organic	23	21	0.79	1.49	1.052565217	1.141	95% Student's-t UCL
TNX[i]	CdV-16-1(i)	Organic	21	19	0.163	0.362	0.232190476	0.251	95% BCA Bootstrap UCL
Toluene	CdV-16-1(i)	Organic	23	9	0.268	119	6.960782609	22.9	95% BCA Bootstrap UCL
Tritium	CdV-16-1(i)	Rad	8	8	26.645	68.264	55.3415	67.03	95% Student's-t UCL
Uranium	CdV-16-1(i)	Inorganic	41	40	0.3	0.62	0.436720488	0.463	95% Student's-t UCL
Uranium-234	CdV-16-1(i)	Rad	8	8	0.293	0.462	0.397625	0.436	95% Student's-t UCL
Uranium-238	CdV-16-1(i)	Rad	8	8	0.112	0.28	0.17175	0.214	95% BCA Bootstrap UCL
Zinc	CdV-16-1(i)	Inorganic	41	36	4.9	70.7	21.6215122	26.33	95% BCA Bootstrap UCL
Acetone	CdV-16-2(i)r	Organic	23	1	7.81	7.81	3.712608696	7.81	Max detected concentration
Amino-2,6-dinitrotoluene[4-]	CdV-16-2(i)r	Organic	33	20	0.0958	0.166	0.134042424	0.142	95% Student's-t UCL
Amino-4,6-dinitrotoluene[2-]	CdV-16-2(i)r	Organic	32	1	0.182	0.182	0.114332813	0.182	Max detected concentration
Barium	CdV-16-2(i)r	Inorganic	24	24	1.95	3.55	2.5175	2.671	95% BCA Bootstrap UCL
Boron	CdV-16-2(i)r	Inorganic	24	21	17.7	37.5	26	28.08	95% Student's-t UCL
Butanone[2-]	CdV-16-2(i)r	Organic	23	1	11.7	11.7	2.519565217	11.7	Max detected concentration
Chloromethane	CdV-16-2(i)r	Organic	23	1	2.7	2.7	0.519565217	2.7	Max detected concentration
DNX	CdV-16-2(i)r	Organic	26	20	0.081	0.385	0.197080769	0.226	95% BCA Bootstrap UCL
HMX	CdV-16-2(i)r	Organic	33	32	0.155	1.98	0.820093939	0.969	95% Student's-t UCL
Iron	CdV-16-2(i)r	Inorganic	24	3	54.5	176	54.02083333	176	Max detected concentration
Methyl tert-butyl ether	CdV-16-2(i)r	Organic	19	16	0.31	0.64	0.463684211	0.513	95% Student's-t UCL
Methyl-2-pentanone[4-]	CdV-16-2(i)r	Organic	23	1	5.35	5.35	2.243478261	5.35	Max detected concentration
MNX	CdV-16-2(i)r	Organic	26	23	0.16	0.667	0.388888462	0.439	95% Student's-t UCL
Nickel	CdV-16-2(i)r	Inorganic	24	10	0.52	1.8	0.78575	0.922	95% Student's-t UCL
Nitrate-nitrite as nitrogen	CdV-16-2(i)r	Inorganic	19	19	498	763	626.6842105	654	95% Student's-t UCL
Perchlorate	CdV-16-2(i)r	Inorganic	19	19	0.242	0.385	0.312105263	0.324	95% Student's-t UCL
Perfluorooctanoic acid	CdV-16-2(i)r	Organic	1	1	0.0108	0.0108	0.0108	0.0108	Max detected concentration

Table 4.5-1 (continued)

COPC Name	Site Well	Category	No. of Analyses[a]	No. of Detects[b]	Min Detect (µg/L)	Max Detect (µg/L)	Mean Concentration[c] (µg/L)	EPC[d] (µg/L)	EPC Method[e]
RDX	CdV-16-2(i)r	Organic	33	32	1.34	128	81.27242424	128	Max detected concentration[j]
Strontium	CdV-16-2(i)r	Inorganic	24	24	56.1	67.8	61.84583333	62.91	95% Student's-t UCL
Sulfate	CdV-16-2(i)r	Inorganic	19	19	3190	5000	4217.368421	4377	95% Student's-t UCL
Tetrachloroethene	CdV-16-2(i)r	Organic	23	22	0.289	0.92	0.555565217	0.612	95% BCA Bootstrap UCL
TNX	CdV-16-2(i)r	Organic	26	19	0.0887	0.193	0.150365385	0.171	95% BCA Bootstrap UCL
Toluene	CdV-16-2(i)r	Organic	23	15	0.321	12	2.124391304	3.423	95% BCA Bootstrap UCL
Trichloroethene	CdV-16-2(i)r	Organic	23	14	0.293	0.57	0.404043478	0.446	95% Student's-t UCL
Trinitrobenzene[1,3,5-]	CdV-16-2(i)r	Organic	32	10	0.0856	0.16	0.116792188	0.13	95% Student's-t UCL
Tritium	CdV-16-2(i)r	Rad	11	9	4.993	8.4686	10.7242	8.4686	UCL greater than max detect
Uranium	CdV-16-2(i)r	Inorganic	24	21	0.214	0.394	0.271791667	0.294	95% Student's-t UCL
Uranium-234	CdV-16-2(i)r	Rad	9	8	0.139	0.348	0.202888889	0.247	95% BCA Bootstrap UCL
Uranium-238	CdV-16-2(i)r	Rad	9	9	0.0714	0.203	0.113633333	0.14	95% Student's-t UCL
Zinc	CdV-16-2(i)r	Inorganic	24	24	9.19	33.3	17.29958333	19.58	95% BCA Bootstrap UCL
Acetone	CDV-16-4ip	Organic	20	2	10.5	68.7	7.35125	68.7	Max detected concentration
Amino-2,6-dinitrotoluene[4-]	CDV-16-4ip	Organic	29	28	1.47	2.67	1.90637931	2.06	95% Student's-t UCL
Barium	CDV-16-4ip	Inorganic	28	27	2.2	8.56	3.9425	4.674	95% BCA Bootstrap UCL
Boron	CDV-16-4ip	Inorganic	28	27	15.1	115	63.95	70.14	95% Student's-t UCL
DNX	CDV-16-4ip	Organic	24	24	0.202	0.578	0.305833333	0.344	95% BCA Bootstrap UCL
HMX	CDV-16-4ip	Organic	29	29	6.33	11.8	9.064137931	9.445	95% Student's-t UCL
Iron	CDV-16-4ip	Inorganic	28	2	33.9	105	45.13928571	105	Max detected concentration
Methyl tert-butyl ether	CDV-16-4ip	Organic	20	18	0.32	0.8	0.5595	0.616	95% Student's-t UCL
MNX	CDV-16-4ip	Organic	24	24	0.273	0.92	0.587416667	0.631	95% Student's-t UCL
Nickel	CDV-16-4ip	Inorganic	28	17	0.526	1.19	0.690767857	0.772	95% BCA Bootstrap UCL
Nitrate-nitrite as nitrogen	CDV-16-4ip	Inorganic	28	28	433	1120	868.7142857	917.6	95% Student's-t UCL
Perchlorate	CDV-16-4ip	Inorganic	28	28	0.246	0.397	0.35375	0.365	95% Student's-t UCL
Perfluorooctanoic acid	CDV-16-4ip	Organic	1	1	0.0117	0.0117	0.0117	0.0117	Max detected concentration

Table 4.5-1 (continued)

COPC Name	Site Well	Category	No. of Analyses[a]	No. of Detects[b]	Min Detect (µg/L)	Max Detect (µg/L)	Mean Concentration[c] (µg/L)	EPC[d] (µg/L)	EPC Method[e]
RDX	CDV-16-4ip	Organic	29	29	104	177	132.2413793	137.6	95% BCA Bootstrap UCL
Strontium	CDV-16-4ip	Inorganic	28	28	55.7	71.9	61.45	62.79	95% BCA Bootstrap UCL
Sulfate	CDV-16-4ip	Inorganic	28	28	2410	5660	3693.214286	3878	95% BCA Bootstrap UCL
Tetrachloroethene	CDV-16-4ip	Organic	20	20	0.73	1.12	0.9145	0.961	95% Student's-t UCL
TNX	CDV-16-4ip	Organic	24	24	0.129	1.1	0.261083333	0.371	95% BCA Bootstrap UCL
Trichlorobenzene[1,2,3-]	CDV-16-4ip	Organic	20	1	0.9	0.9	0.4325	0.9	Max detected concentration
Trichloroethene	CDV-16-4ip	Organic	20	20	0.45	0.79	0.6435	0.68	95% Student's-t UCL
Trinitrobenzene[1,3,5-]	CDV-16-4ip	Organic	28	12	0.0867	0.158	0.109471429	0.121	95% Student's-t UCL
Tritium	CDV-16-4ip	Rad	7	7	8.407	33.114	13.72457143	33.114	Max detected concentration
Uranium	CDV-16-4ip	Inorganic	28	27	0.36	0.705	0.474464286	0.502	95% Student's-t UCL
Uranium-234	CDV-16-4ip	Rad	5	5	0.239	0.346	0.2814	0.346	Max detected concentration
Uranium-238	CDV-16-4ip	Rad	5	5	0.141	0.197	0.1712	0.197	Max detected concentration
Zinc	CDV-16-4ip	Inorganic	28	4	4.02	12.4	4.716071429	12.4	Max detected concentration
Acetone	CDV-37-1(i)	Organic	11	2	2.47	4.41	3.173636364	4.41	Max detected concentration
Barium	CDV-37-1(i)	Inorganic	17	17	6.44	18.6	9.628823529	11.27	95% BCA Bootstrap UCL
Boron	CDV-37-1(i)	Inorganic	17	1	17.4	17.4	19.40588235	17.4	Max detected concentration
Iron	CDV-37-1(i)	Inorganic	17	5	31	62.9	37.48235294	44.74	95% Student's-t UCL
Nickel	CDV-37-1(i)	Inorganic	17	17	1.41	7.07	3.625882353	4.436	95% BCA Bootstrap UCL
Nitrate-nitrite as nitrogen	CDV-37-1(i)	Inorganic	17	16	27.4	255	134.2647059	159.5	95% BCA Bootstrap UCL
Perchlorate	CDV-37-1(i)	Inorganic	16	16	0.108	0.257	0.134625	0.159	95% BCA Bootstrap UCL
Strontium	CDV-37-1(i)	Inorganic	17	17	45.6	51	48.6	49.34	95% Student's-t UCL
Sulfate	CDV-37-1(i)	Inorganic	17	17	1430	5130	2505.294118	2971	95% BCA Bootstrap UCL
Uranium	CDV-37-1(i)	Inorganic	17	16	0.293	0.623	0.422823529	0.475	95% Student's-t UCL
Uranium-234	CDV-37-1(i)	Rad	4	4	0.243	0.282	0.26375	0.282	Max detected concentration
Uranium-238	CDV-37-1(i)	Rad	4	3	0.152	0.168	0.1285375	0.168	Max detected concentration
Zinc	CDV-37-1(i)	Inorganic	17	15	3.61	30.7	10.66470588	14.25	95% BCA Bootstrap UCL

Table 4.5-1 (continued)

COPC Name	Site Well	Category	No. of Analyses[a]	No. of Detects[b]	Min Detect (µg/L)	Max Detect (µg/L)	Mean Concentration[c] (µg/L)	EPC[d] (µg/L)	EPC Method[e]
Acetone	CDV-9-1(i)	Organic	12	2	2.59	18.5	4.5075	18.5	Max detected concentration
Amino-2,6-dinitrotoluene[4-]	CDV-9-1(i)	Organic	17	17	0.199	0.769	0.351941176	0.426	95% BCA Bootstrap UCL
Amino-4,6-dinitrotoluene[2-]	CDV-9-1(i)	Organic	17	17	0.29	0.47	0.342882353	0.365	95% BCA Bootstrap UCL
Barium	CDV-9-1(i)	Inorganic	12	12	2.94	7.07	4.928333333	5.434	95% Student's-t UCL
Boron	CDV-9-1(i)	Inorganic	12	10	27.5	52.4	30.48333333	37.49	95% Student's-t UCL
Butanone[2-]	CDV-9-1(i)	Organic	12	1	4.35	4.35	1.925	4.35	Max detected concentration
Carbon disulfide	CDV-9-1(i)	Organic	12	1	1.5	1.5	1.6875	1.5	Max detected concentration
DNX	CDV-9-1(i)	Organic	17	4	0.0892	0.179	0.086747059	0.179	Max detected concentration
Gross alpha	CDV-9-1(i)	Rad	4	1	2.01	2.01	0.969	2.01	Max detected concentration
HMX	CDV-9-1(i)	Organic	17	17	0.728	3.46	1.478647059	1.821	95% BCA Bootstrap UCL
Iron	CDV-9-1(i)	Inorganic	12	2	50.8	126	41.81666667	126	Max detected concentration
Methyl tert-butyl ether	CDV-9-1(i)	Organic	12	11	0.36	1.24	0.755	0.926	95% Student's-t UCL
MNX	CDV-9-1(i)	Organic	17	14	0.0852	0.414	0.147635294	0.192	95% BCA Bootstrap UCL
Nickel	CDV-9-1(i)	Inorganic	12	8	0.547	1.17	0.662416667	0.808	95% Student's-t UCL
Nitrate-nitrite as nitrogen	CDV-9-1(i)	Inorganic	12	12	945	1650	1133.083333	1252	95% BCA Bootstrap UCL
Nitrotoluene[2-]	CDV-9-1(i)	Organic	17	2	0.0941	0.121	0.076758824	0.121	Max detected concentration
Perchlorate	CDV-9-1(i)	Inorganic	12	12	0.404	0.532	0.451916667	0.472	95% Student's-t UCL
Perfluorooctanoic acid	CDV-9-1(i)	Organic	1	1	0.00217	0.00217	0.00217	0.0022	Max detected concentration
RDX	CDV-9-1(i)	Organic	17	17	8.03	37.3	19.74294118	22.78	95% BCA Bootstrap UCL
Strontium	CDV-9-1(i)	Inorganic	12	12	47.7	104	82.05833333	90.02	95% Student's-t UCL
Sulfate	CDV-9-1(i)	Inorganic	12	12	6470	9490	7625.833333	8097	95% BCA Bootstrap UCL
Tetrachloroethene	CDV-9-1(i)	Organic	12	12	0.87	1.35	1.081666667	1.164	95% Student's-t UCL
TNX	CDV-9-1(i)	Organic	16	5	0.0863	0.35	0.0938625	0.143	95% BCA Bootstrap UCL
Toluene	CDV-9-1(i)	Organic	12	1	0.85	0.85	0.383333333	0.85	Max detected concentration
Trichloroethene	CDV-9-1(i)	Organic	12	12	0.31	0.74	0.508333333	0.567	95% Student's-t UCL
Trinitrotoluene[2,4,6-]	CDV-9-1(i)	Organic	17	6	0.0897	0.209	0.102464706	0.123	95% Student's-t UCL

Table 4.5-1 (continued)

COPC Name	Site Well	Category	No. of Analyses[a]	No. of Detects[b]	Min Detect (µg/L)	Max Detect (µg/L)	Mean Concentration[c] (µg/L)	EPC[d] (µg/L)	EPC Method[e]
Tritium	CDV-9-1(i)	Rad	6	6	7.472	16.423	14.29516667	16.423	Max detected concentration
Uranium	CDV-9-1(i)	Inorganic	12	11	0.526	0.967	0.7205	0.812	95% Student's-t UCL
Uranium-234	CDV-9-1(i)	Rad	4	4	0.49	0.684	0.56575	0.684	Max detected concentration
Uranium-238	CDV-9-1(i)	Rad	4	4	0.252	0.406	0.32675	0.406	Max detected concentration
Zinc	CDV-9-1(i)	Inorganic	12	7	3.49	7.83	5.108333333	5.763	95% BCA Bootstrap UCL
Acetone	R-19	Organic	9	1	3.1	3.1	7.417222222	3.1	Max detected concentration
Anthracene	R-19	Organic	8	1	0.2	0.2	2.2373125	0.2	Max detected concentration
Barium	R-19	Inorganic	22	22	22.4	28.2	25.09090909	25.61	95% Student's-t UCL
Bis(2-ethylhexyl)phthalate	R-19	Organic	6	2	0.17	0.61	3.021666667	0.61	Max detected concentration
Boron	R-19	Inorganic	22	11	12.7	20.9	20.51363636	20.9	UCL greater than max detect
Fluoranthene	R-19	Organic	8	1	0.19	0.19	2.1752	0.19	Max detected concentration
Fluoride	R-19	Inorganic	17	17	409	849	571.1176471	618.3	95% BCA Bootstrap UCL
Gross alpha	R-19	Rad	16	3	3.51	9.7	1.37365625	9.7	Max detected concentration
Iron	R-19	Inorganic	22	5	25	281	51.94545455	84.42	95% BCA Bootstrap UCL
Nickel	R-19	Inorganic	22	11	0.51	28.6	2.124886364	5.936	95% BCA Bootstrap UCL
Nitrate-nitrite as nitrogen	R-19	Inorganic	17	17	128	496	356.1176471	390.9	95% Student's-t UCL
Perchlorate	R-19	Inorganic	17	16	0.299	0.381	0.437764706	0.381	UCL greater than max detect
Phenanthrene	R-19	Organic	8	1	0.24	0.24	2.2423125	0.24	Max detected concentration
Pyrene	R-19	Organic	8	1	0.19	0.19	2.1752	0.19	Max detected concentration
RDX	R-19	Organic	14	1	0.098	0.098	0.107592857	0.098	Max detected concentration
Strontium	R-19	Inorganic	22	22	56.6	77.2	70.30909091	71.95	95% Student's-t UCL
Sulfate	R-19	Inorganic	17	17	2570	3560	3226.470588	3316	95% Student's-t UCL
Toluene	R-19	Organic	9	1	0.54	0.54	1.132222222	0.54	Max detected concentration
Uranium	R-19	Inorganic	22	22	0.214	0.344	0.277318182	0.29	95% Student's-t UCL
Uranium-234	R-19	Rad	19	19	0.192	0.332	0.262526316	0.278	95% Student's-t UCL
Uranium-238	R-19	Rad	19	17	0.0786	0.171	0.105042105	0.118	95% Student's-t UCL

Table 4.5-1 (continued)

COPC Name	Site Well	Category	No. of Analyses[a]	No. of Detects[b]	Min Detect (µg/L)	Max Detect (µg/L)	Mean Concentration[c] (µg/L)	EPC[d] (µg/L)	EPC Method[e]
Zinc	R-19	Inorganic	21	15	3	44.4	8.044285714	13.47	95% BCA Bootstrap UCL
Acetone	R-25	Organic	18	2	2.01	3.4	6.411666667	3.4	Max detected concentration
Aluminum	R-25	Inorganic	24	4	76	604	111.625	604	Max detected concentration
Amino-2,6-dinitrotoluene[4-]	R-25	Organic	20	2	0.389	0.6	0.184075	0.6	Max detected concentration
Amino-4,6-dinitrotoluene[2-]	R-25	Organic	20	4	0.093	0.65	0.1767	0.65	Max detected concentration
Barium	R-25	Inorganic	24	24	18.7	40.4	21.70833333	24.11	95% BCA Bootstrap UCL
Boron	R-25	Inorganic	24	24	12.3	61.6	29.15	32.84	95% BCA Bootstrap UCL
Carbon disulfide	R-25	Organic	18	1	1.36	1.36	2.436666667	1.36	Max detected concentration
Chlorobenzene	R-25	Organic	18	3	0.73	2.3	0.745555556	2.3	Max detected concentration
Cobalt	R-25	Inorganic	24	4	1.18	19.7	2.975854167	19.7	Max detected concentration
DNX	R-25	Organic	11	6	0.101	0.18	0.162136364	0.18	UCL greater than max detect
Gross alpha	R-25	Rad	7	1	3.09	3.09	0.835285714	3.09	Max detected concentration
HMX	R-25	Organic	20	7	0.115	4.9	0.4897	1.346	95% BCA Bootstrap UCL
Iron	R-25	Inorganic	24	13	32.3	524	103.31875	161.9	95% BCA Bootstrap UCL
Manganese	R-25	Inorganic	24	20	2	52.7	16.26208333	23.13	95% BCA Bootstrap UCL
Methyl tert-butyl ether	R-25	Organic	9	9	0.94	1.31	1.104444444	1.177	95% Student's-t UCL
Methylene chloride	R-25	Organic	18	1	0.85	0.85	3.222222222	0.85	Max detected concentration
MNX	R-25	Organic	11	10	0.13	0.42	0.223	0.275	95% BCA Bootstrap UCL
Nickel	R-25	Inorganic	24	21	0.75	11	3.031875	4.072	95% BCA Bootstrap UCL
Nitrate-nitrite as nitrogen	R-25	Inorganic	16	12	58.5	1230	519.28125	700.4	95% Student's-t UCL
Nitrotoluene[2-]	R-25	Organic	20	2	0.104	1.1	0.236025	1.1	Max detected concentration
Perchlorate	R-25	Inorganic	15	13	0.0521	0.53	0.444553333	0.53	UCL greater than max detect
RDX	R-25	Organic	20	18	1.9	26.7	13.1505	26.7	Max detected concentration[j]
Strontium	R-25	Inorganic	24	24	96.9	366	139.6708333	168.7	95% BCA Bootstrap UCL
Styrene	R-25	Organic	18	1	1	1	0.861111111	1	Max detected concentration
Sulfate	R-25	Inorganic	16	16	9310	207000	30841.25	66423	95% BCA Bootstrap UCL

Table 4.5-1 (continued)

COPC Name	Site Well	Category	No. of Analyses[a]	No. of Detects[b]	Min Detect (µg/L)	Max Detect (µg/L)	Mean Concentration[c] (µg/L)	EPC[d] (µg/L)	EPC Method[e]
Tetrachloroethene	R-25	Organic	18	11	0.31	1.21	1.106666667	1.21	UCL greater than max detect
TNX	R-25	Organic	11	8	0.12	0.2	0.156636364	0.19	95% Student's-t UCL
Toluene	R-25	Organic	17	5	0.24	15	1.561470588	4.35	95% BCA Bootstrap UCL
Trichloroethene	R-25	Organic	18	12	0.31	0.9	1.013611111	0.9	UCL greater than max detect
Trinitrobenzene[1,3,5-]	R-25	Organic	20	1	0.315	0.315	0.157125	0.315	Max detected concentration
Trinitrotoluene[2,4,6-]	R-25	Organic	20	1	0.36	0.36	0.159375	0.36	Max detected concentration
Tritium	R-25	Rad	11	10	30.6544	67.942	34.92821818	43.48	95% Student's-t UCL
Uranium	R-25	Inorganic	24	23	0.127	0.812	0.566083333	0.634	95% Student's-t UCL
Uranium-234	R-25	Rad	15	13	0.315	0.733	0.400943333	0.488	95% Student's-t UCL
Uranium-238	R-25	Rad	15	14	0.15	0.47	0.258992	0.32	95% Student's-t UCL
Zinc	R-25	Inorganic	24	19	2.4	20.1	7.436875	9.171	95% BCA Bootstrap UCL
Aluminum	R-25b	Inorganic	19	8	111	1010	226.6842105	357.7	95% BCA Bootstrap UCL
Amino-2,6-dinitrotoluene[4-]	R-25b	Organic	11	2	0.117	0.169	0.134818182	0.169	Max detected concentration
Amino-4,6-dinitrotoluene[2-]	R-25b	Organic	11	1	0.165	0.165	0.141272727	0.165	Max detected concentration
Barium	R-25b	Inorganic	19	18	8.41	40.6	16.55368421	21.57	95% BCA Bootstrap UCL
Boron	R-25b	Inorganic	19	12	15.5	51.4	23.42894737	27.72	95% BCA Bootstrap UCL
Bromodichloromethane	R-25b	Organic	11	2	1.08	2.18	0.705454545	2.18	Max detected concentration
Bromoform	R-25b	Organic	11	2	0.72	1.79	0.637272727	1.79	Max detected concentration
Chlorodibromomethane	R-25b	Organic	11	2	1.47	3.04	0.819090909	3.04	Max detected concentration
Chloroform	R-25b	Organic	11	2	1.62	4.09	0.928181818	4.09	Max detected concentration
Copper	R-25b	Inorganic	19	7	3.99	15.9	6.361578947	8.103	95% BCA Bootstrap UCL
Gross alpha	R-25b	Rad	3	1	3.92	3.92	1.539416667	3.92	Max detected concentration
HMX	R-25b	Organic	12	9	0.155	0.656	0.282416667	0.376	95% BCA Bootstrap UCL
Iron	R-25b	Inorganic	19	10	32.5	600	135.0657895	214.4	95% BCA Bootstrap UCL
Manganese	R-25b	Inorganic	19	10	4.3	102	22.13210526	37.6	95% BCA Bootstrap UCL
Nickel	R-25b	Inorganic	19	15	0.627	5.6	2.011684211	2.696	95% BCA Bootstrap UCL

Table 4.5-1 (continued)

COPC Name	Site Well	Category	No. of Analyses[a]	No. of Detects[b]	Min Detect (µg/L)	Max Detect (µg/L)	Mean Concentration[c] (µg/L)	EPC[d] (µg/L)	EPC Method[e]
Nitrate-nitrite as nitrogen	R-25b	Inorganic	18	17	41.3	930	528.8777778	632.5	95% Student's-t UCL
Perchlorate	R-25b	Inorganic	16	16	0.208	0.313	0.2810625	0.293	95% Student's-t UCL
RDX	R-25b	Organic	12	12	0.144	8.49	3.520166667	4.873	95% Student's-t UCL
Strontium	R-25b	Inorganic	19	19	50.8	91.9	73.45789474	77.24	95% Student's-t UCL
Sulfate	R-25b	Inorganic	18	18	2250	21000	7283.333333	10077	95% BCA Bootstrap UCL
Tetrachloroethene	R-25b	Organic	11	3	0.32	0.38	0.457272727	0.38	Max detected concentration
Uranium	R-25b	Inorganic	19	19	0.264	3.12	1.137684211	1.454	95% BCA Bootstrap UCL
Uranium-234	R-25b	Rad	4	4	0.207	1.77	1.10425	1.77	Max detected concentration
Uranium-238	R-25b	Rad	4	4	0.13	0.554	0.3875	0.554	Max detected concentration
Zinc	R-25b	Inorganic	19	18	7.5	1420	105.3473684	327.7	95% BCA Bootstrap UCL
Acetone	R-63i	Organic	1	1	1.92	1.92	1.92	1.92	Max detected concentration
Barium	R-63i	Inorganic	1	1	10.9	10.9	10.9	10.9	Max detected concentration
Iron	R-63i	Inorganic	1	1	37.3	37.3	37.3	37.3	Max detected concentration
Methylene chloride	R-63i	Organic	1	1	1.42	1.42	1.42	1.42	Max detected concentration
Nickel	R-63i	Inorganic	1	1	0.75	0.75	0.75	0.75	Max detected concentration
Nitrate-nitrite as nitrogen	R-63i	Inorganic	1	1	561	561	561	561	Max detected concentration
Perchlorate	R-63i	Inorganic	1	1	0.223	0.223	0.223	0.223	Max detected concentration

Table 4.5-1 (continued)

COPC Name	Site Well	Category	No. of Analyses[a]	No. of Detects[b]	Min Detect (µg/L)	Max Detect (µg/L)	Mean Concentration[c] (µg/L)	EPC[d] (µg/L)	EPC Method[e]
RDX	R-63i	Organic	1	1	0.31	0.31	0.31	0.31	Max detected concentration
Strontium	R-63i	Inorganic	1	1	66.3	66.3	66.3	66.3	Max detected concentration
Sulfate	R-63i	Inorganic	1	1	3730	3730	3730	3730	Max detected concentration
Uranium	R-63i	Inorganic	1	1	0.943	0.943	0.943	0.943	Max detected concentration

[a] No. of Analyses = The number of samples for the analyte.

[b] No. of Detects = Number of detected results (values with validation qualifiers other than those containing "U").

[c] The arithmetic mean was calculated using one-half of the detection limit to represent the concentration of U-qualified (non-detect) results. Because ProUCL software uses various methods to represent the concentration for nondetections, some of these mean values could be below the 95% UCL estimate when detected concentrations are small relative to the detection limit.

[d] EPC = Exposure point concentration. The 95% UCL if there were at least eight samples and five detected values; otherwise the maximum detected value.

[e] EPC Method = Basis of the 95% UCL calculation. See ProUCL software output for details.

[f] DNX = Hexahydro-1,3-dinitro-5-nitro-1,3,5-triazine.

[g] HMX = Her Majesty's Explosive.

[h] MNX = Hexahydro-1-nitroso-3,5-dinitro-1,3,5-triazine.

[i] TNX = 2,4,6-trinitroxylene.

[j] A 95% UCL was not calculated because trend tests indicate RDX concentrations in this well are increasing with time (see section 4.2.1.1).

Table 4.6-1
Summary of Screening-Level Risk Assessment Results

	Screening Results for Chemical COPCs					Screening Results for Radionuclide COPCs		
	Cancer Risk		Hazard Index				Cancer Risk	
Well	Cancer Risk (using Max Detect)	Cancer Risk (using EPCs)	Sum of Ratios (using Max Detect)	Sum of Ratios (using EPCs)	Well		Cancer Risk (using Max Detect)	Cancer Risk (using EPCs)
CdV-16-1(i)	5E-05	5E-05	1	0.8	CdV-16-1(i)		6E-06	6E-06
CdV-16-2(i)r	1E-04	1E-04	2	2	CdV-16-2(i)r		3E-06	1E-06
CDV-16-4ip	2E-04	1E-04	3	2	CDV-16-4ip		3E-06	3E-06
CDV-37-1(i)	0E+00	0E+00	0.09	0.06	CDV-37-1(i)		7E-07	7E-07
CDV-9-1(i)	4E-05	3E-05	1	0.8	CDV-9-1(i)		3E-06	3E-06
R-19	2E-07	2E-07	1	0.9	R-19		7E-07	6E-07
R-25	4E-05	4E-05	4	4	R-25		6E-06	4E-06
R-25b	6E-05	6E-05	0.8	0.4	R-25b		3E-06	3E-06
R-63i	4E-07	4E-07	0.1	0.1	R-63i		NA*	NA

Notes: Purple shading indicates chemical hazard index > 1. Blue shading indicates chemical cancer risk > 1E-05.

*NA = Not available.

Table 4.6-2
Cumulative Risk Assessment Screening for Chemicals in Well CdV-16-1(i)

COPC Name	Category	Cancer Risk (Max)	Cancer Risk (EPC)	Non-cancer Risk (Max)	Non-cancer Risk (EPC)
Naphthalenedisulfonic acid[1,5-]	Organic	NA[a]	NA	NA	NA
Acetone	Organic	NA	NA	1.31E-04	1.31E-04
Amino-2,6-dinitrotoluene[4-]	Organic	NA	NA	7.49E-03	5.08E-03
Amino-4,6-dinitrotoluene[2-]	Organic	NA	NA	4.95E-03	3.18E-03
Barium	Inorganic	NA	NA	5.46E-03	5.10E-03
Bis(2-ethylhexyl)phthalate	Organic	7.89E-07	7.89E-07	1.09E-02	1.09E-02
Boron	Inorganic	NA	NA	2.00E-02	1.61E-02
Butanone[2-]	Organic	NA	NA	2.08E-03	2.08E-03

Table 4.6-2 (continued)

COPC Name	Category	Cancer Risk (Max)	Cancer Risk (EPC)	Non-cancer Risk (Max)	Non-cancer Risk (EPC)
Copper	Inorganic	NA	NA	8.00E-02	2.05E-02
DNX[b]	Organic	4.68E-07	2.35E-07	5.68E-03	2.85E-03
Heptachlor	Organic	7.46E-06	7.46E-06	6.07E-03	6.07E-03
HMX[c]	Organic	NA	NA	2.53E-03	1.83E-03
Iron	Inorganic	NA	NA	1.99E-01	2.42E-02
Manganese	Inorganic	NA	NA	6.74E-03	2.64E-03
Methyl tert-butyl ether	Organic	1.03E-07	8.63E-08	2.37E-04	1.97E-04
MNX[d]	Organic	4.05E-07	3.25E-07	4.91E-03	3.94E-03
Nickel	Inorganic	NA	NA	3.55E-02	1.53E-02
Nitrate-nitrite as nitrogen	Inorganic	NA	NA	6.49E-02	5.33E-02
Perchlorate	Inorganic	NA	NA	4.17E-02	3.82E-02
Perfluorooctanoic acid	Organic	NA	NA	1.64E-02	1.64E-02
RDX	Organic	3.87E-05	3.87E-05	4.70E-01	4.70E-01
Strontium	Inorganic	NA	NA	9.28E-03	8.09E-03
Sulfate	Inorganic	NA	NA	NA	NA
Tetrachloroethene	Organic	1.32E-07	1.01E-07	3.70E-02	2.83E-02
TNX[e]	Organic	3.75E-07	2.60E-07	4.55E-03	3.15E-03
Toluene	Organic	NA	NA	1.09E-01	2.09E-02
Uranium	Inorganic	NA	NA	1.05E-02	7.82E-03
Zinc	Inorganic	NA	NA	1.19E-02	4.42E-03
Risk/Hazard		**5E-05**	**5E-05**	**1**	**0.8**

[a] NA = Not available.

[b] DNX = Hexahydro-1,3-dinitro-5-nitro-1,3,5-triazine.

[c] HMX = Her Majesty's Explosive.

[d] MNX = Hexahydro-1-nitroso-3,5-dinitro-1,3,5-triazine.

[e] TNX = 2,4,6-trinitroxylene.

Table 4.6-3
Cumulative Risk Assessment Screening for Chemicals in Well CdV-16-2(i)r

COPC Name	Category	Cancer Risk (Max)	Cancer Risk (EPC)	Non-cancer Risk (Max)	Non-cancer Risk (EPC)
Acetone	Organic	NA[a]	NA	5.55E-04	5.55E-04
Amino-2,6-dinitrotoluene[4-]	Organic	NA	NA	4.26E-03	3.64E-03
Amino-4,6-dinitrotoluene[2-]	Organic	NA	NA	4.67E-03	4.67E-03
Barium	Inorganic	NA	NA	1.08E-03	8.15E-04
Boron	Inorganic	NA	NA	9.50E-03	7.11E-03
Butanone[2-]	Organic	NA	NA	2.10E-03	2.10E-03
Chloromethane	Organic	1.33E-06	1.33E-06	1.44E-02	1.44E-02
DNX[b]	Organic	3.99E-07	2.34E-07	4.84E-03	2.84E-03
HMX[c]	Organic	NA	NA	1.98E-03	9.68E-04
Iron	Inorganic	NA	NA	1.27E-02	1.27E-02
Methyl tert-butyl ether	Organic	4.47E-08	3.59E-08	1.02E-04	8.20E-05
Methyl-2-pentanone[4-]	Organic	NA	NA	4.30E-03	4.30E-03
MNX[d]	Organic	6.91E-07	4.55E-07	8.38E-03	5.52E-03
Nickel	Inorganic	NA	NA	4.84E-03	2.48E-03
Nitrate-nitrite as nitrogen	Inorganic	NA	NA	4.55E-02	3.90E-02
Perchlorate	Inorganic	NA	NA	2.79E-02	2.34E-02
Perfluorooctanoic acid	Organic	NA	NA	1.54E-01	1.54E-01
RDX	Organic	1.33E-04	1.33E-04	1.61E+00	1.61E+00
Strontium	Inorganic	NA	NA	5.72E-03	5.31E-03
Sulfate	Inorganic	NA	NA	NA	NA
Tetrachloroethene	Organic	8.15E-08	5.42E-08	2.28E-02	1.52E-02
TNX[e]	Organic	2.00E-07	1.77E-07	2.42E-03	2.15E-03
Toluene	Organic	NA	NA	1.10E-02	3.13E-03

Table 4.6-3 (continued)

COPC Name	Category	Cancer Risk (Max)	Cancer Risk (EPC)	Non-cancer Risk (Max)	Non-cancer Risk (EPC)
Trichloroethene	Organic	2.20E-06	1.72E-06	2.02E-01	1.58E-01
Trinitrobenzene[1,3,5-]	Organic	NA	NA	2.71E-04	2.20E-04
Uranium	Inorganic	NA	NA	6.65E-03	4.96E-03
Zinc	Inorganic	NA	NA	5.59E-03	3.28E-03
Risk/Hazard		**1E-04**	**1E-04**	**2**	**2**

[a] NA = Not available.

[b] DNX = Hexahydro-1,3-dinitro-5-nitro-1,3,5-triazine.

[c] HMX = Her Majesty's Explosive.

[d] MNX = Hexahydro-1-nitroso-3,5-dinitro-1,3,5-triazine.

[e] TNX = 2,4,6-trinitroxylene.

Table 4.6-4
Cumulative Risk Assessment Screening for Chemicals in Well CdV-16-4ip

COPC Name	Category	Cancer Risk (Max)	Cancer Risk (EPC)	Non-cancer Risk (Max)	Non-cancer Risk (EPC)
Acetone	Organic	NA[a]	NA	4.88E-03	4.88E-03
Amino-2,6-dinitrotoluene[4-]	Organic	NA	NA	6.85E-02	5.28E-02
Barium	Inorganic	NA	NA	2.61E-03	1.43E-03
Boron	Inorganic	NA	NA	2.91E-02	1.78E-02
DNX[b]	Organic	5.98E-07	3.56E-07	7.26E-03	4.32E-03
HMX[c]	Organic	NA	NA	1.18E-02	9.43E-03
Iron	Inorganic	NA	NA	7.60E-03	7.60E-03
Methyl tert-butyl ether	Organic	5.59E-08	4.31E-08	1.28E-04	9.84E-05
MNX[d]	Organic	9.53E-07	6.53E-07	1.16E-02	7.93E-03
Nickel	Inorganic	NA	NA	3.20E-03	2.08E-03
Nitrate-nitrite as nitrogen	Inorganic	NA	NA	6.67E-02	5.47E-02

Table 4.6-4 (continued)

COPC Name	Category	Cancer Risk (Max)	Cancer Risk (EPC)	Non-cancer Risk (Max)	Non-cancer Risk (EPC)
Perchlorate	Inorganic	NA	NA	2.87E-02	2.64E-02
Perfluorooctanoic acid	Organic	NA	NA	1.67E-01	1.67E-01
RDX	Organic	1.83E-04	1.42E-04	2.22E+00	1.73E+00
Strontium	Inorganic	NA	NA	6.07E-03	5.30E-03
Sulfate	Inorganic	NA	NA	NA	NA
Tetrachloroethene	Organic	9.92E-08	8.51E-08	2.78E-02	2.38E-02
TNX[e]	Organic	1.14E-06	3.84E-07	1.38E-02	4.66E-03
Trichlorobenzene[1,2,3-]	Organic	NA	NA	1.29E-01	1.29E-01
Trichloroethene	Organic	3.05E-06	2.62E-06	2.80E-01	2.41E-01
Trinitrobenzene[1,3,5-]	Organic	NA	NA	2.68E-04	2.05E-04
Uranium	Inorganic	NA	NA	1.19E-02	8.47E-03
Zinc	Inorganic	NA	NA	2.08E-03	2.08E-03
Risk/Hazard		**2E-04**	**1E-04**	**3**	**2.5**

[a] NA = Not available.

[b] DNX = Hexahydro-1,3-dinitro-5-nitro-1,3,5-triazine.

[c] HMX = Her Majesty's Explosive.

[d] MNX = Hexahydro-1-nitroso-3,5-dinitro-1,3,5-triazine.

[e] TNX = 2,4,6-trinitroxylene.

Table 4.6-5
Cumulative Risk Assessment Screening for Chemicals in Well CdV-37-1(i)

COPC Name	Category	Cancer Risk (Max)	Cancer Risk (EPC)	Non-cancer Risk (Max)	Non-cancer Risk (EPC)
Acetone	Organic	NA*	NA	3.14E-04	3.14E-04
Barium	Inorganic	NA	NA	5.68E-03	3.44E-03
Boron	Inorganic	NA	NA	4.41E-03	4.41E-03
Iron	Inorganic	NA	NA	4.55E-03	3.24E-03
Nickel	Inorganic	NA	NA	1.90E-02	1.19E-02
Nitrate-nitrite as nitrogen	Inorganic	NA	NA	1.52E-02	9.50E-03
Perchlorate	Inorganic	NA	NA	1.86E-02	1.15E-02
Strontium	Inorganic	NA	NA	4.30E-03	4.16E-03
Sulfate	Inorganic	NA	NA	NA	NA
Uranium	Inorganic	NA	NA	1.05E-02	8.02E-03
Zinc	Inorganic	NA	NA	5.15E-03	2.39E-03
Risk/Hazard		**0E+00**	**0E+00**	**0.09**	**0.06**

* NA = Not available.

Table 4.6-6
Cumulative Risk Assessment Screening for Chemicals in Well CdV-9-1(i)

COPC Name	Category	Cancer Risk (Max)	Cancer Risk (EPC)	Non-cancer Risk (Max)	Non-cancer Risk (EPC)
Acetone	Organic	NA[a]	NA	1.32E-03	1.32E-03
Amino-2,6-dinitrotoluene[4-]	Organic	NA	NA	1.97E-02	1.09E-02
Amino-4,6-dinitrotoluene[2-]	Organic	NA	NA	1.21E-02	9.36E-03
Barium	Inorganic	NA	NA	2.16E-03	1.66E-03
Boron	Inorganic	NA	NA	1.33E-02	9.49E-03
Butanone[2-]	Organic	NA	NA	7.82E-04	7.82E-04
Carbon disulfide	Organic	NA	NA	1.85E-03	1.85E-03

Table 4.6-6 (continued)

COPC Name	Category	Cancer Risk (Max)	Cancer Risk (EPC)	Non-cancer Risk (Max)	Non-cancer Risk (EPC)
DNX[b]	Organic	1.85E-07	1.85E-07	2.25E-03	2.25E-03
HMX[c]	Organic	NA	NA	3.46E-03	1.82E-03
Iron	Inorganic	NA	NA	9.12E-03	9.12E-03
Methyl tert-butyl ether	Organic	8.67E-08	6.47E-08	1.98E-04	1.48E-04
MNX[d]	Organic	4.29E-07	1.99E-07	5.20E-03	2.41E-03
Nickel	Inorganic	NA	NA	3.15E-03	2.17E-03
Nitrate-nitrite as nitrogen	Inorganic	NA	NA	9.83E-02	7.46E-02
Nitrotoluene[2-]	Organic	3.85E-07	3.85E-07	7.52E-03	7.52E-03
Perchlorate	Inorganic	NA	NA	3.85E-02	3.41E-02
Perfluorooctanoic acid	Organic	NA	NA	3.10E-02	3.10E-02
RDX	Organic	3.86E-05	2.36E-05	4.69E-01	2.86E-01
Strontium	Inorganic	NA	NA	8.78E-03	7.60E-03
Sulfate	Inorganic	NA	NA	NA	NA
Tetrachloroethene	Organic	1.20E-07	1.03E-07	3.35E-02	2.89E-02
TNX[e]	Organic	3.62E-07	1.48E-07	4.40E-03	1.80E-03
Toluene	Organic	NA	NA	7.78E-04	7.78E-04
Trichloroethene	Organic	2.86E-06	2.19E-06	2.62E-01	2.01E-01
Trinitrotoluene[2,4,6-]	Organic	8.24E-08	4.85E-08	2.13E-02	1.26E-02
Uranium	Inorganic	NA	NA	1.63E-02	1.37E-02
Zinc	Inorganic	NA	NA	1.31E-03	9.67E-04
Risk/Hazard		**4E-05**	**3E-05**	**1**	**0.8**

[a] NA = Not available.

[b] DNX = Hexahydro-1,3-dinitro-5-nitro-1,3,5-triazine.

[c] HMX = Her Majesty's Explosive.

[d] MNX = Hexahydro-1-nitroso-3,5-dinitro-1,3,5-triazine.

[e] TNX = 2,4,6-trinitroxylene.

Table 4.6-7
Cumulative Risk Assessment Screening for Chemicals in Well R-19

COPC Name	Category	Cancer Risk (Max)	Cancer Risk (EPC)	Non-cancer Risk (Max)	Non-cancer Risk (EPC)
Acetone	Organic	NA*	NA	2.20E-04	2.20E-04
Anthracene	Organic	NA	NA	1.16E-04	1.16E-04
Barium	Inorganic	NA	NA	8.60E-03	7.81E-03
Bis(2-ethylhexyl)phthalate	Organic	1.10E-07	1.10E-07	1.52E-03	1.52E-03
Boron	Inorganic	NA	NA	5.29E-03	5.29E-03
Fluoranthene	Organic	NA	NA	2.37E-04	2.37E-04
Fluoride	Inorganic	NA	NA	1.06E+00	7.73E-01
Iron	Inorganic	NA	NA	2.03E-02	6.11E-03
Nickel	Inorganic	NA	NA	7.69E-02	1.60E-02
Nitrate-nitrite as nitrogen	Inorganic	NA	NA	2.96E-02	2.33E-02
Perchlorate	Inorganic	NA	NA	2.76E-02	2.76E-02
Phenanthrene	Organic	NA	NA	1.41E-03	1.41E-03
Pyrene	Organic	NA	NA	1.62E-03	1.62E-03
RDX	Organic	1.01E-07	1.01E-07	1.23E-03	1.23E-03
Strontium	Inorganic	NA	NA	6.52E-03	6.07E-03
Sulfate	Inorganic	NA	NA	NA	NA
Toluene	Organic	NA	NA	4.94E-04	4.94E-04
Uranium	Inorganic	NA	NA	5.81E-03	4.90E-03
Zinc	Inorganic	NA	NA	7.45E-03	2.26E-03
Risk/Hazard		**2E-07**	**2E-07**	**1**	**0.9**

* NA = Not available.

Table 4.6-8
Cumulative Risk Assessment Screening for Chemicals in Well R-25

COPC Name	Category	Cancer Risk (Max)	Cancer Risk (EPC)	Non-cancer Risk (Max)	Non-cancer Risk (EPC)
Acetone	Organic	NA[a]	NA	2.42E-04	2.42E-04
Aluminum	Inorganic	NA	NA	3.03E-02	3.03E-02
Amino-2,6-dinitrotoluene[4-]	Organic	NA	NA	1.54E-02	1.54E-02
Amino-4,6-dinitrotoluene[2-]	Organic	NA	NA	1.67E-02	1.67E-02
Barium	Inorganic	NA	NA	1.23E-02	7.36E-03
Boron	Inorganic	NA	NA	1.56E-02	8.32E-03
Carbon disulfide	Organic	NA	NA	1.68E-03	1.68E-03
Chlorobenzene	Organic	NA	NA	2.96E-02	2.96E-02
Cobalt	Inorganic	NA	NA	3.29E+00	3.29E+00
DNX[b]	Organic	1.86E-07	1.86E-07	2.26E-03	2.26E-03
HMX[c]	Organic	NA	NA	4.89E-03	1.34E-03
Iron	Inorganic	NA	NA	3.79E-02	1.17E-02
Manganese	Inorganic	NA	NA	2.61E-02	1.15E-02
Methyl tert-butyl ether	Organic	9.16E-08	8.23E-08	2.09E-04	1.88E-04
Methylene chloride	Organic	7.21E-08	7.21E-08	7.98E-03	7.98E-03
MNX[d]	Organic	4.35E-07	2.85E-07	5.28E-03	3.45E-03
Nickel	Inorganic	NA	NA	2.96E-02	1.09E-02
Nitrate-nitrite as nitrogen	Inorganic	NA	NA	7.33E-02	4.17E-02
Nitrotoluene[2-]	Organic	3.50E-06	3.50E-06	6.83E-02	6.83E-02
Perchlorate	Inorganic	NA	NA	3.83E-02	3.83E-02
RDX	Organic	2.76E-05	2.76E-05	3.35E-01	3.35E-01
Strontium	Inorganic	NA	NA	3.09E-02	1.42E-02
Styrene	Organic	NA	NA	8.30E-04	8.30E-04
Sulfate	Inorganic	NA	NA	NA	NA
Tetrachloroethene	Organic	1.07E-07	1.07E-07	3.00E-02	3.00E-02
TNX[e]	Organic	2.07E-07	1.97E-07	2.51E-03	2.39E-03

Table 4.6-8 (continued)

COPC Name	Category	Cancer Risk (Max)	Cancer Risk (EPC)	Non-cancer Risk (Max)	Non-cancer Risk (EPC)
Toluene	Organic	NA	NA	1.37E-02	3.98E-03
Trichloroethene	Organic	3.47E-06	3.47E-06	3.19E-01	3.19E-01
Trinitrobenzene[1,3,5-]	Organic	NA	NA	5.34E-04	5.34E-04
Trinitrotoluene[2,4,6-]	Organic	1.42E-07	1.42E-07	3.67E-02	3.67E-02
Uranium	Inorganic	NA	NA	1.37E-02	1.07E-02
Zinc	Inorganic	NA	NA	3.37E-03	1.54E-03
Risk/Hazard		**4E-05**	**4E-05**	**4**	**4**

[a] NA = Not available.

[b] DNX = Hexahydro-1,3-dinitro-5-nitro-1,3,5-triazine.

[c] HMX = Her Majesty's Explosive.

[d] MNX = Hexahydro-1-nitroso-3,5-dinitro-1,3,5-triazine.

[e] TNX = 2,4,6-trinitroxylene.

Table 4.6-9
Cumulative Risk Assessment Screening for Chemicals in Well R-25b

COPC Name	Category	Cancer Risk (Max)	Cancer Risk (EPC)	Non-cancer Risk (Max)	Non-cancer Risk (EPC)
Aluminum	Inorganic	NA[a]	NA	5.07E-02	1.80E-02
Amino-2,6-dinitrotoluene[4-]	Organic	NA	NA	4.33E-03	4.33E-03
Amino-4,6-dinitrotoluene[2-]	Organic	NA	NA	4.23E-03	4.23E-03
Barium	Inorganic	NA	NA	1.24E-02	6.58E-03
Boron	Inorganic	NA	NA	1.30E-02	7.02E-03
Bromodichloromethane	Organic	1.62E-05	1.62E-05	5.78E-03	5.78E-03
Bromoform	Organic	5.45E-07	5.45E-07	4.76E-03	4.76E-03
Chlorodibromomethane	Organic	1.81E-05	1.81E-05	8.05E-03	8.05E-03
Chloroform	Organic	1.78E-05	1.78E-05	4.21E-02	4.21E-02
Copper	Inorganic	NA	NA	2.01E-02	1.03E-02
HMX[b]	Organic	NA	NA	6.55E-04	3.76E-04
Iron	Inorganic	NA	NA	4.34E-02	1.55E-02
Manganese	Inorganic	NA	NA	5.06E-02	1.86E-02
Nickel	Inorganic	NA	NA	1.51E-02	7.25E-03
Nitrate-nitrite as nitrogen	Inorganic	NA	NA	5.54E-02	3.77E-02
Perchlorate	Inorganic	NA	NA	2.26E-02	2.12E-02
RDX	Organic	8.79E-06	5.05E-06	1.07E-01	6.12E-02
Strontium	Inorganic	NA	NA	7.76E-03	6.52E-03
Sulfate	Inorganic	NA	NA	NA	NA
Tetrachloroethene	Organic	3.37E-08	3.37E-08	9.42E-03	9.42E-03
Uranium	Inorganic	NA	NA	5.27E-02	2.45E-02
Zinc	Inorganic	NA	NA	2.38E-01	5.50E-02
Risk/Hazard		**6E-05**	**6E-05**	**0.8**	**0.4**

[a] NA = Not available.

[b] HMX = Her Majesty's Explosive.

Table 4.6-10
Cumulative Risk Assessment Screening for Chemicals in Well R-63i

COPC Name	Category	Cancer Risk (Max)	Cancer Risk (EPC)	Non-cancer Risk (Max)	Non-cancer Risk (EPC)
Acetone	Organic	NA*	NA	1.37E-04	1.37E-04
Barium	Inorganic	NA	NA	3.33E-03	3.33E-03
Iron	Inorganic	NA	NA	2.70E-03	2.70E-03
Methylene chloride	Organic	1.20E-07	1.20E-07	1.33E-02	1.33E-02
Nickel	Inorganic	NA	NA	2.02E-03	2.02E-03
Nitrate-nitrite as nitrogen	Inorganic	NA	NA	3.34E-02	3.34E-02
Perchlorate	Inorganic	NA	NA	1.61E-02	1.61E-02
RDX	Organic	3.21E-07	3.21E-07	3.89E-03	3.89E-03
Strontium	Inorganic	NA	NA	5.60E-03	5.60E-03
Sulfate	Inorganic	NA	NA	NA	NA
Uranium	Inorganic	NA	NA	1.59E-02	1.59E-02
	Risk/Hazard	**4E-07**	**4E-07**	**0.1**	**0.1**

* NA = Not available.

Table 4.6-11
Major Contributors to Calculated
Health Effects Above Threshold in Site Wells

CdV-16-1(i)	
Cancer Risk	**HI**
5E-05	0.8
RDX Contribution to Risk	**RDX Contribution to HI**
81%	61%
Risk From All Other COPCs	**HI From All Other COPCs**
9E-06	0.3
CdV-16-2(i)r	
Cancer Risk	**HI**
1E-04	1.6
RDX Contribution to Risk	**RDX Contribution to HI**
97%	77%
Risk From All Other COPCs	**HI From All Other COPCs**
4E-06	0.5
CdV-16-4ip	
Cancer Risk	**HI**
1E-04	2.5
RDX Contribution to Risk	**RDX Contribution to HI**
97%	69%
Risk From All Other COPCs	**Hi From All Other COPCs**
4E-06	0.8
CdV-37-1(i)	
Cancer Risk	**HI**
0E+00	0.1
R-19	
Cancer Risk	**HI**
2E-07	0.9
R-63i	
Cancer Risk	**HI**
4E-07	0.1

Table 4.6-11 (continued)

CdV-9-1(i)		
Cancer Risk	**HI**	
3E-05	0.8	
RDX Contribution to Risk	**RDX Contribution to HI**	**Tricholorethene Contribution to HI**
88%	38%	27%
Risk From All Other COPCs	**HI From All Other COPCs**	
3E-06	0.3	
R-25		
Cancer Risk	**HI**	
4E-05	4	
RDX Contribution to Risk	**Cobalt Contribution to HI**	**Tricholorethene and RDX Contribution to HI**
77%	76%	15%
Risk From All Other COPCs	**HI From All Other COPCs**	
8E-06	0.4	
R-25b		
Cancer Risk	**HI**	
6E-05	0.4	
Chlorodibromomethane Contribution to Risk	**Chloroform Contribution to Risk**	
31%	31%	
Bromodichloromethane Contribution to Risk	**Risk From All Other COPCs**	
28%	6E-06	

Table 4.6-12
Cumulative Risk Assessment Screening for Radionuclides, All Wells

COPC Name	Site Well	Cancer Risk (using Max and PRG)	Cancer Risk (using EPC and PRG)
Gross alpha	CdV-16-1(i)	NA*	NA
Tritium	CdV-16-1(i)	4.71E-06	4.62E-06
Uranium-234	CdV-16-1(i)	6.25E-07	5.90E-07
Uranium-238	CdV-16-1(i)	4.78E-07	3.65E-07
Total Excess Cancer Risk		**6E-06**	**6E-06**
Tritium	CdV-16-2(i)r	2.44E-06	5.84E-07
Uranium-234	CdV-16-2(i)r	4.71E-07	3.34E-07
Uranium-238	CdV-16-2(i)r	3.47E-07	2.39E-07
Total Excess Cancer Risk		**3E-06**	**1E-06**
Tritium	CDV-16-4ip	2.28E-06	2.28E-06
Uranium-234	CDV-16-4ip	4.68E-07	4.68E-07
Uranium-238	CDV-16-4ip	3.36E-07	3.36E-07
Total Excess Cancer Risk		**3E-06**	**3E-06**
Uranium-234	CDV-37-1(i)	3.82E-07	3.82E-07
Uranium-238	CDV-37-1(i)	2.87E-07	2.87E-07
Total Excess Cancer Risk		**7E-07**	**7E-07**
Gross alpha	CDV-9-1(i)	NA	NA
Tritium	CDV-9-1(i)	1.13E-06	1.13E-06
Uranium-234	CDV-9-1(i)	9.26E-07	9.26E-07
Uranium-238	CDV-9-1(i)	6.93E-07	6.93E-07
Total Excess Cancer Risk		**3E-06**	**3E-06**
Gross alpha	R-19	NA	NA
Uranium-234	R-19	4.49E-07	3.76E-07
Uranium-238	R-19	2.92E-07	2.02E-07
Total Excess Cancer Risk		**7E-07**	**7E-07**
Gross alpha	R-25	NA	NA
Tritium	R-25	4.69E-06	3.00E-06
Uranium-234	R-25	9.92E-07	6.60E-07
Uranium-238	R-25	8.03E-07	5.46E-07
Total Excess Cancer Risk		**6E-06**	**4E-06**
Gross alpha	R-25b	NA	NA
Uranium-234	R-25b	2.40E-06	2.40E-06
Uranium-238	R-25b	9.46E-07	9.46E-07
Total Excess Cancer Risk		**3E-06**	**3E-06**

* NA = Not available.

Table 4.6-13
Comparison of EPCs for Site Wells with Regulatory Standards

COPC Name	Site Well	EPC (µg/L or pCi/L)	NMAC; Part A (µg/L)	NMAC; Part B (µg/L)	Primary MCL or TT[a] (µg/L)	Secondary MCL (µg/L)
Naphthalenedisulfonic acid[1,5-]	CdV-16-1(i)	2.1E+04	NA[b]	NA	NA	NA
Acetone	CdV-16-1(i)	1.8E+00	NA	NA	NA	NA
Amino-2,6-dinitrotoluene[4-]	CdV-16-1(i)	2.0E-01	NA	NA	NA	NA
Amino-4,6-dinitrotoluene[2-]	CdV-16-1(i)	1.2E-01	NA	NA	NA	NA
Barium	CdV-16-1(i)	1.7E+01	2.0E+03	NA	2.0E+03	NA
Bis(2-ethylhexyl)phthalate	CdV-16-1(i)	4.4E+00	NA	NA	4.0E+02	NA
Boron	CdV-16-1(i)	6.3E+01	NA	NA	NA	NA
Butanone[2-]	CdV-16-1(i)	1.2E+01	NA	NA	NA	NA
Copper	CdV-16-1(i)	1.6E+01	NA	1.0E+03	1.3E+03	1.0E+03
DNX[c]	CdV-16-1(i)	2.3E-01	NA	NA	NA	NA
Heptachlor	CdV-16-1(i)	1.7E-02	NA	NA	4.0E-01	NA
HMX[d]	CdV-16-1(i)	1.8E+00	NA	NA	NA	NA
Iron	CdV-16-1(i)	3.3E+02	NA	1.0E+03	NA	3.0E+02
Manganese	CdV-16-1(i)	5.3E+00	NA	2.0E+02	NA	5.0E+01
Methyl tert-butyl ether	CdV-16-1(i)	1.2E+00	NA	1.0E+02	NA	NA
MNX[e]	CdV-16-1(i)	3.1E-01	NA	NA	NA	NA
Nickel	CdV-16-1(i)	5.7E+00	NA	NA	NA	NA
Nitrate-nitrite as nitrogen	CdV-16-1(i)	8.9E+02	1.0E+03	NA	1.0E+03	NA
Perchlorate	CdV-16-1(i)	5.3E-01	NA	NA	NA	NA
Perfluorooctanoic acid	CdV-16-1(i)	1.2E-03	NA	NA	NA	NA
RDX	CdV-16-1(i)	3.7E+01	NA	NA	NA	NA
Strontium	CdV-16-1(i)	9.6E+01	NA	NA	NA	NA
Sulfate	CdV-16-1(i)	1.0E+04	NA	6.0E+05	NA	2.5E+05
Tetrachloroethene	CdV-16-1(i)	1.1E+00	5.0E+00	NA	5.0E+00	NA
TNX[f]	CdV-16-1(i)	2.5E-01	NA	NA	NA	NA

Table 4.6-13 (continued)

COPC Name	Site Well	EPC (µg/L or pCi/L)	NMAC; Part A (µg/L)	NMAC; Part B (µg/L)	Primary MCL or TT (µg/L)	Secondary MCL (µg/L)
Toluene	CdV-16-1(i)	2.3E+01	1.0E+03	NA	1.0E+03	NA
Uranium	CdV-16-1(i)	4.6E-01	3.0E+01	NA	3.0E+01	NA
Zinc	CdV-16-1(i)	2.6E+01	NA	1.0E+04	NA	5.0E+03
Gross alpha	CdV-16-1(i)	4.2E+00	NA	NA	1.5E+01	NA
Tritium	CdV-16-1(i)	6.7E+01	NA	NA	2.0E+04	NA
Uranium-234	CdV-16-1(i)	4.4E-01	NA	NA	NA	NA
Uranium-238	CdV-16-1(i)	2.1E-01	NA	NA	NA	NA
Acetone	CdV-16-2(i)r	7.8E+00	NA	NA	NA	NA
Amino-2,6-dinitrotoluene[4-]	CdV-16-2(i)r	1.4E-01	NA	NA	NA	NA
Amino-4,6-dinitrotoluene[2-]	CdV-16-2(i)r	1.8E-01	NA	NA	NA	NA
Barium	CdV-16-2(i)r	2.7E+00	2.0E+03	NA	2.0E+03	NA
Boron	CdV-16-2(i)r	2.8E+01	NA	NA	NA	NA
Butanone[2-]	CdV-16-2(i)r	1.2E+01	NA	NA	NA	NA
Chloromethane	CdV-16-2(i)r	2.7E+00	NA	NA	NA	NA
DNX	CdV-16-2(i)r	2.3E-01	NA	NA	NA	NA
HMX	CdV-16-2(i)r	9.7E-01	NA	NA	NA	NA
Iron	CdV-16-2(i)r	1.8E+02	NA	1.0E+03	NA	3.0E+02
Methyl tert-butyl ether	CdV-16-2(i)r	5.1E-01	NA	1.0E+02	NA	NA
Methyl-2-pentanone[4-]	CdV-16-2(i)r	5.4E+00	NA	NA	NA	NA
MNX	CdV-16-2(i)r	4.4E-01	NA	NA	NA	NA
Nickel	CdV-16-2(i)r	9.2E-01	NA	NA	NA	NA
Nitrate-nitrite as nitrogen	CdV-16-2(i)r	6.5E+02	1.0E+03	NA	1.0E+03	NA
Perchlorate	CdV-16-2(i)r	3.2E-01	NA	NA	NA	NA
Perfluorooctanoic acid	CdV-16-2(i)r	1.1E-02	NA	NA	NA	NA
RDX	CdV-16-2(i)r	1.3E+02	NA	NA	NA	NA
Strontium	CdV-16-2(i)r	6.3E+01	NA	NA	NA	NA

Table 4.6-13 (continued)

COPC Name	Site Well	EPC (µg/L or pCi/L)	NMAC; Part A (µg/L)	NMAC; Part B (µg/L)	Primary MCL or TT (µg/L)	Secondary MCL (µg/L)
Sulfate	CdV-16-2(i)r	4.4E+03	NA	6.0E+05	NA	2.5E+05
Tetrachloroethene	CdV-16-2(i)r	6.1E-01	5.0E+00	NA	5.0E+00	NA
TNX	CdV-16-2(i)r	1.7E-01	NA	NA	NA	NA
Toluene	CdV-16-2(i)r	3.4E+00	1.0E+03	NA	1.0E+03	NA
Trichloroethene	CdV-16-2(i)r	4.5E-01	5.0E+00	NA	5.0E+00	NA
Trinitrobenzene[1,3,5-]	CdV-16-2(i)r	1.3E-01	NA	NA	NA	NA
Uranium	CdV-16-2(i)r	2.9E-01	3.0E+01	NA	3.0E+01	NA
Zinc	CdV-16-2(i)r	2.0E+01	NA	1.0E+04	NA	5.0E+03
Tritium	CdV-16-2(i)r	8.5E+00	NA	NA	2.0E+04	NA
Uranium-234	CdV-16-2(i)r	2.5E-01	NA	NA	NA	NA
Uranium-238	CdV-16-2(i)r	1.4E-01	NA	NA	NA	NA
Acetone	CDV-16-4ip	6.9E+01	NA	NA	NA	NA
Amino-2,6-dinitrotoluene[4-]	CDV-16-4ip	2.1E+00	NA	NA	NA	NA
Barium	CDV-16-4ip	4.7E+00	2.0E+03	NA	2.0E+03	NA
Boron	CDV-16-4ip	7.0E+01	NA	NA	NA	NA
DNX	CDV-16-4ip	3.4E-01	NA	NA	NA	NA
HMX	CDV-16-4ip	9.4E+00	NA	NA	NA	NA
Iron	CDV-16-4ip	1.1E+02	NA	1.0E+03	NA	3.0E+02
Methyl tert-butyl ether	CDV-16-4ip	6.2E-01	NA	1.0E+02	NA	NA
MNX	CDV-16-4ip	6.3E-01	NA	NA	NA	NA
Nickel	CDV-16-4ip	7.7E-01	NA	NA	NA	NA
Nitrate-nitrite as nitrogen	CDV-16-4ip	9.2E+02	1.0E+03	NA	1.0E+03	NA
Perchlorate	CDV-16-4ip	3.7E-01	NA	NA	NA	NA
Perfluorooctanoic acid	CDV-16-4ip	1.2E-02	NA	NA	NA	NA
RDX	CDV-16-4ip	1.4E+02	NA	NA	NA	NA
Strontium	CDV-16-4ip	6.3E+01	NA	NA	NA	NA

Table 4.6-13 (continued)

COPC Name	Site Well	EPC (µg/L or pCi/L)	NMAC; Part A (µg/L)	NMAC; Part B (µg/L)	Primary MCL or TT (µg/L)	Secondary MCL (µg/L)
Sulfate	CDV-16-4ip	3.9E+03	NA	6.0E+05	NA	2.5E+05
Tetrachloroethene	CDV-16-4ip	9.6E-01	5.0E+00	NA	5.0E+00	NA
TNX	CDV-16-4ip	3.7E-01	NA	NA	NA	NA
Trichlorobenzene[1,2,3-]	CDV-16-4ip	9.0E-01	NA	NA	NA	NA
Trichloroethene	CDV-16-4ip	6.8E-01	5.0E+00	NA	5.0E+00	NA
Trinitrobenzene[1,3,5-]	CDV-16-4ip	1.2E-01	NA	NA	NA	NA
Uranium	CDV-16-4ip	5.0E-01	3.0E+01	NA	3.0E+01	NA
Zinc	CDV-16-4ip	1.2E+01	NA	1.0E+04	NA	5.0E+03
Tritium	CDV-16-4ip	3.3E+01	NA	NA	2.0E+04	NA
Uranium-234	CDV-16-4ip	3.5E-01	NA	NA	NA	NA
Uranium-238	CDV-16-4ip	2.0E-01	NA	NA	NA	NA
Acetone	CDV-37-1(i)	4.4E+00	NA	NA	NA	NA
Barium	CDV-37-1(i)	1.1E+01	2.0E+03	NA	2.0E+03	NA
Boron	CDV-37-1(i)	1.7E+01	NA	NA	NA	NA
Iron	CDV-37-1(i)	4.5E+01	NA	1.0E+03	NA	3.0E+02
Nickel	CDV-37-1(i)	4.4E+00	NA	NA	NA	NA
Nitrate-nitrite as nitrogen	CDV-37-1(i)	1.6E+02	1.0E+03	NA	1.0E+03	NA
Perchlorate	CDV-37-1(i)	1.6E-01	NA	NA	NA	NA
Strontium	CDV-37-1(i)	4.9E+01	NA	NA	NA	NA
Sulfate	CDV-37-1(i)	3.0E+03	NA	6.0E+05	NA	2.5E+05
Uranium	CDV-37-1(i)	4.8E-01	3.0E+01	NA	3.0E+01	NA
Zinc	CDV-37-1(i)	1.4E+01	NA	1.0E+04	NA	5.0E+03
Uranium-234	CDV-37-1(i)	2.8E-01	NA	NA	NA	NA
Uranium-238	CDV-37-1(i)	1.7E-01	NA	NA	NA	NA
Acetone	CDV-9-1(i)	1.9E+01	NA	NA	NA	NA
Amino-2,6-dinitrotoluene[4-]	CDV-9-1(i)	4.3E-01	NA	NA	NA	NA

Table 4.6-13 (continued)

COPC Name	Site Well	EPC (µg/L or pCi/L)	NMAC; Part A (µg/L)	NMAC; Part B (µg/L)	Primary MCL or TT (µg/L)	Secondary MCL (µg/L)
Amino-4,6-dinitrotoluene[2-]	CDV-9-1(i)	3.7E-01	NA	NA	NA	NA
Barium	CDV-9-1(i)	5.4E+00	2.0E+03	NA	2.0E+03	NA
Boron	CDV-9-1(i)	3.7E+01	NA	NA	NA	NA
Butanone[2-]	CDV-9-1(i)	4.4E+00	NA	NA	NA	NA
Carbon disulfide	CDV-9-1(i)	1.5E+00	NA	NA	NA	NA
DNX	CDV-9-1(i)	1.8E-01	NA	NA	NA	NA
HMX	CDV-9-1(i)	1.8E+00	NA	NA	NA	NA
Iron	CDV-9-1(i)	1.3E+02	NA	1.0E+03	NA	3.0E+02
Methyl tert-butyl ether	CDV-9-1(i)	9.3E-01	NA	1.0E+02	NA	NA
MNX	CDV-9-1(i)	1.9E-01	NA	NA	NA	NA
Nickel	CDV-9-1(i)	8.1E-01	NA	NA	NA	NA
Nitrate-nitrite as nitrogen	CDV-9-1(i)	1.3E+03	1.0E+03	NA	1.0E+03	NA
Nitrotoluene[2-]	CDV-9-1(i)	1.2E-01	NA	NA	NA	NA
Perchlorate	CDV-9-1(i)	4.7E-01	NA	NA	NA	NA
Perfluorooctanoic acid	CDV-9-1(i)	2.2E-03	NA	NA	NA	NA
RDX	CDV-9-1(i)	2.3E+01	NA	NA	NA	NA
Strontium	CDV-9-1(i)	9.0E+01	NA	NA	NA	NA
Sulfate	CDV-9-1(i)	8.1E+03	NA	6.0E+05	NA	2.5E+05
Tetrachloroethene	CDV-9-1(i)	1.2E+00	5.0E+00	NA	5.0E+00	NA
TNX	CDV-9-1(i)	1.4E-01	NA	NA	NA	NA
Toluene	CDV-9-1(i)	8.5E-01	1.0E+03	NA	1.0E+03	NA
Trichloroethene	CDV-9-1(i)	5.7E-01	5.0E+00	NA	5.0E+00	NA
Trinitrotoluene[2,4,6-]	CDV-9-1(i)	1.2E-01	NA	NA	NA	NA
Uranium	CDV-9-1(i)	8.1E-01	3.0E+01	NA	3.0E+01	NA
Zinc	CDV-9-1(i)	5.8E+00	NA	1.0E+04	NA	5.0E+03
Gross alpha	CDV-9-1(i)	2.0E+00	NA	NA	1.5E+01	NA

Table 4.6-13 (continued)

COPC Name	Site Well	EPC (µg/L or pCi/L)	NMAC; Part A (µg/L)	NMAC; Part B (µg/L)	Primary MCL or TT (µg/L)	Secondary MCL (µg/L)
Tritium	CDV-9-1(i)	1.6E+01	NA	NA	2.0E+04	NA
Uranium-234	CDV-9-1(i)	6.8E-01	NA	NA	NA	NA
Uranium-238	CDV-9-1(i)	4.1E-01	NA	NA	NA	NA
Acetone	R-19	3.1E+00	NA	NA	NA	NA
Anthracene	R-19	2.0E-01	NA	NA	NA	NA
Barium	R-19	2.6E+01	2.0E+03	NA	2.0E+03	NA
Bis(2-ethylhexyl)phthalate	R-19	6.1E-01	NA	NA	4.0E+02	NA
Boron	R-19	2.1E+01	NA	NA	NA	NA
Fluoranthene	R-19	1.9E-01	NA	NA	NA	NA
Fluoride	R-19	6.2E+02	1.6E+03	NA	4.0E+03	2.0E+03
Iron	R-19	8.4E+01	NA	1.0E+03	NA	3.0E+02
Nickel	R-19	5.9E+00	NA	NA	NA	NA
Nitrate-nitrite as nitrogen	R-19	3.9E+02	1.0E+03	NA	1.0E+03	NA
Perchlorate	R-19	3.8E-01	NA	NA	NA	NA
Phenanthrene	R-19	2.4E-01	NA	NA	NA	NA
Pyrene	R-19	1.9E-01	NA	NA	NA	NA
RDX	R-19	9.8E-02	NA	NA	NA	NA
Strontium	R-19	7.2E+01	NA	NA	NA	NA
Sulfate	R-19	3.3E+03	NA	6.0E+05	NA	2.5E+05
Toluene	R-19	5.4E-01	1.0E+03	NA	1.0E+03	NA
Uranium	R-19	2.9E-01	3.0E+01	NA	3.0E+01	NA
Zinc	R-19	1.3E+01	NA	1.0E+04	NA	5.0E+03
Gross alpha	R-19	9.7E+00	NA	NA	1.5E+01	NA
Uranium-234	R-19	2.8E-01	NA	NA	NA	NA
Uranium-238	R-19	1.2E-01	NA	NA	NA	NA
Acetone	R-25	3.4E+00	NA	NA	NA	NA

Table 4.6-13 (continued)

COPC Name	Site Well	EPC (µg/L or pCi/L)	NMAC; Part A (µg/L)	NMAC; Part B (µg/L)	Primary MCL or TT (µg/L)	Secondary MCL (µg/L)
Aluminum	R-25	6.0E+02	NA	NA	NA	5.0E+01
Amino-2,6-dinitrotoluene[4-]	R-25	6.0E-01	NA	NA	NA	NA
Amino-4,6-dinitrotoluene[2-]	R-25	6.5E-01	NA	NA	NA	NA
Barium	R-25	2.4E+01	2.0E+03	NA	2.0E+03	NA
Boron	R-25	3.3E+01	NA	NA	NA	NA
Carbon disulfide	R-25	1.4E+00	NA	NA	NA	NA
Chlorobenzene	R-25	2.3E+00	NA	NA	1.0E+02	NA
Cobalt	R-25	9.7E+00	NA	NA	NA	NA
DNX	R-25	1.8E-01	NA	NA	NA	NA
HMX	R-25	1.3E+00	NA	NA	NA	NA
Iron	R-25	1.6E+02	NA	1.0E+03	NA	3.0E+02
Manganese	R-25	2.3E+01	NA	2.0E+02	NA	5.0E+01
Methyl tert-butyl ether	R-25	1.2E+00	NA	1.0E+02	NA	NA
Methylene chloride	R-25	8.5E-01	5.0E+00	NA	5.0E+00	NA
MNX	R-25	2.8E-01	NA	NA	NA	NA
Nickel	R-25	4.1E+00	NA	NA	NA	NA
Nitrate-nitrite as nitrogen	R-25	7.0E+02	1.0E+03	NA	1.0E+03	NA
Nitrotoluene[2-]	R-25	1.1E+00	NA	NA	NA	NA
Perchlorate	R-25	5.3E-01	NA	NA	NA	NA
RDX	R-25	2.7E+01	NA	NA	NA	NA
Strontium	R-25	1.7E+02	NA	NA	NA	NA
Styrene	R-25	1.0E+00	1.0E+02	NA	1.0E+02	NA
Sulfate	R-25	6.6E+04	NA	6.0E+05	NA	2.5E+05
Tetrachloroethene	R-25	1.2E+00	5.0E+00	NA	5.0E+00	NA
TNX	R-25	1.9E-01	NA	NA	NA	NA
Toluene	R-25	4.4E+00	1.0E+03	NA	1.0E+03	NA

Table 4.6-13 (continued)

COPC Name	Site Well	EPC (µg/L or pCi/L)	NMAC; Part A (µg/L)	NMAC; Part B (µg/L)	Primary MCL or TT (µg/L)	Secondary MCL (µg/L)
Trichloroethene	R-25	9.0E-01	5.0E+00	NA	5.0E+00	NA
Trinitrobenzene[1,3,5-]	R-25	3.2E-01	NA	NA	NA	NA
Trinitrotoluene[2,4,6-]	R-25	3.6E-01	NA	NA	NA	NA
Uranium	R-25	6.3E-01	3.0E+01	NA	3.0E+01	NA
Zinc	R-25	9.2E+00	NA	1.0E+04	NA	5.0E+03
Gross alpha	R-25	3.1E+00	NA	NA	1.5E+01	NA
Tritium	R-25	4.3E+01	NA	NA	2.0E+04	NA
Uranium-234	R-25	4.9E-01	NA	NA	NA	NA
Uranium-238	R-25	3.2E-01	NA	NA	NA	NA
Aluminum	R-25b	3.6E+02	NA	NA	NA	5.0E+01
Amino-2,6-dinitrotoluene[4-]	R-25b	1.7E-01	NA	NA	NA	NA
Amino-4,6-dinitrotoluene[2-]	R-25b	1.7E-01	NA	NA	NA	NA
Barium	R-25b	2.2E+01	2.0E+03	NA	2.0E+03	NA
Boron	R-25b	2.8E+01	NA	NA	NA	NA
Bromodichloromethane	R-25b	2.2E+00	NA	NA	NA	NA
Bromoform	R-25b	1.8E+00	NA	NA	NA	NA
Chlorodibromomethane	R-25b	3.0E+00	NA	NA	NA	NA
Chloroform	R-25b	4.1E+00	1.0E+02	NA	NA	NA
Copper	R-25b	8.1E+00	NA	1.0E+03	1.3E+03	1.0E+03
HMX	R-25b	3.8E-01	NA	NA	NA	NA
Iron	R-25b	2.1E+02	NA	1.0E+03	NA	3.0E+02
Manganese	R-25b	3.8E+01	NA	2.0E+02	NA	5.0E+01
Nickel	R-25b	2.7E+00	NA	NA	NA	NA
Nitrate-nitrite as nitrogen	R-25b	6.3E+02	1.0E+03	NA	1.0E+03	NA
Perchlorate	R-25b	2.9E-01	NA	NA	NA	NA
RDX	R-25b	4.9E+00	NA	NA	NA	NA

Table 4.6-13 (continued)

COPC Name	Site Well	EPC (µg/L or pCi/L)	NMAC; Part A (µg/L)	NMAC; Part B (µg/L)	Primary MCL or TT (µg/L)	Secondary MCL (µg/L)
Strontium	R-25b	7.7E+01	NA	NA	NA	NA
Sulfate	R-25b	1.0E+04	NA	6.0E+05	NA	2.5E+05
Tetrachloroethene	R-25b	3.8E-01	5.0E+00	NA	5.0E+00	NA
Uranium	R-25b	1.5E+00	3.0E+01	NA	3.0E+01	NA
Zinc	R-25b	3.3E+02	NA	1.0E+04	NA	5.0E+03
Gross alpha	R-25b	3.9E+00	NA	NA	1.5E+01	NA
Uranium-234	R-25b	1.8E+00	NA	NA	NA	NA
Uranium-238	R-25b	5.5E-01	NA	NA	NA	NA
Acetone	R-63i	1.9E+00	NA	NA	NA	NA
Barium	R-63i	1.1E+01	2.0E+03	NA	2.0E+03	NA
Iron	R-63i	3.7E+01	NA	1.0E+03	NA	3.0E+02
Methylene chloride	R-63i	1.4E+00	5.0E+00	NA	5.0E+00	NA
Nickel	R-63i	7.5E-01	NA	NA	NA	NA
Nitrate-nitrite as nitrogen	R-63i	5.6E+02	1.0E+03	NA	1.0E+03	NA
Perchlorate	R-63i	2.2E-01	NA	NA	NA	NA
RDX	R-63i	3.1E-01	NA	NA	NA	NA
Strontium	R-63i	6.6E+01	NA	NA	NA	NA
Sulfate	R-63i	3.7E+03	NA	6.0E+05	NA	2.5E+05
Uranium	R-63i	9.4E-01	3.0E+01	NA	3.0E+01	NA

[a] TT = Treatment technique.

[b] NA = Not available.

[c] DNX = Hexahydro-1,3-dinitro-5-nitro-1,3,5-triazine.

[d] HMX = Her Majesty's Explosive.

[e] MNX = Hexahydro-1-nitroso-3,5-dinitro-1,3,5-triazine.

[f] TNX = 2,4,6-trinitroxylene.

Appendix A

Acronyms and Abbreviations,
Metric Conversion Table, and Data Qualifier Definitions

A-1.0 ACRONYMS AND ABBREVIATIONS

1-D	one-dimensional
2-D	two-dimensional
3-D	three-dimensional
amsl	above mean sea level
ASTM	American Society for Testing and Materials
BCA	bias-corrected and accelerated
bgs	below ground surface
CAS	Chemical Abstracts Service
CB	consistent Bayes
CdV	Cañon de Valle
CME	corrective measures evaluation
CMR	combinable magnetic resonance porosity
Consent Order	Compliance Order on Consent
COPC	chemical of potential concern
CSM	conceptual site model
DGIR	deep groundwater investigation report
DOE	Department of Energy (U.S.)
DNX	hexahydro-1,3-dinitro-5-nitro-1,3,5-triazine
DPHZ	density porosity
EES	Earth and Environmental Sciences (LANL division)
EIM	Environmental Information Management (database)
ELAN	Elemental Log Analysis (software)
EM-LA	Environmental Management Los Alamos Field Office (DOE)
ENPH	epithermal neutron porosity
EPA	Environmental Protection Agency (U.S.)
EPC	exposure point concentration
FEHM	Finite Element Heat and Mass transfer code
GFM	geologic framework model
HASL	Health and Safety Laboratory
HE	high explosives
HI	hazard index
HMX	Her Majesty's Explosive
HPC	high-performance computing
HQ	hazard quotient
IQR	Inner Quartile Range (method)
IRIS	Integrated Risk Information System (EPA database)
LANL	Los Alamos National Laboratory

LCMS/MS	liquid chromatography mass spectrometry/mass spectrometry
LCS	laboratory control sample
LM	Levenberg-Marquardt
LPZ	lower perched-intermediate zone
LR	literature review (RRM source type)
MADS	Model Analysis and Decision Support
MBR	mountain block recharge
MC	Monte Carlo
MCL	maximum contaminant level
MCMC	Markov Chain Monte Carlo
MDC	minimum detectable concentration
MFR	mountain front recharge
ML	machine learning
MLE	maximum likelihood estimation
MLMM	machine learning meta model
M-K	Mann-Kendall trend test
MNX	hexahydro-1-nitroso-3,5-dinitro-1,3,5-triazine
N3B	Newport News Nuclear BWXT-Los Alamos, LLC
NA	not available
NC	not calculated
ND	nondetection
NL	not listed
NMAC	New Mexico Administrative Code
NMED	New Mexico Environment Department
NPHI	thermal neutron porosity
OF	objective function
OLS	ordinary least squares regression
P&D	Pipe and Disk (analytical screening tool)
PAH	polycyclic aromatic hydrocarbon
PCB	polychlorinated biphenyl
PFAS	per- and polyfluoroalkyl substances
PRG	preliminary remediation goal
PZ	piezometer
RDX	Royal Demolition Explosive
RFI	Resource Conservation and Recovery Act facility investigation
RL	reporting limit
RPD	relative percent difference
RRM	RDX regional aquifer model

RSL	regional screening level (EPA)
RVZM	RDX Vadose Zone Model
S	screen (also sedimentary materials [strata classification])
SA	sensitivity analysis
SD	standard deviation
SIM	secondary ion mass spectrometry
SL	screening level
STL	seasonal decomposition of time series by loess
SVOC	semivolatile organic compound
SZ	saturated zone
TA	technical area
TCMR	combinable magnetic resonance total porosity
TNX	2,4,6-trinitroxylene
T-S	Theil-Sen trend test
TT	treatment technique
UCL	upper confidence limit
UPZ	upper perched-intermediate zone
UZ	unsaturated zone
V	volcanics
VOC	volatile organic compound
VOI	value of information
VU	values used (RRM source type)
VZ	vadose zone
XGB	extreme gradient boosting

A-2.0 METRIC CONVERSION TABLE

Multiply SI (Metric) Unit	by	To Obtain U.S. Customary Unit
kilometers (km)	0.622	miles (mi)
kilometers (km)	3281	feet (ft)
meters (m)	3.281	feet (ft)
meters (m)	39.37	inches (in.)
centimeters (cm)	0.03281	feet (ft)
centimeters (cm)	0.394	inches (in.)
millimeters (mm)	0.0394	inches (in.)
micrometers or microns (µm)	0.0000394	inches (in.)
square kilometers (km^2)	0.3861	square miles (mi^2)
hectares (ha)	2.5	acres
square meters (m^2)	10.764	square feet (ft^2)
cubic meters (m^3)	35.31	cubic feet (ft^3)
kilograms (kg)	2.2046	pounds (lb)
grams (g)	0.0353	ounces (oz)
grams per cubic centimeter (g/cm^3)	62.422	pounds per cubic foot (lb/ft^3)
milligrams per kilogram (mg/kg)	1	parts per million (ppm)
micrograms per gram (µg/g)	1	parts per million (ppm)
liters (L)	0.26	gallons (gal.)
milligrams per liter (mg/L)	1	parts per million (ppm)
degrees Celsius (°C)	9/5 + 32	degrees Fahrenheit (°F)

A-3.0   DATA QUALIFIER DEFINITIONS

Data Qualifier	Definition
U	The analyte was analyzed for but not detected.
J	The analyte was positively identified, and the associated numerical value is estimated to be more uncertain than would normally be expected for that analysis.
J+	The analyte was positively identified, and the result is likely to be biased high.
J-	The analyte was positively identified, and the result is likely to be biased low.
UJ	The analyte was not positively identified in the sample, and the associated value is an estimate of the sample-specific detection or quantitation limit.
R	The data are rejected as a result of major problems with quality assurance/quality control parameters.

Appendix B

Data Preparation Protocol, Time Plots, Box Plots,
and ProUCL Files for Chemicals of Potential Concern

B-1.0 DATA PREPARATION PROTOCOL

The data preparation protocol applied to the Environmental Information Management (EIM) data query is similar to that described in section 3.1 of the "Investigation Report for Royal Demolition Explosive in Deep Groundwater" (N3B 2019, 700561):

The data set evaluated to screening values included the following filters: (1) sample purpose – regular (REG), (2) sample type – water (W) and groundwater (WG), (3) best value – yes, and (4) sample usage code – investigation (INV) or blank. No screening values, test data, or field duplicates were included in the data set.

For the data set created by the EIM data query for this assessment, a "removal_flag" field was added to the data file and flagged with Y (yes, remove from data set) or N (no, do not remove from data set) to indicate records that should be removed because they are not applicable to evaluating current groundwater conditions. The removal_flag = Y reasons based on the initial review are provided in the following list:

- SAMPLE_TYPE

  - ❖ Remove EM (engineered material), R (rock), S (soil), and WIP (industrial process water)
  - ❖ Keep WG (groundwater), W (water)

- EXCAVATED_FLAG

  - ❖ Keep N (no)
  - ❖ Keep NA (not available)
  - ❖ Remove Y (yes)

- SAMPLE_PURPOSE

  - ❖ Remove EQB (equipment blank), FB (field blank), PEB (performance equipment blank), FTB (field trip blank), FD (field duplicate), and TEST
  - ❖ Keep REG

- LAB_MATRIX

  - ❖ Remove GAS, SD (solid)
  - ❖ Keep W (water)

- VALIDATION_STATUS_CODE

  - ❖ Remove NOVAL (not validated)
  - ❖ Keep VAL (validated)
  - ❖ Keep NA (not available)

- SAMPLE_USAGE_CODE

  - ❖ Remove CONST (well under construction)
  - ❖ Remove DEV (well development)
  - ❖ Remove PUMT (pump/aquifer test)

❖ Remove QC (quality control)

❖ Remove SCR (screening samples for screening purposes only)

❖ Remove TEST (well testing samples collected from sampling system, not for monitoring)

❖ Remove TRACER (tracer study for groundwater wells for the purpose of water dispersion studies)

❖ Remove WST (waste classification samples collected for waste determination purposes only)

❖ Keep INV (investigation)

❖ Keep NA (not available)

- SAMPLE_PLAN_NAME

    ❖ Remove CDV-9-1i Initial Drilling and Purge Sampling

    ❖ Remove FY09; Direct waste Decon Fluids for Well PCI-2, TA-18

    ❖ Remove R-25(b) Well Development

    ❖ Remove R-26 Piezometer Sampling

    ❖ Remove R-26 Piezometer Sampling 2

    ❖ Remove Westbay Reliability Assessment Part 1: No-Purge Samples

    ❖ Remove Westbay Reliability Assessment Part 2: Sampling during Initial Purge

    ❖ Remove R-63-i – Bailed Sample

    ❖ Keep all other sampling plan names

- BEST_VALUE_FLAG

    ❖ Remove N (no)

    ❖ Remove NA (not available)

    ❖ Keep Y (yes)

- USE_FLAG

    ❖ Remove N (no)

    ❖ Keep Y (yes)

B-1.1 Evaluation of Preferred Analytical Method

In some instances, an analyte was measured by multiple analytical methods for the same sample. The following analytes were analyzed by more than one method in a single sample:

- High explosives – 2,4-dinitrotoluene; 2,6-dinitrotoluene

    ❖ Analyzed by 8321/8270 or 8330/8270

- Polycyclic aromatic hydrocarbons (PAHs) – acenaphthene, acenaphthylene, anthracene, benzo(g,h,i)perylene, chrysene, fluoranthene, phenanthrene, pyrene

    ❖ Analyzed by 8270/8270SIM

- Volatile organic compounds (VOCs)/Semivolatile organic compounds (SVOCs) – hexachlorobutadiene; 1,2-dichlorobenzene

  - ❖ Analyzed by 8260/8270

- Metals – antimony, beryllium, cadmium, lead, thallium

  - ❖ Analyzed by 6010/6020

- Radionuclide – americium-241 (Am-241)

  - ❖ Analyzed by generic gamma spectroscopy/Health and Safety Laboratory (HASL) 300 Am-241 (alpha spectroscopy)

- Radionuclide – radium-226 (Ra-226)

  - ❖ Analyzed by 901.1 and 903.1

- Radionuclide – uranium-238 (U-238)

  - ❖ Analyzed by 901.1 and generic alpha spectroscopy

- Metal/radionuclide – uranium

  - ❖ Analyzed by American Society for Testing and Materials (ASTM) D3972-90 (alpha spectroscopy)/6020

Table B-1.1-1 provides a summary of the analytical methods selected for these analytes. Details of the selection rationale are provided below.

High explosives – 2,4-dinitrotoluene; 2,6-dinitrotoluene

- Prefer 8231 over 8270

  - ❖ All results are nondetections (ND).

  - ❖ Reporting limits (RLs) for 8321 are ~3✕ lower.

  - ❖ No qualifications of particular concern are in the data chosen for retention.

  - ❖ One 8321 result was qualified UJ for a holding-time exceedance.

- Prefer 8330 over 8270

  - ❖ All results are ND.

  - ❖ RLs for 8330 are ~5–10✕ lower.

  - ❖ Most 8330 analyses used a mass spectrometer detector, which gives greater certainty in the identification.

  - ❖ No qualifications of particular concern have been applied to the data chosen for retention.

- Comparability – The data seem to be split across these three analyses.

PAHs – acenaphthene, acenaphthylene, anthracene, benzo(g,h,i)perylene, chrysene, fluoranthene, phenanthrene, pyrene

- Prefer 8270SIM over 8270

    - All results are ND.

    - RLs for secondary ion mass spectrometry (SIMS) are generally 3–10✕ lower.

    - No qualifications.

- Comparability – Most results are from 8270 analyses and not SIMS. However, the preparation and separation portions of the analyses are the same and both also use a mass spectrometer for detection. In SIMS, the mass spectrometer looks only for the selected masses, which provides the greater sensitivity. (There were some analyses by 8310; this analysis has problems with interferences.)

VOCs/SVOCs – hexachlorobutadiene, 1,2-dichlorobenzene

- Prefer 8260 over 8270

    - Most results are ND.

    - RLs for 8260 are ~10✕ lower.

    - No qualifications of particular concern are in the data chosen for retention. A few 8260 results are qualified for either holding-time exceedance or low laboratory control sample (LCS) recovery.

- Comparability – Looking at the full water matrix data set, most analyses per performed by 8260.

Metals – antimony, beryllium, cadmium, lead, thallium

- Prefer 6020 over 6010

    - Most results are ND.

    - 6020 generally has lower RLs.

    - No qualifications of particular concern are in the data chosen for retention. A few results qualified for a high duplicate relative percent difference (RPD).

    - 6020 detected results are often (but not exclusively) higher than the paired 6010 result, but not substantially higher.

- Comparability – Both 6010 and 6020 use the same "separation" process (plasma) but have different detectors so, analytically, they are slightly less comparable. Method 6010 is more robust for groundwater analyses when there are high concentrations of dissolved solids, but the total dissolved solids results in the database are fairly low, so that is probably not an issue. The mass spectrometer is more sensitive than the optical system used in 6010, so 6020 usually has lower detection limits. Analytically, these are reasonably comparable methods.

    - Beryllium was analyzed more by 6010.

    - Antimony, cadmium, lead, thallium were analyzed more by 6020.

Perchlorate

- Prefer 6850 over 314.0

    ❖ 6580 has lower RLs.

    ❖ No qualifications of particular concern. A few results were qualified, but the reason codes were not defined. Likely the qualifications were for a low LCS recovery and/or RPD between the LCS and LCS duplicate.

- Comparability – Most analyses were performed by 6850.

Total phosphate as phosphorus

- Prefer 365.4 over 300.0

    ❖ 365.4 specific to phosphate

    ❖ Fewer interferences since phosphate is the only analyte

    ❖ One result was censored for a method blank detection. No other qualifications were of concern.

- Comparability – Most results were reported by 365.4.

Radionuclide – Am-241

- Prefer HASL 300 over generic gamma spectroscopy

    ❖ HASL method uses a chemical separation specific for americium.

    ❖ Minimum detectable concentration (MDC) and uncertainties are orders of magnitude lower.

    ❖ No qualifications

- Comparability – The methods are not analytically comparable.

    ❖ There are four results above the MDC. Two detections were by HASL in samples where the result was <gamma MDC and the gamma result was <MDC. The other two detections were in the same sample, with the gamma result 3 orders of magnitude higher.

    ❖ Most analyses were performed by alpha spectroscopy.

Radionuclide – Ra-226

- Prefer 903.1 over 901.1

    ❖ 901.1 is a gamma spectroscopy screening method while 903.1 performs a chemical separation of Ra-226 and then counts it via alpha spectrometry.

    ❖ MDC and uncertainties are orders of magnitude lower.

    ❖ No qualifications

- Comparability – most analyses performed by 903.1

Radionuclide – U-238

- Prefer generic alpha spectroscopy over 901.1

    - 901.1 is a gamma spectroscopy screening method while even a generic alpha spectroscopy probably performs a chemical separation of uranium and then counts it via alpha spectrometry.

    - MDC and uncertainties are orders of magnitude lower.

    - The result was qualified, but the code is not defined. The laboratory may have qualified the result as a nondetection even though it was above the MDC. This is not a concern.

- Comparability – Most analyses were performed by HASL 300, which is an alpha spectroscopy method.

Metal/radionuclide – uranium

- Use either ASTM D3972-90 (alpha spectroscopy) or 6020.

    - Only one affected sample was analyzed twice by 6020 and once by an alpha spectroscopy method; the three results are virtually the same.

    - None of the results are qualified.

    - Alpha spectroscopy may have better identification because there is a chemical speciation before counting.

- Comparability – Of the analyses reporting nonspeciated uranium, about 90% were performed by either 6010 or 6020.

Evaluation of temporal trends in the prepared data set was performed by review of time plots that show potential patterns of increasing or decreasing concentrations over time for each analyte. The plots were reviewed to identify early sample results that are not representative of current conditions for specific analytes or analytical suites, and these results were then removed to produce the trimmed data set used in the screening assessment. Attachment B-1 shows the time plots for data trimming. (on CD included with this document).

B-2.0 DESCRIPTION OF STATISTICAL TESTS USED FOR BACKGROUND COMPARISONS

The following four tests were used to support evaluation of whether concentrations of inorganic chemicals and radionuclides in groundwater from the site wells were elevated relative to corresponding concentrations in the background wells. Tests that evaluate a shift in the central tendency of the data (t-test and Gehan test) address whether concentrations in the site wells are broadly elevated. This is complemented by the use of tests that evaluate shifts in the upper tails of the distributions (quantile and slippage tests) to determine whether concentrations in one or a few wells might be elevated, even if there are relatively few samples from these wells. Box plots comparing the analytical results of site wells and background wells are shown in Attachment B-2 (on CD included with this document).

Student's two sample t-test. The t-test tests for equality of the means of the site and background concentrations. The theoretical basis of the test assumes that concentrations are normally distributed at both site and background locations, though the test is fairly robust with respect to this assumption, if sufficient data are available. This test does not directly accommodate data reported as nondetections (i.e., data reported as below some detection limit). A substitution method is required for the censored

data. In practice, a value of one-half the detection limit (censoring limit) is commonly used. The t-test is run as a one-sided test, significant only if the site mean concentration is higher than the background mean, not assuming equal variances for the site and background distributions.

Gehan test. The Gehan test is a modification of the Wilcoxon rank sum test that tests for a location shift in the site concentrations (i.e., a shift of the entire distribution), and was first presented in "A Generalized Wilcoxon Test for Comparing Arbitrarily Singly-Censored Samples" (Gehan 1965, 055611). This nonparametric test ignores the actual concentrations measured and uses only the rank of the concentrations, and thus it can detect any upward shift of the site concentration distribution with respect to background. The Gehan test is less efficient than the t-test (i.e., it generally requires more data than the t-test to detect a difference between site and background), but it is more robust to outliers (i.e., less likely to produce a spurious significant result because of one or two outliers).

Quantile Test. The quantile test is a nonparametric test of the equality of some quantile of the site and background distributions (Gilbert and Simpson 1992, 054952). That is, it statistically compares the numbers of values greater than the specified quantile that come from the site and background data. Any quantile can be tested if sufficient data are available—the more extreme the quantile, the greater the sample size required. Commonly used quantiles are the 75th, 80th, or 90th percentiles. For purposes of this report, the 75th and 90th percentiles are discussed. The quantile test can accommodate nondetections provided that the detection limit is below the appropriate quantile of the background data set. If the detection limit is higher than the quantile, the nondetection data point is not used by the test.

Slippage Test. The slippage test is a nonparametric test that compares the extreme tails of the site and background distributions (Gilbert and Simpson 1992, 054952). Since the tail of a distribution can be estimated well only with a very large data set, the slippage test has low power for small data sets. The test statistic relies on the maximum concentration in the background data, and thus it is not robust to outliers in the background data set. The test is robust to outliers in the site data set. Nondetections for the slippage test are handled in the same way as the quantile test. The nondetection is used if the detection limit is below the maximum detected concentration in the background data set.

Attachment B-3 (on CD included with this document) presents time plots for the final data set used in the screening, subsequent to data trimming supported by the plots described in Attachment B-1 (on CD included with this document). Attachment B-4 (on CD included with this document) presents box plots for chemicals of potential concern that include the 95% upper confidence limit (UCL) line. These plots support review of the reasonableness of the calculated 95% UCL by displaying the value relative to the underlying data distribution. Attachment B-5 (on CD included with this document) presents the ProUCL software output files associated with the 95% UCL calculations.

B-3.0 REFERENCES

The following reference list includes documents cited in this appendix. Parenthetical information following each reference provides the author(s), publication date, and ERID, ESHID, or EMID. ERIDs were assigned by Los Alamos National Laboratory's (the Laboratory's) Associate Directorate for Environmental Management (IDs through 599999); ESHIDs were assigned by the Laboratory's Associate Directorate for Environment, Safety, and Health (IDs 600000 through 699999); and EMIDs are assigned by N3B (IDs 700000 and above).

Gehan, E.A., June 1965. "A Generalized Wilcoxon Test for Comparing Arbitrarily Singly-Censored Samples," *Biometrika,* Vol. 52, No. 1 and 2, pp. 203–223. (Gehan 1965, 055611)

Gilbert, R.O., and J.C. Simpson, December 1992. "Statistical Methods for Evaluating the Attainment of Cleanup Standards, Volume 3: Reference-Based Standards for Soils and Solid Media," document prepared for the U.S. Environmental Protection Agency, Pacific Northwest Laboratory, Richland, Washington. (Gilbert and Simpson 1992, 054952)

N3B (Newport News Nuclear BWXT-Los Alamos, LLC), August 2019. "Investigation Report for Royal Demolition Explosive in Deep Groundwater," Newport News Nuclear BWXT-Los Alamos, LLC, document EM2019-0235, Los Alamos, New Mexico. (N3B 2019, 700561)

Table B-1.1-1
Identification of Preferred Analytical Method for
Analytes with Multiple Measurements in a Single Sample

Analytical Group	Compounds/Analytes	Methods Used	Method to Retain
High Explosive	2,4-dinitrotoluene 2,6-dinitrotoluene	8231 and 8270	8231
High Explosive	2,4-dinitrotoluene 2,6-dinitrotoluene	8330 and 8270	8330
PAHs	Acenaphthene Acenaphthylene Anthracene Benzo(g,h,i)perylene Chrysene Fluoranthene Phenanthrene Pyrene	8270 and 8270SIM	8270SIM
VOC/SVOC	Hexachlorobutadiene 1,2-dichlorobenzene	8260 and 8270	8260
Metals	Antimony Beryllium Cadmium Lead Thallium	6010 and 6020	6010
General Chemistry	Perchlorate	314.0 and 6850	6850
	Total phosphate as phosphorous	300.0 and 365.4	365.4
Radionuclides	Am-241	Generic gamma spectroscopy and HASL 300 Am-241	HASL 300 Am-241
	Ra-226	901.1 and 903.1	903.1
	U-238	901.1 and generic alpha spectroscopy	Alpha spectroscopy
Radionuclide/Metal	Uranium	ASTM D3972-90 and 6020	6020

Attachment B-1

Time Plots for Data Trimming
(on CD included with this document)

Attachment B-2

Box Plots
(on CD included with this document)

Attachment B-3

Time Plot Final Data Set
(on CD included with this document)

Attachment B-4

Box Plots with 95% UCL Line
(on CD included with this document)

Attachment B-5

ProUCL Files
(on CD included with this document)

Appendix C

Probabilistic Groundwater Modeling
of the Royal Demotion Explosive Plume at
Los Alamos National Laboratory to Support Risk Assessment

EXECUTIVE SUMMARY

A dissolved phase plume of the organic compound hexahydro-1,3,5-trinitro-1,3,5-triazine (Royal Demolition Explosive [RDX]) with concentrations greater than the New Mexico tap water drinking standard of 9.66 ppb is present in the upper portions of the regional aquifer near the southwestern boundary of Los Alamos National Laboratory (LANL). This risk assessment for exposure to regional aquifer groundwater is supported with long-term predictions of RDX concentrations from a calibrated, probabilistic, numerical fate and transport model run to the year 2200. The fate and transport modeling of the regional aquifer is conducted with computational and statistical methods that use high-performance computing resources. This modeling leverages prior work with extensive updates in terms of data, software, model, and analytical tools. Results of the calibration demonstrate excellent matches to concentration data, water levels, drawdown responses to water-supply pumping, and hydraulic gradients. The model is also compared with validation data sets to verify its appropriateness for predictive use. Uncertainty is quantified using a Bayesian approach that includes different model conceptualizations (unique flow fields and source terms are independently calibrated) and uncertainty in transport parameters using a Markov Chain Monte Carlo (MCMC) sampler. Ultimately this results in four deterministic calibrations and over 4000 posterior parameter sets for predictive modeling into the future. Results are presented as likelihoods determined by a percentage of predictive runs.

The RDX regional aquifer model (RRM) was developed to incorporate all relevant data and conceptual site knowledge in a transparent framework, to predict future plume migration with uncertainty, and to support decision-making. Notably, this revision calibrates monitoring well drawdown to supply well pumping tests and incorporates long-term pumping at Los Alamos County water-supply wells. The model is calibrated using data through December 2019 and validated with data through May 2022. Model input parameters are described by prior distributions that compile available data and information to constrain the plausible range and likelihood of input parameter values at the site. Where data are scarce, other lines of evidence and prior work are used to inform the distributions, including the multiphase RDX Vadose Zone Model (RVZM) and the Pipe and Disk (P&D) analytical screening tool.

Calibration is performed with a Bayesian approach. First, a classical nonlinear optimization using a Levenberg-Marquardt (LM) algorithm is performed, which is then used to initialize an MCMC sampler. The LM calibrations estimate model uncertainty and the MCMC calibration estimates parameter uncertainty, ultimately providing updated posterior distributions for input parameters. Uncertainty in the conceptual model is explored by identifying four top calibrations before the MCMC is initialized. The challenges of the calibration include high temporal and spatial resolution, high-dimensional parameter space (including spatially heterogeneous hydraulic conductivities), comparatively sparse data, and low RDX concentrations. The results of the predictive forward runs are estimates of head and concentration with uncertainty at all modeled points in space and time.

LM calibration results show very close matches between simulated and observed targets at the site. All wells with observed RDX concentrations are well matched in the modeled results. Hydraulic gradients local to the plume are also matched in both direction and magnitude. This is significant because the overall regional gradient is from west to east, but local to the plume there is a northeast gradient of variable magnitude between wells where RDX has been observed in the regional aquifer. Water levels match closely, with 97% of simulated heads within 0.5 m of observed data. The model is validated through detailed comparisons between the conceptual site model and numerical model, including final source locations and hydraulic gradients. Additionally the model is validated against data between December 2019 and present, which were excluded from the target data sets. These data are well matched across runs with uncertainty, with only a few validation points at R-18 falling outside the range of all runs. Further calibration of the model incorporating new data would continue to improve the predictive power of the model.

No simulations predict breakthrough of the plume (9.66-ppb contour) at water-supply wells between now and the end of the simulation in year 2200. Median RDX concentrations are below 0.25 ppb at all supply wells and the middle 50% of simulations fall below 0.5 ppb, suggesting that if RDX were ever to reach these wells it would likely be below detection limits.

CONTENTS

Figures

Table

C-1.0 INTRODUCTION

C-1.1 Background

This revision to the May 2020 risk assessment report for Royal Demolition Explosive (RDX) contamination in deep groundwater at Los Alamos National Laboratory (LANL or the Laboratory) Technical Area 16 (TA-16) (N3B 2020, 700925) fulfills a requirement of the 2016 Compliance Order on Consent (Consent Order) Appendix B milestones and targets for fiscal year 2022. Appendix B Milestone 10 requires a report that incorporates updates to the risk assessment and groundwater model reflecting discussions and draft comments received from the New Mexico Environment Department (NMED).

In 2019, Newport News Nuclear BWXT-Los Alamos, LLC (N3B) submitted the "Investigation Report for Royal Demolition Explosive in Deep Groundwater" (hereafter, DGIR) to NMED (N3B 2019, 700561). The DGIR presented results of previous investigations and studies, including analysis of the nature and extent of RDX in deep groundwater and an updated conceptual site model (CSM). The predictive modeling of the RDX plume at LANL, which is summarized in this report, draws from prior work, includes new characterization activities, and supports the continual evaluation of RDX in groundwater, including Scenario 3 in this risk assessment report. Scenario 3 applies the results of this RDX fate and transport modeling in the regional aquifer to evaluate the probability that the RDX plume, specified by the 9.66-ppb contour, could reach regional aquifer water-supply wells at some time in the future (predictive modeling is run to the year 2200). The modeling conducted for this report draws from a conceptual model that derives from work that began in 1998 and reflects refinements from ongoing characterization to the present day. Any updates to the model that are not described in previous reports are described here. This appendix presents an overview of the fate and transport model and simulation results, while appendix D provides extensive supplementary information about all the analyses that informed the model.

C-1.2 Conceptual Site Model

Early activities at TA-16 supported the development of the first implosion-type atomic bombs. The high explosives (HE) components of the implosion design were developed, manufactured, and tested at TA-16 during World War II.

Building 260, located on the north side of TA-16, has been used for processing and machining HE since 1951, including RDX (hexahydro-1,3,5-trinitro-1,3,5-triazine). Water is used in the machining process. The HE is slightly water soluble, and effluent from machining operations contains dissolved and entrained HE cuttings. At building 260, effluent treatment consists of routing the effluent to 13 settling sumps to recover any entrained HE cuttings. From 1951 to 1996, the water from these sumps was discharged to the 260 Outfall that drained into Cañon de Valle, with millions of gallons discharged per year. The 260 Outfall is the primary source of HE that impacted groundwater at TA-16 (LANL 2011, 203711), releasing large quantities of contaminants, particularly RDX, at high concentrations and large volumes of water that provided a significant hydrologic driving force for infiltration (LANL 2011, 203711; LANL 2012, 213573).

The physical systems presented in the CSM describe the fate and transport of RDX in groundwater beneath the TA-16 area. The development of the CSM began with Phase I site characterization (LANL 2011, 206324). Subsequent soil, sediment, surface water, springs, alluvial groundwater, shallow- and deep- perched-intermediate groundwater, and regional groundwater investigations formed and continue to influence the current CSM.

The following sections summarize the geologic and hydrological context of the CSM, which are discussed in detail in Appendix D.

C-1.2.1   Geologic Context

The RDX project area lies on the western edge of the Pajarito Plateau. Underlying the plateau is a geologic feature consisting of roughly 250 m of varying sequences of poorly consolidated tuffaceous materials known as the Bandelier Tuff. Below the Bandelier Tuff in the RDX project area lies the Puye Formation, which is the dominant geologic unit affecting flow and transport in the plume area. The Puye Formation consists of unconsolidated alluvial sediments sourced from the Jemez Mountains volcanic field to the west that predate the deposition of the Bandelier Tuff. The Tschicoma Formation, a thick lobe of massive to brecciated dacite lavas, lies deep in the stratigraphic section beneath the project area to the south of the plume.

Following the deposition of the Bandelier Tuff, erosion and faulting have modified the geology. Erosion of the tuff has created fingerlike mesas and canyons that extend west to east. TA-16 sits on one of these mesas located south of, and adjacent to, Cañon de Valle. The TA-16 260 Outfall discharged directly into the Cañon de Valle canyon bottom. The 260 Outfall is located in the TA-09 graben, an area that is suspected to be coincident with an area of high infiltration due to faulting and fractures (Figure C-1.2-1).

C-1.2.2   Hydrologic Context

The hydrologic system in the watershed includes surface water, springs, alluvial groundwater, vadose zone water, perched-intermediate groundwater, and regional aquifer groundwater.

Perched groundwater occurs at both shallow (referred to as shallow bedrock) and deep (referred to as perched-intermediate) levels of the vadose zone in the TA-16 area. Perched-intermediate groundwater occurs at depths of generally 600 ft below ground surface (bgs) in the lower part of the vadose zone, primarily in the Cerro Toledo Formation, the Otowi Member of the Bandelier Tuff, and the Puye Formation (Appendix D section D-1.3, Figure D-1.3-1) Groundwater in the two perched-intermediate zones is a mixture of mountain block recharge and mountain front recharge. Mountain block recharge originates in the highlands west of the Pajarito fault zone and consists of diffuse subsurface infiltration of snowmelt and surface water that percolates through the rock and recharges the regional aquifer. Mountain front recharge consists of mountain overland flow (generally streamflow) that infiltrates at the mountain front and the adjacent basin.

RDX containing wastewater was discharged from the 260 Outfall into Cañon de Valle, where it mixed with surface waters from the canyon and then infiltrated into the upper vadose zone. Vertical movement is primarily controlled by gravity in unsaturated zones. However, water has the potential to move laterally at bedding contacts and in zones of perched water, which are driven by hydraulic gradients that generally trend to the east (LANL 2018, 602963). The result is that water tends to stairstep down through the vadose zone through a series of perched zones, likely expanding the lateral extent of the contaminant plume and creating zones of preferential recharge to the regional aquifer. Other evidence, such as mounding at R-25 and strong vertical gradients at the site, also support the conceptualization of preferential zones of recharge. The CSM for the RDX regional aquifer model (RRM) includes both RDX-free and RDX-contaminated sources of recharge from the perched-intermediate groundwater to the regional aquifer. More detail on the vadose zone hydrology is described in Appendix D.

The regional groundwater system is large, heterogeneous, and complex, with unconfined conditions near the water table and semiconfined conditions with depth (LANL 2011, 207069). The main direction of groundwater flow in the aquifer is from west, where regional recharge enters the aquifer from the mountain block of Sierra de los Valles at an elevation of approximately 6600 ft above mean sea level (amsl) at the Pajarito fault, to east, where discharge occurs along the Rio Grande River (approximately 5500 ft amsl at the Rio Grande) and White Rock Canyon springs. This distance is about 9.3 mi laterally.

At TA-16, the regional water table is located between 1000 and 1300 ft bgs, with higher water-table levels to the west creating flow from west to east and local northeastern gradients.

The regional aquifer produces large volumes of water; Los Alamos County supply wells pull nearly 1 billion gal. from the regional aquifer every year. Slow but steady long-term decline in water levels has also been observed in well screens across the Pajarito Plateau for decades. Differences in rates of long-term decline observed between wells across the plateau suggest that decline is not uniform across the regional aquifer (Appendix D Section D-2.3.1). In order to better understand and quantify potential impacts of supply wells on present-day and future RDX transport, a detailed study of hydraulic head data and county pumping is presented in Appendix D; a brief summary is included below.

C-1.2.3 Hydraulic Gradients Study Summary

An analysis of long-term water table decline finds that across the Pajarito Plateau, on average, the water table has been declining at a rate of approximately 0.33 ft (0.1 m) per year over the last few decades, which could be expected to continue at similar rates into the future. Declining water levels suggest the potential for a "hinge effect" in the aquifer system; if water levels below the Pajarito Plateau were to decline at substantially greater rates than regions close to the mountain block (where heads are sustained from mountain recharge), this could cause a shift in overall hydraulic gradient magnitudes across the plateau. An extensive study interrogating (1) potential trends and variability in long-term water table decline and (2) lateral and vertical hydraulic gradients is conducted in Appendix D using hydraulic head data at monitoring wells and pumping data at Los Alamos County water-supply wells. The focus of the study is to determine the magnitude of impact that supply wells have on hydraulic gradients in the portion of the regional aquifer from the RDX plume in the west, extending east to supply wells PM-2, PM-4, and PM-5. The goals of this study are to characterize long-term trends in lateral and vertical gradients across the site, identify mechanisms responsible for producing the vertical gradients observed in wells near the RDX plume (such as R-69 and R-25), and to evaluate whether county supply well pumping influences hydraulic gradients, both vertical and lateral, at the RDX plume site or the region between the plume and PM-2, PM-4, and PM-5.

The study uses the method of Heath (1983, 700907) to calculate lateral gradients between well triplets at 3 different aquifer depths (Figure C-1.2-2). Similarly, vertical gradients are calculated at every multiscreened interval available, as well as single-screened wells that are close laterally but screened at different depths in the aquifer [Figure C-1.2-3(A)]. These 30 lateral gradients across 3 depths and 24 vertical gradients are explored temporally for the entire period of record and compared with county supply well pumping records to answer the following three questions:

1. Do regional aquifer gradients change through time enough to meaningfully affect flow and transport?

2. Can any systematic changes in gradients be correlated to county supply well pumping?

3. For the purposes of Scenario 3 in the risk assessment, should long-term county supply well pumping be included in model simulations because it is likely to impact RDX transport in the next several hundred years?

In addition to addressing these questions directly, this type of hydraulic analysis provides important context for modeling, including the magnitude of gradients throughout the aquifer, insight into the spatial components of long-term water table declines, and the correlation between supply well pumping and subregions in the aquifer. All of these inform the CSM and are considered when designing the RRM to accurately represent transport in the regional aquifer.

Results of the analysis of long-term decline suggest that there may be a relationship between water table decline and proximity to county water-supply wells. The relationship diminishes somewhere west of R-19 and east of CdV-R-15-3 (Appendix D section D-2.3.1, Figure D-2.3-4), suggesting that hydraulic gradients west of R-17 may not be affected by county supply pumping.

The estimated magnitude of lateral hydraulic gradients ranges from 0.001 to 0.048 across the area of study, and for most well triplets there is a statistically significant increasing trend in gradient magnitude through time. Although there exists statistical evidence that gradients/azimuths are increasing/decreasing over time, in all cases the magnitude of change is not practically meaningful for the period of simulation in the model. Estimated changes through time for lateral gradient magnitudes in the RDX plume and downgradient region west of R-17 are on the order of 10^{-6} to 10^{-8} per year across the three depth zones. This indicates that while changes in hydraulic gradients are quantifiable, the magnitude of change is negligible over the period of modeling for the RRM (~250 yr). Similarly, changes in azimuth in this region are generally less than a few degrees over the period of record. Tests for a relationship between supply well pumping and changes in lateral hydraulic gradient magnitude and azimuth indicate that higher correlation is seen at distances close to the PM water-supply wells, where larger changes in magnitude and azimuth are observed; the relationship diminishes with distance, particularly in the south where the Tschicoma Formation is coincident with the water table. Low correlation values combined with very small changes through time suggests that the supply wells have little to no effect on lateral gradients in the RDX plume and downgradient region west of R-17. These water table declines and lateral gradients provide insight on the potential "hinge" effect mentioned above. While some analyses show correlation at some monitoring wells, the magnitude of any effect is so small as to be negligible for transport calculations over the next few hundred years.

Vertical gradients are also critical to scrutinize, especially since these are very high (between −0.07 and −0.26) near the plume. Magnitudes throughout the site indicate high, downward vertical gradients near the mountain block, a flatter gradient in the center of the aquifer, and an upward gradient where the regional aquifer reaches the Rio Grande. Vertical gradients in multiscreened wells like R-17 and R-19, which are very close to county supply wells, are 1–2 orders of magnitude below those observed near the plume. Analysis of correlation to water-supply pumping showed that these small gradients near the supply wells are strongly correlated to pumping rates and that the high gradients near the plume are not correlated to pumping [Figure C-1.2-3(B)]. This is consistent with the CSM that gradients in the RDX plume and downgradient area are driven by a combination of mountain block recharge and, likely to a lesser extent, localized/preferential infiltration under canyons at the ground surface that travels through the vadose zone and arrives as preferential recharge to the regional aquifer through hydraulic windows.

Overall, the hydraulic analyses conclusions are as follows:

1. Regional aquifer gradients do not change through time enough to meaningfully affect flow and transport. Rates of change in magnitude and direction are small enough to be considered negligible and this type of transience is not needed in the RRM to accurately simulate RDX transport until the year 2200.

2. Minor systematic changes or impacts on hydraulic gradients can be correlated/attributed to county supply well pumping near the wells. However, lateral and vertical hydraulic gradient magnitudes in the RDX plume area are 1–2 orders of magnitude higher than any observed at closer distances to supply wells. Therefore, any impact the supply wells may have on hydraulic gradients in the regional aquifer is negligible in the context of the RDX plume. Hydraulic gradients in the RDX plume and downgradient area are driven by mountain block recharge and local sources of infiltration from the surface.

3. Long-term water table declines do not affect lateral or vertical hydraulic gradients near the RDX plume or in most of the region between the plume and the county supply wells. Despite this result, long-term county water-supply pumping is included in the RRM for thoroughness.

C-2.0 METHODS, ANALYSIS, AND DISCUSSION

C-2.1 Approach to Modeling

The modeling approach is designed to integrate all possible sources of information available to inform the decision in a hierarchical structure represented in Figure C-2.1-1. This structure is used to predict RDX fate and transport in both space and time, quantify the uncertainty associated with model predictions, and quantify the sensitivity of parameters and the value of information. The numerical RRM is built using the Finite Element Heat and Mass transfer code (FEHM) [(Zyvoloski 2007, 700904); https://fehm.lanl.gov/] and is calibrated using the Model Analysis and Decision Support (MADS) software, available at https://mads.lanl.gov/.

The steps developed for the RRM modeling leverage all the lines of evidence available, including data, the RDX Vadose Zone Model (RVZM), site CSM and expert knowledge, as well as other available information (such as the focused study on hydraulic gradients). This site information is combined into the modeling framework, which includes the model structure such as boundary and initial conditions, discretization in space and time, and assumptions. The model is calibrated against site data ("calibration targets") and validated with conceptual information and data that were not used as a calibration target. Modeling is inherently an iterative process and analytical tools are used at every step to improve process representation, input parameterization, and assumptions. Within each step of the process there are internal iterative loops, including detailed quality assessment and control. Many of these tools are described briefly in section C-2.5 and described in detail in Appendix D section D-5.4.

C-2.2 Model Domain and Grid

The upper surface of the RRM represents the regional aquifer water table, which is approximately 300–400 m below the land surface. Water table elevations range from 1920 m amsl near the western edge of the domain, which approaches the mountain block, to 1616 m amsl near the Rio Grande, whose x, y coordinates define the eastern model boundary. The model covers an area of 221 km^2 horizontally and extends from the water table down to 1000 m amsl in the vertical direction. While the plume covers only a small portion of the regional aquifer, a large domain size with successive levels of refinement was used to provide detailed characterization in the plume region as well as to avoid boundary effects in flow and transport modeling. Including the entire regional aquifer in the model allows for selection of physically significant boundaries (such as the Rio Grande to the east), and the use of selective refinement minimizes the computational burdens associated with a large domain on a regular grid.

The model is discretized into a tetrahedral mesh with lateral spacing at 125 m using the LANL LaGriT mesh generator available at https://lagrit.lanl.gov/ (Gable et al. 1996, 700887). Two levels of refinement are used in areas of interest, which increases lateral resolution to 62.5 m and 31.25 m respectively. The z direction is variably refined, ranging from 6 to 24 m in thickness with higher resolution at the top of the regional aquifer. The grid is connected according to Delaunay criteria and is quality tested both in terms of Voronoi volumes and negative coefficients. Materials are assigned to each node in the mesh based on the 13 hydrogeological units in the Geological Framework Model for the LANL region; the vast majority of RDX modeling occurs in the Puye Formation, with some influence from the Tschicoma lobe to the south of the RDX plume. The total number of nodes for the RRM mesh is 510,226 and the total number of

elements is 2,883,589. The entire RRM and an inset in the region of interest for monitoring RDX concentrations is shown in Figure C-2.2-1.

A water table surface developed for the regional aquifer previously (LANL 2018, 602964) was discretized with two zones of the 2014 average water table levels. The year 2014 is used because this is the same year used to develop water table targets and it represents the most thorough description of the water table (interpolated between data points) available from recent years. The model is run to steady-state flow conditions (see section C-2.1.3), as opposed to using transient flow solutions. An average water table decline of 0.33 ft per yr is observed across the site, and a uniform change in water table elevation is not expected to alter flow directions for RDX transport. This assumption is interrogated in the hydraulic gradients study, which is briefly summarized in section C-1.2.3 and described fully in section D-2.3.1. Gradients are found not to vary significantly in the RDX region in a way that alters flow directions for RDX transport.

The water table surface was smoothed to a resolution appropriate for the grid spacing. Using the Los Alamos Grid Toolbox (LaGriT) (https://lagrit.lanl.gov/), the 125-m by 125-m grid was interpolated onto the water table surface, and the surface was clipped to the shape of the RRM. Next, a process of two-dimensional (2-D) refinement was performed to balance the total number of nodes on the mesh (fewer nodes result in more tractable runtimes) with detail, especially local to the plume, to resolve transport simulations of RDX in the regional aquifer. After refining these regions in 2-D, copies are made and stacked at every z-coordinate needed for the orthogonal mesh (21 layers of 6.5 m beginning at the water table, 10 layers of 15 m, 4 layers of 30 m, and 8 layers of 65 m). The resulting orthogonal, tetrahedral mesh passes all quality checks and represents an appropriate compromise between detail and computational efficiency (more detail in Appendix D).

C-2.3 Model Operation, Initial, and Boundary Conditions

The FEHM code (Zyvoloski 2007, 700904) is used to simulate flow and transport in the RRM. The model represents the regional aquifer and is saturated at every node. Most boundary conditions, like other model parameters, use input distributions that limit parameters to plausible values. The boundary conditions are listed here, but their parameterization is described in detail in Appendix D section D-3.1. The main flow gradient in the model is developed by assigning constant head conditions to the western (mountain block) and eastern (Rio Grande) boundaries. On the eastern boundary, a uniform head is applied at nodes from the top (water table) to the bottom of the model. On the western boundary, vertical gradients are observed in wells near the western boundary (R-25, R-69, etc.), which are formed by recharge at the mountain block and, to a lesser extent, preferential recharge zones (Appendix D section D-2.0). To enforce this behavior observed in the data, a vertical gradient is set on the western boundary. No-flow boundaries are set approximately parallel to regional flow (north and south model edges) and the base of the model, which is sufficiently deep so it does not interfere with plume transport behavior. On the surface of the RRM, elliptical hydraulic windows representing preferential recharge from the vadose zone, both contaminated with RDX and clean, are applied.

Additional boundary conditions include the month-long pumping tests at PM-2 and PM-4, and long-term pumping at PM-2, PM-4, and PM-5. Drawdown observed in regional wells during the PM-2 and PM-4 tests is matched as calibration targets (section C-2.5.1). Although impacts from the county supply well pumping on the RDX plume and future transport were determined to be negligible (section C-1.2.3 and Appendix D), long-term supply well pumping is incorporated into the model for thoroughness. Pumping rates continue throughout model simulations (until 2200) with the expectation that supply pumping will continue at similar rates to those in the present day. Incorporating daily, weekly, or even monthly pumping from supply wells, however, would result in intractable model runtimes that would severely limit the future

simulated timeframe. Therefore, to include supply well pumping, pumping is incorporated by aggregating rates to a decadal scale for wells PM-2, PM-4, and PM-5 (Appendix D).

Some material and transport properties are assigned on a node-by-node basis; others are homogeneous throughout the domain. Details of these assignments, along with the data that inform the distributions, are discussed in Section C-2.4. Material properties parameters include advective porosity, dispersivity, lateral and vertical hydraulic conductivity (***K****)*, specific storage (S_s), and kriging parameters that are used to interpolate ***K*** and S_s. Additionally, an RDX sorption coefficient (K_d) and diffusivity are defined for the model.

A distribution is developed for the total mass of RDX that could impact the regional aquifer based on inventory estimates throughout the TA-16 site (surficial, vadose zone, and regional aquifer). This distribution is the only input parameter that is reserved for use in the predictive modeling. Present-day upward trends of RDX, plus relatively low inventory in the regional aquifer, indicate that mass is likely to impact the regional aquifer for decades or more. Other input parameters are used for the calibration and uncertainty quantification steps, but total mass is implemented only for the predictive forward runs, which are run far into the future to the year 2200. This distribution is listed in the input parameter table, but the discussion and accompanying figure can be found in section C-2.7.

Heads measured in February 2014 are spun up to a hydrostatic condition at the beginning of the model run, and then the transient portion of the simulation begins, starting in the year 1956 and running through the calibration period (i.e., until the end of 2019). The transient simulation includes the PM-2 and PM-4 pump tests (McLin 2005, 090073; McLin 2006, 092218), long-term water-supply pumping, and RDX transport. Time series of RDX concentrations and water levels are output for every well within the domain.

C-2.4 Input Parameter Distribution Development

All input parameters to the RRM are described using distributions that inform the range and likelihood of plausible values given existing site data. Though there are 423 unique parameters, some parameters are represented by the same input distribution. Table C-2.4-1 lists every unique distribution used in the RRM along with the parameter, model key, median, and the 1st and 99th percentiles of the distribution, which are used to set the bounds on how far the parameter can be moved by the Levenberg-Marquardt (LM) algorithm during the calibration process (section C-2.5). Distributions are developed using a rigorous process of gathering all available sources of information, including data, published literature values, and, where data are not available, elicitation of possible values from site experts; sources of information for each distribution are listed in Table C-2.4-1.

Modelers and statisticians work together to make decisions regarding the relevance and usage of data. Combining subject matter modeling expertise and statistical expertise ensures that the distribution used adequately represents, but does not overstate, uncertainty in the parameter of interest. Each of these decisions regarding available data for a given parameter is described explicitly in the Appendix D. Additionally, more extensive discussion of the distribution development process can be found in Appendix D or in "Scaling Input Distributions for Probabilistic Models" (Black et al. 2019, 700892).

Material property parameters include hydraulic conductivity, specific storage, dispersivity, and kriging parameters (see paragraph below on implementation of a heterogeneous hydraulic conductivity field). Boundary condition parameters include constant head at the four corners of the domain, a vertical gradient in the top 100 m of the western boundary, and hydraulic window characteristics. The RRM domain begins at the top of the regional aquifer, where it is assumed that RDX has traveled through the vadose zone to the regional aquifer water table. These pathways are referred to as "hydraulic windows" or "drip points." Their footprints on the regional aquifer are referred to as the "source(s)" of RDX at the water table. The hydraulic windows in the RRM are represented as ellipses to provide a range of spatial

configurations of RDX addition to the aquifer. The variability in the spatial extent of the ellipses, as controlled by the center coordinates and xy radii, are shown in Figure C-2.4-1.

Three hydraulic windows are conceptualized in the RRM – a clean source of recharge under Cañon de Valle, a primary contaminated source, and the possibility of a second contaminated source (Figure C-2.4-1). Preferential flow paths are consistent with the CSM, either as small regions of fractured or connected high *K* flow paths from the surface or spatially consistent with perched zones above the regional aquifer. The presence of preferential windows is also corroborated by results from the RVZM (Appendix D section D-3.2.2, Figure D-3.2-3), which found highly nonuniform rates of recharge to the regional aquifer. Certain portions of the RVZM contain recharge rates to the regional aquifer at more than an order of magnitude above the minimal background rates observed elsewhere at the intersection with the regional aquifer. The primary source of RDX is likely to be relatively compact with higher concentrations, based on the clear, low-noise trend in RDX concentrations observed at R-18, coupled with relatively higher values of RDX concentration at R-68 and R-69 and no observed RDX at R-47 above detection limits. Given the proximity of these wells to each other (Figure C-2.2-1), and the fact that they contain the highest measured RDX, it is hypothesized that a primary source is responsible for the trends observed. Given the high concentrations arriving at the regional aquifer through a vertically extensive, 300–400-m vadose zone, this source is conceptualized as MFR, arriving at the regional aquifer via preferential pathways and as having primarily surface infiltration as the water source. To account for uncertainty in the conceptual model, to match the observed arrival of RDX concentrations at a much lower order of magnitude at R-25 and R-63, and to acknowledge the possibility that a surface source may have mixed with perched water during migration from the surface to the regional aquifer, a potential, lower-concentration secondary source is also conceptualized. Details on the conceptualization and data sets that informed the distributions for these hydraulic windows are discussed extensively in Appendix D.

Given the heterogeneity of the Puye Formation, and the sensitivity of flow and transport to local hydraulic conductivity, a heterogeneous field of *K* is generated on a node-by-node basis using the pilot point approach (Doherty 2003, 700894). The method is employed by sampling from narrower distributions at well locations that are informed by hydraulic conductivity estimates derived from aquifer tests at that particular location (referred to as "anchor points") and sampling from wider distributions derived from all relevant site data at locations between the well anchor points (referred to as "pilot points") (Figures C-2.4-2 and C-2.4-3). The distribution for the Puye Formation can range from 0.022 ft/day to 1380 ft/day, though final values do not extend through this entire range (Figure C-2.4-3). For each simulation, the values drawn at anchor and pilot points are then kriged to form a heterogeneous *K* field that honors the available estimates, their spatial locations, and the associated uncertainty. The kriging model uses a spherical variogram with a calibrated range parameter. A scaling factor applied to the range parameter in the z direction (i.e., anisotropy) is utilized to allow for the layering behavior present from the alluvial deposition of the Puye Formation—i.e., more correlation in the lateral directions than the vertical direction. The *K* and S_s fields are kriged independently (Appendix D). For pilot points in the Tschicoma Formation and deeper volcanic units in the domain, very little applicable data are available to inform plausible ranges for the model. For that reason, pilot points that fall into these units are described by a wide, uniform range determined from the literature. Distributions for specific storage and the kriging parameters are shown in Figure C-2.4-4.

C-2.5 Calibration

Model development and calibration is an iterative process targeted at evolving the CSM and its implementation in the RRM. This process includes both qualitative and quantitative components that span lines of evidence based on expert knowledge, monitoring data, laboratory experiments, and geophysical data. The RRM integrates these lines of evidence by providing a quantitative calibration of the conceptual model to data (Figure C-2.1-1) and estimating the uncertainty associated with input parameters.

Calibration is a learning process that employs several qualitative and quantitative approaches. Typically, a classical calibration fits a nonlinear regression model to target data. This section will provide an overview of target data sets and a brief discussion of the tools used in calibration and uncertainty quantification, including the LM algorithm and Markov Chain Monte Carlo (MCMC) sampler. More details of the calibration workflow, along with analyses used throughout to qualitatively and quantitatively validate that the RRM realistically simulates the expected physical behaviors, are provided in Appendix D.

C-2.5.1   Target Development

The objective function (OF), which drives the calibration by measuring how well the model matches observed data sets, is composed of target variables. These targets relate model results to observed data. The main form of data available for the RRM is from monitoring wells at the LANL site. Water level data and chemical data with concentrations of RDX are available for screened intervals in these wells or boreholes drilled on the Pajarito Plateau. The data from these wells is made available publicly on the Intellus website (https://intellusnm.com).

Target development takes place alongside distribution development in an iterative process. The spatial and temporal scales of targets are important to represent the observed data at a similar scale to the model for a successful calibration. Currently, the RRM uses 231 targets that can be classified into the following five groups:

1. RDX concentration for each well screen for each observed year (157 targets)

2. RDX concentration slope trends in wells of interest (2 targets)

3. Hydraulic head gradients between wells of interest (8 targets)

4. Hydraulic head within each well screen for February 2014 (20 targets)

5. Hydraulic head drawdown responses measured during the PM-2 and PM-4 aquifer tests in monitoring wells (44 targets)

Each of these groups of targets can be weighted differently to define an OF that is most appropriate for the calibration. For example, if the calibration can match hydraulic head targets but not concentration targets, weights for concentration data can be increased relative to the hydraulic head targets. These are called the "group weights." Within each group, individual targets (certain wells, or certain times) can also be weighted differently. These are called the "preference weights." The weights and the targets are also standardized, so that different units of measurement or scales of data do not have a different impact on the OF. This is called the "meaningful difference" between targets. The OF therefore is a grouped, weighted average of residuals that measure how closely the simulation matches the observed data.

Final weighting schemes are identified to prioritize data points that have a larger influence on maintaining the CSM, encouraging important physical behaviors, and matching responses to supply well pumping. The approximate target priorities follow:

1. Concentrations in

    a. R-68, R-69 screen 1 and screen 2 to constrain source concentrations and total inventory; these wells have the highest RDX concentrations in the regional aquifer.

    b. R-18 to constrain the timing/advancement of the plume; R-18 is the furthest downgradient well with a clearly increasing trend in concentration.

    c. R-63 low but increasing trend in RDX

      d. R-25 (low levels), oldest measured concentrations of RDX

      e. Lack of RDX (zero concentration targets)

          i. CdV-R-15-3, CdV-R-37-2, R-17, R-19, R-29, R-47, R-48, R-58, R-60

2. Hydraulic gradient magnitude and azimuth

      a. General flow direction in regional aquifer is west to east. Local to the RDX plume, flow is approximately northeast.

3. Concentration slopes

      a. R-18 is the plume leading-edge monitoring well that shows a clear increasing trend

      b. R-63 shows a small increasing trend.

4. Water levels

      a. RDX plume region multiscreened wells R-69 and R-25

      b. Downgradient multiscreened wells R-17 and R-19

      c. RDX plume region single-screened wells: R-18, R-47, R-48, R-58, R-63, R-68

      d. Downgradient wells R-29 and R-60

5. Drawdown responses to supply well pumping

      a. PM-4 test

          i. Responses at PM-2, PM-5, R-14, R-18, R-19, R-20 and zero response at R-18, CdV-R-37-2, CdV-R-15-3

      b. PM-2 test

          i. Responses at PM-4, PM-5, and R-20 screen 3

RDX Concentration and Trend Targets

Concentration targets are developed using data pulled from the publicly available Intellus database (https://intellusnm.com). The data were obtained in December 2019 and include sample results through November 1st, 2019. The database contains many results that need to be filtered. Data filtering is detailed in Appendix D. Calibration targets are developed by averaging all results for a given year at each well with detectable levels of RDX. If *only* nondetections are observed at a given well, a calibration target of zero is used for each year having nondetect data. The wells with zero calibration targets are CdV-R-15-3 screen 4, CdV-R-37-2 screen 2, R-60, R-17 screen 1, R-17 screen 2, R-29, R-19 screen 3, R-19 screen 4, R-19 screen 5, R-47, R-48, and R-58.

For wells with both nondetections and detections, the yearly average of the sample results defines the calibration target for that year. Results from both detected and nondetected samples are used in calculating the average. If no samples were collected in a given year, no calibration target is developed for that year. The wells with detected RDX and non-zero calibration targets are R-25 screen 5, R-25 screen 6, R-18, R-63, R-68, R-69 screen 1, and R-69 screen 2 (Figure C-2.5-1). Full details on data processing are included in Appendix D.

In addition to RDX concentrations, concentration trends with time are also used as targets. This is intended to allow the calibration to separately weight behavior such as rising or falling concentrations independently from the raw concentrations themselves. Slopes are calculated from the RDX concentration targets for wells with a long enough time history to support trend analysis. The wells with concentration trend targets used in the RRM are R-63 and R-18. The slopes are calculated by polynomial fitting with degree of 1 (i.e., a linear fit to the time/concentration data). Figure C-2.5-2 shows the computed slopes against the target data.

Hydraulic Head and Hydraulic Gradient Targets

Hydraulic head targets were derived for monitoring well screens located west of the county water-supply wells. Each target represents the average head (meters amsl) observed within the well screen during February 2014. High-temporal resolution head data obtained from Intellus were aggregated to a monthly average target value by iteratively averaging values using the following successive temporal windows: (1) 2-hr interval within a calendar day, (2) calendar day, (3) month of February. For instances of wells without head values during the period of interest, values were imputed via regression analysis using nearby wells with a long period of record (Appendix D).

Additionally, lateral hydraulic gradients were derived using the hydraulic head target values for a subset of well screens located within the core of the plume (these gradients are shown with results in Figure C-2.5-3). Hydraulic gradients are computed for specified triplets of well screens using the three-point method detailed in Heath (1983, 700907). Target values for a given triplet consist of both a gradient magnitude and azimuth, each of which are weighted independently within the OF. The hydraulic gradient targets serve to provide an additional constraint on the hydraulic head target values to ensure that the northeast gradient local to the plume is also honored.

Drawdown Responses to PM-2 and PM-4 Aquifer Tests

In addition to hydraulic head and hydraulic gradient targets, the RRM is structured to match observed drawdown responses in regional aquifer monitoring wells due to pumping from supply wells. A drawdown target consists of an intercept and slope, obtained from a regression of drawdown observed in a monitoring well versus the logarithm of time since pumping began (similar in nature to the Cooper and Jacob late-time approximation of the Theis equation). The intercept and slope of this fitted linear model characterizes the magnitude and timing of the drawdown response. Water level responses to pumping are developed into drawdown targets for (1) wells R-20 screen 3, PM-4, and PM-5 in response to the PM-2 pump test and (2) PM-2, PM-5, R-14 screens 1–2, R-19 screens 4–7, and R-20 screens 1–3 in response to the PM-4 pump test. Wells with no observed drawdown in response to county pumping are also included as targets; these include CdV-R-15-3 screens 4–6, CdV-R-37-2 screens 2–4, R-18, and R-19 screen 3. These targets are shown with their calibrated model results in section C-3.1.

Note that this approach does not make any simplifying assumptions regarding the structure of the aquifer. Traditional hydrologic methods typically derive a transmissivity/hydraulic conductivity and/or storativity/specific storage estimate of the aquifer system from a drawdown response using simplifying assumptions about the aquifer structure and an analytical solution. The derived parameters are subsequently used to parameterize a groundwater model. In the RRM, drawdown targets specify only the timing and magnitude of water level change that is observed at a monitoring location in response to a nearby pump test. The RRM calibrates drawdown response (timing and magnitude) explicitly using a spatially heterogeneous K and S_s field that is also constrained by aquifer test data (section C-2.4 and Appendix D).

C-2.5.2   Method and Uncertainty Quantification

A classical calibration involves identifying a deterministic model with one set of input parameters that minimizes the error between observations (target data) and simulation (RRM). In the RRM, hydrologists vary parameters according to site-specific knowledge and compare model results with available data. This process involves sweeps of all parameter space, filtering, then hand-tuning. The parameter values selected through this process (see Appendix D section D-5.4) are then adjusted through LM calibration to further minimize the error between observations (target data) and simulation. This process facilitates selection of parameter sets that are conceptually meaningful, in agreement with available data, and have been closely examined by subject matter experts for hydrologic reasonability and conformance with the CSM. Other analyses are used throughout to provide conceptual and statistical tests of the validity of each potential parameter set for the calibrated RRM. These are described in detail in Appendix D, section D-5.4. Results from the classical calibration are used to initialize a sampler to quantify uncertainty, as described below.

A Bayesian approach is taken to quantifying uncertainty. Uncertainty in parameters related to hydraulic conductivities, specific storages, boundary conditions, and rates of recharge from hydraulic windows is addressed from a conceptual model perspective in the classical calibration. That is, these parameters are optimized through the iterative process described in the preceding paragraph, and multiple conceptualizations of these parameters are identified that all meet the criteria of a well-calibrated model (e.g., parameters are physically realistic, simulated values compare closely with observed data, and the CSM is honored). Ultimately, four top calibrations are identified and the OF is minimized using the LM algorithm. These four discrete, equally well performing, deterministic solutions quantify uncertainty in flow field parameters and can be thought of as different conceptualizations of hydraulic properties. This is an improvement over identifying a single deterministic calibration because it captures more uncertainty, which is critical to any future predictive modeling.

Uncertainty in transport parameters, along with some transport-relevant boundary conditions—dispersivity, source concentration, advective porosity, time of RDX arrival, and free water diffusion coefficient—are estimated using an MCMC sampler. Contaminant transport is most heavily influenced by these parameters, and quantitative estimates of their uncertainty are important to predictive modeling of plume transport and migration into the future. Uncertainty in these parameters is characterized with continuous prior probability distributions to form a joint posterior distribution for the parameters. Uncertainty in the hydraulic conductivities, specific storages, boundary conditions, and rates of recharge from hydraulic windows are characterized by the discrete parameter sets described by the top four calibrations (these act as prior probability distributions in an updated Bayesian model; see Appendix D for more details on this topic).

Ultimately the calibration and uncertainty quantification process involves a variety of tools and numerical techniques to arrive at results that characterize uncertainty through a statistical model but also provide the necessary prior constraints to ensure physical accuracy. Regardless of whether the approach is thought of as a model averaging approach or a restrictive prior approach, the posterior predictive uncertainty captures uncertainty both within and across models.

C-2.6   Validation

There are two major data sets withheld from calibration for use in validating the model. These are concentrations between December 2019 and May 2022 (shown as pink dots in Figure C-2.5-1) and hydraulic gradients between the plume and the water-supply wells (averages for the period of record are shown in Figure C-1.2-2). Lastly, all input parameters, especially source characteristics, are reviewed in

detail to verify consistency with the CSM. Results of these validation exercises, including figures, are presented alongside calibration results in section C-3.1. Additionally, the analyses to diagnose and improve model performance, including sensitivity, forward modeling, etc., provide an additional opportunity for model validation. These are described in Appendix D.

C-2.7 Predictive Forward Modeling

The posterior predictive mean, 5th, and 95th percentiles are evaluated to estimate the present and future extent of the RDX plume and determine the likelihood of plume arrival at the county water-supply wells. This means out of all 4061 predictive forward runs covering uncertainty, the mean, 5th, and 95th result at each point in space and time are presented, instead of plotting all 4061 runs. To make final predictions of RDX concentrations in space and time using the RRM, a probabilistic suite of forward models is launched from the posterior parameter distributions developed with the MCMC sampler (posterior parameter distributions are shown and discussed in section C-3.2). While the prior parameter distributions described in section C-2.4, Input Parameter Distribution Development, represent the compilation of prior knowledge for a given parameter based on all existing lines of evidence, the posteriors represent a probability distribution of parameter values that combines this prior information with all the learning during the model calibration process, specifically the target data and physically based flow and transport equations.

The total mass of RDX expected to enter the regional aquifer is generated by taking random draws directly from a prior distribution (Table C-2.4-1 and Figure C-2.7-1). It is not possible to estimate a posterior distribution since concentrations are still increasing at wells local to the RDX plume (R-18 and R-63) and it is assumed that mass is still arriving in the present day. Therefore, mass is continuously added to the RRM during the LM and MCMC routines (which run to 2019) and the posterior distribution is the same as the prior distribution. In the predictive forward runs (run to the year 2200), the draw for total mass is compared with the mass added each year by the source windows, and the sources are turned off once this total mass draw is reached. The distribution was developed based on inventory estimates made in 2017 throughout the entire system (surface, vadose zone, and regional aquifer) with a focus on how much mass could reach the regional aquifer at any time in the future. Most of the distribution's density lies between 500 and 2500 kg (more detail on total mass distribution in Appendix D).

Other parameters are selected using samples from the posterior parameter distributions produced from the MCMC. These forward runs can then be analyzed at critical times and places where decision makers need predictions of plume migration and concentration. At a given time and place of interest, the forward runs are combined into a probability distribution which identifies a predicted scenario of plume migration that characterizes the uncertainty associated with that prediction, providing much needed context and associated uncertainty for decision makers.

C-3.0 RESULTS

C-3.1 LM Calibration and Validation Results

The LM calibration is measured by the minimum of the OF, which is in turn a metric of how well the simulation matches the observed target data given the weighting scheme described in the calibration methods. Many different starting points are selected based on the best forward runs available, including some manually calibrated starting locations. The LM calibration gradually improves the matches to data through iterations of runs. Four local minima, referred to as "top calibrations," are identified representing unique source configurations and flow pathways to represent a range of possible solutions. All these are consistent with the CSM and all closely match target data sets. The top calibrations are randomly

numbered 1–4, and the numbers do not reflect confidence in the model. These four solutions form the initialization state for the MCMC sampler, as described in section C-2.5.2.

Specific matches to specific data sets are discussed in the following paragraphs. Overall, the goodness of fit of the calibration provides confidence in the predictive ability of the model. Weighting the data sets as described in section C-2.5.1 increases the importance of data points that are most likely to impact the predictive ability of the model. Confidence in the model is then further built through the use of validation data sets. The model shows the best matches to data local to the plume, with decreasing accuracy distal to the plume. This is driven by the data availability local to the plume (high) compared with data distal to the plume region (lower).

Matching concentrations of RDX in the regional aquifer is the main priority for the simulation. Figure C-3.1-1 shows the results of the top four LM calibrations plotted against the raw, target, and validation data. Raw data are plotted in black, target data points are plotted in green, and validation data are plotted in pink. Detection limits vary depending on the analytical method used; for the method usually applied to RDX, sample accuracy is lost below 0.33 ppb (LANL 2018, 602963), and this value is used in any discussion of results. The OF compares simulated results only to target data (not to raw data or validation data).

The highest observed concentrations, between 15 and 25 ppb at R-68 and R-69, have excellent matches to data. The trend observed across the three target years at R-68 is likely noise and not signal, especially given that the validation data fall in a narrower range centered near the yearly averaged targets, indicating that all calibrations match R-68. A notable pattern in the target data set is that R-69 exhibits a vertical concentration gradient (R-69 screen 2 target near 20 ppb and R-69 screen 1 target near 13 ppb) in the first year of collection, which is the only year in the target data set. It has been observed at the LANL site that early data from a well may not be as reliable as later data, and the validation data seem to settle with both screens around, or slightly above, 15 ppb. The calibrations cover these validation points well, with only calibration 4 missing the validation data set entirely; interestingly, this calibration that performs worst when compared with the validation data set has the smallest residuals for the concentration targets, so the OF considers calibration 4 the best match at R-69.

R-18 has the most pronounced trend, increasing with little noise from the first data point (2006) up to the last target data (2019), and then continuing this upward trend smoothly into 2022 in the validation data. Calibrations 1 and 4 match the target data trend nearly perfectly, calibration 3 misses the early data but hits the main trend well, and calibration 2 underpredicts the final two targets by approximately 0.1 and 0.4 ppb, respectively. All four calibrations underestimate the validation data set at R-18 by between 0.2 and 0.8 ppb. Calibration 4 captures the trend in the validation data best, continuing upward at the same rate, while the other three calibrations show a slower rate of increase, underestimating the trend in the validation data.

At R-47, despite being close to wells with high levels of RDX and also being directly east of these wells, no RDX has been detected to the present day. Therefore, R-47 provides a constraint on the eastern edge of the plume and adds evidence of a northeast gradient local to the plume. All calibrations do well at matching the 0-ppb target at R-47. R-63 and R-25 have lower concentrations than the wells described previously; however, they are still important to match. The calibrations are able to match the data at R-63 as well as at R-25 within 0.5 ppb. At R-63 there is a trend that continues into the validation data set. While none of the calibrations capture this trend well, calibration 1 is most effective and it hits some of the validation data. Calibration 3 was not expected to hit the low concentrations of RDX at these two wells since it uses only a single contaminated source of RDX, but overall it does very well at both. Results at R-25 are marginally less accurate than results at other wells; the RDX measured at R-25 is very near the detection limit of 0.33 ppb, and the data also appear noisy, so accuracy in the target data at this well

cannot be assumed. Matches to calibration trends are very close across all four calibrations for both R-18 and R-63 (Figure C-3.1-2), but these trends were calculated only from target data and thus underestimate the higher validation data points. These trend targets may contribute to constraining the model to a lower slope that misses the validation data set.

Water levels in the LM calibrations also match closely, with almost all simulated values (19 observations across 4 calibrations) falling within 0.5 m of target data throughout the domain. The two exceptions are both in calibration 2: R-25 screen 6 residual at 0.67 m, and R-17 screen 2 residual at 0.51 m (Figure C-3.1-3). The best head measurements are in calibration 4 where all simulated heads are within 0.22 m of the observed data.

In addition to the water levels, the hydraulic gradient local to the plume is also an important target. Gradient targets are especially critical because the dominant direction of flow in the model is west to east; however, local to the plume the gradient is southwest to northeast, so an accurate representation of plume transport is dependent on representing this gradient. Figure C-2.5-3 shows the hydraulic gradient targets (as black arrows) and the four calibrated model results. The simulation gradients are plotted as black arrows and are difficult to see below the target arrows because the results are nearly perfect in both magnitude and direction. The strong vertical gradients observed in the plume area also match well compared with observed data; for example, all calibrations match the downward vertical gradient at R-69 (−0.16 average gradient over period of record) and R-25 screens (−0.26, and −0.21) within 0.05. In the models these gradients are driven primarily by preferential recharge rather than the vertical gradient on the western boundary, since most of the calibrations ended at values for the western boundary condition that were less than −0.06. Calibration 2 is the exception, which set a strong gradient at the western edge of the model at −0.18.

Additional gradients (besides the targets shown above) can be used as validation of the RRM since they were not used as targets. The results show that hydraulic gradients are well matched in the RDX plume area and the downgradient region to approximately the x-coordinate of R-17. Further east observed gradients are much smaller and the model overestimates these gradients considerably (Figure C-3.1-4). Additionally, predictive forward modeling results (section C-3.3) show that the model is very accurate throughout the region where the RDX plume migrates over the next 200 yr.

Drawdown targets for the 2005 PM-4 and 2003 PM-2 pump tests are shown for each monitoring well with a thick solid line next to the top four calibrated results in Figure C-3.1-5. The most difficult to match, and perhaps the most critical to establishing the gradually increasing confining conditions observed in the aquifer, is the varied, multiscreen responses at R-19. Screen 3, at the water table, has no drawdown in response to the pump test (all calibrations match this perfectly), while deeper screens respond more as depth increases (and proximity to PM-4's long screen increases). Screen 7 has more than 0.75 m of drawdown in response to the pump test. Calibration 1 (thin solid line) reproduces observed drawdown best, hitting screens 3, 4, 5, and 7 nearly perfectly. All four calibrations struggle to hit screen 6, while they all predict greater drawdown at screen 7 than screen 6; calibrations 2 and 4 overpredict screen 7 drawdown but are close to hitting the difference between the two screens; and calibrations 1 and 3 accurately hit screen 7 drawdown but overpredict screen 6 (missing the difference between the two screens). R-20 and R-14 also have multiscreen responses. Despite the large difference between screens 1, 2, and 3 in R-20, all four models do well at replicating drawdown response (again, calibration 1 does best). At R-14, most of the calibrations struggle to differentiate the response difference between screen 1 and screen 2, with only calibration 4 hitting it accurately, and calibrations 1–3 estimating similar responses at both screens (note: the response at R-14 is small, only 0.05 and 0.07 m respectively). All models perfectly match the no-drawdown wells (R-18, CdV-R-37-2, and CdV-R-15-2) along with the largest drawdown responses observed at fellow county supply wells PM-5 and PM-2. During the

PM-2 test, there were only three monitoring wells relevant to the RDX site that were in operation for observing drawdown (PM-5, PM-4, and R-20), and all four calibrations are effective in matching drawdown at these wells.

Another important metric that can be used to understand and analyze the LM results is the source locations in the context of the CSM. Figure C-3.1-6 shows the final locations in each of the top four calibrations of the primary, secondary, and preferential recharge hydraulic windows for the top LM calibrations (as also shown in Figure C-2.4-1). Calibration 3 uses only a single source arrival of RDX (primary window) to the regional aquifer to calibrate, and, while some concentrations are not as perfectly matched (Figure C-3.1-1), this solution is important because it represents a simpler conceptualization of the hydraulic windows.

All four conceptualizations have the primary source centered near R-68 where the highest measured concentrations are observed. The maximum concentration of RDX for the primary source ranges from 106 to 286 ppb across calibrations. Note: concentrations are not applied uniformly across the spatial extend of the hydraulic window; assigned concentrations are highest in the center of the modeled hydraulic windows and decrease by one standard deviation at the edge of the windows. The calibrations range in terms of the mechanisms that hit the magnitudes at R-68, R-69, and the increasing trend at R-18. For example, calibration 1 has little overlap between the preferential recharge and primary sources, and RDX arrives on top of R-68 and R-69, so this calibration is likely to represent a lower inventory conceptualization since the sources are coincident with the observations. In contrast, calibration 4 has higher rates of recharge that likely push the bulk of inventory deeper into the aquifer (potentially below these monitoring locations), and the source is located slightly downgradient of R-68, so only the lower concentration edges hit the monitoring locations. This represents a higher inventory case. Uncertainty in inventory is further varied through the MCMC sampler transport parameters and the draw for total mass of RDX made in the predictive forward runs, as described above in section C-2.7.

The secondary source location, time of arrival, and concentration is more variable, with all of these parameters varying notably across the three calibrations that include a secondary source. While all of the preferential clean recharge sources are located near the location of preferential infiltration at the surface under Cañon de Valle, they vary in shape and size, which reflects uncertainty in the movement of water through the vadose zone before reaching the regional aquifer.

Final calibrated hydraulic conductivity values are shown for all pilot and anchor points in Figure C-2.4-3 as small, grey Xs. Additionally, figures of K_x, K_y, and K_z in all four top calibrations for three depths (water table, 30 m below the water table, and 60 m below the water table) are shown in Appendix D. They are omitted here for brevity.

The RDX site is complex, and the calibrated RRM matches most of the 231 total targets well. This includes concentrations at wells of interest, hydraulic head data, and drawdown responses from county supply aquifer tests. The model also does well against validation data, despite not using this data explicitly in the calibration process. It could improve against the validation data set at R-18, and, to a lesser extent, at R-63. The LM calibration covers uncertainty in flow field parameters across the four deterministic solutions presented here, and more uncertainty in transport parameterization will be discussed in the next section. Overall, flow and transport are well parameterized, using plausible values for inputs that are consistent with the CSM, in the RRM.

C-3.2 MCMC Calibration Results

The MCMC sampler is implemented using an affine-invariant ensemble method (Goodman and Weare 2010, 700890). This method has been shown to work well when parameters are on very different scales, and it can also be significantly faster than other MCMC methods. The MCMC sampler is initialized using the top four LM calibration results presented in the previous section and is run with an ensemble of 60 "walkers" and 50 iterations, with the first 10 iterations discarded as burn-in. With nine parameters varied within each ensemble, this is well within the recommended rule of thumb of twice the number of walkers as parameters and is shown to be sufficient for convergence in Figure C-3.2-1. Forward modeling is then conducted with the resulting set of accepted parameter sets (i.e., samples from the parameter posterior distributions) to generate posterior predictive distributions for the model endpoints (section C-3.3).

For each of the four calibration endpoints, one of the 60 walkers is initialized at the LM calibration result, and the remaining walkers are initialized by a draw from a generalized beta distribution defined by a sigma parameter of 0.001, a mean equal to the LM calibration result, and a minimum and maximum defined by the 1st and 99th percentiles of the corresponding prior distribution. In each step of the algorithm, an affine transformation is applied with a tuning parameter, a, and the walker movement takes place in the transformed space. The a parameter provides control over the region of the multi-dimensional parameter space that is explored and thus allows tuning of the walker proposal acceptance rate. After analyzing the movement of the walkers when a = 2 is used, this parameterization is found to be appropriate following Foreman-Mackey et al. (2013, 700906). The proposed set of parameter values for an individual walker depends both on the previous parameter set for that walker and on the position of the other walkers in the ensemble.

The movement of each walker, with each iteration, is displayed in Figure C-3.2-1 for the primary source maximum concentration parameter as an example. The algorithm had an overall acceptance rate of 41.4%, indicating that the walker moved to the proposed set in 41.4% of all iterations. If the proposed parameter set is rejected, the walker stays in place, resulting in the horizontal lines in Figure C-3.2-1 Higher posterior density is indicated by parameter sets where the walker remains stuck for multiple iterations. Though the algorithm allows a walker to move from higher to lower likelihood (likelihood that the simulation matches available data), it is much more likely to move towards higher likelihood. This method leads to posterior distributions with higher density in regions that tend to increase the likelihood function and to lower density in regions where results are still possible but less likely. The method gives more weight to parameter sets that are most consistent with observed data but does not exclude the possibility of parameter sets that could, but are less likely to, produce observed RDX concentrations. Marginal posterior distributions for all nine parameters varied in the MCMC sampler are displayed in Figure C-3.2-2.

Posterior predictive distributions are developed by processing MCMC results into a unique "chain" of parameter sets for predictive modeling. The chain includes 4061 unique parameter sets that include both the conceptual uncertainty from the four LM calibrations and quantitative uncertainty from the MCMC sampler. Predictive forward runs are launched from each unique set, and final results are weighted by the frequency of occurrence of the parameter set from which they were derived such that predictive runs with better matches to the data occur more frequently in the predictive forward runs. Results of the predictive runs are discussed in the following section.

C-3.3   Predictive Forward Results

After removing duplicates, the chain produced from the MCMC calibration resulted in parameter sets for 4061 predictive model runs. Draws from these posterior parameter sets along with a prior parameter draw for total mass are run through the model until the year 2200. Results characterize uncertainty in RDX concentrations everywhere in the model domain. Spatial output at every node was produced for years 2022 (present-day conditions), 2025, 2030, 2040, 2050, 2100, 2150 and 2200 (end of simulation conditions). The extent of the plume is defined by the 9.66-ppb contour, though discussion of the extent of RDX above the approximate detection limit of 0.33 ppb is also included here for completeness.

The extent of the plume in the present day (2022) is plotted with uncertainty, defined by the MCMC sampler, for each of the four LM calibration endpoints in Figure C-3.3-1. These figures show the median estimate as a red line, the middle 50% of runs plotted as a dark grey shaded region, and the middle 95% of runs shown as a light grey shaded region. Though the plot is a 2-D plan view, the values used for estimating percentiles are the maximum RDX observed at any depth (note: the depth plots for these four plume endpoints are shown in Figure C-3.3-2). In the year 2022, which is constrained by target data through the end of 2019, uncertainty in the flow field (hydraulic window parameters, K and S field) is larger than that from the MCMC sampler across transport parameters. In other words, differences between these discrete endpoints of the four top calibrations are larger than the variability within each across transport parameters. The plume shapes are different across the four calibrations. Calibration 1 shows a tight plume that just reaches R-18 and is shallow until the northeast edge near R-18. Calibration 2 is a shallow plume throughout that runs to the northeast just above and around R-18. Calibration 3 is very deep and moves far to the northeast, forming the largest plume observed across the four calibrations. Calibration 4 has a similar shape to calibration 1 but is generally a deeper plume than calibration 1 throughout.

Figure C-3.3-3 shows probabilistic time series for all predictive forward runs with target and validation points. As with the LM calibration results, predictive forward runs match target and validation points at all wells except the validation data at R-18. While some runs in the 95% band cover some of the validation points at R-18, most (middle 50%) underestimate all points. Comparing the shape of the plumes in Figures C-3.3-1 and C-3.3-2 with these time-series traces shows that the underestimate of R-18 validation data does not suggest, as it may first appear, an underestimation of the leading edge of the plume; three of the four calibrations show a plume that extends well beyond R-18. Rather, it appears that this underestimate is a calibrated effect, possibly due to the lower target data and thus the low concentration trend enforced by the calibration. Calibrations 2, 3, and 4 all show plumes that dodge near and then beyond R-18, likely in order to match the lower target data sets. Unfortunately, this results in a miss of the validation data at R-18. Only calibration 1 suggests that the plume is constrained to a smaller shape, with the leading edge arriving at R-18 and thus underestimating the validation points by constraining the plume to a smaller shape. An updated calibration that uses the new data at R-18 as a target will likely be able to match these validation data in an LM calibration with minor adjustments to the parameter space.

R-69 screens show excellent matches between predictive runs and validation data. Screen 2 shows the opposite effect to R-18, with the predictive models performing better at the validation data (fully covered by the middle 50%) than the target data point (well within the 95% band, but outside the middle 50%). R-69 screen 1 is well matched at both the target and validation data despite the (potential) upward trend in recent validation data. Predictive runs are able to cover the noisy data at R-25 and the validation data at R-63, though the trend observed at R-63 could be improved by the middle 50%. Some concentrations at wells with 0-ppb targets are observed in the predictive runs outside the middle 50% (see e.g., CdV-R-15-3 screen 4 and R-17 screen 2). These low-likelihood simulated concentrations max out near

the detection limit of 0.33 ppb and are thus consistent with observed data of 0 ppb RDX. High downgradient concentrations generally come from calibration 3, which shows a faster flow field and larger inventory/time than the other calibrations. None of the other three calibrations shows any RDX above 0.33 ppb (detection limit) past the x-coordinate of CdV-R-15-3 (Figure C-3.3-4). Figures of RDX above 0.33 ppb into the future are shown in Appendix D; they are omitted here for brevity.

Figure C-3.3-5 combines the predictive runs across all four LM solutions and MCMC samples (resulting in predictions made using over 4000 individual runs) and plots the likelihood of the 9.66-ppb contour as well as the depth where the maximum concentration is observed for the years 2025, 2050, 2100, 2150, and 2200.

These plots show that the plume expands slowly from the present day until 2100, where only 1% of simulations show the plume extending beyond the CdV-R-15-3 x-coordinate. By 2150 the plume shrinks because some simulations have exhausted available inventory of RDX by this point in time. By 2200 the plume shrinks even more across the predictive runs. In the final year of simulation (2200), 70% of the predictive forward runs have exhausted RDX inventory. Most of the runs initialized by calibrations 2 and 3 are exhausted (98% and 91% of runs respectively), suggesting that these runs had "hotter" sources with more RDX input per time than calibrations 1 and 4, which probably represent more "slow and steady" input of RDX. For calibrations 1 and 4, more than half of the simulations are still adding RDX to the system in the year 2200 (59% and 51% respectively). As RDX spreads out and disperses in the regional aquifer, concentrations are diluted to levels below 9.66 ppb by natural attenuation, reducing the plume footprint.

For Scenario 3 of the risk assessment, the decision locations of interest are the nearest county water-supply wells—PM-2, PM-4, and PM-5. Figure C-3.3-6 shows predictive time series of all runs at these wells. No simulation shows breakthrough of the plume (9.66-ppb contour) at water-supply wells between now and the end of the simulation in year 2200. Concentrations are calculated as the average of all nodes in the well screen. The median concentrations fall below 0.25 ppb at all supply wells and the middle 50% of simulations fall below 0.5 ppb, suggesting that if RDX were ever to reach these wells it would likely be below detection limits.

A breakout of these results by LM calibration shows that calibration 3, the high inventory case discussed above as the largest extent of the plume in the present day, is responsible for nearly all of the breakthrough observed in predictive runs at the water-supply wells (Figure C-3.3-7). Interestingly, this calibration also predicts a reduction in concentrations (median maximum around 1 ppb) of RDX at the water-supply wells beginning between 2100 and 2150 when inventory in this calibration is exhausted.

C-4.0 CONCLUSIONS

The RRM presented here is a robust approach to gathering all available data into a numerical model constrained by physics to maximize the value of information at a complex site. It is used to generate predictive results to inform the risk assessment described by the main report. Model structure and boundary conditions are informed by years of data and analyses, particularly the hydraulic analysis which quantifies the magnitude of shifts in hydraulic gradients through time and investigates the relationship to county supply pumping. These combine to develop a thorough CSM. All 423 model input parameters go through a detailed process to incorporate all available data and lines of evidence (distribution development results in 54 unique distributions) such that they are constrained to physically realistic, site-specific values. The structure, boundary conditions, and parameters are all vetted closely during the calibration process, which includes hand-tuning of parameters by experts, suites of model runs covering the entire input parameter space, spatial correlation structures for the conductivity field based on aquifer

test data, a variety of different sensitivity analyses, and comparison with a validation data set. The LM and MCMC calibrations result in posterior distributions that quantify uncertainty across the input parameter space and form the initialization of forward model runs to predict the future transport of RDX in space and time.

Results from the LM and MCMC calibrations demonstrate exceptional matches to target and validation data for concentrations, hydraulic gradients, drawdown responses to water-supply pumping, and hydraulic heads, providing confidence in the modeling. Predictive forward results suggest that the plume, as defined by the 9.66-ppb contour, does not expand quickly or extend east of CdV-R-15-3, and 0% of predictive runs see plume arrival at any water-supply well by the year 2200. While low concentrations of RDX are predicted by some runs to reach water-supply wells, results suggest that any arrival is likely to be below typical detection limits.

C-5.0 REFERENCES

The following reference list includes documents cited in this appendix. Parenthetical information following each reference provides the author(s), publication date, and ERID, ESHID, or EMID. ERIDs were assigned by the Laboratory's Associate Directorate for Environmental Management (IDs through 599999); ESHIDs were assigned by the Laboratory's Associate Directorate for Environment, Safety, and Health (IDs 600000 through 699999); and EMIDs are assigned by N3B (IDs 700000 and above).

Abbaspour, K.C., M.T. van Genuchten, R. Schulin, and E. Schläppi, August 1, 1997. "A Sequential Uncertainty Domain Inverse Procedure for Estimating Subsurface Flow and Transport Parameters," *Water Resources Research,* Vol. 33, No. 8, pp. 1879-1892. (Abbaspour et al. 1997, 700898)

Aistleitner, C., M. Hofer, and R. Tichy, 2012. "A Central Limit Theorem for Latin Hypercube Sampling with Dependence and Application to Exotic Basket Option Pricing," *International Journal of Theoretical and Applied Finance,* Vol. 15, No. 7. (Aistleitner et al. 2012, 700896)

Bates, S.J., J. Sienz, and V.V. Toropov, April 19–22, 2004. "Formulation of the Optimal Latin Hypercube Design of Experiments Using a Permutation Genetic Algorithm," 45th AIAA/ASME/ASCE/AHS/ ASC Structures, Structural Dynamics and Materials Conference, April 19–22, 2004, Palm Springs, California. (Bates et al. 2004, 700895)

Birdsell, K.H., K.M. Bower, A.V. Wolfsberg, W.E. Soll, T.A. Cherry, and T.W. Orr, July 1999. "Simulations of Groundwater Flow and Radionuclide Transport in the Vadose and Saturated Zones Beneath Area G, Los Alamos National Laboratory," Los Alamos National Laboratory report LA-13299-MS, Los Alamos, New Mexico. (Birdsell et al. 1999, 069792)

Birdsell, K.H., B.D. Newman, D.E. Broxton, and B.A. Robinson, 2005. "Conceptual Models of Vadose Zone Flow and Transport beneath the Pajarito Plateau, Los Alamos, New Mexico," *Vadose Zone Journal,* Vol. 4, pp. 620–636. (Birdsell et al. 2005, 092048)

Black, P., K. Catlett, D. Anderson, P. Duffy, T. Stockton, and S. Van Sickle, March 3–7, 2019. "Scaling Input Distributions for Probabilistic Models-19472," Waste Management 2019 Conference, March 3–7, 2019, Phoenix, Arizona. (Black et al. 2019, 700892)

Bromly, M., C. Hinz, and L.A.G. Aylmore, February 2007. "Relation of Dispersivity to Properties of Homogeneous Saturated Repacked Soil Columns," *European Journal of Soil Science,* Vol. 58, No. 1, pp. 293-301. (Bromly et al. 2007, 700902)

Broxton, D., R. Warren, P. Longmire, R. Gilkeson, S. Johnson, D. Rogers, W. Stone, B. Newman, M. Everett, D. Vaniman, S. McLin, J. Skalski, and D. Larssen, March 2002. "Characterization Well R-25 Completion Report," Los Alamos National Laboratory report LA-13909-MS, Los Alamos, New Mexico. (Broxton et al. 2002, 072640)

Butler, T., J. Jakeman, and T. Wildey, April 2018. "Combining Push-forward Measures and Bayes' Rule to Construct Consistent Solutions to Stochastic Inverse Problems," *SIAM Journal on Scientific Computing,* Vol. 40, No. 2, pp. A984-A1011. (Butler et al. 2018, 700905)

Chen, T., and C. Guestrin, August 13-17, 2016. "XGBoost: A Scalable Tree Boosting System," KDD '16: Proceedings of the 22nd ACM SIGKDD International Conference on Knowledge Discovery and Data Mining, August 13-17, 2016, San Francisco, California. (Chen and Guestrin 2016, 700897)

Cressie, N., 1993. *Statistics for Spatial Data*, John Wiley and Sons Inc., New York, New York. (Cressie 1993, 700911)

DOE (U.S. Department of Energy), January 2010. "Final Environmental Impact Statement for Decommissioning and/or Long-Term Stewardship at the West Valley Demonstration Project and Western New York Nuclear Service Center," Volume 2 (Appendices A through R), DOE/EIS-0226, West Valley, New York. (DOE 2010, 700880)

Doherty, J., March-April 2003. "Ground Water Model Calibration Using Pilot Points and Regularization," *Ground Water,* Vol. 41, No. 2, pp. 170-177. (Doherty 2003, 700894)

Fetter, C.W., *Applied Hydrogeology*, Third ed., Prentice Hall, Upper Saddle River, New Jersey. (Fetter 1994, 070942)

Fetter, C.W., 2008. *Contaminant Hydrogeology*, Second Edition, Waveland Press Inc., Long Grove, Illinois. (Fetter 2008, 700912)

Foreman-Mackey, D., D.W. Hogg, D. Lang, and J. Goodman, March 2013. "emcee: The MCMC Hammer," *Publications of the Astonomical Society of the Pacific,* Vol. 125, No. 925, pp. 306-312. (Foreman-Mackey et al. 2013, 700906)

Franke, O.L., T.E. Reilly, and D. Bennett, 1987. "Chapter B5, Definition of Boundary and Initial Conditions in the Analysis of Saturated Ground-Water Flow Systems—An Introduction," in *Techniques of Water-Resources Investigations of the United States Geological Survey*, United States Geological Survey, United States Government Printing Office, Washington, D.C. (Franke et al. 1987, 700886)

Freeze, R.A., and J.A. Cherry, January 1979. *Groundwater*, Prentice-Hall, Inc., Englewood Cliffs, New Jersey. (Freeze and Cherry 1979, 088742)

French, S., R. Shuman, G.L. Cole, K.J. Crowell, M.S. Day, C.W. Gable, M.O. Gard, J.J. Whicker, D.G. Levitt, B.D. Newman, B.A. Robinson, E.P. Springer, and P.H. Stauffer, October 2008. "Performance Assessment and Composite Analysis for Los Alamos National Laboratory Material Disposal, Area G, Revision 4," Los Alamos National Laboratory document LA-UR-08-06764, Los Alamos, New Mexico. (French et al. 2008, 106890)

Fujinawa, K., 2010. "Anthroscape of the Mediterranean Coastal Area in the Context of Hydrogeology: Projected Impacts of Climate Change," in *Sustainable Land Management*, S. Kapur, H. Eswaran, and W. Blum (Eds.), Springer, Berlin, Heidelberg. (Fujinawa 2010, 700903)

Gable, C.W., H.E. Trease, and T.A. Cherry, June 1996. "Geological Applications of Automatic Grid Generation Tools for Finite Elements Applied to Porous Flow Modeling," in *Numerical Grid Generation in Computational Fluid Dynamics and Related Fields*, B.K. Soni, J.F. Thompson, H. Hausser, and P.R. Eiseman (Eds.), Mississippi State University Press, Jackson, Mississippi. (Gable et al. 1996, 700887)

Gains-Germain, L., A. Jordan, M. Higgs, P. Meeks, P. Black, and T. Stockton, March 18–22, 2018. "Explicitly Accounting for Multiple Spatial Scales in Data Informing Kd Distribution Development – 18414," Waste Management 2018 Conference, March 18–22, 2018, Phoenix, Arizona. (Gains-Germain et al. 2018, 700888)

Gard, M.O., and B.D. Newman, November 2005. "The High Explosives Source Term at TA-16," Los Alamos National Laboratory document LA-UR-05-9433, Los Alamos, New Mexico. (Gard and Newman 2005, 093651)

Gardner, J.N., A. Lavine, G. WoldeGabriel, D. Krier, J., D.T. Vaniman, F.A. Caporuscio, C.J. Lewis, M.R. Reneau, E.C. Kluk, and M.J. Snow, March 1999. "Structural Geology of the Northwestern Portion of Los Alamos National Laboratory, Rio Grande Rift, New Mexico: Implications for Seismic Surface Rupture Potential from TA-3 to TA-55," Los Alamos National Laboratory report LA-13589-MS, Los Alamos, New Mexico. (Gardner et al. 1999, 063492)

Gelhar, L.W., C. Welty, and K.R. Rehfeldt, July 1992. "A Critical Review of Data on Field-Scale Dispersion in Aquifers," *Water Resources Research,* Vol. 28, No. 7, pp. 1955–1974. (Gelhar et al. 1992, 102465)

Goodman, J., and J. Weare, 2010. "Ensemble Samplers with Affine Invariance," *Communications in Applied Mathematics and Computational Science,* Vol. 5, No. 1, pp. 65-80. (Goodman and Weare 2010, 700890)

Heath, R.C., 1983. "Basic Ground-Water Hydrology," prepared in cooperation with the North Carolina Department of Natural Resources and Community Development, U.S. Geological Survey Water-Supply Paper 2220, Reston, Virginia. (Heath 1983, 700907)

Heerspink, B.P., S. Pandey, H. Boukhalfa, D.S. Ware, O. Marina, G. Perkins, V.V. Vesselinov, and G. WoldeGabriel, May 2, 2017. "Fate and Transport of Hexahydro-1,3,5-trinitro-1,3,5-triazine (RDX) and Its Degradation Products in Sedimentary and Volcanic Rocks, Los Alamos, New Mexico," *Chemosphere,* Vol. 182, pp. 276-283. (Heerspink et al. 2017, 602560)

Ho, C.K., R.G. Baca, S.H. Conrad, G.A. Smith, L.-J. Shyr, and T.A. Wheeler, January 1999. "Stochastic Parameter Development for PORFLOW Simulations of the Hanford AX Tank Farm," Sandia National Laboratories Report No. SAND98-2880, Albuquerque, New Mexico. (Ho et al. 1999, 700883)

Jordan, A., S. Fitchett, K. Catlett, D. Levitt, G. Occhiogrosso, J. Tauxe, P. Meeks, M. Higgs, and P. Black, March 5–9, 2017. "Realistic Geochemical Paramater Uncertainty for Performance Assessment Modeling – 17066," Waste Management 2017 Conference, March 5–9, 2017, Phoenix, Arizona. (Jordan et al. 2017, 700881)

Keramat, M., and R. Kielbasa, 1997. "Latin Hypercube Sampling Monte Carlo Estimation of Average Quality Index for Integrated Circuits," *Analog Integrated Circuits and Signal Processing,* Vol. 14, pp. 131-142. (Keramat and Kielbasa 1997, 700908)

Kleinfelder, January 25, 2005. "Final Well R-26 Completion Report, Revision No. 1," report prepared for Los Alamos National Laboratory, Project No. 37151, Albuquerque, New Mexico. (Kleinfelder 2005, 087846)

Kwicklis, E., M. Witkowski, K. Birdsell, B. Newman, and D. Walther, August 2005. "Development of an Infiltration Map for the Los Alamos Area, New Mexico," *Vadose Zone Journal,* Vol. 4, pp. 672–693. (Kwicklis et al. 2005, 090069)

LANL (Los Alamos National Laboratory), September 1998. "Work Plan for Pajarito Canyon," Los Alamos National Laboratory document LA-UR-98-2550, Los Alamos, New Mexico. (LANL 1998, 059577)

LANL (Los Alamos National Laboratory), September 2003. "Phase III RFI Report for Solid Waste Management Unit 16-021(c)-99," Los Alamos National Laboratory document LA-UR-03-5248, Los Alamos, New Mexico. (LANL 2003, 077965)

LANL (Los Alamos National Laboratory), June 2008. "Supplemental Investigation Work Plan for Intermediate and Regional Groundwater at Consolidated Unit 16-021(c)-99," Los Alamos National Laboratory document LA-UR-08-3991, Los Alamos, New Mexico. (LANL 2008, 103165)

LANL (Los Alamos National Laboratory), August 2009. "Pajarito Canyon Investigation Report, Revision 1," Los Alamos National Laboratory document LA-UR-09-4670, Los Alamos, New Mexico. (LANL 2009, 106939)

LANL (Los Alamos National Laboratory), June 2011. "Hydrologic Testing Report for Consolidated Unit 16-021(c)-99," Los Alamos National Laboratory document LA-UR-11-3072, Los Alamos, New Mexico. (LANL 2011, 203711)

LANL (Los Alamos National Laboratory), September 2011. "Corrective Measures Evaluation Report for Material Disposal Area G, Solid Waste Management Unit 54-013(b)-99, at Technical Area 54, Revision 3," Los Alamos National Laboratory document LA-UR-11-4910, Los Alamos, New Mexico. (LANL 2011, 206324)

LANL (Los Alamos National Laboratory), September 2011. "Investigation Report for Water Canyon/ Cañon de Valle," Los Alamos National Laboratory document LA-UR-11-5478, Los Alamos, New Mexico. (LANL 2011, 207069)

LANL (Los Alamos National Laboratory), March 2012. "Technical Area 16 Well Network Evaluation and Recommendations," Los Alamos National Laboratory document LA-UR-12-1082, Los Alamos, New Mexico. (LANL 2012, 213573)

LANL (Los Alamos National Laboratory), July 27, 2017. "Completion Report for Regional Aquifer Well R-68," Los Alamos National Laboratory document LA-UR-17-26063, Los Alamos, New Mexico. (LANL 2017, 602539)

LANL (Los Alamos National Laboratory), March 2018. "Compendium of Technical Reports Related to the Deep Groundwater Investigation for the RDX Project at Los Alamos National Laboratory," Los Alamos National Laboratory document LA-UR-18-21326, Los Alamos, New Mexico. (LANL 2018, 602963)

LANL (Los Alamos National Laboratory), March 2018. "Compendium of Technical Reports Conducted Under the Work Plan for Chromium Plume Center Characterization," Los Alamos National Laboratory document LA-UR-18-21450, Los Alamos, New Mexico. (LANL 2018, 602964)

Levitt, D.G., September 2011. "Modeling the Movement of Transient Moisture through Disposal Units at Los Alamos National Laboratory Technical Area 54, Area G," Los Alamos National Laboratory document LA-UR-11-05424, Los Alamos, New Mexico. (Levitt 2011, 700879)

Lewis, C.L., J.N. Gardner, E.S. Schultz-Fellenz, A. Lavine, and S.L. Reneau, June 2009. "Fault Interaction and Along-Strike Variation in Throw in the Pajarito Fault System, Rio Grande Rift, New Mexico," *Geosphere,* Vol. 5, No. 3, pp. 252–269. (Lewis et al. 2009, 111708)

Lin, Y., D. O'Malley, and V.V. Vesselinov, September 15, 2016. "A Computationally Efficient Parallel Levenberg-Marquardt Algorithm for Highly Parameterized Inverse Model Analyses," *Water Resources Research,* Vol. 52, pp. 6948-6977. (Lin et al. 2016, 700889)

Manteufel, R.D., April 3-6, 2000. "Evaluating the Convergence of Latin Hypercube Sampling," 41st Structures, Structural Dynamics, and Materials Conference and Exhibit, April 3-6, 2000, Atlanta, Georgia. (Manteufel 2000, 700909)

McGehee, E.D., S. McCarthy, K. Towery, J. Ronquillo, K.L.M. Garcia, and J. Isaacson, March 28, 2003. "Sentinels of the Atomic Dawn: A Multiple-Property Evaluation of the Remaining Manhattan Project Properties at Los Alamos (1942-1946)," Historic Building Survey Report No. 215, Los Alamos National Laboratory document LA-UR-03-0726, Los Alamos, New Mexico. (McGehee et al. 2003, 700541)

McLin, S., July 2005. "Analyses of the PM-2 Aquifer Test Using Multiple Observation Wells," Los Alamos National Laboratory report LA-14225-MS, Los Alamos, New Mexico. (McLin 2005, 090073)

McLin, S., January 2006. "Analyses of the PM-4 Aquifer Test Using Multiple Observation Wells," Los Alamos National Laboratory report LA-14252-MS, Los Alamos, New Mexico. (McLin 2006, 092218)

Meyer, B.R., C.A.R. Bain, A.S.M. De Jesus, and D. Stephenson, 1981. "Radiotracer Evaluation of Groundwater Dispersion in a Multi-Layered Aquifer," *Journal of Hydrology,* Vol. 50, pp. 259-271. (Meyer et al. 1981, 700901)

Millington, R.J., and J.P. Quirk, 1961. "Permeability of Porous Solids," *Transactions of the Faraday Society,* Vol. 57, pp. 1200–1207. (Millington and Quirk 1961, 110521)

N3B (Newport News Nuclear BWXT-Los Alamos, LLC), August 2019. "Investigation Report for Royal Demolition Explosive in Deep Groundwater," Newport News Nuclear BWXT-Los Alamos, LLC, document EM2019-0235, Los Alamos, New Mexico. (N3B 2019, 700561)

N3B (Newport News Nuclear BWXT-Los Alamos, LLC), May 2020. "Fate and Transport Modeling and Risk Assessment Report for RDX Contamination in Deep Groundwater," Newport News Nuclear BWXT-Los Alamos, LLC, document EM2020-0135, Los Alamos, New Mexico. (N3B 2020, 700925)

Neptune (Neptune and Company, Inc.), September 30, 2018. "File Transfer Report for Chromium and RDX Project Hydrologic Modeling," Neptune and Company, Inc., report no. NAC-0124_R0, Los Alamos, New Mexico. (Neptune 2018, 700878)

Neuman, S.P., August 1990. "Universal Scaling of Hydraulic Conductivities and Dispersivities in Geologic Media," *Water Resources Research,* Vol. 26, No. 8, pp. 1749-1758. (Neuman 1990, 090184)

NRC (U.S. Nuclear Regulatory Commission), April 1987. "Modeling Study of Solute Transport in the Unsaturated Zone," Workshop Proceedings, NUREG/CR-4615, LA-10730-MS, Washington, D.C. (NRC 1987, 700882)

O'Malley, D., and V.V. Vesselinov, March 7, 2014. "Analytical Solutions for Anomalous Dispersion Transport," *Advances in Water Resources,* Vol. 68, pp. 13–23. (O'Malley and Vesselinov 2014, 700891)

Reimus, P.W., M.J. Haga, A.I. Adams, T.J. Callahan, H.J. Turin, and D.A. Counce, April–May 2003. "Testing and Parameterizing a Conceptual Solute Transport Model in Saturated Fractured Tuff Using Sorbing and Nonsorbing Tracers in Cross-Hole Tracer Tests," *Journal of Contaminant Hydrology,* Vol. 62–63, pp. 613–636. (Reimus et al. 2003, 210315)

Reneau, S.L., E.V. McDonald, J.N. Gardner, T.R. Kolbe, J.S. Carney, P.M. Watt, and P.A. Longmire, 1996. "Erosion and Deposition on the Pajarito Plateau, New Mexico, and Implications for Geomorphic Responses to Late Quaternary Climatic Changes," New Mexico Geological Society Guidebook: 47th Field Conference, Jemez Mountains Region, New Mexico, pp. 391-398. (Reneau et al. 1996, 055539)

Robinson, B.A., S.G. McLin, and H.S. Viswanathan, 2005. "Hydrologic Behavior of Unsaturated, Fractured Tuff: Interpretation and Modeling of a Wellbore Injection Test," *Vadose Zone Journal,* Vol. 4, pp. 694–707. (Robinson et al. 2005, 092040)

Schulze-Makuch, D., D.A. Carlson, D.S. Cherkauer, and P. Malik, November--December 1999. "Scale Dependency of Hydraulic Conductivity in Heterogeneous Media," *Ground Water,* Vol. 37, No. 6, pp. 904-919. (Schulze-Makuch et al. 1999, 700893)

Schwartz, F.W., and H. Zhang, 2002. *Fundamentals of Ground Water*, John Wiley and Sons Inc., New York, New York. (Schwartz and Zhang 2002, 700913)

Springer, E.P., 2005. "Statistical Exploration of Matrix Hydrologic Properties for the Bandelier Tuff, Los Alamos, New Mexico," *Vadose Zone Journal,* Vol. 4, pp. 505–521. (Springer 2005, 098534)

Stephens, D.B., 1995. *Vadose Zone Hydrology*, CRC Press Inc., Boca Raton, Florida. (Stephens 1995, 700914)

Umari, A., M.F. Fahy, J.D. Earle, and P. Tucci, 2008. "Analysis of Conservative Tracer Tests in the Bullfrog, Tram, and Prow Pass Tuffs, 1996 to 1998, Yucca Mountain, Nye County, Nevada," report prepared for the U.S. Department of the Interior and the U.S. Geological Survey in cooperation with the U.S. Department of Energy, Scientific Investigations Report 2007-5280, Weston, Virginia. (Umari et al. 2008, 700899)

Waldrop, W.R., L.W. Gelhar, A. Mantogiou, C. Welty, and K.R. Rehfeldt, August 1985. "A Review of Field-Scale Physical Solute Transport Processes In Saturated and Unsaturated Porous Media," report prepared by Tennessee Valley Authority and Massachusetts Institute of Technology for the Electric Power Research Institute, final report EA-4190, Palo Alto, California. (Waldrop et al. 1985, 700900)

Zyvoloski, G., May 18, 2007. "FEHM: A Control Volume Finite Element Code for Simulating Subsurface Multi-Phase Multi-Fluid Heat and Mass Transfer," Los Alamos National Laboratory document LA-UR-07-3359, Los Alamos, New Mexico. (Zyvoloski 2007, 700904)
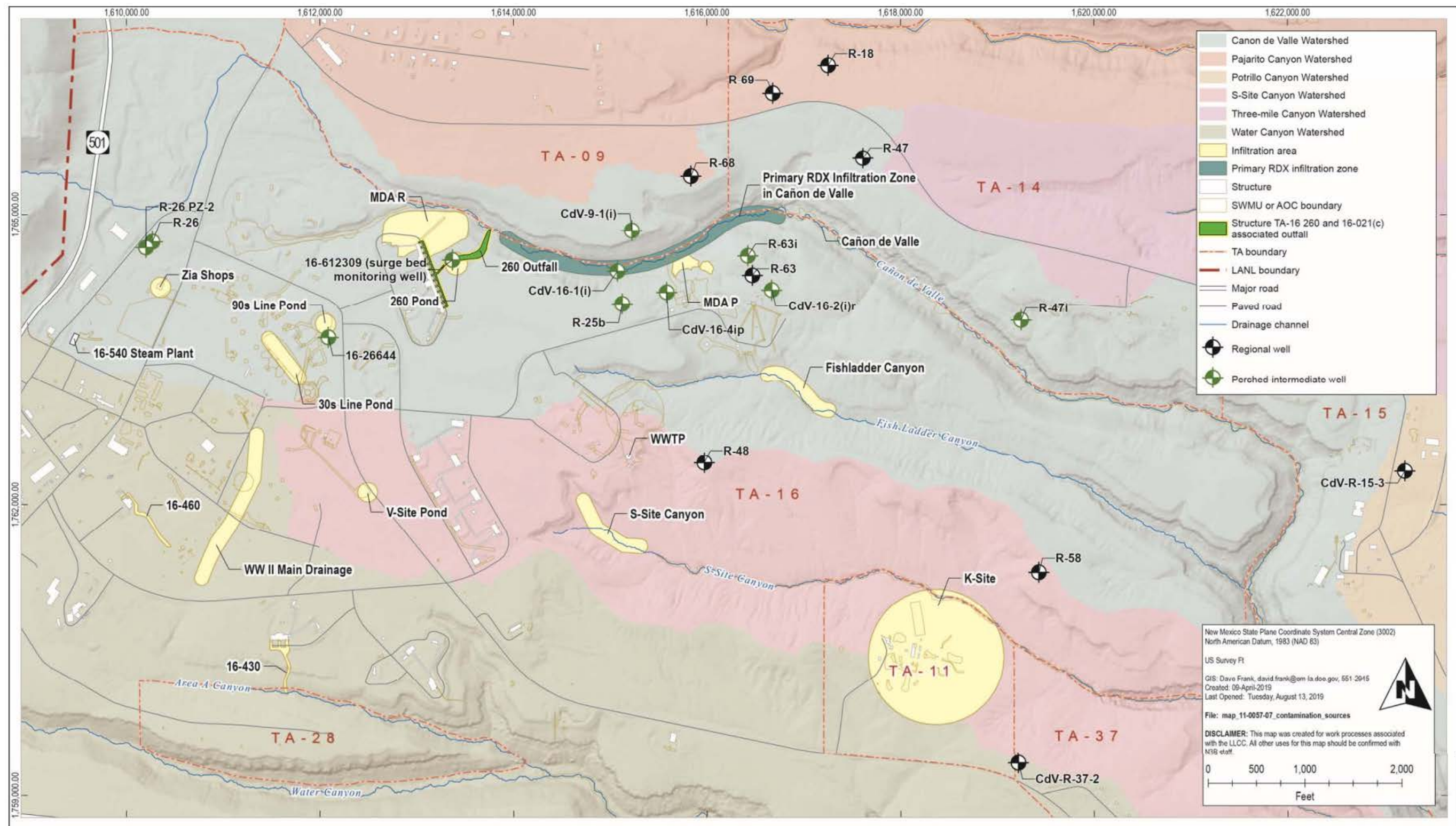
Figure C-1.2-1   A potential area of higher infiltration of surface water is shown downcanyon of the 260 Outfall, within the area of the TA-09 graben. RDX-contaminated discharges from the 260 Outfall, combined with surface water of Cañon de Valle, were thought to infiltrate somewhere within the indicated zone.
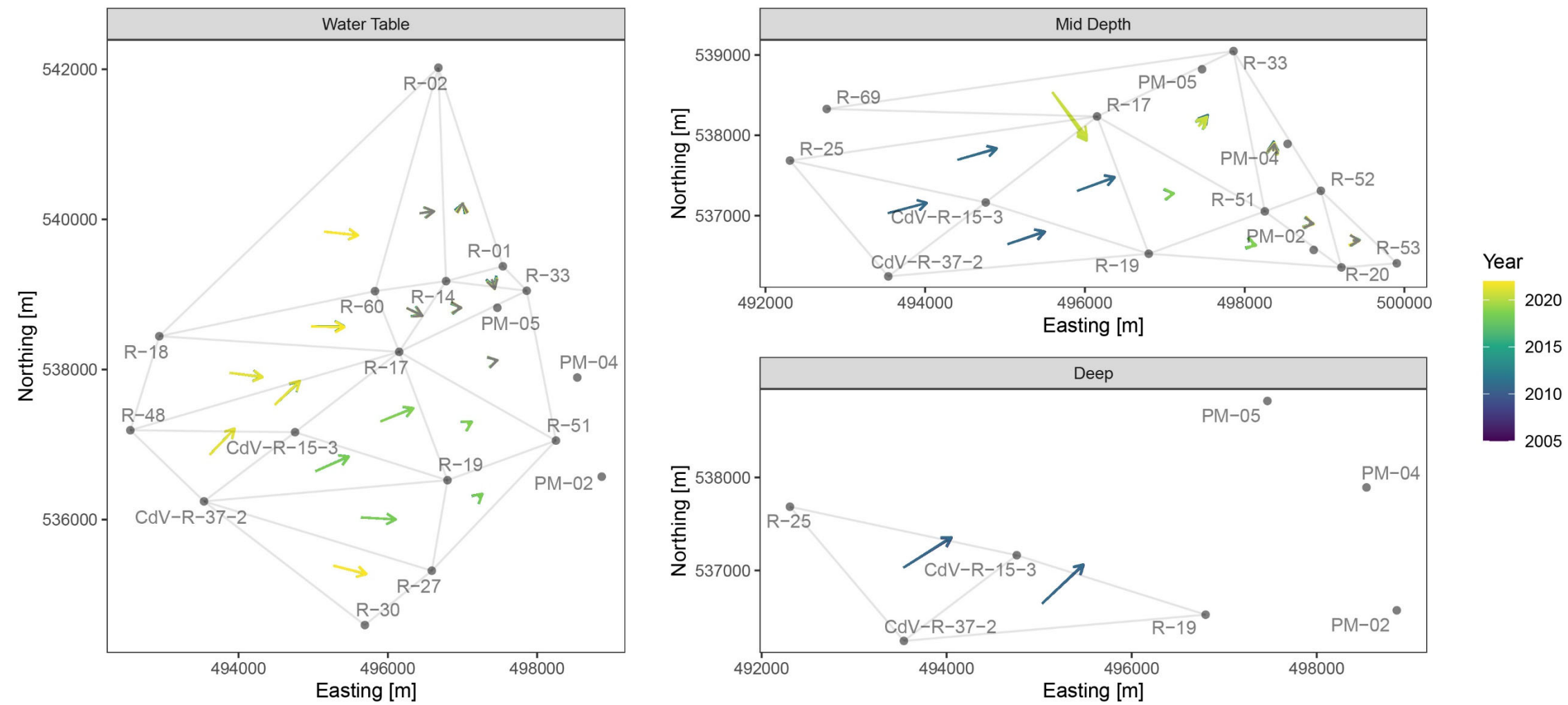
Figure C-1.2-2   Weekly averaged lateral water table gradients for the entire period of record show minimal changes through time (weekly arrows are plotted on top of each other , indicating negligible changes through time) for lateral gradients at any depth
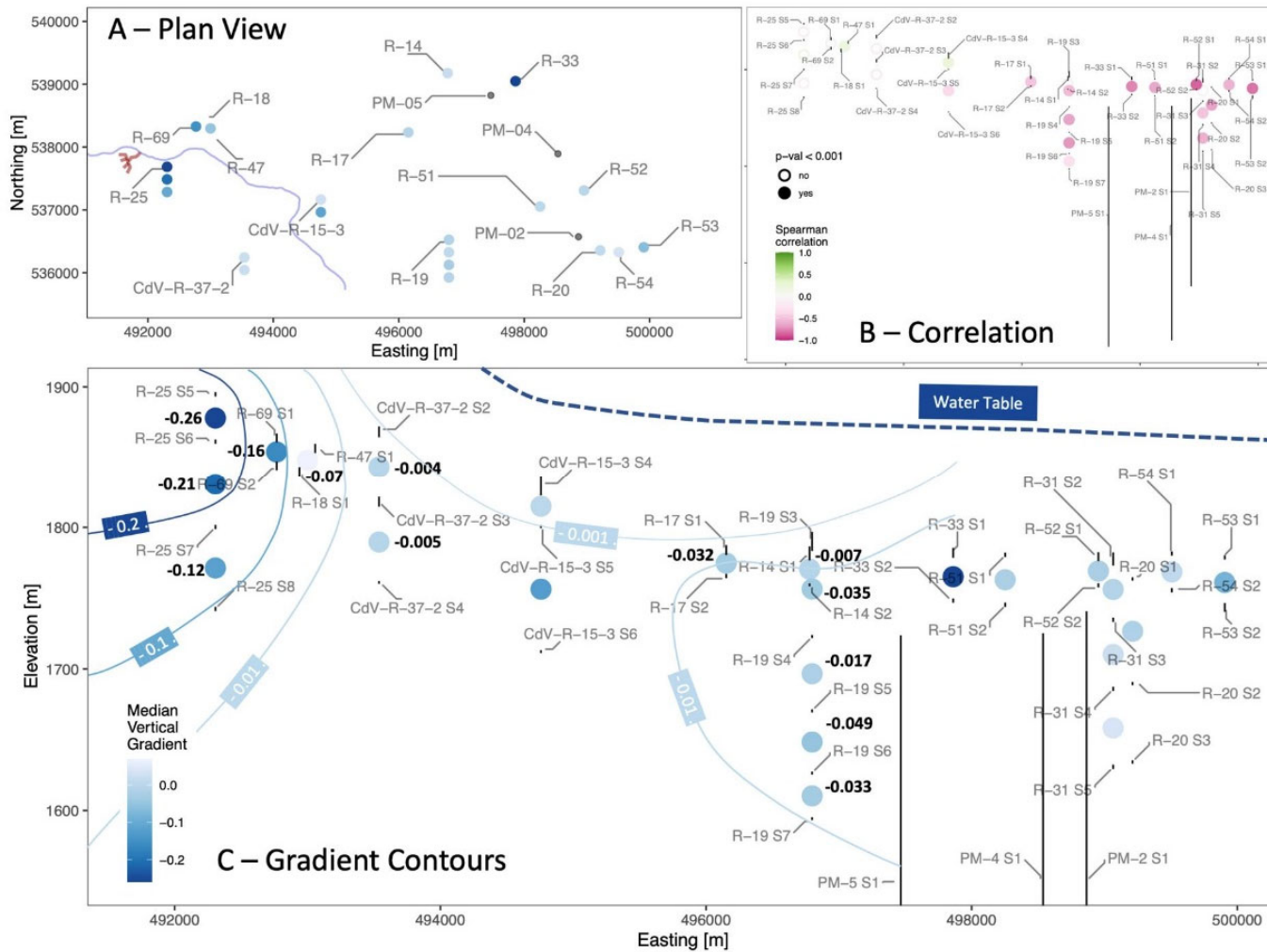
Figure C-1.2-3 **(a) Median vertical gradients throughout the RDX site show that gradients in the plume area are 2 orders of magnitude larger than those in wells near water-supply wells (i.e. R-19). (b) Correlation of vertical gradients to water-supply pumping shows no correlation near RDX plume, high correlation close to supply wells, and low correlation at intermediate distances. (c) Large vertical gradients near the plume are driven by mountain block processes, and low gradients at R-19 are driven by supply pumping.**
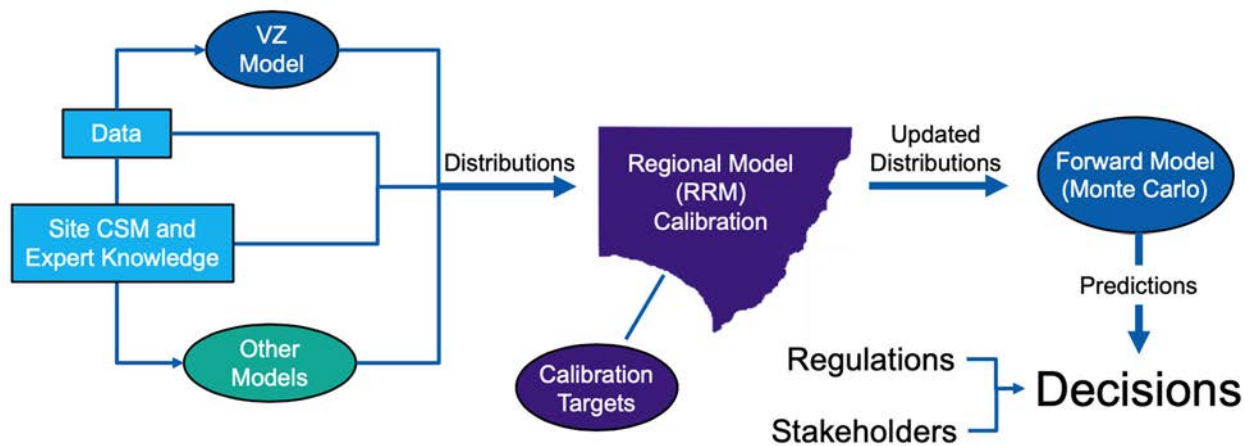
Figure C-2.1-1   Conceptualization of modeling framework
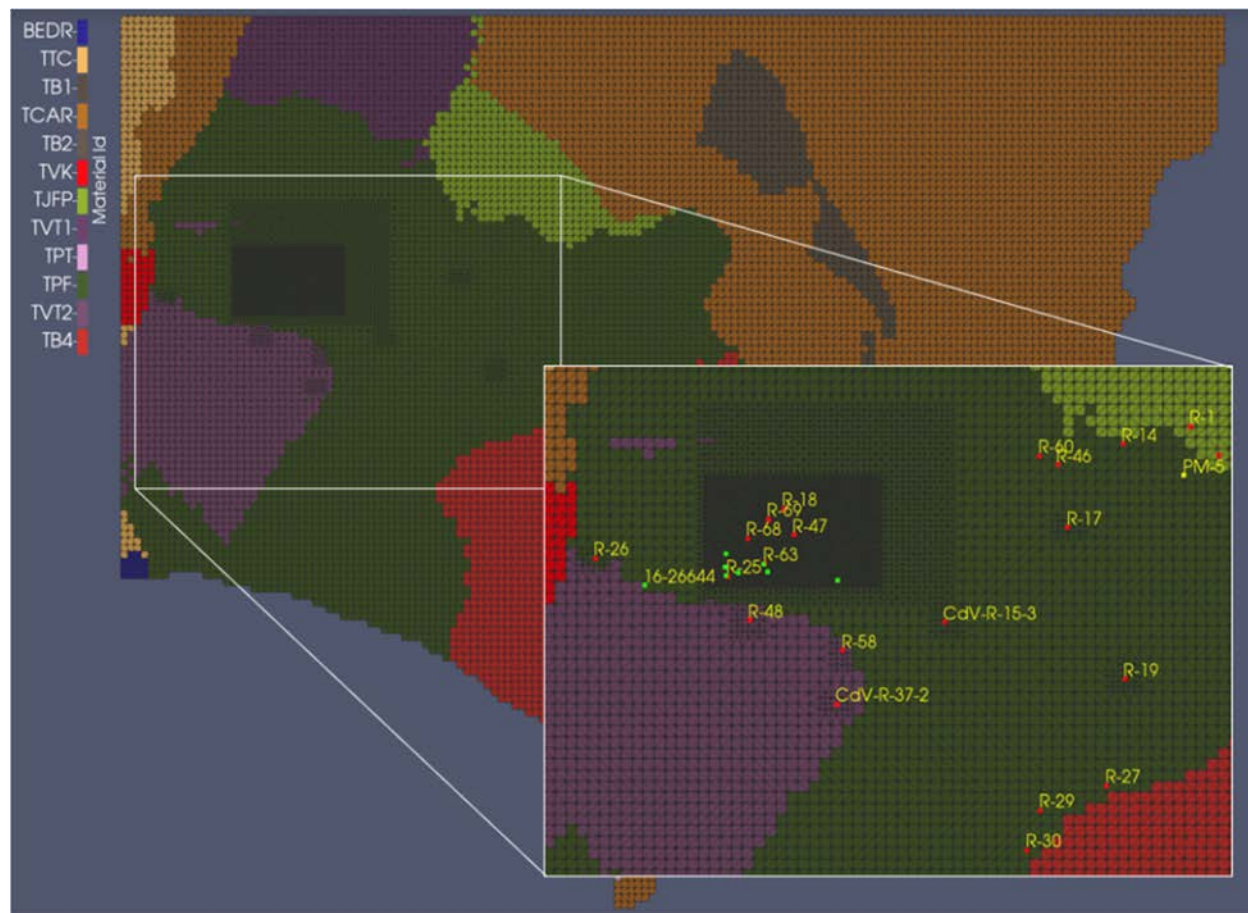
Figure C-2.2-1   RRM discretization and geologic properties. Inset shows refined region with well locations marked in red if screened in the regional aquifer or in green if in the perched-intermediate [well labels removed for clarity: CdV-16-4ip, CdV-9-1(i), R-47i, R-25b, CdV-16-1(i), R-63(i) and CdV-16-2(i)r].
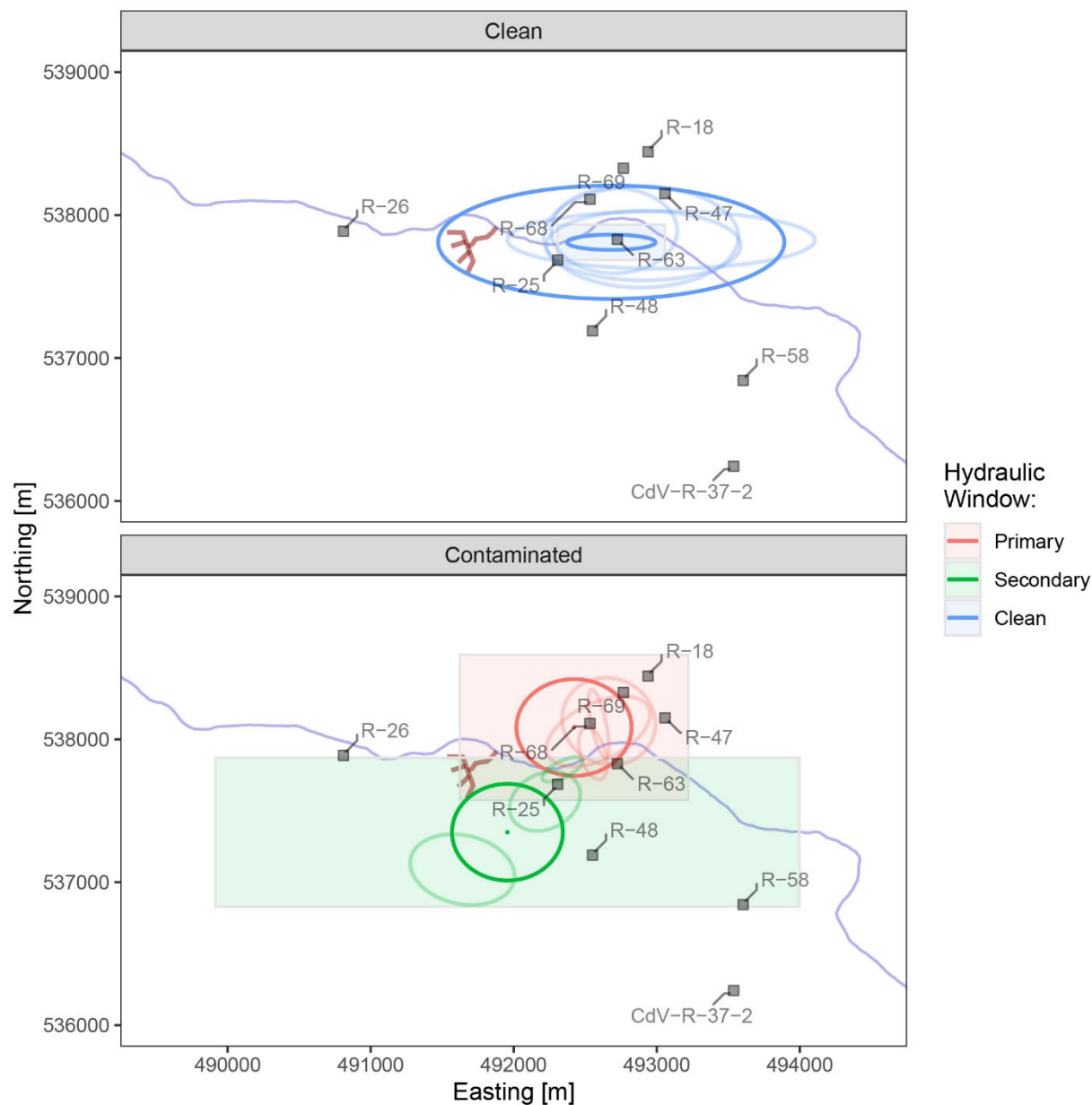
Notes: Decision locations where output is produced (PM wells, CdV-R-15-3, D-A, and D-C) are shown. The 260 Outfall and Cañon de Valle are also plotted for reference. Dotted lines represent potential regions where future monitoring could occur.

Figure C-2.4-1   Clean recharge (top), and RDX-contaminated (bottom) hydraulic window location distributions for spatial input parameters. The shaded rectangle shows the range of allowed center coordinate locations, and the darker ellipses show the allowed range of x and y radii. The final four calibrated hydraulic windows are shown for each source as transparent ellipses.

Figure C-2.4-2 **Map of anchor and pilot points used in the RRM. The underlying *K* field is created using a spatial model of the central value of each anchor point in the domain (although this plot is in plan view, there are pilot and anchor points at depth and the kriged field is 3 dimensional).**
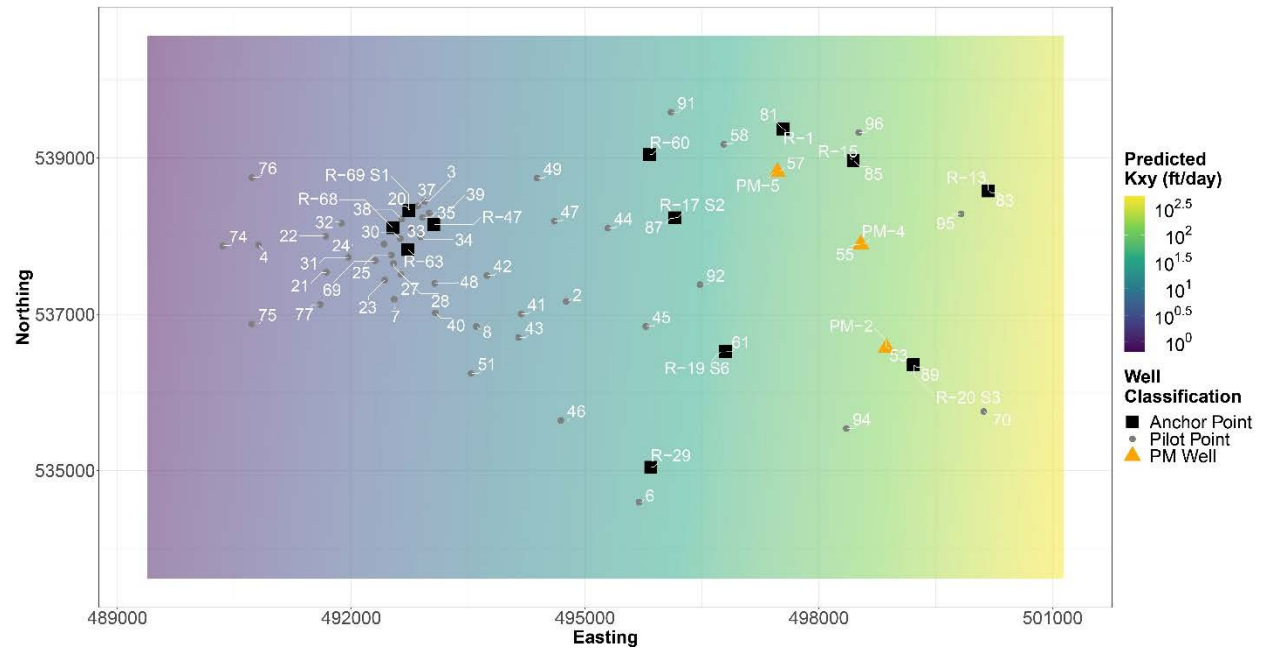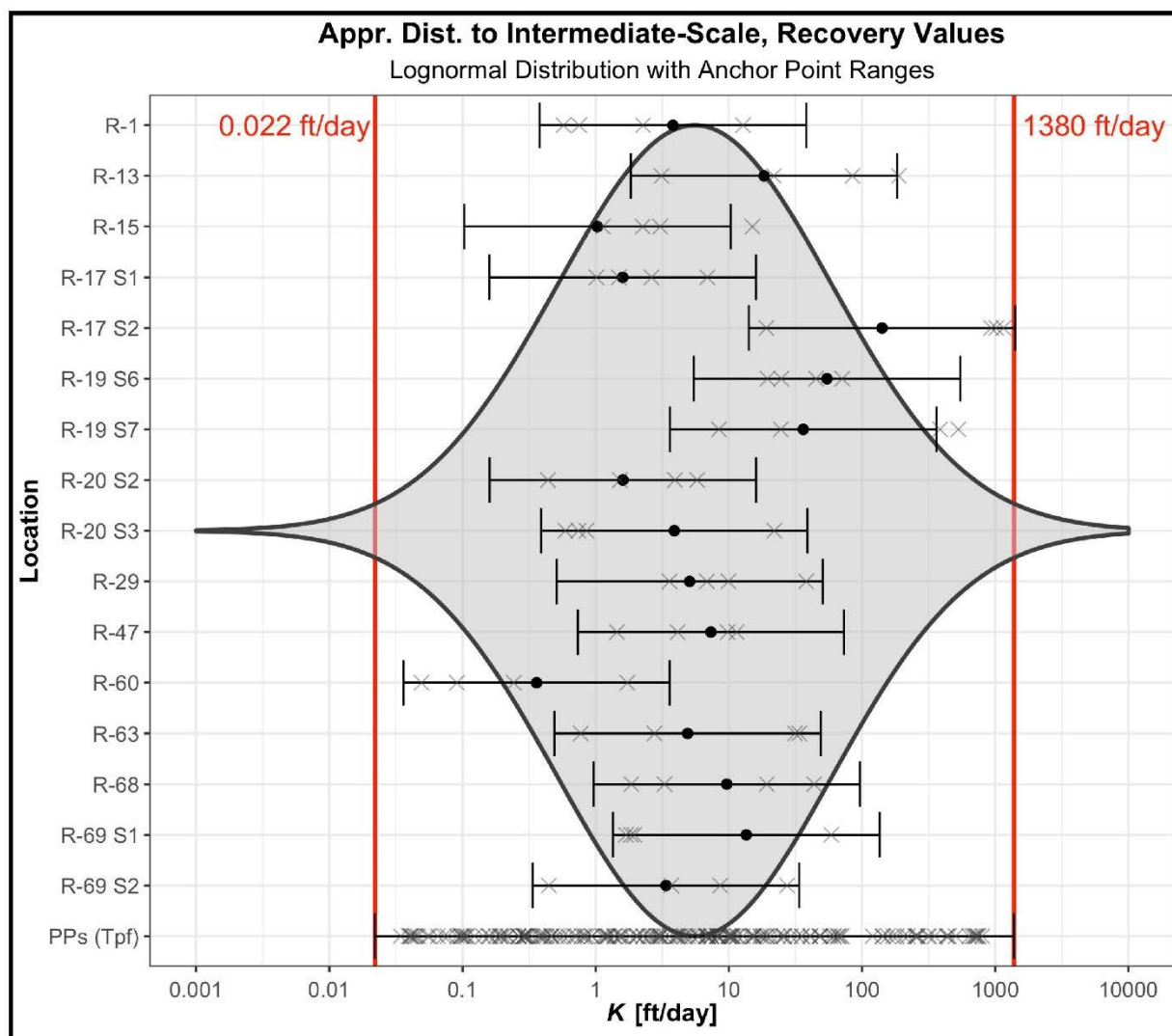
Figure C-2.4-3 **Anchor point hydraulic conductivity distributions at well locations (horizontal bars), which combine to form the overall distribution for the Puye Formation that informs pilot points with no spatially explicit data (bottom bar and shaded gray violin plot). The 1st and 99th percentiles, used to limit the calibration movement, are shown as red lines. Final initialization points of the top four calibrations are shown as grey Xs for all anchor and pilot points.**
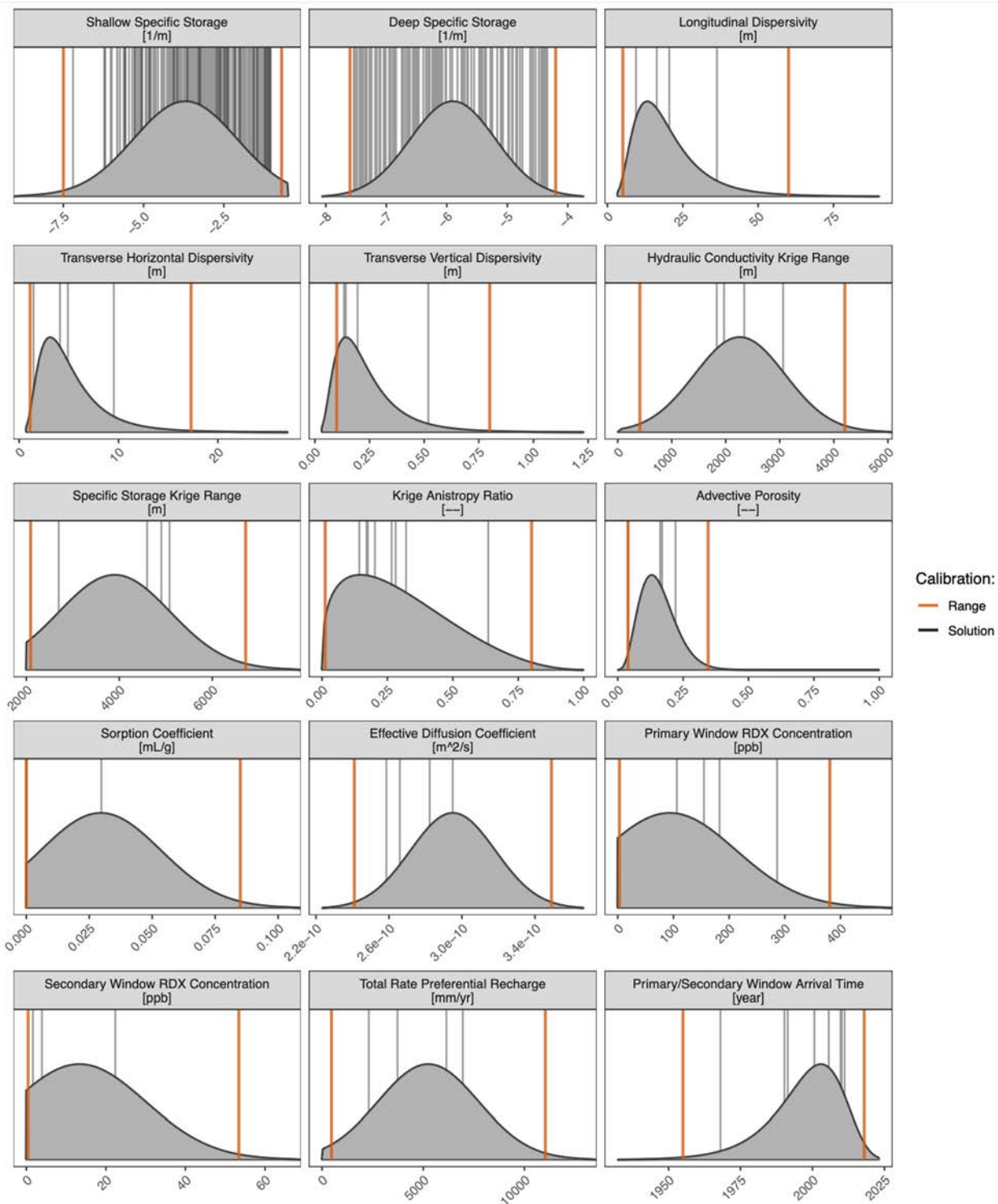
Note: Uniform distributions are listed in the table but are not shown, as they simply run from a minimum to a maximum value.

Figure C-2.4-4   Parameter distributions not shown in other figures. The 1st and 99th percentiles are indicated by orange vertical lines and constrain the range of the LM calibration. Final values for four top calibrations are shown as grey lines behind the distribution.
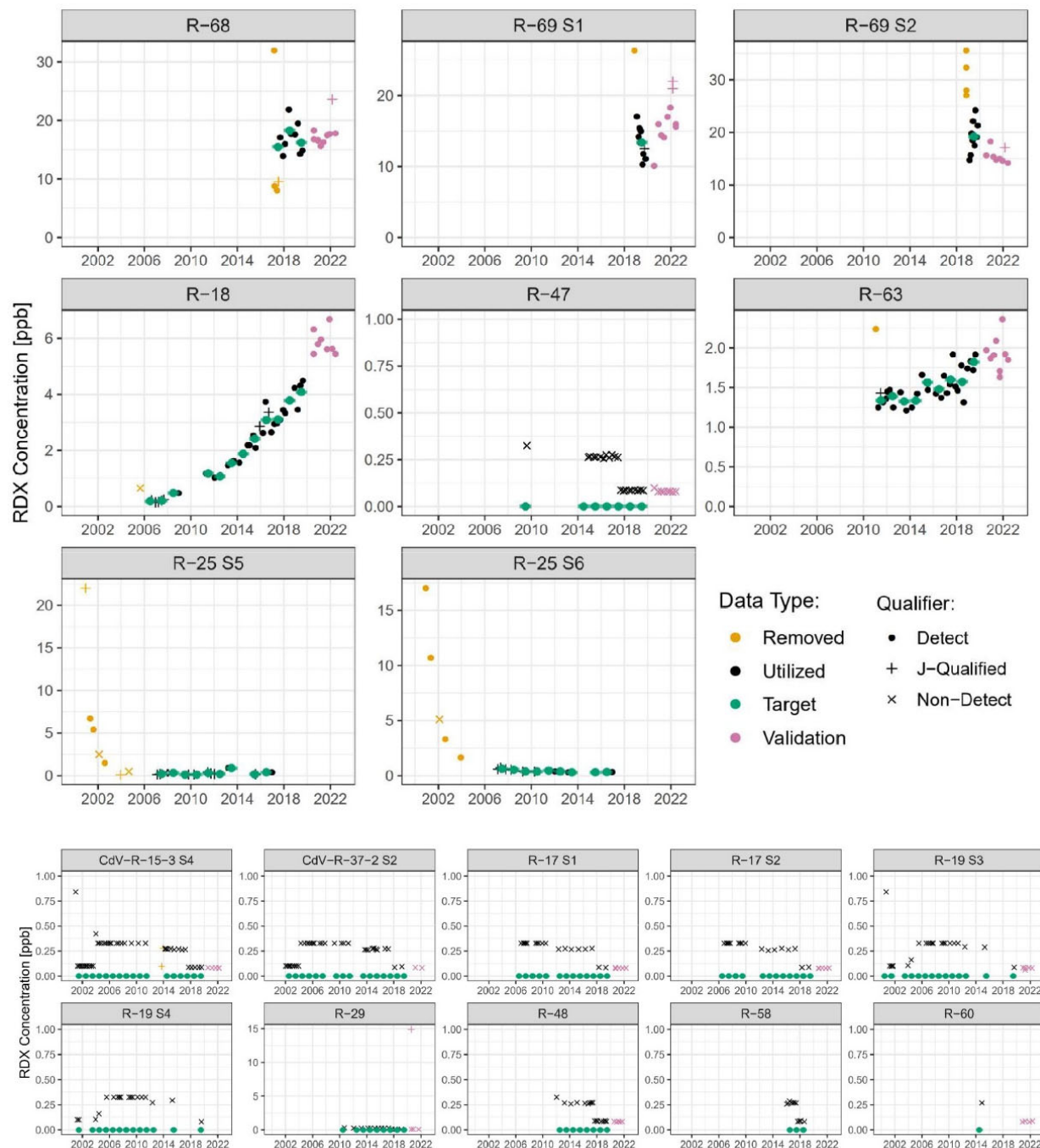
Figure C-2.5-1   Yearly-averaged RDX concentration targets (green) derived from raw data at monitoring wells throughout the domain (black). Data through the end of 2019 are used as targets and data collection after that point is used as validation for the calibration.
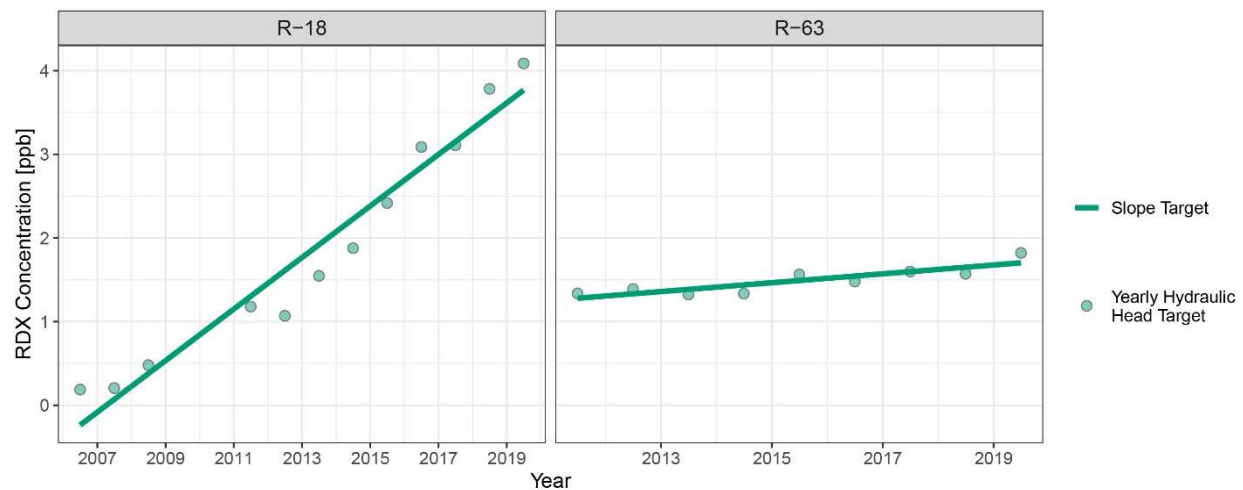
Figure C-2.5-2   Concentration trend targets derived from the slopes of the concentration targets
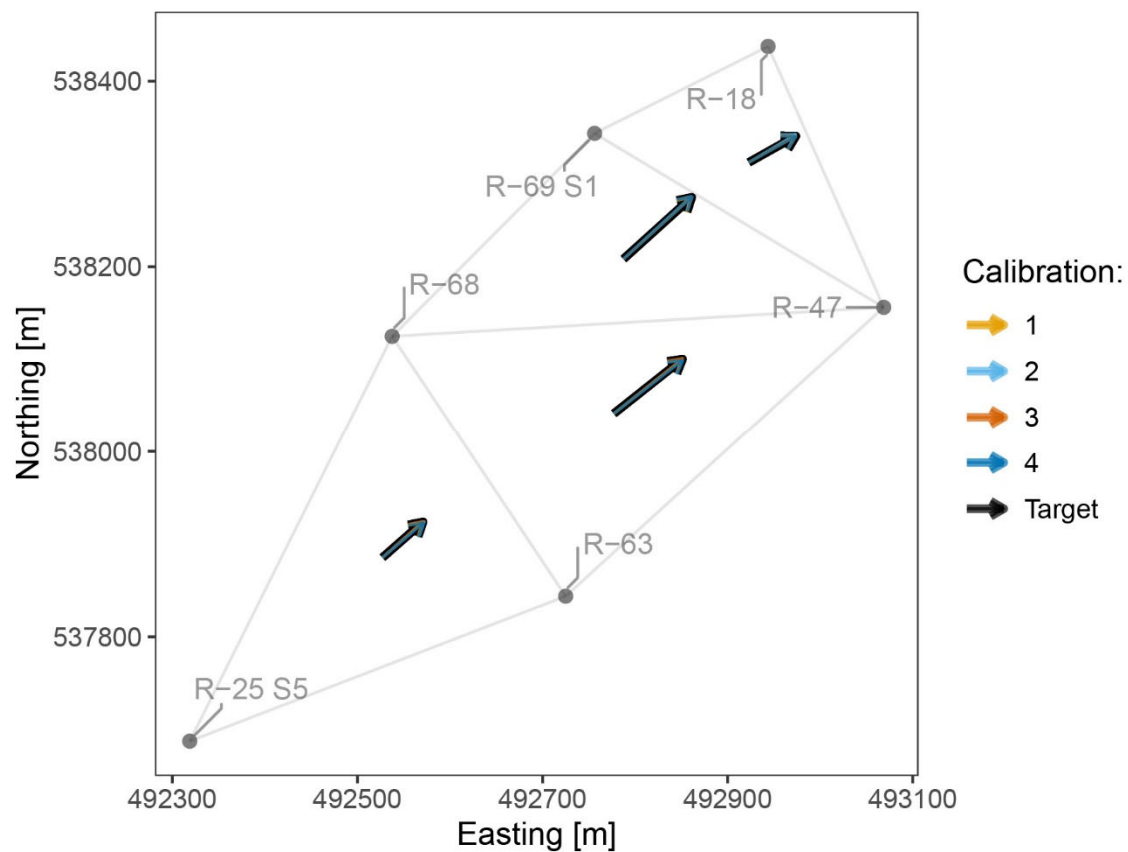
Figure C-2.5-3   LM calibration results (colored arrows) match hydraulic gradient targets (black arrows) perfectly in both magnitude and direction, such that it is nearly impossible to see the differences between the arrows.
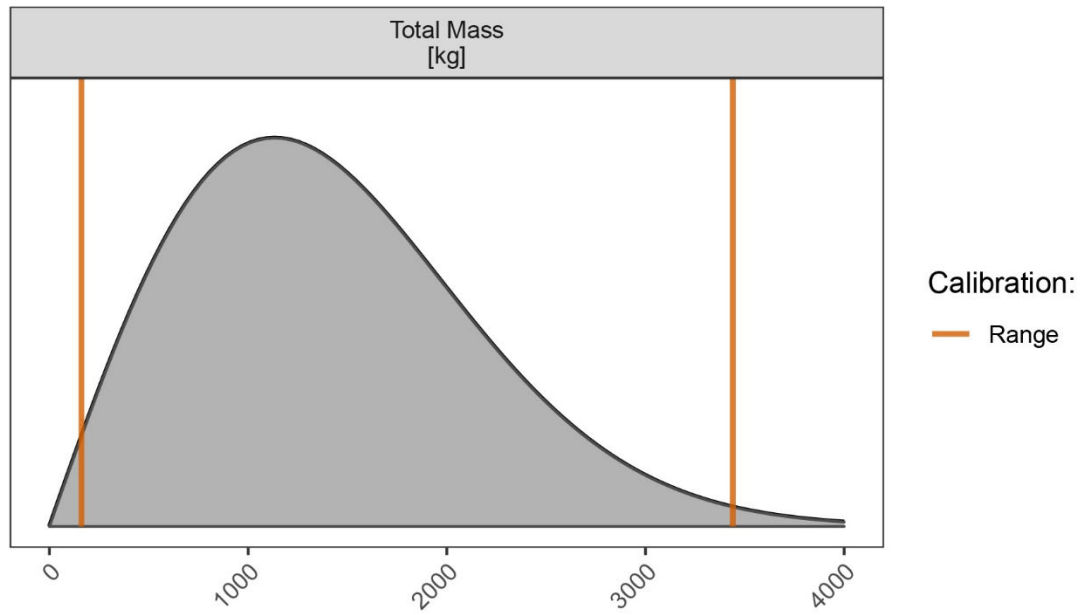
Figure C-2.7-1   Prior distribution for total mass developed to inform how long RDX is added to the system through hydraulic windows in predictive forward runs
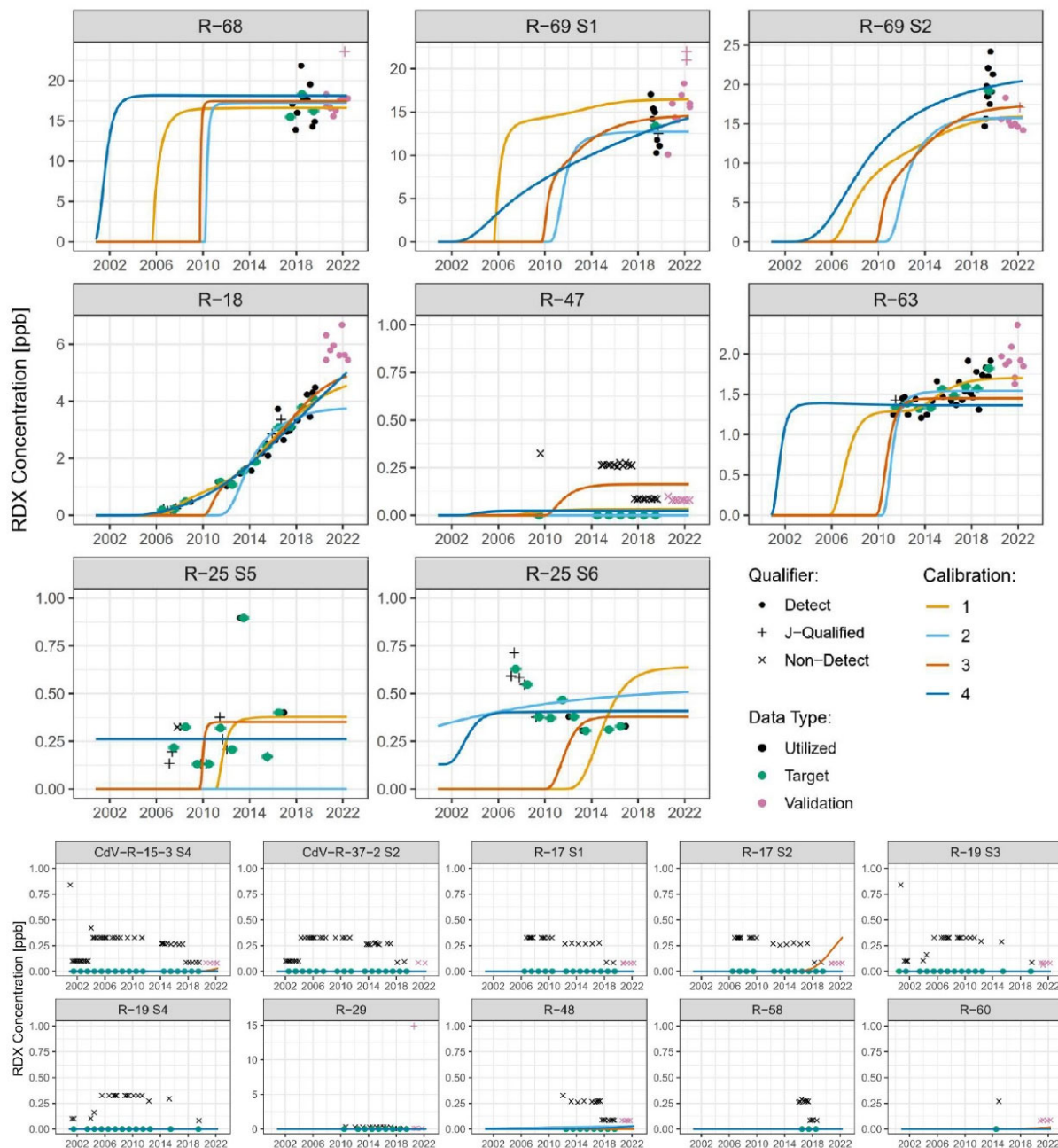
Figure C-3.1-1   Top four calibrated model results show close agreement with all wells in the modeling domain. Validation data are well matched in R-68, R-69 screen 1, and R-69 screen 2 and are close but underpredicted at R-18 and R-63.
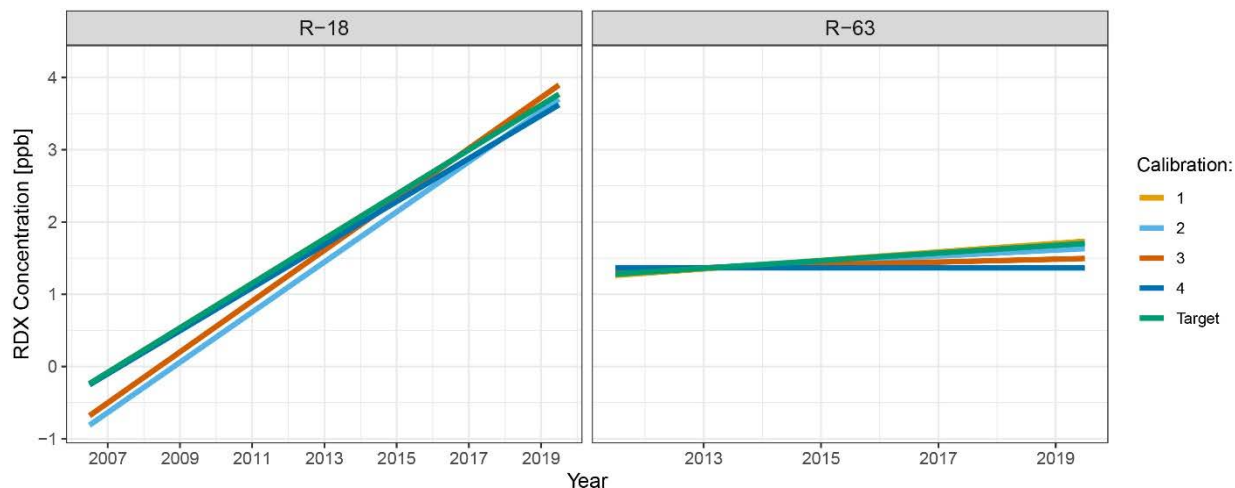
Figure C-3.1-2   LM calibration results compared with concentration slope targets
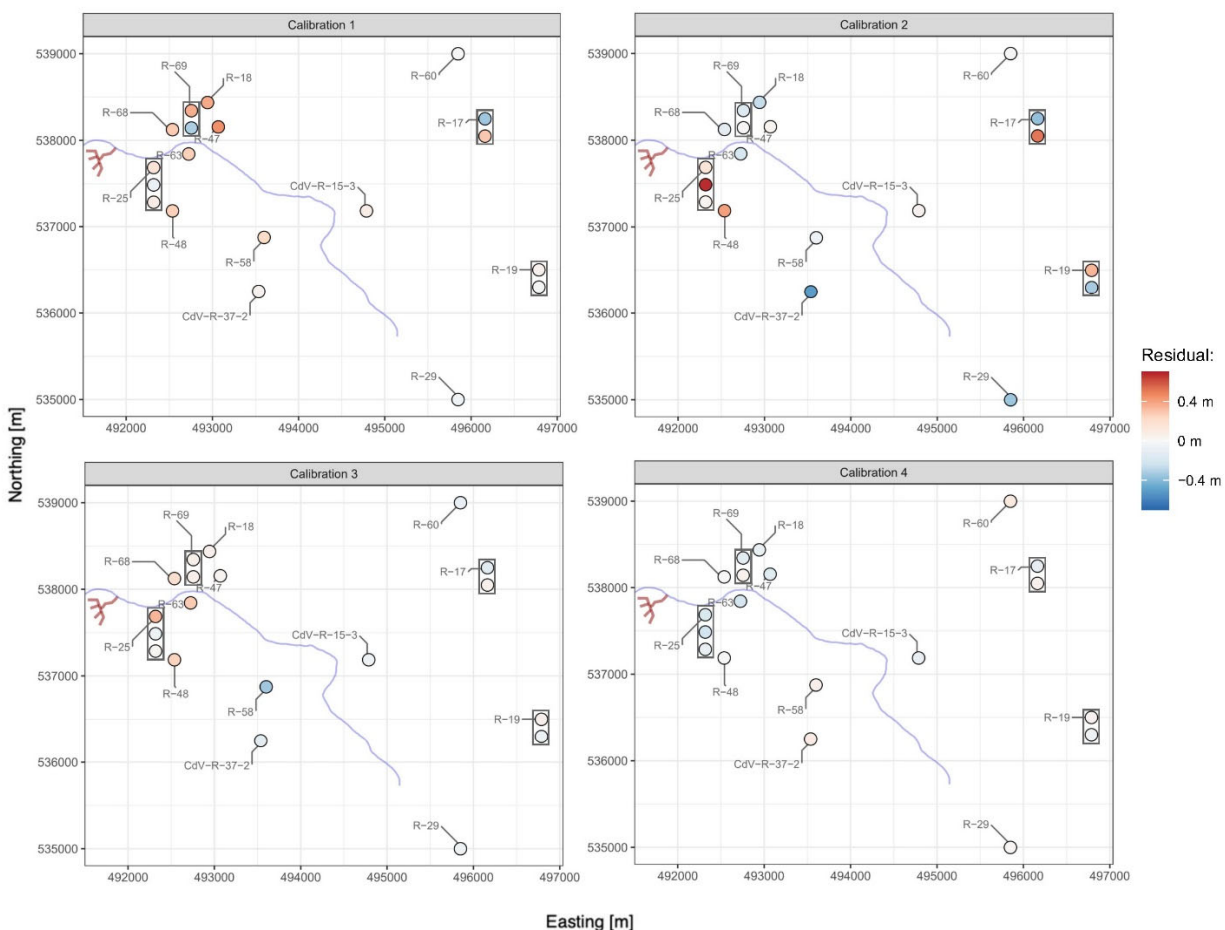
Figure C-3.1-3   Top four calibrated models show close agreement with head data at all screens, including deeper screens. All screens are within 0.5 m of observed data except two points in calibration 2 (R-25 screen 6 residual at 0.67 m, and R-17 screen 2 residual at 0.51 m).
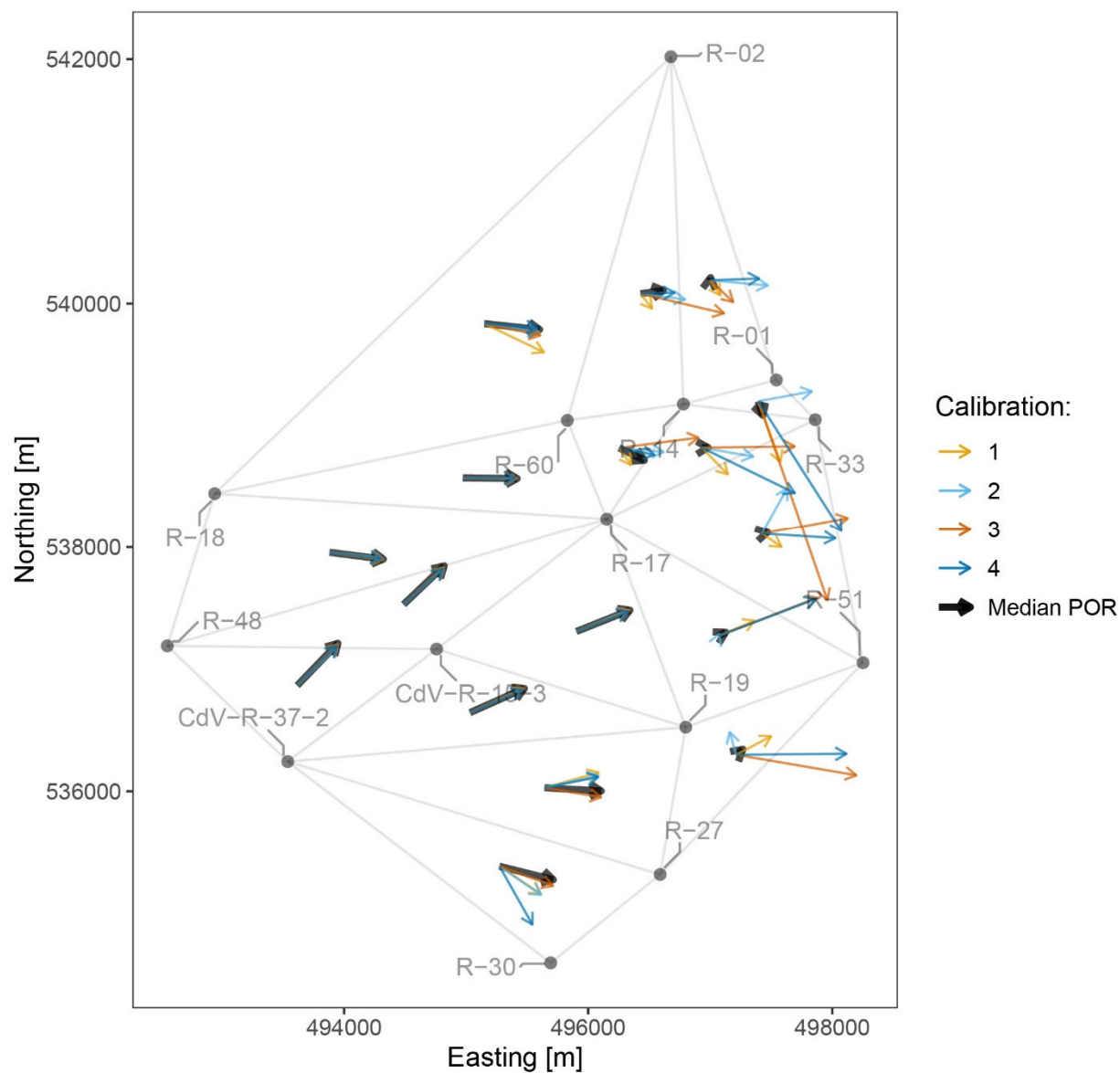
Figure C-3.1-4   Validation lateral gradients are shown in black (the median of the period of record for each well triplet) with calibration results. Calibrations are excellent on the western side of the site near the RDX plume and are large overestimates of the gradients in the region approaching the PM wells.
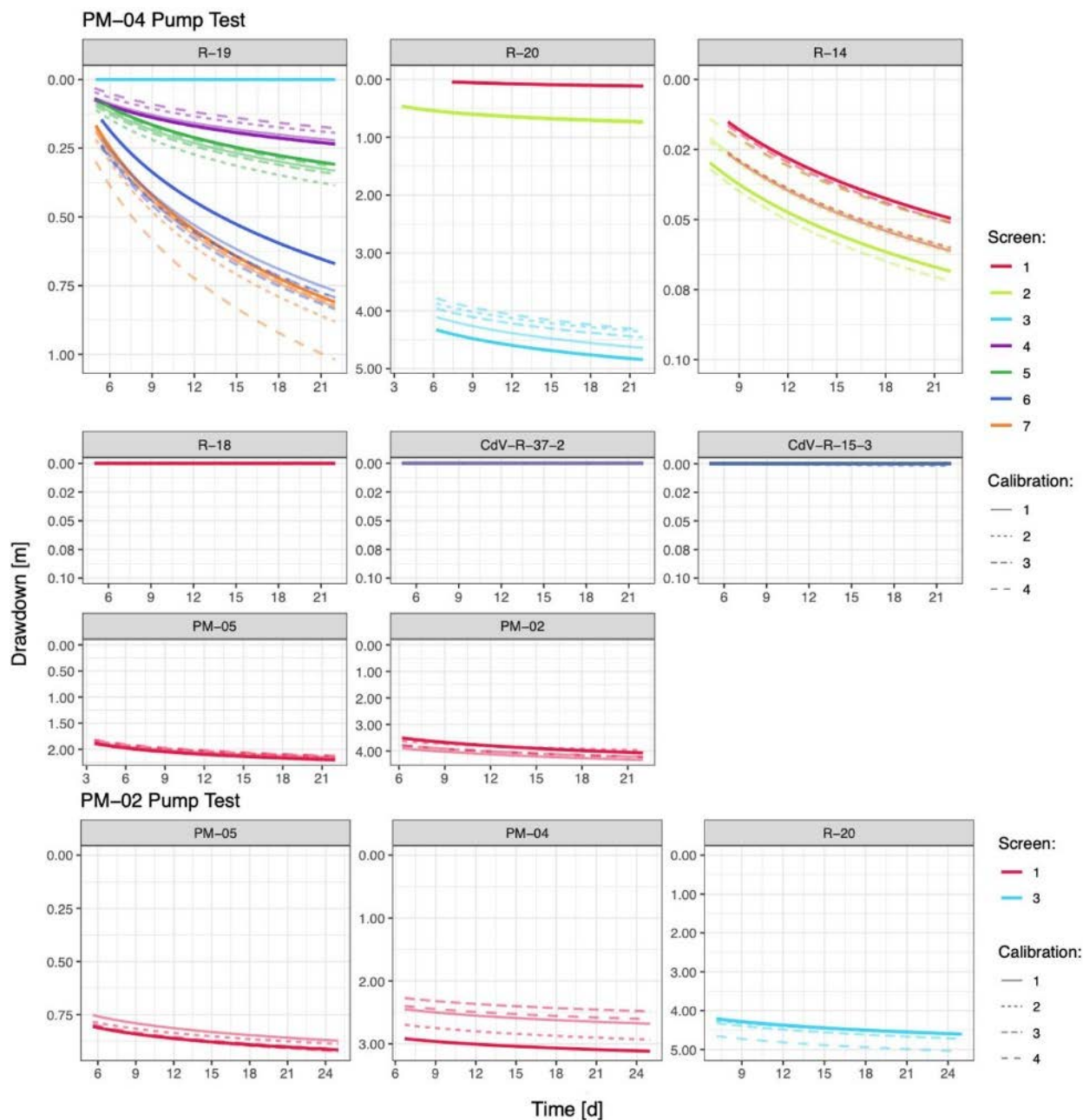
Figure C-3.1-5 **Drawdown responses at monitoring locations to the PM-4 pump test conducted in 2005 (including 3 wells where no drawdown was observed). The last three plots show drawdown responses to the PM-2 pump test conducted in 2003. Observations are plotted as heavy solid lines for each screen and calibration results are plotted.**
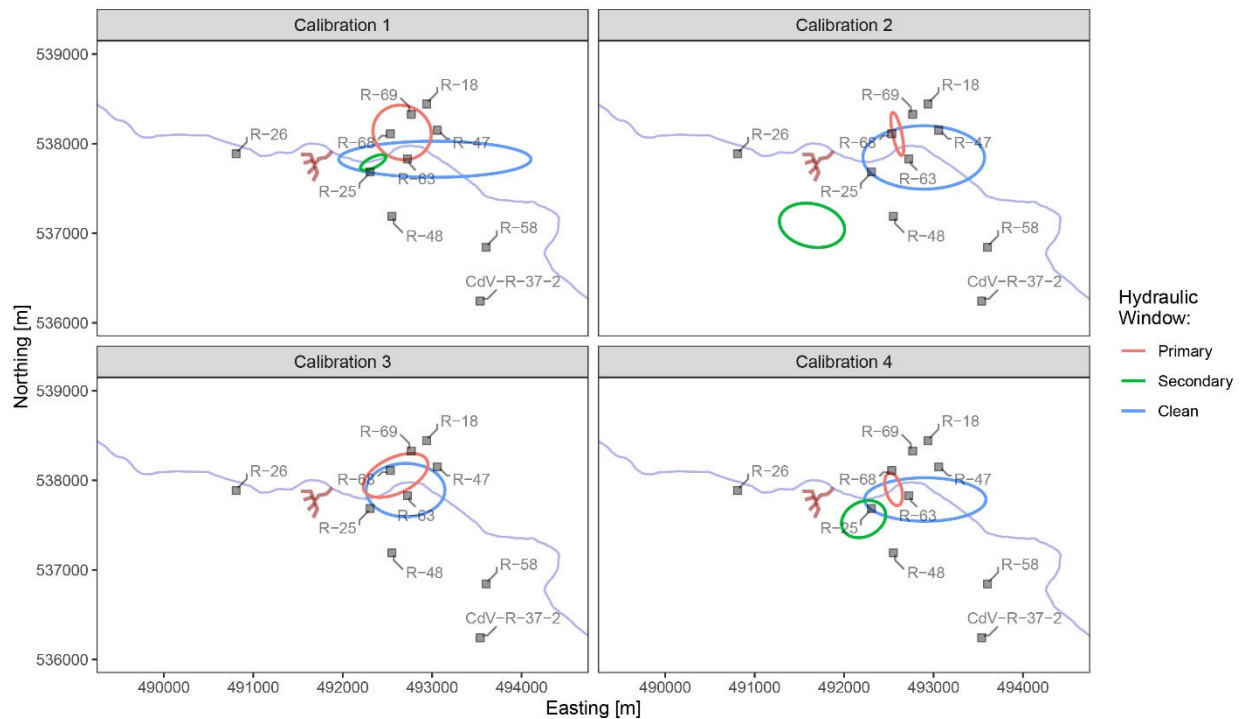
Figure C-3.1-6 **Input parameterizations of the hydraulic windows for the top four calibrations shown with the well locations, 260 Outfall, and Cañon de Valle**
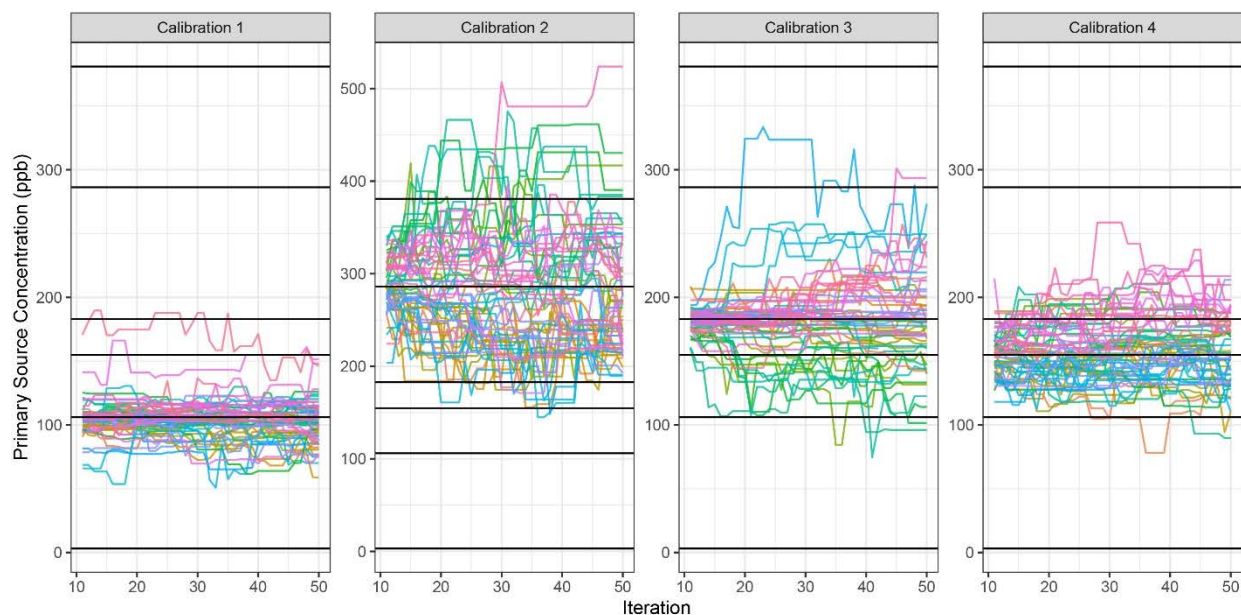
Figure C-3.2-1 **The movement of each walker within the ensemble for each of the four calibrations. Horizontal lines indicate that the walker stayed in place. The color of the line indicates the machine that ran the simulations.**
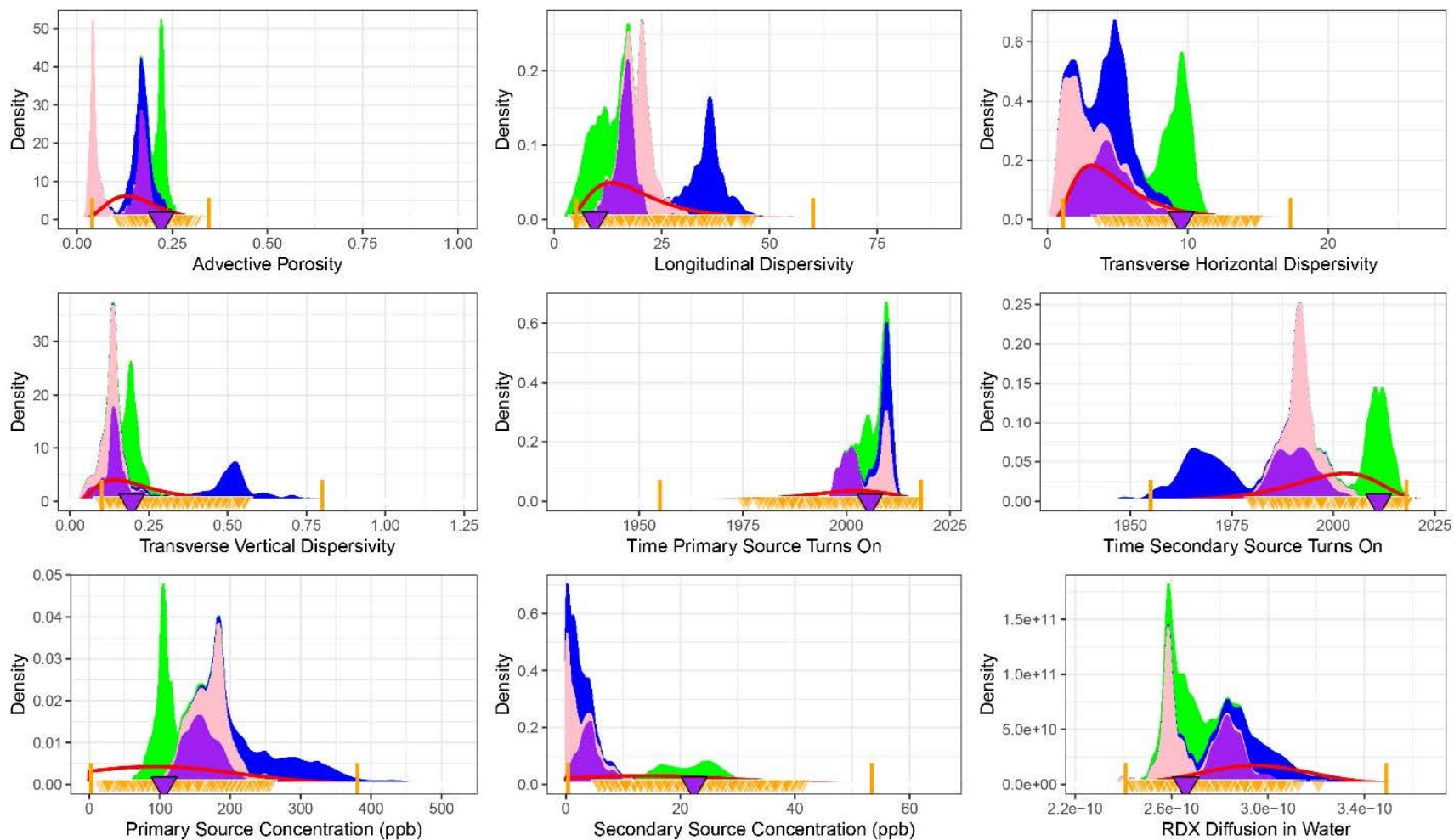
Figure C-3.2-2   Posterior parameter distributions for the nine parameters varied continuously in the MCMC for each of the four LM endpoints. As an example, the purple triangle represents the initialization point from calibration 1 and the orange triangles represent the initial values of the other walkers in calibration 1's ensemble. The green density plot shows the parameter density for calibration 1, blue shows calibration 2, pink shows calibration 3, and purple shows calibration 4.
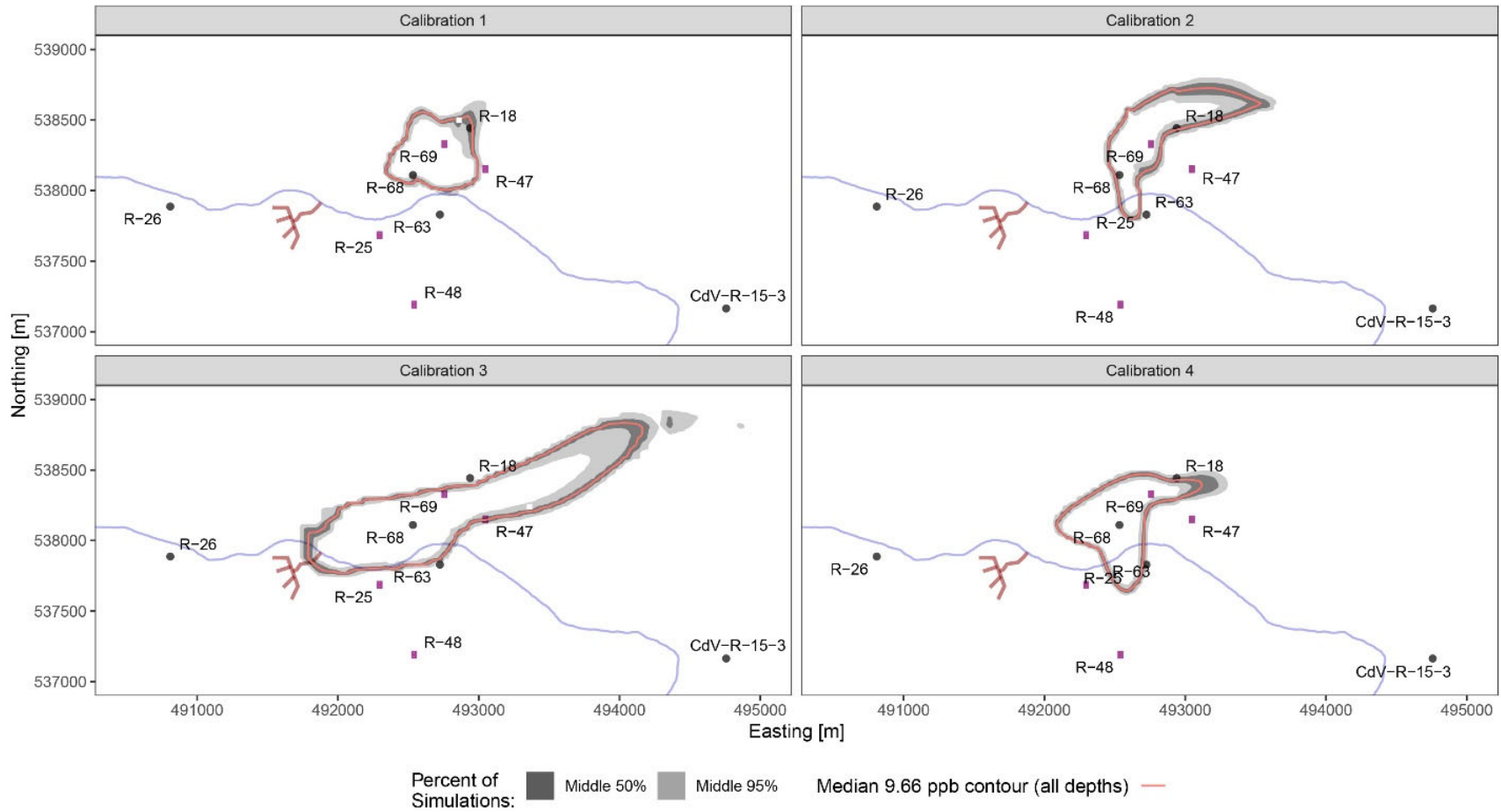
Figure C-3.3-1   Maximum RDX observed at any depth is plotted probabilistically across all predictive forward runs for the present day for each of the four LM calibration endpoints
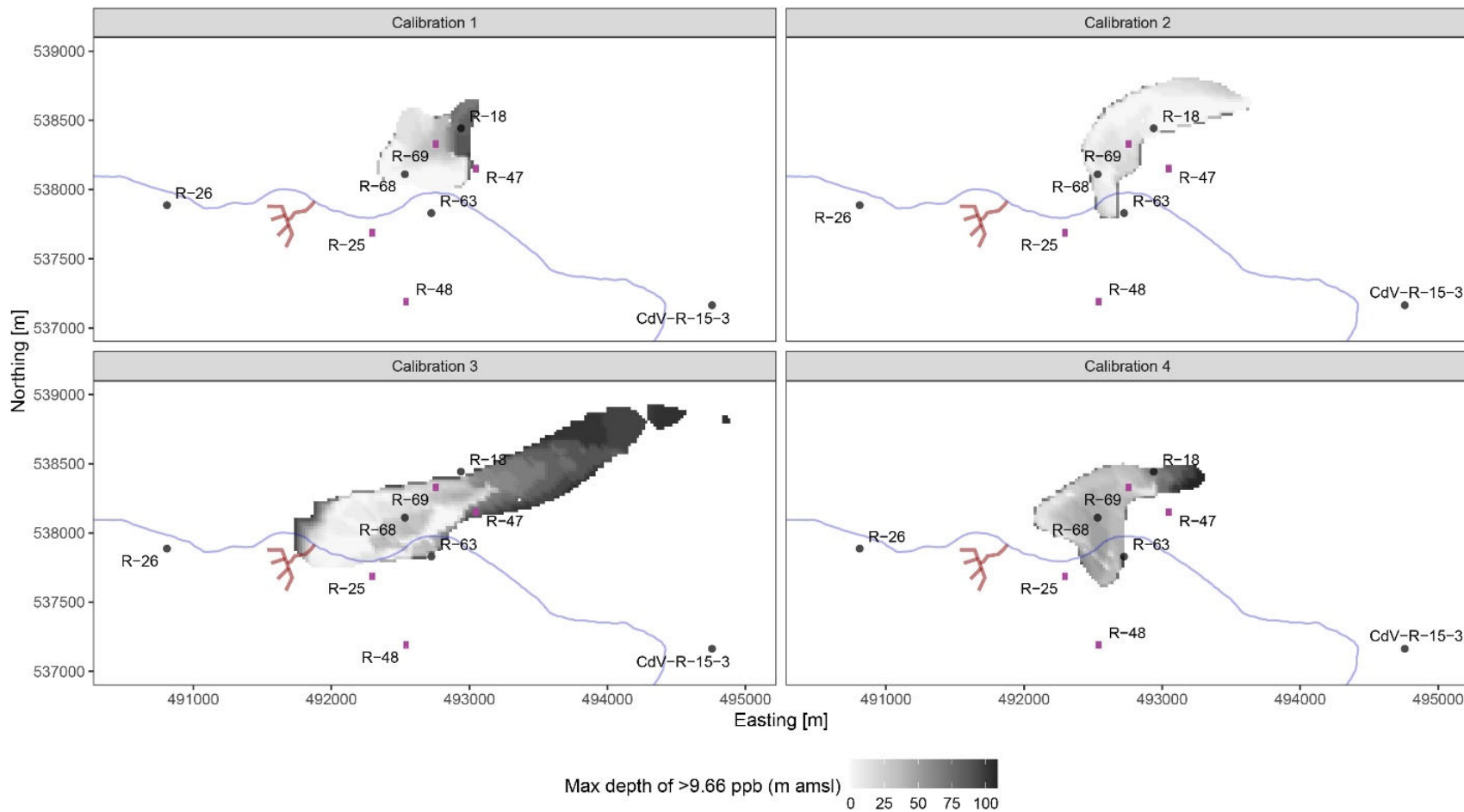
Figure C-3.3-2   Depth of 9.66-ppb RDX for the plume shown in plan view in Figure C-3.3-1 for each LM calibration endpoint
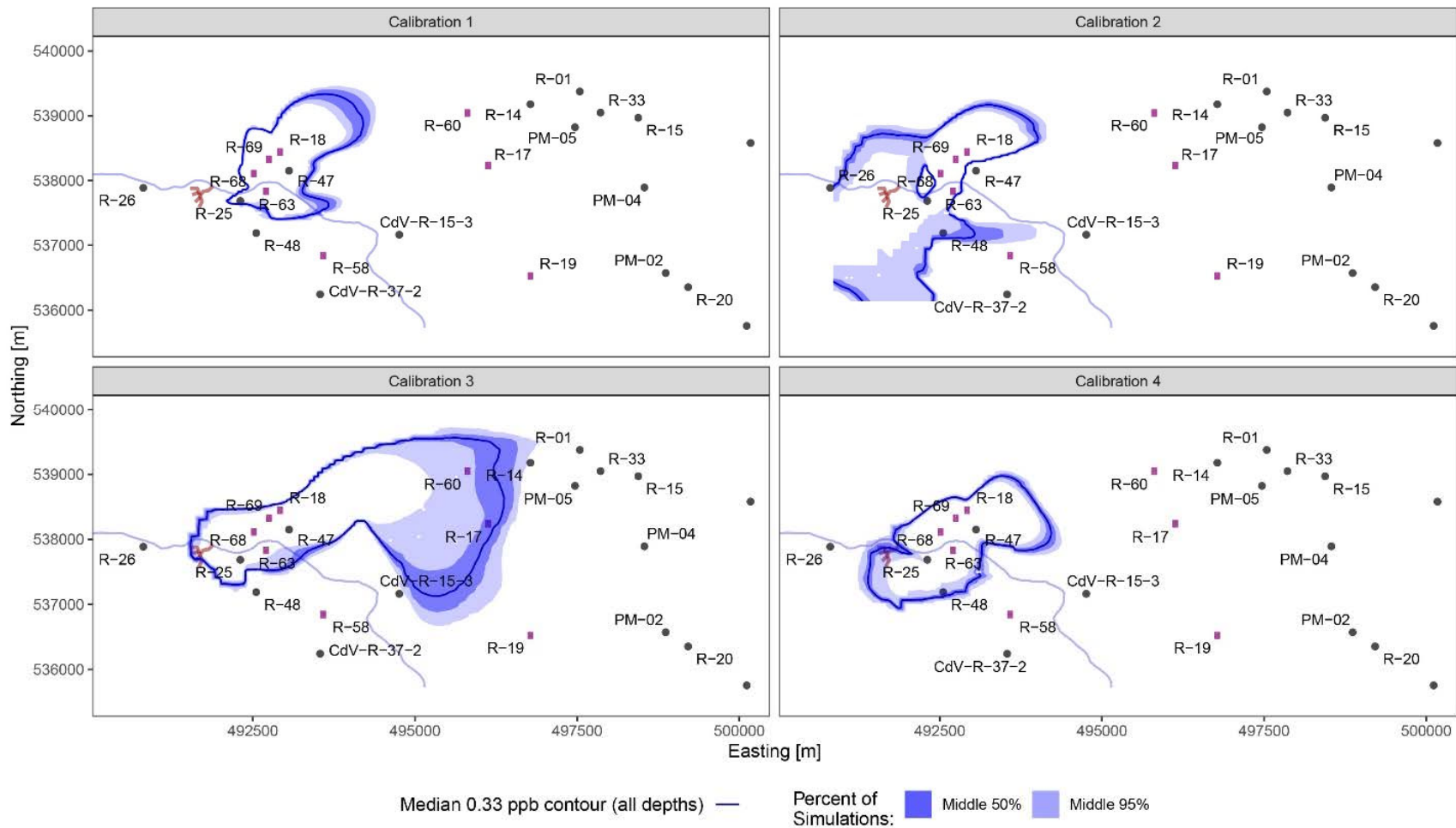
Figure C-3.3-4   Likelihood of RDX above 0.33 ppb (detection limit) for each calibration in 2022
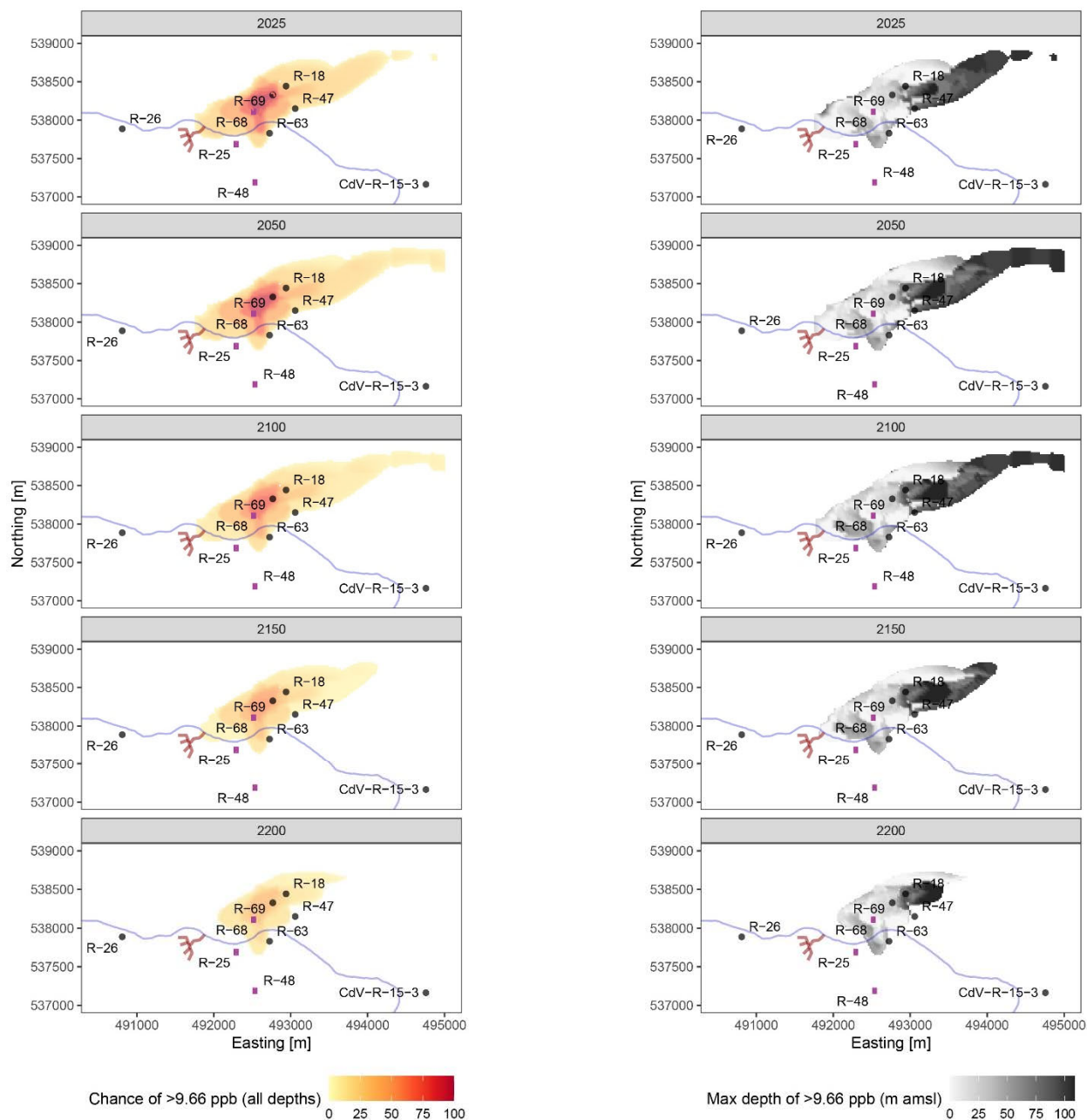
Note: The figure combines the predictive runs across all four LM solutions and MCMC samples (resulting in predictions made using over 4000 individual runs) and plots the likelihood of the 9.66-ppb contour as well as the depth where the maximum concentration is observed for the years 2025, 2050, 2100, 2150, and 2200.

Figure C-3.3-5   Plume extent across all predictive future runs, plotted as a likelihood of being greater than 9.66 ppb across all depths for all runs (left panels). The depth of the plume is plotted next to each plume map (right panels).
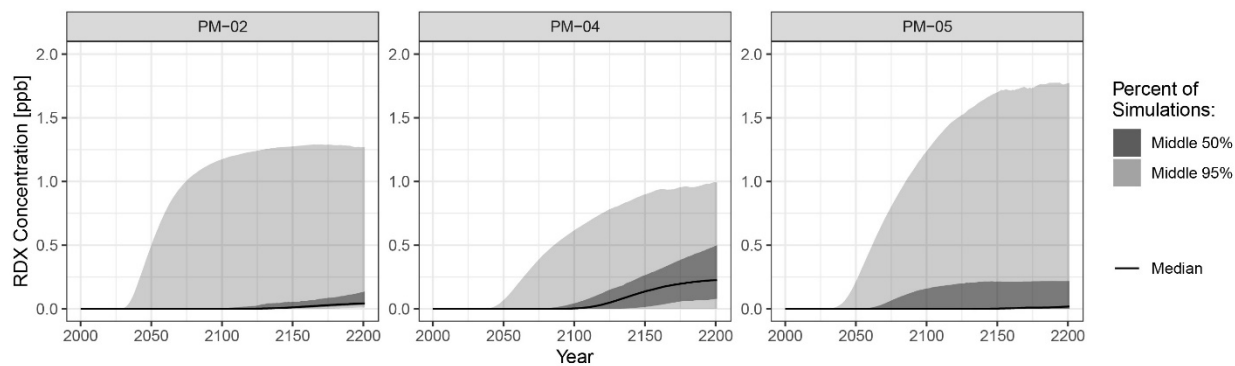
Figure C-3.3-6 **Predictive summary of results at county supply wells nearest to the RDX plume shows that RDX is not likely to arrive at levels above the detection limit at any well and is 95% likely to remain below 2 ppb if it ever arrives.**
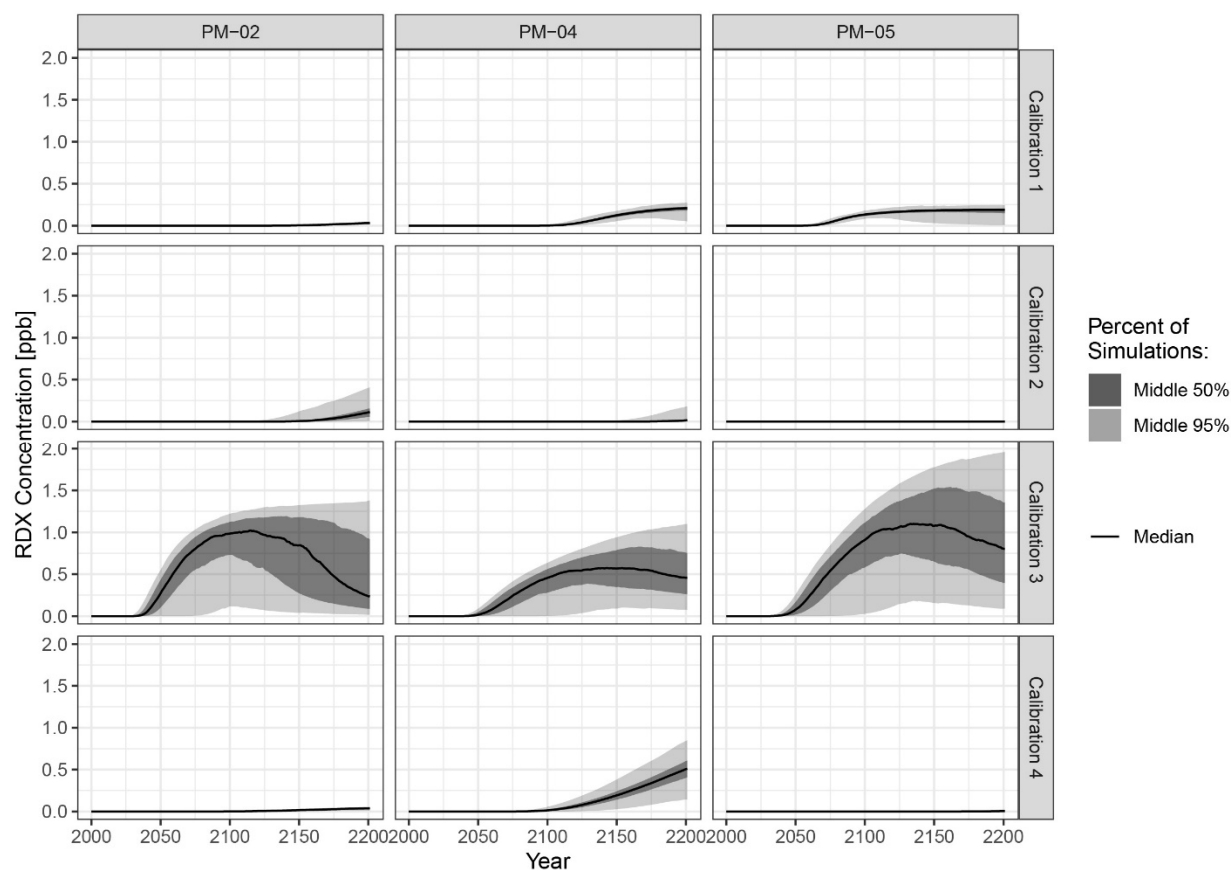
Figure C-3.3-7 **Likelihood of RDX arrival at each of the county supply wells, by calibration**

Table C-2.4-1
Input Parameter Distributions

Material Properties Parameters					
Parameter	Model Notation	Median	1st, 99th%	Unit	Source of Information
Hydraulic conductivity[1]					
Puye Formation (pilot points)	(kx, ky)(pp#)	12	0.2, 1382	ft/day	Well data, literature
Volcanic formations or Unknown (pilot points)	(kx, ky)(pp#)	10	3E-6, 3000	ft/day	Literature, modeling
Anchor points (all in Puye)	(kx, ky)(ap#)	0.35–153	See Figure C-2.4-2.	ft/day	Well data, literature
Specific Storage					
Shallow (unconfined to semiconfined)[2]	s(pp#)	−3.7	−7.5, −0.7	1/m	Well data, literature
Deep (confined to semiconfined)	s(pp#)	−5.9	−4.2, −7.6	1/m	Well data, literature
Dispersivity[1]					
Longitudinal	disp_long	17.5	5.1, 60.1	m	Literature
Transverse horizontal	disp_trans_hor	4.4	1.1, 17.3	m	Literature
Transverse vertical	disp_trans_vert	0.2	0.1, 0.8	m	Literature
Other					
Hydraulic conductivity krige scale[2]	krige_rangeK	2264	410, 4204	m	Literature, modeling
Specific storage krige scale[2]	krige_rangeS	3985	2093, 6718	m	Literature, modeling
Krige anisotrophy ratio[3]	krige_v(K,S)_semiaxis	0.27	0.01, 0.8	m/s	Literature, modeling
Advective porosity[3]	adv_por	0.15	0.04, 0.35	—	Well data, literature
Diffusivity	diff_w	2.96E-10	2.41E-10, 3.49E-10	m^2/s	literature
RDX sorption coefficient	Kd	0.030	0, 0.085	mL/g	literature

Table C-2.4-1 (continued)

Boundary Condition Parameters					
Long Name	**Parameter Name**	**Median**	**1st, 99th%**	**Unit**	**Source of Information**
Primary window centroid coordinates	s1(x,y)0	(492421, 538082)	x(491623, 493220) y(537574, 538592)	State Plane NAD83	Well data, CSM, hydraulic gradient, P&D
Secondary window centroid coordinates	s2(x,y)0	(491956, 537872)	x(489915, 493997) y(536829, 537872)	State Plane NAD83	CSM, surface locations, P&D
Preferential recharge centroid coordinates[4]	s3(x,y)0	(492682, 537810)	x(492306, 493097) y(537686, 537934)	State Plane NAD83	CSM, modeling
Primary window elipse radii	s1r(x,y)	(95,61)	x(3, 403) y(2, 338)	m	RVZM, P&D, CSM
Secondary window elipse radii	s2r(x,y)	(77,61)	x(3, 388) y(2, 338)	m	RVZM, P&D, CSM
Preferential recharge window elipse radii[4]	s3r(x,y)	−760,225	x(309, 1211) y(54, 397)	m	CSM
Primary window Cr concentration[2]	s1c	126	3, 381	ppb	RVZM
Secondary window Cr concentration[2]	s2c	18	0.45, 53	ppb	RVZM
Total rate of preferential recharge[2]	totip	5303	469, 11036	mm/yr	RVZM
Percent of recharge in primary source[4]	s1p	10	1, 19	%	Geochemistry, literature, CSM
Percent of recharge in preferential source[4]	s3p	73	65, 81	%	Geochemistry, literature, CSM
Primary/secondary window arrival time[5]	t0s(1-2)	1999	1956, 2019	yr	RVZM, P&D
Window eccentricity (tilt)	s(1-3)corr	0	−1, 1	—*	RVZM, P&D
Western constant head[4]	wHead(N,S)	1895	1860, 1930	m	Data, literature, modeling
Eastern constant head[4]	eHead(N,S)	1580	1470, 1690	m	Data, literature, modeling
Percent of supply well screen pumped[4]	pm_pct	93	0, 100	%	Data, Literature
Mountain block vertical gradient[4]	wHeavGrad	−0.16	0, −0.3	—	Data, literature, modeling
Total mass of RDX available[5]	totalmass	1327	152, 3506	kg	Literature

Note: Parameter distributions are normal unless marked as follows: (1) lognormal, (2) truncnormal, (3) beta, (4)uniform , (5) Weibull.

* — = Not applicable.

Appendix D

Supplementary Information to Support Appendix C

CONTENTS

Figures

Tables

D-1.0 CONCEPTUAL SITE MODEL

D-1.1   Geologic Context

The Royal Demolition Explosive (RDX) project area lies on the western edge of the Pajarito Plateau. Underlying the plateau is a geologic feature consisting of roughly 250 m of varying sequences of poorly consolidated tuffaceous materials known as the Bandelier Tuff. The sequences of the Bandelier Tuff were deposited from volcanic eruptions roughly 1.25 and 1.6 million yr ago from the Valles Caldera to the west and can be generally classified into two members: the lower (1.6 million yr) Otowi Member and the upper (1.25 million yr) Tshirege Member. Separating the deposition of these two members was a brief pause in geologic activity when the Cerro Toledo Formation erosional sediments were deposited.

There is a large variety of surficial deposits at Technical Area 16 (TA-16), in both the canyons and on top of mesas. Modern alluvium and colluvium can be found within the canyons, while older alluvial fans compose part of the mesa-top sediment. The poorly sorted alluvium within Cañon de Valle and other local drainages is made up of medium- and fine-grained sands and volcanic cobbles, gravels, and sands derived from the Tshirege Member and the Tschicoma Formation. These sediments come from extensive outcrops of these units in the mountains to the west of TA-16, which form a large part of the Cañon de Valle watershed. Within the canyons proximal to the RDX site, this alluvium ranges between 5 and 9 ft in thickness (LANL 1998, 059577). These deposits perennially store alluvial groundwater. Mesa tops at TA-16 include widespread remnants of gravel deposits from early Pleistocene streams draining the Sierra de los Valles, which predated the incision of the modern canyons (Reneau et al. 1996, 055539). Because of their thickness and high porosity, mesa-top alluvial fans may also play a role in storing water from storm runoff and snowmelt (N3B 2019, 700561). Figure D-1.1-1 shows a vertical profile of the geologic sequences of the Bandelier Tuff and the underlying coarse alluvial Puye Formation sediments that pre-date the formation of the Bandelier Tuff. In the RDX plume area, the regional groundwater aquifer is largely within the Puye Formation sediments, with the exception of an area south of the plume where the water table intersects the volcanoclastic deposits of the Tschicoma Formation. Regional groundwater hydrology is discussed in further detail in sections D-1.2 and D-2.

Following the deposition of the Bandelier Tuff, erosion and faulting have modified the geology. Erosion of the tuff has created fingerlike mesas and canyons that extend west to east. TA-16 sits on one of these mesas located south of, and adjacent to, Cañon de Valle. The TA-16 260 Outfall discharged directly into the Cañon de Valle canyon bottom.

Extensive faulting has also been observed at the western edge of the Pajarito Plateau, known as the Pajarito Fault System (Figure D-1.1-2). The Pajarito Fault System is a narrow band of normal faults that trend to the north/northeast. Deep-seated normal faulting is expressed at the surface level by a mix of normal faults of variable magnitudes and monoclines (Gardner et al. 1999, 063492).

The Pajarito fault has extensive influence on the thickness and relative location of geologic units at the mountain block/plateau interface. It is the principal structural feature in the area and most likely plays a key role in the transfer of groundwater from the mountain block to the plateau. Because of intense fracturing, the fault zone probably is also an important infiltration zone for mountain front recharge (N3B 2019, 700561). Faulting has the ability to create fast pathways or hydraulic windows to the subsurface. The 260 Outfall is located in the TA-09 graben, an area that is suspected to be coincident with an area of high infiltration due to faulting and fractures (Figure D-1.1-3).

D-1.2   Hydrologic Context

The hydrologic system in the watershed includes surface water, springs, alluvial groundwater, vadose zone water, perched-intermediate groundwater, and regional aquifer groundwater. Water Canyon and its main tributary, Cañon de Valle, have their headwaters west of the Laboratory in the Sierra de los Valles within the Santa Fe National Forest. Surface water in Cañon de Valle is predominantly ephemeral and seasonally dependent on snowmelt and storm runoff. Only short reaches with perennial flow occur in Cañon de Valle, and these reaches are dependent on spring discharges. Alluvial groundwater in Cañon de Valle is recharged by streamflow and runoff from local precipitation and snowmelt.

Perched groundwater occurs at both shallow (referred to as shallow bedrock) and deep (referred to as perched-intermediate) levels of the vadose zone in the TA-16 area. Shallow bedrock groundwater zones occur at depths of 200 ft below ground surface (bgs) in upper units of the Tshirege Member of the Bandelier Tuff. Groundwater from these zones includes springs that discharge into canyons and small zones of saturation in tuff that are penetrated by shallow wells. Perched-intermediate groundwater occurs at depths of generally 600 ft bgs in the lower part of the vadose zone, primarily in the Cerro Toledo Formation, the Otowi Member of the Bandelier Tuff, and the Puye Formation. Groundwater in the two perched-intermediate zones is a mixture of mountain block recharge and mountain front recharge. Mountain block recharge originates in the highlands west of the Pajarito fault zone and consists of diffuse subsurface infiltration of snowmelt and surface water that percolates through the rock and recharges the regional aquifer. Mountain front recharge consists of mountain overland flow (generally streamflow) that infiltrates at the mountain front and the adjacent basin.

RDX-contaminated water initially entered the hydrologic system at the land surface and was transported down to the regional aquifer. The deposition of a significant inventory of water containing RDX occurred in mesa-top settling ponds or within sediments in small drainages near outfalls. RDX from the 260 Outfall that mixed with surface water and alluvial groundwater in Cañon de Valle acted as a hydraulic driver for a source of recharge to the vadose zone. The infiltration of surface water at outfalls in the surrounding areas moved soluble contaminants down into the shallow perched groundwater in the upper Tshirege Member. Infiltration into this perched zone mainly occurs through fast pathways such as Pajarito fault-related faulting and fractures.

Ultimately, this resulted in the deposition of RDX within the vadose zone. Previous reports have divided the vadose zone into two parts: upper and lower. The upper vadose zone is defined as extending from the surface to a depth of about 600 ft bgs. This section is composed of variably welded Bandelier Tuff and Cerro Toledo fluvial deposits. The upper vadose zone is, for the most part, unsaturated but contains thin ribbon-like zones of perched groundwater, some of which daylight as springs in the canyons.

The lower vadose zone extends from 600 ft bgs to the top of the regional aquifer (between 1000 and 1300 ft bgs) and includes the lowermost deposits of the Bandelier Tuff as well as thick sequences of generally coarse and highly heterogeneous fluvial sediments of the Puye Formation. The lower vadose zone, as defined here, includes both of the perched-intermediate groundwater bodies that are often referred to as the upper and lower perched zones. Significant amounts of RDX have been observed in these zones.

D-1.2.1   Upper Vadose Zone

Dissolved-phase RDX initially migrated into the subsurface through the surface water and alluvial groundwater pathways described above. Infiltration is more significant beneath canyons and gullies than mesa tops. The shallow bedrock beneath Cañon de Valle is composed of welded and relatively impermeable tuffs, and infiltration in this canyon bottom is thought to be strongest in areas where bedrock

has been fractured. In the RDX site, faults along the TA-09 graben cut roughly perpendicular to the canyon axis, and large amounts of stream and alluvial water loss occur in this part of the canyon (N3B 2019, 700561). Infiltration also occurs outside of the canyon bottoms at the mesa tops in locations where sufficient water is stored or accumulates. This type of ponding creates higher hydrologic heads with the ability to drive infiltration. The 260 Outfall pond and adjacent drainages are two examples of locations with enough inundation to allow varying amounts of seepage.

RDX containing wastewater was discharged from the 260 Outfall into Cañon de Valle, where it mixed with surface waters coming up from the canyon. The combined waters infiltrated into the alluvium and from there into the upper vadose zone. The amount of water that migrates through these vertical pathways is temporally variable and spatially dependent. Vertical movement is primarily controlled by gravity in unsaturated zones. However, water has the potential to move laterally at bedding contacts and in zones of perched water, which are driven by hydraulic gradients that generally trend to the east (LANL 2018, 602963). The result is that water tends to stairstep down through the vadose zone through a series of perched zones, likely expanding the lateral extent of the contaminant plume. This process occurs to a small degree in the upper vadose zone compared with the lower vadose zone, where much larger perched zones have been observed.

D-1.2.2   Lower Vadose Zone and Perched-Intermediate Groundwater

Two discrete perched-intermediate groundwater zones are believed to be below the RDX site in the lower vadose zone. The upper and lower perched-intermediate zones are separated by 80–150 ft of variably saturated rocks. Both zones have the potential to create a lateral pathway for contaminant transport. Because of the potential for lateral transport, contaminated water may leave the perched zones at a spatial location that is different from where the source entered the perched zone. Contaminated water eventually travels vertically from these zones, resulting in contaminated recharge to the regional aquifer.

Of the two perched-intermediate zones, the upper perched-intermediate zone is larger and more important for RDX lateral transport because of the spatial extent of saturation. The lower perched-intermediate zone is thought to be much smaller in its extent of saturation compared with the upper. The perched zones are generally continuous and in direct hydraulic communication locally, although that communication can be variable as a result of the heterogeneous geology present and the variable levels of saturation spatially. Perched groundwater appears to be supported by leaky confining beds made up of thin silt beds that are limited in their lateral extent.

The primary source of recharge to the perched-intermediate groundwater is thought to be dominated by mountain block recharge and mountain front recharge (N3B 2019, 700561). Monitoring of water levels in the perched-intermediate zones suggests that recharge from precipitation events at the surface is slow, and travel times are long, although there is evidence of fast pathways from the surface to the regional aquifer as well. These fast pathways could be the results of localized fault-related fracture networks. Geochemical analysis also suggests a large fraction of the perched water is similar to water sourced from the mountain block rather than from vertical infiltration sources above (LANL 2018, 602963). Mountain block recharge and mountain front recharge are thought to occur where steep gradients in the regional water table intersect gently dipping transmissive geologic strata (N3B 2019, 700561), creating the perched-intermediate zones. That is, as groundwater flows eastward from the mountain block towards TA-16, some groundwater is diverted laterally into the vadose zone. While mountain block recharge is similar to mountain front recharge, mountain front recharge is considered to be recharge, which occurs more shallowly than mountain block recharge.

Mountain front recharge is characterized by streamflow infiltration from upcanyon Cañon de Valle watershed drainages and the infiltration of overland flows. The mountain front recharge to the perched-intermediate groundwater occurs in an area extending from the Pajarito fault zone to the TA-16 area. Mountain block recharge is thought to make up approximately 66% of perched groundwater, with local mountain front recharge making up 34% (LANL 2018, 602963).

During the period of active releases at the 260 Outfall, wastewater containing RDX that had comingled with surface water infiltrated vertically and mixed with perched-intermediate water sustained by clean mountain block recharge and mountain front recharge, resulting in diluted RDX concentrations in the perched-intermediate groundwater. This contaminated water eventually flows from the perched-intermediate zones downward in vadose zone pathways and laterally in perched zones to recharge the regional aquifer.

D-1.2.3   Regional Aquifer Groundwater

The Puye Formation begins in the lower vadose zone and is characterized by coarse and highly heterogeneous alluvial fan sediments. The Puye Formation is up to several thousand feet thick in some locations (LANL 2018, 602963). The regional aquifer water table at the RDX site is mostly within the Puye Formation.

The shape of the regional water table is predominantly controlled by hydrologic recharge at the western boundary and discharge to the east. At the western boundary of the regional aquifer, recharge from the Sierra de los Valles mountain block provides higher hydraulic heads that force an overall west-to-east gradient. At the eastern boundary, the regional aquifer contributes to gaining stream conditions below the Rio Grande and is also expressed at the surface as discharges from springs in White Rock Canyon. Aside from the overall west-to-east hydraulic gradient within the aquifer, regional flows may also be influenced by local areas of infiltration (beneath canyons), heterogeneous lithology, and anisotropic aquifer properties. Pumping tests have shown a higher degree of lateral connectivity than vertical connectivity within the aquifer, suggesting hydraulic conductivities are generally higher laterally than vertically. Vertical differences in hydraulic heads and a lack of vertical propagation of pumping drawdown indicate some level of hydraulic stratification. This vertical anisotropy within the aquifer is likely caused by the depositional layering of the stratigraphic units that contain the regional aquifer.

D-1.3   RDX Transport Conceptual Model

RDX has been detected in surface water, springs, sediments, and alluvial, perched-intermediate, and regional groundwater at the site. The focus of the risk assessment is on RDX detected in the perched-intermediate zones and regional aquifer. The RDX transport conceptual model described here aims to briefly summarize the conceptualized modes and paths of RDX transport in these systems.

The primary source for RDX that has been detected in the perched-intermediate and regional groundwater at the site is largely thought to be the result of discharges of wastewater containing RDX from the TA-16 260 Outfall and pond to Cañon de Valle (Figure D-1.1-3). At the outfall, the water containing RDX was directly discharged into Cañon de Valle, where it mixed with surface water and alluvial groundwater in Cañon de Valle and infiltrated into the subsurface near the TA-09 graben (faults of the TA-09 graben are shown in the lower-right map of Figure D-1.3-1). Faulting in the TA-09 graben area intersects the canyon bottom, and significant stream loss has been observed in the vicinity of the faults (Figure D-1.1-3).

After infiltrating to the subsurface, water containing RDX is transported vertically via partially saturated flow through the porous geologic material of the Bandelier Tuff until it reaches saturated conditions in the perched-intermediate zones, though the potential exists for faster transport through fractures. There are two main perched zones at the RDX site, an upper and a lower zone (Figure D-1.3-2 and sections D-1.2.1 and D-1.2.2). The upper perched-intermediate zone occurs around 600 ft bgs, and hydraulic heads in the lower perched-intermediate zone indicate that zone is roughly 200 to 280 ft lower, 800 to 880 ft bgs (N3B 2019, 700561). A large portion of recharge to the perched-intermediate aquifers is understood to come from mountain front recharge and mountain block recharge that have no RDX (Figure D-1.3-1). This recharge composes the majority of total recharge to the perched zones, so it is most likely that water containing RDX is successively diluted by mountain front recharge and mountain block recharge each time it arrives at a perched zone.

The upper of the two perched-intermediate zones is larger and more extensive (Figure D-1.3-2). Concentrations over 100 ppb have been detected in the upper perched-intermediate zone in intermediate wells CdV-16-2(i)r and CdV-16-4ip. The lower perched-intermediate zone is much smaller in extent, and lower concentrations of RDX have been detected compared with the upper zone. Only a few monitoring wells have been completed in the lower perched-intermediate zone, with RDX concentrations detected around 20–23 ppb (R-25 screen 4 and CdV-16-4ip screen 2). Limited data exist for the lower zone, as the two well screens completed in this zone have been abandoned.

Once RDX arrives in the perched-intermediate saturated zones, it has a higher potential for lateral movement via saturated flow (Figure D-1.3-1). Eventual downward percolation from these perched zones provides contaminated recharge to the regional aquifer. Because of the potential for lateral transport in the perched-intermediate aquifer systems, RDX may not arrive at the regional aquifer in the same spatial location as it first infiltrated into the subsurface.

The degree of hydraulic communication between the perched-intermediate zones and the regional aquifer is thought to be relatively poor and spatially variable, depending on local hydrogeologic conditions and associated hydrostratigraphy (Figure D-1.3-1) (N3B 2019, 700561). Downward percolation and recharge to the regional aquifer is thought to occur through regions of preferential recharge or "hydraulic windows," although these flows have not been directly observed.

Once water containing RDX reaches the regional aquifer, it mixes with and is diluted by clean regional groundwater as it is being transported via hydraulic gradients. Lateral hydraulic connectivity within the regional aquifer has been demonstrated through observed drawdown during drilling, well development, and well pump tests (N3B 2019, 700561). Water level data from regional wells show a steep hydraulic gradient at the RDX site that flattens out near R-17 and R-19 just before the Los Alamos County supply wells; however, aquifer heterogeneity and sources of recharge to the regional aquifer have the potential to modify gradients locally. Section D-2 presents an in-depth discussion of hydraulic analyses of lateral and vertical gradients through time. To date, concentrations up to 22 ppb (regional well R-69 screen 2) have been detected in the regional aquifer. Figures D-1.3-3 and D-1.3-4 show the estimated horizontal and vertical extent of RDX in the regional aquifer in map view and cross-section, respectively.

D-2.0   HYDRAULIC ANALYSES OF LATERAL AND VERTICAL GRADIENTS

D-2.1   Introduction

Regional groundwater flow beneath the Pajarito Plateau is complicated and highly complex, as is typical in mountainous environments. As discussed in section D-1.2, groundwater flow typically originates at points of recharge in upland elevations and flows to points of discharge at lower elevations. At larger scales (>1 km), simplified approaches to conceptualizing flow patterns are valid enough to understand

regional flow patterns; however, these approaches require many limiting and simplifying assumptions to be made about the aquifer system. Assumptions include that the aquifer system is relatively homogeneous and isotropic, or at most has a simple layered configuration, that the water table approximately follows the topography of the land, that slopes of the ground surface are small compared with density of flow lines and equipotential lines used to characterize flow, and that under these ideal conditions simple algebraic functions are valid enough to approximate flow (Freeze and Cherry 1979, 088742). In most environments, these simplifying assumptions do not hold true at smaller scales (<1000 m) because of the heterogeneity of aquifer materials, geologic contacts between dissimilar units, the presence of faults, and/or localized recharge. After a broad pattern of groundwater flow is conceptualized at a site, water level observations can be used to test whether the conceptual model accurately reflects the observed data. If observations do not match the conceptual model, the conceptual model must be updated and refined to reflect the observations.

Using water levels from regional aquifer monitoring wells, hydraulic analyses can characterize magnitudes and trends of hydraulic gradients in the regional aquifer so that representative gradients can be simulated in the RDX regional aquifer model (RRM) such that the model accurately reflects actual conditions observed in the regional aquifer. Hydraulic analyses can also inform the conceptual model of interactions between the mountain block, RDX plume-area wells (some of which have strong, downward vertical gradients), and downgradient Los Alamos County water-supply wells. For this study, lateral and vertical gradients were investigated in detail in the western portion of the regional aquifer to determine if any long-term trends can be observed and to assess whether natural recharge mechanisms or supply well pumping are driving gradients that affect RDX transport.

Figure D-2.1-1 (modified from Freeze and Cherry 1979, 088742) shows the basic concepts of aquifer hydraulic head distributions in a site with upland recharge and lowland discharge to a river, such as the case on the Pajarito Plateau. The diagram depicts downward flow and the production of downward (negative) vertical gradients near the upland plateau shown on the right-hand side of the figure (region 1). At depth, bedrock prevents continued downward flow; groundwater flow is ultimately deflected horizontally (region 2), and no vertical gradients are observed. As groundwater flow approaches the discharge zone, flow turns upward and groundwater discharges to the valley stream shown on the left-hand side of the figure (region 3). In this region, equipotential contours are expected to increase with depth, indicating that upward (positive) vertical gradients are present that result in groundwater discharge to the stream. This example is a mirror image of the Pajarito Plateau, which has upland recharge to the west and lowland discharge to a river to the east.

In the western Pajarito Plateau, close to the mountain front where the RDX plume resides, the regional aquifer lies up to 1000 ft below the surface (Figure D-2.1-2). The large distance between the ground surface and the regional aquifer system means that topography likely has little to no impact on the regional aquifer water table.

The RDX plume lies close to the mountain front, where mountain block and mountain front recharge occur (Figure D-2.1-2). According to the conceptual model as seen in Figure D-2.1-1, this recharge should produce downward vertical hydraulic gradients in the regional aquifer at the site. Further east along the Pajarito Plateau, surface flows and recharge become greatly diminished because of the semi-arid climate at the surface; regional groundwater flow is expected to transition to largely horizontal flow in this region, with little to no vertical gradients present. Further to the east as the Rio Grande is approached, upward vertical gradients are expected as groundwater discharges to the river. Artesian wells have been observed in the Buckman well field, which supports the conceptual model of this area being a zone of discharge.

The steep canyons between mesas on the Pajarito Plateau channelize and concentrate flow at the surface into the canyon bottoms, resulting in focused recharge. Near the RDX plume, large amounts of recharge in Cañon de Valle have been observed along the streambed, resulting in perched zones of saturation within the vadose zone (Figure D-2.1-2) and water table mounding in the regional aquifer at R-25 (N3B 2019, 700561). Geologic heterogeneity and stratigraphy, contacts between units, and faulting can also alter the aquifer structure and impact local flow. While much of the regional aquifer system lies within alluvial and fluvial sediments of the Puye Formation in the RDX plume region, the Puye Formation is intersected by dacite flows from volcanic activity to the west. Contacts between highly conductive sands and gravels of the alluvial and fluvial Puye Formation sediments and the fine-grained poorly conductive volcanic formations have potential to alter flow patterns. Structural contours of the top of the Tschicoma Formation are shown in plan view in Figure D-2.1-3, and in cross-section in Figure D-2.1-4. Regional aquifer wells R-48, R-58, CdV-R-37-2, and CdV-R-15-3 are completed in the more permeable brecciated portions of the Tschicoma Formation.

In the following hydraulic analyses, the conceptual model of regional groundwater flow outlined above is tested and refined by analyzing the available groundwater level observation data. This is critical to ensuring that the regional aquifer hydraulic conceptual site model (CSM) is accurately depicted in the RRM. While the RRM or any aquifer model of a complex site must make simplifications in order to be numerically tractable, it is important to justify the simplifications with a thorough analysis of site data. In particular

1. The RRM uses hydraulic head boundary conditions to the east and west of the site to simulate the sloping water table.

2. Downward vertical gradients observed at the RDX site are generated in the model by (a) a vertical gradient where the aquifer intersects the mountain block quantified, with uncertainty, by these analyses, and (b) recharge sources at the water table.

3. Transient municipal water-supply pumping is included in the RRM, and the model is calibrated to match observed relationships between pumping events and water level changes. This includes a lack of response to transient events (short-term response) at any of the wells at the RDX site west of R-17.

Lateral and vertical hydraulic gradients are estimated at various depths in the aquifer system through time, time series are assessed for potential trends including long-term water level decline, and correlation between changes in hydraulic gradients and groundwater pumping from county supply wells through time is assessed.

The focus of the hydraulic gradient analyses presented in this section are to characterize and quantify long-term sustained trends and shifts in lateral and vertical hydraulic gradients. This is in contrast to immediate aquifer responses (e.g., During pumping, do gradients change?) which are typically followed by a period of recovery. The focus here is on long-term responses in the aquifer that result in more permanent shifts in hydraulic gradients.

D-2.2   Methods

To test the conceptual model outlined in the previous section, groundwater level data are analyzed to estimate lateral and vertical hydraulic gradients in the regional aquifer.

D-2.2.1   Water Level Data

Water level data from monitoring wells across the Pajarito Plateau are publicly available on IntellusNM, the public version of Los Alamos National Laboratory's (the Laboratory's or LANL's) Environmental Information Management (EIM) database (https://intellusnm.com).

Initially, water levels are not filtered or corrected as part of an exploratory data analysis presented to briefly look at long-term water table decline across the Pajarito Plateau. For this initial analysis, water levels for each screen port are aggregated to a monthly scale using a series of mean values. First the mean water level is calculated at 2-hr intervals in the day. Next the mean of the 2-hr means is calculated for each day. Lastly, the mean of the daily means is calculated for each month. The monthly mean results for some months in several wells appear to be anomalous results, therefore Cook's distance is used to identify monthly means to exclude from these analyses. A Cook's distance greater than or equal to 0.1 is used to identify outliers.

For the remaining analyses that involve calculating lateral and vertical hydraulic gradients, a more robust treatment and filtering of the water level data is performed. For these analysis, water level observations are filtered based on method and data quality. For instances where screen ports are replaced over time (e.g., multiscreened Westbay wells are converted to single completion wells), the port with the longest time series is utilized. Bad data and observation jumps (e.g., transducer slips) are removed and corrected for, respectively, based on manual review of the data. Because additional erroneous data records exist within a screen's time series, anomalous records are detected and removed using the anomalize R package (https://cran.r-project.org/web/packages/anomalize/anomalize.pdf). Specifically, the IQR (Inner Quartile Range) method is applied to the residuals from a STL (seasonal decomposition of time series by loess) decomposition of the water level time series. This results in the removal of observations that fall outside the limits of six times the interquartile range after removing both seasonality and trends from the time series. In some instances, visual inspection of the time series indicated that anomalous observations still existed, and such instances are manually removed. Water levels are then barometrically corrected by regression deconvolution (Toll and Rasmussen 2007, 104799) using publicly available tidal data and barometric pressures from LANL's TA-54 weather station. Water levels for each screen port are then aggregated to a weekly scale using the median value of all head values within a calendar week.

D-2.2.2   Horizontal Gradients – Three-Point Method

The three-point method detailed in Heath (1983, 700907) is used to calculate the magnitude and direction (azimuth) of lateral hydraulic gradients in the aquifer system. This method requires a set of three wells, each with known water level and geographic location (Figure D-2.2-1). A summary of the steps to compute the hydraulic gradient is as follows:

1. Rank wells based on water level: high, intermediate, low (1, 2, and 3 in the figure).
2. Draw a line between the high and low wells (gray line in the figure). Calculate location on this line where the water level is equal to the intermediate well's water level (red dot in the figure).
3. Draw a line from the intermediate well through the location computed in step 2 (red line in the figure); this represents a contour of water level equal to the intermediate well.
4. Draw a line perpendicular to the contour in step 3 through the low well's location (blue line in the figure).
5. Magnitude is equal to the difference in head between the intermediate and low wells, divided by the distance between the low well and the contour. Direction is equal to the azimuth of the line from step 4.

Well triplets are constructed using well screens at the same approximate depth below the water table. Well screens allow three depths to be investigated within the regional aquifer: the first at the water table, represented by the first regional aquifer screen in multiscreened wells; the second depth, referred to here as "mid-depth," represented by the second regional aquifer screen in multiscreened wells; and the third depth, referred to here as "deep," represented by the third regional aquifer screen in multiscreened wells.

First the well triplets used to establish the RRM hydraulic gradient targets are analyzed. Data for these well screens is limited in time since the RDX plume is relatively new and few wells have been drilled in the region to characterize the plume. However, further afield, regional wells have been installed for a much longer time. Therefore, the spatial context of analysis is expanded to include well screens with longer historic records. This expanded scope characterizes lateral and vertical hydraulic gradients in the RDX plume and downgradient region, focusing on the portion of the regional aquifer that lies between the RDX plume and supply wells PM-2, PM-4, and PM-5 to the east.

D-2.2.3   Vertical Gradients

The presence of vertical gradients can be assessed in the regional aquifer using wells with multiple screens, along with single-screened wells near to one another that are screened in different depths in the aquifer.

Vertical hydraulic gradients are calculated by taking the difference in observed water levels in the two screens (lower screen minus upper screen), divided by the absolute distance between the midpoint elevation of the screened intervals (Figure D-2.2-2). Negative vertical gradients occur when the lower screen has a lower measured water level compared with the upper screen, indicating downward flow in the aquifer, and vice versa for upward gradients.

Few multiscreened wells that have a long period of record for water levels exist near the RDX plume. Since vertical gradients are of particular importance for understanding RDX fate and transport, R-18 and R-47 are used to estimate the vertical hydraulic gradient in the RDX plume (Figure D-2.2-3).

D-2.2.4   Correlation to PM Well Pumping

The combined weekly gallons pumped for PM-2, PM-4, and PM-5 are computed using the daily pumped gallons reported by Los Alamos County (Figure D-2.2-4). A Spearman rank correlation is used to quantify the strength and direction of a monotonic relationship (i.e., linear or nonlinear) between total PM well pumping and lateral hydraulic gradient magnitudes and directions and vertical hydraulic gradient magnitudes. The sign of the Spearman correlation indicates the direction of association such that positive values indicate gradient magnitudes/directions tend to increase with increased total PM well pumping (and vice versa). A correlation of zero indicates no tendency of the gradient magnitudes/directions to increase or decrease when total PM well pumping increases. The correlation's absolute value increases towards 1 as the gradient magnitude/direction becomes a more perfect monotone function of total PM well pumping. Each Spearman rank correlation is accompanied by a statistical test to determine whether the correlation is statistically different from zero. If the *p*-value from the test is below the alpha level (0.001), the conclusion is that there is evidence of a monotonic association between the hydraulic gradient magnitude/direction and total PM well pumping.

D-2.2.5   Trends and Estimated Linear Changes

The Mann-Kendall (M-K) test for trend is utilized to quantify whether hydraulic gradients monotonically increase or decrease over time. Positive (negative) values of the test statistic indicate that the magnitude/direction tends to consistently increase (decrease) over time, but the trend may or may not be

linear. Each M-K statistic is accompanied by a statistical test to determine whether the statistic is statistically different from zero. A *p*-value from the test that is below the alpha level (0.001) indicates a monotonic trend in gradient magnitude/direction over time.

Sen's method (https://influentialpoints.com/Training/sens_estimator_of_slope.htm), with a 95% confidence interval for Sen's slope parameter, is utilized to estimate the linear rate of change in gradient magnitude/direction over the period of interest.

D-2.3   Results

In this section, results are presented for the hydraulic analysis investigations. First, long-term decline is analyzed using individual well screens at the water table. Next, lateral gradient results in space and time are presented using the three-point method described above. Finally, vertical gradients are analyzed for temporal trends.

D-2.3.1   Long-Term Water Table Decline

Long-term decline of water levels in the regional aquifer has been observed across the Pajarito Plateau for decades (Collins et al. 2005, 092028; Koch and Schmeer 2010, 108926). Previous work has largely concluded that supply well pumping is responsible for long-term decline; however, this ignores potential additional factors that could influence long-term water balance in the regional aquifer, such as reduced overall recharge due to higher evapotranspiration from an evolving climate at the surface, or reduced infiltration from precipitation due to extreme landscape changes from the Cerro Grande and Las Conchas wildfires in 2000 and 2011, respectively. Nevertheless, declining water levels suggest the potential for a "hinge effect" in the aquifer system: if water levels below the Pajarito Plateau were to decline at substantially greater rates than regions close to the mountain block (where heads are sustained from mountain recharge), this could cause a shift in overall hydraulic gradient magnitudes across the plateau.

Figure D-2.3-1 shows monthly average water levels for single completion (single-screen) wells in the regional aquifer, and the uppermost regional aquifer screen in wells with multiple screens. Red dots indicate outliers (based on Cook's distance greater than or equal to 0.1) and are excluded in the analysis. A linear regression line is fit to each time series, and the rates of change are plotted as a histogram in Figure D-2.3-2. Rates of change range from just above zero at R-69 screen 1 (suggesting increasing water levels) to close to −0.7 ft/yr at R-61 screen 1, with a mean of −0.354 (R-5 being representative of the mean at −0.349 ft/yr) and median of −0.375 ft/yr (R-14 being a representative of the median at −0.399 ft/yr). Results suggest that across the site, the regional aquifer water table is declining by about 0.34 ft per year.

The estimated linear rates of decline are plotted spatially in Figure D-2.3-3. The estimated rates are plotted against a weighted sum distance from PM wells (Figure D-2.3-4), where the weights are based on the annual average pumping from each well (Table D-2.3-1). Both plots suggest that the regional aquifer near PM well pumping shows greater rates of water table decline.

Results suggest there is a spatial component to these long-term declines, with larger rates observed within close proximity to county water supply wells. However, the relationship appears to diminish somewhere west of R-19 and east of CdV-R-15-3 (Figure D-2.3-4). This suggests that hydraulic gradients west of R-17 may not be affected by county supply pumping. The following analyses aim to (1) quantitatively assess the impact of PM well pumping on regional flow patterns in the RDX and downgradient region using water level data to estimate lateral and vertical hydraulic gradients through time and (2) test for correlation with supply well pumping. This will help determine whether a "hinge effect" is occurring due to spatial trends in water level decline, and if so, quantify the magnitude of that effect.

D-2.3.2   Lateral Gradient

Lateral gradient vectors (azimuth and magnitude) have been calculated specifically for the purpose of RRM targets, as well as more generally across the site. The gradients used as RRM targets in the plume area require the model to match the observed flow direction and magnitude. This, in turn, helps ensure that modeled velocities and RDX travel times are reasonable.

The following sections discuss the calculation and temporal analysis on RRM lateral gradient targets, and the wider sitewide targets, to determine whether changes in time due to PM well pumping are significant for model accuracy and predictive power.

RRM Targets

The RRM targets are the well triplets used as model calibration targets in the RDX plume for hydraulic gradient magnitude and direction. Time series of magnitude (Figure D-2.3-5) and azimuth (Figure D-2.3-6) for these vectors are plotted along with total nearby supply well pumping (PM-2 + PM-4 + PM-5). Supply well pumping is scaled to the range of gradient magnitude/azimuth values in plots to make them easily readable. A complete time series of supply well pumping including pumping magnitudes is shown in Figure D-2.2-4. Figure D-2.3-7 shows a plot of all computed hydraulic gradients for RRM target triplets over the period of record. Data availability for these well screens spans from 2018 to 2022; however, three of four triplets are limited to less than 3 yr of data.

Estimated hydraulic gradient magnitudes for RRM target triplets range from 0.028 to 0.048 between well triplets; estimated changes through time, however are on the order of 10^{-6} to 10^{-7} per year within each triplet. As discussed in the next section, these gradients in the RDX plume area are the strongest lateral hydraulic gradients that are measured in the regional aquifer throughout this analysis. Estimated azimuths range from 50.25 to 64.5 degrees; within each triplet, the estimated azimuth varies by less than 2 degrees through time.

For the purposes of modeling, the RRM hydraulic gradient targets are based on estimated 2014 water level conditions (N3B 2020, 700925); however, they are very similar to the computed medians in magnitude and azimuth. The median computed hydraulic gradients for RRM model target triplets are compared with model targets in Table D-2.3-2 and compared visually in Figure D-2.3-8. This suggests that the gradients the model is calibrated against are an accurate long-term representation of the flow system.

Trends Through Time

Data are limited in time to assess long-term trends for the RRM hydraulic gradient targets: while triplet {R-47, R-63, R-68} has almost 5 yr of data, the remaining have less than 3 yr of data, with {R-25 S5 (screen 5), R-63, R-68} having less than 1 yr of data. While the amount of data is sufficient to estimate the magnitude and direction of the hydraulic gradients for the purposes of determining model targets, additional data will need to be collected to assess potential trends. The tests for trend results presented here should be considered preliminary, uncertain, and subject to change with time as more data are collected.

Both the M-K test and linear estimates suggest decreasing hydraulic gradient magnitude over the period of record for all triplets except for {R-18, R-47, R-69 S1}, which is not statistically significant (Table D-2.3-3).

Correlation to PM Well Pumping

The limited data available for RDX plume hydraulic gradient triplets also prevents assessing confident assessment of the correlation with PM well pumping. As with the trend results, the correlation results presented here should be considered preliminary, uncertain, and subject to change with time as more data are collected.

Two gradient magnitude triplets ({R-18, R-47, R-69 S1} and {R-47, R-63, R-68}) have high *p*-values suggesting no evidence of correlation (Table D-2.3-3). Triplet {R-47, R-68, R-69 S1} shows a small negative correlation with PM well pumping, meaning that increases in PM well pumping correlate with decreasing lateral hydraulic gradient magnitude. The mechanism for why PM well pumping would be correlated to a decrease in hydraulic gradient is unclear. This result is likely erroneous because of the limited period of record.

The triplet {R-25 S5, R-63, R-68} shows positive correlation with PM well pumping but has less than a year of available data. Since R-25 screen 5 has been abandoned, no further data will be available for this triplet in the future.

Gradient azimuth correlation is shown in Table D-2.3-4. Three of the four gradient azimuth triplets indicate small but significant correlation with PM pumping; however, all target triplet azimuths vary less than 1 degree over the period of record (Figure D-2.3-6), indicating high regularity in direction.

Water Table Triplets

Because of the limited data mentioned above, the analysis has been extended to additional wells in the RDX plume region, and areas downgradient of the RDX plume in the direction of the PM wells to the east. In this expanded region, much more data are available, and well triplets are selected with a focus on obtaining screens with particularly long water level records so that trends and correlation with PM well pumping can be assessed. Well triplets are constructed using well screens at the same approximate depth below the water table. This section focuses on screens at the water table, represented by the first/highest-elevation regional aquifer screen in multiscreened wells and by single-screened regional aquifer wells.

Time series of magnitude (Figure D-2.3-9) and azimuth (Figure D-2.3-10) are plotted along with total nearby supply well pumping (PM-2 + PM-4 + PM-5). Supply well pumping is scaled to range of gradient magnitude/azimuth values in plots to make them easily readable. A complete time series of supply well pumping that includes pumping magnitude is shown in Figure D-2.2-4. Figure D-2.3-11 shows a plot of all computed hydraulic gradients for RRM target triplets over the period of record. Data availability for these well screens spans from 2008 to 2022 with most triplets having 10+ years of data.

Estimated hydraulic gradient magnitudes at the water table are higher in triplets located to the west of a roughly vertical line made by wells R-2, R-60, R-17, R-19, and R-27, compared with triplets located to the east of these wells (Figure D-2.3-11). The triplets to the west of this line are immediately downgradient of the RDX plume and range in magnitude from 0.022 to 0.025 m/m, slightly less than those measured upgradient in the RDX plume, as discussed in the previous section on model targets. Hydraulic gradient azimuths range from 43 to 104 degrees between well triplets in the west, most generally pointing east-northeast.

To the east of wells R-2, R-60, R-17, R-19, and R-27, hydraulic gradients are estimated to be about an order of magnitude less compared with the west, ranging from <0.001 to 0.01 m/m with most falling between 0.001 and 0.006 m/m. Hydraulic gradient azimuths range from −5 to 165 degrees, but most generally point east-northeast.

The median hydraulic gradients west of wells R-2, R-60, R-17, R-19, and R-27 match well with modeled gradients in the RRM (Figure D-2.3-12). East of these wells, measured hydraulic gradients are much smaller compared with those modeled. This is due to a lack of water level targets in this portion of the model and a lack of degrees of freedom (e.g., ability to calibrate; see Appendix C regarding RRM structure) in the hydraulic conductivity field for this portion of the regional aquifer. Since model simulations out to 2200 do not indicate RDX will come anywhere close to this area of regional aquifer, this area is not the focus of model development.

Trends Through Time

Hydraulic gradients at the water table are highly regular, though long-term time series indicate small steady increases in magnitude through time for most areas of the regional aquifer between the RDX plume and the PM wells. Immediately downgradient of the RDX plume at well triplet {R-60, R-17 S1, R-18}, the estimated hydraulic gradient magnitude increases approximately 1.8% from 0.022 to 0.0224 m/m, over the 10+-yr period of record from 2011 to 2022 (Figure D-2.3-9), at an estimated linear rate of 6.13E-07 yr^{-1} (Table D-2.3-5). While gradients generally decline in magnitude to the east, time series plots indicate small increases in time throughout the region. The estimated magnitude of the next downgradient triplet {R-60, R-17 S1, R-14} is approximately half of well triplet {R-60, R-17 S1, R-18} and increases approximately 7.2% from 0.011 to 0.0118, over the 10+-yr period of record, at an estimated linear rate of 1.28E-06 yr^{-1}.

Trends in azimuth indicate that some areas are trending more northward (decreasing azimuth), and some areas are trending more southward (increasing azimuth), but overall, the direction of flow through time is highly regular. For triplets west of wells R-2, R-60, R-17, R-19 and R-27, changes in azimuth are very small, on the order of 1–2 deg over a 10+-yr period. To the east of these wells, azimuth varies several degrees over the 10+-yr record, with triplet {R-2, R-1, R-14} varying up to 20 deg and {R-33 S1, R-17 S1, R-14} varying up to 10 deg. Both triplets are near PM-4 and PM-5, which are known to impact water levels to some degree in this region.

Correlation to PM Well Pumping

The results of tests for correlation between changes in hydraulic gradient magnitude and azimuth and total supply well pumping (PM-2 + PM-4 + PM-5) are shown in Tables D-2.3-5 and D-2.3-6, respectively, and in Figure D-2.3-13. Statistically significant positive correlation (*p*-value <0.001) is generally observed in hydraulic gradient magnitudes in the north and east, meaning that increases in PM well pumping are correlated to increases in observed hydraulic gradient magnitudes. Significant correlation is also generally seen with changes in azimuth in the north and east meaning that increases in PM well pumping are correlated to changes in the direction of hydraulic gradients. Significant correlation with magnitude and azimuth is generally not seen in southwest triplets that include well screens from R-48, CdV-R-37-2, and CdV-R-15-3. While hydraulic gradient magnitudes for triplets that include these wells are increasing (Figure D-2.3-9 and Table D-2.3-5), changes through time do not appear to be correlated to PM well pumping. Most wells in this region are completed in the Puye Formation, whereas the R-48, CdV-R-37-2, and CdV-R-15-3 water table screens are located in the Tschicoma Formation (Figure D-2.1-3). Therefore, local geology may have a large impact on how drawdown from PM well pumping is propagated through the regional aquifer in this region.

Mid-Depth Triplets

This section addresses well screen triplets using screens from wells that have at least a second screen in the regional aquifer, referred to here as "mid-depth." The screens selected include the lower-elevation regional aquifer screen in dual-screened wells and the second regional aquifer screen for wells that have multiple screens in the regional aquifer.

Time series of magnitude and azimuth are plotted along with total nearby supply well pumping (PM-2 + PM-4 + PM-5) in Figures D-2.3-14 and D-2.3-15. Supply well pumping is scaled to the range of gradient magnitude/azimuth values in plots to make them easily readable. A complete time series of supply well pumping that includes pumping magnitude is shown in Figure D-2.2-4. Figure D-2.3-16 shows a plot of all computed hydraulic gradients for RRM target triplets over the period of record. Data availability for these wells' screens spans from 2004 to 2022; however, none of the triplets span that entire period. Triplets to the east of R-17 and R-19 have about 10 yr of data, and triplets in the west have about 5 yr of data. The triplet including R-69 screen 2 spans the west and east regions, and data are limited to about 2 yr. Azimuth results from this triplet should be considered extremely approximate given the narrow proportions of this triplet and the large distance over which the hydraulic gradient is estimated.

The estimated hydraulic gradient magnitude at mid-depth is higher in triplets located to the west of R-17 and R-19 compared with triplets located to the east of these wells (Figure D-2.3-16), though the available mid-depth screen data is limited to wells largely to the south of the RDX plume and not directly downgradient. Nevertheless, the estimated hydraulic gradient magnitudes are very steady in this region, ranging only from 0.024 to 0.026, consistent with the estimated lateral gradients at the water table at the same approximate distance from the mountain front. Hydraulic gradient azimuths also appear very regular in this region to the west, ranging only from 73 to 76 deg between well triplets.

To the east of R-17 and R-19, hydraulic gradients are estimated to be about an order of magnitude less compared with the west, ranging from 0.002 to 0.009 with most falling between 0.002 and 0.006. Hydraulic gradient azimuths range from 5 to 110 deg, with most generally pointing east and northeast.

Trends Through Time

Though limited in time, neither substantial changes nor trends in magnitude and azimuth are apparent over the period of record (Tables D-2.3-7 and D-2.3-8). The Mann-Kendall and estimated linear change results are inconclusive and inconsistent with one another, suggesting no overall trend is present in magnitude or azimuth. Despite the limited amount of data in time, observed gradient magnitudes are extremely consistent in triplets to the west of R-17 and R-19, varying only by about 1–2% over the period of record. To the east of R-17 and R-19, hydraulic gradient magnitudes appear much lower and more variable in time. For example, {R-20 S2, R-19 S4, R-51 S2} is one of the more regular triplets to the east of R-17 and R-19; however, gradients change up to 16% over time, fluctuating between 0.0024 and 0.0028 (Figure D-2.3-14). Well triplet {R-17 S2, R-33 S2, R-51 S2} appears the most variable, with gradient magnitude changing up to 50% over time, fluctuating between 0.006 and 0.009. The Mann-Kendall test suggests roughly a third of the triplets have no trend in magnitude or azimuth, and estimated linear changes range from positive to negative.

Correlation to PM Well Pumping

The results of tests for correlation between changes in hydraulic gradient magnitude and azimuth and total supply well pumping (PM-2 + PM-4 + PM-5) are shown in Tables D-2.3-7 and D-2.3-8, respectively, and in Figure D-2.3-17. While trends in time are not apparent in the hydraulic gradient magnitude and azimuth in mid-depth well screen triplets, supply well pumping shows high correlation to changes and thus appears to have a stronger influence on gradients at this depth.

Statistically significant positive correlation (*p*-value <0.001) with PM well pumping and hydraulic gradient magnitude are observed in nearly all mid-depth well triplets, meaning that increases in PM well pumping are correlated to increases in observed hydraulic gradient magnitudes. The exceptions are (1) the well triplet containing R-69 screen 2, which because of its limited data in time should not be considered conclusive and (2) well triplet {R-20 S2, R-52 S2, R-53 S3} which, because it is to the east of the PM wells, makes plausible a negative correlation indicating PM wells are correlated with decreasing

gradients. Significant correlation is also generally seen with changes in azimuth in nearly all mid-depth well triplets. PM well pumping in the north appears to be correlated to decreasing (more northerly) changes in direction of hydraulic gradients, and in the south to increasing (more southerly) changes in direction. Greater correlation with magnitude and azimuth is seen in the western triplets that include well screens from CdV-R-37-2 and CdV-R-15-3, compared with those estimated at the water table. Despite CdV-R-37-2 and CdV-R-15-3 screens being in the Tschicoma Formation (Figure D-2.1-3), PM well pumping appears to have a greater influence on hydraulic gradients in the regional aquifer at this depth.

Deep Triplets

This section includes well screen triplets using screens from wells that have a third screen in the regional aquifer, referred to here as "deep"; however, data are extremely limited for this depth. Between the RDX plume and the PM supply wells, only four wells contain a third screen in the regional aquifer. Data availability for both triplets span from 2005 to 2011. Time series of magnitude and azimuth are plotted along with total nearby supply well pumping (PM-2 + PM-4 + PM-5) in Figures D-2.3-18 and D-2.3-19. Figure D-2.3-20 shows a plot of all computed hydraulic gradients for RRM target triplets over the period of record.

The estimated hydraulic gradient magnitudes are very similar between the two triplets, ranging from only 0.0305 to 0.0307 between the two, and appear highly regular through time. Magnitudes are similar to estimated gradients at the water table and mid-depth at the same approximate distance from the mountain front. Hydraulic gradient azimuth also appears very regular in time for the two triplets. Triplet {CdV-R-37-2 S3, R-19 S4, CdV-R-15-3 S5} fluctuates only between 46.5 to 47.25 deg over the 6-yr period, and {CdV-R-37-2 S3, R-25 S6, CdV-R-15-3 S5} fluctuates much less but shows an apparent slow and steady decrease from about 58.2 deg down to 57.5 over the period of record.

Trends Through Time

Neither strong trends nor substantial changes in magnitude or azimuth are apparent over the period of record for deep triplets (Tables D-2.3-9 and D-2.3-10). The Mann-Kendall test for triplet {CdV-R-37-2 S3, R-19 S4, CdV-R-15-3 S5} indicates a lack of significant trend in magnitude through time, though the estimated azimuth through time suggests an overall small rate of decline. The Mann-Kendall test and linear estimates for triplet {CdV-R-37-2 S3, R-25 S6, CdV-R-15-3 S5} both suggest slightly decreasing gradient magnitudes through time, and estimates of azimuth also appear to be decreasing through time. In both triplets, the estimated hydraulic gradient magnitude and azimuth are extremely regular through time, varying less than 1–2% over the period of record.

Correlation to PM Well Pumping

The results of tests for correlation between changes in hydraulic gradient magnitude and azimuth and total supply well pumping (PM-2 + PM-4 + PM-5) are shown in Tables D-2.3-9 and D-2.3-10, respectively, and in Figure D-2.3-21.

Statistically significant positive correlation (*p*-value <0.001) with PM well pumping and hydraulic gradient magnitude is observed only in triplet {CdV-R-37-2 S3, R-25 S6, CdV-R-15-3 S5}, and significant correlation with azimuth is observed only in triplet {CdV-R-37-2 S3, R-19 S4, CdV-R-15-3 S5}. While some changes in magnitude and azimuth appear to be correlated to PM well pumping at this depth, deep triplets show very little change in gradient magnitude and azimuth through time, indicating any impact is likely quite small in magnitude.

D-2.3.3   Vertical Gradient

Vertical gradients are calculated using vertical well screen pairs from wells that have at least two screens in the regional aquifer. Between the RDX plume and the PM supply wells, several multiscreened wells are available for analysis, and data availability spans from 2000 to 2022. Not all well screen pairs have water level records over this entire period; however, most pairs have at least 10 yr of data. Time series of vertical gradient magnitude are plotted along with total nearby supply well pumping (PM-2 + PM-4 + PM-5) in Figure D-2.3-22. Figure D-2.3-23 shows a cross-section plot showing the median computed vertical gradient and the wells' easting.

The estimated vertical gradients are highest in the west and decrease rapidly to the east. R-25 is the closest well to the mountain front, and screens 2 and 3 have the largest measured vertical gradient; magnitudes appear to decline rapidly with distance from the mountain front.

Trends Through Time

While spatial patterns are evident in vertical gradients, magnitudes appear much more variable through time compared with the variability in lateral gradients. Note that this could be due to different barometric influences (e.g., well barometric efficiency), especially when deep screens are involved. In other portions of the regional aquifer where more recent modern wells are located with high barometric efficiency, changes are so similar in construction that the barometric influence tends to be in lockstep. However in the RDX and downgradient region, older wells (like R-25, the Cañon de Valle [CdV] wells, etc.) could have different barometric responses. While barometric correction is performed on the water level data here, it is an inexact correction.

Despite large changes in magnitude, and water level records that span 10+ yr, long-term trends in vertical gradient are not apparent over the period of record. While the Mann-Kendall test indicates significant trends in magnitude through time, the estimated linear changes are very small (Table D-2.3-11) In the time series, the variability in gradients appears to overwhelm any small trends that might be apparent through time.

Correlation to PM Well Pumping

The Spearman test for correlation is used to look at whether the observed high variability in vertical gradients may be related to supply well pumping. The results of tests for correlation between changes in vertical gradient magnitude and total supply well pumping (PM-2 + PM-4 + PM-5) are shown in Table D-2.3-11 and in Figure D-2.3-24.

Statistically significant positive correlation (p-value <0.001) with PM well pumping and hydraulic gradient magnitude is observed only in wells near the supply wells. As distance increases, less correlation is observed. In the RDX plume region, changes in vertical gradients appear uncorrelated to downgradient supply well pumping.

D-2.4   Discussion

The hydraulic analysis results presented above show that strong lateral gradients are present in the western portion of the regional aquifer, close to the mountain block where the RDX plume is located, and that lateral gradient magnitudes dissipate quickly with distance from the mountain front. Combining all lateral gradients at all depth horizons into a single plot, a strong decline in lateral magnitude from west to east is clearly evident (Figure D-2.4-1). A similar pattern is observed spatially with vertical gradients in the regional aquifer, which have been hand-contoured in Figure D-2.4-2. The largest vertical gradients are observed in R-25, the closest multiscreened well to the mountain block, and drop rapidly with distance

from the mountain front. Further to the east, vertical gradients are small, but measurable and consistent. Estimated vertical gradients at R-17 and R-19 are roughly an order of magnitude less than those observed in the RDX plume area.

The presence of strong lateral and downward vertical gradients in the RDX plume region agrees with the conceptual understanding of regional groundwater flow patterns and expected structure of equipotential contours from recharge in mountainous environments. In this type of environment, recharge is expected to occur close to the mountain front, producing strong lateral and vertical gradients locally that quickly dissipate with distance away from the mountain block. While generally flow is expected to occur from west to east, local to the RDX plume and immediately downgradient, flow appears to be deflected to the northeast. This is likely a combination of spatially variable recharge and heterogeneous geology of the regional aquifer; the large low-permeability Tschicoma dacite unit to the south likely affects regional flow patterns.

Tests for correlation between supply well pumping and changes in lateral gradients indicate supply well pumping does have some degree of influence on gradients across the site. However, the influence diminishes rapidly with distance. At the water table, statistically significant positive correlation (*p*-value <0.001) is observed in hydraulic gradient magnitudes and azimuths to the north and east. Significant correlation with gradient and azimuth is generally not seen in triplets to the southwest that include well screens from R-48, CdV-R-37-2, and CdV-R-15-3. The large low-permeability Tschicoma dacite unit to the south likely impacts how drawdown from PM well pumping is propagated through the regional aquifer in this region.

Results for mid-depth triplets in general show higher correlation with PM pumping compared with the water table triplets, including triplets with well screens from R-48, CdV-R-37-2, and CdV-R-15-3. This is consistent with previous observations in the regional aquifer where lower screens show greater response to supply well pumping compared with screens at the water table (McLin 2005, 090073; McLin 2006, 092218). While gradients appear more correlated to PM well pumping at this depth, long-term trends are less apparent. The two deep triplets show weak or no correlation with PM well pumping with magnitude; however, the triplet closer to the supply wells, {CdV-R-37-2 S3, R-19 S4, CdV-R-15-3 S5} shows relatively high correlation between azimuth and supply well pumping. Despite the high correlation, the magnitude of variability in azimuth is extremely low, ranging less than 1 deg over the 6-yr period of record. Therefore, while highly correlated, the apparent magnitude of impact from pumping appears very small.

Testing for correlation with PM well pumping and vertical gradients in the RDX plume and immediate downgradient region show no correlation with supply well pumping. However, vertical gradients in wells further downgradient and in closer proximity to PM wells show higher correlation to supply well pumping. Wells in very close proximity to the supply wells that are clearly impacted by supply well pumping, such as R-20 screen 2 and screen 3, show very high correlation (−0.926) to supply well pumping.

D-2.5   Conclusions

Though small long-term trends are evident, the regularity of hydraulic gradients in the regional aquifer suggests that impacts from supply well pumping are quite minimal in the RDX plume and downgradient area of the regional aquifer. Additionally, the observed lateral and vertical gradients in the RDX plume region are roughly 1–2 orders of magnitude higher than those downgradient and near to the supply wells. Recharge mechanisms at the mountain front are therefore far more likely to control the magnitude and direction of groundwater flow in this region of the aquifer compared with supply well pumping. The results do indicate that supply well pumping has a measurable impact on hydraulic gradients in the regional aquifer; however, the impact diminishes quickly with distance from the supply wells. For most triplets in

the RDX plume and downgradient, linear estimates project changes on the order of 10^{-6} to 10^{-8} m/m per year across all depth horizons. In the context of contaminant fate and transport modeling, a difference of this magnitude in modeled hydraulic gradient is negligible.

Given the highly regular observed gradients in the regional aquifer, and minimal meaningful impact from wells, a steady-state assumption of groundwater flow would likely be a valid approach for purpose of modeling ambient transport of RDX in the regional aquifer for the length of time investigated by the RRM (70 yr). Despite its lack of influence on groundwater flow in the RDX plume area, supply well pumping from PM-2, PM-4, and PM-5 will nonetheless also be added to the RRM. The results of the analysis presented here are used to inform how PM well pumping will be included and calibrated against in the model.

Lastly, the results of this analysis suggest that the way the western head boundary condition was modeled in previous iterations of the RRM should be modified to more accurately reflect the observed vertical gradients present in the regional aquifer. Previously in the RRM, the western head was treated as a constant head with uniform pressure with depth (no vertical gradient). Based on a review of the conceptual understanding of the site, a vertical head gradient is more appropriate for this boundary condition, and a vertical gradient has now been included in the RDX plume western boundary (section D-4.8).

D-3.0   MODEL CONSTRUCTION ADDITIONAL DETAILS

The first level of refinement for the RRM mesh covers a larger area of interest (from 492100 to 494800 m easting and from 537300 to 539600 m northing in New Mexico State Plane coordinates) as well as major wells in the wider region of interest (R-17, R-19, CdV-R-15-3, CdV-R-37-2, R-58, R-48, and R-26). Note that no RDX has been detected at these wells. The second level of refinement includes wells where RDX has been detected (R-68, R-69, R-18, R-63, and R-25) as well as some area downstream of these wells (from 492100 to 494000 m easting and from 537600 to 538000 m northing).

Reducing resolution deeper in the aquifer increases computational efficiency. The orthogonal mesh has faster runtimes than an irregular mesh. It also amounts to 30% fewer nodes than an equivalent irregular mesh for the same vertical resolution in the area of interest. This mesh is then converted from a hexagonal mesh to a tetrahedral mesh for use in the Finite Element Heat and Mass transfer code (FEHM) [(Zyvoloski 2007, 700904); https://fehm.lanl.gov/]. Detailed quality checks on the mesh are made throughout the process, verifying that LaGriT correctly tags nodes as inside or outside the domain, tags facies and geologic units correctly, and maintains high aspect ratios (>0.5) and positive volumes in all elements [(Gable et al. 1996, 700887); https://lagrit.lanl.gov/]. Errors in the meshing step can affect FEHM groundwater modeling calculations, so verifying the accuracy of the mesh is a critical step for a robust groundwater model.

Figure D-3.0-1 shows the vertical dimension mesh refinement in cross-section, with 4× vertical exaggeration for visual clarity. The model layering is designed to provide finer resolution near the surface in the plume area with increasing grid cell size at depth in order to make model runtimes tractable. Units from the geologic framework model (GFM) are shown, although the model makes use of the pilot point method (described in section D-3.2.3) to assign hydrologic material properties rather than linking them to specific model layers (geology is used to define volcanic and sedimentary unit distributions for hydraulic conductivity). The plume area is entirely within the Puye Formation, and is not predicted to expand into other units (although the Tschicoma [Tvt2] formation to the south of the plume area may play a role in hydraulic behavior in that area). Therefore, the specific delineation of separate hydrostratigraphic units using conforming model layers is not performed nor is it related to the vertical mesh refinement scheme.

D-3.1 RDX Regional Model Input Parameter Distribution Development

The purpose of the RRM is to simulate the transport of RDX in the future towards potential downgradient points of compliance in the regional aquifer.

D-3.1.1 Overview

Table D-2.5-1 presents all model input distributions, and Appendix C, section C-2.4, presents a brief overview of the distribution development process for model input parameters. This section covers distribution development in much more detail, including an overview of modeling tools used to inform RRM parameters (RDX Vadose Zone Model [RVZM] and the Pipe & Disk Tool) and a detailed explanation of all decisions made during distribution development for each parameter individually. Representing uncertainty in model inputs often means finding a balance between uncertainty and physical reality. Developing wide distributions may seem conservative in principle, but this approach can lead to unrealistic model results. Characterizing the current state of knowledge of stochastic inputs presents many challenges, especially if the data available are limited or have limited relevance to the site. Relationships among these inputs may also be important to represent but are typically complex or difficult to define. Often special adjustments must be made to account for reduced credibility in particular data. If parameters are strongly related to one another, a correlation structure may be developed for input to the model. Other techniques such as regression models may be used to incorporate relationships between the information available and the desired parameters.

The RRM necessarily represents a simplification of the coupled hydrogeologic and chemical processes in the regional aquifer. From a statistical perspective, the model parameters are "conditioned" on this simplification that defines the physical process the parameter is intended to represent. No matter the amount or quality of data available, there is no way to know the true value of the parameter to be represented. The data available represent a sample of the population as defined by the conditioning on the model structure. This disconnect is referred to as sampling error—the uncertainty resulting from not knowing every value in the population. Although it is not possible to explicitly address sampling error in distribution development, assuming the sample is unbiased and representative, makes inferences possible about the population using a variety of techniques.

Because the distribution of the average is typically of interest, bootstrapping methods are useful in distribution development. Bootstrapping methods sample the data with replacement and calculate the statistic of interest (in this case the average) from a particular data set. This process can be repeated many times (usually 1000 or more) to produce representative averages. Bootstrapping is particularly useful for data sets smaller than n=30 but should not be used for data sets smaller than n=7 or 8.

In some cases, the data represent measures of uncertainty rather than the raw data themselves, and this uncertainty should be accounted for in distribution development. Depending on the parameter and the source, this uncertainty may be a standard deviation or variance of raw values in a study that measured the parameter of interest directly for several individuals or areas. Some studies from which data are gathered for the RRM distribution development use models to derive values for the parameter, in which case the study may provide a single estimate of the parameter and a standard error of estimation. Other studies may have been conducted for some purpose other than estimating the parameter of interest, but they may provide the parameter for reference. In these cases, it is common to find a table with the estimate(s) of the parameter and some associated uncertainty without an explanation of what that uncertainty is meant to represent. This makes accounting for the uncertainty in distribution development challenging, and professional judgement may be required to make assumptions on the most likely meaning of the reported uncertainty.

When uncertainty estimates are available, Monte Carlo (MC) simulation is a useful technique to develop a distribution. Just as MC simulations can propagate uncertainty throughout a model, this method is also useful for representing uncertainty on a smaller scale, such as for a single parameter. By assuming some distributional form applies to the individual measurements reported, MC simulation techniques can be used to develop the distribution of interest. Typically, a normal or lognormal distribution is applied to each measurement. A draw is taken for each measurement to represent a plausible average from that source, and the average across all sources is taken to represent a plausible average for the parameter suitable for input to the model. This process is repeated many times to obtain a set of averages, which a final distribution can be fit to.

Modelers and statisticians work in conjunction to make decisions regarding the relevance and usage of sparse data. Combining subject matter modeling expertise and statistical expertise ensures that the distribution used adequately represents, but does not overstate, uncertainty in the parameter of interest. Although these decisions inevitably introduce subjectivity into the process, the resulting distribution tends to be more representative of the most likely values of the parameter of interest. Further discussion of the distribution development process can be found in "Scaling Input Distributions for Probabilistic Models" (Black et al. 2019, 700892).

D-3.1.2   Available Data and Other Lines of Evidence

Distribution development combines all sources of available information, here called "lines of evidence," into probability distributions representing the possible values of a given parameter at the spatial and temporal scale of the model. For the RRM, lines of evidence include observational data at the site, information or data from reviews of available literature, the RVZM, and the Pipe and Disk (P&D) analytical screening tool. Distributions are needed for each of the calibrated parameters in the RRM. While there are 423 calibrated parameters, some share the same input distribution when there is not enough available information to develop a separate distribution. For example, in the case of lateral hydraulic conductivity, K_x and K_y at a pilot point location use unique parameter draws during each calibration iteration; however, there are no data to develop separate distributions for K_x and K_y, so their distributions are identical, even though their draws and, ultimately, calibrated values, will differ. All unique distributions are shown in Table D-2.5-1 and are discussed individually in the sections that follow.

The RVZM is used as a line of evidence for some of the RRM parameters. It also makes use of distribution development for other parameters, especially material properties, many of which it shares with the RRM. Parameters that are used in both the RVZM and RRM will include discussion of distribution development for both models.

D-3.1.3   Well Data and Literature

There is extensive data to be found in the literature for RRM distribution development. The data is considered in the context of the CSM and, if needed for a given distribution, additional lines of evidence are also considered. Literature used to inform distribution development varied by parameter; however, LANL site-specific data were always preferred. Some sources of information in the literature include borehole data (core samples), geophysical methods, and pumping test data. Databases are built to collect, store, and update this type of observational data. For all parameters, the RDX compendium, a collection of studies pertaining to the RDX project site and performed by LANL (LANL 2018, 602963), was searched for data and information. Many additional LANL reports were also used in data collection and are referenced and described in subsequent sections of this report. Peer-reviewed scientific literature and reports from analogous sites (e.g., the Nevada National Security Site) were reviewed, and data and/or information were extracted where they pertained to the RDX site and/or could be used to inform

distribution development. Well-drilling logs were used for geophysical measurements taken, as wells were drilled in or near the RDX site. Finally, expert opinion, especially from LANL scientists and engineers, was used as source of information and to interpret data, for example in selection of representative porosity measurements from geophysical logs.

D-3.2   RDX Vadose Zone Model

The RVZM is considered as another line of evidence in distribution development where no data or literature previously exist to inform the parameter. In particular, it is used to estimate travel times and pathways of RDX from its infiltration below the surficial alluvial aquifer to the top of the regional aquifer water table and to help formulate distributions of RDX concentration and recharge fluxes to the RRM.

The RVZM was initially developed by LANL and solves saturated/unsaturated isothermal flow and RDX transport in a near-rectangular prism whose west-east long axis follows Cañon de Valle between the Pajarito fault to the west and the extent of the Cañon de Valle alluvial aquifer to the east (LANL 2018, 602963). The estimated north-south extent of saturated perched-intermediate groundwater defines the model extent in that direction. The model domain is approximately 3 km long between the eastern and western boundaries, 1 km from north to south, and 650 m deep, extending from the land surface to about 40 m below the water table. The model uses the geologic framework WC15c (LANL 2018, 602963), which in the TA-16 area is based on the geologic mapping of Lewis et al. (2009, 111708) and well logs (Figure D-3.2-1). The model includes 13 hydrogeological units discretized over 41 vertical layers using the LaGriT mesh generator (Figure D-3.2-2). The Delaunay mesh has 345,050 tetrahedral elements and 60,516 nodes. Vertical layer resolution ranges from about 1 m to 16 m. Horizontal resolution is 40 m. The mesh conforms to the land surface, the top of Qbof (Otowi) and Tpf 3 (Puye), and to the water table surface of the regional aquifer. All other geological units are interpolated onto the elements of the mesh.

FEHM is used to solve for flow and transport using the Richards equation, which calculates water pressure and saturation at every node of the domain as well as water fluxes (Zyvoloski 2007, 700904). The model uses van Genuchten parameterization of the water retention curve to link water pressure and water content. The Mualem model is used to calculate unsaturated permeability as a function of water content.

D-3.2.1   Model Function to Inform the RDX Regional Model

The RVZM is an important tool to help develop certain highly uncertain distributions in the RRM, given the lack of other evidence to inform source (hydraulic window) characteristics. Source characteristics include the timing of arrival, concentration, recharge rate, location, radius, and shape of hydraulic windows containing RDX and arriving at the regional aquifer. While the extent of the RVZM, whose northern boundary does not cover the highest measured RDX in the regional aquifer (R-69 screen 2), precludes it from being used for location distributions, it can still provide useful information for the other source parameters. Travel times and recharge rates are constrained by the flow physics of the RVZM. The RVZM is therefore also used in conjunction with the P&D tool to inform the travel time of RDX from the land surface to the regional aquifer. Recharge rates are also constrained by the physics in the RVZM, which uses infiltration distributions informed by surface data and maintenance of the observed perched zones. Because of these realistic constraints, and the accurately represented physics of flow, recharge rate distributions for the RRM use RVZM output. The calibration attempts to match concentrations throughout the RVZM, making it an appropriate tool to estimate concentration where the vadose zone and regional aquifer intersect. Given that it is one of the only available lines of evidence, that it explicitly accounts for uncertainty, and that it appropriately constrains the flow and transport with detailed physical calculations, the RVZM is an appropriate line of evidence for the aforementioned distributions.

D-3.2.2   Initial and Boundary Conditions

The CSM informs flow and transport boundary and initial conditions for the different zones of the model. In the RVZM, the representation of the regional aquifer is simplified: The regional aquifer has a nearly flat water table surface, below which all nodes are assigned full saturation and hydrostatic pressure (with atmospheric pressure at the top of the regional aquifer), and the water table elevation at nodes of side boundaries is fixed. Flow of groundwater is allowed to enter and leave the regional aquifer through the side boundaries. The bottom of the domain, about 40 m below the water table surface, is a no-flow boundary.

Perched-intermediate saturated zones above the regional aquifer are initially assigned full saturation and hydrostatic pressure condition. Two perched zones, upper and lower, referred to as the UPZ and LPZ, are initially defined based on the estimates of Lewis et al. (2009, 111708). As in the regional aquifer, pressure and saturation of nodes in these perched saturated zones that intersect the side boundaries are kept fixed. The perched zone saturated thickness can vary in space and time during the simulation and depends on influx of water at the land surface and at side boundaries. To maintain the extent of the perched zones and prevent drainage, a permeability reduction factor at the bottom of the UPZ and LPZ is assigned to nodes that define the bottom of these perched zones. The bottom of the UPZ cuts across multiple geological units. On the western boundary, a flux of water representing mountain block recharge is imposed at the nodes of the upper perched saturated zone shown in Figure D-3.2-3. All other UPZ boundary nodes have constant saturation and pressure, allowing water to either enter or leave this perched zone there. The LPZ does not intersect any side boundaries.

Three other fluxes of water are specified at the top boundary (Figure D-3.2-3). One defines background infiltration and is imposed over all top boundary nodes. A second flux sets the canyon infiltration, except over Cañon de Valle. The third flux controls infiltration over Cañon de Valle. These three water fluxes are constant in time. Distribution development for these fluxes is described in section D-4.6.

Initially, the concentration of RDX is set to zero for the entire domain. RDX enters the model domain via two areas, the 260 Outfall over Cañon de Valle, and the 260 Pond (modeled as one single node). The mass of RDX entering the top surface at these two locations is calculated as the product of the volume of RDX solution that entered the system times the RDX concentration. RDX is assumed to be at the solubility limit (44 mg/L). This mass of RDX is time dependent and depends on the estimated production conditions at these two locations.

D-3.2.3   RVZM Parameterization and Distribution Development

Distributions that are developed together for the RVZM and RRM include *Kd* and dispersivity; these are discussed in section D-4. For other parameters, more distributions for the RVZM are required because of additional geologic units in the vadose zone, unsaturated properties, or a difference in treatment of the parameter for this model. These include infiltration, aqueous diffusivity, and hydraulic conductivity. These are discussed in the sections below for the RVZM, and separately for the RRM in section D-4.

The van Genuchten parameters, residual and saturated water content, porosity, and rock density of each of the 13 hydrostratigraphic units are given as fixed quantities in the RVZM (Table D-3.2-1), as described in the RDX compendium (LANL 2018, 602963).

RVZM Infiltration

Infiltration is the entry of water into the subsurface from the ground surface (e.g., Freeze and Cherry 1979, 088742, p. 211). It is a parameter used only in the RVZM, and not the RRM, because the vadose zone separates the ground surface from the saturated zone of the regional aquifer. Water reaching the regional aquifer is termed recharge.

Sources of information for infiltration include field studies conducted as part of the investigation report for Water Canyon and Cañon de Valle (LANL 2011, 206324), values used in modeling studies, simulation results (Levitt 2011, 700879), and literature review (Birdsell et al. 2005, 092048). One source (Kwicklis et al. 2005, 090069) combined field measurements and literature review. These authors made a composite of point estimates of infiltration at higher elevation areas (e.g., mesa tops) with estimates of streamflow gains and losses in channels to generate an infiltration map, which included the RDX project site and surrounding areas. Geochemical data were also collected to inform distribution development. Estimates from mixing models indicate that the regional aquifer is composed of 90% mountain block recharge (LANL 2018, 602963, Attachment 3, section 6, and Tables 6.2-1, 6.2-2, and 6.3-2), which does not percolate through the vadose zone at the RDX site and is expected to mitigate RDX concentrations in the regional aquifer via dilution.

All of the nodes at the land surface in the RVZM have an assigned value of infiltration. Each node is classified in one of four topographical groupings identified in Figure D-3.2-3: background, canyon, Cañon de Valle, or MBR (mountain block recharge). Background infiltration is associated with mesa tops surrounding the RDX project site, and it has the lowest mean value of the four groups. Canyon infiltration is associated with locations at the ground surface in canyons but is not specific to Cañon de Valle and the location downstream of the 260 Outfall. Cañon de Valle infiltration is specific to Cañon de Valle and the location downstream of the 260 Outfall. MBR is groundwater flow sourced from diffuse precipitation falling over the upgradient mountain block. MBR feeds the upper perched zones (and the regional aquifer) and comes in at the upstream, left-hand side of the RVZM (Figure D-3.2-3) in accordance with the CSM (Figure D-1.3-1).

For infiltration into the RVZM, raw data are available from 16 different references (e.g., LANL 2011, 206324), collected in a comprehensive literature review. A probability distribution was developed for the mean infiltration rate for each grouping of infiltration in the RVZM. The distributions are intended to describe the spatio-temporal average of infiltration for each grouping, and a double bootstrap method is employed. This method estimates uncertainty in the mean while accounting for the fact that data values were taken from different references. Truncated normal distributions are selected to fit the distribution of bootstrap sample means because sampling distributions of the mean typically follow a normal distribution—when the sample size is large enough (or when the sample size is small, and the independence and normality assumptions are met). The fitted distributions are displayed over the bootstrapped means and the collected data in Figure D-3.2-4.

RVZM Diffusivity in Variably Saturated Porous Media

The effective diffusion coefficient (D_e) is used for calculating the movement of solutes in water because of differences in concentration gradient in a porous medium. This section describes parameter distribution development for the RDX D_e distribution used in the RVZM. Diffusion in water in the RRM is discussed separately in section D-4.10, which includes additional detail on background information about the effective diffusion coefficient, including how the diffusion coefficient is calculated from other parameters, a description of data compilation and calculations used to inform distribution development, and the approach taken to produce input distributions for contaminants in the probabilistic model.

The spatial and temporal scales captured by the distributions should align with the scale of the model and with how individual draws from these distributions are used. For each realization of the RRM and RVZM, a single D_e will be sampled from a distribution and applied to all model cells in the domain, regardless of actual geologic material. D_e is assumed to be homogeneous in space and constant in time. Because D_e depends on tortuosity, which depends on porosity, the choice of homogeneous porosity for the RRM is related to the selection of homogeneous diffusivity. For the RVZM, which includes multiple geologic units with different porosities, a separate (wider) distribution for diffusivity is developed. In both cases, because realistic variability in site D_e values is expected to occur at spatial scales much smaller than the model domain over which they are applied, these individual values are intended to represent possible average values. D_e must be >0; therefore, negative D_e values will not be entered into the FEHM model, and there are no physical upper limits of D_e values.

Salinity, temperature, and pressure have the potential to change the density of water, which in turn can change the rate of diffusion of a given substance in water. For the RRM and RVZM, the magnitude of change of these parameters over the domain of the models has a negligible effect on density. Factors relating to the porous media (such as porosity and volumetric water content) provide the primary source of spatial variability in diffusivity.

The RVZM is expected to contain a greater variability of effective diffusivity over the path of RDX migration compared with the RRM, since it covers a much greater range of porosity in widely different geologic materials as well as a wide range of volumetric water content (θ_w). As this is a calibrated parameter, the classical calibration of the RVZM will select a diffusion coefficient consistent with history-matching of the site RDX data in conjunction with all other parameters. The effective liquid-phase diffusion coefficient in the RVZM is not expected to be a sensitive parameter, and therefore a wide range is selected for calibration of the RVZM. A uniform distribution with range (1E-11, 1E-9 m^2/s) was selected, which is expected to be wider than plausible average values for the entire model domain and reflects a great deal of uncertainty in appropriate average values for this parameter for the RVZM. The selected coefficient was evaluated for reasonability given the current state of knowledge of diffusivity through the materials in the RVZM.

RVZM Hydraulic Conductivity

There are additional geologic units in the RVZM that require hydraulic conductivity distributions, which are grouped based on similarities to each other. In the RVZM, each geology group receives a single draw from the appropriate distribution (i.e., one value of K is used to represent an average for the volume of the unit). Vertical scales of the units range from 1 m to hundreds of m, and the horizontal scale is on the order of 1 km.

Methods, information collection, and distribution development are described in the parameterization of K for the RRM in section D-4.1. Table D-3.2-2 gives the results for K_{xy} (horizontal) and K_z (vertical) in the geologic units present in the RVZM. The distributions are normal with mean and standard deviation given in ft/day. For use in the model, the distributions are transformed to the log10 scale and therefore represent a lognormal distribution.

D-3.2.4 RVZM Calibration

The RVZM is calibrated by adjusting a set of input parameters to best-fit predefined targets. For the RVZM, this includes time-dependent RDX concentrations at wells and thicknesses of perched saturated zones, as described below. Calibration is performed using the Levenberg-Marquardt (LM) technique with random initial guesses implemented in the Model Analysis and Decision Support (MADS) software

(https://mads.lanl.gov/), which minimizes an objective function (OF) that measures the fit of model results to targets. The LM calibration is conducted in a similar manner to that of the RRM.

Calibrated input parameters in the RVZM include

- the horizontal and vertical permeability for 16 units (13 hydrostratigraphic units and 3 additional zones in the Puye Formation),

- 3 permeability reduction factors at two perched saturated zones (including a 3 × 3-node "window" in the upper perched zone),

- 10 RDX partition coefficients,

- 1 RDX matrix diffusion coefficient,

- 4 boundary fluxes, and

- 3 dispersivity coefficients (1 for each axis direction, identical for all geological units).

In the results shown in Figure D-3.2-5 and Table D-3.2-3, 42 dispersivity coefficients, 1 for each axis direction and for each of the 13 hydrostratigraphic units plus the regional aquifer, were calibrated. These calibrations are discussed in detail below.

Targets

Two types of targets are used for calibration of the RVZM: (1) saturated thickness of perched-intermediate water zones and (2) RDX concentrations measured at wells. Upper- and lower-perched zone saturated thickness data are interpolated onto each node of a horizontal plane of the mesh. This yields 2252 target values (1126 for each perched zone). Time-dependent RDX concentrations at wells add another 226 to 350 targets, depending on when the data set was processed, as discussed below. RDX concentration target values use monthly averages. Wells include intermediate well screens CdV-16-1(i), CdV-16-2(i)r, CdV-16-4ip, CdV-9-1(i), R-25 screen 1 through screen 4, and R47i and regional well screens R-25 screen 5 through screen 8, R-63, and R-68. Weighting is used to prioritize matches to data most relevant to the purpose of the RVZM in estimating quantities for the RRM. While this weighting could be revisited in future work, for the results presented here, saturated thicknesses are assigned a weight of 1 and RDX concentrations a weight of 5, except where noted otherwise.

D-3.2.5   RVZM Results

Three calibrations were used to inform distributions for the RRM. The first calibration uses the same set of calibrated parameters as the calibration described in Attachment 8 of the RDX compendium (LANL 2018, 602963) with added RDX concentration targets for regional well R-68. In this calibration the total number of targets for RDX concentration is 350 over the period from September 30, 1998, to December 31, 2018. This calibration uses a unique set of dispersivity for all hydrostratigraphic units. The second calibration uses an updated set of RDX concentration targets, which contained 347 data points collected between November 31, 2000, and December 31, 2018. This calibration uses 14 layer-specific dispersivities along the 3 orientation axes. Finally, the third calibration improves over the second calibration by assigning higher weights (25) to intermediate well CdV-9-1(i) and regional well R-68 in an attempt to obtain a better match at these important locations. The number of targets for RDX concentration for this third calibration is 226 based on data pulled in March 2019 that include RDX concentration between February 28, 2002, and March 31, 2019.

Results

Values of calibrated parameters are given for the best calibration with the lowest value of the OF (Calibration 3) in Tables D-3.2-3 through D-3.2-7. These tables also include values of calibrated parameters of earlier calibrations reported in the RDX compendium (LANL 2018, 602963, Attachment 8, Tables 4.0-1 and 4.0-2), and an improved calibration from LANL's Earth and Environmental Sciences (EES) Division (Neptune 2018, 700878), for comparison. In general, calibrated values show similar trends to earlier calibrations. Results from calibrations indicate that many possible combinations of parameter values yield good fits to the data and thus, more than one set of parameter values is possible. Note that Calibration 3 yields overall smaller values of sorption coefficients (Table D-3.2-7) in better accordance with data (Heerspink et al. 2017, 602560). Calibrations 2 and 3, which assign three dispersivities to each of the hydrostratigraphic units, also seem to yield a better fit.

To illustrate the goodness of fit, Figure D-3.2-5 shows targets versus simulated RDX concentration for the lowest OF value of Calibration 3, and Figure D-3.2-6 shows the time-dependent targets and simulated values for all the wells. The model reproduces measured RDX concentration relatively well. A perfect fit would show all colored data points in Figures D-3.2-5 and D-3.2-6 on the diagonal line. Three wells, R-25 screen 1, R-63, and R-68, have values of RDX concentration that are underestimated. One well, R-25b, has trends that are unlikely to be represented with a continuum model such as that used here. Note also that Calibration 3, whose results are shown in Figures D-3.2-5 and D-3.2-6, is the only calibration that resulted in a good fit for well CdV-9-1(i) screen 1, perhaps owing to the large weight assigned to this well. Modeled RDX concentration for well R-68 was zero in all calibrations, which is a result attributed to the model structure, as the simplified representation of the regional aquifer may not permit movement of contaminated water towards R-68.

The best calibrations on the basis of smallest OF value (all eight seeds from Calibration 1 and 2; four seeds from Calibration 3), were run in a forward mode to compute fluxes and RDX concentration entering the regional aquifer. These forward model results are used to inform distributions for the RRM.

D-3.3   Pipe and Disk Analytical Tool

Another line of evidence used to constrain the inputs to the RRM is the P&D screening tool. The P&D tool was developed by LANL to represent contaminant transport pathways through the vadose zone. The P&D approach, as described in the RDX compendium (LANL 2018, 602963), is a simplified model that uses analytical solutions for fast computational analyses of problems that would be cumbersome to set up and test in a full three-dimensional (3-D) VZ/SZ model. The P&D tool has been previously used to roughly estimate plausible source timing and location relative to R-18 and R-68 RDX concentration data (LANL 2018, 602963).

The setup of the model is that arbitrary numbers of pathways can be established in unsaturated zones ("pipes") between arbitrary numbers of saturated lenses ("disks"), such as the case at the RDX site. Figure D-3.2-7 shows a schematic of an example model geometry for a case with several pipes and disks. The bottom disk always represents the regional aquifer. The locations, footprint, and fluxes in the pipes can be calibrated against observed data.

The unsaturated (VZ) pipes are simulated as one-dimensional (1-D), vertical conduits, which have discrete contaminant transfer and diffusion properties. The disks representing the saturated zones represent a homogenous lateral flow field within each disk. The analytical solutions used by the P&D tool incorporate advanced concepts of anomalous diffusion to better represent the observed behavior of contaminant transport in porous media (O'Malley and Vesselinov 2014, 700891). However, the tool as a whole does not presently allow for important MBR dilution processes in the SZs or other complexities in

the CSM. However, because of its simplicity, the model is computationally efficient and therefore can be run thousands of times to generate distributions of possible pathways through a VZ, where the user can constrain the potential number and locations of pipes and/or disks.

The P&D tool was used to inform the distribution for time of onset of RDX concentration at surface of the regional aquifer. Although some historical data on land surface RDX releases are available to inform this parameter, they do not provide information about travel times through the thick VZ to the regional aquifer. Inferring the time of contaminant arrival at the regional aquifer from well data is not possible because these data are incomplete in their spatial and temporal coverage, and their reliability can be questionable because of incidental and temporary contamination as a result of drilling issues. The tool was also used to inform the source locations and source sizes.

D-4.0   RRM PARAMETERIZATION AND DISTRIBUTION DEVELOPMENT

Distribution development is the process shown at the far left third of Figure D-4.0-1 where available lines of evidence are combined to describe the range and likelihood of plausible values for each input parameter to the RRM. Figure D-4.0-2 presents the distribution development workflow.

Note that the data, methodology, and distributions are identical to those in the chromium project area at LANL. This is justified because of the proximity of the two sites, similar geology, and sparsity of specific storage data on the Pajarito Plateau.

An iterative approach to parameter distribution development is used for the RRM for the purpose of focusing effort where it will have the greatest benefit for reducing uncertainty in risk and dose. After a target or goal for the distribution for the input parameter is defined, the method has four main steps that result in model implementation. In the first step, *screening*, high-level decisions are used to limit the scope of information collection. For example, will data collection be limited to certain contaminants, locations, or types of properties? Expert judgment or prior sensitivity analysis (SA) results may be used during screening. During the next step, *data collection*, the most relevant available sources are gathered. To determine relevance, some site assessment is performed first to identify the expected media types and aqueous environmental conditions at the site (usually part of the CSM development). In the *filtering* step, data are culled based on the site assessment with consideration to the amount of data available, data quality, and relevance to the site. Exploratory data analysis is extremely useful for determining whether categorizations of the data have been appropriate, and new choices may be made if necessary. Finally, the data subsets are ready for the final step, *statistical analysis*, where distributions are developed using the statistical techniques deemed most appropriate for meeting the distributional goal and for the intended usage of the parameter in the model. The distributions are implemented in the model, and results are used to identify new areas of focus for parameter development, based on sensitivity and/or value of information analysis. More extensive explanation of this process is described by Jordan et al. (2017, 700881).

In the case of the RRM, these steps are described in detail for every parameter below. These steps include incorporating the CSM, gathering lines of evidence, filtering the data, and also applying the analytical tools used to understand the distributions in the context of the modeling described in section D-5.4.

In this section, each parameter in the RRM requiring a unique distribution is described in detail, including all available lines of evidence, data, statistical modeling, and final distribution. While there are 423 calibrated parameters, many of these use the same distribution (for example, *K* values are drawn for points throughout the model; however, these are based on four unique distributions). All unique distributions, and their central value, units, and sources of information, are shown in Table D-2.5-1.

The spatial and temporal scale of the model parameter versus the data, correlations between parameters, and quality of data are all considered during the distribution development process. Many parameters in the RRM at LANL take a single draw and apply that draw to all space and time over which the model is run, for a single simulation. Defining the distributional goals as they relate to the modeling process is the crucial first step. Distribution development requires consideration of many sources of data or information on the parameter where available, ideally from multiple references. Depending on these conditions and the reliability or relevance of particular references, different sources of data may each contribute valuable information but may have varying relevance to the site. In these cases, weighting data is a useful way to incorporate the value of different sources of information.

In some cases, the data represent measures of uncertainty rather than the raw data themselves, and this uncertainty should be accounted for in distribution development. Some studies from which data are gathered for the RRM distribution development use models to derive values for the parameter, in which case the study may provide a single estimate of the parameter and a standard error of estimation. Other studies may have been conducted for some purpose other than estimating the parameter of interest, but they may provide the parameter for reference. In these cases, it is common to find a table with the estimate(s) of the parameter and some associated uncertainty without an explanation of what that uncertainty is meant to represent. This makes accounting for the uncertainty in distribution development challenging, and professional judgement may be required to make assumptions on the most likely meaning of the reported uncertainty.

D-4.1   Hydraulic Conductivity

Distributions are needed for hydraulic conductivity (K_x, K_y, and K_z) because these parameters are required to model flow and RDX transport at the site. Their values are uncertain, and K is likely to be a sensitive parameter. The distributions will be used to build a heterogeneous K field for the model domain using the pilot and anchor point concept. Anchor points represent location in the model with associated K data, typically from aquifer test estimates. These points will have distributions developed based on uncertainty in the data, including whether they represent the appropriate spatial scale as used in the model. Pilot points are locations in between anchor points where K data do not exist. K values for these locations are drawn from wider distributions that represent the appropriate geologic material being represented. After draws are made at pilot and anchor points, kriging is used to interpolate K values onto all model nodes.

The spatial scale over which a K value applies is determined by a combination of pilot/anchor point density and kriging parameters. Pilot and anchor points in the model are separated by tens to hundreds of meters. The density of pilot points was selected based on a combination of cross-hole connections between pairs, triplets, and quadruplets of wells at which data exist. The goal is to allow enough degrees of freedom for the model calibration to match cross-hole responses to site activities (pumping and injection) and observed RDX migration. The temporal scale of the model is tens to hundreds of years. Temporal variability in K is not considered for this model on these timescales.

Hydraulic conductivities in the aquifer materials present at the site are expected to be highly heterogeneous on spatial scales considerably smaller than model nodes [see, e.g., (LANL 2018, 602963), Attachment 3: high resolution stratigraphy]. At larger spatial scales, heterogeneity may be caused by additional factors related to the depositional environment. Sources of uncertainty include the use of expert judgment in the analysis and interpretation of K estimates from the raw data (e.g., pump test analysis) and the appropriateness of the spatial scale of the data to the model scale. There is a recognized scale dependence of hydraulic conductivity (Schulze-Makuch et al. 1999, 700893), wherein average K is generally larger over greater distances in heterogeneous media. This is because of the dominance of connected fast paths in the overall hydraulic behavior.

The distributions should represent plausible values for mean hydraulic conductivity at the appropriate scale described above.

D-4.1.1   Method

Hydraulic conductivity is the coefficient of proportionality between the hydraulic head gradient and fluid flux in Darcy's Law (in one dimension),

$$q = -K \frac{dh}{dl} \, , \qquad \qquad \textbf{Equation D-1}$$

Where, q = fluid flux [length (L)/time (T)],

      K = the hydraulic conductivity along the direction of flow [L/T], and

      dh/dl = the hydraulic head gradient [unitless].

Hydraulic conductivity is dependent on both the properties of the porous medium and the fluid of interest. For this reason, Equation D-1 is also commonly expressed in terms of intrinsic permeability k, where

$$k = K \frac{\mu}{\rho g} \, , \qquad \qquad \textbf{Equation D-2}$$

where, k = intrinsic permeability [L^2],

      μ = the fluid viscosity [mass (M)/L·T],

      ρ = the fluid density [M/L^3], and

      g = the acceleration due to gravity [L/T^2].

The laboratory standard for hydraulic conductivity is defined as pure water at a temperature of 15.6°C (Fetter 1994, 070942). Hydraulic conductivities determined from pumping tests are assumed to be at in-situ subsurface temperatures. Conversions between K and k for the models are made using an equation of state defined in the FEHM model with reference temperature set to 20°C and pressure 1.0 MPa.

Extension of Equation D-2 into three dimensions turns scalar K into a tensor, $\mathbf{K}$, of which the diagonal components K_x, K_y, and K_z are used as model inputs. If $K_x = K_y = K_z$, the system is isotropic. Since the implementation does not allow the off-diagonal elements of the tensor to be model inputs, the assumption is implicitly made that the coordinate axes are aligned with the principal directions of anisotropy (or that the system is isotropic). Based on assumptions about the anisotropy of geologic materials at the site, one distribution is developed for both K_x and K_y (referred to as the K_{xy} distribution) and another for K_z.

The RRM uses the pilot point method as described in Doherty (2003, 700894). Pilot points are located between monitoring wells, and they receive a broad distribution that reflects plausible hydraulic conductivity values for the geologic material in which they are located. Pilot points are not randomly distributed but rather should be considered "connectors" in between locations with data (anchor points). The density of pilot points should be greater in areas of higher interest, measurement density, and heterogeneity (Doherty 2003, 700894). The pilot points are necessary because cross-hole connector values may need to be significantly different from anchor point values in order to obtain the observed drawdowns or RDX transport, which is also in line with the observations in the heterogeneous aquifer that values around the site can be highly variable even at the spatial scale of pumping tests. By allowing these values to vary via a distribution, the calibration may be relied upon to select appropriate combinations.

The anchor points are well locations with hydraulic conductivity estimates; these receive narrower distributions that reflect the state of uncertainty in the data. Despite the name "anchor," which implies certainty*, these are still stochastic and allowed to vary across their range during calibration.*

Once values are drawn from the distributions for all pilot and anchor points, hydraulic conductivities at *all* nodes in a model realization are assigned by using ordinary kriging to interpolate.

A sitewide GFM, known as WC15c, forms the basis for assigning nodes in the model to geologic units; however, more recent work has identified changes to the elevations of geologic contacts and as a result there is some discrepancy between the current understanding of which units well screens are found in and which they are assigned in the model. The effects of this discrepancy are discussed below. Because of the pilot point approach, the effects are minimal, as hydraulic conductivities are not required to obey strict geologic boundaries as defined in the GFM; additionally, there is significant overlap in the expected hydraulic properties of the geologic units, which also minimizes the effect of the old GFM. This is a major benefit to the pilot point approach as it does not rely on uncertain geologic unit boundaries across the site.

Figure D-4.1-1 shows the model GFM in the RDX area. Selected pilot and anchor point locations are shown in black and gray, respectively. The geologic formations most relevant to the RRM pilot and anchor points include the Puye Formation (Tpf) and Tschicoma Formation (Tvt). Other units in which pilot points are found in the RRM include the Cerros del Rio (Tb4), late Miocene basalts (Tb2), Miocene Chamita (Tcar), Miocene Pumiceous (Tjfp), and the Keres group volcanics (Tvk).

D-4.1.2   Information Collection

Hydraulic conductivity information was gathered from analyses performed on well data across the Pajarito Plateau. Sources of information include single- and multiwell aquifer tests, geophysical well logging, and laboratory-scale analysis on extracted core. These were compiled into a database that included metadata such as well location, geologic formation, type of measurement, and data reference.

Information is typically not given that would help identify whether the measurement represents K_x or K_y relative to any coordinate system, and therefore K values are assumed to be for any horizontal direction and are used for a single distribution for K_{xy}. Vertical anisotropy is difficult to estimate from pumping tests and was typically not within the scope of K estimations made for LANL well completion reports (e.g., Broxton et al. 2002, 072640), but several of the pumping test analyses do provide rough anisotropy estimates (e.g., LANL 2007, 098129; LANL 2009, 105079). These provide the basis for the K_z distributions, as discussed below, along with literature reviews. If specific storage or storativity estimates are also given in the same reference, they are also entered into the database, as discussed in section D-4.2.

Methods for measuring hydraulic conductivity are divided into three categories that correspond to the spatial scale represented by the measurement: small, intermediate, and site-scale. Measurements based on aquifer pumping tests were considered "intermediate" scale. These pumping tests, typically of 24 hr duration (although sometimes longer), are expected to interrogate the aquifer at scales of hundreds of meters (depending on the pumping rate and hydraulic properties of the media). This is observed by the drawdown response in nearby pumping wells from the pumping test. For example, the R-70 pumping tests in the upper and lower screens were observed to cause drawdown at wells such as R-13 and possibly R-44 screen 2, which are approximately 500 m away (N3B 2021, 701506).

Estimates of *K* from corehole samples in the chromium area were performed using particle-size distribution analysis and the Kozeny-Carmen equation (LANL 2018, 602964). Estimates were made for each 6-in. section of core. The scale of these is classified as "small." Methods other than the Kozeny-Carmen approach were also tested and found to produce variability in absolute *K* values of up to an order of magnitude, but the *relative* distribution of *K* values remained similar across multiple methods (Broxton et al. 2021, 701441).

Potential site-scale *K* estimates would be ones for which the value is estimated across the entire formation or at a much larger scale than the intermediate. These could include published model-estimated values for an entire formation or estimates from the literature that summarize formation-scale data. None of these apply to the RRM in the database.

D-4.1.3   Discussion

Once the LANL-area *K* information is collected, exploratory data analysis is performed to visualize the data and determine what filtering should be performed to subset the database to the most relevant and appropriate data for the scale and geologic units present at the area.

Geologic Units

All pilot and anchor points in the model are shown in Figure D-4.1-1. The GFM of the model which identifies which nodes fall within which units has not been updated to new information presented in (LANL 2018, 602963), and therefore node assignments to certain geologic units may have discrepancies with the most current GFM. The effect of this is different for pilot versus anchor points. For anchor points (i.e., wells), distributions for K_{xy} are developed directly from the data at these locations, and so these are not affected by which geologic unit they are located in. For pilot points, the initialized value of K_{xy} for the calibration is based on the geologic unit in which it is found, as well as K_z. Therefore, for pilot points, a mis-assignment of geologic unit could result in the other distribution being used. However, a close eye will be kept on any pilot points in the model that move to the edges of their allowable distributions, suggesting that higher or lower values at that location would be possible.

Exploratory data analysis was performed to determine how distributions would be developed with respect to geologic units present in the RRM. Sedimentary units such as Tpf, Tjfp, and Tcar were grouped into one distribution referred to as "sedimentary." Similarly, the volcanic units were grouped together into one broad, generic volcanics distribution. Table D-4.1-1 lists the geologic units that are assigned the volcanics distribution and the sedimentary distribution.

Collected *K* estimates for volcanics are likely biased high. This is because screened intervals in wells that are in the volcanic units tend to be targeted at productive zones, i.e., fractured or brecciated portions of the unit. These may not represent appropriate bulk/upscaled *K* values for massive portions of the unit, and so *K* estimates from aquifer testing in the screened intervals are considered unreliable for determining a range of plausible values for use in the model, where nodes may be in massive or brecciated portions of the unit (or mixtures of the two). Additionally, no location in the volcanics units can be considered an anchor point even if data exist (e.g., R-48, R-58). They are all treated as pilot points.

There are several estimates of *K* values for certain volcanic units at LANL, e.g., (Birdsell et al. 2005, 092048), that include massive portions of the lavas (as opposed to brecciated). A distribution was desired that would span from massive to brecciated. Freeze and Cherry (1979, 088742) suggest that unfractured igneous materials can have *K* values from 10^{-9} to 10^{-5} ft/day (10^{-14} to 10^{-10} m/s) while fractured basalt, on the other extreme end, can range from 10^{-2} to 10^3 ft/day (10^{-7} to 10^{-2} m/s). A wide range was selected as the plausible range for the volcanics in the model, as described below.

Spatial Distribution

The hydraulic conductivity database contains information from wells across the Pajarito Plateau, including some that are far from the RDX area. Exploratory data analysis was performed to test whether data should be filtered based on proximity to the RDX area. Figure D-4.1-2 shows intermediate-scale data compared for the RDX area and other areas around the site. Although there appears to be smaller average hydraulic conductivity in the RDX area than around the site, the decision was made to not filter by location. RDX-area K data are weighted twice that of data from other areas for the purpose of pilot point distribution development.

Figure D-4.1-3 shows the spatial distribution of K_{xy} data across the RDX site. Because the spatial location of wells appeared to be correlated with the wells' K_{xy} values, a spatial model was used to initialize the values of pilot points at these locations.

Scale

Small-scale corehole data from the chromium area were added to the database for completeness and comparison, but they are not expected to represent the spatial scale over which the parameter is applied in the model when compared with the aquifer test data, which covers a scale much more similar to the pilot point density. Therefore, filtering was performed to exclude the small-scale data from distribution development.

Figure D-4.1-4 compares the small-scale data from the chromium area with the intermediate-scale data for the Puye Formation. Estimates of K from the small-scale data are significantly smaller, on average, than the intermediate-scale data. The significant difference between the groups suggests filtering for the most appropriate scale of data, and therefore the small-scale K data are not used in distribution development.

Type of Aquifer Test Analysis

Aquifer tests at the LANL site have been performed by many analysts over many years, resulting in a variety of interpretation approaches. Recently, the New Mexico Environment Department has called into question the validity of analyses from the drawdown portion of an aquifer test. Because many of the aquifer test analyses also include K estimates based on the recovery portion of the test, exploratory data analysis was performed to compare drawdown with recovery estimates.

Figure D-4.1-5 shows well locations with K estimates. The type of measurement is red if based on allowable recovery data or blue if coded as any other type of analysis. This figure shows which wells would be eliminated from anchor point consideration if all nonrecovery estimates are rejected (any well without red data). It also shows how the mean at each location differs when either recovery or other types of estimates are considered.

Anisotropy

Horizontal anisotropy is not included in this iteration of the hydraulic conductivity analysis. However, there may be conceptual lines of evidence to support an anisotropic horizontal hydraulic conductivity tensor in the future. The Puye Formation is composed of alluvial fan deposits from a large volcanic center to the west/northwest. With distance from the source, the alluvial fan deposits become less channelized and more sheet-like, with potentially decreasing anisotropy downgradient.

North-south trending faults could also potentially play a role, causing north-south hydraulic conductivity to be larger than east-west permeability, although the effect has not been directly observed (Keating et al. 2005, 090039). A single distribution is developed for both K_x and K_y and is referred to as K_{xy}.

On the other hand, vertical anisotropy (K_z/K_{xy}) in the aquifer materials at the Pajarito Plateau is firmly established in the prior literature based on multiple lines of evidence (e.g., Birdsell et al. 2005, 092048; Keating et al. 2005, 090039; McLin 2006, 092218; LANL 2018, 602963, Attachment 1). However, quantitative estimates of K_z are highly uncertain. When estimated as part of pumping test analysis, there are typically nonunique solutions where anisotropy and storage coefficient are both variable and depend on each other, e.g., as at R-44 (LANL 2009, 105079). However, some pumping test analyses suggest that a particular anisotropy ratio or range provides the best fit to the pumping test data. Where vertical anisotropy estimates are discussed in well completion reports, they are included in the database. Table D-4.1-2 shows anisotropy estimates from well completion reports in the Tpf, Tjfp, and Tcar formations. Where more than one anisotropy estimate exists for a location, they have been averaged.

Although the estimates from highly uncertain aquifer test analyses do not range lower than 0.0004, Keating et al. (2005, 090039) presents even lower estimates (down to 0.00005) and discusses the possibility of a scale dependence of anisotropy. Therefore, the data in Table D-4.1-2 are not directly used to compute an anisotropy distribution to develop K_z values but are used to inform the process described for distribution development below.

D-4.1.4 Distribution Development

Final filtering decisions based on the discussions above are given in Table D-4.1-3.

Based on the filtering decisions in Table D-4.1-3, a well/screen location could be an anchor point only if it had intermediate-scale, recovery-only data. Anchor point initialization values are set to the mean of the data that meet those criteria, available at those locations. The allowable range is set to ±1 order of magnitude for the LM calibration. This range was determined based on subject matter expert interpretation of the uncertainty associated with K estimates, including the appropriateness of scale for the model. If any anchor point values are seen to move to the edges of their distribution, this may be re-evaluated. Figure D-4.1-6 shows the anchor point distributions along with the pilot point distributions.

Sedimentary Distribution

For the pilot points in sedimentary geologic units, a distribution was fit to the data based on the filtering criteria in Table D-4.1-3. Based on the methods used to measure the intermediate-scale data, intermediate-scale K_{xy} values were on the closest scale as an average. This distribution was used to determine the ranges used for the LM calibration based on the 1st and 99th percentiles. This range is assumed to represent plausible values at the appropriate scale for K_{xy} at these locations at which data do not exist.

As many sample locations had more than one measurement method reported on the same set of data, there were concerns for treating these observations as independent and identically distributed. Instead of fitting a distribution to all K_{xy} values reported from each well, a location average was calculated within each well on which the distribution would be informed.

Several parametric distributions were considered for fitting to the intermediate-scale K_{xy} values: lognormal, gamma, and truncated normal with lower bound set to 0 ft/day. Each choice was bounded below by 0 ft/day, which is consistent with the natural range of K_{xy} values.

The distributions were fit using maximum likelihood estimation (MLE) via the fitdistrplus R package (https://www.jstatsoft.org/article/view/v064i04). The lognormal distribution is available in the base R package (http://www.r-project.org/index.html).

The optimal lognormal and gamma fits are shown in Figure D-4.1-7 and described in Table D-4.1-4. The truncated normal distribution is not shown. In the figure, all sedimentary, intermediate-scale K_{xy} data are shown as ticks along the bottom of the plots, and histograms are shown in the background. The distributions for all data, recovery-only analysis types, and other (i.e., drawdown and other types of analyses) are also shown. Dashed lines indicate the 1st and 99th percentiles for each distribution.

The gamma and lognormal distributions fit using MLE are shown in shown in Table D-4.1-4. The calibration ranges (LM min and LM max) for pilot points will use the 1st and 99th percentiles of the selected distribution. While the lognormal distribution may provide unusually high estimates for K, the upper end of the distribution range was determined to still remain plausible. The gamma distribution provides more coverage on the low end but the lognormal was determined to provide a better fit to the site data, and it is consistent with the way in which K data are frequently assumed to be distributed.

The pilot point distribution in Figure D-4.1-6 is shown as a violin-density curve for the MLE-fit, lognormal distribution reported in Table D-4.1-4. The vertical red lines show the 1st and 99th percentiles of the distribution, which are used as the minimum and maximum for the LM calibration. Initial values are set using the spatial model described below.

Volcanics Distribution

As discussed above, aquifer test data collected in the volcanic units are likely biased high because of screen interval choices. Because of the inapplicability of the data to inform averages of the type needed for the model, literature ranges were used instead, with a uniform distribution from 10^{-11} to 10^{-2} m/s (10^{-6} to 10^3 ft/day). Initial values are set using the spatial model described below.

Spatial Model

The lognormal distribution established the range of plausible K_{xy} ranges to be implemented in the LM calibration for the pilot points, but it did not establish the values to be used at each pilot point to initialize the model, which may be correlated by spatial location. A spatial model based on all data was used during the calibration process to initialize pilot points, which are then allowed to vary within the ranges set by the distribution described above.

The basis for the spatial model is an ordinary least squares regression model that uses K_{xy} values from the wells in the area. The regression model included spatial coordinates in (x,y) to estimate any spatial trends in K_{xy} values in the RDX area to assist in interpolating an average K_{xy} between anchor points at the pilot point locations. The geologic layer and depth of samples were also implemented in the model for capturing trends.

K_z Distribution

Because of the limited and uncertain data available for anisotropy as described above, the distribution for K_z is an uncertainty range based on orders of magnitude. For pilot points and anchor points in the sedimentary units, the initial value of K_z is set to 0.1 times the initial value of K_{xy}. The maximum anisotropy for all points is allowed to be 1 (i.e., $K_z = K_{xy}$ for the maximum allowed value of K_{xy}). The minimum is allowed to range four orders of magnitude below the minimum value at that location, i.e., 0.0001 times the minimum K_{xy}. For pilot points in the volcanic units, the initial value of K_z is also set to 0.1 times the initial

value of K_{xy}, the maximum anisotropy for all points is also allowed to be 1, and the minimum is allowed to range two orders of magnitude of the minimum value at that location, i.e., 0.01 times the minimum K_{xy}.

K_z values are allowed to be drawn independently of K_{xy}, which means, in theory, a value larger than 1 of anisotropy may be permissible in the model. This allows additional degrees of freedom in calibration. In practice, it has not been seen that the model calibration favors anisotropy greater than 1.

D-4.2   Specific Storage

The RRM requires a distribution for specific storage because it is an important and uncertain parameter. Storage properties are particularly important in the context of transient pressure pulses introduced by, for example, non-steady pumping of the PM wells in the area. Furthermore, aquifer storage affects the speed of a pressure pulse through groundwater, much like the hydraulic conductivity. In fact, the hydraulic conductivity divided by the specific storage is the hydraulic diffusivity (Freeze and Cherry 1979, 088742), which can be used to estimate pressure pulse propagation speed. Therefore, the combination of hydraulic conductivity and specific storage can affect water levels, drawdowns, and the transport of chemicals in groundwater.

There are several terms that describe the storage of water in an aquifer. In this document "aquifer storage" is used as a general term that describes how much water an aquifer can store and release. In contrast, the terms "storativity," "specific yield," and "specific storage" all have precise mathematical definitions that reflect various aspects of aquifer storage. The storativity (S) is composed of (1) the specific yield (S_y), which describes how much water is released from an unconfined aquifer through the dewatering of pores by the force of gravity, and (2) the specific storage (S_s) times the aquifer thickness, which describes how much water comes from storage through the compression of water and the aquifer pore space. The RRM uses specific storage, and distributions for specific storage are discussed in section D-4.2.4. All three measures of aquifer storage are described in more detail below along with a justification of the use of specific storage to capture the aquifer storage effects.

Despite the importance of aquifer storage on groundwater flow and transport, specific storage is difficult to estimate precisely and can vary over several orders of magnitude. The storage is often measured with pumping tests that involve extracting water from one well while monitoring the transient response in the water level at both the pumping well and, if possible, nearby observation wells. Water level data are typically used to fit analytic solutions that have been developed for various scenarios that allow for the calculation of aquifer properties including storage properties. Single-well tests in which there are no observation wells can be unreliable (LANL 2017, 602595; LANL 2017; 602258; McLin 2005, 702324) and therefore, it is preferable to use field tests that measure water level responses at nearby observation wells, when available. Even when multiwell tests are available, interpreting the results via fitting to analytical solutions is complicated by the fact that real systems never obey the strict assumptions upon which the solutions were developed (e.g., 1-D radially symmetric behavior, homogeneity, infinite lateral aquifer extent, leaky or non-leaky confining units, fully or partially penetrating wells, etc.) and the resulting estimate of storage properties will depend on choice of method and on other choices made by the analyst (e.g., assigning an effective aquifer thickness). The usefulness of properties derived from fitting pump test field data to analytical solutions thus rests on how closely the real system conforms to the assumptions of the chosen solution. While these estimates can be useful, note that inverse modeling like the LM calibration employed in this modeling effort is likely to produce more realistic parameter estimates, as the model structure allows for 3-D heterogeneous assignment of aquifer properties such as would be found in the real system. This suggests that aquifer property distributions based on values derived from analytical solution fits should not be allowed to over-constrain the calibration since these values are based on a collapsing of system complexity to the strictures of the analytical solutions.

Finally, there are additional sources of uncertainty in the application of storage parameters to the RRM, such as (1) aquifer thickness and (2) the transition in aquifer type from unconfined, to partially confined, to fully confined, which are discussed in more detail below.

The specific storage is used in the pilot point method (section D-4.1) to construct a heterogeneous, 3-D field for the RRM of RDX transport at the site. The specific storage in the aquifer materials present at the site are expected to be heterogeneous on spatial scales considerably smaller than model nodes. The distribution should represent plausible values for mean specific storage at the appropriate scale (i.e., the pilot point scale).

Specific storage values are drawn from two distributions. One distribution represents the relatively shallow, unconfined or partially confined aquifers near the water table of the regional aquifer, and the other distribution represents the deeper, partially or fully confined aquifers. The aquifer is believed to transition from unconfined, to partially confined, to fully confined as depth increases (Vesselinov 2004, 090040). This gradual transition is due to the depositional history of the site, which resulted in high- and low- hydraulic conductivity horizontal layers. It is well known that a system of high and low K horizontal layers has an effective horizontal conductivity that is larger than the effective vertical conductivity (Freeze and Cherry 1979, 088742, Section 2.4). Because of this layering and effective hydraulic conductivity, the aquifers are believed to transition from unconfined to confined behavior near 50−70 m below the regional water table (Vesselinov 2004, 090040).

The specific storage is applied to all pilot and anchor points in the model. Model nodes in between these points will have specific storage values that are determined by interpolation using kriging, which uses stochastic parameters "range" and "v_semiaxis" to reflect the scale and the anisotropy of the kriging approach, respectively (see section D-2.4.3). Note that a separate set of kriging parameters is used for S_s and for hydraulic conductivity. The distribution for S_s is used (1) to provide ranges (min/max) and initialization values for the LM calibration, (2) as a prior distribution for the Markov Chain Monte Carlo (MCMC), and (3) to run the model in forward mode across realistic/plausible ranges.

D-4.2.1   Method

As mentioned previously, there are three measures of aquifer storage, but for the RRM, specific storage was selected as the sole storage parameter. Storativity is the broadest of the storage categories and encompasses the specific yield and the specific storage, but the numerical model does not have an option to use storativity directly. Specific yield applies to unconfined aquifers and describes water draining out of the pore space, which becomes unsaturated. Since deeper parts of the aquifer are partially or fully confined, the specific yield does not apply for the full extent of the aquifer (because the pore space will not become unsaturated in these confined aquifers) and is not used in the numerical model. In contrast, specific storage can be applied to both unconfined and confined aquifers, which is why distributions were developed around specific storage.

However, the specific storage must be applied with care, particularly in the unconfined and partially confined regions of the aquifer. Physically, the specific storage describes the storage or release of water from saturated pores through two mechanisms: (1) aquifer compressibility (i.e., pores expanding or contracting due to changes in effective stress) and (2) fluid compressibility (i.e., the water in the pore space expanding or contracting under changes in fluid pressure). In many unconfined aquifers, the specific storage is orders of magnitude smaller than the specific yield. Therefore, the "effective specific storage" concept (discussed in more detail below) allows specific storage to be larger than is typical in the unconfined and partially confined aquifers to account for the larger storage potential of S_y.

The storativity of a saturated aquifer is the volume of water that an aquifer releases from storage per unit surface area of aquifer per unit decline in the hydraulic head (Freeze and Cherry 1979, 088742). It is composed of two parts, as seen in the equation below (Fetter 1994, 070942).

$$S = S_s b + S_y \; ,$$ **Equation D-3**

where, S_s is the specific storage [L^{-1}],

b is thickness of the saturated aquifer [L], and

S_y is the specific yield [–].

The specific storage and the effective specific storage can be estimated in several ways, depending on the aquifer type (confined or unconfined) and the type of data available. To this end, four data types are described in the subsections below, which define the specific storage or effective specific storage. Data type 1 applies to both shallow and deep aquifers, whereas data types 2 through 4 apply to only deep or shallow. Data types 1 and 2 come from manipulations of Equation D-3 above. The specific storage is a highly uncertain parameter, especially in the deeper regions where there are few observations, and therefore using multiple data types to calculate the specific storage honors the wide range of uncertainty.

Data Type 1: Calculation of Specific Storage from Storativity

Neptune and Company, Inc., has collected a rich data set of aquifer storativity estimates from the literature for the LANL area. The storativity can be used to calculate the specific storage by manipulating Equation D-3. In deep, confined aquifers the specific yield is zero by definition, and S_s can be calculated from estimates of the storativity and the aquifer thickness as shown in Equation D-4.

$$S_s = \frac{S}{b}$$ **Equation D-4**

Equation D-4 is also applied to shallow aquifers when there is a pumping test that leads to a storativity value. The storativity data and estimates of the aquifer thickness are discussed below.

Data Type 2: Calculation of Effective Specific Storage from Specific Yield

In portions of the shallow subsurface with unconfined aquifers, the pore-draining physics described by the specific yield are expected to dominate the storativity. To capture this behavior, the assumption is that $S_y \gg S_s$ in these shallow, unconfined aquifers so that $S = S_y$. This assumption allows the assignment of an effective specific storage ($S_{s,eff}$) by manipulating Equation D-4 to get Equation D-5.

$$S_{s,eff} = \frac{S}{b} = \frac{S_y}{b}$$ **Equation D-5**

Equation D-5 above applies only to the shallow distribution. Data sources are discussed below.

Data Type 3: Calculation of Specific Storage from Compressibility Literature Values

It is possible to calculate the specific storage for a wide range of rock from literature values according to Equation D-6.

$$S_s = \rho g (\alpha + n\beta) \, ,$$ **Equation D-6**

Where, ρ is the density of water [ML^{-3}],

   g is the acceleration of gravity [L^2/T],

   α is the aquifer compressibility [M/L/T^2],

   n is the porosity [–], and

   β is the compressibility of water [M/L/T^2].

Equation D-6 is used for the deep portions of the aquifer with partially or fully confined behavior.

Data Type 4: Specific Storage Data

In rare cases, S_s data are reported directly, which means that no additional calculation is required. Data type 4 exists only for the deep regions represented within Neptune and Company's database.

D-4.2.2   Information Collection

Information for the specific storage distribution comes primarily from a literature review of site data and from textbook values. In rare cases, storativity site data are removed from consideration because the reference indicates that the data are unreliable. Aquifer thickness estimates are required to calculate specific storage from storativity and are informed by literature review and expert elicitation. The subsections below describe data sources for each data type and the aquifer thickness estimates.

Data Collection for Data Type 1

Most of the data for deep regions of the subsurface come from data type 1. Pumping tests were performed on PM-2, PM-4, PM-5, O-1, and O-4 and were interpreted with myriad analysis methods (e.g., Neuman-Witherspoon, Hantush-Jacob, Moench, and Theis) to estimate storativity values (Frenzel 1995, 056028, pp. 14–16; McLin 2005, 090073; McLin 2006, 092218, Table 7). The PM wells are screened in the Tp, Tpp, Tpt, and Tf formations, and O-4 is screened in the Tsf formation. Note that some of these wells, particularly PM-2, O-1, and O-4 are located far from the chromium plume, but their data are included because (1) there are few deep data points, (2) the data are expected to be reflective of the deep subsurface below the chromium plume, and (3) the RRM includes a region that is much larger than the chromium plume.

The shallow region also uses pumping test data for data type 1. Many wells on the Pajarito Plateau provide data including R-15, R-44, R-70, CrEX-2, CrEX-3, CrEX-4, CrIN-1, CrIN-2, CrIN-3, CrIN-4, and CrIN-5 (Longmire et al. 2001, 070103; LANL 2016, 601778; LANL 2017, 602595; LANL 2017, 602258, Table D-16; N3B 2019, 700721) (LANL 2017b, Table D-16; LANL 2016). These references note that some of the storativity estimates are unrealistically low and are unreliable because they are based on only a single-well pumping test. Therefore, a subset of the pumping test S estimates from CrEX-2 (LANL 2017, 602595), CrIN-1, CrIN-2, CrIN-3, CrIN-4, and CrIN-5 (LANL 2017,602258, page D-35) are removed from consideration for distribution development.

As noted previously, properties estimated from pumping test analysis are subject to considerable uncertainty because of the analysis methods in which the field data are fit to analytical solutions that were generally developed for idealized 1-D radially symmetrical systems with various assumptions depending on the solution employed.

Data Collection for Data Type 2

Data type 2 for the shallow subsurface uses textbook values for specific yield, which can range from 0.01 to 0.3 (Freeze and Cherry 1979, 088742; Fetter 1994, 070942). Note that the theoretical upper bound of the specific yield is the maximum porosity at the site. Therefore, the maximum porosity of 0.32 (LANL 2017, 602258, page D-35) is consistent with the maximum specific yield (0.3).

Data Collection for Data Type 3

The data for data type 3 comes primarily from Freeze and Cherry (1979, 088742; Table 2.5). The aquifer compressibility for sound and jointed rock ranges from 10^{-11} to 10^{-8} Pa^{-1}, and the compressibility of water is $4.4 \cdot 10^{-10}$ Pa^{-1}. The maximum porosity in the Puye Formation is 0.32 (LANL 2017, 602258, page D-35), and a lower bound porosity of 0.01 is assumed. Using these values and Equation D-6 specific storage values are calculated ranging from $10^{-7.4}$ to $10^{-4.0}$ m^{-1}.

Data Collection for Data Type 4

Data type 4 uses S_s data from Keating et al. (2005, 090039) and the references within. The data come from pumping tests for the deep, water supply wells on the Pajarito Plateau from the Otowi and Los Alamos Canyon well fields. Wells O-1 and O-4 are in the Otowi field, and there is a good agreement between the specific storage from data type 1 at O-1 and O-4 and data type 4 in the Otowi field, thereby giving confidence to these approaches.

Aquifer Thickness

Defining the aquifer thickness is important when calculating the specific storage with Equations D-4 or D-5 (data types 1 and 2). Thickness is estimated from site knowledge of the hydrogeology and from well screen length. The RRM uses a thickness for the shallow aquifers ranging from 3 to 100 m, and for the deep aquifers from 10 to 1000 m. These ranges should capture the uncertainty in the aquifer thickness, and the rationale is presented in the paragraphs below. While assigning an aquifer thickness is required to apply the equations outlined above based on analytical techniques, doing so applies some implicit idealizations to the system's behavior (e.g., that there are well-defined aquifers and aquitards), whereas the reality is more complicated. As such, the thickness ranges stated above were used to provide a corresponding range of resulting specific storage values in light of these complications.

At shallow depths, the typical screen length is on the order of 10–100 ft (3–30 m). Pumping tests carried out using these screens could tap multiple aquifers, or they could be partially penetrating (i.e., the screen length spans only part of a thicker well-defined water-bearing unit). Nevertheless, the pumping tests offer a ballpark estimate of the shallow aquifer thicknesses, as they would preferentially draw water from the screened interval, especially if there is any lateral hydraulic conductivity that exceeds the vertical. Applying a thickness to use for type 2 data of (specific yield) is more uncertain still, as the stored water associated with specific yield is that which is drained from (or taken into) the pore space of the vadose zone at the water table. How deep below the water table these storage effects would be evident is not often addressed, though it would surely depend on the degree of vertical heterogeneity. Furthermore, the high and low conductivity layers of the shallow regions below the regional water table could act like a series of thin aquifers with poor hydraulic communication, or they could act like a thicker aquifer if the hydraulic communication is good. If the latter case is true, then a reasonable upper bound on aquifer thickness should be 100 m.

In the deep portions below the regional water table, screen lengths can range from 200 to 500 m (Vesselinov 2004, 090040). For example, PM-4 has a 260-m screen. As with the shallow screens, the screens could be partially penetrating, meaning the aquifer is thicker than hundreds of meters, or they could penetrate multiple aquifers, meaning the aquifers are thinner than 100 m. Geologically, the semi-confined and fully confined behavior starts deeper than 50 m below the regional water table (Vesselinov 2004, 090040). However, the maximum depth to the bottom of the regional aquifer is uncertain, and the PM wells did not drill to bedrock. Therefore, these aquifers could be very thick, assumedly up to 1000 m.

As noted previously, the uncertainties associated with these choices suggest that a wider range of values is appropriate for the modeling effort so as not to constrain the model's efficacy as a tool to elucidate the system properties, allowing for more complicated and arguably more realistic behaviors than, for example, pumping test analyses based on analytical solutions.

D-4.2.3 Discussion

Geologic Units

Geologic units are not explicitly considered in the RRM anchor and pilot point approach. However, the gradual transition from unconfined, to semi-confined, to fully confined with depth is honored by the shallow and deep specific storage distributions.

Spatial Distribution

All pilot or anchor points less than 50 m were assigned "shallow" distributions, and all deeper than 70 m were assigned "deep" distributions, based on this designation. Two points fell within this range. The first, CdV-R-37 screen 3, was classified as shallow because it was only 51 m below the water table. The second point was R-32 screen 3, which was 58 m below the water table. The depth of the transition becomes shallower from west to east. So in the middle of the domain it is not unreasonable to classify 58 m as shallow behavior. Additionally, there is a pilot point deeper in the model at this same latitude and longitude, which allows the model enough degrees of freedom to define the transition between unconfined and confined aquifer responses.

Aquifer Thickness

The aquifer thicknesses are intentionally chosen to have a wide range to cover some of the uncertainty in the transition from unconfined to semi-confined to fully confined aquifer behavior. It may have been possible to research the hydrogeology more in depth and develop narrower bounds on aquifer thickness. However, by choosing large ranges of aquifer thickness, the specific storage distributions have more overlap than if the aquifer thickness were chosen to be narrower. These wide ranges allow the inverse modeling associated with the LM algorithm to produce specific storage parameter estimates that account for the 3-D heterogeneous nature of the subsurface in the RDX plume area, as discussed previously.

D-4.2.4 Distribution Development

The distributions for specific storage are developed in log10 space because the reservoir simulator accepts the parameters in the log10 format as input.

For the deep subsurface, data came from data types 1, 3, and 4. The storativity from data type 1 had to be converted into specific storage values according to Equation D-4. This involved an MC simulation that drew from a uniform distribution of deep aquifer thickness that ranged from 10 to 1000 m. Each data value for storativity was combined with a random draw for the aquifer thickness; the ratio is taken and

transformed to log10 space to represent specific storage. Data type 3 was used to calculate a range for specific storage based on textbook compressibility data, as discussed previously. Since data types 3 and 4 were already in terms of specific storage, no transformation was necessary. Once all data types were converted to specific storage, each data point was weighted equally, and a normal distribution was fit (Figure D-4.2-1).

The shallow subsurface distribution used data types 1 and 2. The data are processed separately, and then combined to a final distribution.

For data type 1, the aquifer thickness is assumed to be represented by a uniform distribution with a lower value of 3 m and an upper value of 100 m. The storativity given from the data is combined with a random draw from the distribution of aquifer thickness; the log10 of the ratio is then taken. This is repeated for each data value (n = 16) to produce 16 representative values of specific storage in log10 space based on available data.

For data type 2, the aquifer thickness is again taken from a uniform distribution with a lower value of 3 m and an upper value of 100 m, and specific yield is assumed to be represented by a uniform distribution with a lower value of 0.01 and an upper bound of 0.3. An MC simulation is performed by taking a draw from each distribution. The ratio of specific yield and aquifer thickness is then taken and transformed to log10 space. This process was repeated 1000 times to produce 1000 representative values of specific storage in log10 space based on conceptual knowledge.

Conceptual knowledge of shallow regions below the water table guided the decision to use a truncated normal distribution. An upper bound of the effective specific storage is set to 0.3, based on physical considerations. This corresponds to a specific yield at its upper bound (0.3), and an aquifer thickness of 1 m (Equation D-4), which is very thin and is below the ranges discussed previously (i.e., 3–100 m for shallow aquifers and 10–1000 m for deep aquifers). In log10 space, this corresponds to a truncation at −0.5.

Data types 1 and 2 represent somewhat different physics. Data type 1 comes from data that could represent unconfined or semi-confined aquifers, whereas data type 2 represents only the specific yield of unconfined aquifers.

Because different sets of physics are reflected, these two data types were weighted equally and fit with a truncated normal distribution (Figure D-4.2-2). Since there are 1000 values from data type 2 but only 16 values from data type 1, each value from data type 1 is weighted 62 times more than each value from data type 2 to achieve equal weighting of the two methods.

D-4.3   Kriging Parameterization

Kriging is used to interpolate values of hydraulic conductivity and specific storage to every node within the RRM domain from discrete values at the anchor and pilot point locations (described in section D-4.1).

Spatial interpolation via ordinary kriging is performed using the GeoStats package in Julia (https://juliaearth.github.io/GeoStats.jl). A spherical variogram is utilized and consists of three parameters: range, sill, and nugget. The range parameter defines the distance at which pairs of points are no longer spatially correlated and is calibrated (i.e., not estimated from data) separately for K and S. The sill defines the maximum variance between pairs of points. The sill parameter is set equal to 1 since its value has no impact on spatial predictions (Cressie 1993, 700911). The nugget parameter defines small-scale variability and is set equal to zero.

To allow for directionally dependent correlation structure (i.e., anisotropy), an ellipsoid distance is used instead of the standard Euclidean distance for computing distances between points. The ellipsoid is parameterized by semiaxis scalars and angles of rotation. The scalars are values in [0,1] that scale the range parameter in the x, y, and z directions. Within the RRM, the x and y direction scalars are set equal to 1 because isotropic conditions are assumed in the lateral direction. The z direction scalar is calibrated within the model separately for K and S. Angles of rotation for each semiaxis are set to zero.

Distributions are developed for kriging range and semiaxis for both hydraulic conductivity and specific storage using subject matter expert elicitation. A shiny application developed using the SHELF package in R allows the user to customize a histogram representing plausible values and obtain a parameterized distribution for the customized histogram (https://jeremy-oakley.shinyapps.io/SHELF-single/; https://cran.r-project.org/web/packages/SHELF/index.html). A single beta distribution was developed for semiaxis for both hydraulic conductivity and specific storage (Figure D-4.3-1). Separate zero-truncated normal distributions were developed for range for hydraulic conductivity (mean = 2260, standard deviation = 835) and specific storage (mean = 3900, standard deviation = 1200), as shown in Figure D-4.3-2.

The control points consist of anchor points and pilot points. Anchor points are located at wells, where enough local information is available to develop an independent distribution for each anchor point. Pilot points are placed throughout the area of interest to provide additional heterogeneity options in the aquifer at locations without local data, where **K** values are less certain. Pilot points are assigned aquifer parameter distributions based on the geologic layer they are placed within. For example, a pilot point placed in the Puye Formation would be assigned parameter distributions for hydraulic conductivity developed for the Puye Formation. Based on the central estimate of each anchor point, a spatial model is developed that predicts values for each point in the domain that honors any spatial trend in aquifer test data at the site. In forward model suite runs, initializations of K for calibration points in data-rich portions near the RDX plume are set with draws that honor the spatial model that accounts for the spatial correlation structure, while initializations of K for calibration points in data-poor portions near the plume are set with independent draws based on the estimated K domain in the area.

For each model run, hydraulic conductivities (K_x, K_y, K_z) and specific storage (S_s) at each anchor point and pilot point are drawn from their respective distributions (K_x and K_y are drawn from the same distribution, K_{xy}). Because of limited information about the kriging parameters, uniform distributions from previous modeling studies in the area were used for the range parameter for both K and S_s (LANL 2018, 602964). A uniform distribution over [0,1] was specified for the vertical semiaxis scalar parameter for both K and S_s. This distribution allows the calibration flexibility to determine whether anisotropic or isotropic vertical structure in K and S_s is needed. The control points and kriging parameters are then used to develop a continuous field for K and S_s. Areas that extend beyond the distance specified by the (x,y,z) range parameters from the control points are treated as homogeneous and equal the overall mean K or S_s value. Figure D-4.3-3 shows K values derived from the spatial model for lateral hydraulic conductivity at two depths along with all the pilot and anchor points in the domain.

Specific storage kriging scale distributions are wider than those of hydraulic conductivity in order to replicate drawdown responses to pumping at the RDX site. Specifically, a combination of a low-scaling parameter (anisotropy ratio, krige_v_semiaxis key in the model) and a higher-scale parameter are required to match the drawdown responses to the PM-2 and PM-4 pump tests in the aquifer. This is likely necessary to mimic the shift in aquifer confinement at different depths in the aquifer (i.e. unconfined at the surface, semi-confined with depth, and confined at depth).

D-4.4   Advective Porosity

Total porosity, ϕ, defines the volume fraction of a cell that is not occupied by solid rock material. In contrast, advective porosity, also referred to as mobile or effective porosity (ϕ_e), is the porosity through which advective transport may occur. In earlier versions of the RRM that did not include any pumping, total porosity was a direct input to the model, and distributions were developed for this parameter, along with advective porosity expressed as a fraction of total porosity. In the current version, only advective porosity is used as a direct input, and total porosity is calculated dynamically using the specific storage model *ppor* in FEHM (Zyvoloski 2007, 700904). The total porosity and fractional advective porosity distributions previously developed are now combined to generate the single advective porosity distribution that is used in the RRM. This approach was used because there is correlation between the total porosity and the advective porosity, and data are available for total porosity/fractional advective porosity rather than advective porosity directly.

The subsections below present: (1) methodology, including data collection; (2) distribution development for total porosity, fractional advective porosity, and advective porosity; and (3) results. The goal is to develop a distribution for advective porosity following these steps:

1.   Develop a distribution for total porosity (Figure D-4.4-1).

2.   Develop a distribution for fractional advective porosity (Figure D-4.4-2).

3.   Develop a distribution for the advective porosity, which is done by taking the product of random draws of the previous two distributions. This is used in the RRM model and is shown in Figure D-4.4-3 and Table D-4.4-1.

The spatial and temporal scales described by the advective porosity distribution should align with the spatial and temporal scales of the FEHM model. The relationship between the distribution and the model must also include how individual draws from the distribution are used in model development.

Advective porosity is the quantity linking Darcy velocity to average linear ("advective") velocity through porous media. Its theoretical minimum and maximum range from zero to 1, but advective porosity is smaller than the total porosity because the total porosity may include dead-end pores or regions dominated by non-advective (i.e., diffusive) transport.

Advective porosity can be estimated at a given point in the subsurface using borehole data for effective porosity. However, a point measurement will probably not accurately reflect advective porosity at the field scale. Considerable error may be introduced to transport calculations, especially for highly heterogeneous materials such as the primary geologic stratum of interest for the RDX regional aquifer modeling, the Puye Formation (Tpf). Therefore, a combination of field-scale measurements, modeling studies, and statistical analysis of borehole data with appropriate scaling is recommended to constrain advective porosity.

In the RRM, one draw from the advective porosity distribution is used for the entire model domain (~220 km^2 area by ~800 m thick) for the entire timescale of simulation (tens to hundreds of years). Sources of spatial variability in porosity (and hence advective porosity) include differences between the geologic formations present in the RRM domain, intra-formation differences due to geographic setting, factors during deposition, and long-term evolution of the formation. Sources of spatial variability particular to advective porosity include the presence of dead-end pore space, capillary barriers, and diffusive transport regimes. The diffusive regimes commonly exist in low-porosity zones such as clay lenses, which are minimal in the Puye Formation.

While advective porosity variability with time is possible, it is expected to be negligible when compared with the spatial variability described previously in this hydrogeologic setting and timescale. Therefore, the assumption is made that material properties will stay constant over the modeled future.

D-4.4.1   Method

Accurate estimates of advective porosity are difficult to obtain. Geophysical methods are used to estimate "effective" porosity, which may differ somewhat from "advective" porosity but is considered similar enough to be interchangeable for the sake of determining an advective porosity distribution as a function of total porosity. Effective porosity is the porosity available for fluid flow, whereas advective porosity is the void space through which advective flow occurs. For single-porosity, fully saturated, single-phase (i.e., with no mobile air-phase or non-aqueous phase liquid) media, where molecules of the fluid in question (e.g., water) are smaller than pore throats, the two terms are identical. Some confusion is added because of the similarity of the terms and the tendency of computational hydrologists to prefer the term "advective" and field hydrologists to prefer the term "effective" porosity.

Information Collection

The primary material of importance in the regional aquifer in the RDX site is the Puye Formation, although sections of Tschicoma dacite lavas are also present in the area. Total porosity and effective porosity data were entered broadly for all units where available, and a focus was made on obtaining Puye Formation data in the RDX area for the RDX regional model. Since only one draw for advective porosity is made for the entire domain, it is intended to reflect the primary material in the area.

Types of available porosity information include geophysical data from borehole logs obtained during the drilling of wells in the LANL area; other processed experimental data from the site, usually on small-scale samples; and model values used in previous studies. Each of these types of information is discussed in the sections below.

Geophysical Methods

During the construction of many LANL monitoring wells, routine geophysical methods were used to log the borehole for geologic information and estimation of hydraulic properties. Folders containing all geophysical log files were obtained from the publicly available Intellus database (https://intellusnm.com) or several wells in the RDX and chromium site areas. Not all boreholes provide high-quality geophysical data: cased holes such as R-42, for example, should not be used because the geophysical data are unreliable.

Interpretation of the geophysical log data is extremely complex. R-18 is shown as an example. The file labeled R-18_10811506_PEX_REEPAT_005LUP.las contains measurements for density porosity (DPHZ), thermal neutron porosity (NPHI), and epithermal neutron porosity (ENPH). The file R-18_10811506_CMR_REPEAT_010PUP.las contains measurements for combinable magnetic resonance total porosity (TCMR). These represent raw (unprocessed) porosity estimates and they can vary considerably. Figure D-4.4-4 compares porosity measurements for these four methods, both in the entire borehole (VZ and regional [left plot]) and the regional aquifer only (right plot). Density porosity, which is based on density measurements paired with estimated rock unit grain densities to derive porosity, yields better estimates of porosity in the vadose zone compared with the other methods (Figure D-4.4-4, left plot). However, the various measurements converge in the regional aquifer (right plot) where presumably all the pore space is water-filled. The two neutron porosity measurements (NPHI and ENPH) track closely and the values are reasonable compared with what is commonly seen in the Puye Formation. The density porosity (DPHZ) shows a bit more scatter but is generally the same as the

two neutron porosities. The combinable magnetic resonance (CMR) porosity is generally considered the best estimate of porosity in saturated rocks, but in this case it is the clear outlier in the methods. It is a shallow reading tool and is very sensitive to borehole washouts.

When possible, processed porosity and effective porosity data from the Elemental Log Analysis (ELAN) program were found in the geophysical log files and entered into the database. The ELAN analysis applies borehole and environmental corrections and takes the best characteristics of multiple measurements (e.g., the four separate porosity measurements) to come up with a best estimate of geophysical parameters. For example, density porosity is the best estimate of porosity in the unsaturated rocks because the other three measurements (thermal and epithermal neutrons and CMR) measure water in pores. In saturated rocks, the thermal and epithermal neutrons and CMR are considered to be better porosity estimates. Nevertheless, all geophysical estimates of porosity and effective porosity must be considered to have an unknown amount of measurement error. Kleinfelder (2005, 087846) notes "…Interpretations should be made from the ELAN results with the understanding that the mineral-fluid model represents a mathematically optimized solution that is not necessarily a physically accurate representation of the native geologic formation. Within this context, the ELAN model is a robust estimate of the bulk mineral-fluid composition that accounts for the combined response from all geophysical measurements." ELAN and other geophysical measurements of porosity are considered small on a spatial scale because they cover 0.5-ft sections down the length of the borehole.

Geophysical data are also subject to other measurement errors, particularly related to the strength of the material and quality of the borehole. Where material is soft and less consolidated, borehole "washouts" may be more frequent and can often affect the porosity data. The washouts may be identified in geophysical logs using caliper or gamma data. Figure D-4.4-5 shows a section of geophysical log from R-19 where washouts have been identified. These correspond to unrealistic spikes in porosity data. All geophysical data were evaluated for appropriateness, and data selected for filtering are indicated in the sections that follow.

Other Experimental Data

Other experimental methods for calculating porosity from a rock sample include helium injection, imbibition (to calculate saturated water content), or using measured bulk density (using oven-dry analysis) and assumed particle density to calculate porosity. In the latter approach,

$$\phi = 1 - \frac{\rho_b}{\rho_g},$$ **Equation D-7**

where, ρ_b is bulk density [g cm^{-3}] and

ρ_g is grain density [g cm^{-3}].

An assumed grain density of 2.65 g cm^{-3} was used.

Modeling Values

There are two types of "values used" (VU) data entered in the database. The first would be estimates determined by expert judgement to be the best representative value (or distribution) for use in a model. These values are suspect because the methods used to determine them are not always known, and it is frequently the case that conservative assumptions are embedded in the data. Therefore, this type of VU information is generally considered the lowest quality type of information.

The second type of model VU data in the database is based on model calibration. While potentially these values could represent a higher-quality source of information (e.g., upscaling to the proper scale is already accounted for), there are many other variables and parameters that may be correlated with porosity and therefore the magnitude of the calibrated values could be reflective of other processes, especially ones that are not modeled. For example, if advective porosity is not modeled, a value reported as a total porosity may essentially represent an effective tracer porosity if concentrations were matched in the model calibration.

Therefore, all VU information is considered low quality, but values are collected and reported in the data set to show as comparisons alongside other collected information. During exploratory data analysis, if the VU data are observed to fall far outside the ranges of the experimental/geophysical data, the values may be filtered out based on assumptions of quality.

Methods Discussion

Although the RRM contains data on multiple different geologic formations (as described above), the plume is primarily found in an area containing Puye Formation fanglomerate aquifer materials with some nearby Tschicoma Formation (Miocene-age dacite) to the south and other units within the model domain further downgradient or at depths far below the plume (see Appendix C, section C-1.2.1).

It is not expected that the plume presently resides in non-Puye Formation units or will reach downgradient locations in other units in appreciable concentrations, and as a single advective porosity value is applied for the model domain, only Puye Formation data are considered for the distribution. During geophysical sampling, point data were taken every 0.5 ft so the sample size is small and there are few wells available to inform distributions. Because a single value is applied to the entire spatial domain of the model, the distribution of the average is developed.

The relationship between advective porosity and total porosity is incorporated by developing a distribution for the proportion of total porosity equal to advective porosity. The underlying distribution for this relationship is developed.

D-4.4.2   Distribution Development

As described previously, the RRM requires a distribution for advective porosity. However, the advective porosity distribution was developed by combining the total porosity distribution and the fractional advective porosity distributions from a previous version of the RRM. Therefore, the subsections below describe the distributions for the total porosity and the fractional advective porosity. After that, the advective porosity distribution, which is developed by drawing from the previous distributions, is presented.

Total Porosity

For the RRM, a single distribution is developed for total porosity in the Puye Formation. The data used in distribution development are shown in Figure D-4.4-6. Data classified as "Non-Well Info" are values used deterministically from other model calibrations.

Sample size considerations are especially important in the development of a distribution for the average. As sample size increases, so does confidence in the value of the average. However, this principle depends on the assumption that each value is independent from one another. Although $n = 1919$ estimates for porosity are available, these were taken from only eight boreholes and two additional values from separate model calibrations. For measurements taken within the same borehole, similar biases and measurement error are expected, so these values cannot be assumed to be independent. Different

boreholes should have independent values. Therefore, the effective sample size to inform variation around the average is the number of independent pieces of information (8 boreholes + 2 calibrations, *n* = 9).

The distribution was developed via a bootstrap simulation within boreholes. For each borehole, a random measured value for porosity was sampled from the empirical distribution. For each of the two model calibrations, the measured value was recorded. The weighted average was then calculated across all boreholes/model calibrations. Each borehole/model calibration was weighted according to its sample size. The sample sizes within boreholes ranged from 2 to 1339. This process was repeated 1000 times to obtain 1000 weighted averages, and a normal distribution was fit to the weighted averages.

The distribution developed for total porosity is shown in Figure D-4.4-1. The histogram and points show all the data used to inform distributions.

Fractional Advective Porosity

Advective porosity must be less than total porosity. Depending on the material, advective porosity may also be highly correlated with total porosity. The data available are shown in Figure D-4.4-7. In the Tpf, advective porosity appears to be correlated with total porosity, and there appears to be no correlation between total porosity and advective porosity as a percent of total porosity.

Because it is not realistic for advective porosity to be equal to total porosity, the paired measurements where this condition was met were excluded from distribution development. The underlying distribution is developed for the remainder of paired measurements. The data used to inform the distribution are shown in Figure D-4.4-8. The distribution of the data appears approximately normal; however, since the underlying distribution is developed rather than the distribution of the average, gamma, Weibull, and generalized beta distribution fits were also tested. Goodness-of-fit statistics and visual examination showed normal was the best-fitting distribution, so a normal distribution was fit to data. The final distribution is shown in Figure D-4.4-2.

Advective Porosity

Since total porosity is no longer used in the RRM, a single distribution for advective porosity was developed from the total porosity and fractional advective porosity distributions (presented above) from the RDX model via simulation. Ten thousand draws were taken from each distribution and 10,000 products were calculated. These products represent plausible values for advective porosity in itself. The distribution of the products was skewed and follows a beta (4.38, 23.3) distribution (Figure D-4.4-3). The beta distribution is naturally truncated at 0 and 1. The 1st and 99th percentiles of the distribution are 0.04 and 0.35, respectively.

D-4.4.3   Results

The distributions developed are given in Table D-4.4-1. Only the advective porosity distribution is directly sampled in the RRM.

D-4.5   Aqueous Dispersivity

Aqueous-phase (i.e., dissolved) RDX may be transported by advection. Therefore, it is subject to dispersive processes in the porous materials that compose the VZ and SZs of the RVZM and RRM. The RVZM contains both SZ and VZ regions, whereas the RRM is saturated everywhere. Dispersion is a process that spreads out an advecting solute front as it migrates through a porous material. It arises from (1) differing pore sizes with correspondingly different flow velocities, and the existence of mobile and

immobile zones to flow, (2) differing solute speeds within individual pores because of the no-slip boundary condition, (3) different path lengths for different tortuous routes taken through the pores, and (4) heterogeneity in the material (Fetter 1994, 070942). The dispersion coefficient has units of length (m) and is defined in three directions relative to the flow path: longitudinal (α_L), transverse horizontal (α_H), and transverse vertical (α_V).

D-4.5.1   Flow-Direction and Length-Scale Dependencies

Dispersivities are typically larger in the longitudinal (same direction as flow) direction than in transverse (perpendicular to flow) directions. For the 3-D RDX models (both RVZM and RRM), dispersivities are required in each direction. The relative importance of longitudinal dispersivity in a given transport situation depends on the Péclet number, a dimensionless ratio that compares the effectiveness of advective versus diffusive transport (Fetter 2008, 700912). When liquid infiltration rates and hence velocities are very low, the effect of aqueous dispersion on solute transport is small, and the effect of diffusive transport is relatively higher. Where higher infiltration rates and velocities are found, dispersive transport would be expected to increase accordingly, and diffusive transport would be less influential.

For the RRM, the length scale of interest for the calculation of aqueous dispersivity is defined by the distance RDX transport occurs from an RDX source to a given downstream location of interest, which is on the order of hundreds to thousands of meters. In the RVZM, transport occurs predominately downward, and the length scale of interest is the average vertical thickness of each geologic unit. Exceptions are made for lateral transport in the perched and regional groundwater in the RVZM. In these locations, the length scale of interest is a lateral distance assumed to be on the order of tens to hundreds of meters.

A single distribution is developed for dispersivity for each direction in the saturated zones in both the RRM and RVZM. Each geologic unit in the unsaturated areas of the RVZM will have a separate value drawn for dispersivity. The average dispersivity over the spatial volume of the material in the model is assumed to be the quantity of interest. The value drawn from the distribution of the average will be applied over the entire time the model is run (tens to hundreds of years). This is done under the assumption that material properties will stay close enough to constant over the modeled future.

Dispersivities are also spatial scale-dependent (Gelhar et al. 1992, 102465) and are a function of the material properties (e.g., homogeneity of pore sizes) and water content (Stephens 1995, 700914). Some authors suggest unsaturated zone dispersivities are lower than in the saturated zone (Ho et al. 1999, 700883), while others note a maximum at intermediate saturation or increasing dispersivity with decreasing saturation (Stephens 1995, 700914). Because dispersion produces an apparent diffusive-like distribution of solutes, it is typically combined with diffusion coefficients into a single effective "hydrodynamic" dispersion term in numerical models (Fetter 1994, 070942). The RRM handles dispersion in this way. Diffusion parameters are described separately.

D-4.5.2   Treatment of Uncertainty

Values of dispersivity in the RVZM and RRM are highly uncertain because the primary geologic stratum of interest in the regional aquifer, the Puye Formation (Tpf), and the layers that compose the VZ, are extremely heterogeneous. Therefore, distributions of dispersivity are needed for both the RVZM and RRM. First, available information about aqueous dispersivity coefficients relevant to materials at the RDX project area was assembled. Then distributions were developed that appropriately described the potential values for dispersivity in the RVZM and RRM. In this work, three values of aqueous dispersivities (longitudinal, transverse, and vertical) were developed.

Sources of uncertainty in dispersivity include (1) spatial heterogeneity in geologic materials not captured by the model, (2) uncertainty in velocity and water content, (3) the influence of pore structure (e.g., dead-end pores) and fracturing, (4) whether laboratory-scale samples were tested as undisturbed or repacked materials, (5) experimental error, and (6) variability in methods among sources in the literature. These sources of uncertainty are considered in distribution development in a way that is consistent with the spatial and temporal scales of the RVZM and RRM. Dispersivity data span a wide range of rock types, saturation conditions (VZ, SZ, or both), and experimental conditions and scales. In theory, since dispersivity depends on the porous medium structure, different materials are expected to have different dispersivities. However, site-specific data are rarely available and various rules of thumb for dispersivity are commonly used across materials instead, e.g., $\alpha_L = 0.1L$ (Gelhar et al. 1992, 102465), where L is a length scale. In this work, the relationship between the aqueous dispersivity coefficient and length scale is estimated from available data by weighting information sources according to relevance of the information to the site and relative quality of the information. Uncertainty in the relationship was also quantified and used in developing the distributions of aqueous dispersivity as a function of scale length.

D-4.5.3   Information Collection

An extensive review of both peer-reviewed and white paper literature (e.g., reports from performance assessments) was performed, and dispersivity data from over 16 sources were compiled into a master database. The intention was to include data from a wide range of available sources, so that distributions developed based on the data reflect the uncertainty in the subsurface environment at the site, and to have the database be as complete as possible to promote flexibility in including and excluding data based on expert judgment of the applicability to the site and overall quality of the source. The database sources included the following types of documents, in generally decreasing order of completeness of information:

1. Papers containing original experimental data, typically found in peer-reviewed journals and including extensive information about experimental conditions, methodology, and uncertainty.

2. Literature reviews (LR), which provide references to the original data and generally contain less information about specific experimental conditions and methods.

3. Model description white papers, which describe dispersivity values selected by researchers for a particular modeling application. These papers sometimes provide an explanation of the methods used to select the values, often based on a combination of literature review, such as the papers in category 2 above, site-specific data if available, and expert judgment. This category includes the VU data for previous modeling at Area G (French et al. 2008, 106890).

All data that could be obtained from these source types were entered into the database, including (when available) dispersivity values; type of value (e.g., average, empirical fit); range of values; spread (e.g., standard deviation); number of samples; rock or soil type/texture; location; length scale; saturation (saturated or unsaturated); and other relevant information. When length scale was uncertain, it was inferred based on other information in the source (e.g., model dimensions).

A great deal of dispersivity data are summarized across many rock types in two seminal references (Gelhar et al. 1992, 102465; Neuman 1990, 090184). Both sources give estimated regression equations. The raw data in Gelhar et al. (1992, 102465) were used instead of the regression equation because the raw data are more easily combined with observations from other sources. The raw data from Neuman (1990, 090184) were not available, so the regression equation was used. Because there are so few data that apply specifically to the materials in the RVZM and RRM, groupings for which different distributions are developed are broad. For longitudinal dispersivity, a single distribution is developed for the RRM, and a separate distribution is developed for the RVZM. For transverse horizontal and transverse vertical dispersivity, a single distribution is developed for each direction based on the relationship of each to longitudinal dispersivity.

D-4.5.4   Longitudinal Dispersivity

The data used in distribution development are shown in Figure D-4.5-1. The sizes of the points reflect the relative influence of each in the final distribution, according to quality of information and relevance to the site (see section D-4.5.7 below). The shape of the points indicates source type: papers reporting experiments (Exp), literature reviews (LR), model application papers (Model), and reported values used in modeling (VU). The line is not a regression fit to the points, but rather an additional source of data (Neuman 1990, 090184) used in distribution development.

D-4.5.5   Transverse Dispersivity

Transverse dispersivity values paired with longitudinal dispersivity values were given only in Gelhar et al. (1992, 102465). Because these data were given the same weights for both the SZ and the VZ, the same distribution was applied to both the RVZM and the RRM for each direction. Two distributions are developed: one for the relationship between longitudinal dispersivity and transverse horizontal dispersivity, and the other for the relationship between longitudinal dispersivity and transverse vertical dispersivity. The data available from Gelhar et al. (1992, 102465) are plotted in Figure D-4.5-2 Similar to Figure D-4.5-1 the regression line, which is a "rule of thumb" presented in the literature, represents additional data incorporated into distribution development.

D-4.5.6   Flow-Direction and Length-Scale Analysis

The format for dispersivity used in the RRM is in terms of model coordinate system x, y, and z, rather than having the model determine the direction of flow for longitudinal, transverse horizontal, and transverse vertical. Both are possible options in FEHM's tracer transport module. Therefore, the closest alignment of flow direction to this coordinate system and the direction of expected anisotropy for each material is used to define the corresponding dispersivity distribution that is drawn.

In the RRM, x most closely aligns with the flow direction (west to east), so it is assigned longitudinal dispersivity (αL). The y-direction draws from the transverse horizontal distribution (αH). As the material is highly anisotropic in z, flow is primarily lateral, so this is assigned the transverse vertical distribution (αV). The same distribution is used for the regional aquifer in the RVZM, whether in the Puye or Tschicoma Formations. For unsaturated flow in the RVZM, the direction of flow is primarily vertical, so z is assigned longitudinal dispersivity (αL). Because x and y are isotropic compared with the vertical dimension, both are assigned the transverse horizontal distribution (αH).

For horizontal transport in the Puye Formation in the regional aquifer, length scale would be defined by the distance between the plume source at the regional aquifer and the point of interest for measurement, and/or target locations. This is assumed to range from 500 m to several (up to 6) km, the distance to several water-supply wells (PM-2, PM-4, PM-5). Target data locations are much closer, within a few hundred meters, so length scales overall for the saturated regional aquifer zone are allowed to range from 125 to 6000 m. For the RVZM, scale lengths are the thicknesses of the geologic units and range from 1 to 300 m depending on the unit.

D-4.5.7   Weighting

For distribution development, a weighting scheme was developed to account for the source quality and relevance of the data for the given dispersivity grouping in Table D-4.5-1. The variables in the database used to implement the weighting are value type (e.g., experimental, or value used in another model), rock type, zone type (saturated or unsaturated), and site. Other types of data (e.g., those tabulated as part of a

literature review) are considered based on their similarities to these categories and are usually considered as VU.

Data of the type VU in another model are weighted lower because these are considered the lowest quality information and may be based on data from other sources already in the database. Although considerable expert judgment may have gone into their selection, it is often difficult to know how much subjectivity has been used (e.g., whether the value was selected to be "conservative" or to meet other desired requirements, and is not necessarily reflective of the conditions believed to exist at a site).

Because limited data are available for unsaturated and saturated conditions, all the data are retained within both the VZ and SZ categories for distribution development and are simply up-weighted or down-weighted according to the quality and relevance. The RRM domain is entirely saturated within the regional aquifer, so saturated zone sources are weighted more heavily than unsaturated zone sources for the regional model distribution, while the opposite is true for the RVZM distributions.

The final list of weights used for the sources is given in Table D-4.5-1, along with the length scales represented by that source. The weights were developed using subject matter expertise and professional knowledge about relevance to the site, including soil types used in a study; environmental conditions (e.g., level of saturation); type of study (e.g., laboratory, field, modeling); and reliability. A weight of 1 can be thought of as perfectly representing site conditions.

D-4.5.8   MC Simulation and Bootstrapping

An approach combining MC simulation and bootstrapping (i.e., sampling with replacement) is used to approximate the distributions of the estimated mean aqueous dispersivity as a function of scale length, using the weighting of data sources described above. Separate distributions are developed for the RRM and the RVZM through the use of different weights for the sources. The following steps are taken to develop each distribution, using the associated weights:

1. Sample a source (i.e., reference article or report) with probability proportional to the weights assigned to the sources (see Table D-4.5-1)

2. Sample a record (i.e., row from the database) from the source chosen in step 1 and obtain a dispersivity and scale length pair according to the rules in the next step.

3. Record a scale length and dispersivity pair as follows:

    a. If the record (a row in the data set) provides both scale length and estimated dispersivity, record the pair of values.

    b. If the selected record provides a VU for dispersivity, an associated scale length thought to represent the context within which the value was developed is used. This information is contained as the x-value associated with these dispersivities in Figure D-4.5-1. Record the associated scale length along with the VU dispersivity.

    c. If the selected record reports a distribution for dispersivity at a given scale length, then the reported scale length is used and a random draw from the associated dispersivity distribution is used to obtain a value for dispersivity. Record the reported scale length and the random dispersivity value.

    d. If the selected record provides a formula relating scale length and dispersivity with no specific recorded scale length (Neuman 1990, 090184), then draw a random scale length from a uniform distribution over the range of relevant scale lengths given in Neuman (1990, 090184). Predict the dispersivity from the selected scale length using the stated relationship. Predict the dispersivity by drawing from the predictive distribution at the value of the selected scale length. Record the random draw of scale length and the associated predicted dispersivity.

4. Repeat steps 1–3 to create a single bootstrap sample of the same size as the available number of records by sampling with replacement from all the available records with weights for the sources as described previously.

5. Fit a regression model of dispersivity on scale length to the bootstrap sample, on the log10-log10 scale to obtain an estimated intercept and an estimated slope for the bootstrap sample.

6. Repeat steps 1–5 2000 times to obtain 2000 pairs of bootstrap intercepts and slopes making up the bootstrap distributions of the regression coefficients describing the relationship between the scale length and mean dispersivity. The estimated means, standard errors, and estimated covariance from these distributions are used to specify the final distributions used in the models that describe the distribution of mean aqueous dispersivity for a given scale length.

The bootstrap distributions for the estimated slopes and intercepts, along with the covariance between the two, are used to obtain the distribution for the estimated mean aqueous dispersivity for a given scale length. The variance of the distribution reflects the uncertainty in estimating the mean as a function of length from available information under the weighting.

The general equations used to describe the distributions developed for the two models as a function of scale length (*L*) are:

$$\hat{\mu}(L) = \log_{10}\alpha_w \sim N\big[\hat{\mu}(L), SE_{\hat{\mu}}(L)\big] \text{ ,} \qquad \textbf{Equation D-8}$$

where

$$\hat{\mu}(L) = \ \widehat{\log_{10}\beta_1} \ + \hat{\beta}_2\log_{10}(L) = \ \hat{\gamma}_1 + \ \hat{\gamma}_2\log_{10}(L) \qquad \textbf{Equation D-9}$$

and

$$SE_{\hat{\mu}}(L) = \ sqrt[SE(\hat{\gamma}_1)^2 \ + \ (\log_{10}L)^2\,SE(\hat{\gamma}_2)^2 \ + 2\log_{10}(L)\,Cov(\hat{\gamma}_1,\hat{\gamma}_2)]. \qquad \textbf{Equation D-10}$$

D-4.5.9   Longitudinal Dispersivity Distributions

The bootstrap estimated regression lines for each bootstrap sample are displayed in Figure D-4.5-3. For the RRM, only data with scale lengths between 10 and 1E5 m were used to describe the distance from an RDX source to current wells or potential locations of interest to an order of magnitude approximation. For the RVZM, only data with scale lengths between 1 and 500 m were used as an order magnitude approximation of the distance from the ground surface to the top of the saturated zone. The spread of the collection of red lines associated with a particular scale length represents the spread of the distribution of longitudinal aqueous dispersivity at that scale length.

The values estimated for the distributions are given in Table D-4.5-2. Values for the RRM apply to length scales from 100 to 10,000 m. Draws from this multivariate distribution provide a representative average value of aqueous dispersivity on the log10 scale for a given scale length associated with a given geologic unit, which is then back-transformed to the original scale before use in the FEHM model.

D-4.5.10   Transverse Dispersivity Distributions

The distributions describing the relationship between transverse and longitudinal dispersivity were developed from paired data. However, the only paired data available come from Gelhar et al. (1992, 102465), for which equal weights were used for unsaturated zone (UZ) and SZ distributions; therefore, a single distribution was developed for each direction and each observation was weighted equally. The bootstrap estimated regression lines for each bootstrap sample are displayed in Figure D-4.5-4. The spread of the collection of red lines associated with a longitudinal dispersivity value represents the spread of the distribution of transverse dispersivity at that longitudinal dispersivity. The values estimated for the

distributions are given in Table D-4.5-3. Draws from these multivariate distributions provide a representative average value of transverse dispersivity in each direction on the log10 scale for a given scale length associated with a given geologic unit, which is then back-transformed to the original scale before use in the FEHM model. Figure D-4.5-5 displays distributions on the original scale and log10 scale for selected scale lengths for illustration.

Ultimately, these distributions were used to develop three independent distributions for dispersivity, one for each of the three directions. Distributions were fit to plausible values for each of the three directions. These values were developed using the following process:

1. A representative scale length was drawn from a uniform distribution, with the minimum at 125 m and the maximum at 6000 m, the estimated range of length scales in the Puye Formation (Table D-4.5-1).

2. A draw from the multivariate normal distribution developed for the relationship between length scale and longitudinal dispersivity (regional aquifer) was taken. The length scale from step 1 was transformed into a longitudinal dispersivity using the draws for β_0 and β_1.

3. A draw from the multivariate normal distribution developed for the relationship between transverse horizontal and longitudinal dispersivity was taken. The longitudinal dispersivity from step 2 was transformed into a transverse horizontal dispersivity using the draws for β_0 and β_1.

4. A draw from the multivariate normal distribution developed for the relationship between transverse vertical and longitudinal dispersivity was taken. The longitudinal dispersivity from step 2 was transformed into a transverse vertical dispersivity using the draws for β_0 and β_1.

5. Steps 1–4 were repeated 10,000 times, and the 10,000 values for each direction were combined. A lognormal distribution was fit to each set of values.

The final distributions developed are shown in Figure D-4.5-6 and displayed in Table D-4.5-4.

D-4.6   Hydraulic Window Parameters

The RRM domain begins at the top of the regional aquifer, where it is assumed that RDX has traveled through the VZ (including the perched zones) to the regional water table. These pathways are referred to as "hydraulic windows" or "drip points." Their footprint on the regional aquifer is referred to as the "source" of RDX at the water table. This is distinct from the source of RDX at the land surface. The hydraulic windows in the RRM are characterized as ellipses parameterized by a multivariate normal distribution. Several parameters relating to size, shape, location, RDX concentration, and recharge rate define the source ellipses. Below, each of these characteristics and its distribution development are described in detail.

Previous investigations have addressed the question of whether multiple hydraulic windows are required to match the observed RDX trends in the regional aquifer, or if a single hydraulic window is sufficient to match the data (LANL 2018, 602963). As this question remains uncertain, distributions are developed to allow for two RDX-contaminated hydraulic windows, referred to as "primary" and "secondary," but it is possible to have the secondary source set to zero flux so that a single RDX source is present.

D-4.6.1   Source Location

Multiple lines of evidence are used to develop probability distributions characterizing the location of the source center at the water table. Geostatistical analyses are carried out to combine lines of evidence into a probabilistic representation of the location. The lines of evidence pointing to the location of the primary source are the concentrations at well screens in the regional aquifer, conceptual model information, and conceptual knowledge regarding location of a possible upgradient source. The lines of evidence pointing

to the location of the secondary sources are 800-ft buffer boxes around the low and medium surface sources, along with results from the P&D tool.

The outline of the centroid of RDX mass at the regional aquifer, defined by concentrations in the regional aquifer, is the strongest line of evidence for source location. It is the kidney bean shape with the leading edge at R-18, labeled "C" in Figure D-4.6-1. The CSM information is perhaps the most difficult to capture quantitatively. Geological surfaces and physical structures (faults) likely play a role in transport. Currently, a bounding box is developed to quantitatively describe the limits of source location and is labeled "CSM" in Figure D-4.6-1. The northern boundary of the box is based on an estimation of the possible northern boundary of the source, and it is identified by the northing of well R-18. The southern boundary is based on the nondetected RDX concentrations at the R-25 screen in the regional aquifer. Given that the local gradient is southwest-northeast (as opposed to the regional west-east gradient), a more focused polygon representing a possible upgradient location for the source is developed by expert opinion and is labeled "UpGrad" in Figure D-4.6-1.

For the secondary source, polygons representing 800-ft buffers around each low and medium concentration surface source location identified in LANL (2012, 213573) are used to quantitatively capture uncertainty in the location of surface sources shown in Figure D-4.6-2. These are labeled "SS_Low" and "SS_Med" in Figure D-4.6-3. The choice of 800 ft as a buffer size was based on likely migration distances during infiltration to the water table. The P&D tool also directly provides quantitative information regarding the possible source centers. To incorporate this information into distribution development for source location, a convex hull was drawn around the source centers generated from the P&D model. The source center is assumed to be equally likely at any location in the convex hull. The convex hulls derived from the P&D tool output for the secondary source are pictured in Figure D-4.6-3, labeled "PD2" (LANL 2018, 602963). The P&D output for the stronger source is slightly farther north and is not used in distribution development.

Several lines of evidence are omitted and are not used to inform the location of the primary source. The P&D model output for the primary source is not ultimately used to inform primary source location because site experts deemed the locations too far north to be realistic. Additionally, the 800-ft buffer boxes around the 260 Outfall and the losing reach of Cañon de Valle are classified as high concentration surface source locations but are not used to inform the subsurface location of the primary source. This is because it is likely that the "hotdog" footprint along Cañon de Valle has moved by the time the contamination has infiltrated to the depth of the water table. Lastly, RVZM results are not used as a line of evidence to define source location. The RVZM has a limited extent that does not include the location where the highest RDX has been measured in the regional aquifer, so it is not a line of evidence that can be effectively used to constrain source location.

A regular grid is laid over the area depicted in Figure D-4.6-1 and the number of lines of evidence is recorded for each grid cell. Cells with more overlapping lines of evidence are assumed to have higher probability of being the source center. All lines of evidence are weighted equally, assuming each line of evidence is comparable in its reliability of information. A multivariate normal distribution is fit to the data, where the density is assumed to be represented by the number of overlaps at a grid cell. The method of moments is used to fit the distribution, where the weighted longitude and the weighted latitudes define the mean vector. The weights are the number of overlaps for a given grid cell. The diagonals of the covariance matrix are defined by the weighted variances of the latitudes and longitudes, and the covariance is calculated from a weighted correlation. The weights in all calculations are defined by the number of overlaps for a given grid cell. The wtd.mean() and wtd.var() functions in the Hmisc R package, as well as the corr() function in the boot R package, are used to calculate these quantities.

The density of the fitted multivariate normal distribution on the regular grid is displayed in Figure D-4.6-4 with the color gradient indicating density. The orange ellipse indicates the 68th percentile of the distribution, and the yellow ellipse indicates the 95th percentile of the distribution. Since the MADS framework (https://mads.lanl.gov/) requires hard constraints on both latitude and longitude with no correlation, a bounding box is defined based on the 95th percentile ellipse. The bounding box is slightly larger in area than the ellipse.

Note that the sizes of the ellipses in Figures D-4.6-1 and D-4.6-5 do not represent the sizes of the sources. Rather, the sizes of the ellipses represent uncertainty in the source center (x0, y0). The use of a multivariate normal distribution to quantify uncertainty in the locations of the source centers, as well as to describe the shape of the sources, is coincidental. Distribution development for the radii and source eccentricity are described below.

D-4.6.2   Source Size and Shape

The distributions for source radii in the *x* and *y* directions are informed by the P&D analysis, RVZM results, and the region of high concentrations observed in the regional aquifer.

Results from the P&D analysis (Figures D-4.6-6 and Figure D-4.6-7) illustrate that there is large uncertainty in the source size, depending on both source location and the time of source onset. The first P&D source ranges in size from very small to about 150 m in r_x and about 175 m in r_y. The second source is similar to the first in terms of r_x, but may be larger in r_y, ranging from very small to about 300 m.

Results from the RVZM are also highly variable with time. The sources identified in the RVZM are typically smaller in earlier years and grow with time ((Figure D-4.6-8). The size of the secondary source in the *x*-direction (r_x) is generally smaller than the primary source initially but is larger than the primary source in the later time steps (near 2050).

Since source radius is not allowed to vary with time in the RRM, a distribution for the average radius over time in the *x* and *y* directions is developed. As for source location, one distribution is developed to represent size of the primary source, and a second distribution is developed to represent size of the secondary source. Results from three lines of evidence—the RVZM, the P&D analysis, and well concentrations—are combined to develop one distribution for radius in the *x* and *y* directions.

First, separate distributions are developed for the VZ and P&D tool results, and then the distributions are combined to select a final distribution. The mean of each individual distribution is set to the average radius, and the standard error is the standard deviation divided by the square root of the number of "data" points. The number of "data" points in the P&D model is the number of realizations, and the number of "data" points in the RVZM is the number of time steps.

The distributions are combined in a way so as to retain the variance among the models as a representation of model uncertainty. The mean of the combined distribution is set to the average of the means of the P&D and RVZM distributions. The standard deviation of the combined distribution is calculated by subtracting the smallest 2.5th percentile from the radius defining the kidney bean shape in the regional aquifer and dividing by 4.

The same process is followed for the secondary source, using the same concentration data but using RVZM and P&D results for the secondary source. The *x*-radius of the secondary source has a smaller mean than the primary source, but distributions are fairly comparable (Figures D-4.6-9 and D-4.6-10).

Source shape is highly correlated with source size and source location. Source shape depends heavily on the physical features that are present at specific locations. Although sources are in general expected to have low eccentricity, certain physical features such as the alluvial aquifer at Cañon de Valle, fractures, faults, and perched zones may lead to more elongated shapes. These shapes are highly correlated to the locations of these physical features.

The lines of evidence informing source shape are the results of the P&D tool as well as the RVZM. Source shape somewhat varies with location in the P&D output (Figure D-4.6-6). The source shape identified by the RVZM is also highly dependent upon the fixed source locations.

Source centers (x_0, y_0) are not restricted to a discrete set of locations; rather, center is represented by a bivariate continuous probability distribution. It is thus difficult to correlate center with shape in a continuous way when combining information from lines of evidence that are variable and discrete in both location and shape. For this reason, source shape is characterized by a uniform distribution with a minimum of −0.9 and a maximum of 0.9, reflecting the knowledge that no shape (other than perfectly linear) can be excluded and acknowledging the difficulties in characterizing a source shape that could apply to location in a continuous way. The selection of a uniform distribution also allows the calibration more freedom in initialization. This allows exploration of a wider domain of shapes than might be explored if a distribution with more restrictive percentiles were used to constrain the starting values allowed in the calibration.

D-4.6.3 Source Concentration

Source hydraulic windows have a concentration of RDX when the contaminant plume reaches the surface of the regional aquifer. These sources are conceptualized as having a maximum concentration at the center of the window, which decreases according to a bivariate normal distribution out to the 68th-percentile isopleth. The quantity estimated by this distribution is the peak concentration in the center of the source hydraulic window.

Transport of RDX is calculated via the advection-dispersion equation (Zyvoloski 2007, 700904). Because of its relatively low solubility, RDX is conceptualized as an aqueous-phase solute, with no variation in density based on concentration. RDX is simulated exclusively in the aqueous phase because the maximum concentration of RDX will not exceed the solubility limit. Transport is assumed to be conservative (i.e., no chemical reactions occur or RDX degradation occurs). The degradation of RDX is dependent on environmental variables. RDX has been shown to degrade at higher levels of pH and under anaerobic condition. The regional aquifer in the vicinity of the RDX plume has a neutral pH of 7.5 (Heerspink et al. 2017, 602560). Groundwater in the regional aquifer is well oxygenated (dissolved oxygen varying from 5–7 mg/L) (LANL 2018, 602963). Therefore, no RDX degradation is assumed to occur in the RRM.

There is limited raw data to inform the concentration of RDX once it reaches the regional aquifer. At the surface, RDX was assumed to be released at its solubility limit. Transport through the large VZ is complex and will alter the concentration upon reaching the regional aquifer. Some concentration data have been collected in both the VZ and regional aquifer, providing a small amount of data with which to constrain a distribution. However, these data are sparse and spread out in both time and space, making them useful mostly by comparison with modeled estimates and for use as input to modeling tools for concentration estimates. Given the inability to gather spatially distributed data at the interface of the VZ and the regional aquifer, the main source of information to inform the distribution will be abstracted model results.

The RDX-contaminated sources are conceptualized as a primary source, which is responsible for the consistent, low-noise trend observed in R-18 and the high values at R-68 and R-69. A secondary source is also developed, since it is unknown how many sources arrive at the regional aquifer. This source has more flexibility, both in location and size. Both recharge and concentration have the ability in the model to range from zero to nonzero values, so the calibration can essentially remove the secondary source if this results in better matches to the data (note: Calibration 3 described in the results does use ONLY the primary source to calibrate the RRM). The secondary source is also described by likely preferential recharge below Cañon de Valle.

Distributions for RDX concentration at the primary and secondary source windows (Figure D-4.6-11) were developed using modeled concentrations from 18 different runs of the VZ model. Within each run, concentrations were extracted at the regional aquifer z-slice, assumed to be at 1920 m, at each time point from 1950 to 2072 (i.e., the timescale of the RRM). The primary source location was identified as the node with the highest concentration within year 2070. The secondary source location was identified as the node with the highest concentration within year 2070 after excluding the primary source node with a 10-node radius buffer. Because each source distribution represents an average concentration over time, primary and secondary source concentrations were averaged from the year of onset to 2070. The year of onset was defined as the time point where RDX concentrations at each source first exceeded 0.1 ppb. Because of the physical lower bound of zero for concentration, a truncated normal distribution was fit to the 19 average concentrations. Simultaneous estimation of the truncated normal parameters using maximum likelihood resulted in physically unrealistic values for the mean. Therefore, the distribution mean was instead set equal to the sample median of the average concentrations. The median was used as a robust measure of center because of the skewness present in the average concentration values Figure D-4.6-11. Conditional on the lower truncation point of zero and mean equal to the sample median, the standard deviation was estimated using maximum likelihood.

The highest measured concentration in the VZ is around 150 ppb. While this is the highest observation, it is not likely that one of a very sparse set of spatial locations happens to coincide with maximum RDX in the VZ model. Therefore, the range of values for the primary source from 0 up to approximately 380 ppb at the 99th percentile, with a mean (93 ppb) centered at less than the highest VZ observation and more than the highest regional observation, is consistent with the limited observed data.

D-4.6.4   Source Recharge

The purpose of this section is to describe parameter distribution development for drip points to the regional aquifer below the RDX project area at LANL. The parameter describes water reaching the saturated zone at the surface of the water table, which is the definition of recharge (e.g., Freeze and Cherry 1979, 088742, p. 211), so the term recharge will be used in this document. Recharge may occur from other directions besides the vertical, i.e., from water that has infiltrated upstream and reaches the aquifer laterally or at an angle from the surface. This parameter is alternatively called "infiltration" in model files and reports (e.g., LANL 2018, 602963, Attachment 8). However, "infiltration" is a misnomer for this parameter. Infiltration describes the entry of water into the subsurface from the ground surface (e.g., Freeze and Cherry 1979, 088742, p. 211), and it is distinct from recharge in locations with an unsaturated zone overlying the saturated zone such as occurs in the RDX project area.

Recharge velocity impacts the rate at which RDX transport occurs. Recharge water may dilute discharged RDX concentrations from the LANL TA-16 260 facility outfall; change the water table elevation (i.e., causing "mounding" with locally high saturated elevations below recharge points); and impact head values at the top boundary of the model. These processes have the potential to alter system hydraulics (e.g., increasing pore water velocities, changing direction of groundwater flow, affecting local vertical gradients).

For recharge in the RDX RRM, the spatial scale of interest encompasses all zones where hydraulic windows may occur below the RDX project area. Therefore, it includes parts of Cañon de Valle and extensive upstream surface and groundwater sources such as (1) MBR, which is diffuse subsurface recharge over the mountain block that percolates into the subsurface and flows as groundwater into the basin, and (2) mountain front recharge (MFR), which is overland flow in mountainous terrain that infiltrates at the mountain front. The terrain of interest includes mountains, mesas, and canyons, which leads to spatial variability in recharge rates. For the RRM, the recharge parameter is held constant over the time period of simulation, which is decades to hundreds of years; therefore, the value must represent an average over that time.

A distribution of recharge rates is needed because of the uncertainty in infiltration rates at the ground surface and the fact that flow through the highly heterogeneous VZ separating the ground surface from the water table is not well characterized. This zone is composed of unsaturated regions and perched saturated zones in geologic strata of variable permeability and porosity. Distribution development for recharge at the RDX site must therefore account for the high level of uncertainty in the available information and processes that affect rates of recharge to the regional groundwater aquifer. Recharge distributions, which are used as inputs for the RRM, are based on the output of forward runs of the RVZM, whose water balance is constrained by surface infiltration distributions, calibrating to observed water levels, and flow physics.

Recharge to the regional aquifer is conceptualized as a combination of background and preferential flow paths. This conceptualization in consistent with the CSM as well as with results from the RVZM, which show regions of preferential flow (Figure D-4.6-12).

Preferential Recharge Locations

The geology in the region suggests that certain preferential hydraulic windows of recharge may occur at the regional aquifer. In the RRM, these are conceptualized as three windows: a potential primary and secondary source of RDX and a clean region of higher recharge below Cañon de Valle, called the preferential recharge source hereafter. The three windows could be locations that consolidate small regions of fractured or highly preferential flow from the surface, parts of the unsaturated zone, or parts of the perched zone. Geochemical lines of evidence can provide constraints on the percentage of recharge from each of the three sources out of the total, so distributions for these percentages are developed as well as distributions of preferential recharge.

The primary source is likely to be relatively compact with higher concentrations, based on the clear, low-noise trend in RDX concentrations observed at R-18, coupled with high values of RDX concentrations at R-68 and R-69 and no observed RDX at R-47 above detection limits (Figure D-4.6-13). Given the proximity of these wells to each other, and the fact that they contain the highest measured RDX, it is hypothesized that some primary source is responsible for the trends observed. Given the high concentrations arriving at the regional aquifer through a vertically extensive, 300–400 m VZ, this source is conceptualized as arriving at the regional aquifer via preferential pathways and is conceptualized as having primarily surface infiltration as the water source.

Geochemical studies analyzed water from the regional aquifer and the perched VZ to determine relative contributions from different surface sources, including alluvial, spring, and canyon sources (LANL 2018, 602963). A simple binary mixing model was employed in conjunction with chloride, a conservative tracer. End members of the mixing model used average chloride concentrations from well R-26 screen 1 to represent MBR. This location was selected because of the proximity of R-26 to the mountain front and geochemical results suggesting a lack of local recharge (i.e., no RDX concentrations and no tritium). Additional end members were (1) average chloride concentrations of Cañon de Valle surface water,

(2) alluvial groundwater, and (3) concentrations from springs. Between 86–99% of the regional aquifer water is associated with MBR, leaving between 1–14% from surface sources (LANL 2018, 602963). Additionally, an increasing calcium trend attributed to snowmelt was observed in a deep well (R-25 screen 4), which demonstrates a fast pathway from the Cañon de Valle bottom to the regional aquifer (LANL 2018, 602963). To account for uncertainty in the conceptual model, as well as the potential for a surface source to mix with perched water during migration from the surface to the regional aquifer, an additional 5% was added to the range representing alluvial water reaching the regional aquifer through a preferential pathway. Therefore, the primary source is associated with between 1–19% of the total preferential infiltration. Given that there is very little information to further characterize the likelihood of specific proportions of infiltration sources within this range, a uniform distribution is used.

Preferential Recharge Source

The preferential recharge source described in the previous section likely arrives at the regional aquifer somewhere below Cañon de Valle and the VZ perched zones. Evidence for this source includes localized mounding near R-25 (LANL 2018, 602963; N3B 2019, 700561); a deviation of the regional flow gradient from primarily west-east to southwest-northeast near the wells where RDX is observed in the regional aquifer; preferential surface infiltration in Cañon de Valle; and the large extent of perched zones below Cañon de Valle (N3B 2019, 700561).

Distributions were generated for preferential recharge based on the conceptual model and spatial locations of relevant features. Figure D-4.6-13 shows a base map reproduced from "Investigation Report for Royal Demolition Explosive in Deep Groundwater," (N3B 2019, 700561, Figure 3.2-5) with the distributions for preferential, uncontaminated recharge ("preferential recharge source") plotted over the figure. Surface features and topography are plotted, detailing the location of Cañon de Valle relative to the wells in the regional aquifer. The approximate extent of the VZ perched zones is also plotted. These zones are recharged by MBR primarily and secondarily by MFR and preferential surface infiltration under Cañon de Valle. Without much information to constrain the location of the preferential recharge source, uniform distributions are chosen that overlap the conceptual model understanding of the system and provide enough flexibility to account for uncertainty in this CSM.

Preferential recharge source-center x-coordinates can be anywhere from R-25 to as far downgradient as R-47. Source center y-coordinates are set from R-25 to as far north as CdV-9-1(i). Y-coordinates are selected to cover the higher water table elevations observed near the mounding at R-25. The extents of these distributions are shown in the rectangle constrained by the dotted red line in Figure D-4.6-13.

The size of the source is difficult to constrain. However, some general qualitative features are available. First, based on the west-east orientation of Cañon de Valle and of the water table gradients, the x-radius is likely to be significantly larger than the y-radius. Given the uncertainty in source area, a large range of potential radii are allowed (Figure D-4.6-13). The largest x- and y-radii are plotted as a large ellipse centered at the middle of the location distribution (dotted rectangle). The smallest x- and y-radii ellipse is also shown. No correlation structure is specified between x-radius and y-radius as there is no information to constrain one. The source can vary widely in elliptical shape as a result. If the smallest x-radius is drawn simultaneously to the largest y-radius, there is potential for a longer y-axis in the ellipse. However, the number of draws from the x- and y-radius distributions where this would occur is small. No tilt or "corr" parameter is defined because there is no information to inform this. Additionally, if the shape parameter is allowed to vary, the conceptual constraint on having a smaller y-radius than x-radius across most draws no longer remains, so the shape parameter is fixed at 0 for the preferential recharge source.

The percentage of total infiltration used by the preferential recharge source is constrained using geochemical studies. As discussed above, the primary source can use between 1% and 19% of the total preferential infiltration. As a result, the rest of preferential infiltration must occupy between 81% and 99% of recharge. This percentage is conceptualized as being shared between the preferential recharge source described above as clean, and a secondary source, which is potentially mixed with contaminated perched water before reaching the regional aquifer. The existence of a contaminated secondary source is uncertain. Therefore, the proportion of total recharge allocated to the secondary source is allowed to range anywhere from 0% to 34%. This leaves 65%–81% recharge in the preferential clean source.

Implementation of the percentages is achieved by defining uniform distributions for the primary source, Uniform (0.01, 0.19), and for the preferential recharge source, Uniform (0.65 ,0.81). When the maximum of both distributions is drawn the secondary source is set to 0, essentially removing it as an input to the RRM. For all other draws the secondary source is calculated as the remaining percentage after the primary and preferential clean sources have been drawn.

A decision was made to exclude the secondary source from Calibration 3, and for that reason the preferential recharge distribution had to be altered slightly for that calibration to be consistent with the recharge ranges discussed above. A model without a secondary source is conceptually simpler and is advantageous from a model parsimony perspective, but it may reduce the quality of the fit to the data. However, the sum of the preferential recharge and the secondary source must occupy between 81% and99% of recharge. To achieve this, the preferential recharge distribution was adjusted in Calibration 3 to be Uniform (0.81, 0.99) to compensate for the secondary source being set to 0%.

This setup for recharge allows for significant flexibility in the model to place sources of varying rates. It also constrains the sources using the limited available data (geochemical) and incorporates qualitative information from the CSM. The RVZM then informs the possible amount of recharge, making these values dependent on the physics in the system to move water from the surface, MFR, and MBR to the regional aquifer in the area of interest.

D-4.6.5   Rate of Recharge

The RVZM shows that there is (1) a very low level of background recharge that exists throughout most of the aquifer and (2) several localized, high-flux pathways. Based on these results, the background recharge is assumed to be negligible in the RRM and is neglected; therefore this section focuses on the distribution development for recharge above background levels.

A distribution for the total recharge above background (i.e., the sum of the sources for preferential recharge, primary recharge, and secondary recharge) (Figure D-4.6-14) was developed using estimated steady-state flux (mm/yr) (converted from $m^3/yr*m^2$) from 19 different runs of the RVZM. Within each run, fluxes were extracted at the regional aquifer z-slice, the highest saturated elevation of which was assumed to be at 1920 m above mean sea level (amsl). Because of the structure and domain of the RVZM, nonlinear edge effects arise that are not representative of the fluxes entering the regional aquifer (Figure D-4.6-12). To lessen the impact of edge effects on recharge, a 2-node buffer was applied to the extent of the model and each node was spatially averaged using a 1-node radius (40-m) window.

The total recharge above background is represented as a truncated normal distribution with a mean of 5250 mm/yr and a standard deviation of 2480 mm/yr. While there can be an upward flux of water from the regional aquifer into the VZ because of capillary pressure in dry areas, this was assumed to be minimal and the average flux was truncated at zero.

D-4.6.6 Source Timing

Source timing describes the time at which RDX first reaches the surface of the regional aquifer. Three different sources of information were considered to develop a distribution of year of onset for RDX arrival at the regional aquifer: (1) historical data, (2) P&D screening tool, and (3) FEHM VZ modeling results. Because of the lack of available historical data, the P&D tool results are combined with the RVZM results and are used to develop the distribution.

D-4.6.7 P&D Tool

The P&D tool is a screening tool that uses analytical solutions to link together an arbitrary number of UZs with an arbitrary number of SZs to estimate flow through a complex VZ with perched zone elements. VZ elements are conceptualized as slow vertical flow (pipes) using 1-D advection and dispersion, while SZ elements are conceptualized as more rapid flow (disks) using either two-dimensional or 3-D fully saturated advection and dispersion. A full description and set of equations for the P&D tool has been documented by prior work (LANL 2018, 602963, Attachment 8, Section 2.1) and is summarized in section D-3.3.

Measured concentrations at R-18 and R-68 were used to constrain results from the P&D tool, which was run assuming two sources. Note that groundwater flow velocity is a highly uncertain, but highly sensitive, input to the P&D tool. In the analyses presented here, both high and low groundwater velocities were tested to represent a wider range of possible arrival times. However, low-velocity estimates were ultimately excluded because multiple lines of evidence supported the higher estimate (both the mean velocities in the calibrated model and back-of-envelope calculations. Additionally, during calibration, the RRM consistently selected values for time of onset near the upper end of the distribution, suggesting that later arrival times (which align with the higher-velocity model runs) result in better matches to the data. More detail about the P&D analysis can be found in the RDX compendium (LANL 2018, 602963). Results from the P&D tool run with two different surface sources are shown in Figure D-4.6-15, with each resulting in an independent time of onset.

The RVZM is also used to produce representative values for time of onset at the regional aquifer. Unlike the P&D tool, the RVZM results constrain the path of contamination from the surface through 3-D physics and intensive calibration efforts. Time of onset was derived for both sources using modeled concentrations from 18 different calibration fits of the RVZM. Concentrations were extracted from each model fit at the regional aquifer z-slice for each time point from 1950 to 2072. The primary source location was identified as the node with the highest concentration within year 2072. The secondary source location was identified as the node with the highest concentration in year 2072 after excluding the primary source node with a 10-node radius buffer. The year of onset was defined as the time point when RDX concentrations at each respective source first exceeded the assumed detection limit of 0.1 ppb. The time of onset results from the RVZM are given in Figure D-4.6-16. The primary source results are used to inform the time of onset distribution.

The distribution does not represent a spatial average because different draws are taken for each source. The underlying distribution for time of onset will be used in the model, rather than developing the distribution for the average.

Primary Source

The high-velocity P&D results are shown in Figure D-4.6-17 alongside the RVZM results. Various distributions were fit to the data using the fitdistr function in the fitdistrplus package in R. Weights were developed such that each of the three lines of evidence could be weighted equally in distribution

development. This leads to an effective weight of 2 for the pipe and disk model and 1 for the RVZM. This is intentional for a few reasons; first, as mentioned above, the calibrated model consistently selected times of onset at the upper end of the distribution, suggesting that these results are better aligned with the target data at the site. Second, since the VZ model has only 18 observations while the others have 500, each VZ model observation is given a weight 27.78 times (500/18) that of each high-velocity P&D source observation. The actual weights are 36, 36, 1000.

Weibull, gamma, normal, and lognormal distributions were tested and evaluated alongside the data by visual examination. The Weibull distribution was chosen as the most appropriate fit to the data from both lines of evidence (Figure D-4.6-17).

D-4.7   Western and Eastern Model Boundary Condition—Constant Head

Boundary conditions for the RRM include the head condition prescribed at the western and eastern edges of the model. These boundary conditions are used to define the regional flow gradient. Head values set along the western and eastern boundaries are allowed to vary linearly as described below.

Water level and hydraulic head coincide at the water table of an unconfined aquifer, where no additional gauge pressure is present (other than the weight of the atmosphere, which is assumed to be 0.1 MPa). Shallow depths of the regional aquifer (where most wells are located) are generally characterized as unconfined, and therefore water level and hydraulic head are considered equal at most locations. "Water level" is used to refer to the location of the water table (interface between saturated and unsaturated conditions), whether in terms of depth below ground surface, or relative to a geologic boundary, or in terms of height amsl (i.e., relative to a fixed datum). "Hydraulic head," or "head," is used to refer to the sum of elevation (z) above a datum (e.g., in this case amsl) and pressure head, $p/\rho g$, where p is referred to as "gauge" pressure (Franke et al. 1987, 700886):

$$h = z + p/\rho g. \qquad \textbf{Equation D-11}$$

Temporal variation in pressure head can be attributed to three main sources: (1) seasonal variation as a muted response to land surface seasonality, (2) variation in response to human pumping activities, and (3) gradual changes in pressure head over time. These temporal variations are small compared with the spatial variability over the timeframe of the model and so the flow field of the model is computed as a quasi-steady-state representation of 2014 conditions. Long-term pumping from supply wells PM-2, PM-4, and PM-5 (and pump tests for PM-2 and PM-4) are the only temporal variability represented in the current iteration of the model (section D-4.11). Drawdown targets are established and used to help calibrate aquifer properties using water level responses (and lack of responses) in monitoring wells to month-long supply well pump tests (section D-5.1). While long-term decline is observed in monitoring wells across the plateau, hydraulic analysis of lateral and vertical gradients does not indicate large changes in hydraulic gradient magnitudes or direction across the site in the timeframe of the modeling (until the year 2200). Therefore long-term decline of the water table, transient water levels, and hydraulic gradient targets are included in the model. Water level targets are a temporal average of February 2014 conditions and are matched in the model at the time step closest to February 2014 in the model. While long-term pumping from supply wells is included in the modeling, water levels and hydraulic gradients in the RDX plume and downgradient region change little through time.

Spatially, the east and west boundary conditions for the model are applied to every z-coordinate along a boundary edge. While there are no data points near the edges of the modeling domain, water table maps were generated in 2014 based on all available water level data, topography, and geologic expertise to estimate the water table (Figure D-4.7-1). These contours serve as the main source of information for both west and east head distributions, which are discussed independently below.

While the dominant direction of flow is from west to east, the gradient varies throughout the region. In order to capture this variability, two draws are made for west head—at the northernmost and southernmost points of the model—and similarly two draws are made for east head. The gradient between the two draws is interpolated linearly based on the y-coordinate of every node along the boundary. This method allows for a range of possible gradients that broadly move west to east. Given that the draw for head will be applied to a single point in space, the distributions developed span the range of all plausible values, including the extremes, rather than being distributions of the average.

D-4.7.1 Western Hydraulic Head

The raster data used to produce the 2014 water table maps are used as the main data source in distribution development. The distribution is developed by extracting head values from the raster data for every coordinate along the western boundary. The coordinate locations chosen were 100,000 equally spaced points in order to encompass the entire spatial domain of the boundary. The water table raster data with 10 evenly spaced points along the boundary are shown as an example in Figure D-4.7-2.

The extracted water level values at the western boundary ranged from 1864.462 to 1925.726 m (Figure D-4.7-3). Given that there are no measured data at the boundaries, and no other qualitative information to inform which parts of the distribution are most likely, a uniform distribution (minimum = 1860, maximum = 1930) is chosen to represent the western hydraulic head.

D-4.7.2 Eastern Hydraulic Head

A procedure similar to that of extracting head values from the 2014 water level map for the western boundary was used to extract head values for the eastern boundary. The distribution developed for the eastern head was originally intended as a distribution of the average, so the process is slightly different. Rather than extracting the head at 100,000 different equally spaced locations to represent all head values, five random locations on the eastern boundary were selected and the water level was extracted from the raster data. The average water level was then taken as a plausible value to apply over the entire eastern boundary. This process was then repeated 1000 times and a preliminary distribution was fit to the 1000 average head values. The water table raster data with five randomly selected points along the eastern boundary (yellow) are shown as an example in Figure D-4.7-4. The average water level values at the eastern boundary ranged from 1647 to 1706 m (Figure D-4.7-5).

The eastern boundary of the model, however, is much further from the RDX site than the western boundary. To the east of the RDX site, complex hydrologic and geologic conditions exist in the middle to eastern portion of model domain that result in hydraulic gradients and water table surface conditions that are very different from the RDX site. The RDX site tends to have much steeper hydraulic gradients as it approaches the mountain block. Hydrologic and geologic conditions east of the RDX site were not the focus of the model, and matching the gradient within the model area is of higher priority than accuracy at the eastern boundary, which is many miles from the plume. A lower eastern head value would force a steeper gradient that matches the RDX area gradient more closely. Therefore, a linear regression equation was used to extrapolate east heads at the model boundary to expand the eastern boundary range of values at the low end of the distribution.

Extrapolating East Head using Linear Regression

Outside of the local area of the RDX site, the aquifer system in the RRM is represented using homogeneous properties and therefore does not capture the complex geology and hydrology across the site. Figure D-4.7-1 indicates markedly different hydraulic gradients and water table conditions in the middle and eastern portion of the RRM domain compared with the RDX site. In order to produce a

representative hydraulic gradient in the RDX site, values for the eastern hydraulic head need to be able to reproduce the local hydraulic gradients in the western portion of the RRM where the RDX site is located.

Hydraulic head is estimated for the eastern boundary based on extrapolating the observed hydraulic gradient at the RDX site using hydraulic head target data.

Figure D-4.7-6 shows the spatial distribution of wells used for groundwater level targets in the regression analysis along with the 2014 water level contours across the RRM domain. Well targets for the RRM are shown in red, and well targets for another model being developed in the eastern portion of the domain (the chromium regional model) are shown in green. As discussed above, the contour lines show a steeper hydraulic gradient in the RDX site compared with the chromium site. This can also be visualized by showing the relationship between water level and well location projected along an east/west line (Figure D-4.7-7).

All wells in the RDX area with the exception of R-26 were selected to estimate the local hydraulic gradient at the RDX site. R-26 was initially used as a water level target in the RRM; however, it was ultimately excluded as it may represent semi-perched conditions. The geology complexity between R-26 and the RDX site is not captured in the model.

The linear regression equation fit to the water level target data is shown in Figure D-4.7-8, and statistical summary results for the regression are shown in Table D-4.7-1. Since the eastern boundary is jagged and has multiple x-coordinates, head is estimated at three different coordinates meant to represent the southeastern and northeastern corners, as well as a point towards the middle of the eastern boundary ("east middle"). Results of the extrapolation are provided in Table D-4.7-2. The results of the regression analysis for the eastern heads were used to expand the range of values described above. The final range uses the 99th percentile from the distribution developed using the 2014 water level map (1690 m) as the upper bound, and the lower bound is set by rounding the lowest extrapolated eastern head value (1477.37 m) down to the nearest tens place (1470 m).

D-4.8 Western Vertical Gradient Distribution

The western boundary of the model lies within the mountain block, where strong vertical gradients are observed in nearby wells (R-25, R-69, etc.). These gradients are formed by a combination of recharge at the mountain block and, to a lesser extent, preferential recharge zones (section D-2). In order to match the observed vertical gradients, hydraulic windows of infiltration and a vertical gradient imposed at the western boundary are used in tandem to produce vertical gradients at the RDX site.

The previous section discusses a distribution of water table elevations developed separately for the western and eastern boundaries. On the eastern boundary, a uniform head is applied to all nodes in the vertical direction in order to keep the model simple, since this portion of the model has little bearing on RDX transport. However, for the western boundary, specified heads below the water table are lowered as a function of depth in the first 100 m of the model domain. Below this, a uniform head is specified for the remaining nodes to the bottom of the model.

For example, if the value of vgrad drawn is −0.1 m/m, and the water table elevation at the model surface is 1000 m, then heads will be lowered by 0.1 m per m depth into the aquifer. At a depth 100 m below the water table, a water level elevation of 990 m will be specified. Nodes between the surface and 100 m depth will have specified heads between 990 and 1000 m. For the remaining model nodes below 100 m, a uniform water level elevation of 990 m is applied.

The strongest observed gradients near the western boundary range from −0.1 to −0.3 and are observed in wells R-25 and R-69 (section D-2). The relative contributions that mountain block and mountain front recharge provide are highly uncertain; therefore the distribution of vgrad should at least be inclusive of the observed gradients at the site. Given the large uncertainty for this parameter, a uniform distribution from 0 to −0.3 is used for wHeadvGrad.

D-4.9 Sorption Coefficient (K_d)

Sorption onto solid porous media is represented by solid/water partition coefficient (K_d) values. The purpose of this section is to describe parameter distribution development for the RDX K_d distributions used in the RRM and RVZM. Migration of dissolved contaminants may be impacted by sorption onto the solid phase of minerals within the geologic materials present at the site. Sorption consists of several physicochemical processes including ion exchange, adsorption, and chemisorption. Mineralogy, organic carbon content, particle size and texture, element speciation, pore water pH, redox conditions, and the concentrations of other constituents in pore water contribute to variability in K_d values, as do differing assumptions underlying the calculations used in the various literature sources. Sources of temporal variability in the regional aquifer sediments are expected to be negligible over the timescale of the model.

K_d values used in the RRM and RVZM are determined using distribution development and probabilistic sampling. For each realization of the RRM, a single K_d is sampled from a distribution and is applied to all model cells in the domain, regardless of actual geologic material. Because the area of interest is primarily in the Puye Formation, the distribution is intended to be representative of RDX sorption onto Puye Formation sediments. The spatial scale of the RRM is approximately 220 km^2 in area by 800 m thick, with temporal scale ranging from tens of years to approximately 100 yr. For each realization of the RVZM, one K_d will be sampled for volcanic materials (tuff, dacite, pumice) and one for sedimentary materials, and the single draw will be applied to all geologic units assigned to those materials. Within those categories, K_d values are assumed homogeneous in space and constant in time. The spatial scales within the RVZM are approximately 3 km between the eastern and western boundaries, 1 km from north to south, and 650 m deep, extending from the land surface to approximately 40 m below the water table. The temporal scale is the same as the RRM. Because it is expected that realistic variability in site K_d values will occur at spatial scales much smaller than the model domains over which they are applied, the distributions are intended to represent possible average values. There are no physical limits on possible measured K_d values, but negative K_d values will not be entered into the RVZM and RRM.

The development of a K_d distribution for RDX in volcanic and sedimentary materials follows an approach previously used for other contaminated sites (Gains-Germain et al. 2018, 700888). A literature review of RDX K_d values was conducted to identify all potentially relevant information and was then filtered depending on the applicability, quality, and quantity of the information. RDX sorption onto various geologic materials is presented in the literature for sites external to LANL and specifically for LANL borehole samples (LANL 2011, 207069; Heerspink et al. 2017, 602560). Data were entered from the LANL studies only, because of priority of site-specific information.

D-4.9.1 Assumptions

Strata are lumped broadly into volcanics (V) or sedimentary materials (S). Table D-4.9-1 lists the geologic units found in the RVZM, and to which group they are applied. The Cerro Toledo Formation (Qct), although sedimentary, is grouped with the volcanics because it is composed of reworked Otowi material, pumice, and rhyolite. The RRM is given a K_d sampled from the sedimentary distribution.

The groundwater used in the site-specific RDX K_d experiments in Heerspink et al. (2017, 602560) was obtained from well CdV-16-4ip, with a screened interval in the Puye Formation in the intermediate aquifer. This water is assumed to be appropriately representative of the regional aquifer groundwater across the model domain, as the groundwater chemistry in the intermediate and regional aquifers is "very similar" with slight differences in major cation and anion concentrations (LANL 2018, 602963). The shallow alluvial aquifer system near the ground surface may have substantially different water chemistry and redox conditions than the intermediate and regional aquifers, in which case distributions developed for the deeper aquifers may not be applicable in the shallow alluvial aquifer.

The K_d information entered for RDX included several types of records:

- Data from batch experiments on geologic and separated mineral samples,

- Estimated values from laboratory column experiments, and

- Large-scale model-calibrated values based on observed RDX concentration data and a physics-based flow and transport model.

Batch and column experiments were assumed to be small-scale in the spatial categorization scheme in Gains-Germain et al. (2018, 700888), while the model-calibrated values are considered site-scale.

The RDX data in the database were evaluated for suitability using exploratory data analysis. The site-scale calibrated values from a prior version of the LANL RDX RVZM were excluded because of the underlying assumptions (e.g., model accuracy and calibration uniqueness) inherent in the use of that information. Across all rock types in the RVZM, these values spanned a greater range (2.30×10^{-6} to 4.41 mL/g) (LANL 2018, 602963) than the batch and column experimental data (0 to 0.7 mL/g) (Heerspink et al. 2017, 602560).

Heerspink et al. (2017, 602560) describe the results of experiments on core materials from the LANL site. Three samples from two boreholes were used. The boreholes are SHB3, located to the west of the main RDX area, and R25b. At SHB3, sections of core were taken from the Otowi Formation and from the upper Puye Formation. The SHB3 Puye Formation sample was intended to be representative of materials in the portion of the Puye Formation in which the upper perched zone is found (Heerspink et al. 2017, 602560). However, after additional consultation, the SHB3 upper Puye Formation sample was determined unlikely to be representative of the upper Puye Formation in the RDX plume area. At SHB3, the sample was taken from a fine-grained sandstone layer that has not been observed in boreholes in the main section of the RDX plume, whereas the uppermost Puye Formation contains larger cobbles and gravels. If present, the sandstone layer would be expected to compose only a very small percentage of the entire portion of the Puye Formation in the model. Therefore, the SHB3 Puye Formation data were excluded.

The SHB3 Otowi Formation data are used to develop distributions for the volcanic materials at the site, while the R-25b Puye Formation data are used for sedimentary materials (i.e., Puye Formation) in the RVZM and RRM. For each of these cores, batch and column experiments are performed on the bulk material, and batch experiments are also performed on hand-picked separates. The hand-picked separates for the SHB3 Otowi Formation core include pumice, fines (volcanic glass), and dacite lava fragments. For the R-25b Puye Formation core, the separates are red and black dacite lava fragments. The hand-picked separates are tested for K_d separately from the bulk sediments to distinguish between the individual materials in a geologic formation with respect to K_d values. This can be used to extrapolate or infer the behavior of other materials in which some of the same minerals are found, assuming an estimation may be made of the mass or volume percentages of the separates in the bulk materials. The hand-picked separates generally have higher K_d values than the bulk materials, particularly for the fines. Using the incorrect assumptions about the impact of these separates on the bulk or upscaled K_d can significantly affect the distribution and bias K_d values too high.

For the batch experiments performed on the bulk samples, K_d values are essentially zero, with a standard deviation estimated at 0.050 mL/g (Heerspink et al. 2017, 602560). Values of calibrated parameters are given for the best calibration with the lowest value of the OF (Calibration 3) in Tables D-3.2-3 through D-3.2-7. These tables also include values of calibrated parameters of earlier calibrations reported in the RDX compendium (LANL 2018, 602963, Attachment 8, Tables 4.0-1 and 4.0-2), and an improved calibration from LANL-EES (Neptune 2018, 700878), for comparison. In general, calibrated values show similar trends to earlier calibrations. Results from calibrations indicate that many possible combinations of parameter values yield good fits to the data and, thus, more than one set of parameter values is possible. Note that Calibration 3 yields overall smaller values of sorption coefficients (Table D-3.2-7) in accord with data. Calibrations 2 and 3, which assign three dispersivities to each of the hydrostratigraphic units, also seem to yield a better fit. For the column experiments on bulk materials, estimated K_d values were slightly higher, with K_d = 0.047 mL/g for SHB3 Otowi Formation tuff and K_d = 0.059 mL/g for R25b Puye Formation sedimentary materials.

The K_d values in Heerspink et al. (2017, 602560) are reported as mean values with error. Correspondence with the authors clarified that the number of replicates for each batch experiment was 3 and the error represents one standard deviation. Because of the singular source of data, and based on the manner in which the data were collected, spatial scaling was not considered to be a necessary component of the distribution development. Discussion of the creation of the distribution of the average K_d is as follows.

The observed K_d values for bulk samples are selected and are shown in Figure D-4.9-1. The dots represent the mean values as reported and the horizontal lines represent error bars surrounding the estimate extending two standard errors in both directions ($SE = \frac{SD}{\sqrt{n}}$, where n = sample size and SD = standard deviation) to reflect an approximate 95% confidence interval for the mean. If an estimate for spread was not reported, then no error bars are included. The two Otowi Formation bulk tuff records are used to inform the distribution for volcanic materials and the two Puye Formation bulk sediment records from R-25b are used to inform the distribution for sedimentary materials.

D-4.9.2   Distribution Development

An MC simulation approach is used to generate distributions for the mean K_d value for RDX in volcanic materials and in sedimentary materials. As observed in Figure D-4.9-1, the observed K_d values were higher in the column experiments than in the batch experiments. Additionally, there is no reported uncertainty for column experiment records, unlike for batch experiments.

The distribution for volcanic materials was obtained by combining the Otowi Formation bulk tuff estimates from both batch and column experiments. The representative mean K_d value is equal to (w) × (column K_d value) + (1 − w) × b, where w is the weight assigned to the column value, and b is a random draw from a normal distribution with the reported mean from the batch experiment (0) and standard deviation equal to the standard error for Otowi Formation bulk tuff. This process is repeated 10,000 times to obtain 10,000 representative, mean K_d values for volcanic materials. The weights assigned to the column K_d value were equally spaced values between 0 and 1, in order to incorporate uncertainty in the reliability of each estimate. This approach was taken to allow for the distributions to be informed by the different methods using varying degrees, allowing some of the draws to be less impacted by the point estimate of the batch experiment and others to be largely impacted by the point estimate of the batch experiment.

Variable weights are assigned to the column experiment records and batch experiments weights under the condition that the weights sum to 1. This approach was taken to allow for the distributions to be informed by the different methods using varying degrees, allowing some of the draws to be less impacted by the point estimate of the batch experiment and others to be largely impacted by the point estimate of

the batch experiment. A histogram of the weighted average K_d value for volcanic materials obtained from the process is shown in Figure D-4.9-2, with the observed K_d values from the Otowi Formation bulk tuff materials shown below the histogram. A normal distribution was fit to the histogram, where the mean of the distribution is equal to the average of the collection of weighted means. The standard deviation, in this case, is equal to the standard deviation of the weighted means.

The same process is repeated for sedimentary materials (S), but swapping details regarding Otowi Formation bulk tuff with details regarding Puye Formation bulk sediments. A histogram of the weighted average K_d value for sedimentary materials obtained from the bootstrapping process is shown in Figure D-4.9-3 with the observed K_d values from the Puye Formation bulk sediments shown below the histogram. A normal distribution was then fit to the histogram to represent sedimentary K_d values.

Final distributions for K_d are shown in Table D-4.9-2. Distributions developed may result in negative draws. Negative K_d draws are not allowable in the model, and, as a result, the distributions will be bulldozed at 0 mL/g. Bulldozing, in this sense, refers to the action of taking a negative draw and assigning the draw a value of 0 mL/g. This process will create zero-inflated distributions. Table D-4.9-2 includes the parameters for the normal distributions used for both volcanic and sedimentary materials. The 1st and 99th percentiles of the distribution are given, and the probability of a draw from the distribution being less than 0 mL/g is also included in the table. Figure D-4.9-4 shows the final "bulldozed" distributions for K_d.

D-4.10 Effective Diffusion Coefficient (D_e)

As described in the RVZM description, the effective diffusion coefficient (D_e) is used for calculating the movement of solutes in water because of differences in concentration gradient in a porous medium. This section assembles background information about the effective diffusion coefficient, provides an equation for how it is calculated from other parameters, describes data compilation and calculations used to inform distribution development, and documents the approach taken to produce input distributions for contaminants in the probabilistic model. The purpose is to describe parameter distribution development for the RDX D_e distribution used in the RRM and RVZM.

For transport calculations in porous media, the free water diffusion coefficient, D_w, is scaled by a tortuosity factor and the water content to give the effective diffusion coefficient, D_e, as entered into FEHM as a constant:

$$D_e = D_w \tau_w \,, \hspace{4cm} \textbf{Equation D-12}$$

where D_w is the free water diffusion coefficient [m^2/s] and τ_w is the aqueous-phase tortuosity [–].

Distributions are developed here for the parameter D_e, including effects of tortuosity. Transport by advection in porous media is also subject to dispersion.

Information available for D_e and D_w of RDX is extremely limited. A single value is available for D_e in LANL-area materials (3.88 x 10^{-9} m^2/s) (LANL 2018, 602963), and two values are available for RDX D_w (2.2 × 10^{-10} and 7.15 × 10^{-10} m^2/s). Because of the limited availability of information on D_e, the two D_w values are used in conjunction with the distribution developed for porosity and an estimation of tortuosity in order to calculate a distribution for D_e using Equation D-12.

Multiple models for estimating tortuosity exist in the literature, including, for example, the Millington–Quirk model (Millington and Quirk 1961, 110521), where tortuosity in water (τ_w) is computed as

$$\tau_w = \theta_w^{\frac{7}{3}}/\phi^2 \,, \hspace{4cm} \textbf{Equation D-13}$$

Where ϕ is porosity of the mixture [–] and θ_w is the volumetric water content [–].

In saturated conditions, θ_w is equal to porosity in Equation D-13, and it reduces to

$$\tau_w = \phi^{1/3}$$

Equation D-14

The porosity distribution is used for ϕ in Equation D-14. The distribution developed is then compared with the single value from the RDX compendium (LANL 2018, 602963).

A single draw from the distribution developed for D_e will be applied to the entire model spatial and temporal domain. The distribution is therefore intended to represent a distribution of the average D_e across all space and time in the model. Although D_e is correlated with porosity, not enough information is available to allow the two parameters to be correlated in the model at the time of distribution development. Independent draws are taken from each distribution and applied separately (porosity and D_e) in the model.

The distributions for D_e are used for several purposes in the RRM:

1. They will be used to inform the ranges (uniform draws) allowed in the classical calibration.
2. They will be used as priors in the Bayesian calibration.

For the RRM, the distribution for D_e is developed using an MC simulation technique. For each of the two D_w values available, an independent random value is drawn from the distribution developed for porosity to calculate tortuosity using Equation D-14. The independent random draws for each are multiplied by the value for D_w to obtain a value for D_e. Each D_e is assumed to be equally representative of conditions at the site, so the two D_e values are then averaged to obtain a plausible average, and this process is repeated 1000 times to obtain 1000 averages. Finally, a normal distribution is fit to the 1000 averages. Because the D_w values are relatively close in magnitude, the variation in the final distribution is driven largely by uncertainty in porosity. The low sample size also contributes to the width of the final distribution. The distribution developed is shown in Figure D-4.10-1.

Although the single value for D_e from LANL (2008, 103165), (3.88×10^{-9} m^2/s), does not fall within the distribution, the resulting distribution was considered by professional judgement to be reasonable.

D-4.11 Supply Well Pumping Rates

Additional boundary conditions include pumping from Los Alamos County supply wells. The month-long pumping tests at PM-2 and PM-4 are included at the beginning of the model for calibration purposes, and long-term average pumping rates are incorporated using historical records for wells PM-2, PM-4, and PM-5.

Drawdown observed in regional wells during the PM-2 and PM-4 tests (occurring in 2003 and 2005, respectively) is matched as calibration targets and these targets are described in section D-5.1. The actual pumping rates used in the pump test are specified in the model for these two tests. The PM-2 and PM-4 pump tests are simulated very early in the model; 1957 and 1959, respectively. Drawdown targets are agnostic to the actual timing of the pump test, and therefore pump tests can be simulated at any time since the timing and magnitude of the response is what is meaningful. Moving these tests to the beginning of the model allows for the inclusion of pump tests in the calibration as part of the specific storage and hydraulic conductivity field calibration, while permitting long-term average pumping to be used in the model.

Though impacts from the county supply well pumping on the RDX plume and future transport was determined to be negligible (section D-2), long-term supply well pumping is incorporated into the model for thoroughness. Supply well pumping records include historical records that report an annual total of gallons pumped for the year on a well-by-well basis (these records start from the first year of a supply well's operation through approximately year 2000). Beginning around 2000, daily total gallons pumped are reported and continue to the present. Incorporating daily, weekly, or even monthly pumping from supply wells, however, would result in intractable model run times that would severely limit the future simulated timeframe. Therefore, to include supply well pumping, pumping is incorporated by aggregating rates to a decadal scale for wells PM-2, PM-4, and PM-5.

For each well, the total number of gallons pumped within a 10-yr span (1955–1965, 1965–1975, etc.) are calculated, and the equivalent constant rate is determined that would result in an equivalent amount of water pumped from the aquifer. In the RRM, pumping rates are specified every 6 months in the model to enforce reasonable time-stepping to better capture long-term aquifer decline due to pumping. Table D-4.11-1 presents long-term equivalent pumping rates .

D-4.12 Preferential Pumping from Water Supply Well Screens

The calibrated RDX model includes pumping at water-supply wells PM-2, PM-4, and PM-5. Each of wells has long screens of around 1000 to 1500 ft effective length (Figure D-4.12-1 [adapted from McLin 2005, 090073, Figure 4]). A spinner log experiment was performed at PM-4 only among those three wells. The results of the spinner log indicated that approximately 93% of the total production at PM-3 originates from *above* the uppermost Miocene basalt (Tb2) layer in the well.

This is important for model calibration because preferential pumping from certain screen zones would affect the model's ability to match the pumping test targets and produce accurate predictions of the effect of water-supply pumping. The nodes in the model corresponding to PM-2, PM-4, and PM-5 were discretized into two zones depending on the position of the uppermost basalts in those well locations: the zone "upper" is above the first basalt layer, and the zone "lower" is everything else. A percentage parameter is used to allocate discharge due to pumping to the upper or lower zone. For example, to correspond to the spinner log in PM-4, 93% of the well's discharge would come from the upper zone and 7% from the lower zone. The model was initialized with 93% as the value for the upper zone in all three wells, although this is highly uncertain for PM-5 and PM-2. The parameter was allowed to vary as a uniform distribution between 0 and 100% because of the lack of information. (At 100%, all discharge is assigned to the upper zone and no pumping occurs in the lower zone.)

D-4.13 Total Mass of RDX

The predictive forward simulations are a tool to understand RDX migration until the year 2200. As previously noted, if simulations are run for that time with continuous RDX injection, the total mass of RDX in the regional aquifer model could become unrealistically high, limiting the utility of the simulation for understanding downgradient fate and transport, defining risk, and making decisions.

This distribution development leverages estimates of RDX mass in the subsurface environment to constrain the amount of total mass injected into the regional aquifer model. The primary information source for this distribution is from Attachment 1 of the 2018 Compendium of Technical Reports Related to the Deep Groundwater Investigation for the RDX Project at Los Alamos National Laboratory (LANL 2018, 602963) titled 2017 Update of the RDX Inventory Report, which describes an estimate of the RDX inventory completed in 2017. This analysis supersedes a similar analysis that was completed in 2005. While the 2005 results are provided in the RDX compendium for context, these values were based on fewer data and are not considered relevant for this distribution.

The analysis estimates a range of mass of RDX (minimum and maximum) for each of seven spatial regions. A "simple geometry" approach was applied to all seven regions, while a separate geostatistical approach was applied to three of the seven regions. These values are presented in Table 5.0-1 of the RDX compendium (LANL 2018, 602963), which is reproduced below as Table D-4.13-1. These values, along with consideration of the methodology used to obtain them, were used in an expert elicitation style distribution development process that is described below.

This distribution is used to calculate a time at which RDX injection ceases in the RRM. This calculation is performed during the input file preparation and consists of the following steps:

1. Draw from the subject distribution, which defines the total mass of RDX injected during the model run. This is performed by MADS via an entry in the .mads file and the value is passed to the input file preparation code (runmodelcode.jl).

2. Given the hydraulic window parameters for a given run (e.g., source area definitions, source concentrations, source water flow rates, etc.), a function calculates the total mass in the model at any given model time on an annual basis. The year with RDX inventory closest to the value drawn from the total mass distribution for that simulation is assigned as the time at which RDX injection ceases for that individual simulation. This value is carried into FEHM's input files via the .trac file.

With respect to recharge, the RDX sources are applied continuously. The time computed by the steps above changes only the concentration applied at any given injection node (to zero) at the calculated time. Recharge from the source areas carries on at the same rate throughout the predictive forward run.

D-4.13.1 Discussion of Data and Data Uncertainty

The following brief description of the RDX contamination source is provided to give context to the spatial regions listed in Table D-4.13-1. Additional descriptions can be found in the references below. The source of RDX contamination in the subsurface is wastewater discharged from the machining of high explosives at TA-16. Water was discharged to the 260 Outfall, which conveyed water from the mesa top into a settling pond that drains into Cañon de Valle. The vadose zone under the settling pond and outfall area intermittently discharges via springs in Cañon de Valle.

Remediations of the pond area are described in the "Completion Report for Regional Aquifer Well R-68," (LANL 2017, 602539), which included the installation of a low-permeability cap over the contaminated soils and grouting of the surge bed in the vadose zone below the pond area (~25 ft bgs); the surge bed is a high porosity unit where RDX concentrations in soils have been measured as high as 4500 mg/kg. Long-term monitoring of the vicinity described in the "2019 Annual Long-Term Monitoring and Maintenance Report for the Corrective Measures Implementation at Former 260 Outfall Area" (N3B 2019, 700598) indicated that the cap was in good condition and that no water had been detected in the surge bed monitoring well. The report states: "Based on a review of these data, except for SWSC Spring, it can be concluded that the temporal and spatial trends and conditions in the surface water, alluvial groundwater, and springs are consistent with the concept that RDX concentrations are in long-term decline and are still considered protective of the regional groundwater; however, transient increases in RDX concentrations are observed during wet periods." As shown in Table D-4.13-1, a relatively small mass was estimated in Cañon de Valle sediments and the underlying alluvial aquifer due to contaminated flows from the outfall and upstream springs. Given the apparent effectiveness of the remediation efforts for these near-surface spatial regions, preferential attention was given to the intermediate and regional groundwater zones for the purpose of this distribution development.

The intermediate groundwater zone spans elevations from about 6300 ft to 6900 ft composed of upper and lower perched zones, with the lower zone understood to be considerably thinner in the vertical; see more information above in section D-1. Concentrations in the upper zone are estimated based on information from five wells, while those in the lower zone are based on two wells.

The last row in Table D-4.13-1 is the regional aquifer, which is the domain of the RRM. The 2017 estimate used data from three wells to estimate the mass in the regional aquifer (R-18, R-63, and R-68). The maximum measurement considered was 17.1 ppb. Some data from newly installed R-69 included some reliable measurements as high as 25 ppb, though all data collected since 2020 has been below 20 ppb. Regardless, more mass has likely moved from the vadose zone into the regional aquifer since the inventory estimates were made. Given that the distribution described here is for total mass that could potentially reach the regional aquifer (across the entire system, including vadose zone estimates), this movement into the regional aquifer should not affect the distribution developed.

D-4.13.2 Distribution Development

The SHELF package's online tool at https://jeremy-oakley.shinyapps.io/SHELF-single/ is used to develop the distribution in real time with subject matter expertise.

The roulette method was used with 20 bins to quantify uncertainty regarding total mass of RDX in the regional aquifer based on subject matter expert interpretation of reported RDX quantities in the regional and intermediate aquifers.

Experts estimate a 1st percentile around 150 ppb based on the current model inventory estimates as the lowest possible RDX that should be expected to reach the regional aquifer. Experts estimate a 99th percentile just higher than the estimated mass of the reported "maximum" inventory summed over the regional aquifer and all regions in the vadose zone (3608 kg). Central tendency is estimated around 1131.5 kg, the midpoint of the regional + intermediate mass sum. A skewed distribution is selected with a long right tail because current estimates are likely lower than the true inventory because of uncertainty in nature, extent, and timing.

A continuous probability distribution was selected to represent the histogram generated through the roulette method via subject matter elicitation. The 1st percentile of the selected Weibull distribution is 151.7 kg, and the 99th percentile is 3506 kg. Several other quantiles are displayed in Figure D-4.13-1. The median of this distribution is 1327 kg, slightly greater than the estimated midpoint. This was deemed acceptable because of the uncertainty in the upper tail. Most of the distribution's density lies between 500 and 2500 kg.

D-5.0   CALIBRATION FURTHER DETAILS

D-5.1   Calibration Targets

D-5.1.1   RDX Concentration and Trend Targets

Concentration targets are developed using data pulled from the publicly available Intellus database (https://intellusnm.com). The data were obtained in December 2019 and include sample results through November 1st, 2019. Experts advised removal of the following records: sample purpose of TEST, EQB, PEB, FB; sample type of WIP, WS, EM, R, S, "Qbt"; sample usage code of CLN, COMP, CONST, DEV, ENVSUR, PUMT, QC, REHAB, SCR, TEST, TRACER, WST; sample matrix of SD, SO; validation qualifier of R; and location IDs with "OB" or "WST" prefixes. The initial filtering resulted in the inclusion of the following records: sample purpose of REG and FD; sample type of W, WG; sample usage code of INV

and QC (for FD only); sample matrix of W; and validation qualifier not equal to R (rejected). The sample and field duplicate pairs were matched by location identification, screen top depth, and sample date. The sample and field duplicate results were averaged by analyte for each location, screen top depth, and sample date combination. After this initial filtering and processing, several data points were removed based on conversations with site experts familiar with the wells, drilling, and data. The removed points are displayed in red in Figure D-5.1-1. These data points were deemed non-representative by expert opinion, based on conceptual knowledge of well construction and site dynamics. Data points were removed for the following well screens:

1. CdV-R-15-3 screen 4: two J-qualified detections occurring in September and December 2013

2. R-25 screen 5 and R-25 screen 6: data before 2007 believed to be a result of contamination during drilling

3. R-18: the first sample, a nondetection, collected August 25, 2005

4. R-63: the first sample collected on January 27, 2011

5. R-68: all data collected before September 6, 2017

6. R-69: all data before 2019

Calibration targets are developed by averaging all results for a given year at each well with detectable levels of RDX. If *only* nondetections are observed at a given well, a calibration target of zero is used for each year having nondetection data. The wells with zero calibration targets are CdV-R-15-3 screen 4, CdV-R-37-2 screen 2, R-60, R-17 screen 1, R-17 screen 2, R-29, R-19 screen 3, R-19 screen 4, R-19 screen 5, R-47, R-48, and R-58. For wells with both nondetections and detections, the yearly average of the sample results defines the calibration target for that year. Results from both detected and nondetected samples are used in calculating the average. When nondetections are present in a data set, a value of zero is not reported. Rather, the detection limit or reporting limit value is the value provided for the result. Therefore, when determining averages that include nondetections, the reported values in the database are included in determining an average. A few nondetection values were excluded according to professional judgement. Using all the data irrelevant of detection status has been shown to provide the most accurate estimate of the mean in comparison with other methods for analyzing censored data. If no samples were collected in a given year, no calibration target is developed for that year. The wells with detected RDX and non-zero calibration targets are R-25 screen 5, R-25 screen 6, R-18, R-63, R-68, R-69 screen 1, and R-69 screen 2 (Figure D-5.1-1).

In addition to RDX concentrations, concentration trends with time are also used as targets. This is intended to allow the calibration to separately weight behavior such as rising or falling concentrations independently from the raw concentrations themselves.

Slopes are calculated from the RDX concentration targets for wells with a long enough time history to support trend analysis. The wells with concentration trend targets are listed in Table D-5.1-1. The slopes are calculated by polynomial fitting with degree of 1 (i.e., a linear fit to the time/concentration data). Figure D-4.13-1 shows the computed slopes against the target data.

D-5.1.2   Hydraulic Head and Gradient Targets

Hydraulic head targets provide a value for each well screen that represents average conditions at each well screen location during the month of February 2014. In order to achieve a representative average, hydraulic head values for each well screen are averaged by 2-hr intervals. Next, the 2-hr interval values are averaged within each calendar day to obtain a daily average for each well screen. Finally, the daily averages are averaged for each well screen to obtain a monthly average. The estimated average

hydraulic head values for February 2014 are then selected for each well screen and are used as the hydraulic head targets for each well.

For a well screen lacking hydraulic head data during the February 2014 time period, a nearby well with a long record of water level data is selected to impute an estimated February 2014 hydraulic head. For a well that has a long record of head data but lacks data specifically during February 2014, the head data for that well is used to impute an estimated February 2014 hydraulic head.

To impute hydraulic head for wells lacking February 2014 data, the following steps are taken:

1. The average head and average date are calculated for the well lacking data during the February 2014 time period.

2. A linear regression equation is fit to the data of a nearby well with a long record of hydraulic head data.

3. The slope from the linear regression equation is applied to the average hydraulic head and date to impute a value back to February 2014.

Head data for well R-47 begins at the end of 2014 and continues to the present. R-47's own hydraulic head record was used to impute an estimate for February 2014, and the results are shown in Figure D-5.1-2. Wells R-58, R-68, and R-69 (screen 1 and screen 2) used well data from neighboring wells in order to impute an estimated February 2014 hydraulic head. For R-58, head data from CdV-R-37-2 screen 2 were used (Figure D-5.1-3). For R-68, water level data from R-63 were used (Figure D-5.1-4). For R-69, water level data from R-18 was used for both screen 1 and screen 2 (Figures D-5.1-5 and D-5.1-6). Table D-5.1-2 presents the wells used for hydraulic head targets, the method used to calculate the target value, and the estimated February 2014 hydraulic head.

In addition to calculating water levels, the model is structured to also match the observed hydraulic gradient based on a subset of wells located in the area of interest. Hydraulic gradient targets are constructed using the water level target values, and thus the gradients also represent February 2014 conditions. While simply matching water level targets in a model calibration will produce a similar result to matching hydraulic gradient targets, having them as separate targets allows separate weighting in the OF. This means that, for example, the direction and magnitude of flow can be prioritized (weighted higher) over matching individual water levels. The hydraulic gradient is a vector quantity that consists of both the magnitude (change in head per change in distance) and direction (angle from due north, or azimuth) of groundwater movement. The subset of wells used to construct hydraulic head gradient targets includes R-25 screen 5, R-68, R-63, R-69 screen 1, R-18, and R-47 (Figure D-5.1-7). These six wells were used to compute four hydraulic gradients, resulting in four magnitude targets and four direction targets.

The gradient computation detailed in Heath (1983, 700907) is used to derive the hydraulic gradient target values using water level targets. This method requires a set of three wells, each with known water level and geographic location (Figure D-5.1-8). A summary of the steps to compute the hydraulic gradient follows:

1. Rank wells based on water level: high, intermediate, low.

2. Draw a line between the high well and low well. Calculate location on this line where the water level is equal to the intermediate well's water level.

3. Draw a line (contour) from the intermediate well through the location computed in step 2.

4. Draw a line perpendicular to the contour in step 3 through the low well's location.

5. Magnitude is equal to the difference in head between the intermediate well and low well, divided by the distance between the low well and the contour. Direction is equal to the azimuth of the line from step 4.

D-5.1.3   Drawdown Responses

In addition to calculating hydraulic head and hydraulic gradient targets, the RRM is structured to match observed drawdown responses in regional aquifer monitoring wells due to pumping from supply wells. Water level responses to pumping are developed into drawdown targets for (1) wells R-20 screen 3, PM-4, and PM-5 in response to the PM-2 pump test and (2) PM-2, PM-5, R-14 screens 1–2, R-19 screens 4–7, and R-20 screens 1–3 in response to the PM-4 pump test. Wells with no observed drawdown in response to county pumping are also included as targets; these include CdV-R-15-3 screens 4–6, CdV-R-37-2 screens 2–4, R-18, and R-19 screen 3.

Wells that were operational during each pumping test event are identified using high-temporal resolution head data obtained from the publicly available Intellus database (https://intellusnm.com). Actual pumping start and end times are not available on Intellus and were determined by examining the pumping well's hydraulic head values for initial drawdown and recovery. If head values are unavailable, the reported start and end times from the well completion report are used. Hydraulic head values within each observation well are barometrically corrected using either regression deconvolution (Toll and Rasmussen 2007, 104799) or a basic correction algorithm (which simply converts barometric pressure to feet of water, subtracts from the hydraulic head, and normalizes). Corrections were made using publicly available tidal data and barometric pressures from LANL's TA-54 weather station (Figure D-5.1-9). In some instances, barometric correction resulted in a noisier time series and therefore is not utilized.

For the PM-4 pump test, it is apparent that wells were not fully recovered when the test began since most wells recovered to a higher level than before the test. This means that the observed drawdowns are potentially muted and, if not corrected for, would result in biased drawdown targets in the calibration. To correct for this, a regression is fit between the point at which drawdown began at the response screen (this can be up to approximately 2 days after pumping began for some wells) and the end of the pump test (i.e., when PM wells resumed normal operations). This regression line serves as the reference line off which drawdowns are computed (Figure D-5.1-10). Additionally, removal of any long-term trends is not applicable because of limited data available before either pump test.

The drawdown targets for a given response well consist of an intercept and slope, obtained from a regression of drawdown versus the logarithm (base 10) of time since pumping began. This methodology is similar in nature to the Cooper and Jacob late-time approximation of the Theis equation. To determine the starting point of the late-time approximation, a range of times are specified such that the drawdown curve is approximately linear when plotted as the logarithm of time versus drawdown. A grid search is then used to determine the time that maximizes the fitted linear model's R-squared value (Figure D-5.1-11).

Water level responses to pumping are observed in the model and characterized with the same linear fitting method. The spatially heterogeneous K and S fields are adjusted accordingly in the calibration process such that the simulated water level responses from supply well pumping match the observed responses. The focus of drawdown targets is not only to characterize measured drawdown responses, but equally important, to develop targets from wells that do not show a response to supply well pumping. These "zero drawdown" targets are important to incorporate into the model such that it does not produce a drawdown response in a region where none has been observed.

Note that this approach does not make any simplifying assumptions regarding the structure of the aquifer. Traditional hydrologic methods typically derive a transmissivity/hydraulic conductivity and/or storativity/specific storage estimate of the aquifer system from a drawdown response using simplifying assumptions about the aquifer structure and an analytical solution. The derived parameters are subsequently used to parameterize a groundwater model. In the RRM, drawdown targets specify only the timing and magnitude of water level change that should be expected at a monitoring location as a result

of a nearby pump test. The goal is for the model to reproduce the desired drawdown response (timing and magnitude) observed at monitoring wells while allowing for flexibility in the model to calibrate a spatially heterogeneous K and S field.

Drawdown targets are developed using water level responses from actual month-long pump tests at PM-2 and PM-4 (that occurred in 2003 and 2005, respectively). However, in the RRM, these pump tests are simulated very early in the model (1957 and 1959), before PM-2, PM-4, and PM-5 begin their pumping. Drawdown targets are agnostic to the actual timing of the pump test, and therefore pump tests can be simulated at any time since the timing and magnitude of the response is what is meaningful. This allows for the inclusion of pump tests in the calibration, as part of the specific storage and hydraulic conductivity field calibration, while permitting long-term average pumping to be used in the model.

D-5.2   RDX Mass Balance Analysis

Mass balances for the four calibrations are summarized in Table D-5.2-1. The total mass of RDX injected and the net mass balance are taken directly from FEHM's output file, which gives cumulative solute information at each time step. The mass balance error is calculated as the ratio of the net mass balance to the total mass of RDX injected. At the beginning of calendar year 2020, mass balance errors for the four calibrations ranged from −0.50% to −1.75%, where a negative value indicates a mass deficit in the model compared with the mass calculated from the cumulative injections and extractions. Higher mass balance for Calibration 3 error is possibly attributable to higher RDX flux in the primary source area.

D-5.3   Calibration Tools and Philosophy

D-5.3.1   Levenberg-Marquardt Optimization

The LM algorithm is used extensively for solving nonlinear, least squares problems in groundwater inverse modeling. In this application, the LM algorithm is used to numerically solve the minimization problem:

$$\widehat{\boldsymbol{\beta}} = \arg \min_{\boldsymbol{\beta}} \{\| \mathbf{y} - f(\boldsymbol{\beta}) \|_2^2\}, \qquad \textbf{Equation D-15}$$

where, y represents the observed data vector (i.e., targets, section D-5.1), $f(\boldsymbol{\beta})$ is the predicted data vector with f representing the nonlinear FEHM forward modeling operator, and $\widehat{\boldsymbol{\beta}}$ is the inverted or fitted model parameter vector.

The sum of squared deviations loss function $\|\cdot\|_2^2$ is commonly referred to as the OF, and it represents the degree of misfit between the observed (targets) and predicted data (hereafter referred to as pairs). Because of differences in both the scale of the targets and the priority of individual pair fits, a weighting and normalization scheme is imposed upon the OF to mediate the contributions of each pair within the OF. First, each pair is normalized by dividing by a quantity referred to as a meaningful difference (md). This step places each pair on the same scale and facilitates meaningful comparisons of fit across groups of targets. Meaningful difference values are determined for each group through a combination of expert judgement and quantifying the variability of differences within the target groups using preliminary fits of the FEHM forward model. Second, pairs are weighted within groups using preference weights (pw), which dictate the relative contribution of each pair within a given group. Finally, group weights (gw) are applied to each respective group. The normalization and weights therefore result in a weighted nonlinear least squares problem, i.e.,

$$\arg \min_{\boldsymbol{\beta}} \{\| \mathbf{w}[\mathbf{y} - f(\boldsymbol{\beta})] \|_2^2\}, \qquad \textbf{Equation D-16}$$

with weights equal to

$$w_{i[j]} = \sqrt{\left(\frac{gw_i}{\sum gw_i}\right)\left(\frac{pw_{i[j]}}{\sum pw_{i[j]}}\right)\left(\frac{1}{md_i}\right)},$$ **Equation D-17**

where i denotes the ith group and i[j] the jth pair within group i.

Before the LM algorithm's iterative minimization procedure, the parameter vector $\boldsymbol{\beta}$ is initialized using either manually specified values (e.g., $\hat{\boldsymbol{\beta}}$ from a previous calibration) or random draws from the prior distributions detailed in section D-4. Sampling from the prior distributions is restricted to be within the 1st and 99th percentiles of each distribution. At each iteration step, the parameter vector $\boldsymbol{\beta}$ is adaptively updated by either a gradient descent or Gauss-Newton update. The method used at each step is determined by the damping parameter λ, where small values result in a Gauss-Newton update and large values result in a gradient descent update. The damping factor is adjusted at each iteration based upon the resulting change in the residual. Because of the computational burden associated with this highly parameterized model, an efficient parallel LM algorithm implemented in the MADS computational framework (https://mads.lanl.gov/) is used in order to avoid the sequential selection of λ at each iteration (Lin et al. 2016, 700889). Instead, many damping parameters are generated at each iteration and the algorithm proceeds in the search direction, thus yielding the smallest OF value (which are each computed in parallel). The algorithm iterates until either the specified maximum number of iterations or tolerance thresholds are met.

As is the case with many optimization algorithms, the solution found by the LM algorithm is guaranteed to be only a local minimum. Because of the high dimensionality of the parameter space, multiple minima exist, and the algorithm will converge to the global minimum only if the algorithm is initialized sufficiently close to it. Because of the computational cost of running a single calibration (i.e., completion time for a single LM iteration is on the order of 1–3 hr), repeated random initializations of calibrations is not an effective strategy to explore the parameter space. Instead, candidate parameter vector initializations are identified by computing the OF for many fits of the FEHM forward model. The candidate parameter vector with the smallest OF value is then subsequently used to initialize the MCMC calibration.

D-5.3.2   Markov Chain Monte Carlo Methods

MCMC algorithms can be used to evaluate complex integrals, such as joint probability distributions. This is accomplished by probabilistically generating samples from random variables in the target joint probability distribution. MCMC applied to the RRM generates samples from the marginal posterior parameter distributions based on how well parameters values allow the RRM to match data. The MCMC algorithm used here is based on the Affine-Invariant Ensemble Sampler of Goodman and Weare (2010, 700890) (emcee). The emcee algorithm uses a complementary ensemble of chains, or walkers, to explore the parameter space. Each walker receives an initial parameter set, and initial values must differ for each walker. The emcee algorithm is initialized based on the best calibrated parameter sets from the LM calibration process. At each iteration, the MCMC makes a multivariate proposal for each walker, given its previous position and a scaled difference in position by parameter between the current walker and another randomly selected walker.

The proposal is then accepted or rejected in a Metropolis step. In this step, the ratio of the likelihood in the current iteration to the likelihood in the previous iteration is compared with a draw from a random uniform distribution. If the ratio meets or exceeds the random uniform draw, the proposal is accepted. This method allows the walker to move towards higher or lower likelihood, with greater probability of moving towards higher likelihood. The ensemble methods combined with an affine transformation have been shown, in simple examples with known solutions, to converge more quickly than other methods.

The result is a collection of parameter sets that represent a joint posterior parameter distribution. Forward modeling is conducted with the collection of posterior parameter sets developed by the MCMC calibration to generate posterior predictive distributions. As a matter of logistics, each unique parameter set from the MCMC is run once and the frequency of each set is taken into account when analyzing the forward results.

D-5.4 Analyses to Diagnose and Improve Model Performance

The RRM is a complex, computer resource intensive model; thus, several structural and sensitivity analysis approaches are employed to guide the iterative model calibration process. The following sections outline these various analytical tools and analyses.

D-5.4.1 Manual Calibration

Manual calibration refers to the process of altering parameters one at a time by hand, running individual models, and looking at results individually in great detail. In essence, this is a one-at-a-time SA that is critical for building a better understanding of the model through space and time. Additionally, it offers insight into parameter sensitivity and relationships within the RRM.

Manual calibration was carried out in a "scrum" framework used most commonly in software development teams. Scrums are defined as an agile process framework for managing complex knowledge work. They rely on cross-functional teams to deliver in short cycles, which enables fast feedback, continuous improvement, rapid adaptation to change, and accelerated delivery. Instead of a traditional linear, structured approach to workflow, a scrum allows for organic exploration of a complex problem and is facilitated by collocation and coworking in one space. For the RDX project, four hydrologists and one geologist on staff held an intensive 3-day meeting conducting manual calibrations and leveraging idea sharing with white board space and visualizations. One of the hydrologists who participated was not involved in the RDX work before the scrum and so was able to bring fresh perspective and ideas to the process.

The modeling team planned and monitored the progress and results of these manual-forward iterations using shared tracking documents. By testing hydrologist-supplied theories, within and outside the bounds of the team's statistical distributions (see input parameterization in section D-4), these manual calibrations proved to be an efficient method for exploring parameter space, specifically in areas where the model structure or parameter constraints needed to be improved. A suite of specialized visualization tools was developed in order to quickly analyze and compare the results of the manual forward runs. The model was set up to output more data and these scripts pulled spatiotemporal data from every point in space and time. These outputs were then plotted with concentration, drawdown, water level, and head targets at desired wells in order to identify how responsiveness varied across different runs. Results were also visualized in ParaView, a tool for visualizing complex, 3-D data.

During the manual calibration effort, parameter values were systematically altered with the new sets and were initiated as individual forward model runs. An iterative process, this manual forward run testing was also employed throughout calibration development in order to perform quality assurance checks on certain model conditions and to improve the model structure. These manual calibrations also provided a validation step, ensuring that the model was behaving in a physically realistic manner and that post processing scripts were pulling the correct data. This validation step was key in confirming that there were no nonlinear behaviors in nonphysical regions (for example, regions of shifting positive and negative water additions because of a poorly structured boundary). This process also helped establish proof of concept for the CSM and the effects of boundary conditions. These individual parameter tests aided in verifying the functionality of new iterations of the mesh and other assumptions regarding parameters.

Parameter alterations were done manually within MADS input files. By changing which MADS file was being used to initialize FEHM, modelers were able to run specified and iterative tests starting from specific calibrations and seeds. By isolating the parameter variability to a single or a few field(s), specific end-state concentration and head levels could be directly targeted. Once these tests moved model results closer to observed targets, this new information was incorporated into the distribution development or calibration workflow. The process proved to be particularly useful in refining the model in areas where the heterogeneity of localized physical and hydraulic properties caused irregularities.

Through this individual inspection of the hydrologic and physical parameters within the model, project experts are able to verify that the structure and assumptions of the model adequately portray the site and address the problem.

D-5.4.2   Forward Model Suites

Suites of forward models are launched in order to better understand the parameter space defined by distribution development. In this context, "forward" refers to any run or set of runs where inverse history-matching methods (such as LM) are not used to determine the input parameter values. The suites described here are different from the predictive forward modeling because the parameter sets used as inputs may span large sections of parameter space, where the final predictive forward modeling uses a specific parameter set determined by the results of the LM and MCMC calibrations. Here, results from these suites are used to evaluate parameter sensitivity and behavior and to identify good starting places for the LM algorithm, which is highly sensitive to initialization state. Within the distribution-dictated parameter space, the suites draw initial values and then launch forward runs from a set of parameter values. Different input parameter sets are sampled to explore or calibrate different portions of the model in a step-wise fashion. For example, it was typical to start with calibrating the flow field independently and then calibrate transport. This involved varying only those parameters in forward suites that were relevant to the specific goal of each step of the calibration.

Parameters were drawn using the MC method, where sampling consists of randomly drawing *N* samples from each input parameter distribution. Each draw is independent of the other parameter draws in the space. These suites of forward model runs, generally between 5000 and 50,000 simulations, provide an extensive amount of data that can be used for multiple purposes within the modeling workflow. First, they can help determine whether the parameter space covers all potential targets in the model. If, for example, none of 10,000 runs from the input parameter space, conducted across uniform distributions representing the 1% through the 99% points of the distributions, covers the data range at a given target, it is likely there is a structural or conceptual error in the model that is preventing a match to data. Once this mismatch is identified, manual calibrations can be conducted to diagnose the reasons for the model's inability to match the target data. Identifying specific parameters and targets where the model is unable to match the targets provides a starting place in the high-dimensional parameter space to start investigating structural patterns and behaviors in the model. Without this starting place, the manual calibration step is unlikely to be effective in finding these mismatches. Once it is verified that the input space is able to reach all of the targets, a more targeted approach to forward runs—drawing from input distributions instead of from wide uniform distributions or focusing on particular parameters to explore sensitivity—is used.

Secondly, the best matches from each batch and selection method are analyzed and can then be used as a starting point for new LM calibrations. For this step, the prior distributions are used since they are much more informative than a uniform distribution. Visualization of these forward suites' matches in relation to the target data was conducted by sorting forward runs based on their OF or other metrics depending on the goal of the suite. Top runs are all explored and altered in manual calibration to see if they can be improved before initializing the computationally expensive LM calibration. This method provides effective starting points for the LM calibration, which aids in the search for the best local minima in parameter space.

Thirdly, the forward run suites can be used to test various weighting schemes and model sensitivity. As described above, the runs can be sorted based on their OF. By altering the weights in the script, which calculates the OF for the forward runs, the runs selected as *best/top runs* change. This allows the modeler to identify which targets are most important to match and then to select weights that appropriately prioritize among the many targets. This exploration is helpful in identifying the final weighting choices for each calibration target.

Compared with the LM calibrations and MCMC calibrations, the computational demand of the forward suites is more manageable and the forward suites cover a much larger portion of parameter space. This makes the forward suites a critical tool for diagnosing the distribution development, improving the weighting scheme that directs the LM algorithm, and identifying appropriate initialization states that provide the LM better opportunities to reach minima.

D-5.4.3 Machine Learning Meta Model

Machine learning (ML) approaches applied to RRM output can be used to abstract the most important or sensitive features to a simplified machine learning meta model (MLMM). This simplification allows the uncertainties associated with the key processes of the RRM to be studied in a computationally more efficient manner. The MLMM is applied to both calibration and forward model runs, thus taking advantage of all model simulations. Several ML approaches were explored for use in RRM abstraction, ultimately resulting in the use of extreme gradient boosting (XGB) (Chen and Guestrin 2016, 700897). The XGB approach uses boosting of binary recursive partitioning algorithms, which deconstruct a response into the relative influence from a given set of explanatory variables (i.e., model input parameters). The deconstruction breaks the model into separate parts (branches of the regression tree), and each part is examined separately. This process is repeated with smaller and smaller parts, each analyzed for the relationship between the explanatory variables and the model output (i.e., the response of interest). The deconstructed parts are then collected together to provide estimates of the sensitivity of each explanatory variable for a specific response variable from the model. The XGB approach identifies the most influential explanatory variables within the context of the observed uncertainty of the model output or response. Critically, the XGB method also identifies the range over which the influence is strongest; this can be used to better understand the full effect of a sensitive explanatory variable on the output results. Variance decomposition of the XGB fit is then used to estimate sensitivity indices. Under this decomposition approach, the goal is to identify the most influential explanatory variables within a model.

An advantage of the XGB MLMM approach is that nonlinear causal relationships can be mined and extracted without the constraint of distributional assumptions. A key feature of the XGB meta model is the use of parameter partial dependencies, which represent the marginal contribution of a parameter to predicting the model response. These partial dependencies can be used to understand how complex nonlinear relationships are manifested in the model response.

Finally, since the MLMM is an abstraction of the RRM that focuses on the most important causal processes, its runtime for a single simulation for the MLMM is much faster than the runtime for the RRM. Embedding MLMM in an MCMC simulation is used to more quickly explore parameter sensitivities through the evolution of the posterior distributions. This analysis was used in a qualitative fashion to help understand model sensitivities.

Sensitivity analysis is helpful for evaluating various aspects of the decision context. MLMM SA of the final forward runs would generate partial dependencies for each parameter. These partial dependencies indicate where within its posterior distribution the parameter has the most influence on the model response. Thus, these partial dependencies can be used in a value of information (VOI) analysis to guide decisions on reducing uncertainty in future modeling as well as monitoring. The VOI essentially assigns a

"cost" to reducing each parameter's uncertainty across the distributional range of the parameter. This gives the value of collecting more information on a parameter in terms of reducing the predictive distribution uncertainty and, in turn, the decision uncertainty. A VOI analysis was not conducted as part of this study but could help guide, or optimize, future modeling and monitoring studies if the need to reduce decision uncertainty is an outcome of the risk assessment.

D-5.4.4   Consistent Bayes

A Consistent Bayes (CB) (Butler et al. 2018, 700905) approach is used to help explore and identify parameter sets for both calibration and forward runs that match well targets for single wells (univariate distribution) as well as combinations of wells (multivariate distribution). The CB approach to solving inverse problems constructs a probability measure on the model parameters that is consistent with both the model and the observed data. Consistency is defined in terms of matching the "push-forward" probabilities from the model (i.e., MC-generated forward RRM runs) and the probability measure on the data (i.e., the probability distribution of the data). In a Bayesian fashion, the parameter prior densities are propagated through the model to generate the push-forward probability distribution. "Pull-back" probability distributions for the model parameters are then generated through rejection sampling of the push-forward probability distribution that exactly matches the observed data distribution.

The CB approach is implemented in two steps:

1. Propagate the parameter prior distributions through the RRM using MC simulation to generate the push-forward distribution.
2. Conduct rejection sampling on the push-forward realizations with the acceptance ratio based on the ratio of the model and data densities.

Step 1 (above) can take advantage of existing calibration and forward runs for the push-forward distribution. Step 2 is then a matter of rejection sampling on the existing model runs similar to the Metropolis step in the MCMC approach. Similar to the LM and MCMC calibrations, the CB approach is heavily weighted towards matching the data.

The CB rejection sampling is used to explore model runs that fit monitoring data both for one well at a time (univariate distribution sampling) and for various combinations of wells (multivariate sampling). The CB rejection sampling also generates posterior parameter distributions that can provide a comparison with MCMC-generated posterior distributions. The approach requires specifying a distribution for the observed data. Only wells with concentrations above the detection limit were included in the CB analysis and a normal distribution assumption was made for well data densities.

D-5.4.5   ModelWatcher Visualization Suite

ModelWatcher is a tool developed to track calibration or forward modeling progress in real time. ModelWatcher both parses model output and creates visuals of results. The primary benefit of this is that it streamlines the testing and exploration of various models (VZ, RRM, or forward suites of runs) and of various model configurations. ModelWatcher is an independent software package developed by Neptune that can be used for data management and visualization under any model framework.

For the RRM, calibration and forward model output are stored in text files. These text files are regularly copied from the high-performance computing (HPC) cluster to a server used for model development and research. The files are parsed, and the relevant information, including estimated parameter values, predicted RDX concentrations, and water levels at observation wells and decision locations, is gathered into csv file format in preparation for analysis and visualization. The code for creating the visuals is written

within an R notebook. The R notebook is rendered to html for each seed within a calibration and each forward modeling effort, and a simple webpage provides links to each individual html page. The dashboard provides a straightforward presentation of results that is critical to the model development and calibration process as well as the analysis and interpretation of forward modeling results.

D-6.0 RESULTS

Results are discussed extensively in Appendix C; however Figures D-6.1-1 through D-6-1.4 are included here for further reference. These include figures of hydraulic conductivity across the top four calibrated models at various depths throughout the aquifer and the expansion of the 0.33-ppb RDX contour through time.

D-7.0 REFERENCES

The following reference list includes documents cited in this appendix. Parenthetical information following each reference provides the author(s), publication date, and ERID, ESHID, or EMID. ERIDs were assigned by the Laboratory's Associate Directorate for Environmental Management (IDs through 599999); ESHIDs were assigned by the Laboratory's Associate Directorate for Environment, Safety, and Health (IDs 600000 through 699999); and EMIDs are assigned by N3B (IDs 700000 and above).

Aistleitner, C., M. Hofer, and R. Tichy, 2012. "A Central Limit Theorem for Latin Hypercube Sampling with Dependence and Application to Exotic Basket Option Pricing," *International Journal of Theoretical and Applied Finance,* Vol. 15, No. 7. (Aistleitner et al. 2012, 700896)

Birdsell, K.H., K.M. Bower, A.V. Wolfsberg, W.E. Soll, T.A. Cherry, and T.W. Orr, July 1999. "Simulations of Groundwater Flow and Radionuclide Transport in the Vadose and Saturated Zones Beneath Area G, Los Alamos National Laboratory," Los Alamos National Laboratory report LA-13299-MS, Los Alamos, New Mexico. (Birdsell et al. 1999, 069792)

Birdsell, K.H., B.D. Newman, D.E. Broxton, and B.A. Robinson, 2005. "Conceptual Models of Vadose Zone Flow and Transport beneath the Pajarito Plateau, Los Alamos, New Mexico," *Vadose Zone Journal,* Vol. 4, pp. 620–636. (Birdsell et al. 2005, 092048)

Black, P., K. Catlett, D. Anderson, P. Duffy, T. Stockton, and S. Van Sickle, March 3–7, 2019. "Scaling Input Distributions for Probabilistic Models-19472," Waste Management 2019 Conference, March 3–7, 2019, Phoenix, Arizona. (Black et al. 2019, 700892)

Bromly, M., C. Hinz, and L.A.G. Aylmore, February 2007. "Relation of Dispersivity to Properties of Homogeneous Saturated Repacked Soil Columns," *European Journal of Soil Science,* Vol. 58, No. 1, pp. 293-301. (Bromly et al. 2007, 700902)

Broxton, D., R. Warren, P. Longmire, R. Gilkeson, S. Johnson, D. Rogers, W. Stone, B. Newman, M. Everett, D. Vaniman, S. McLin, J. Skalski, and D. Larssen, March 2002. "Characterization Well R-25 Completion Report," Los Alamos National Laboratory report LA-13909-MS, Los Alamos, New Mexico. (Broxton et al. 2002, 072640)

Broxton, D., G. WoldeGabriel, D. Katzman, and R. Harris, March 8–12, 2021. "Using High-Resolution Stratigraphic Characterization to Inform Remediation Strategies for a Hexavalent Chromium Plume at Los Alamos National Laboratory," Waste Management 2021 Conference, March 8–12, 2021, Phoenix, Arizona. (Broxton et al. 2021, 701441)

Butler, T., J. Jakeman, and T. Wildey, April 2018. "Combining Push-forward Measures and Bayes' Rule to Construct Consistent Solutions to Stochastic Inverse Problems," *SIAM Journal on Scientific Computing,* Vol. 40, No. 2, pp. A984-A1011. (Butler et al. 2018, 700905)

Chen, T., and C. Guestrin, August 13-17, 2016. "XGBoost: A Scalable Tree Boosting System," KDD '16: Proceedings of the 22nd ACM SIGKDD International Conference on Knowledge Discovery and Data Mining, August 13-17, 2016, San Francisco, California. (Chen and Guestrin 2016, 700897)

Collins, K.A., A.M. Simmons, B.A. Robinson, and C.I. Nylander (Eds.), December 2005. "Los Alamos National Laboratory's Hydrogeologic Studies of the Pajarito Plateau: A Synthesis of Hydrogeologic Workplan Activities (1998–2004)," Los Alamos National Laboratory report LA-14263-MS, Los Alamos, New Mexico. (Collins et al. 2005, 092028)

Cressie, N., 1993. *Statistics for Spatial Data*, John Wiley and Sons Inc., New York, New York. (Cressie 1993, 700911)

DOE (U.S. Department of Energy), January 2010. "Final Environmental Impact Statement for Decommissioning and/or Long-Term Stewardship at the West Valley Demonstration Project and Western New York Nuclear Service Center," Volume 2 (Appendices A through R), DOE/EIS-0226, West Valley, New York. (DOE 2010, 700880)

Doherty, J., March-April 2003. "Ground Water Model Calibration Using Pilot Points and Regularization," *Ground Water,* Vol. 41, No. 2, pp. 170-177. (Doherty 2003, 700894)

Fetter, C.W., *Applied Hydrogeology*, Third ed., Prentice Hall, Upper Saddle River, New Jersey. (Fetter 1994, 070942)

Fetter, C.W., 2008. *Contaminant Hydrogeology*, Second Edition, Waveland Press Inc., Long Grove, Illinois. (Fetter 2008, 700912)

Franke, O.L., T.E. Reilly, and D. Bennett, 1987. "Chapter B5, Definition of Boundary and Initial Conditions in the Analysis of Saturated Ground-Water Flow Systems—An Introduction," in *Techniques of Water-Resources Investigations of the United States Geological Survey*, United States Geological Survey, United States Government Printing Office, Washington, D.C. (Franke et al. 1987, 700886)

Freeze, R.A., and J.A. Cherry, January 1979. *Groundwater*, Prentice-Hall, Inc., Englewood Cliffs, New Jersey. (Freeze and Cherry 1979, 088742)

French, S., R. Shuman, G.L. Cole, K.J. Crowell, M.S. Day, C.W. Gable, M.O. Gard, J.J. Whicker, D.G. Levitt, B.D. Newman, B.A. Robinson, E.P. Springer, and P.H. Stauffer, October 2008. "Performance Assessment and Composite Analysis for Los Alamos National Laboratory Material Disposal, Area G, Revision 4," Los Alamos National Laboratory document LA-UR-08-06764, Los Alamos, New Mexico. (French et al. 2008, 106890)

Frenzel, P.F., 1995. "Geohydrology and Simulation of Groundwater Flow near Los Alamos, North-Central New Mexico," U.S. Geological Survey, Water-Resources Investigations Report 95-4091, Albuquerque, New Mexico. (Frenzel 1995, 056028)

Fujinawa, K., 2010. "Anthroscape of the Mediterranean Coastal Area in the Context of Hydrogeology: Projected Impacts of Climate Change," in *Sustainable Land Management*, S. Kapur, H. Eswaran, and W. Blum (Eds.), Springer, Berlin, Heidelberg. (Fujinawa 2010, 700903)

Gable, C.W., H.E. Trease, and T.A. Cherry, June 1996. "Geological Applications of Automatic Grid Generation Tools for Finite Elements Applied to Porous Flow Modeling," in *Numerical Grid Generation in Computational Fluid Dynamics and Related Fields*, B.K. Soni, J.F. Thompson, H. Hausser, and P.R. Eiseman (Eds.), Mississippi State University Press, Jackson, Mississippi. (Gable et al. 1996, 700887)

Gains-Germain, L., A. Jordan, M. Higgs, P. Meeks, P. Black, and T. Stockton, March 18–22, 2018. "Explicitly Accounting for Multiple Spatial Scales in Data Informing Kd Distribution Development – 18414," Waste Management 2018 Conference, March 18–22, 2018, Phoenix, Arizona. (Gains-Germain et al. 2018, 700888)

Gardner, J.N., A. Lavine, G. WoldeGabriel, D. Krier, J., D.T. Vaniman, F.A. Caporuscio, C.J. Lewis, M.R. Reneau, E.C. Kluk, and M.J. Snow, March 1999. "Structural Geology of the Northwestern Portion of Los Alamos National Laboratory, Rio Grande Rift, New Mexico: Implications for Seismic Surface Rupture Potential from TA-3 to TA-55," Los Alamos National Laboratory report LA-13589-MS, Los Alamos, New Mexico. (Gardner et al. 1999, 063492)

Gelhar, L.W., C. Welty, and K.R. Rehfeldt, July 1992. "A Critical Review of Data on Field-Scale Dispersion in Aquifers," *Water Resources Research,* Vol. 28, No. 7, pp. 1955–1974. (Gelhar et al. 1992, 102465)

Goodman, J., and J. Weare, 2010. "Ensemble Samplers with Affine Invariance," *Communications in Applied Mathematics and Computational Science,* Vol. 5, No. 1, pp. 65-80. (Goodman and Weare 2010, 700890)

Heath, R.C., 1983. "Basic Ground-Water Hydrology," prepared in cooperation with the North Carolina Department of Natural Resources and Community Development, U.S. Geological Survey Water-Supply Paper 2220, Reston, Virginia. (Heath 1983, 700907)

Heerspink, B.P., S. Pandey, H. Boukhalfa, D.S. Ware, O. Marina, G. Perkins, V.V. Vesselinov, and G. WoldeGabriel, May 2, 2017. "Fate and Transport of Hexahydro-1,3,5-trinitro-1,3,5-triazine (RDX) and Its Degradation Products in Sedimentary and Volcanic Rocks, Los Alamos, New Mexico," *Chemosphere,* Vol. 182, pp. 276-283. (Heerspink et al. 2017, 602560)

Ho, C.K., R.G. Baca, S.H. Conrad, G.A. Smith, L.-J. Shyr, and T.A. Wheeler, January 1999. "Stochastic Parameter Development for PORFLOW Simulations of the Hanford AX Tank Farm," Sandia National Laboratories Report No. SAND98-2880, Albuquerque, New Mexico. (Ho et al. 1999, 700883)

Jordan, A., S. Fitchett, K. Catlett, D. Levitt, G. Occhiogrosso, J. Tauxe, P. Meeks, M. Higgs, and P. Black, March 5–9, 2017. "Realistic Geochemical Paramater Uncertainty for Performance Assessment Modeling – 17066," Waste Management 2017 Conference, March 5–9, 2017, Phoenix, Arizona. (Jordan et al. 2017, 700881)

Keating, E.H., B.A. Robinson, and V.V. Vesselinov, August 2005. "Development and Application of Numerical Models to Estimate Fluxes through the Regional Aquifer beneath the Pajarito Plateau," *Vadose Zone Journal,* Vol. 4, pp. 653–671. (Keating et al. 2005, 090039)

Kleinfelder, January 25, 2005. "Final Well R-26 Completion Report, Revision No. 1," report prepared for Los Alamos National Laboratory, Project No. 37151, Albuquerque, New Mexico. (Kleinfelder 2005, 087846)

Koch, R.J., and S. Schmeer, March 2010. "Groundwater Level Status Report for 2009, Los Alamos National Laboratory," Los Alamos National Laboratory report LA-14416-PR, Los Alamos, New Mexico. (Koch and Schmeer 2010, 108926)

Kwicklis, E., M. Witkowski, K. Birdsell, B. Newman, and D. Walther, August 2005. "Development of an Infiltration Map for the Los Alamos Area, New Mexico," *Vadose Zone Journal,* Vol. 4, pp. 672–693. (Kwicklis et al. 2005, 090069)

LANL (Los Alamos National Laboratory), September 1998. "Work Plan for Pajarito Canyon," Los Alamos National Laboratory document LA-UR-98-2550, Los Alamos, New Mexico. (LANL 1998, 059577)

LANL (Los Alamos National Laboratory), September 2007. "Completion Report for Regional Aquifer Wells R-35a and R-35b," Los Alamos National Laboratory document LA-UR-07-5324, Los Alamos, New Mexico. (LANL 2007, 098129)

LANL (Los Alamos National Laboratory), June 2008. "Supplemental Investigation Work Plan for Intermediate and Regional Groundwater at Consolidated Unit 16-021(c)-99," Los Alamos National Laboratory document LA-UR-08-3991, Los Alamos, New Mexico. (LANL 2008, 103165)

LANL (Los Alamos National Laboratory), April 2009. "Investigation Work Plan for Lower Sandia Canyon Aggregate Area," Los Alamos National Laboratory document LA-UR-09-2076, Los Alamos, New Mexico. (LANL 2009, 105079)

LANL (Los Alamos National Laboratory), September 2011. "Corrective Measures Evaluation Report for Material Disposal Area G, Solid Waste Management Unit 54-013(b)-99, at Technical Area 54, Revision 3," Los Alamos National Laboratory document LA-UR-11-4910, Los Alamos, New Mexico. (LANL 2011, 206324)

LANL (Los Alamos National Laboratory), September 2011. "Investigation Report for Water Canyon/ Cañon de Valle," Los Alamos National Laboratory document LA-UR-11-5478, Los Alamos, New Mexico. (LANL 2011, 207069)

LANL (Los Alamos National Laboratory), March 2012. "Technical Area 16 Well Network Evaluation and Recommendations," Los Alamos National Laboratory document LA-UR-12-1082, Los Alamos, New Mexico. (LANL 2012, 213573)

LANL (Los Alamos National Laboratory), September 6, 2016. "Completion Report for Groundwater Extraction Well CrEX-3," Los Alamos National Laboratory document LA-UR-16-26486, Los Alamos, New Mexico. (LANL 1016, 601778)

LANL (Los Alamos National Laboratory), March 28, 2017. "Well Completion Report for Chromium Plume Control Interim Measure and Plume-Center Characterization Injection Wells CrIN-2, CrIN-3, CrIN-4, and CrIN-5," Los Alamos National Laboratory document LA-UR-17-22162, Los Alamos, New Mexico. (LANL 1017, 602258)

LANL (Los Alamos National Laboratory), July 27, 2017. "Completion Report for Regional Aquifer Well R-68," Los Alamos National Laboratory document LA-UR-17-26063, Los Alamos, New Mexico. (LANL 2017, 602539)

LANL (Los Alamos National Laboratory), September 2017. "Completion Report for Groundwater Extraction Well CrEX-2," Los Alamos National Laboratory document LA-UR-17-27466, Los Alamos, New Mexico. (LANL 2017, 602595)

LANL (Los Alamos National Laboratory), March 2018. "Compendium of Technical Reports Conducted Under the Work Plan for Chromium Plume Center Characterization," Los Alamos National Laboratory document LA-UR-18-21450, Los Alamos, New Mexico. (LANL 2018, 602964)

LANL (Los Alamos National Laboratory), March 2018. "Compendium of Technical Reports Related to the Deep Groundwater Investigation for the RDX Project at Los Alamos National Laboratory," Los Alamos National Laboratory document LA-UR-18-21326, Los Alamos, New Mexico. (LANL 2018, 602963)

Levitt, D.G., September 2011. "Modeling the Movement of Transient Moisture through Disposal Units at Los Alamos National Laboratory Technical Area 54, Area G," Los Alamos National Laboratory document LA-UR-11-05424, Los Alamos, New Mexico. (Levitt 2011, 700879)

Lewis, C.L., J.N. Gardner, E.S. Schultz-Fellenz, A. Lavine, and S.L. Reneau, June 2009. "Fault Interaction and Along-Strike Variation in Throw in the Pajarito Fault System, Rio Grande Rift, New Mexico," *Geosphere,* Vol. 5, No. 3, pp. 252–269. (Lewis et al. 2009, 111708)

Lin, Y., D. O'Malley, and V.V. Vesselinov, September 15, 2016. "A Computationally Efficient Parallel Levenberg-Marquardt Algorithm for Highly Parameterized Inverse Model Analyses," *Water Resources Research,* Vol. 52, pp. 6948-6977. (Lin et al. 2016, 700889)

Longmire, P., D. Broxton, W. Stone, B. Newman, R. Gilkeson, J. Marin, D. Vaniman, D. Counce, D. Rogers, R. Hull, S. McLin, and R. Warren, May 2001. "Characterization Well R-15 Completion Report," Los Alamos National Laboratory report LA-13749-MS, Los Alamos, New Mexico. (Longmire et al. 2001, 070103)

McLin, S.G., May 2005. "Hydrologic Tests at Characterization Well R-20," Los Alamos National Laboratory report LA-14021-MS, Los Alamos, New Mexico. (McLin 2005, 702324)

McLin, S., July 2005. "Analyses of the PM-2 Aquifer Test Using Multiple Observation Wells," Los Alamos National Laboratory report LA-14225-MS, Los Alamos, New Mexico. (McLin 2005, 090073)

McLin, S., January 2006. "Analyses of the PM-4 Aquifer Test Using Multiple Observation Wells," Los Alamos National Laboratory report LA-14252-MS, Los Alamos, New Mexico. (McLin 2006, 092218)

Meyer, B.R., C.A.R. Bain, A.S.M. De Jesus, and D. Stephenson, 1981. "Radiotracer Evaluation of Groundwater Dispersion in a Multi-Layered Aquifer," *Journal of Hydrology,* Vol. 50, pp. 259-271. (Meyer et al. 1981, 700901)

Millington, R.J., and J.P. Quirk, 1961. "Permeability of Porous Solids," *Transactions of the Faraday Society,* Vol. 57, pp. 1200–1207. (Millington and Quirk 1961, 110521)

N3B (Newport News Nuclear BWXT-Los Alamos, LLC), August 2019. "Investigation Report for Royal Demolition Explosive in Deep Groundwater," Newport News Nuclear BWXT-Los Alamos, LLC, document EM2019-0235, Los Alamos, New Mexico. (N3B 2019, 700561)

N3B (Newport News Nuclear BWXT-Los Alamos, LLC), September 2019. "2019 Annual Long-Term Monitoring and Maintenance Report for the Corrective Measures Implementation at Former 260 Outfall Area," Newport News Nuclear BWXT-Los Alamos, LLC, document EM2019-0316, Los Alamos, New Mexico. (N3B 2019, 700598)

N3B (Newport News Nuclear BWXT-Los Alamos, LLC), December 2019. "Completion Report for Regional Aquifer Well R-70," Newport News Nuclear BWXT-Los Alamos, LLC, document EM2019-0365, Los Alamos, New Mexico. (N3B 2019, 700721)

N3B (Newport News Nuclear BWXT-Los Alamos, LLC), May 2020. "Fate and Transport Modeling and Risk Assessment Report for RDX Contamination in Deep Groundwater," Newport News Nuclear BWXT-Los Alamos, LLC, document EM2020-0135, Los Alamos, New Mexico. (N3B 2020, 700925)

N3B (Newport News Nuclear BWXT-Los Alamos, LLC), June 2021. "Assessment Report for the Evaluation of Conditions in the Regional Aquifer Around Well R-70," Newport News Nuclear BWXT-Los Alamos, LLC, document EM2021-0321, Los Alamos, New Mexico. (N3B 2021, 701506)

Neptune (Neptune and Company, Inc.), September 30, 2018. "File Transfer Report for Chromium and RDX Project Hydrologic Modeling," Neptune and Company, Inc., report no. NAC-0124_R0, Los Alamos, New Mexico. (Neptune 2018, 700878)

Neuman, S.P., August 1990. "Universal Scaling of Hydraulic Conductivities and Dispersivities in Geologic Media," *Water Resources Research,* Vol. 26, No. 8, pp. 1749-1758. (Neuman 1990, 090184)

NRC (U.S. Nuclear Regulatory Commission), April 1987. "Modeling Study of Solute Transport in the Unsaturated Zone," Workshop Proceedings, NUREG/CR-4615, LA-10730-MS, Washington, D.C. (NRC 1987, 700882)

O'Malley, D., and V.V. Vesselinov, March 7, 2014. "Analytical Solutions for Anomalous Dispersion Transport," *Advances in Water Resources,* Vol. 68, pp. 13–23. (O'Malley and Vesselinov 2014, 700891)

Reimus, P.W., M.J. Haga, A.I. Adams, T.J. Callahan, H.J. Turin, and D.A. Counce, April–May 2003. "Testing and Parameterizing a Conceptual Solute Transport Model in Saturated Fractured Tuff Using Sorbing and Nonsorbing Tracers in Cross-Hole Tracer Tests," *Journal of Contaminant Hydrology,* Vol. 62–63, pp. 613–636. (Reimus et al. 2003, 210315)

Reneau, S.L., E.V. McDonald, J.N. Gardner, T.R. Kolbe, J.S. Carney, P.M. Watt, and P.A. Longmire, 1996. "Erosion and Deposition on the Pajarito Plateau, New Mexico, and Implications for Geomorphic Responses to Late Quaternary Climatic Changes," New Mexico Geological Society Guidebook: 47th Field Conference, Jemez Mountains Region, New Mexico, pp. 391-398. (Reneau et al. 1996, 055539)

Schulze-Makuch, D., D.A. Carlson, D.S. Cherkauer, and P. Malik, November--December 1999. "Scale Dependency of Hydraulic Conductivity in Heterogeneous Media," *Ground Water,* Vol. 37, No. 6, pp. 904-919. (Schulze-Makuch et al. 1999, 700893)

Stephens, D.B., 1995. *Vadose Zone Hydrology*, CRC Press Inc., Boca Raton, Florida. (Stephens 1995, 700914)

Toll, N.J., and T.C. Rasmussen, January–February 2007. "Removal of Barometric Pressure Effects and Earth Tides from Observed Water Levels," *Ground Water,* Vol. 45, No. 1, pp. 101–105. (Toll and Rasmussen 2007, 104799)

Umari, A., M.F. Fahy, J.D. Earle, and P. Tucci, 2008. "Analysis of Conservative Tracer Tests in the Bullfrog, Tram, and Prow Pass Tuffs, 1996 to 1998, Yucca Mountain, Nye County, Nevada," report prepared for the U.S. Department of the Interior and the U.S. Geological Survey in cooperation with the U.S. Department of Energy, Scientific Investigations Report 2007-5280, Weston, Virginia. (Umari et al. 2008, 700899)

Vesselinov, V.V., 2004. "An Alternative Conceptual Model of Groundwater Flow and Transport in Saturated Zone Beneath the Pajarito Plateau," Los Alamos National Laboratory document LA-UR-05-6741, Los Alamos, New Mexico. (Vesselinov 2004, 090040)

Waldrop, W.R., L.W. Gelhar, A. Mantogiou, C. Welty, and K.R. Rehfeldt, August 1985. "A Review of Field-Scale Physical Solute Transport Processes In Saturated and Unsaturated Porous Media," report prepared by Tennessee Valley Authority and Massachusetts Institute of Technology for the Electric Power Research Institute, final report EA-4190, Palo Alto, California. (Waldrop et al. 1985, 700900)

Zyvoloski, G., May 18, 2007. "FEHM: A Control Volume Finite Element Code for Simulating Subsurface Multi-Phase Multi-Fluid Heat and Mass Transfer," Los Alamos National Laboratory document LA-UR-07-3359, Los Alamos, New Mexico. (Zyvoloski 2007, 700904)
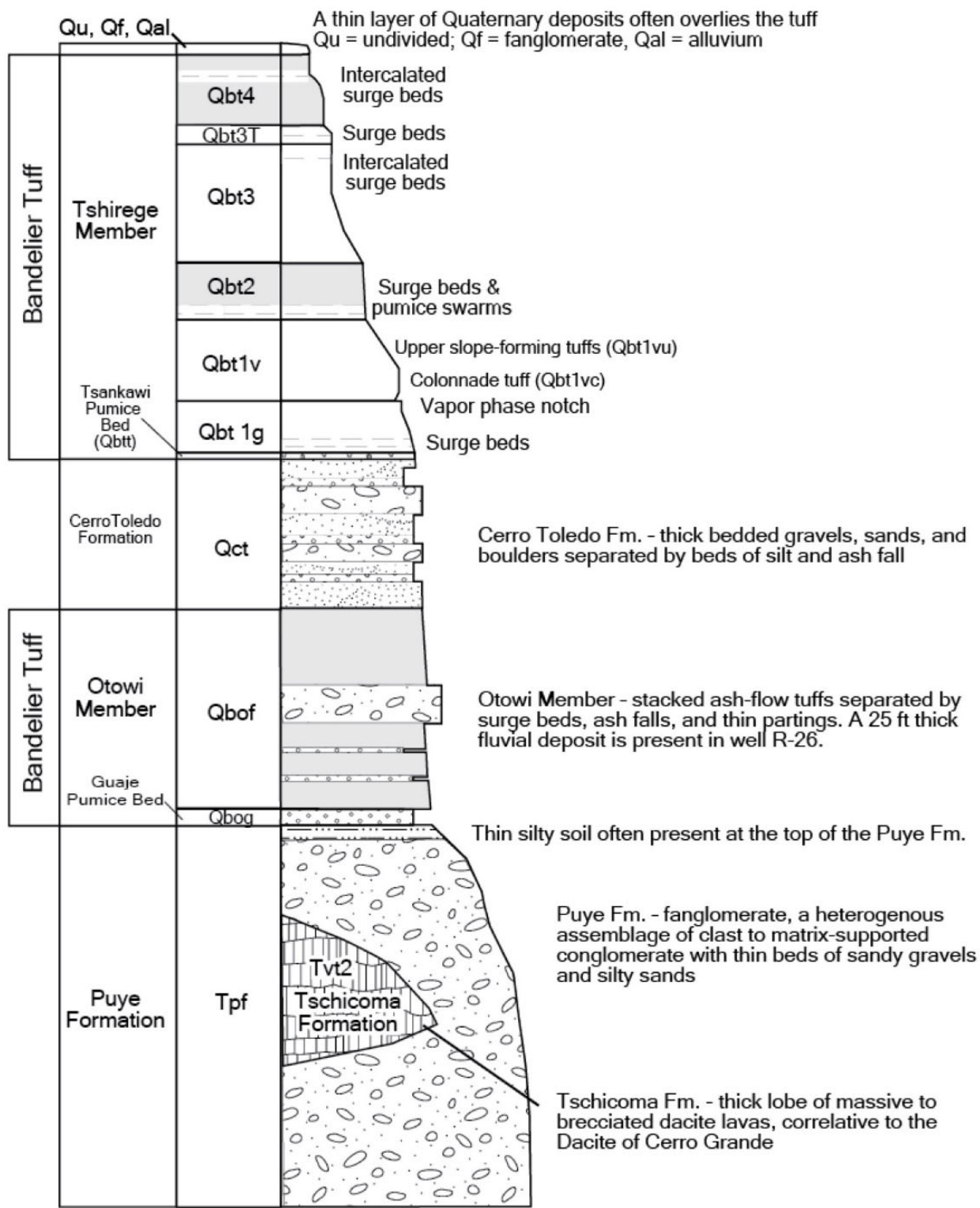
Figure D-1.1-1   Stratigraphy of the geologic units at TA-16

LEGEND

GEOLOGIC & GEOMORPHIC UNITS

	disturbed or fill
	Qal
	Qt
	Qc
	Qls
	Qfy
	Qfi
	Qec
	Qfo
	Qaf
	Qoal
	Qbt4u (w)
	Qbt4u (npw)
	Qbt4u (nw)
	Qbt4u
	Qbt4l (w)
	Qbt4l
	Qbt4
	Qbt3t
	Qbt3
	Qbt2
	Qbt1vw+2
	Qbt1v-c
	Qbt1v
	Qbt1g
	Qbt1
	Qbt
	Qct
	Qbo
	Tpp
	Tpd
	Tpr
	Tka
	not mapped

STRUCTURE

- —— fault
- ---- fault (located approximately)
- ········ fault (concealed)
- fault (uncertain)
- fault zone
- edge of DTW fault zone
- fissure
- fissure (located approximately)
- monocline, bottom hinge
- monocline, bottom hinge (approximate)
- monocline, bottom hinge (concealed)
- monocline, top hinge
- monocline, top hinge (approximate)
- monocline, top hinge (concealed)
- syncline
- ⊢5 Strike & dip of bedding

Most faults with less than 1 m displacement not shown.

OTHER

- —— stream channels
- —— contour lines (200 ft contour interval)
- ● trenches
- ● monitoring well
- —— Roads
- —— Limit of mapping

Modified from Lewis et al. 2009, 111708

Figure D-1.1-2   Pajarito Fault System and TA-09 graben
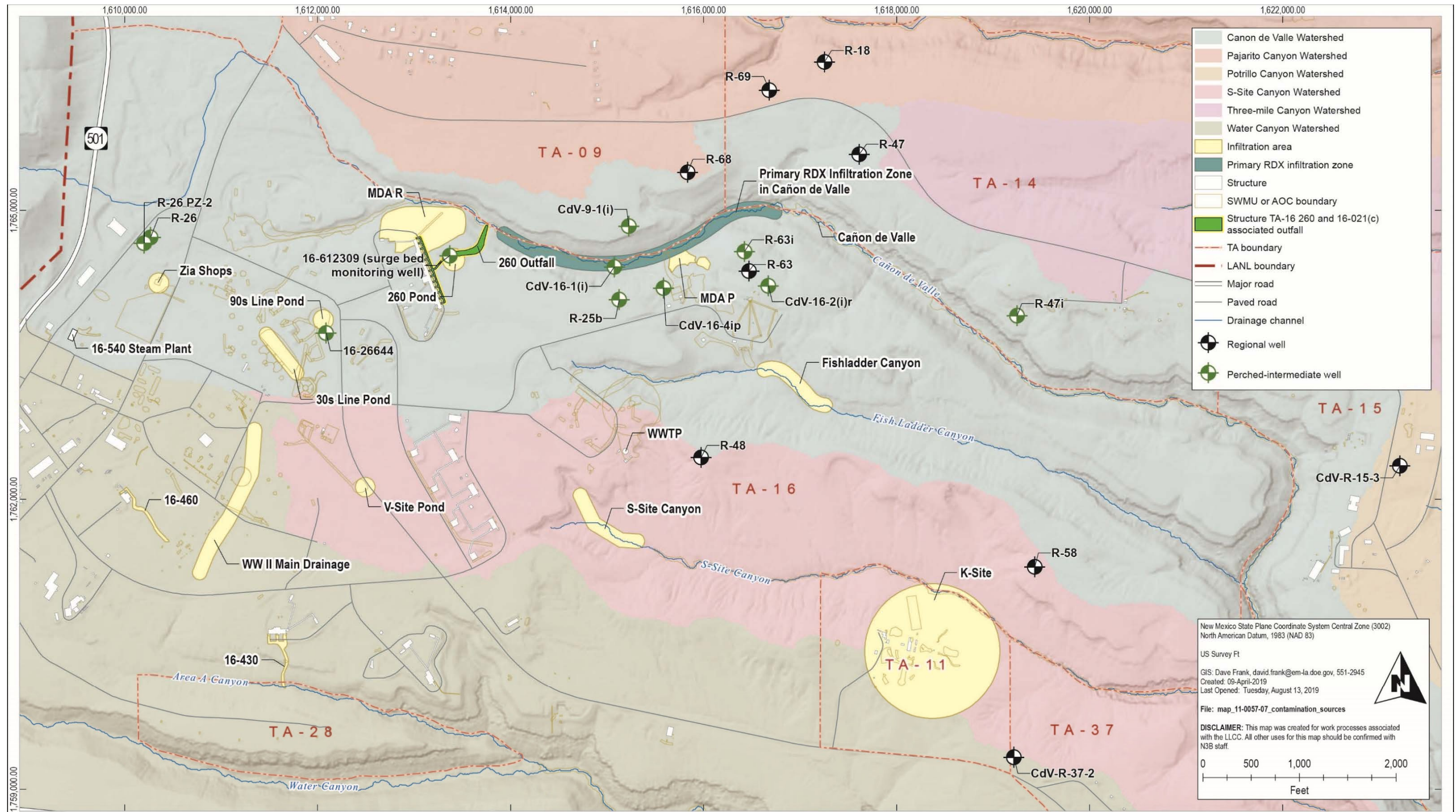
Note: RDX contaminated discharges from the 260 Outfall, combined with surface water of Cañon de Valle, were thought to infiltrate somewhere within the indicated zone.

Figure D-1.1-3   A potential area of higher infiltration of surface water is shown downcanyon of the 260 Outfall, within the area of the TA-09 graben
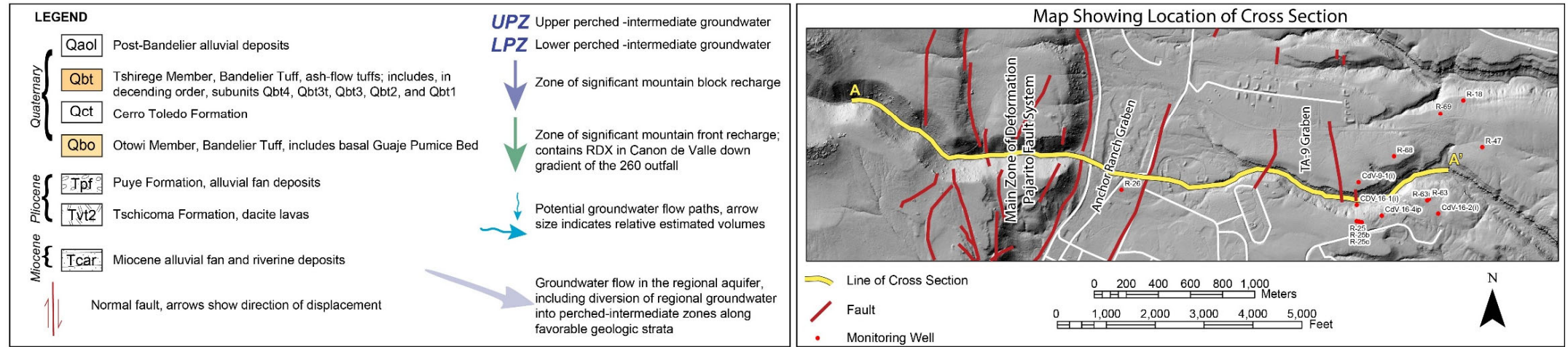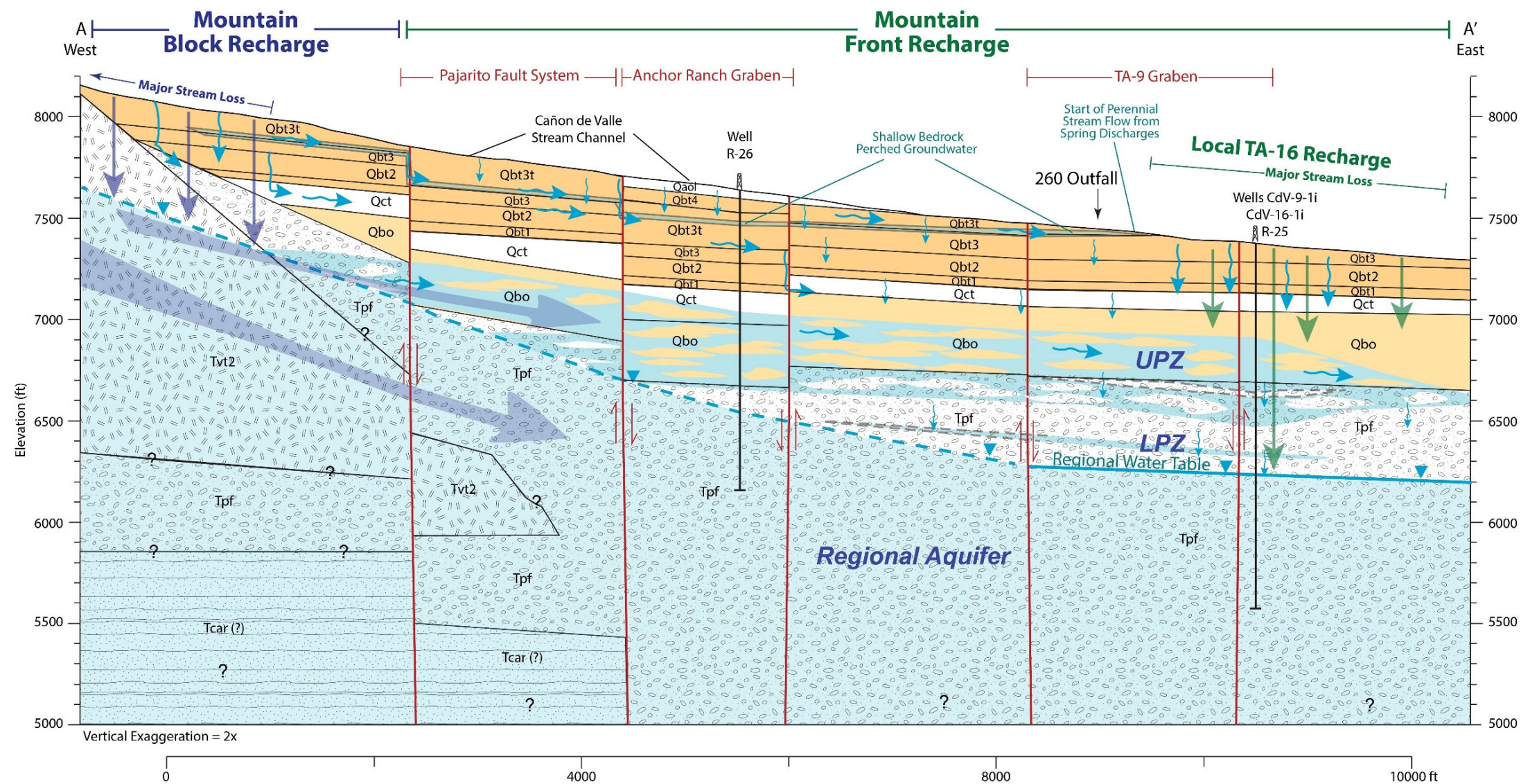
Notes: Mountain-block and mountain-front recharge are shown, along with arrows depicting dominant direction of groundwater flow. Arrows indicate a large source of recharge to the perched zones occurs from mountain-block and mountain-front recharge.

Figure D-1.3-1   Conceptual east-to-west cross-section showing the upper perched-intermediate zone (UPZ), lower perched-intermediate zone (LPZ), and regional aquifer
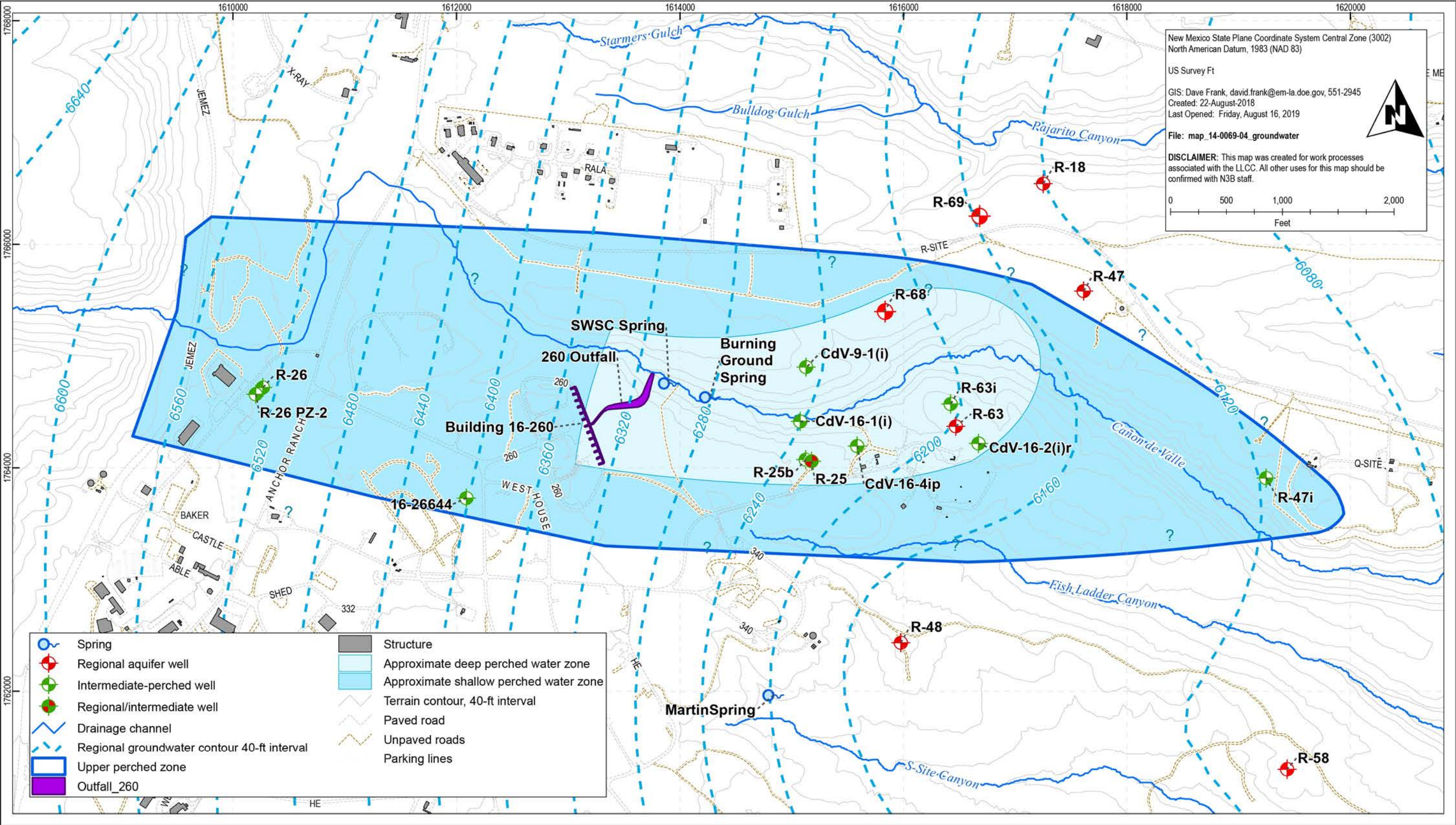
Figure D-1.3-2   Upper and lower extents of perched-intermediate aquifers with regional groundwater contours
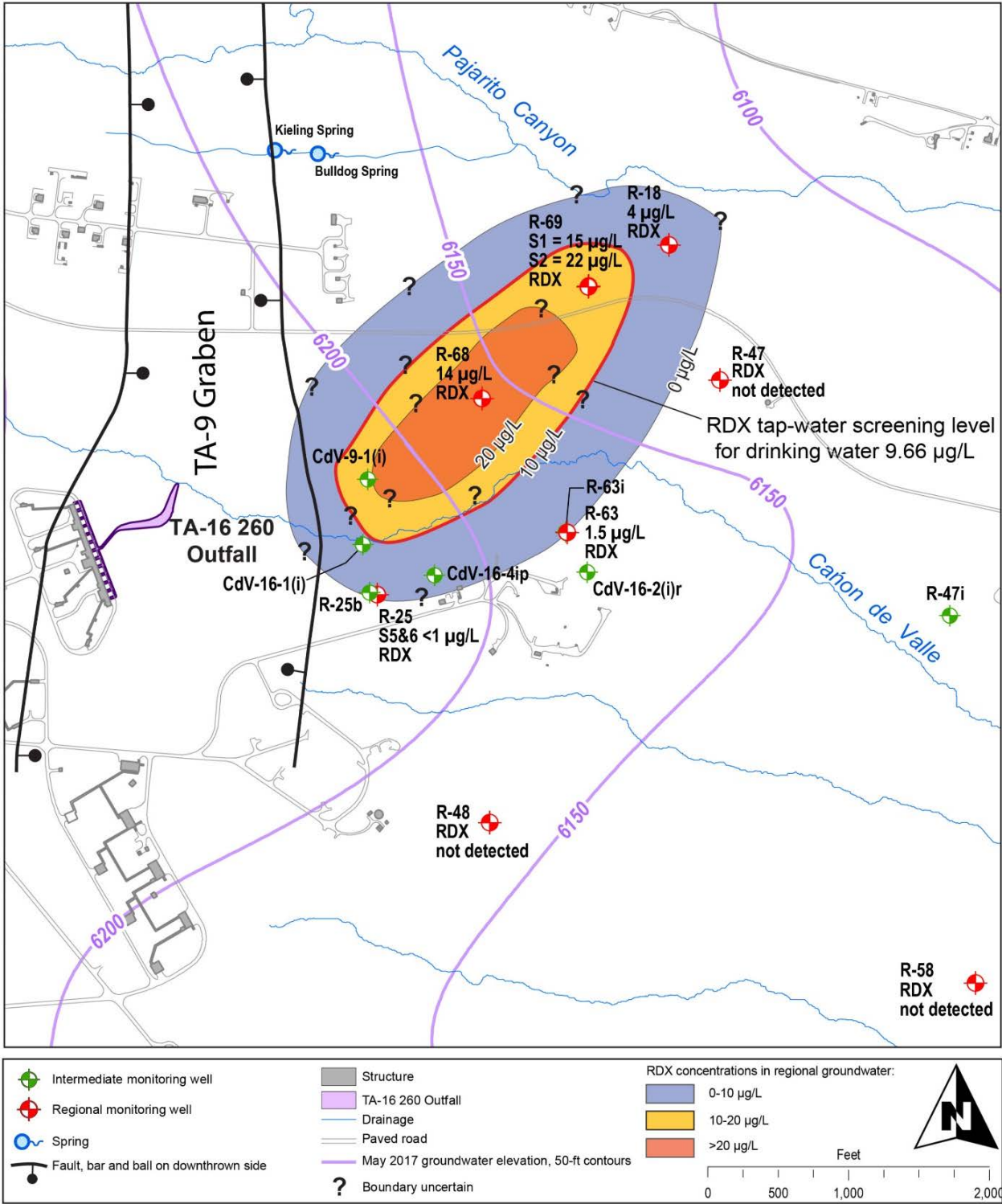
Figure D-1.3-3   Map view of RDX concentrations in the regional aquifer
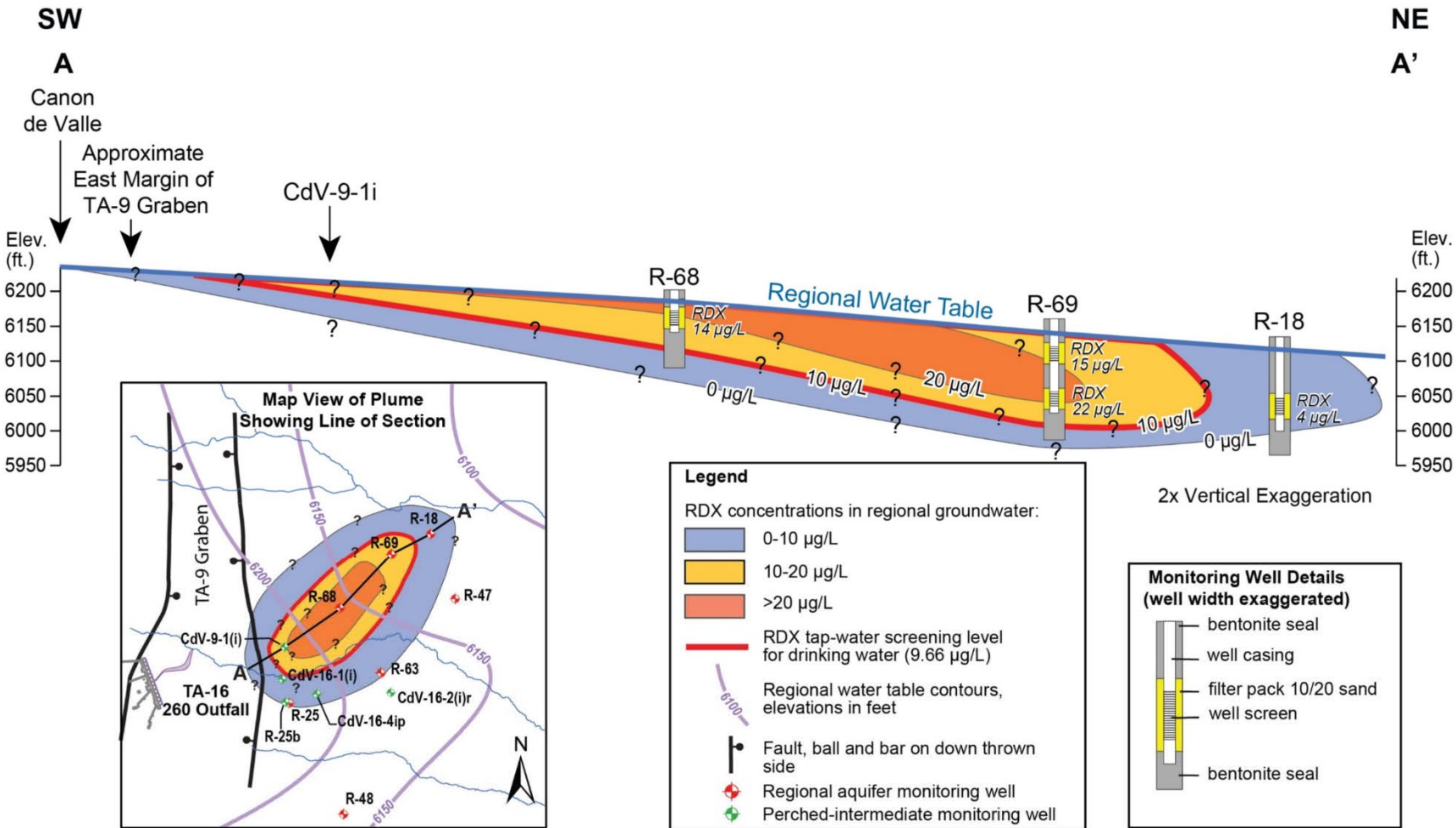
Figure D-1.3-4   Southwest to northeast cross-section of RDX concentrations in the regional aquifer
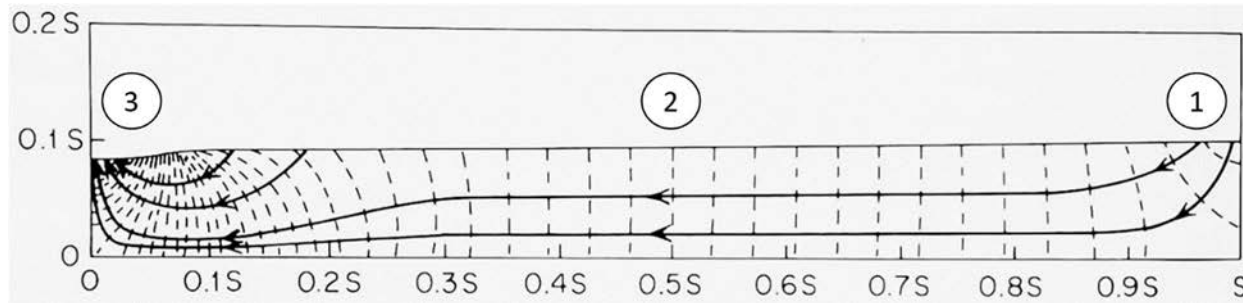
Figure D-2.1-1 The basic concepts of aquifer hydraulic head distributions in a site with upland recharge and lowland discharge to a river are shown. This example is a mirror image of the Pajarito Plateau, which has upland recharge to the west and lowland discharge to a river to the east.
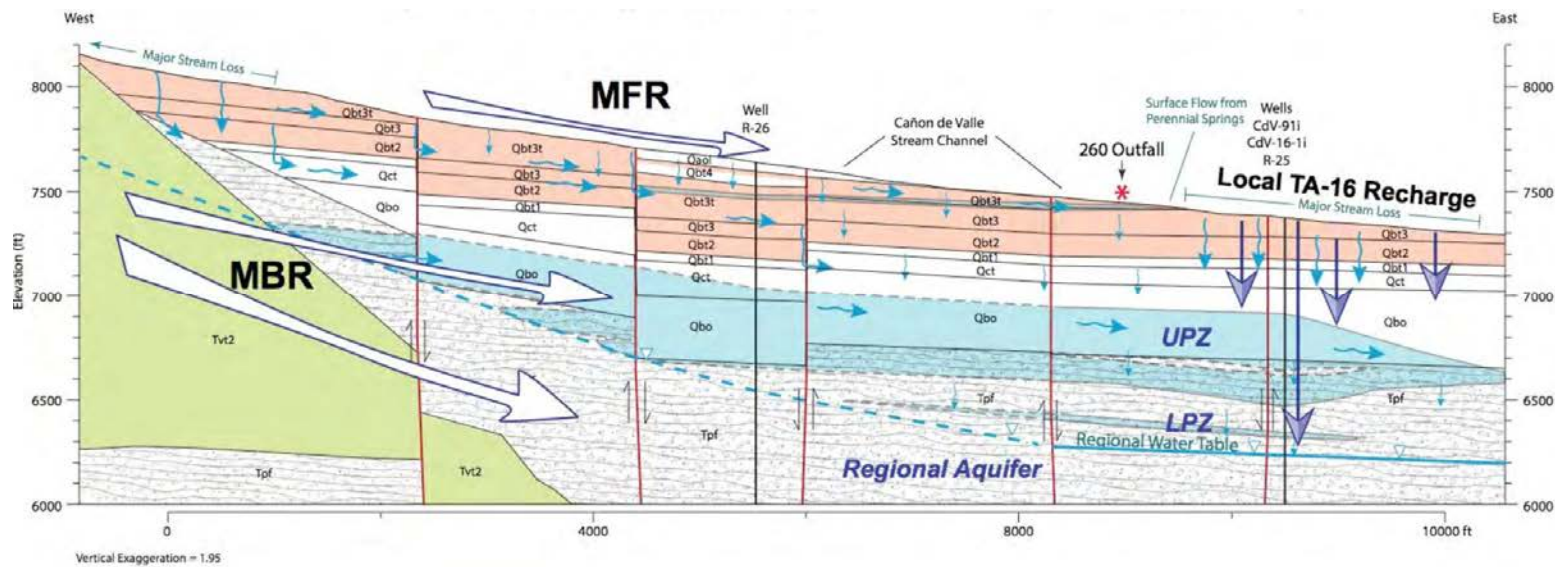
Figure D-2.1-2 Conceptual diagram of mountain block recharge (MBR) and mountain front recharge (MFR)
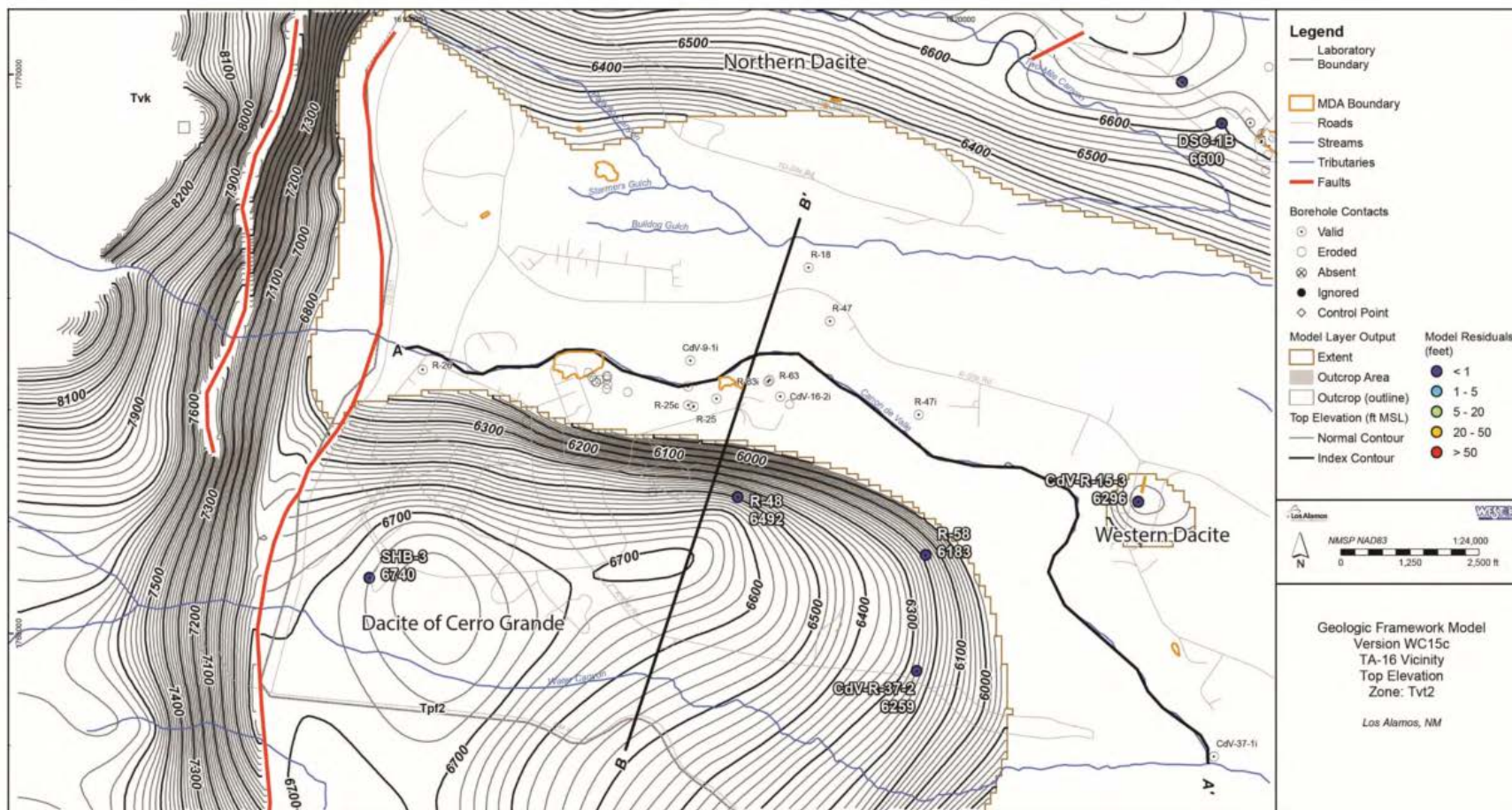
Figure D-2.1-3   Structural contour map of the Tschicoma Formation (Tvt 2), also known as the dacite of Cerro Grande
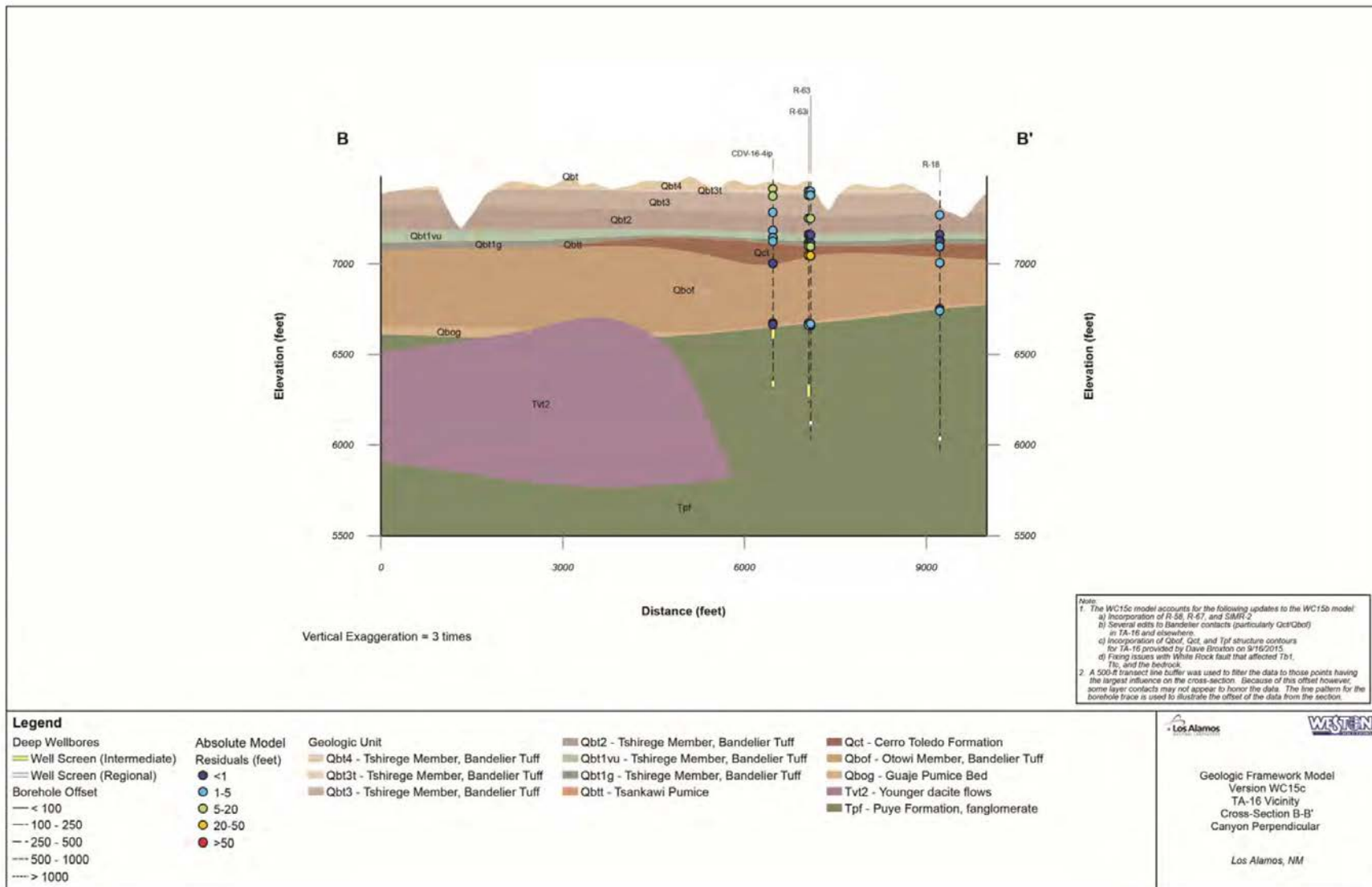
Figure D-2.1-4   Cross-section B-B' in Figure D-2.1-3
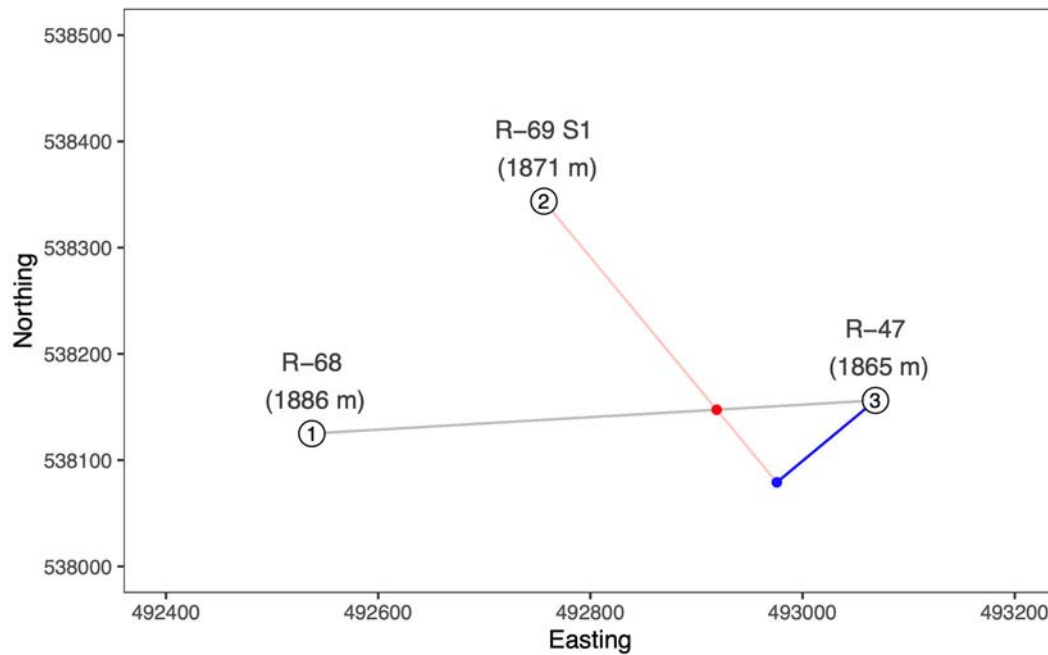
Figure D-2.2-1 **Diagram of gradient computation for wells R-68, R-69 screen 1 (S1), and R-47. Lines referenced in steps 3 and 4 are plotted in red and blue, respectively.**
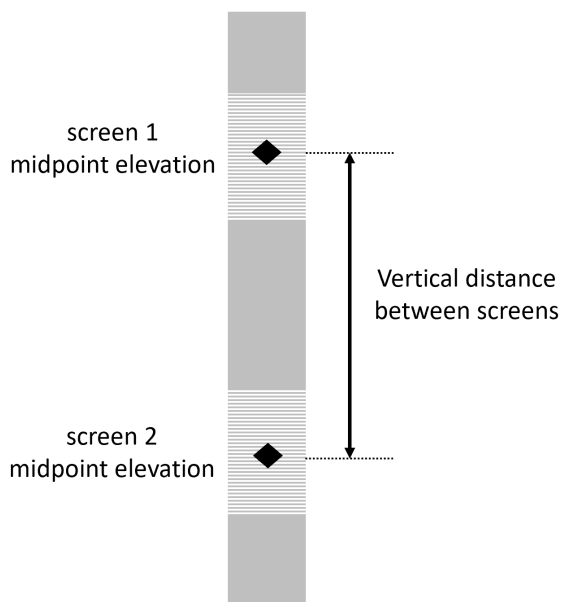
Figure D-2.2-2 **The vertical distance between pairs of screens in a single well is calculated as the distance between the midpoint elevation of the screened interval**
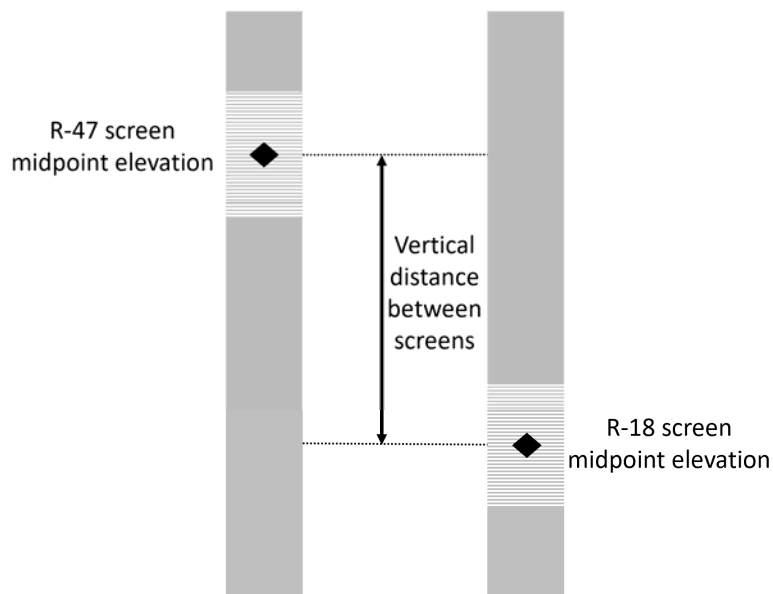
Figure D-2.2-3   The vertical distance between screens in two single completion wells is calculated as the distance between the midpoint elevation of the screened intervals
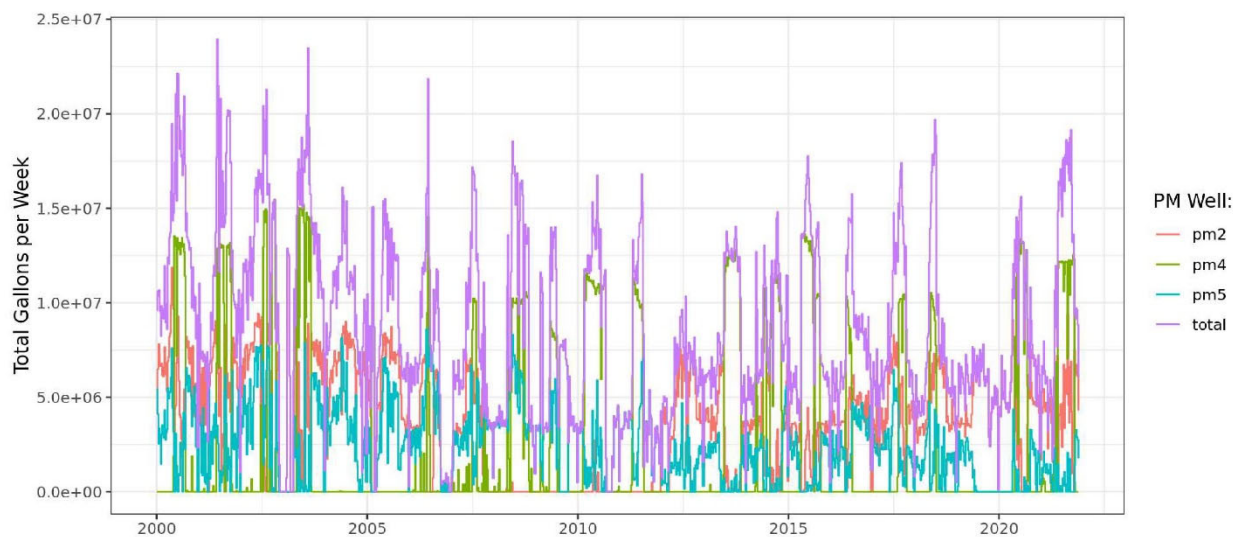
Figure D-2.2-4   Total gallons pumped per week from 2000 through 2022 for supply wells PM-2, PM-4, PM-5, and their sum

Average monthly water levels in regional aquifer water table wells
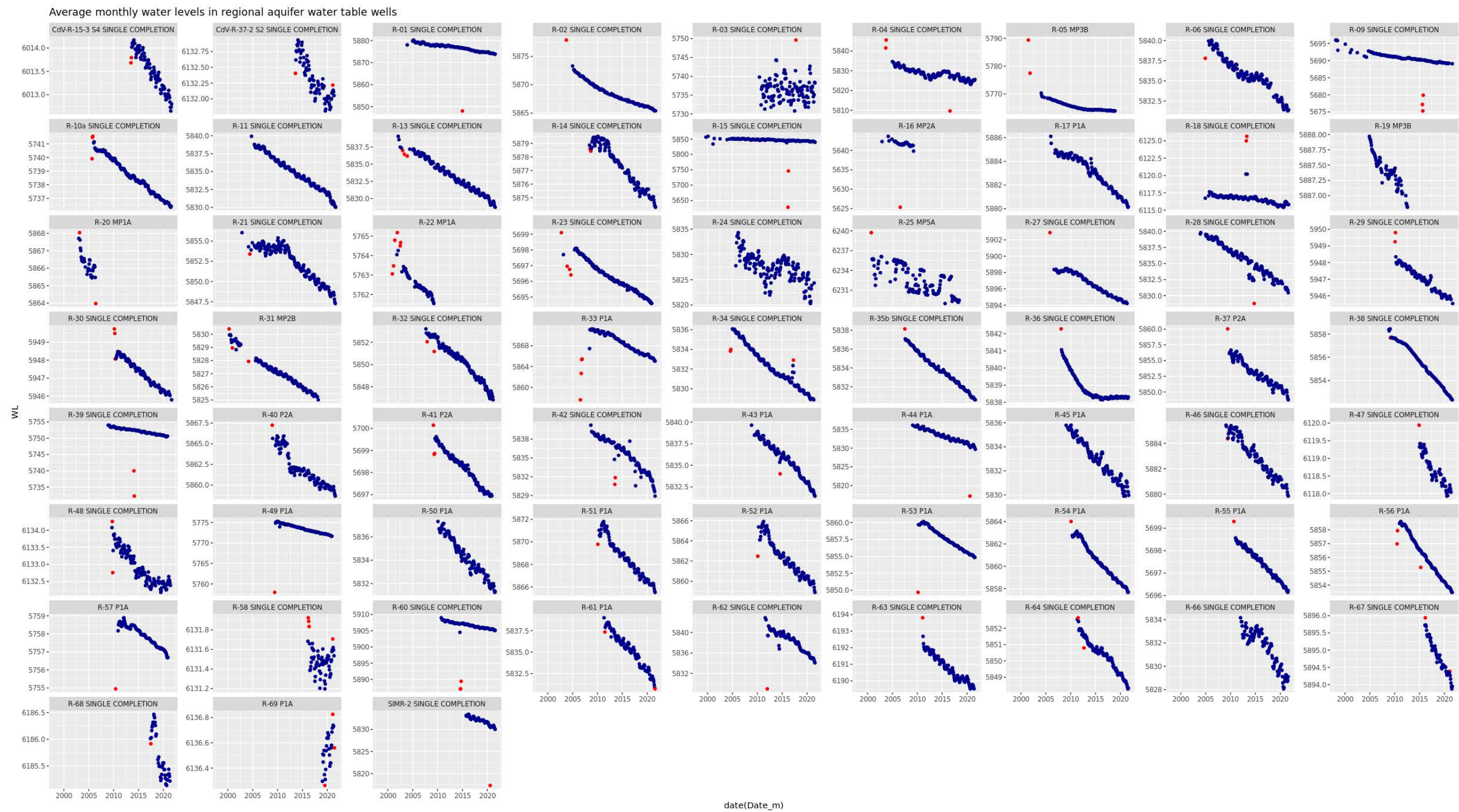
Figure D-2.3-1   Time series plots of monthly average water levels for regional aquifer water table screens
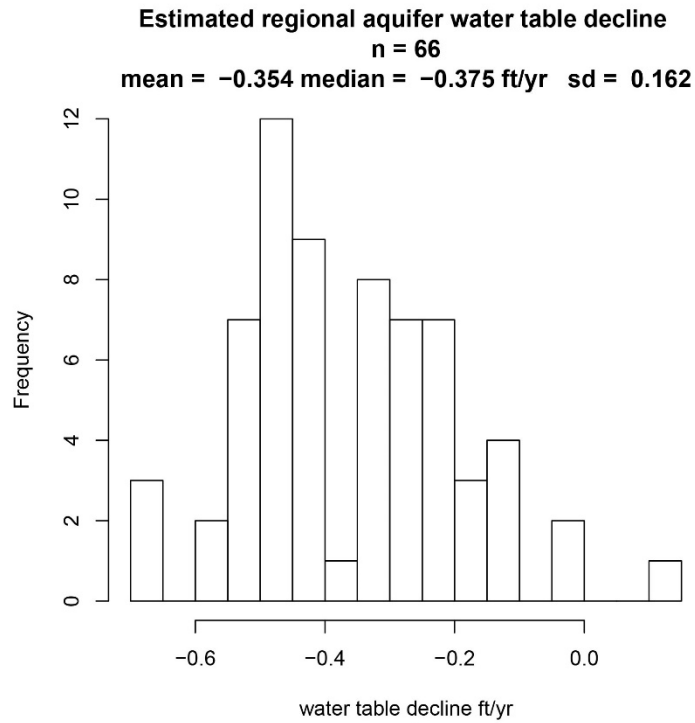
Figure D-2.3-2   Histrogram of estimated linear rates of change for regional aquifer water table screens
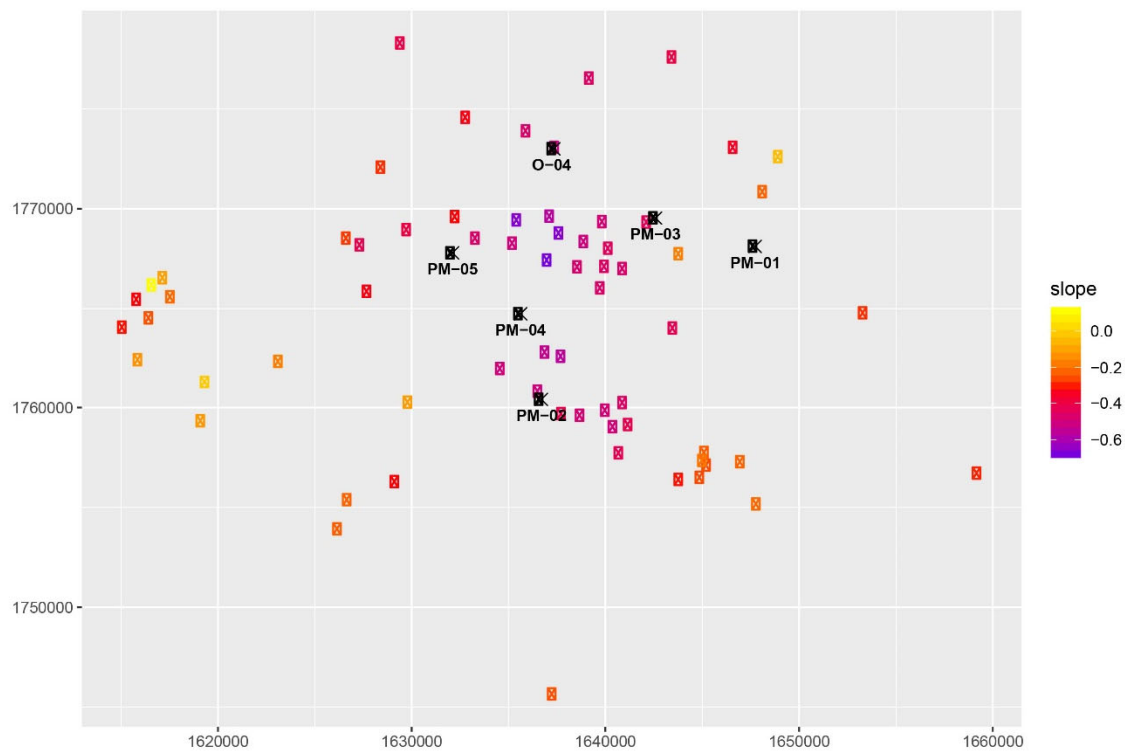
Figure D-2.3-3   Spatial plot of estimated linear rates of change for regional aquifer water table screens
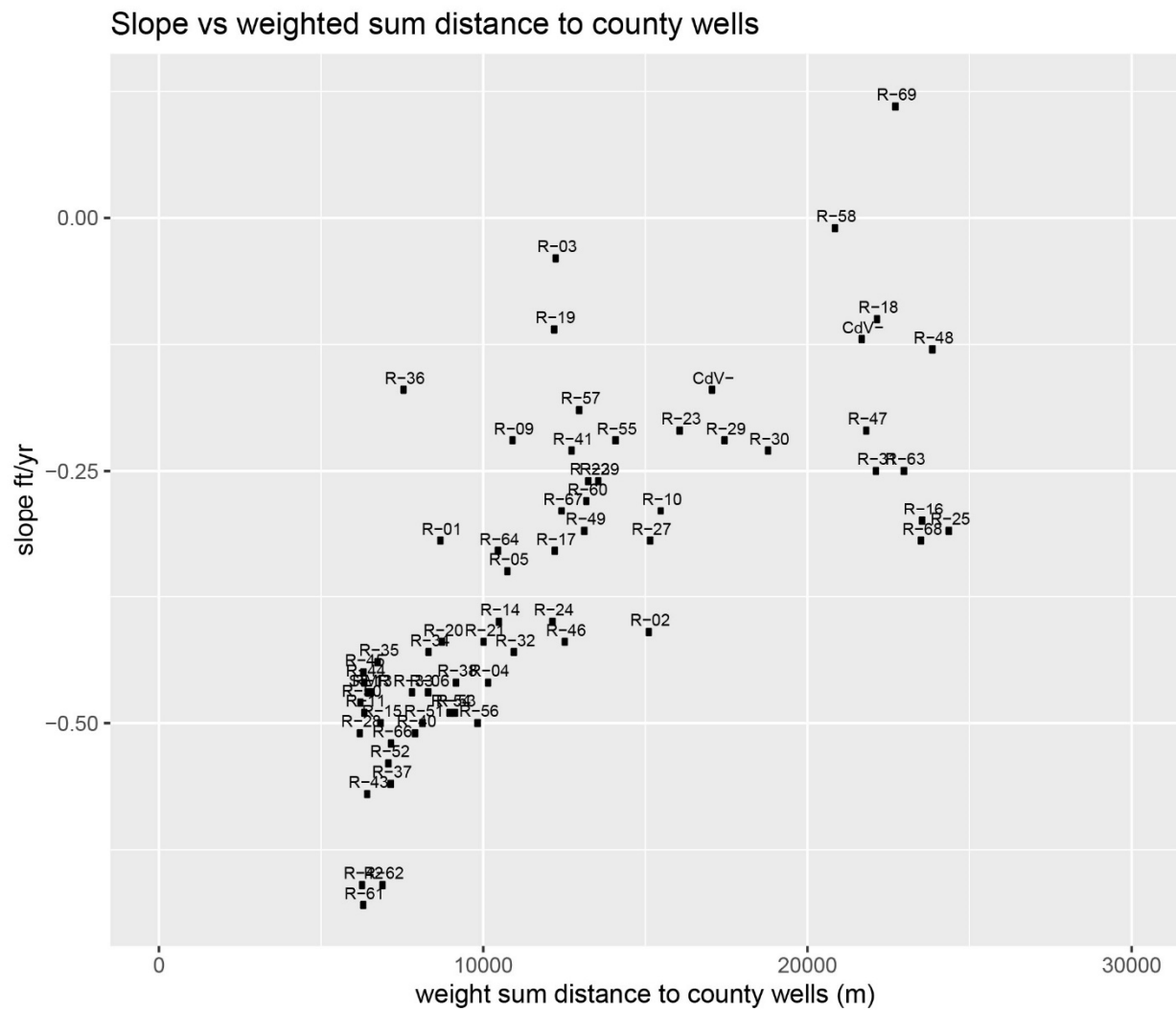
Figure D-2.3-4   Estimated slope (ft/yr) versus weight sum distance to county wells (m)
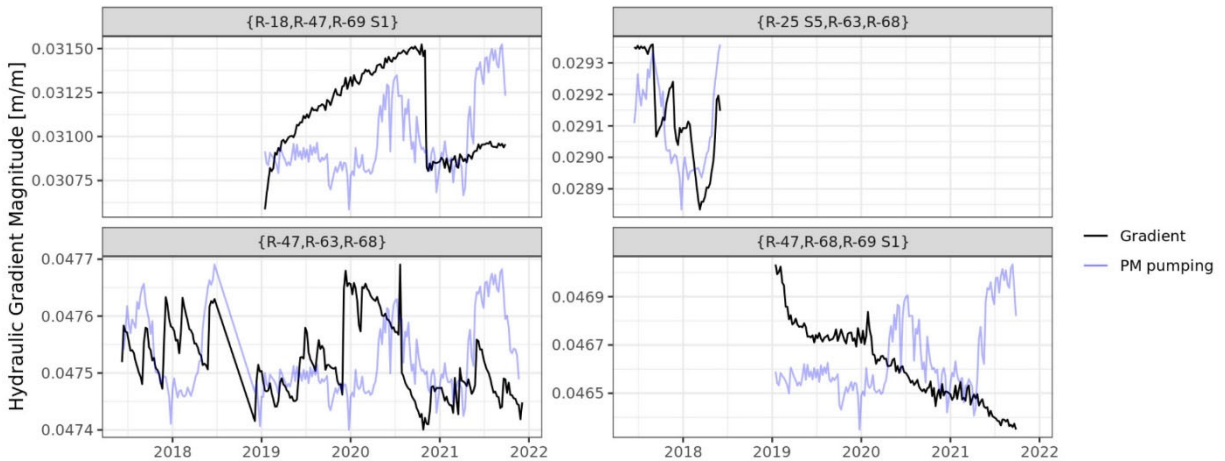
Figure D-2.3-5   Gradient magnitude through time and PM well pumping
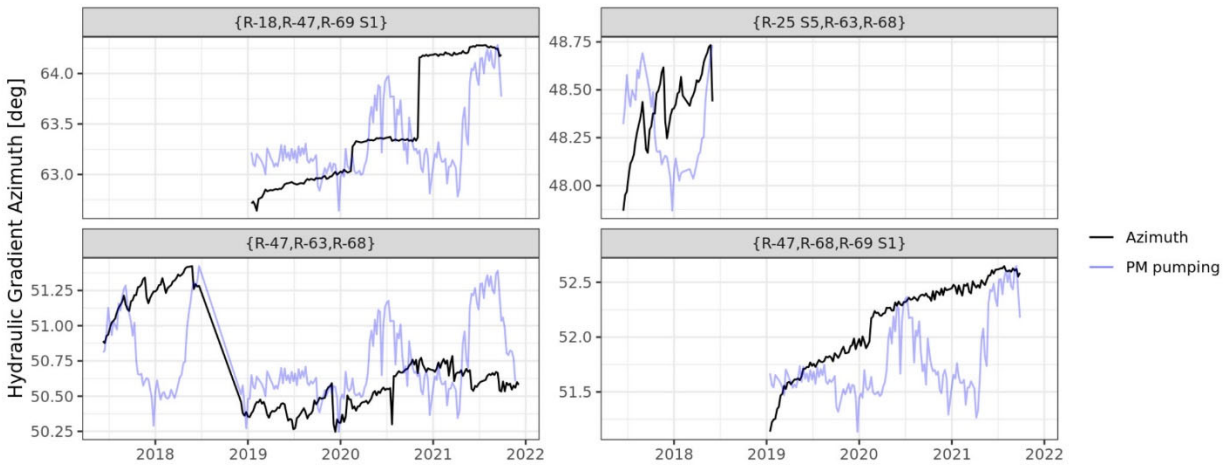
Figure D-2.3-6   Gradient azimuth through time and PM well pumping
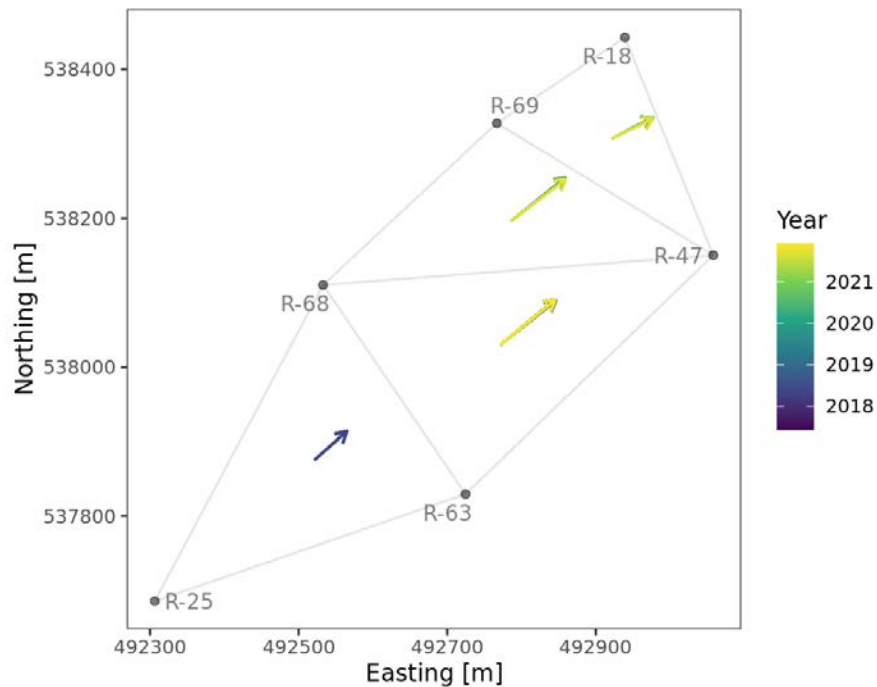
Figure D-2.3-7   Computed hydraulic gradients for RRM target triplets over time
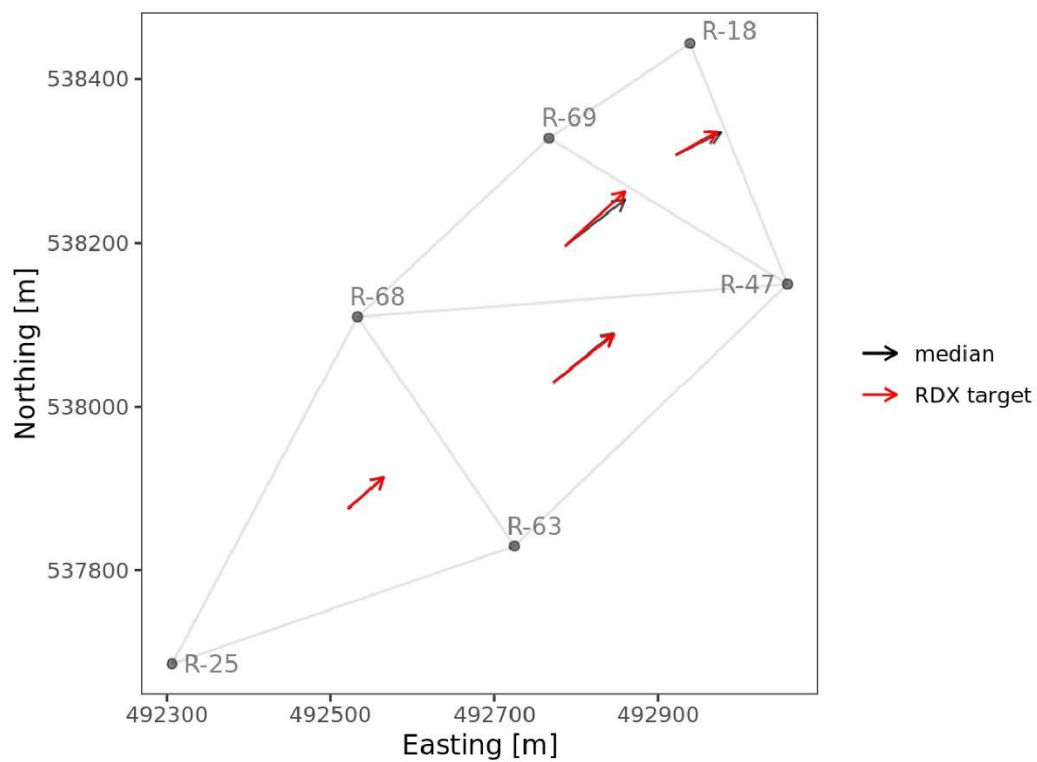
Figure D-2.3-8   Median computed hydraulic gradient for RRM target triplets compared with model targets
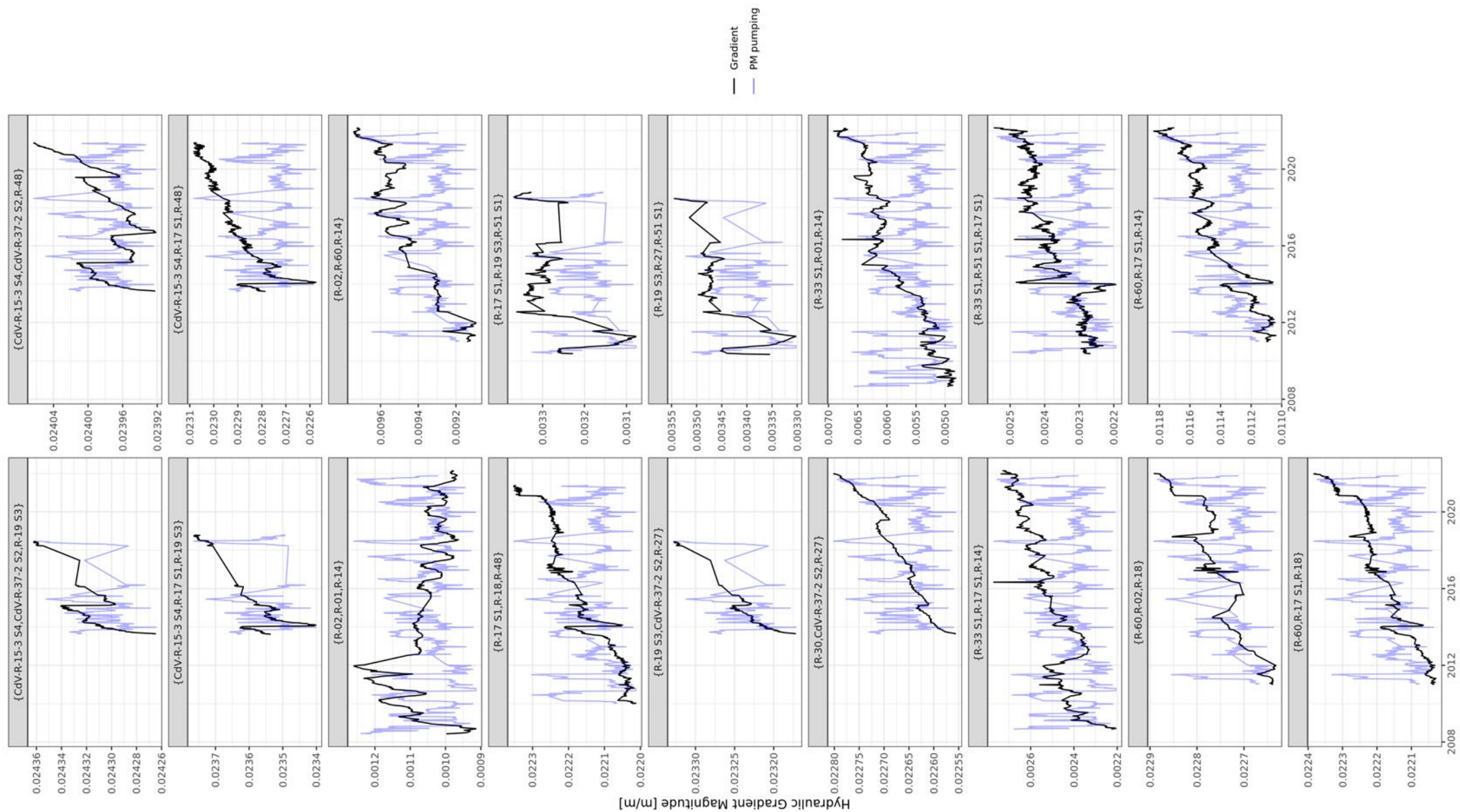
Figure D-2.3-9   Gradient magnitude through time and PM well pumping (PM-2 + PM-4 + PM-5) for water table well screen triplets
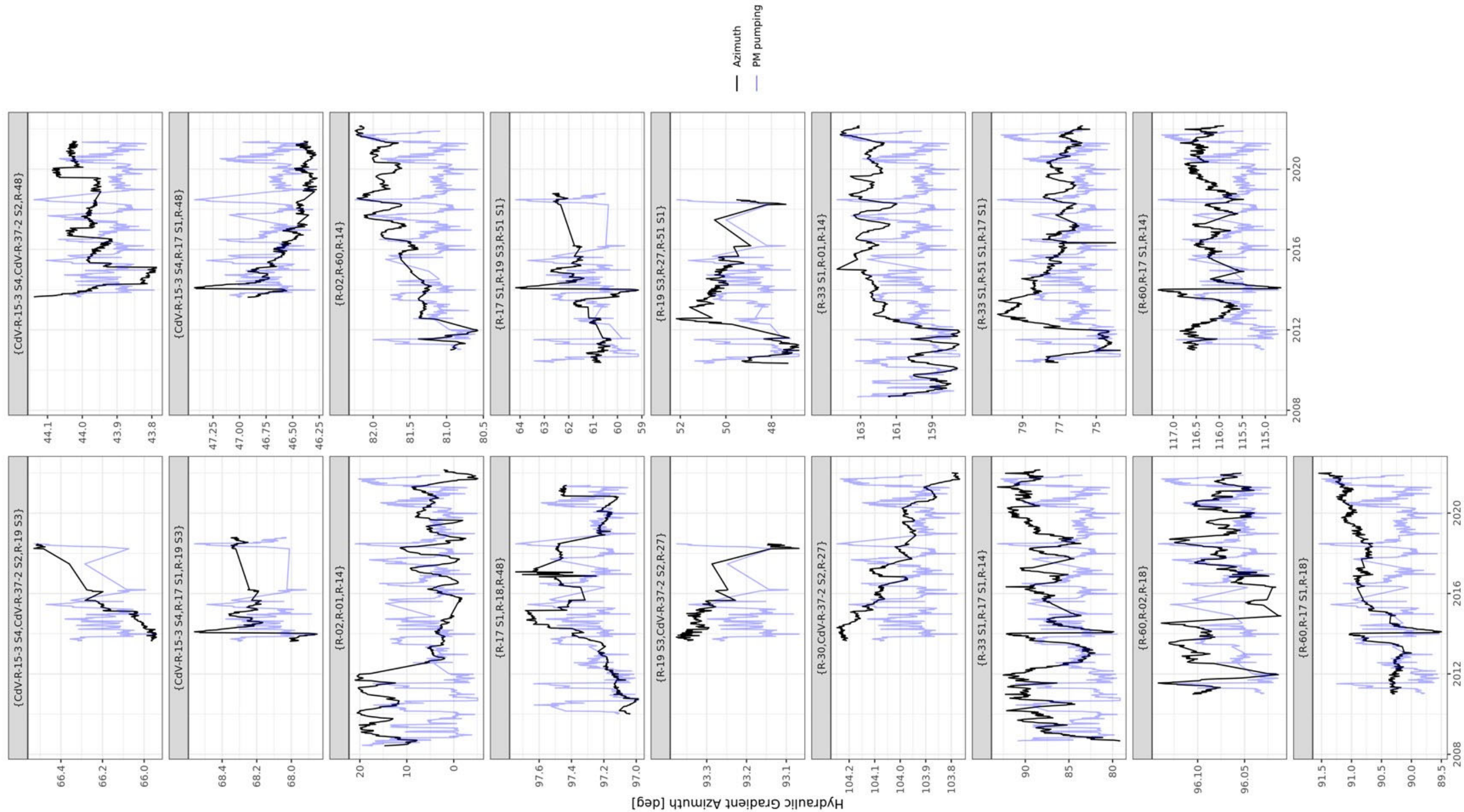
Figure D-2.3-10   Gradient azimuth through time for water table well screen triplets
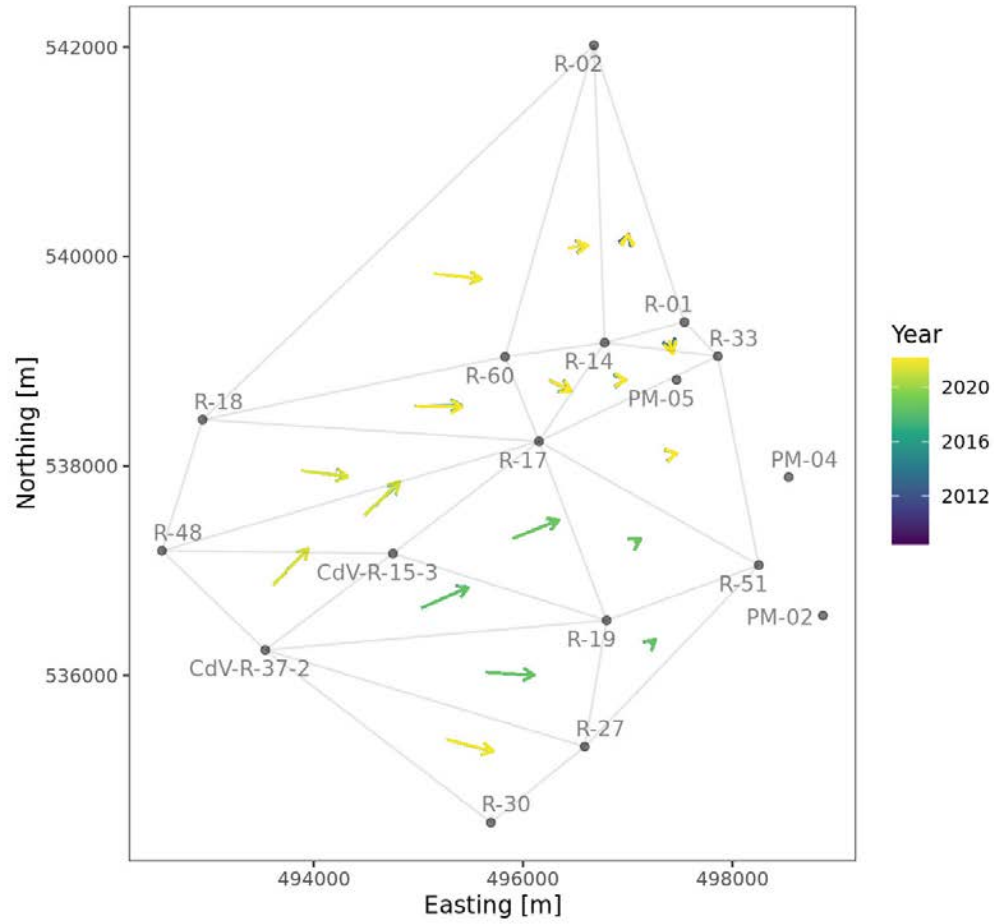
Figure D-2.3-11   Computed hydraulic gradients for water table triplets
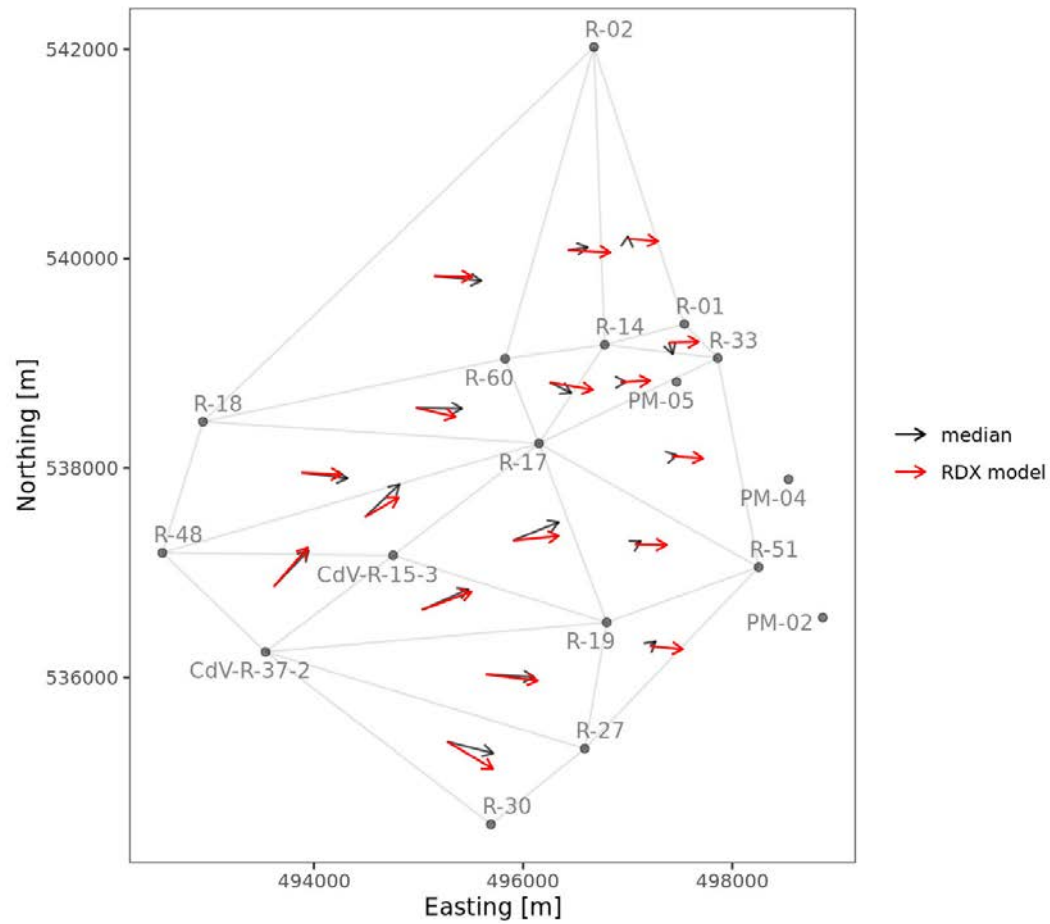
Figure D-2.3-12   Median computed hydraulic gradient for water table triplets compared with modeled gradients
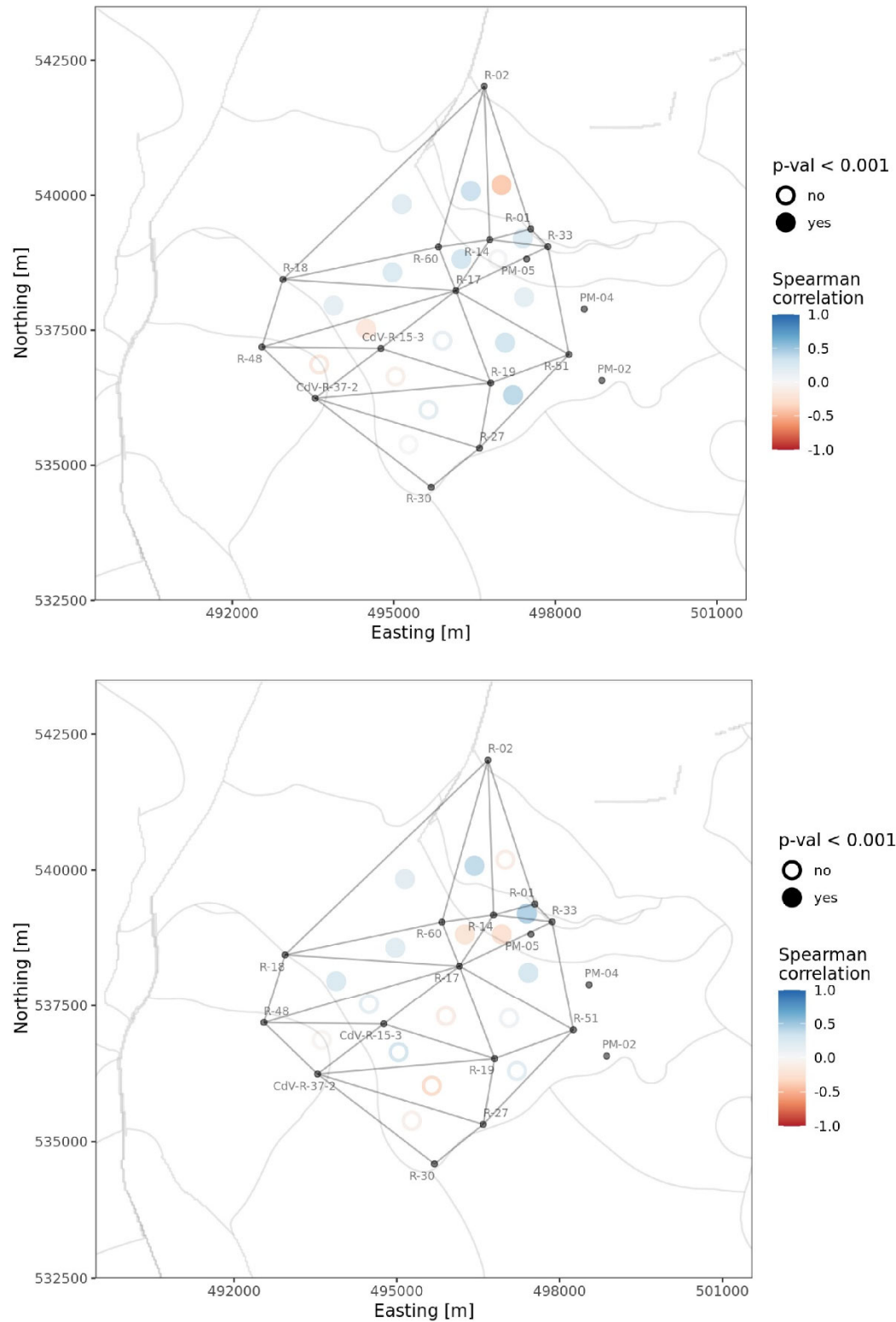
Figure D-2.3-13   Correlation results for gradient magnitude and total PM well pumping (above) and gradient azimuth and total PM well pumping (below) for water table triplets
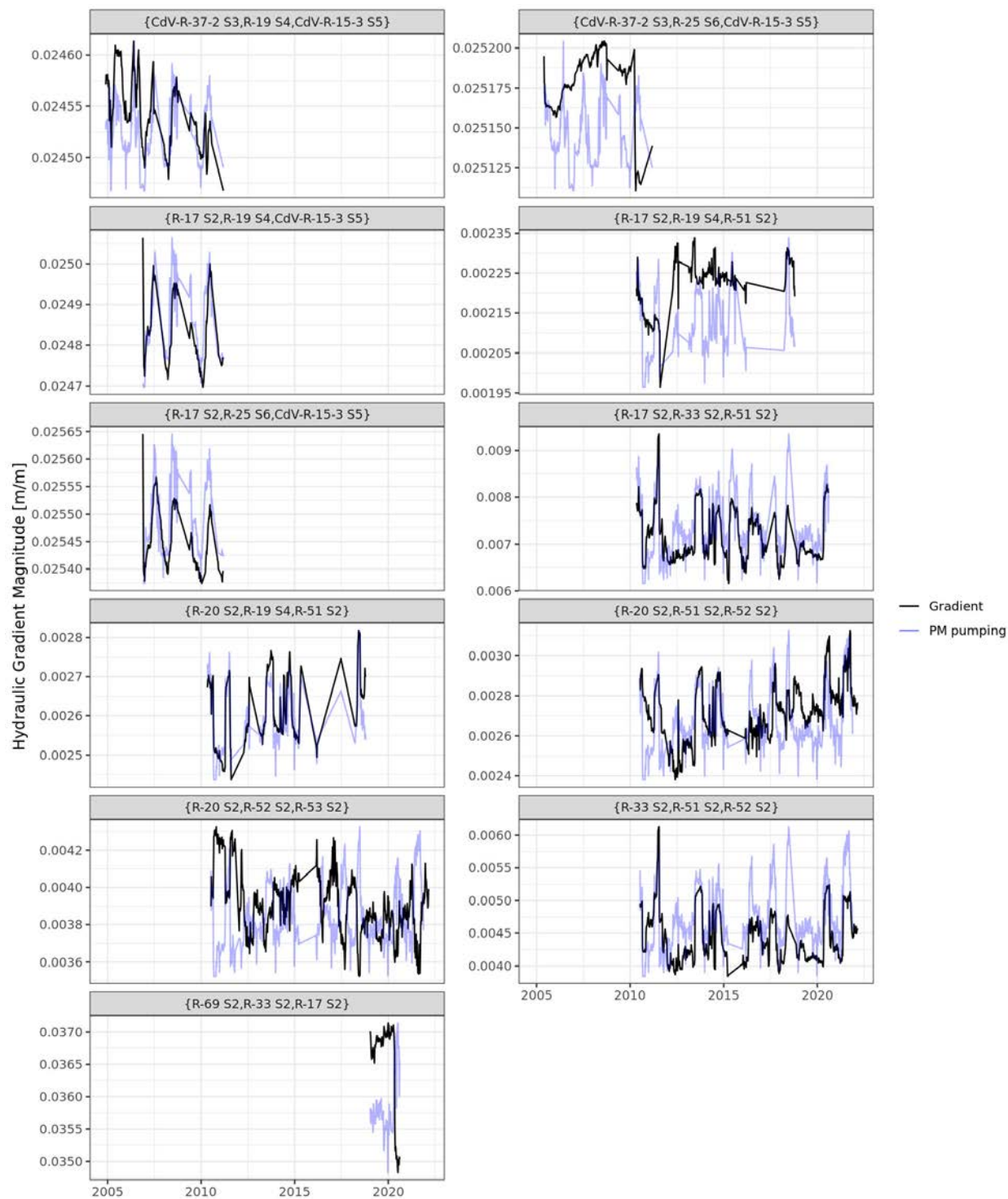
Figure D-2.3-14 **Gradient magnitude through time and PM well pumping (PM-2 + PM-4 + PM-5) for mid-depth well screen triplets**
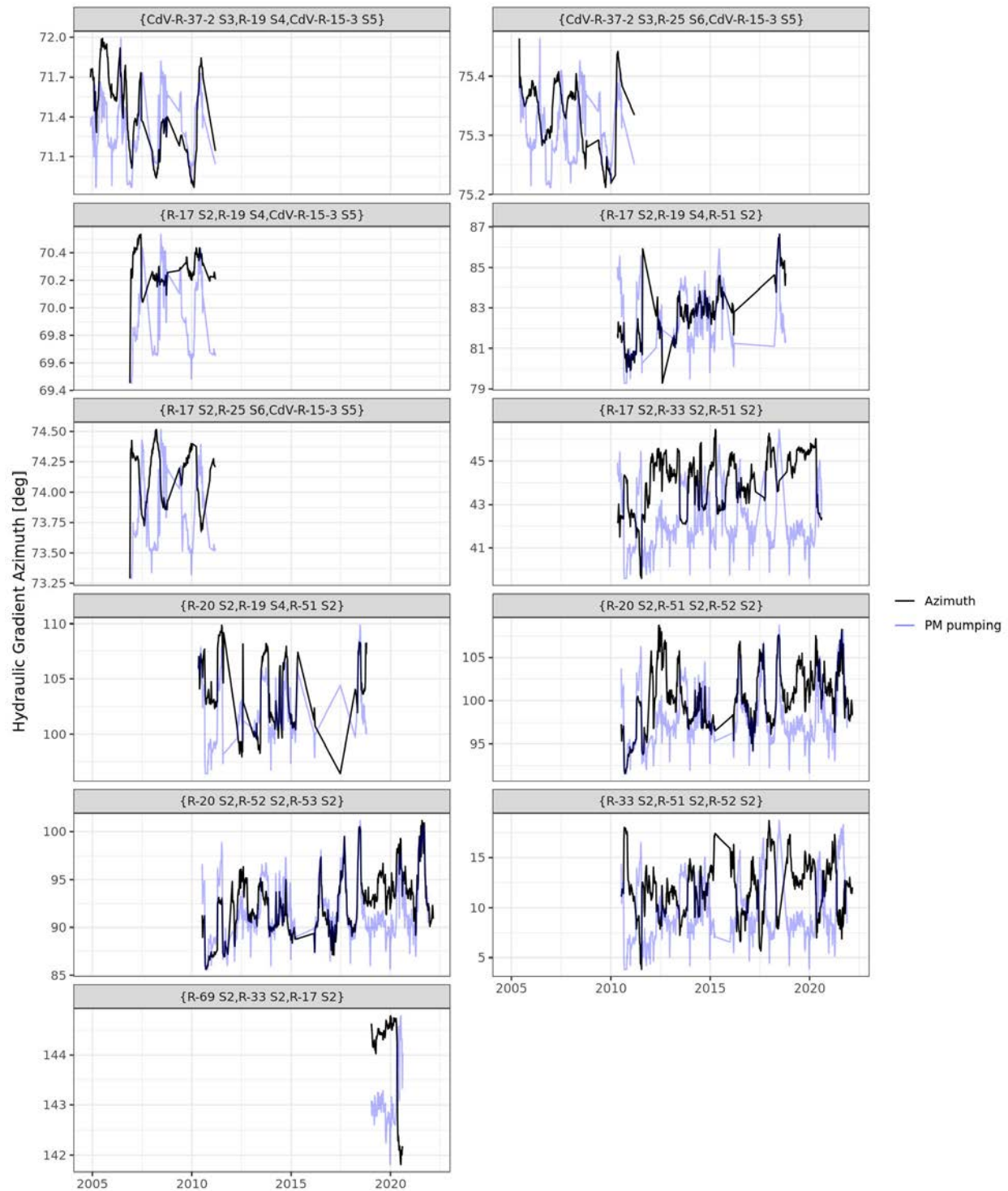
Figure D-2.3-15 **Gradient azimuth through time and PM well pumping (PM-2 + PM-4 + PM-5) for mid-depth well screen triplets**
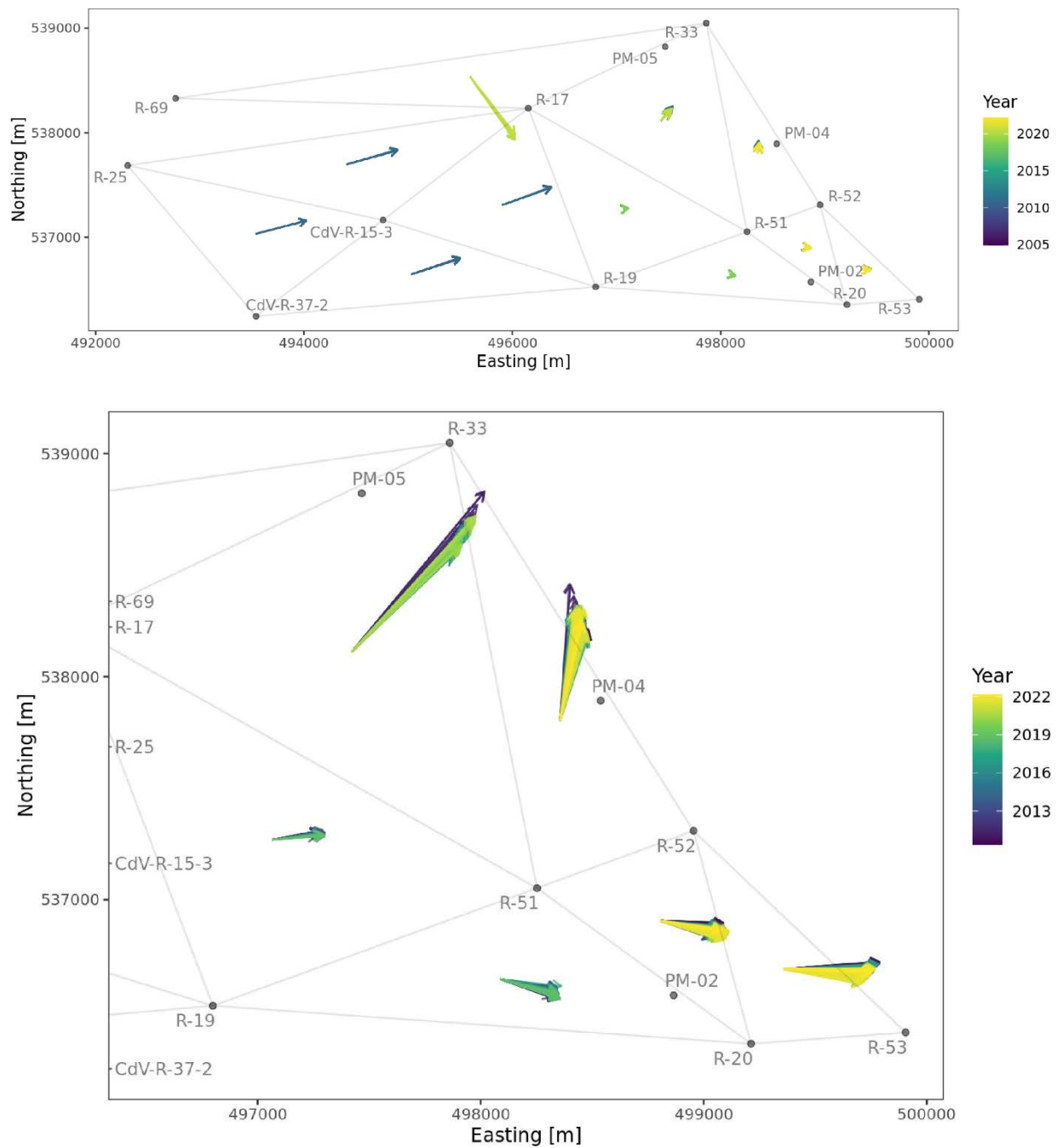
Figure D-2.3-16   Computed hydraulic gradients for mid-depth triplets
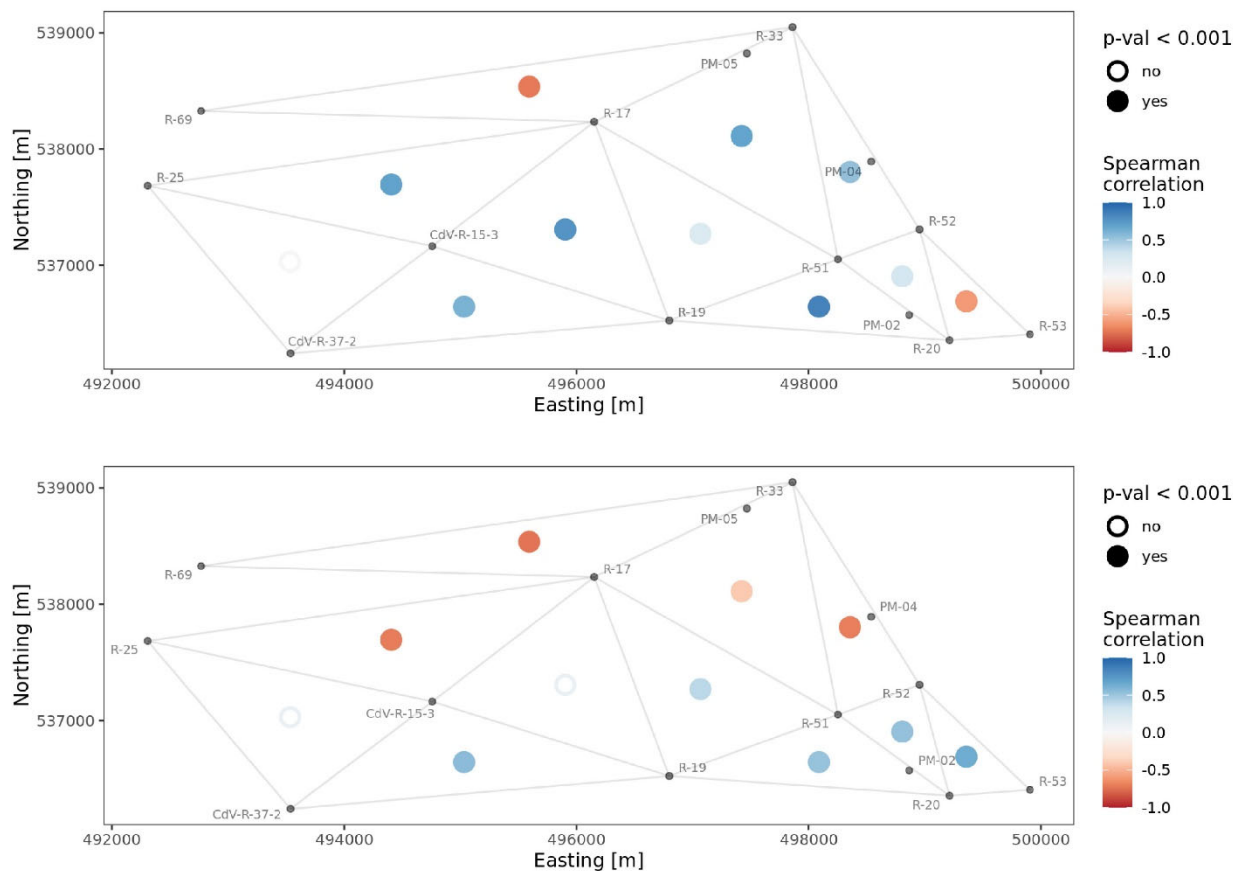
Figure D-2.3-17   Correlation results for gradient magnitude and total PM well pumping (above) and gradient azimuth and total PM well pumping (below) for mid-depth triplets
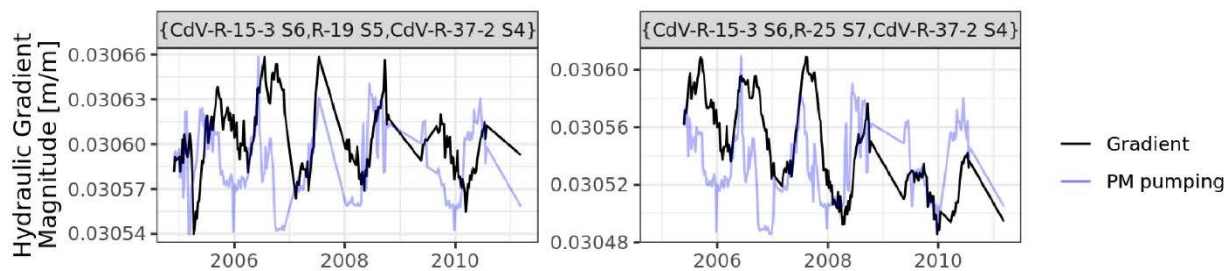
Figure D-2.3-18   Gradient magnitude through time and PM well pumping (PM-2 + PM-4 + PM-5) for deep well screen triplets
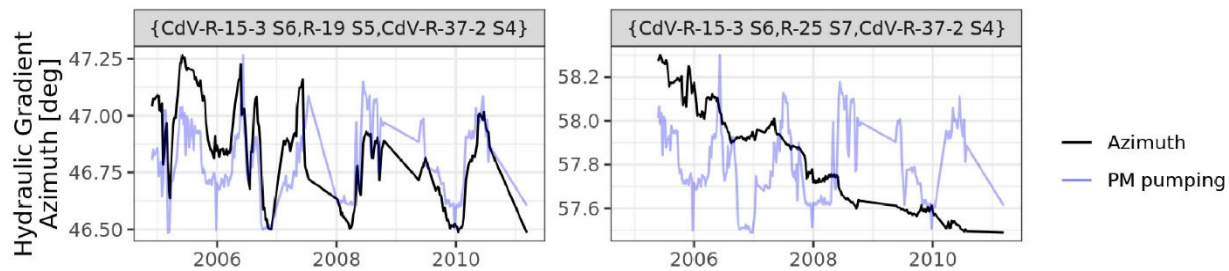
Figure D-2.3-19   Gradient azimuth through time and PM well pumping (PM-2 + PM-4 + PM-5) for deep well screen triplets
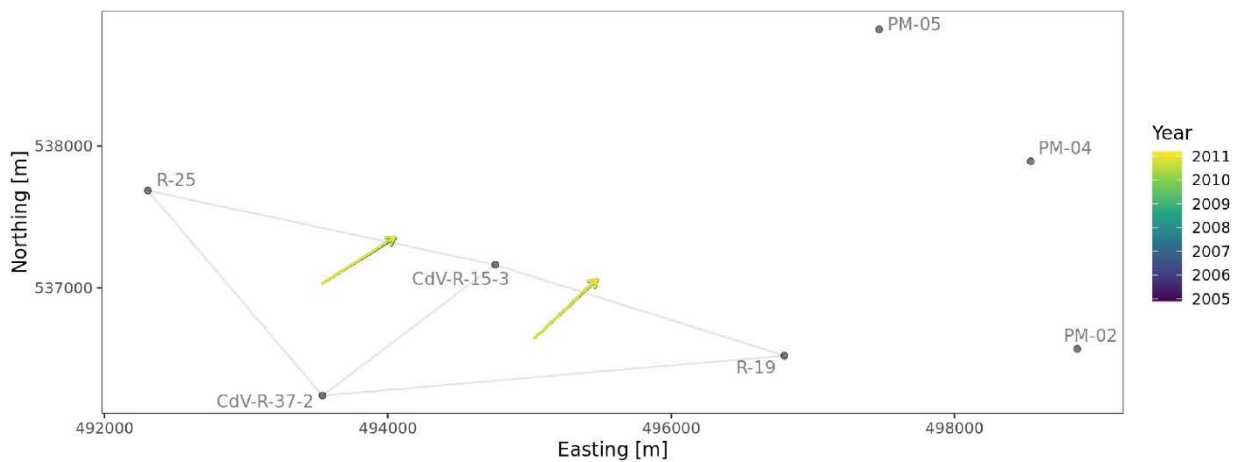
Figure D-2.3-20   Computed hydraulic gradients for deep triplets
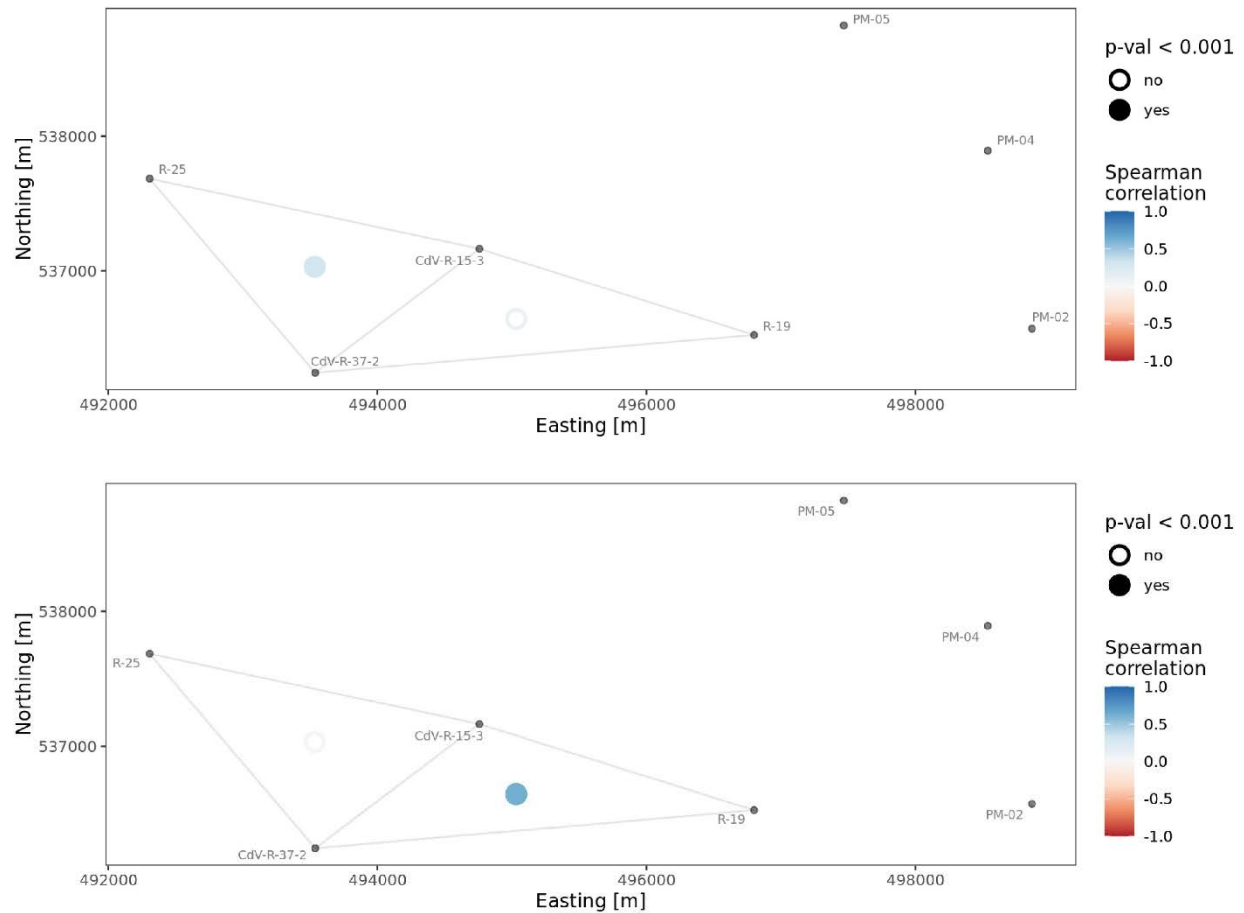
Figure D-2.3-21   Correlation results for gradient magnitude and total PM well pumping (above) and gradient azimuth and total PM well pumping (below) for deep triplets
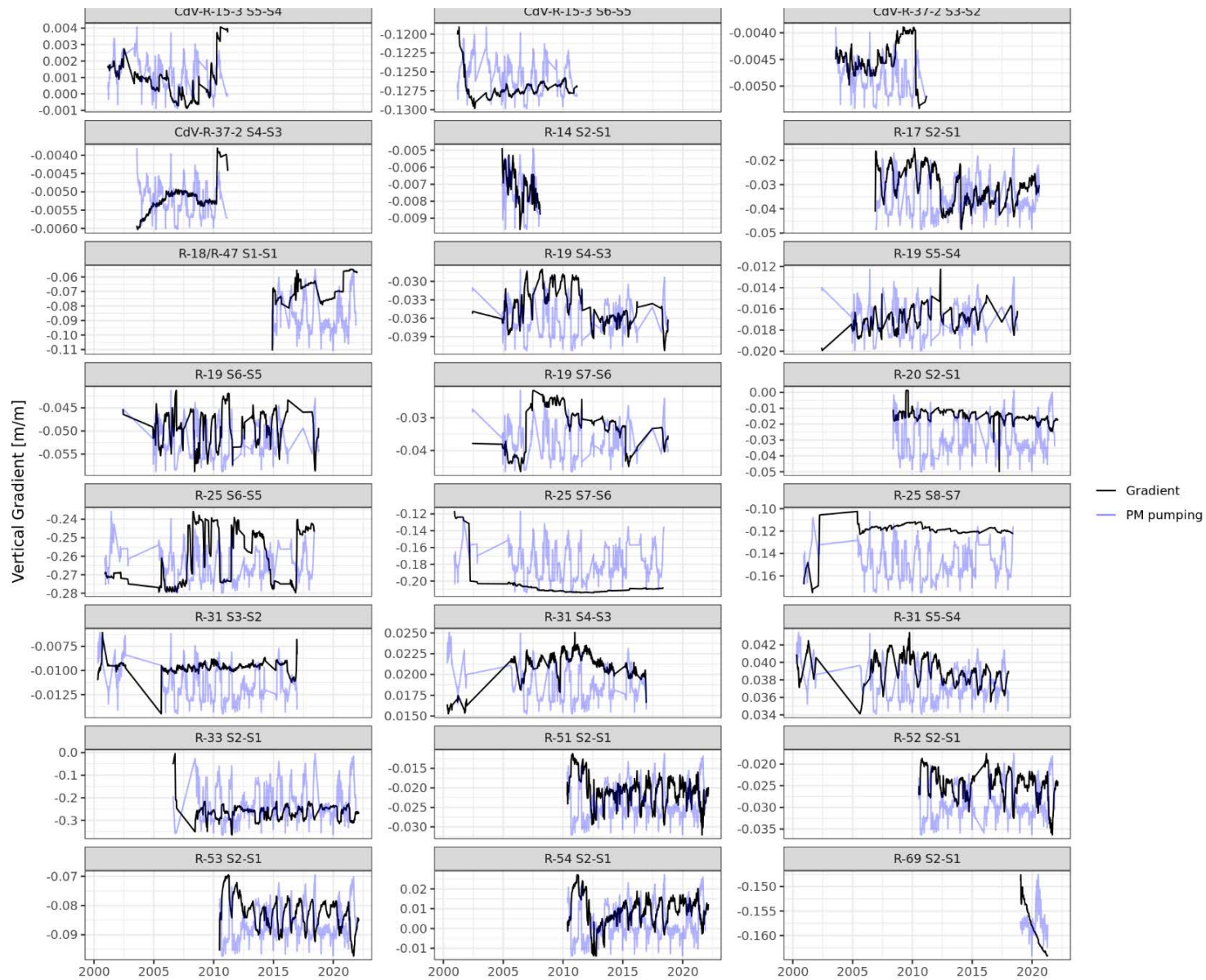
Figure D-2.3-22   Vertical gradient magnitude through time and PM well pumping (PM-2 + PM-4 + PM-5)
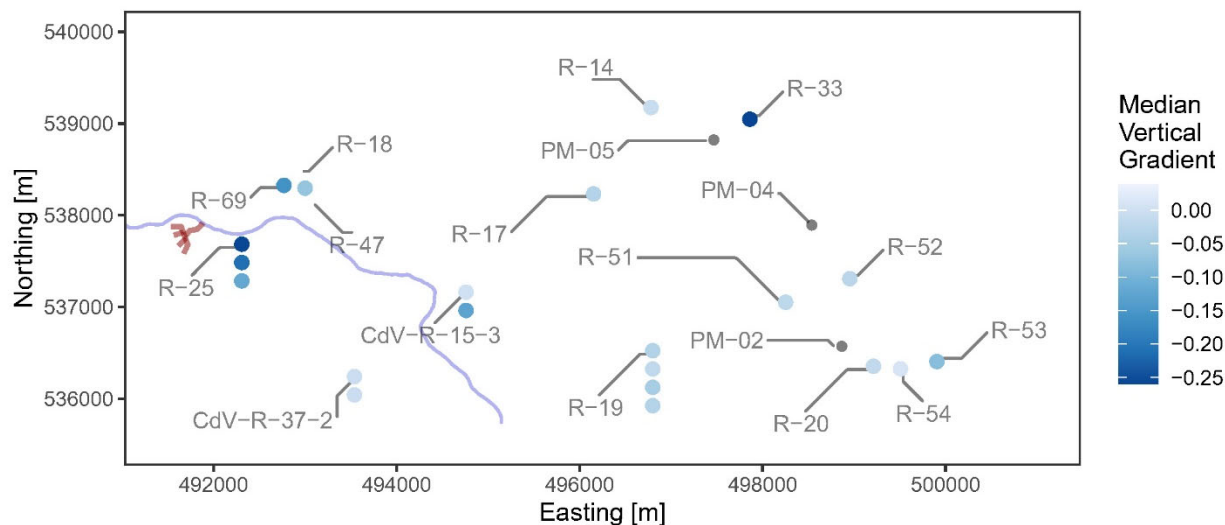
Figure D-2.3-23   Calculated median vertical gradient for wells in the RDX region. Upper portion of the plot shows cross-section of vertical gradients from west to east. The lower portion of the plot shows the vertical gradients spatially. Vertical dots represent the median-calculated vertical gradient between screens. The top dot corresponds to the highest-elevation screen pair, with dots below corresponding to screen pairs deeper in the aquifer at lower elevations.
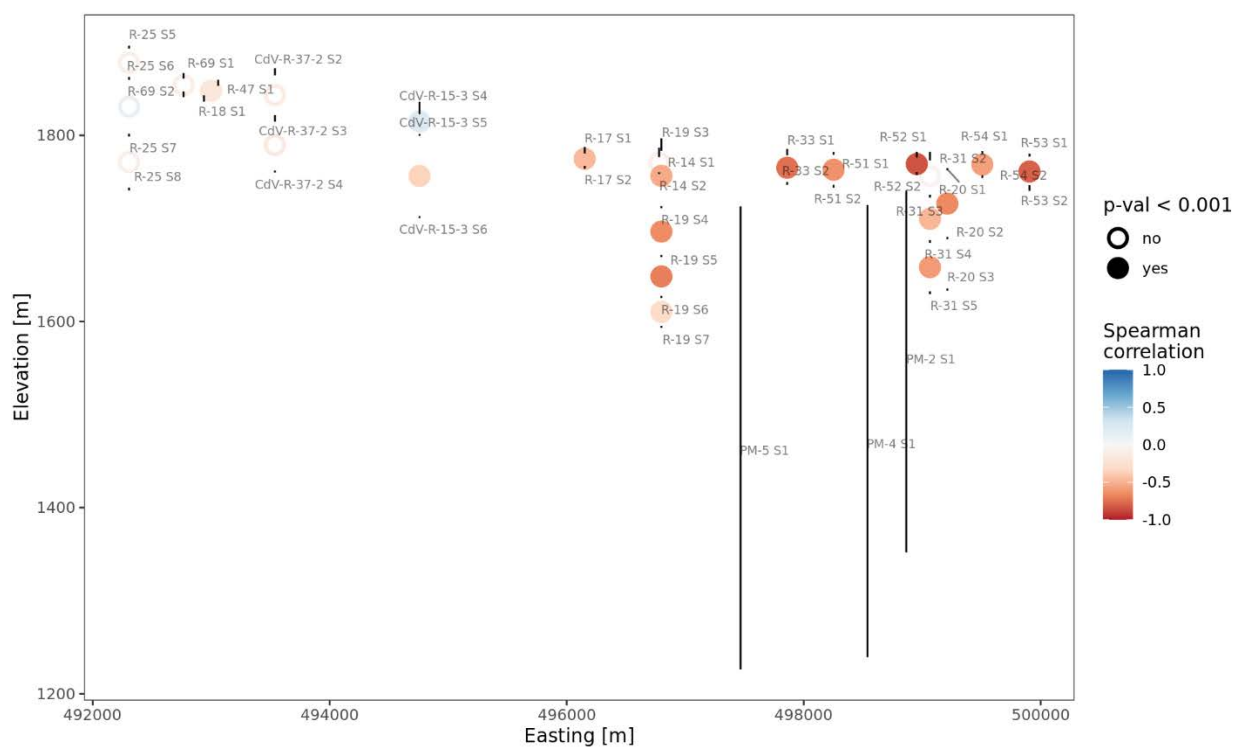
Figure D-2.3-24   Correlation between vertical gradients and total (PM-2 + PM-4 + PM-5) supply well pumping
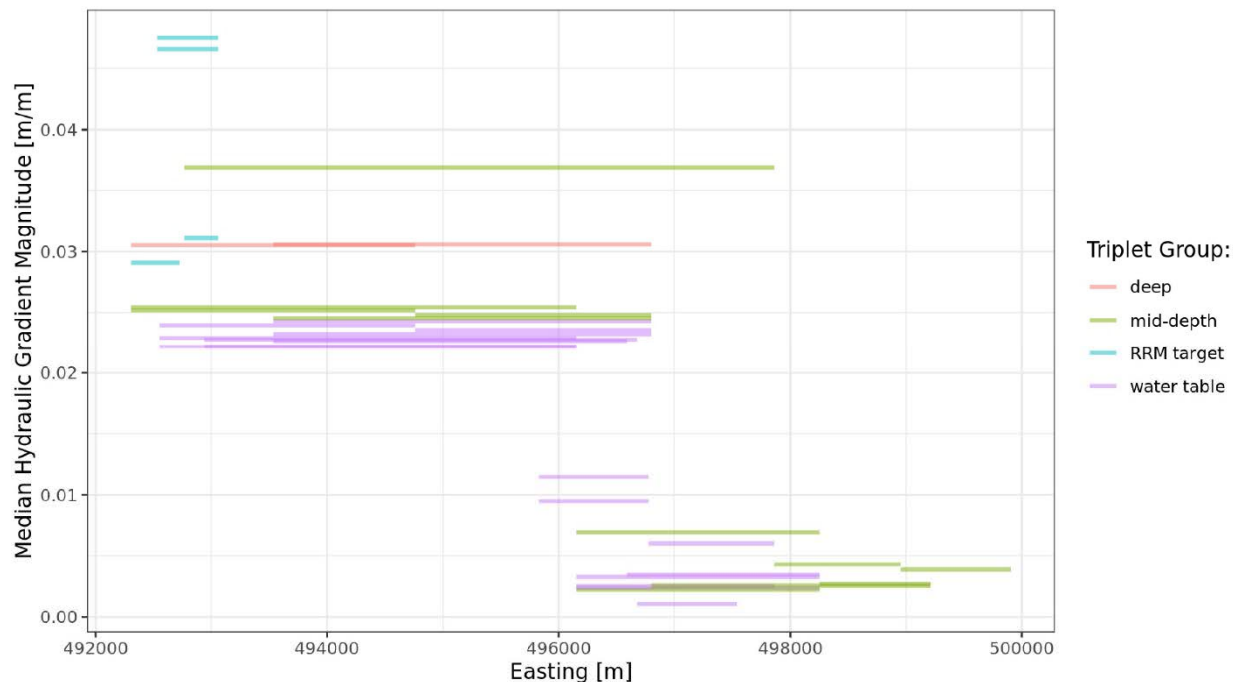
Figure D-2.4-1   **Median-computed hydraulic gradient for each water table triplet (RRM targets are included in the water table category), shown as a line indicating the minimum and maximum easting of which the triplet spans**
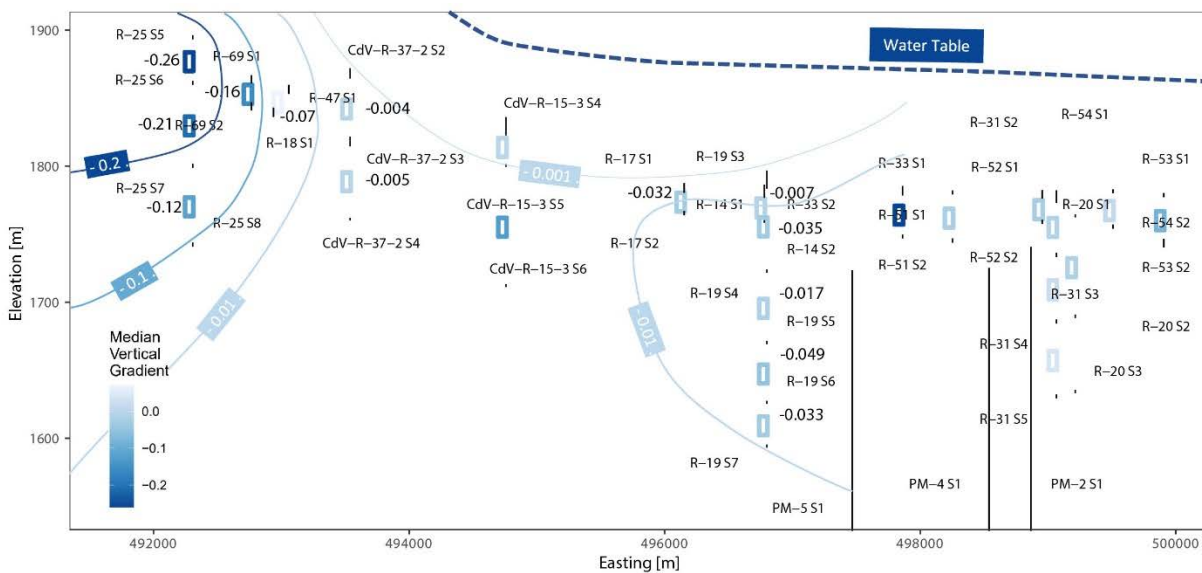
Figure D-2.4-2   **Cross-section view, from west to east, of the median-computed vertical gradient between vertical well screen pairs. Contour lines indicate strong vertical gradients are observed in the west and are about an order of magnitude higher than those in the east near to the supply wells.**
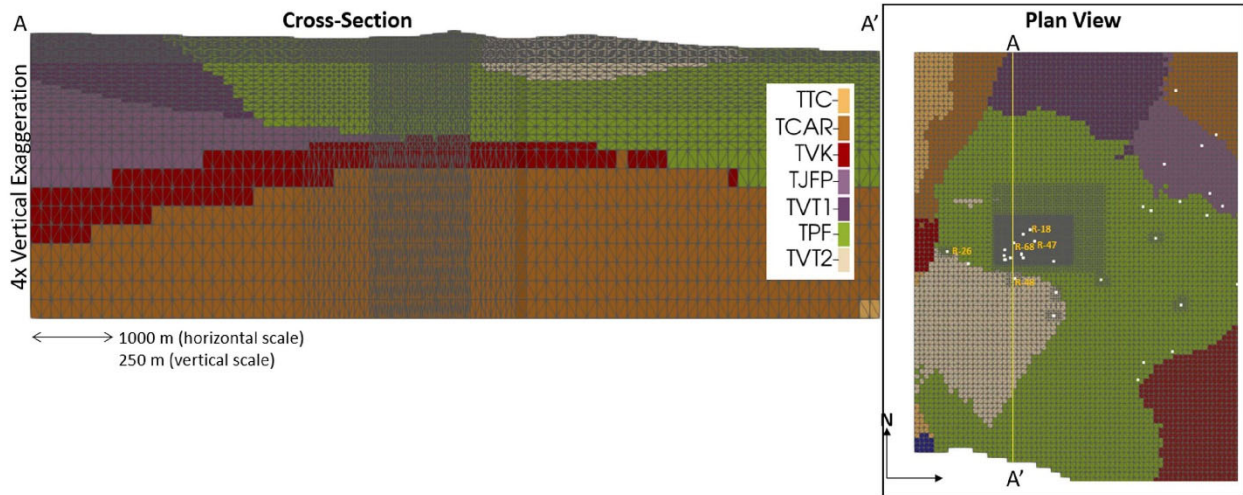
Figure D-3.0-1   Vertical mesh refinement along a cross-section A-A', as shown on inset plan view figure. Vertical exaggeration is 4× to show grid cell size.
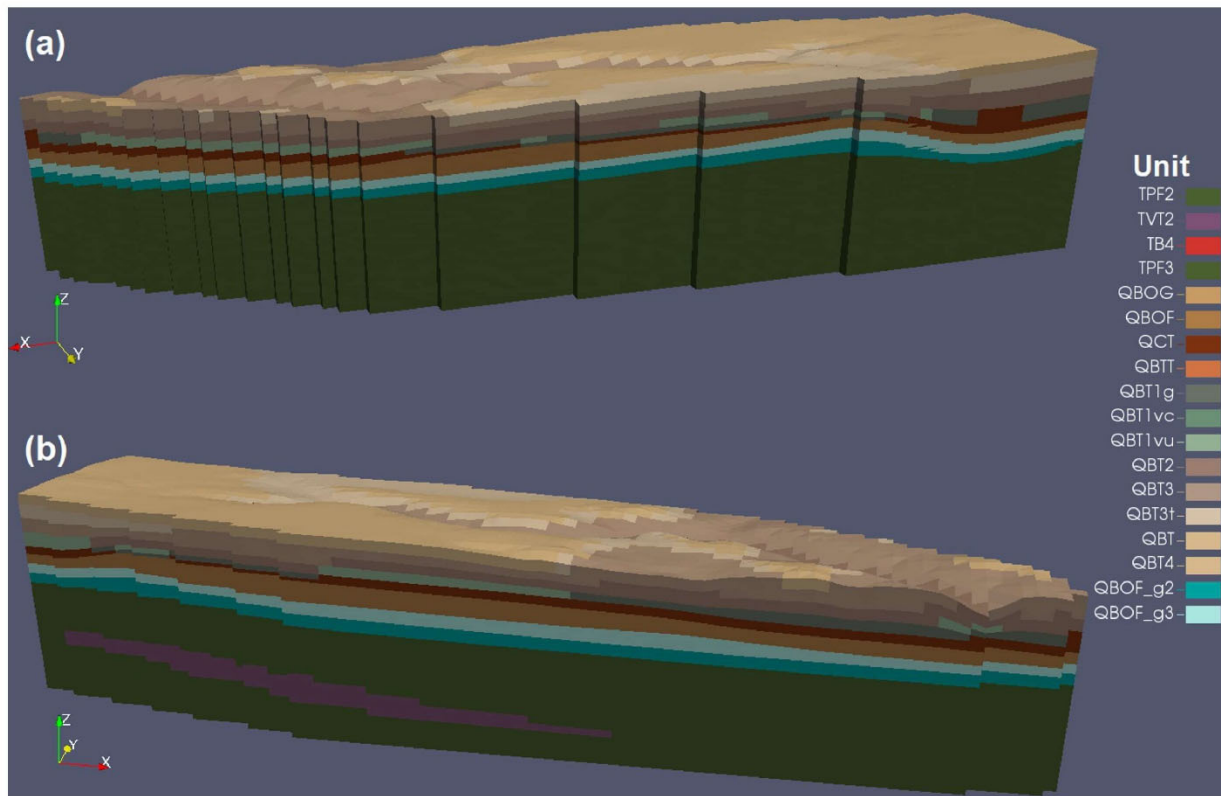
Figure D-3.2-1   RDX vadose zone (VZ)/ saturated zone (SZ) domain and geology, facing (a) the model's northern boundary and (b) the southern boundary
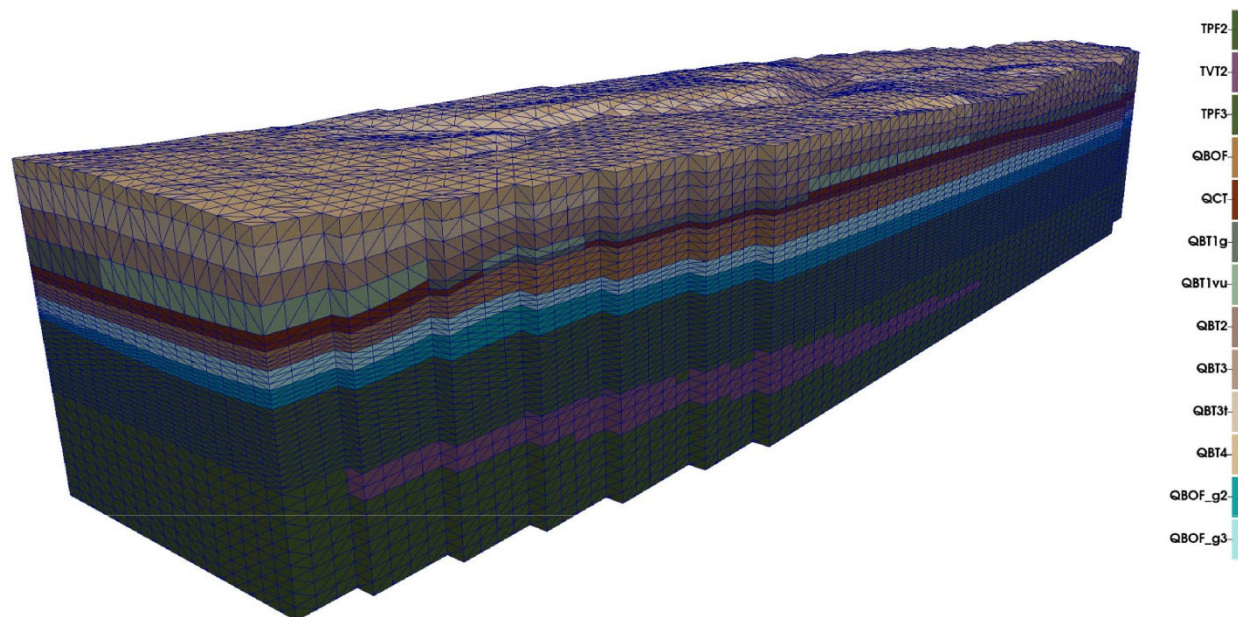
Figure D-3.2-2   RVZM mesh generated by LaGriT and plotted over the geologic framework model
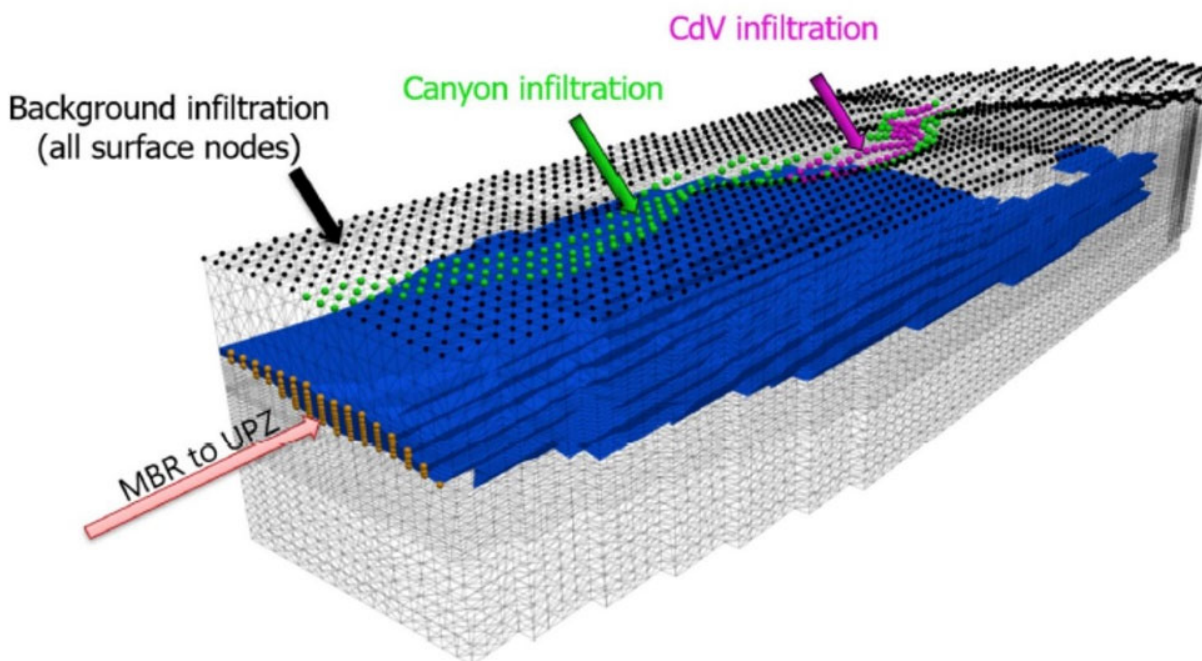
Note: MBR is mountain-block recharge. UPZ is upper perched zone, which is a saturated zone.

Figure D-3.2-3   Variable locations of infiltration in the VZ model of the RDX site
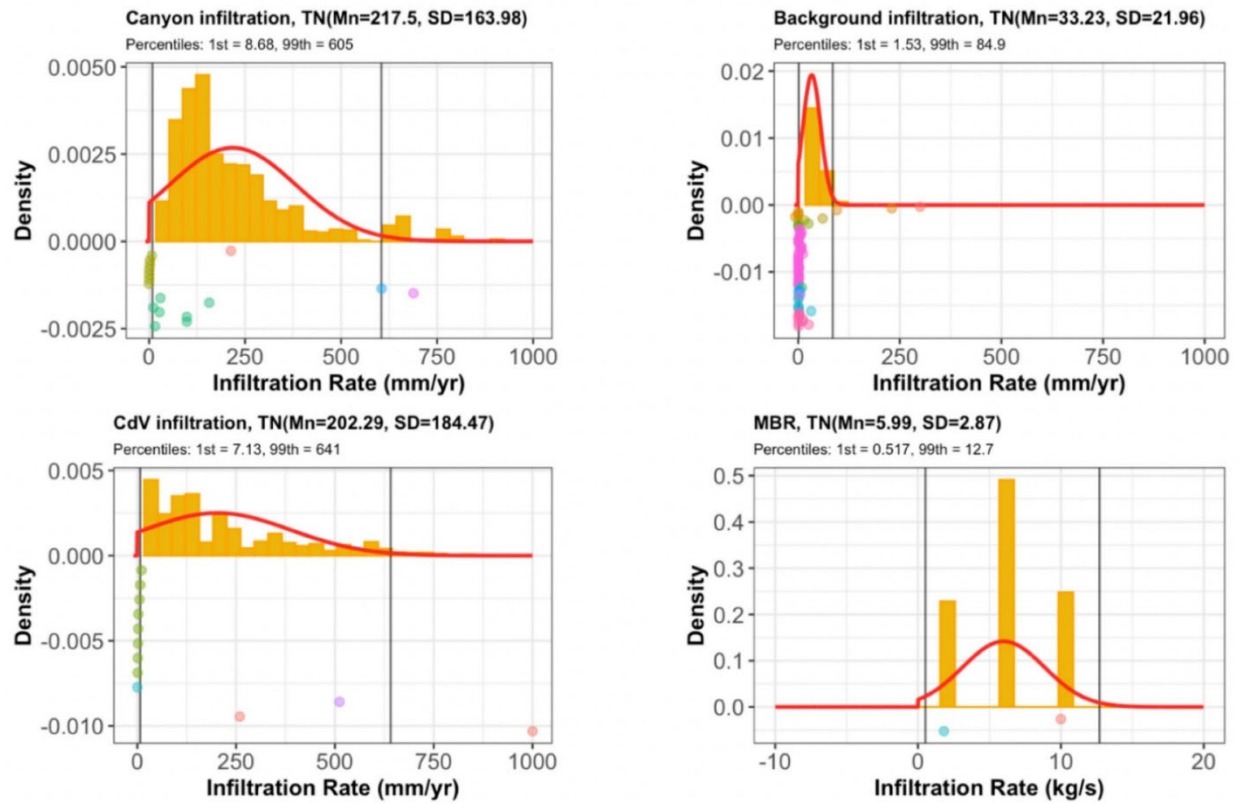
Notes: The distributions for canyon, background, and Cañon de Valle are in units of mm/yr, and the distribution for MBR is in kg/s.
Data are shown below the distributions and are colored by reference source

Figure D-3.2-4   Probability distributions (shown as red lines) for background, canyon, Cañon de Valle, and mountain block recharge infiltration rate for use in the RVZM
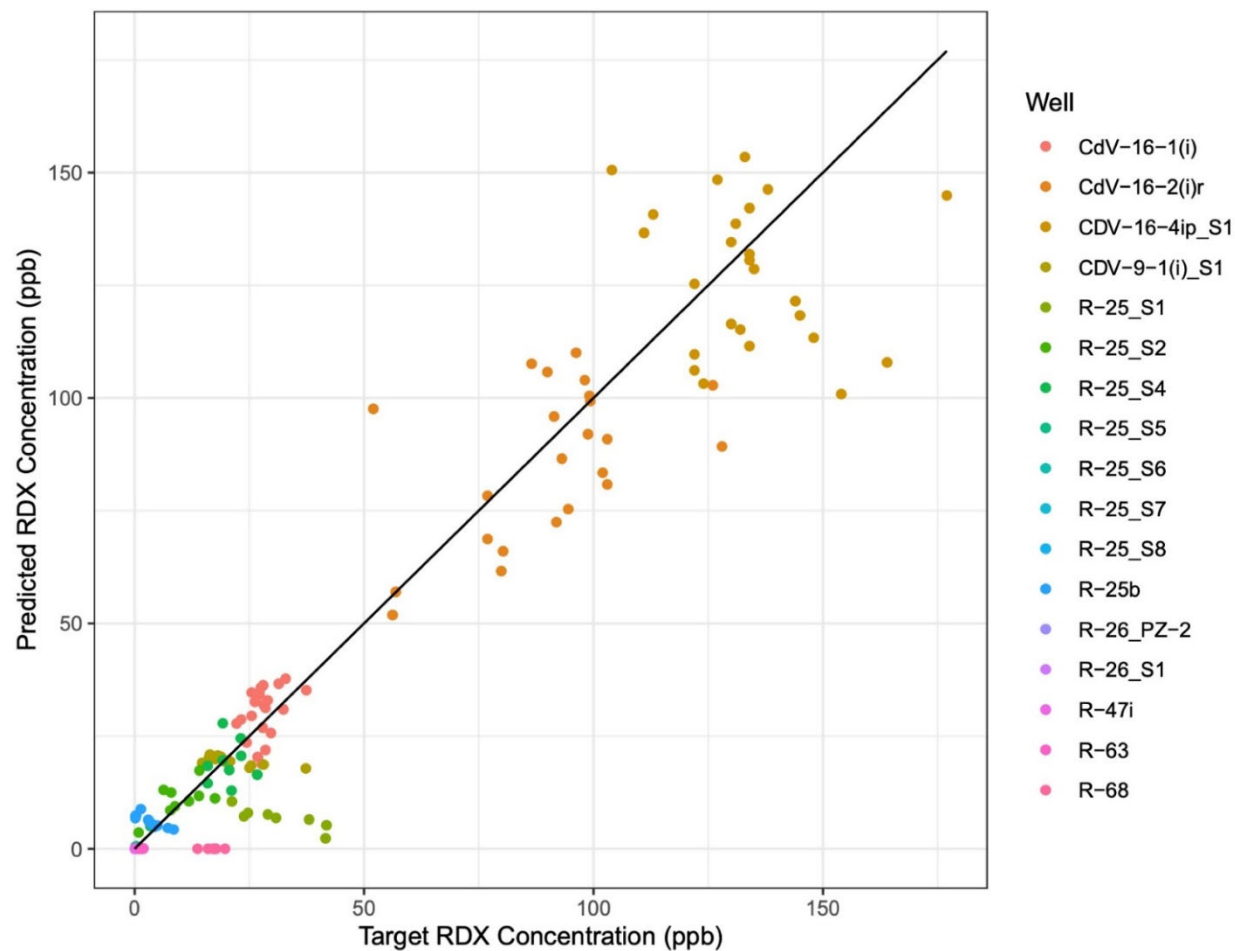
Figure D-3.2-5   Scatter-plot of targets and simulated values of RDX concentration for all wells used in Calibration 3
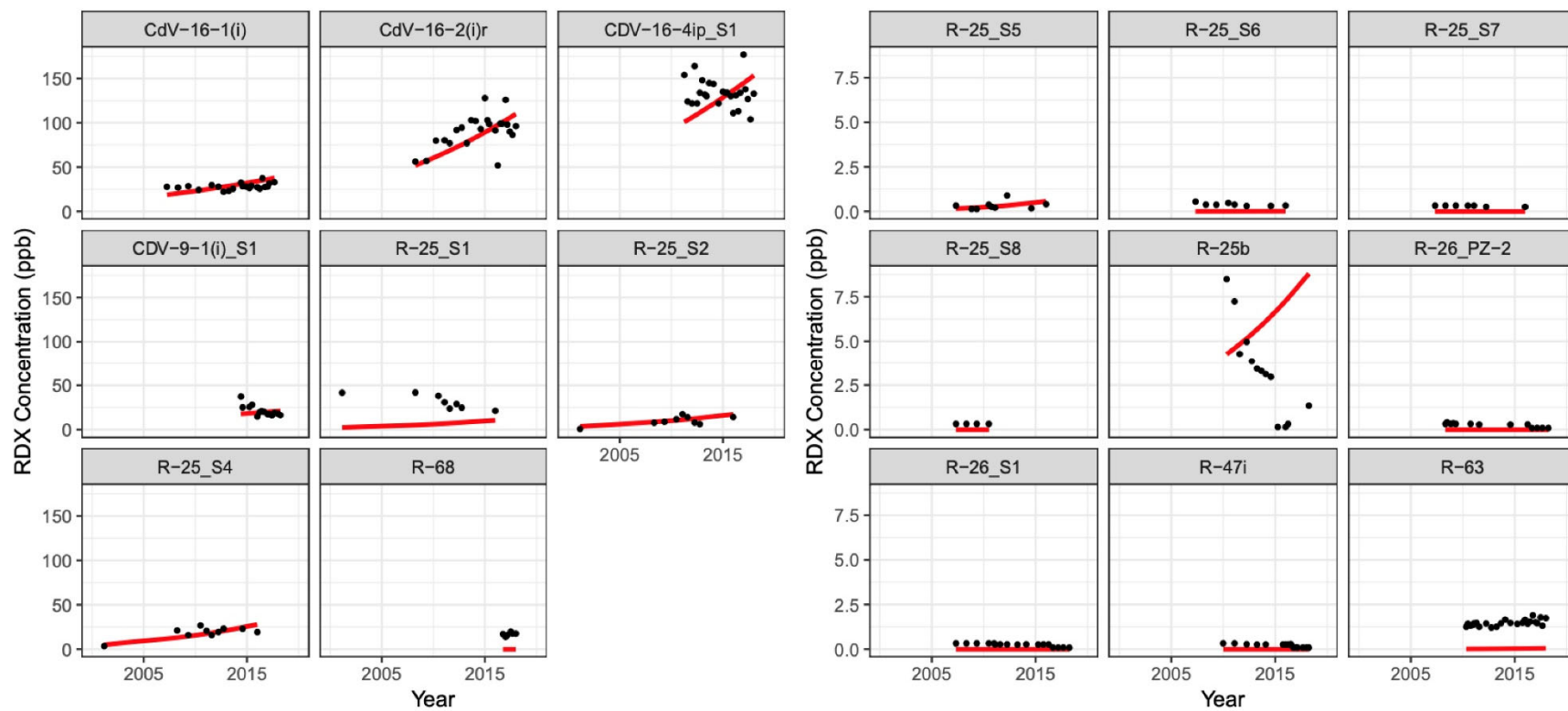
Figure D-3.2-6   Trend plots of targets and simulated values of RDX concentrations for all wells for Calibration 3
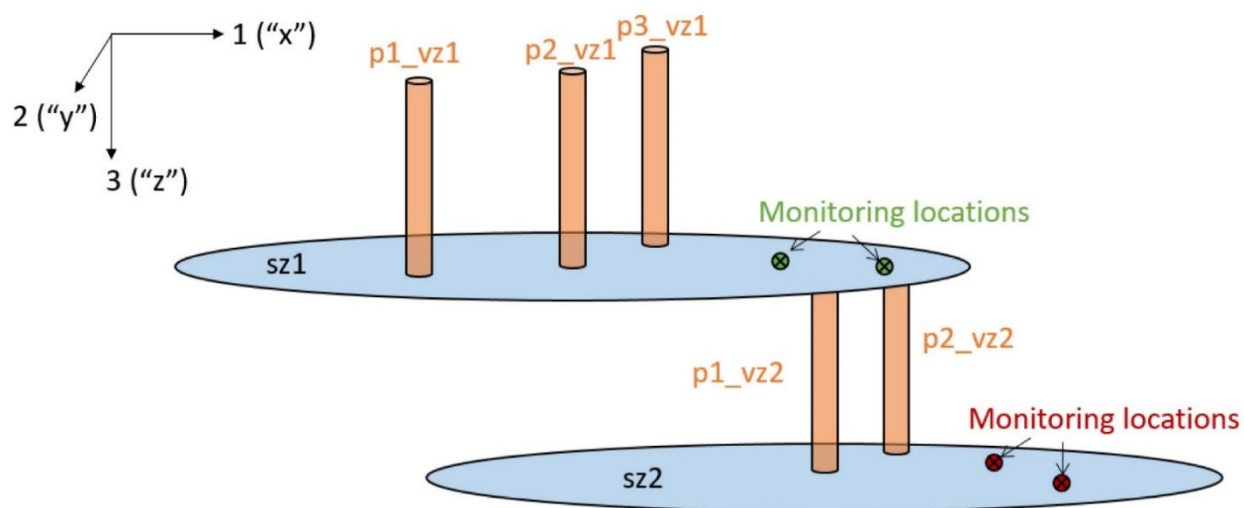
Figure D-3.2-7 **The P&D screening tool allows for fast inverse analysis based on monitoring well data, flexible geometries of vadose zone "drip points," and perched saturated zones**
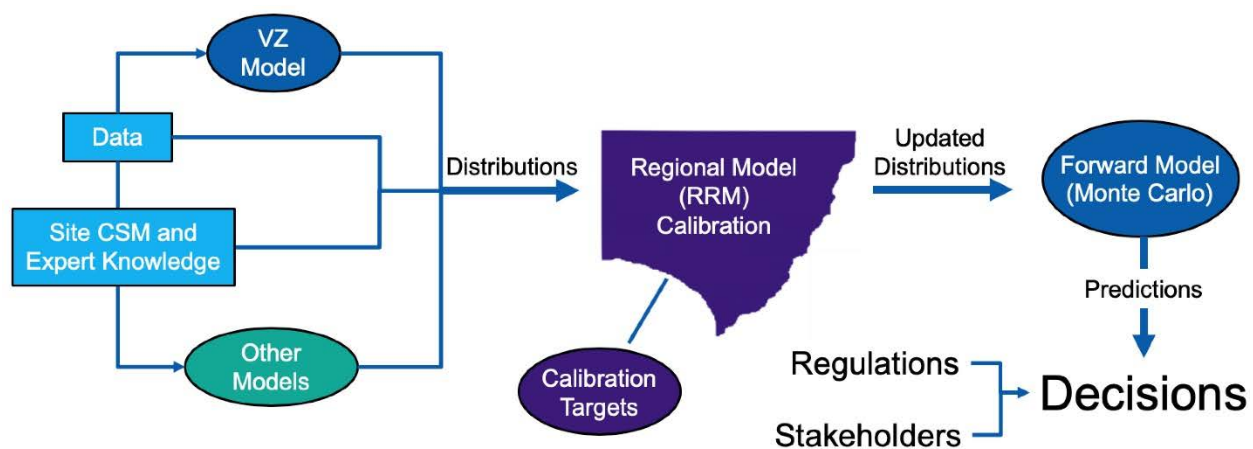
Figure D-4.0-1 **Hierarchical modeling framework**
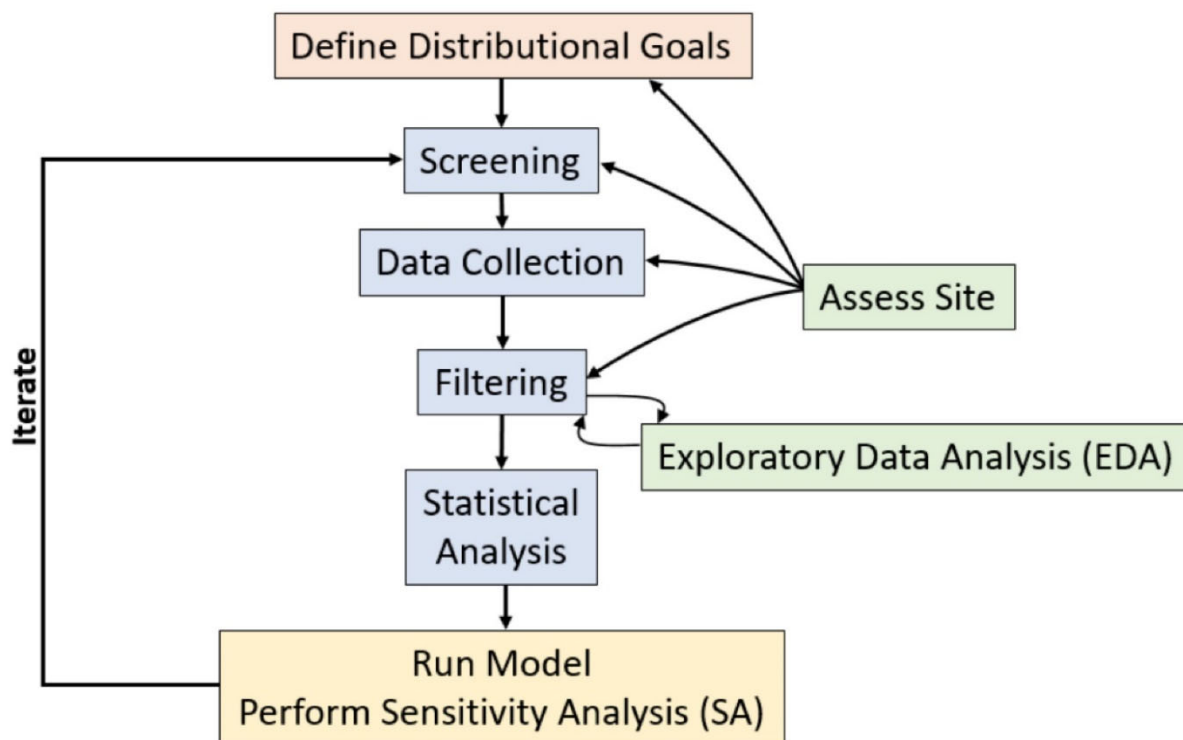
Figure D-4.0-2   Distribution development workflow
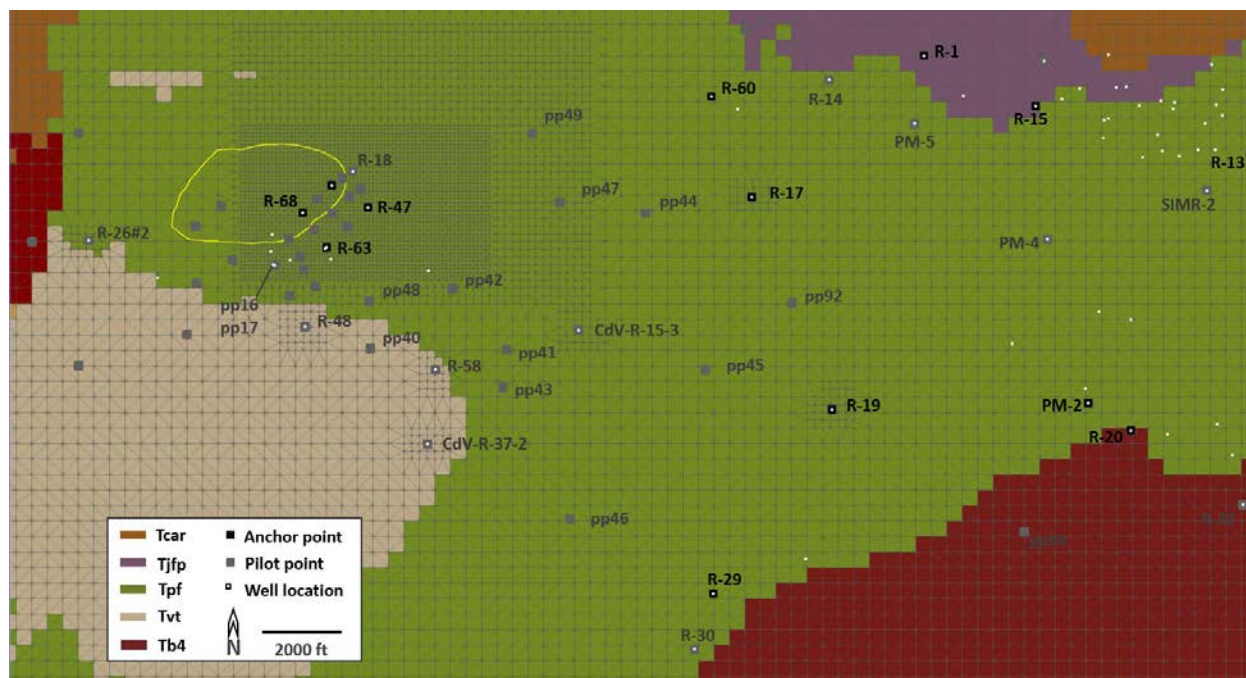
Figure D-4.1-1   Select pilot point (gray) and anchor point (black) locations in the RRM. Pilot and anchor points may be placed at different depths at the same location, e.g., pp16 and pp17. A pilot point location and anchor may be at the same location at different depths.
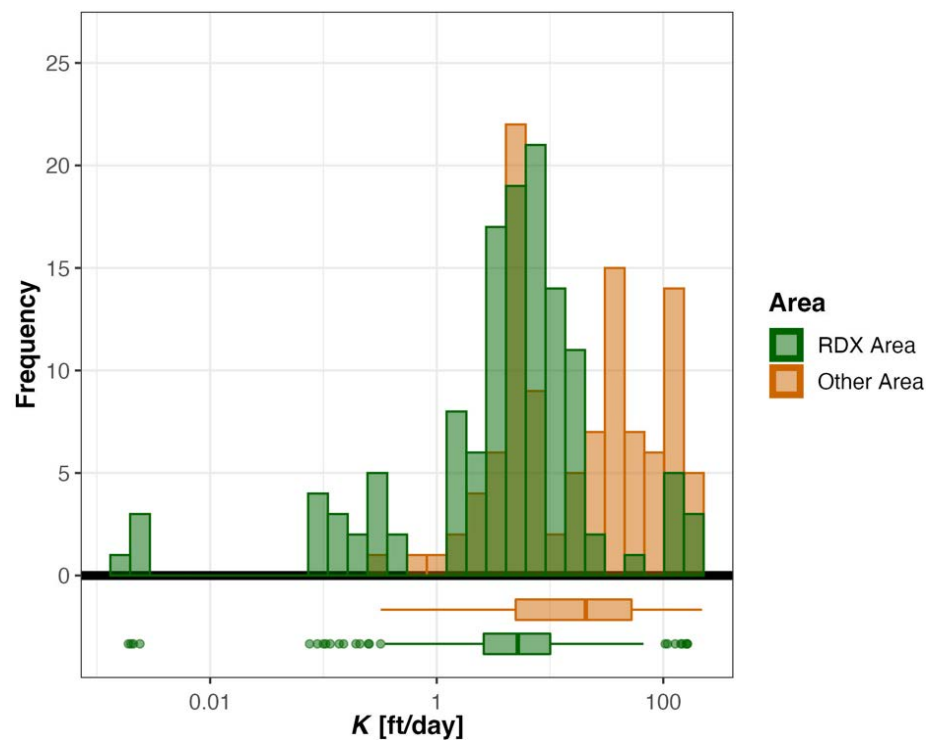
Figure D-4.1-2   Intermediate-scale, Puye formation (Tpf), *K* estimates in the RDX area compared with other locations
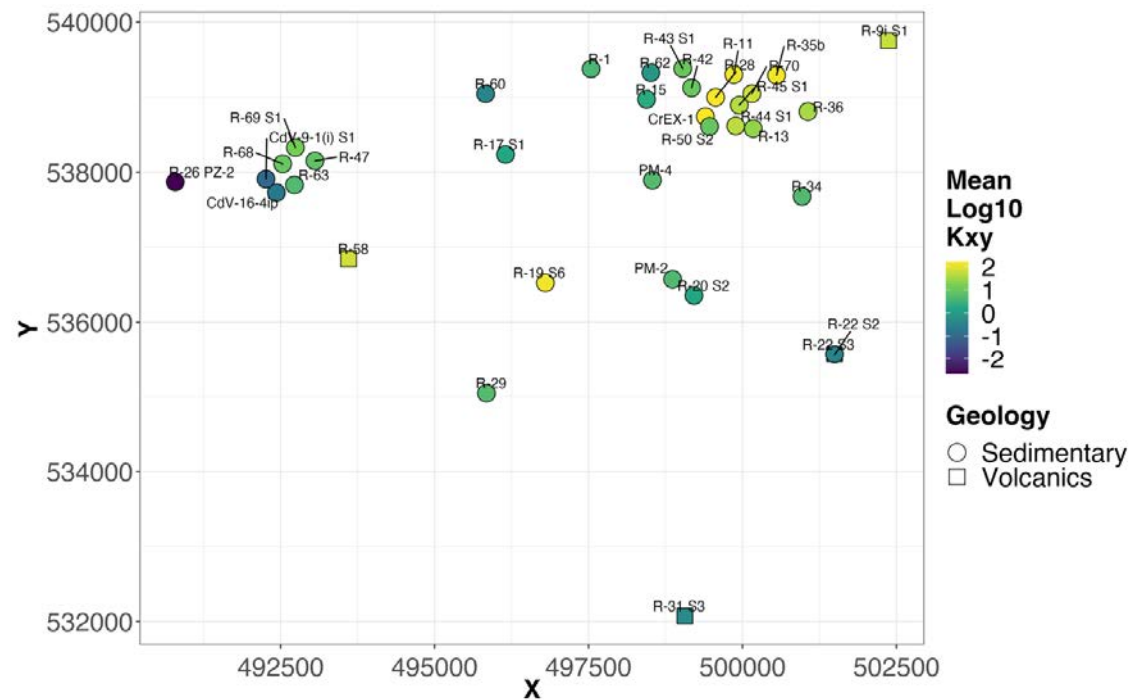
Figure D-4.1-3   Spatial plot with coloring of points indicating the mean *Kxy* at that location on a log₁₀ scale. Wells with recovery data are displayed. If multiple screenings occurred at a location, then only the top layer is displayed.
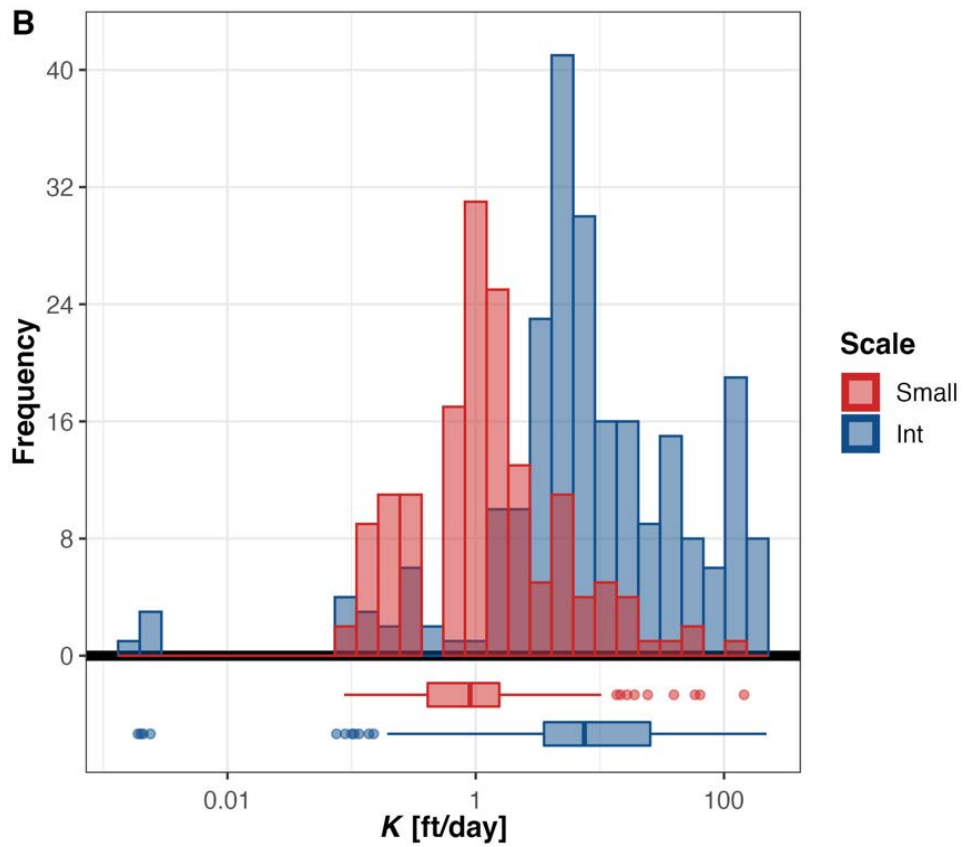
Figure D-4.1-4   Small-scale (corehole and geophysics) data compared with intermediate-scale K estimates (Int) across the LANL site
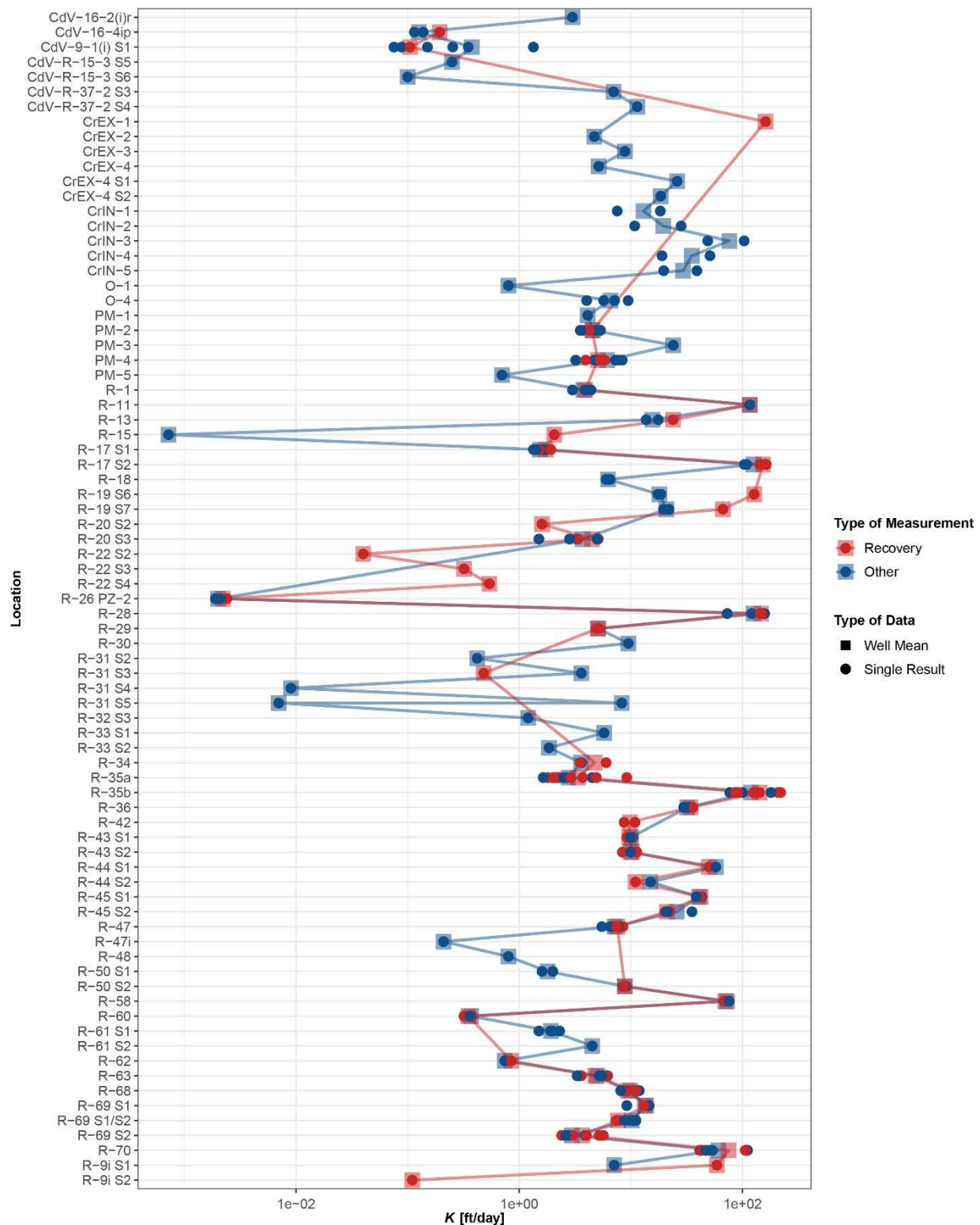
Figure D-4.1-5   Intermediate-scale *K* estimates, coded by type of analysis (recovery or all other types of aquifer test analysis). Individual results are shown as circles while means for the wells are shown as squares for either type.
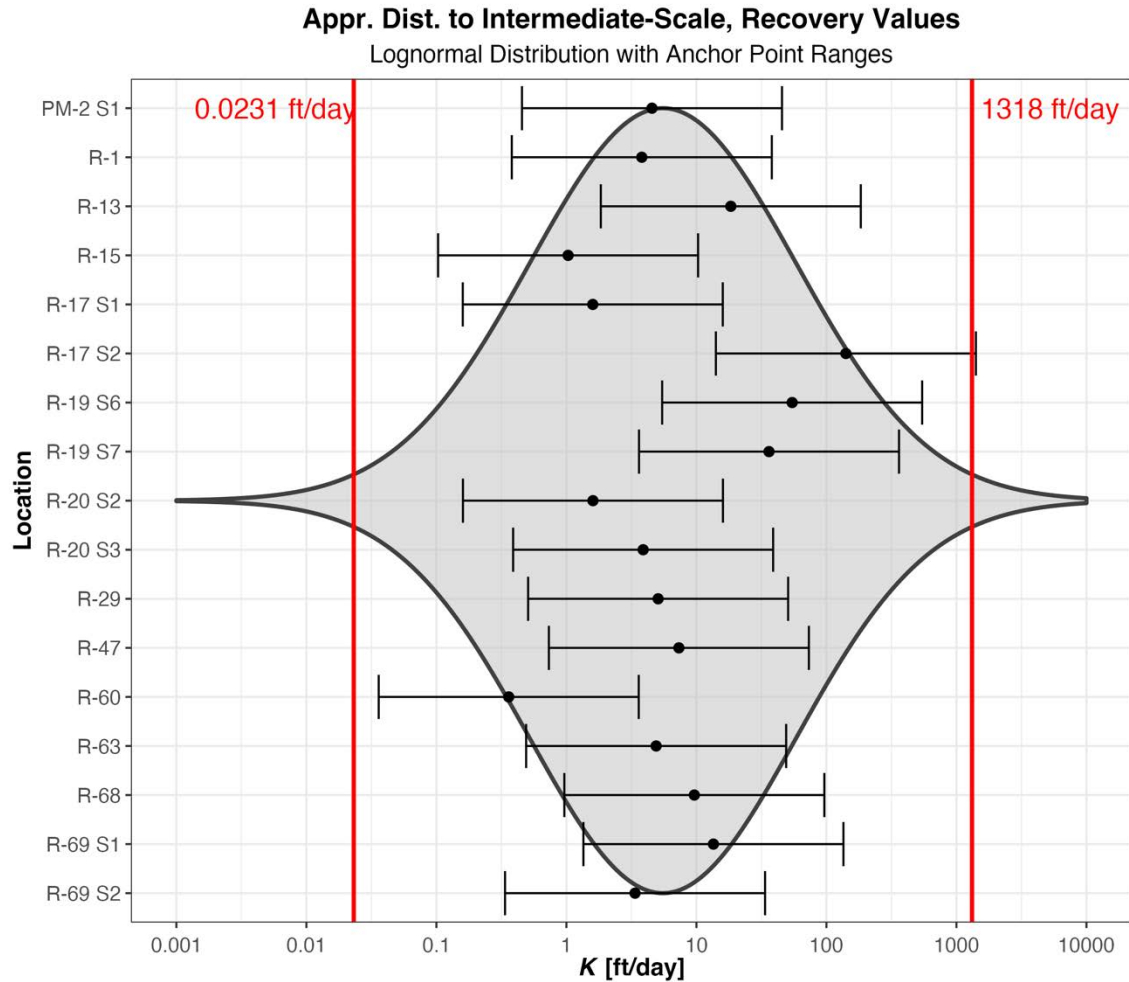
Figure D-4.1-6   **Mean K_{xy} (ft/day) ± one order of magnitude shown on the log10 scale for each anchor point in the RDX area. The final MLE-fit, lognormal distribution for pilot points is included in the background as violin-density plots for comparison. The vertical red lines show the 1st and 99th percentiles of the distribution.**
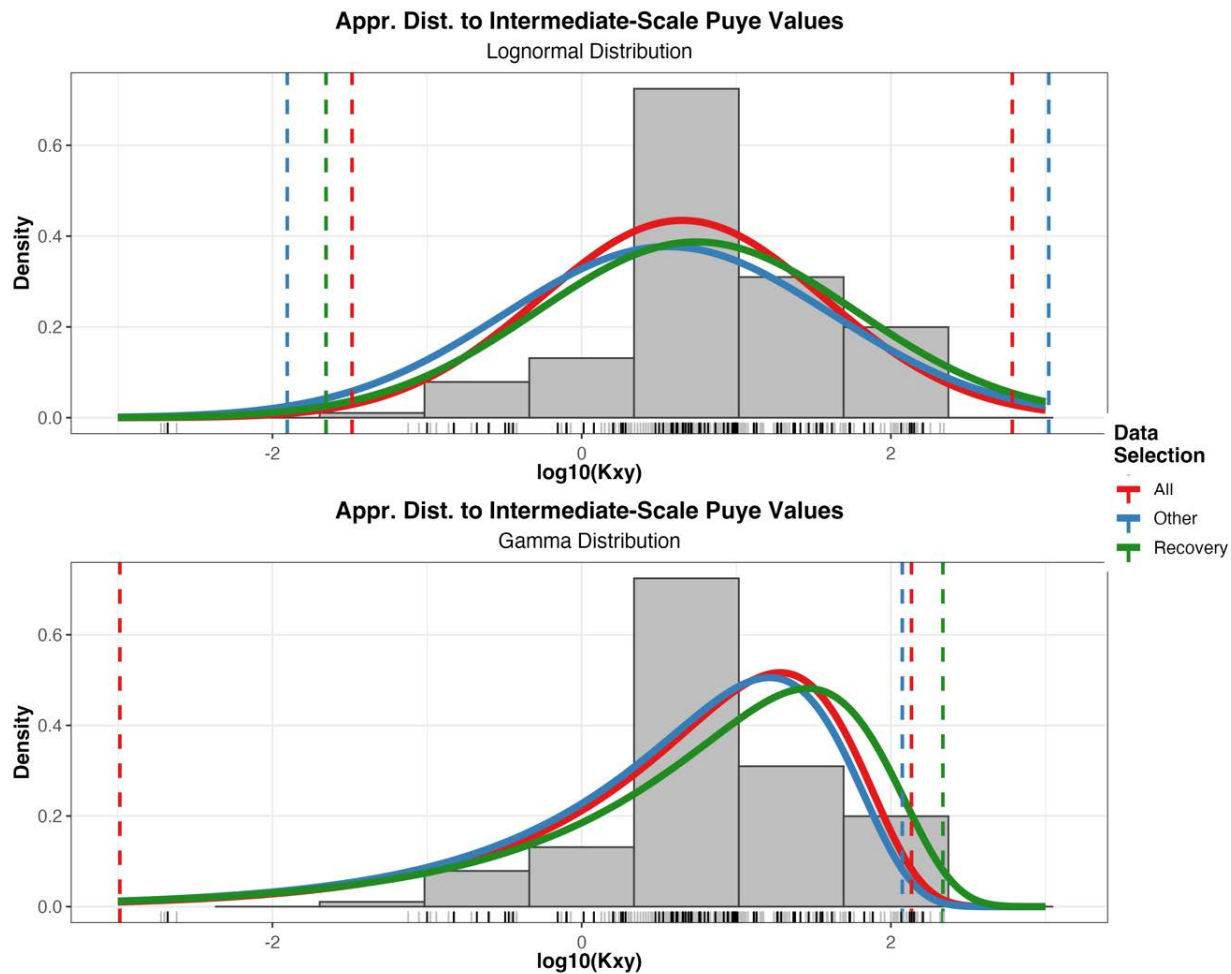
Figure D-4.1-7   Approximate lognormal (top) and gamma (bottom) distributional fits to filtered data on the log10 scale. Histograms and ticks below the histogram represent the filtered data for all types of analyses (both recovery and other). Dashed lines indicate the 1st and 99th percentiles for each distribution. "Puye" is used generally for all sedimentary geologies.
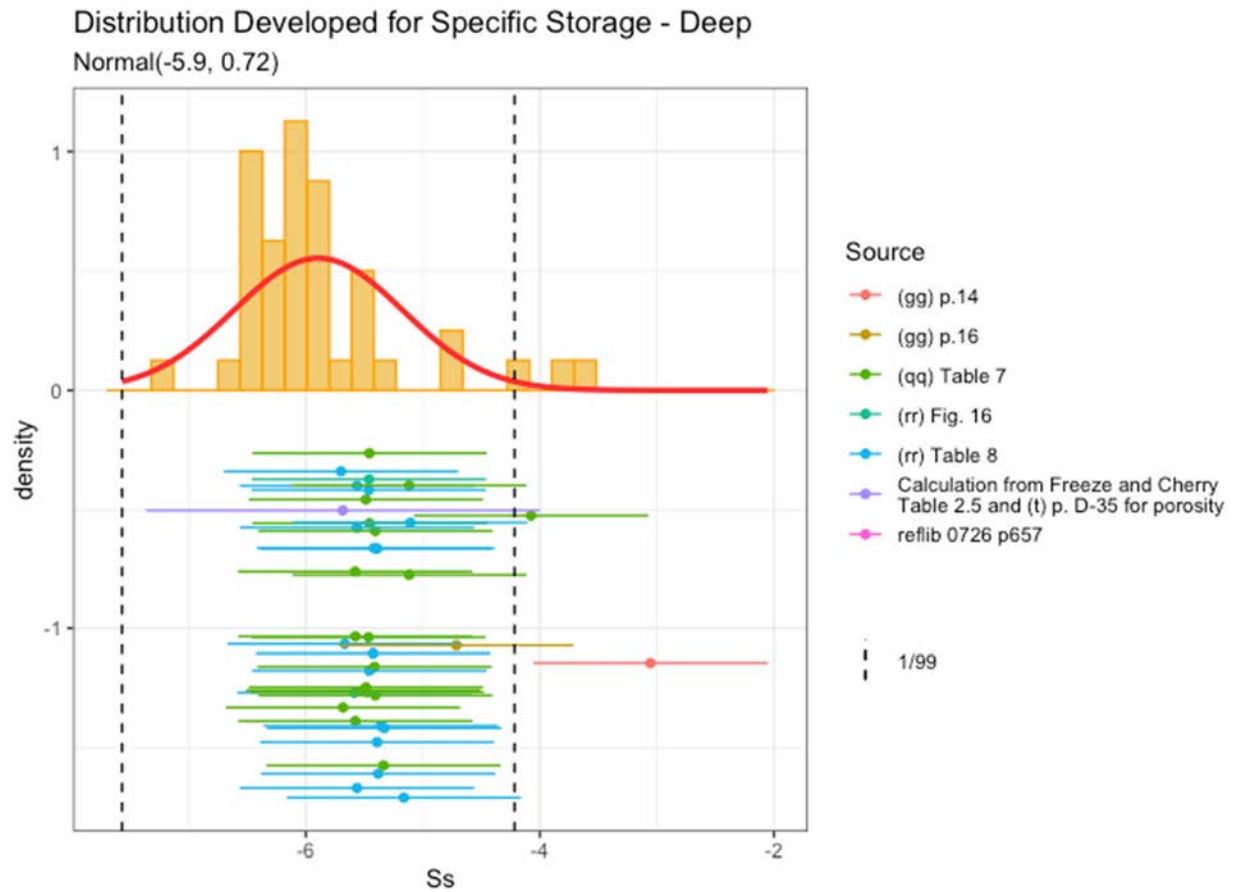
Figure D-4.2-1   Distribution developed for log$_{10}$ of specific storage or effective specific storage with units of m^{-1} (deep)
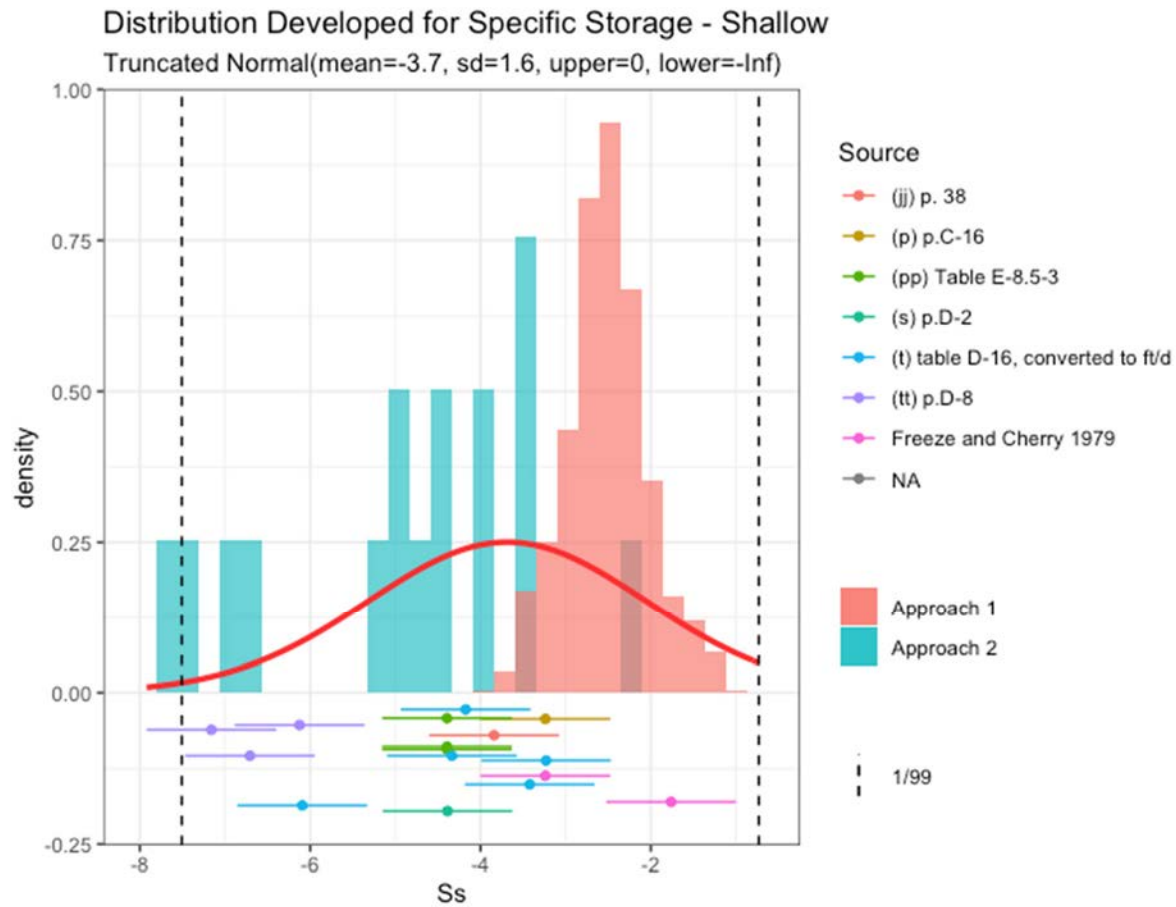
Figure D-4.2-2   Distribution developed for log$_{10}$ of specific storage or effective specific storage with units of m^{-1} (shallow)
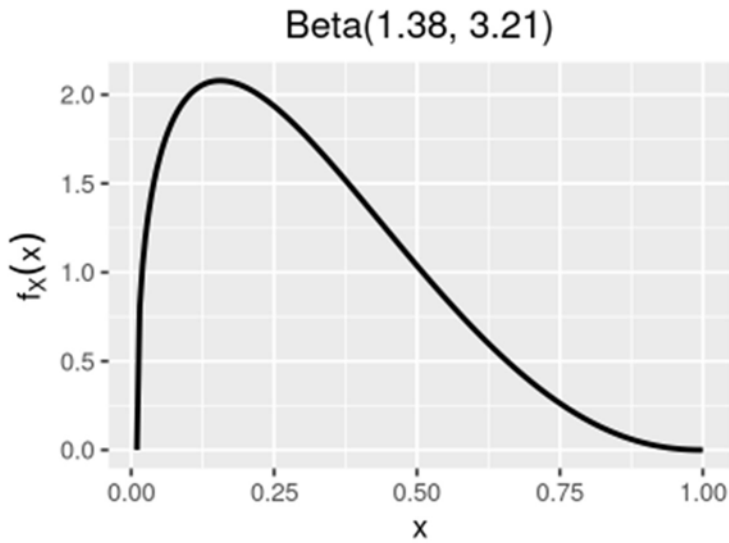
Figure D-4.3-1 **Distribution developed for semiaxis for hydraulic conductivity and specific storage: Beta (1.38, 3.21)**
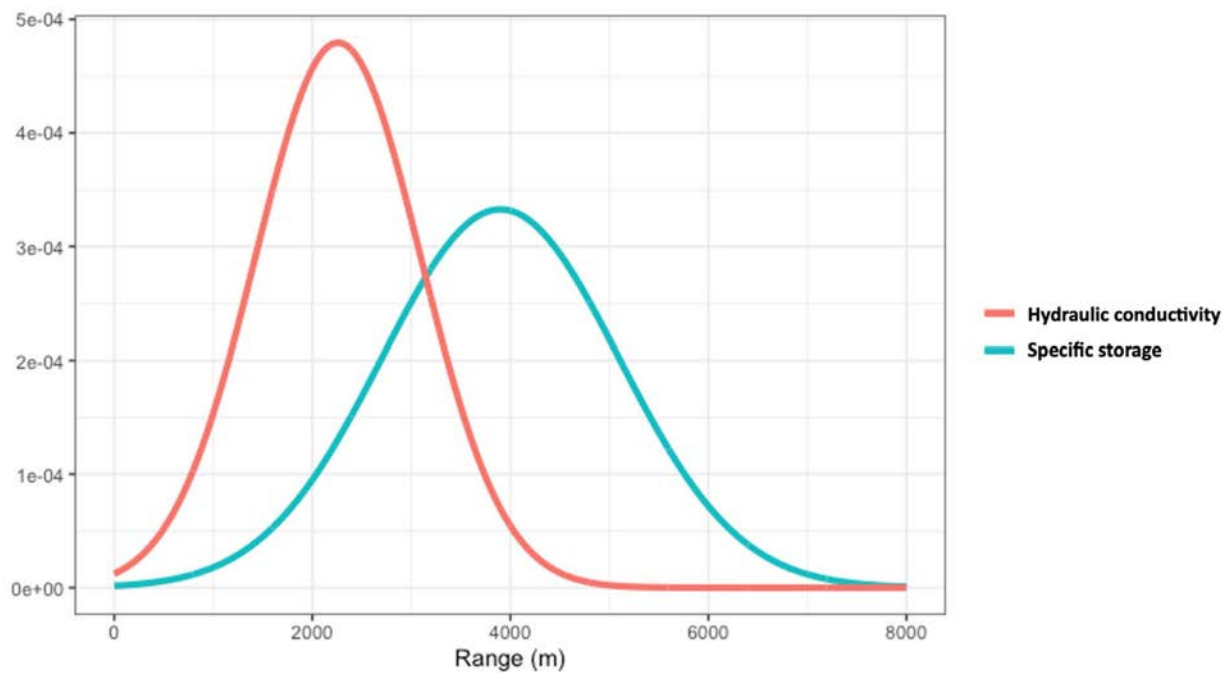
Figure D-4.3-2 **Distributions developed for kriging range**
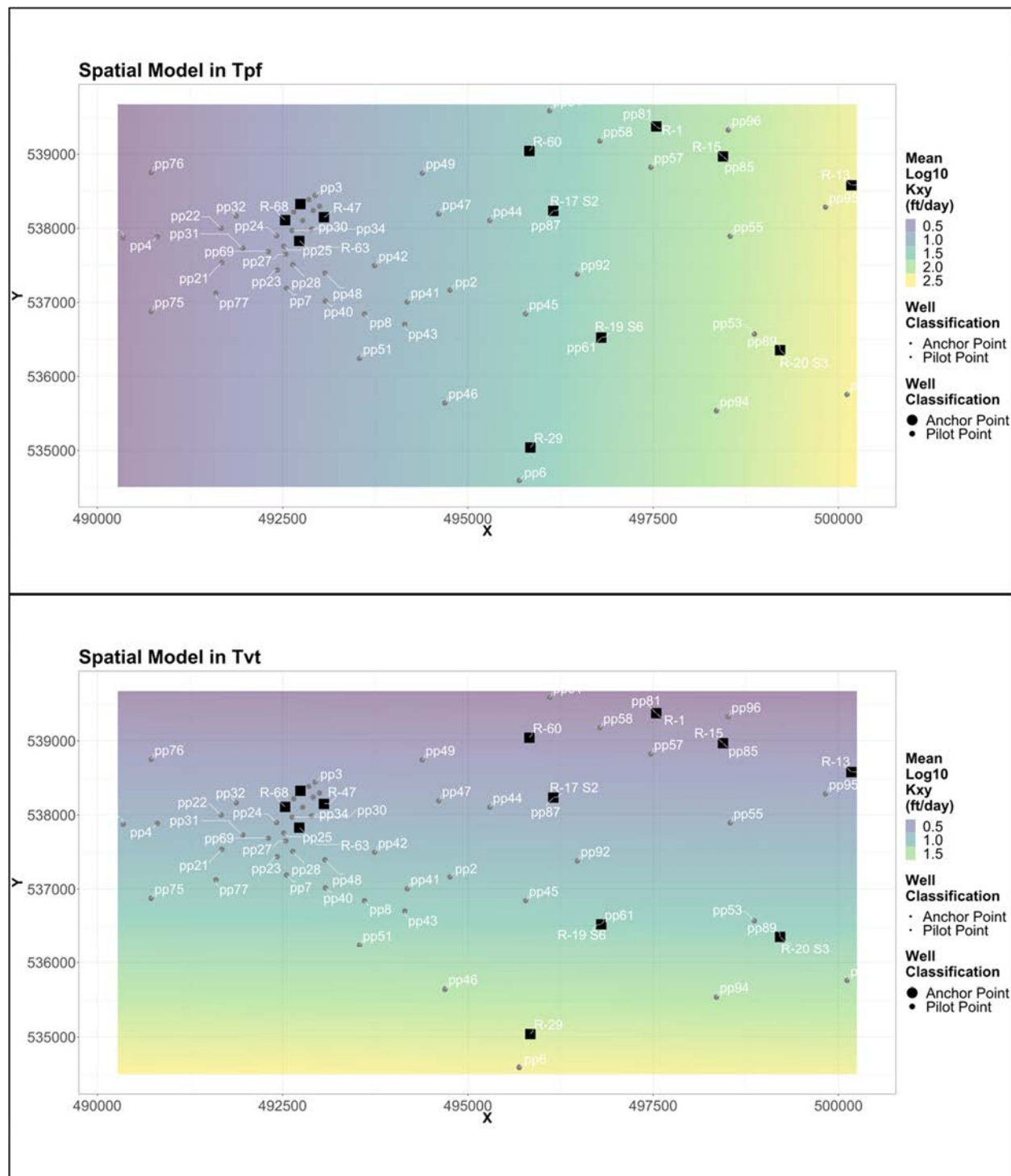
Figure D-4.3-3   Distribution of K values near the surface and at depth in the regional aquifer according to the spatial model of K
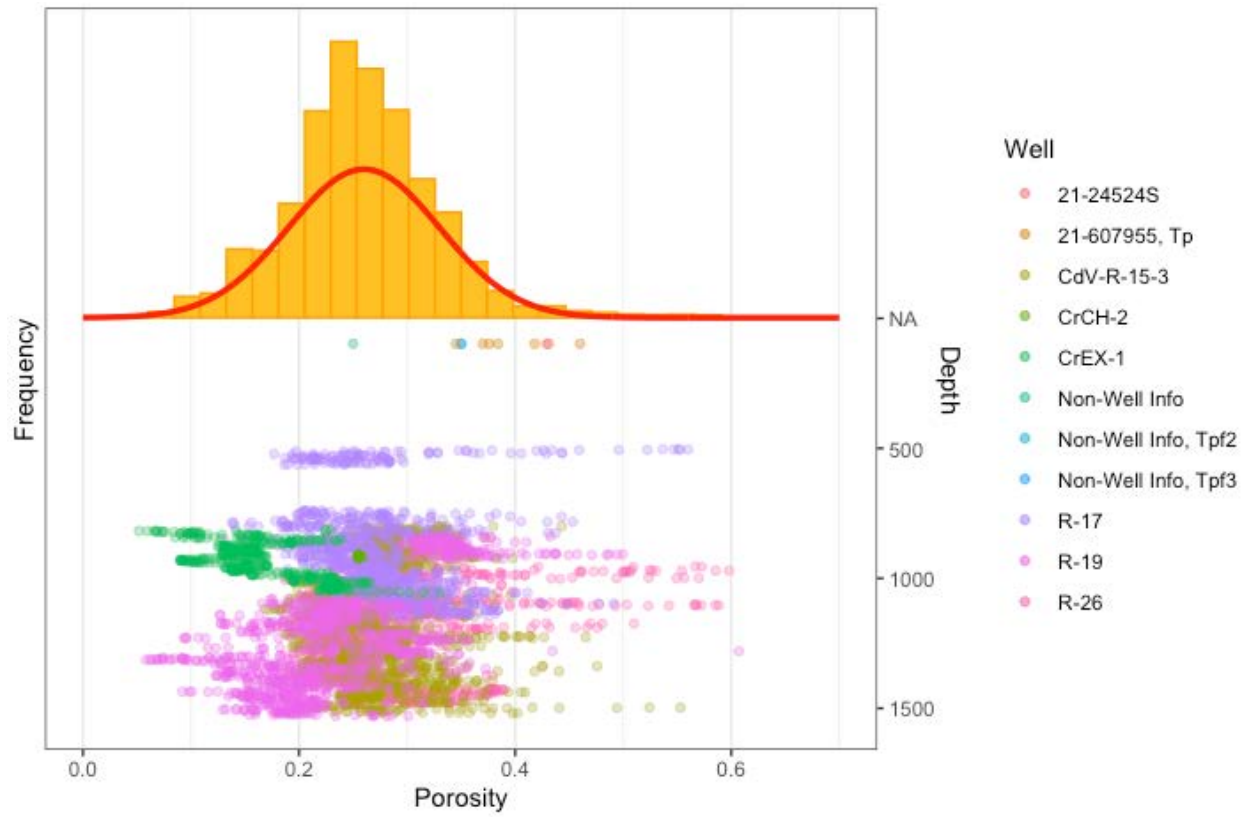
Figure D-4.4-1   Distribution developed for total porosity in the Puye Formation
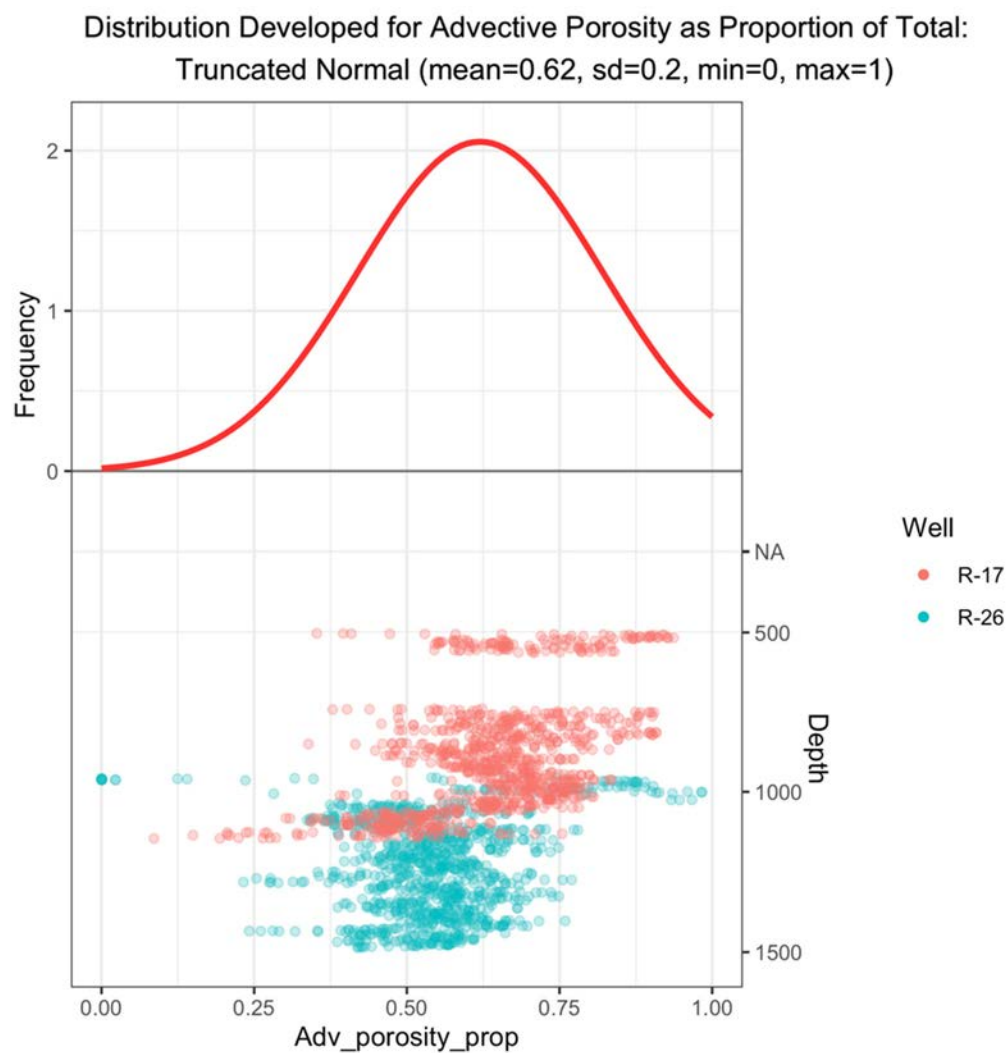
Figure D-4.4-2   Distribution developed for the relationship between total porosity and advective porosity
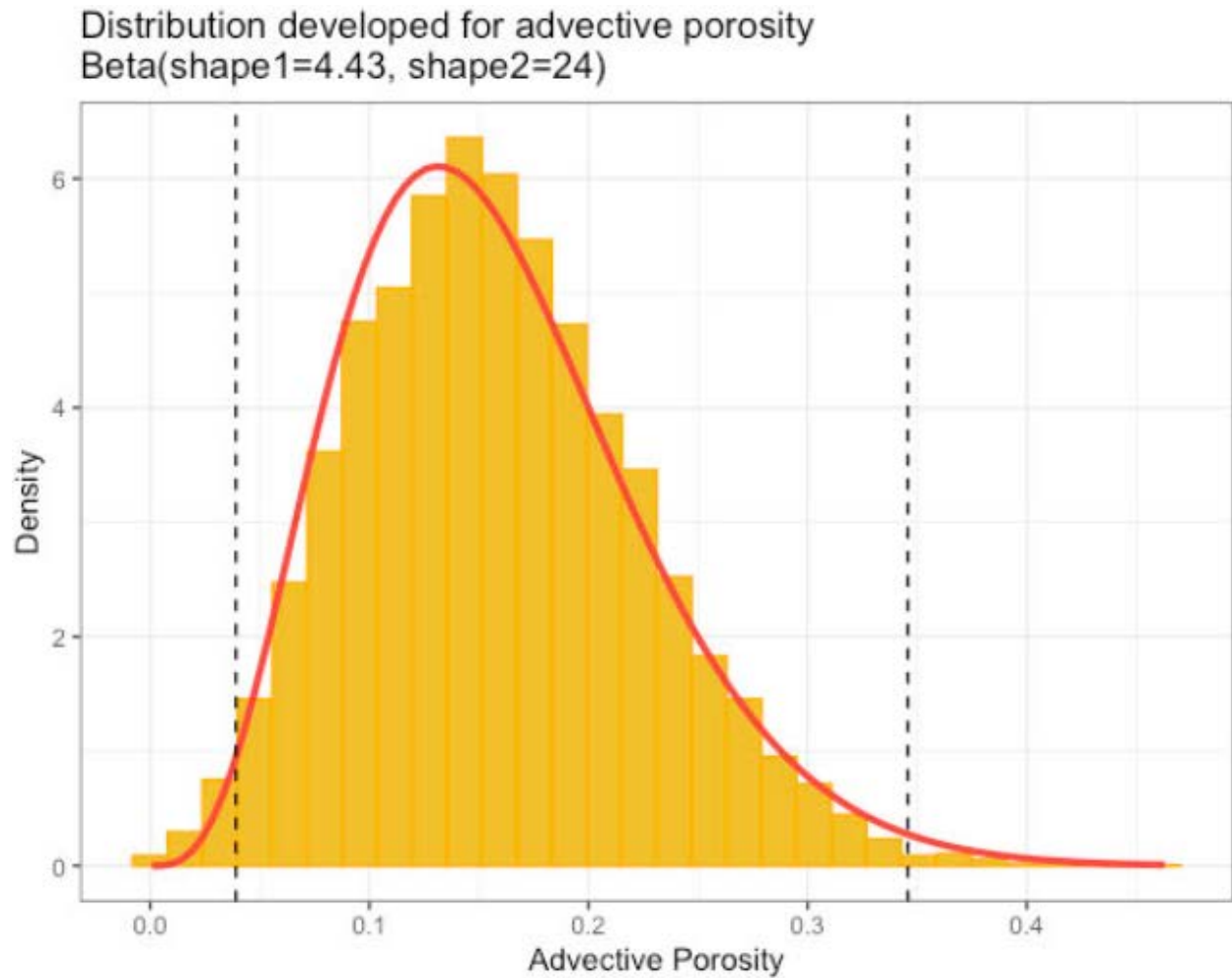
Figure D-4.4-3   **Distribution developed for advective porosity. The histogram shows the distribution of the product of draws from a total porosity distribution and a fractional advective porosity distribution. Vertical bars show the 1st and 99th percentiles used as ranges for the LM calibration (0.04, 0.35).**
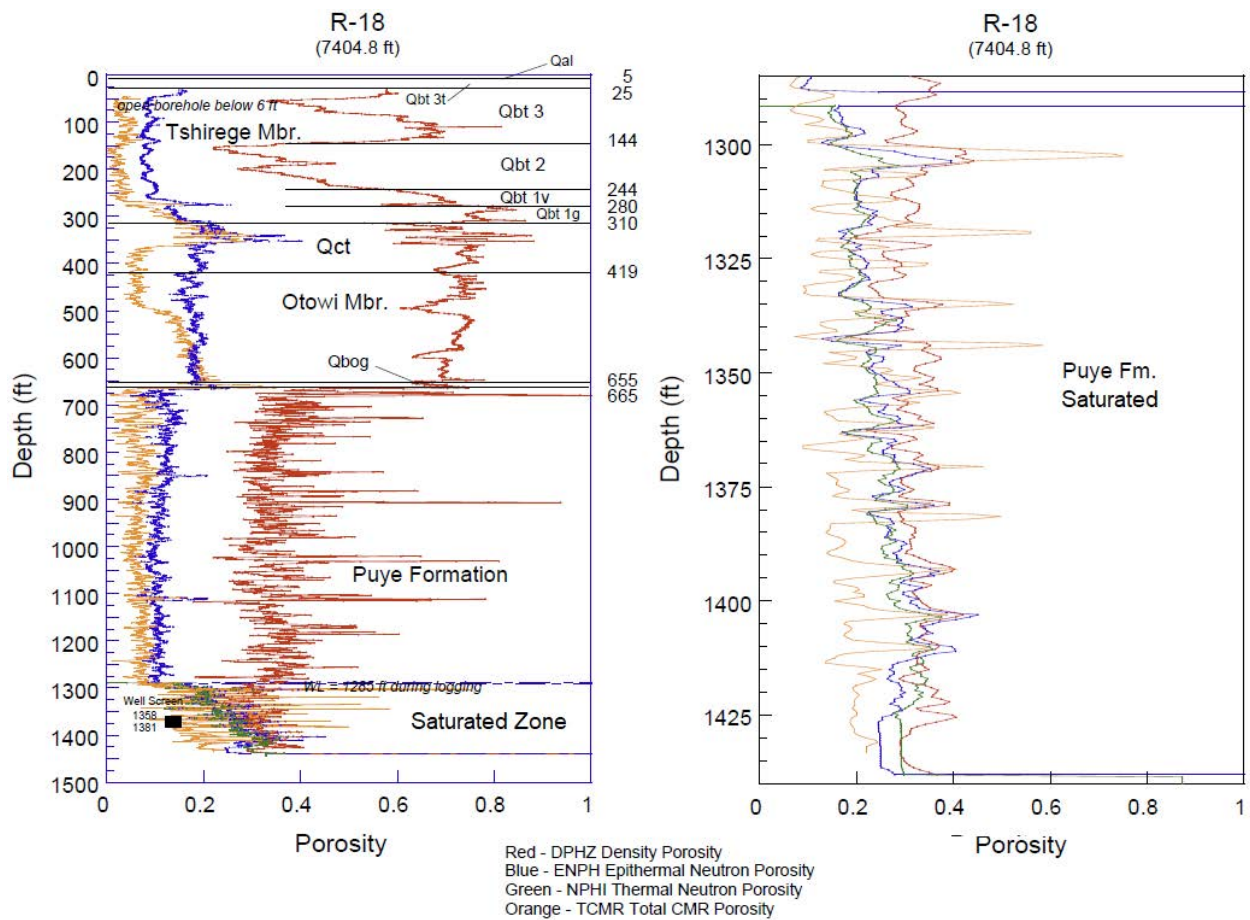
Figure D-4.4-4   R-18 geophysical log data for four types of porosity estimates: (left) full borehole log, (right) regional aquifer saturated zone only
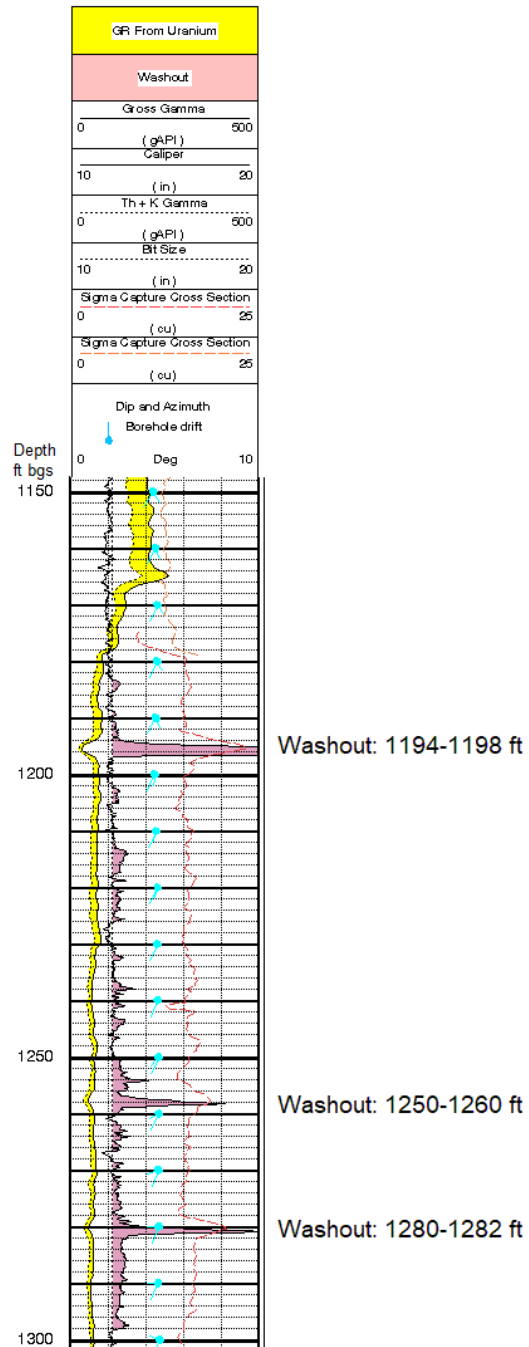
Figure D-4.4-5 **R-19 geophysical log data with washouts estimated by caliper measurements. Washouts removed from the R-19 data set are indicated.**
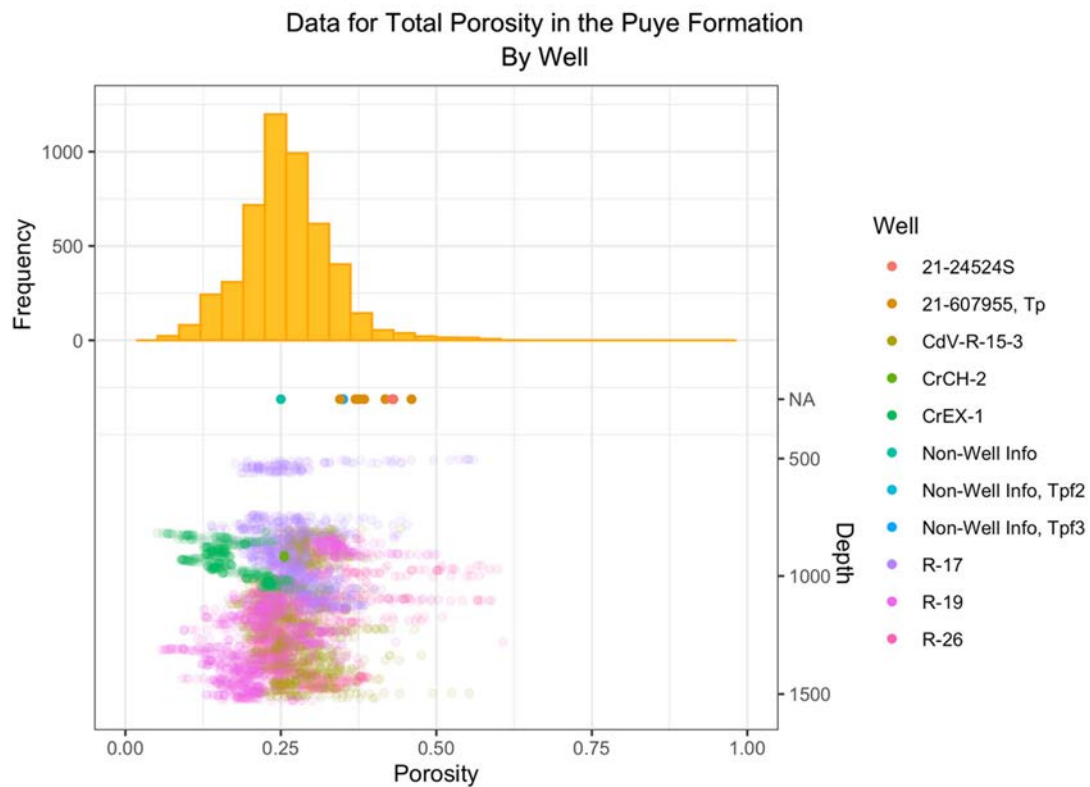
Figure D-4.4-6   Data available for total porosity in the Puye Formation
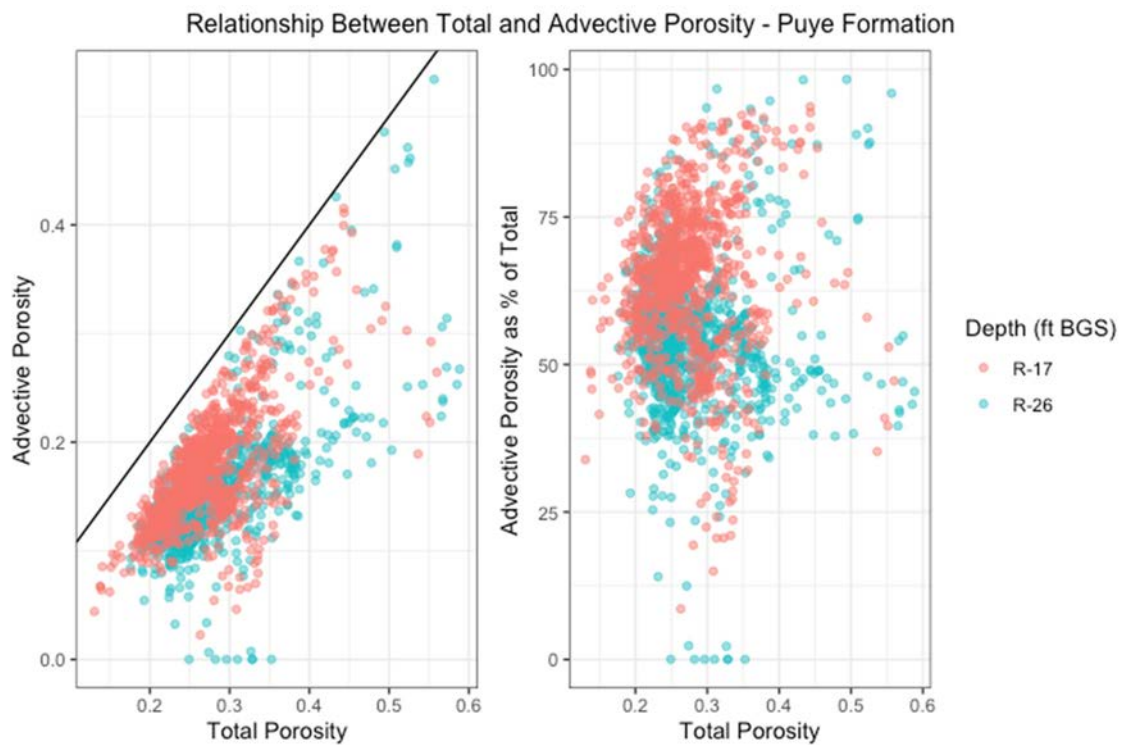
Figure D-4.4-7   Data available to inform the relationship between total and advective porosity
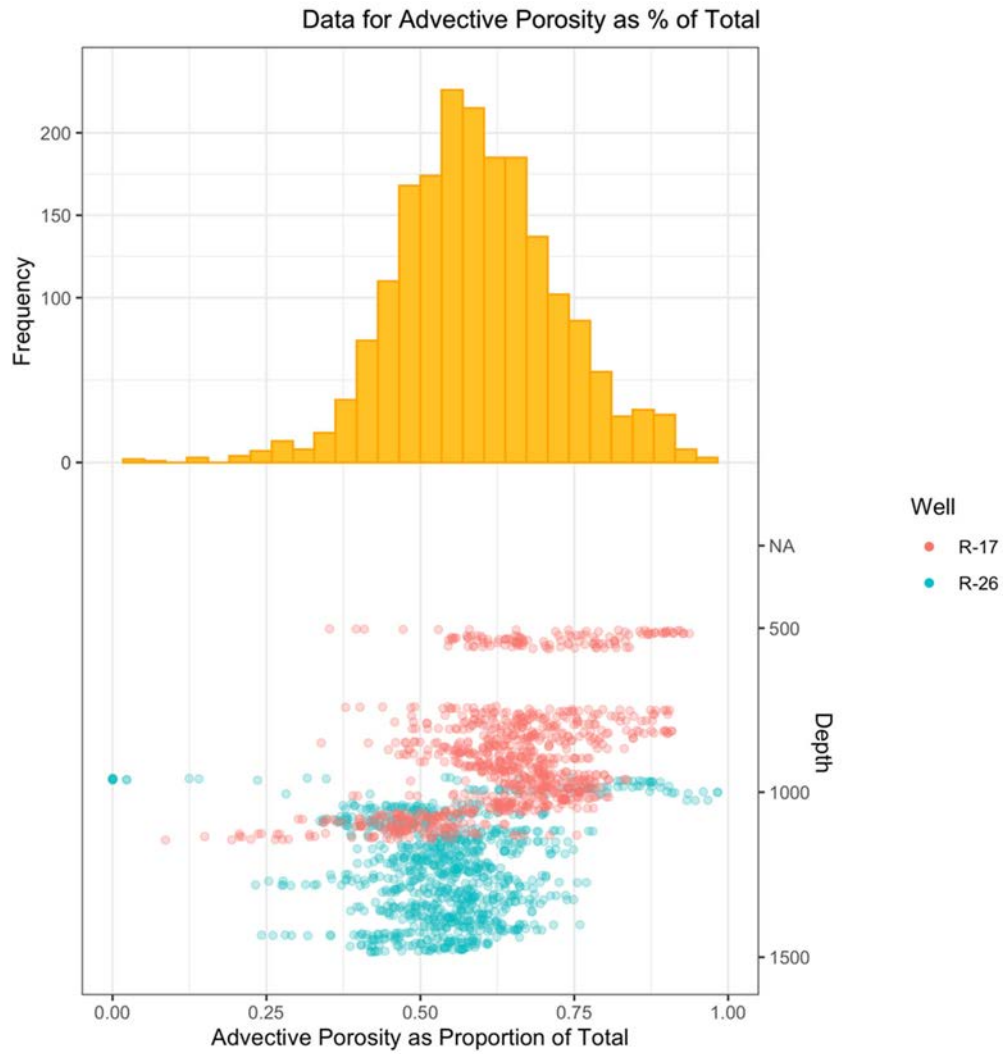
Figure D-4.4-8   Data available to inform the distribution of advective porosity as percent of total porosity
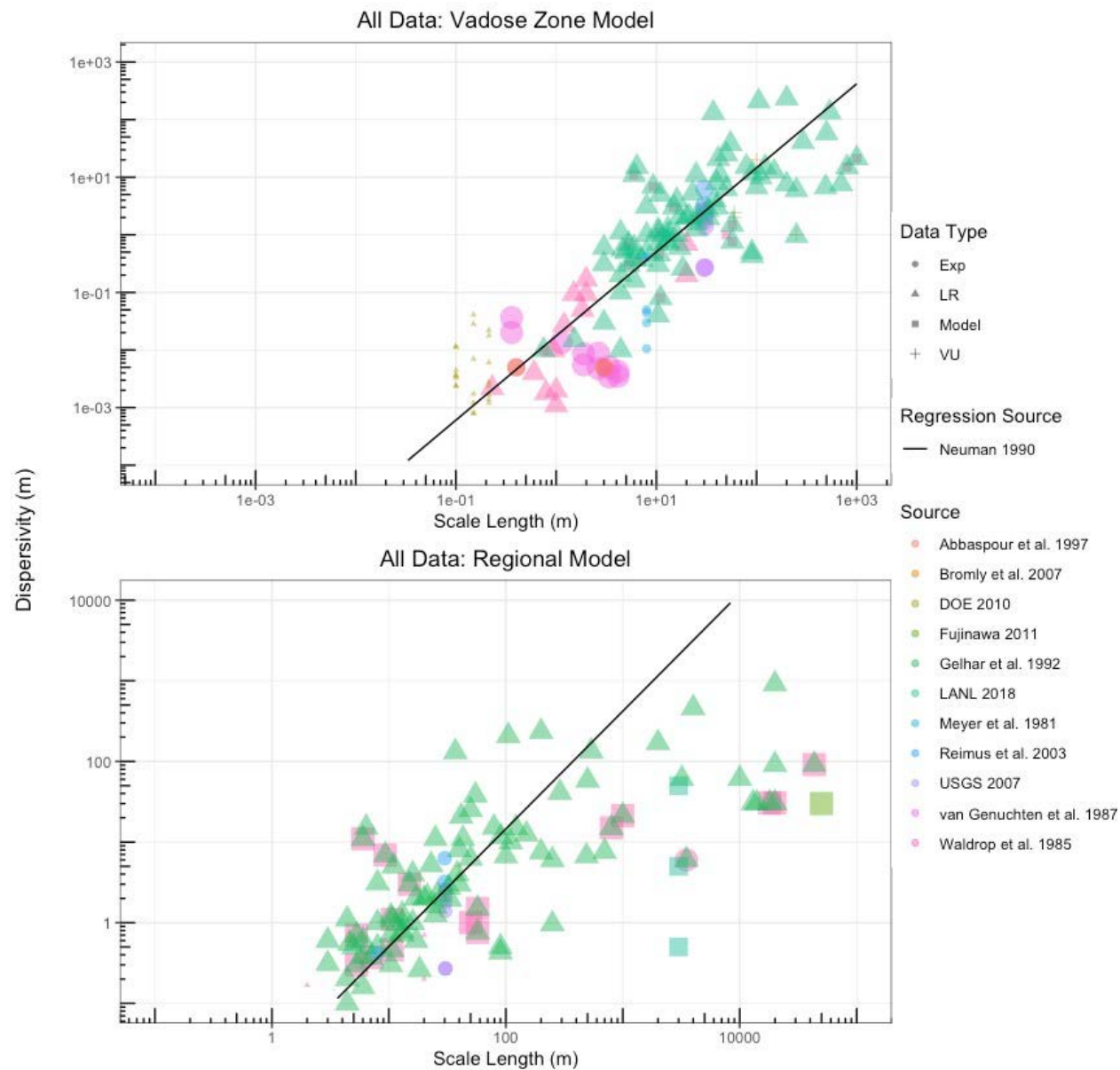
Figure D-4.5-1   Data available to inform the relationship of longitudinal dispersivity and length scale
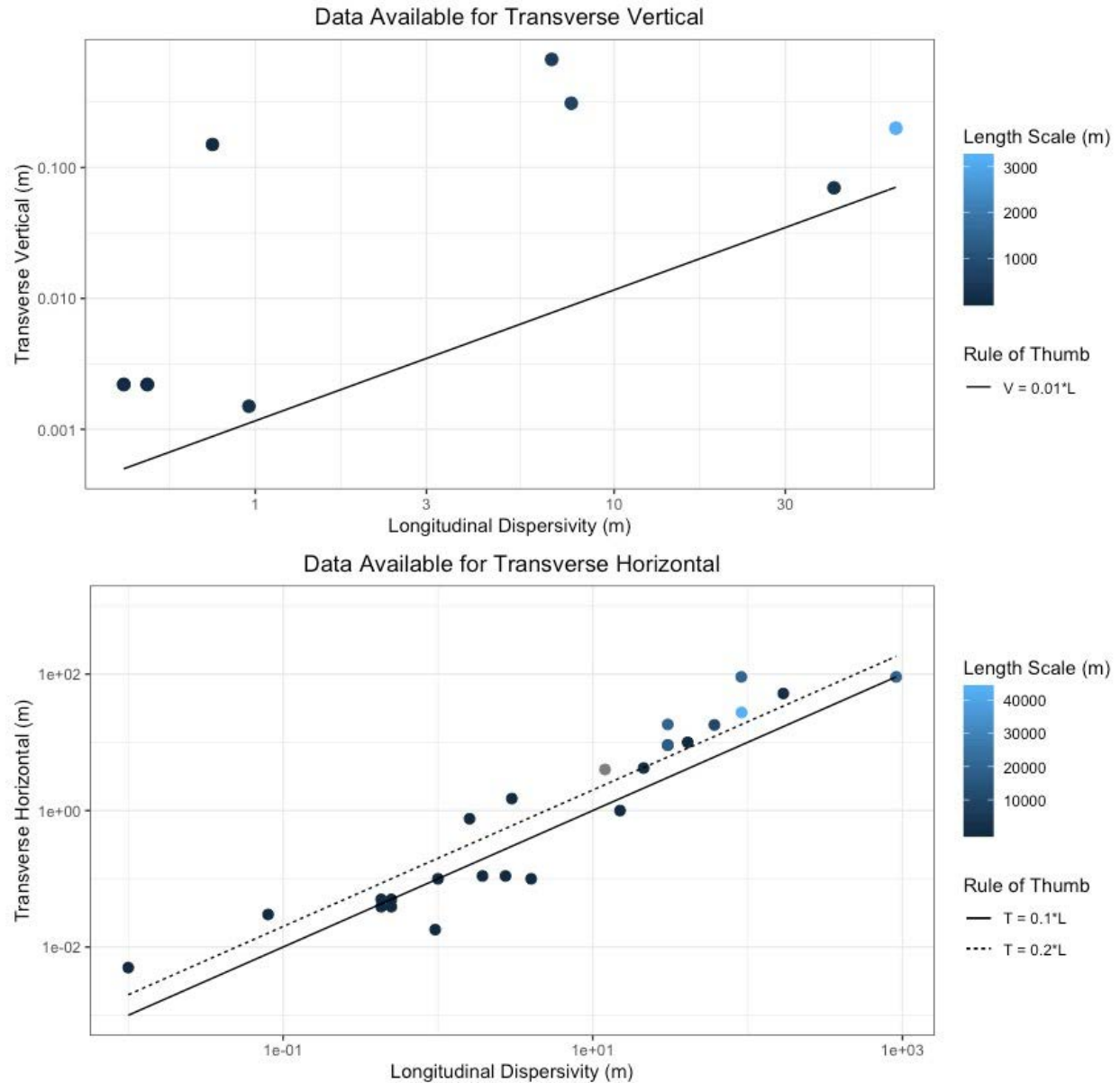
Figure D-4.5-2   Data available to inform the relationships of longitudinal dispersivity and transverse dispersivity in horizontal and vertical directions
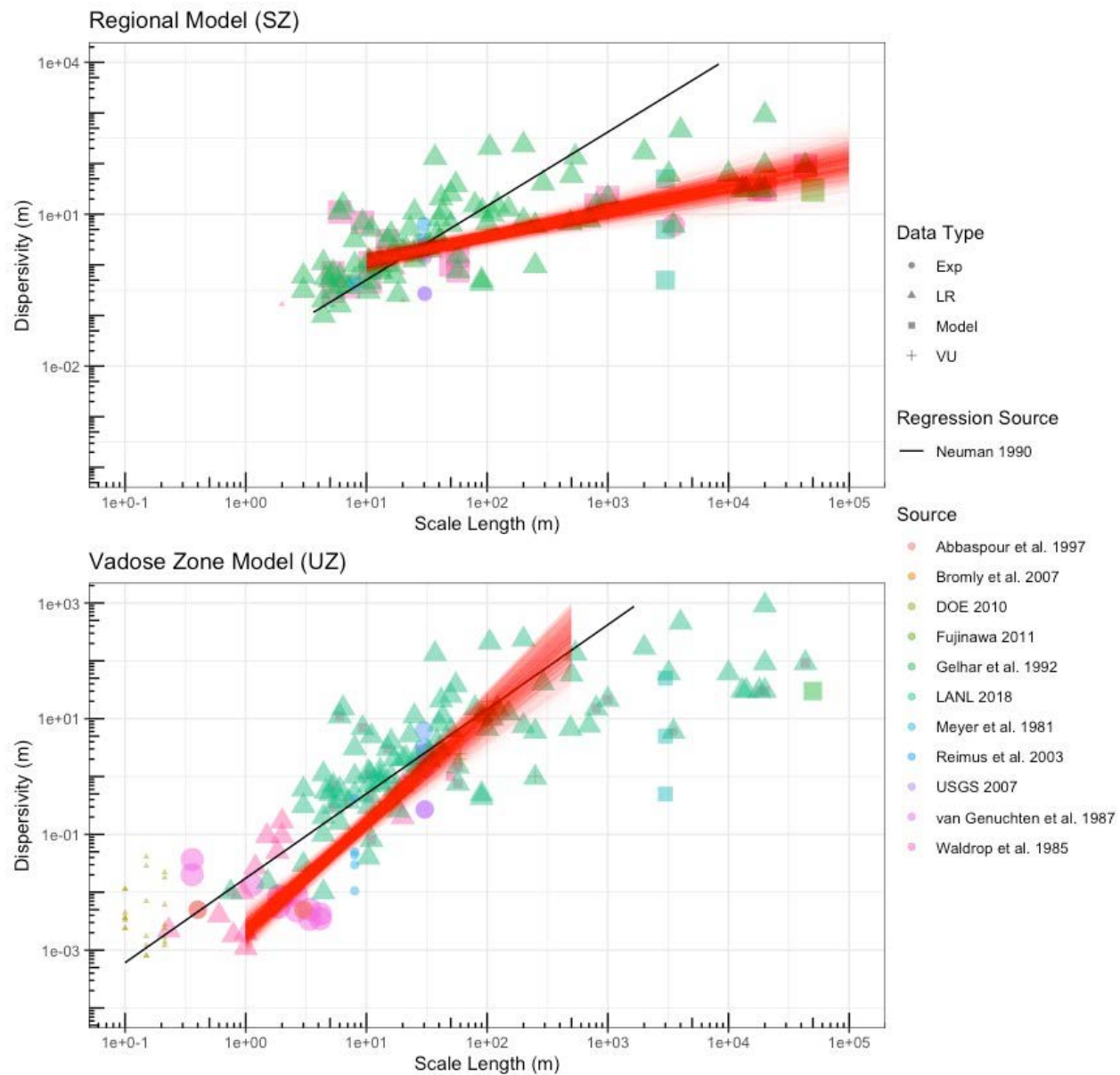
Figure D-4.5-3   Bootstrap estimated regression lines in red for the RRM
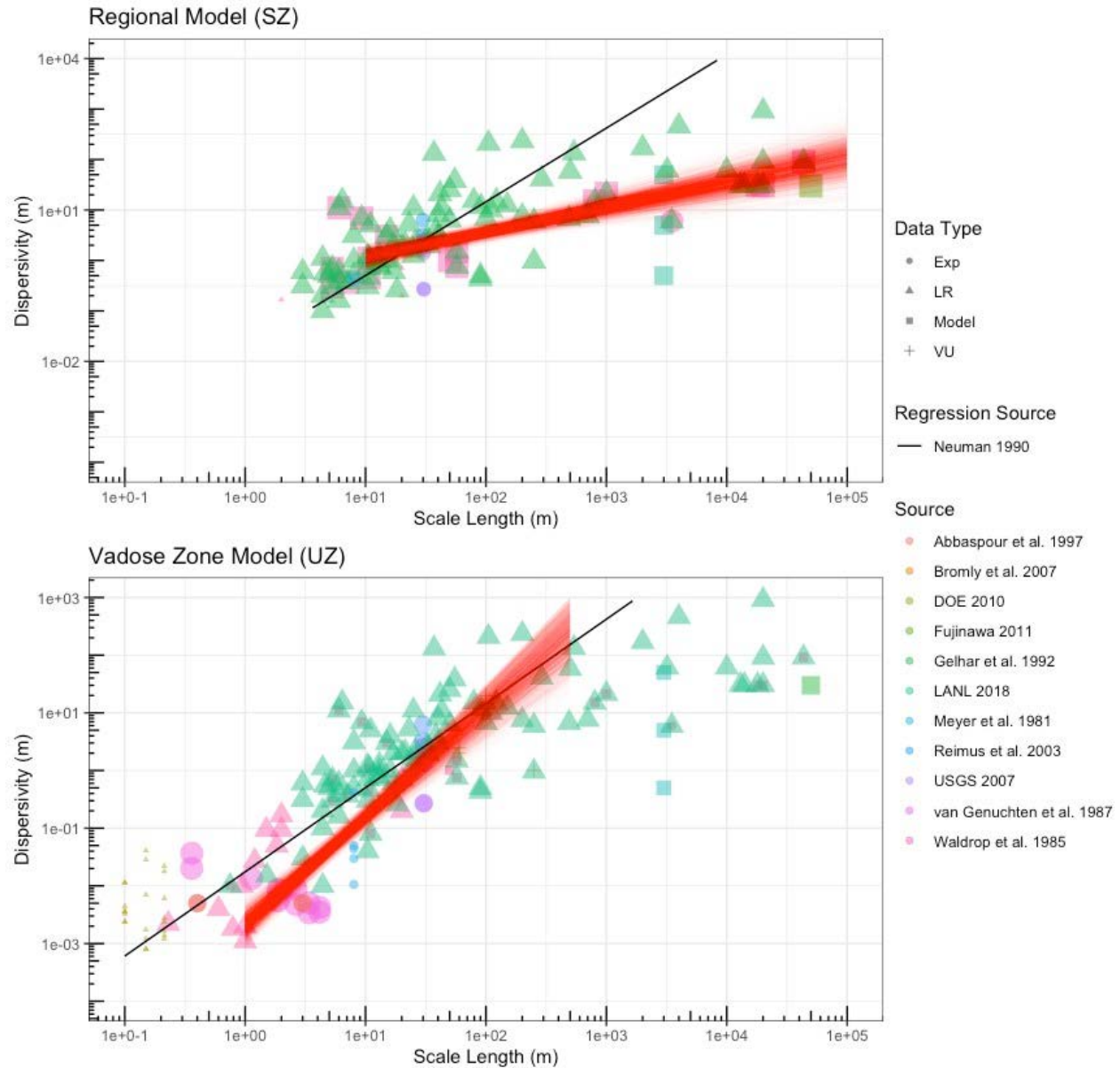
Figure D-4.5-4   Bootstrap estimated regression lines in red for transverse vertical (top) and transverse horizontal (bottom) dispersivities versus longitudinal dispersivity
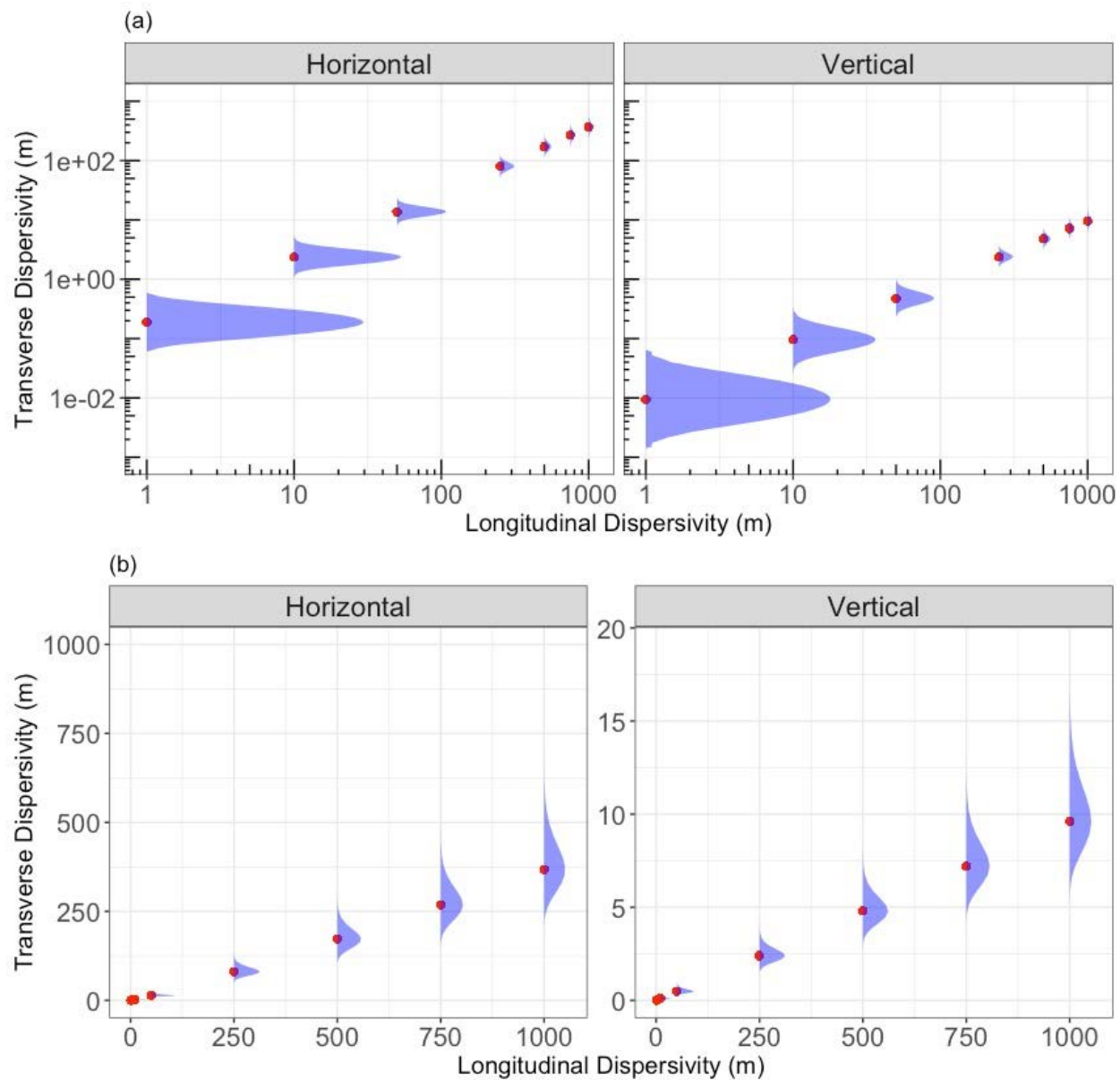
Figure D-4.5-5   Plots of the distributions for transverse dispersivities on the (a) log10 scale and (b) original scale for selected longitudinal dispersivities (1, 10, 50, 250, 500, 750, and 1000 m)
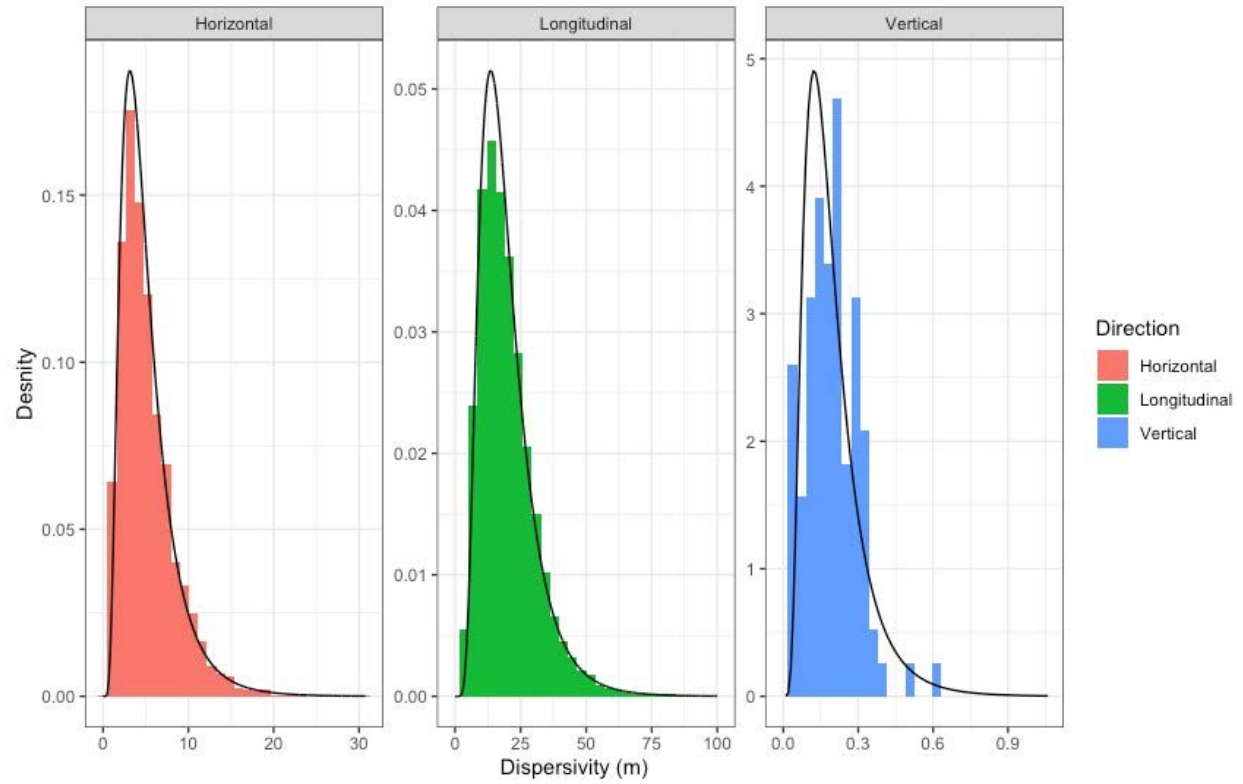
Figure D-4.5-6   Distributions developed for dispersivity in the RRM
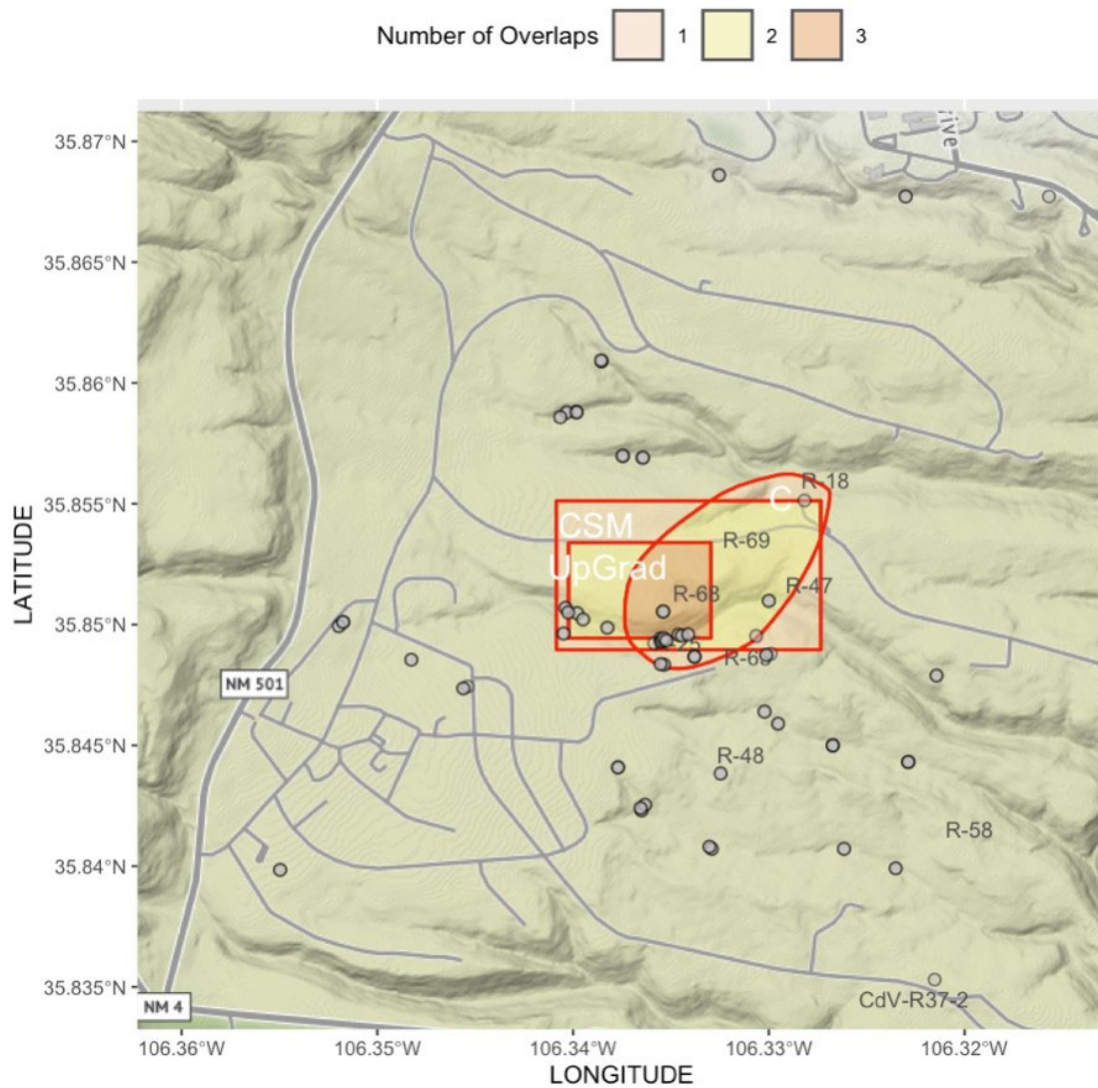
Figure D-4.6-1   Lines of evidence used to inform the primary source location
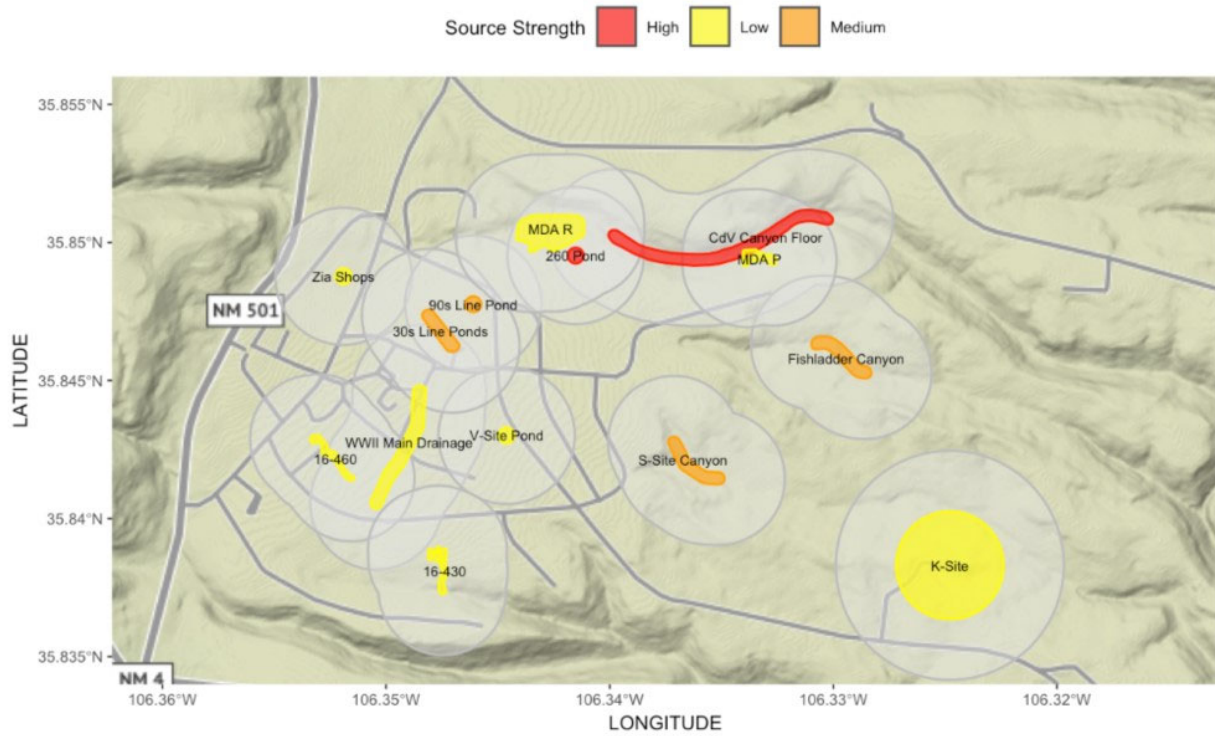
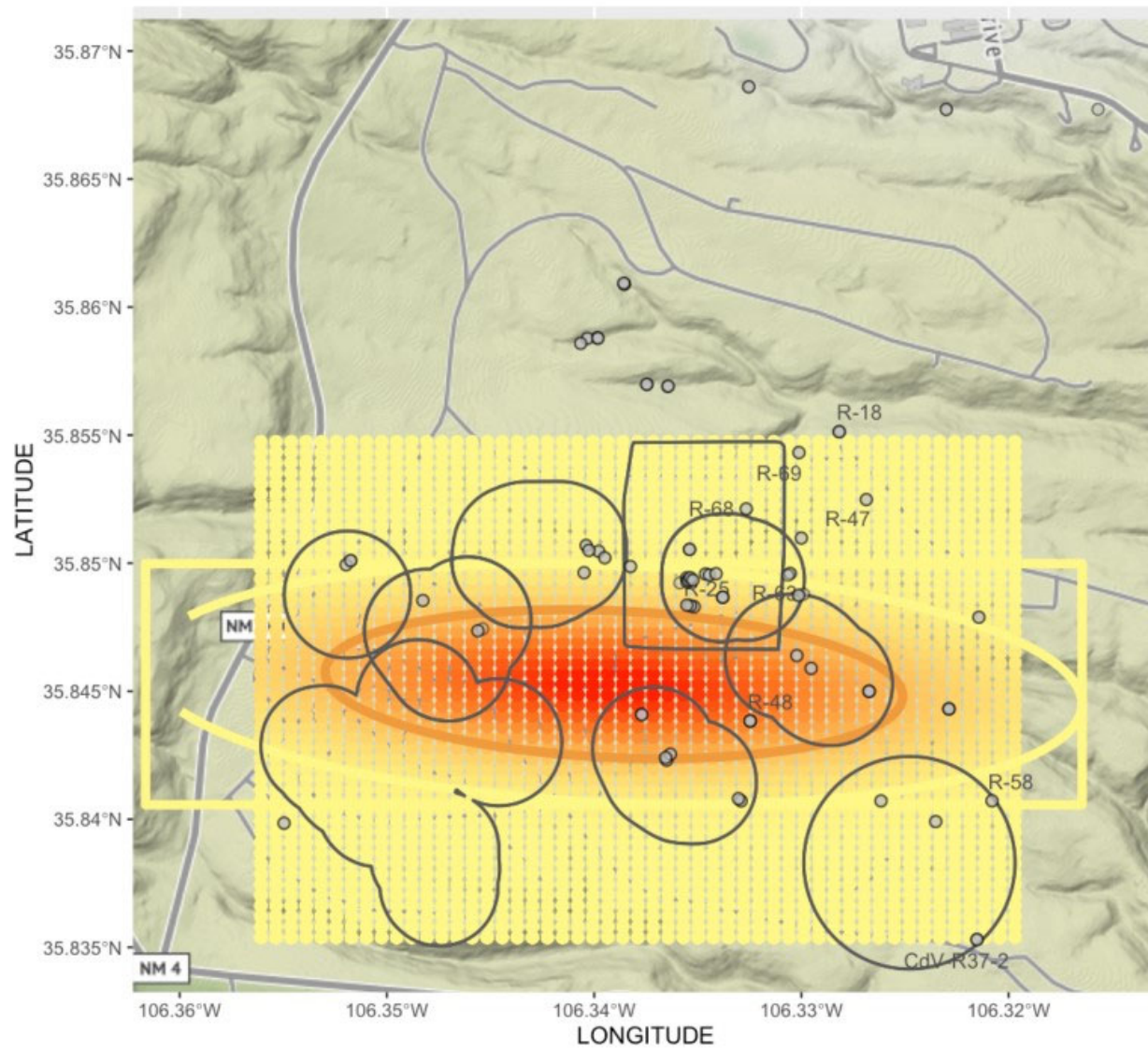**Figure D-4.6-2   Potential sources of surface contamination ranked by their likelihood to contaminate the regional aquifer**
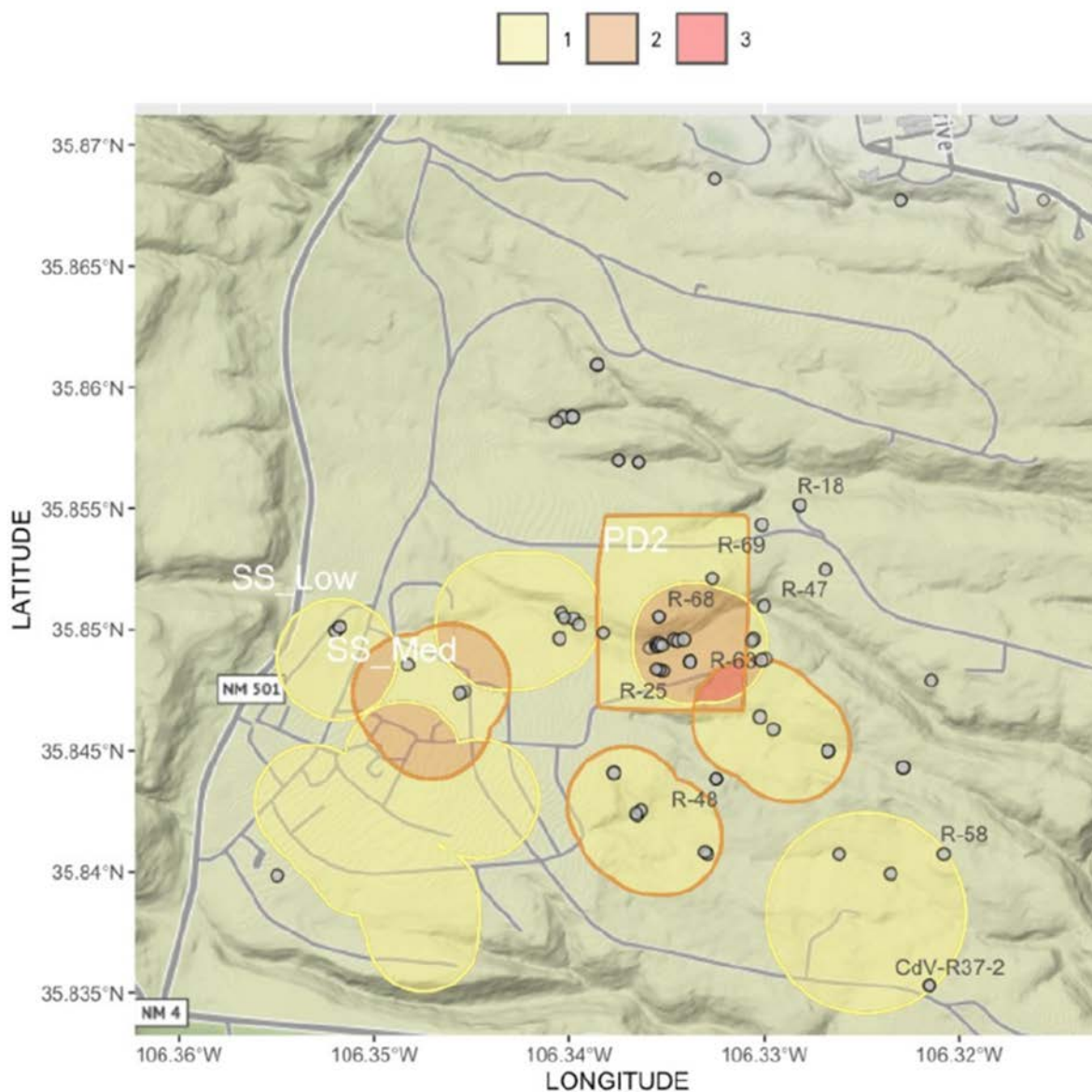
Figure D-4.6-3   Lines of evidence used to inform the secondary source location
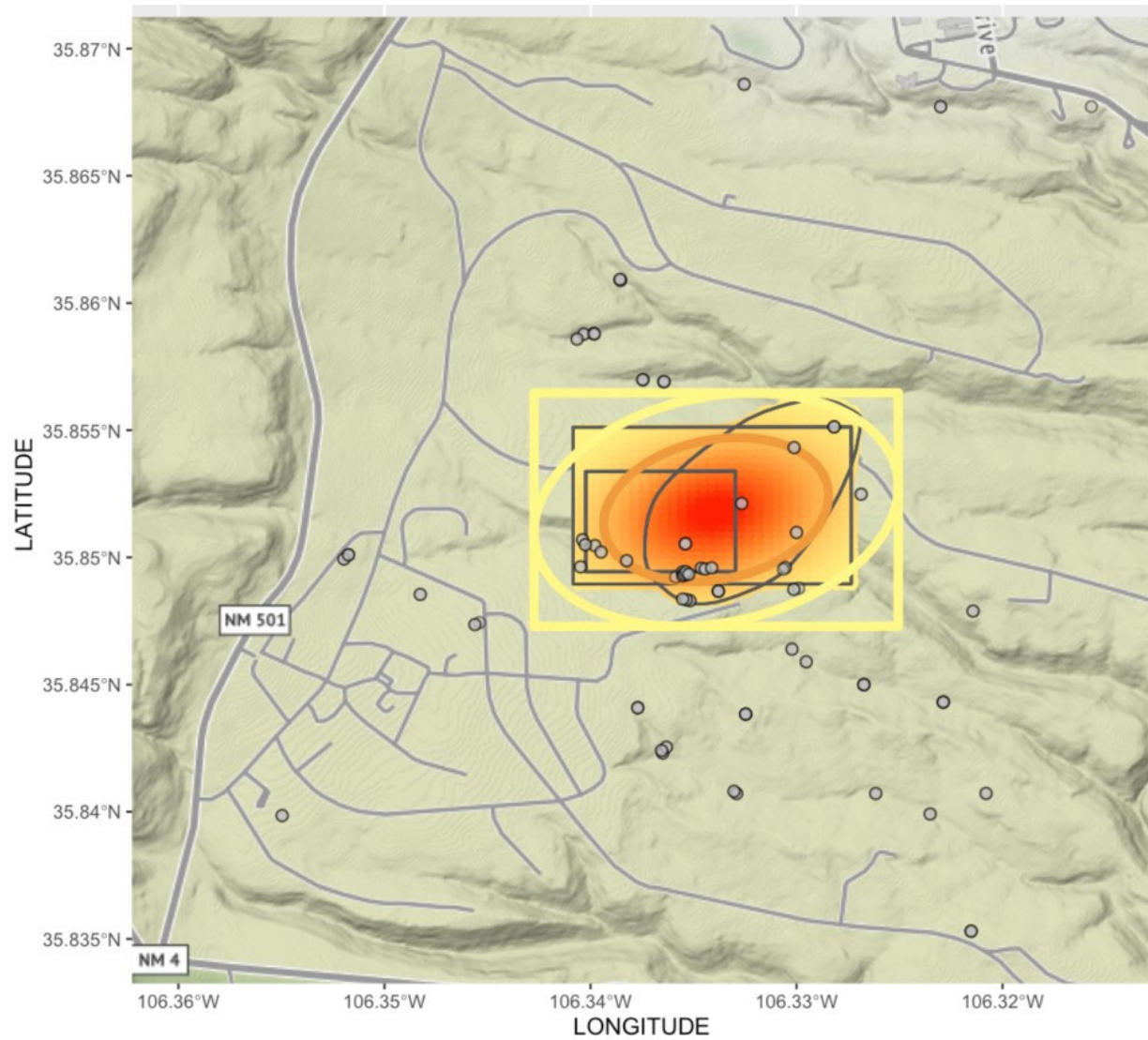
Figure D-4.6-4   Primary source distribution for source center location

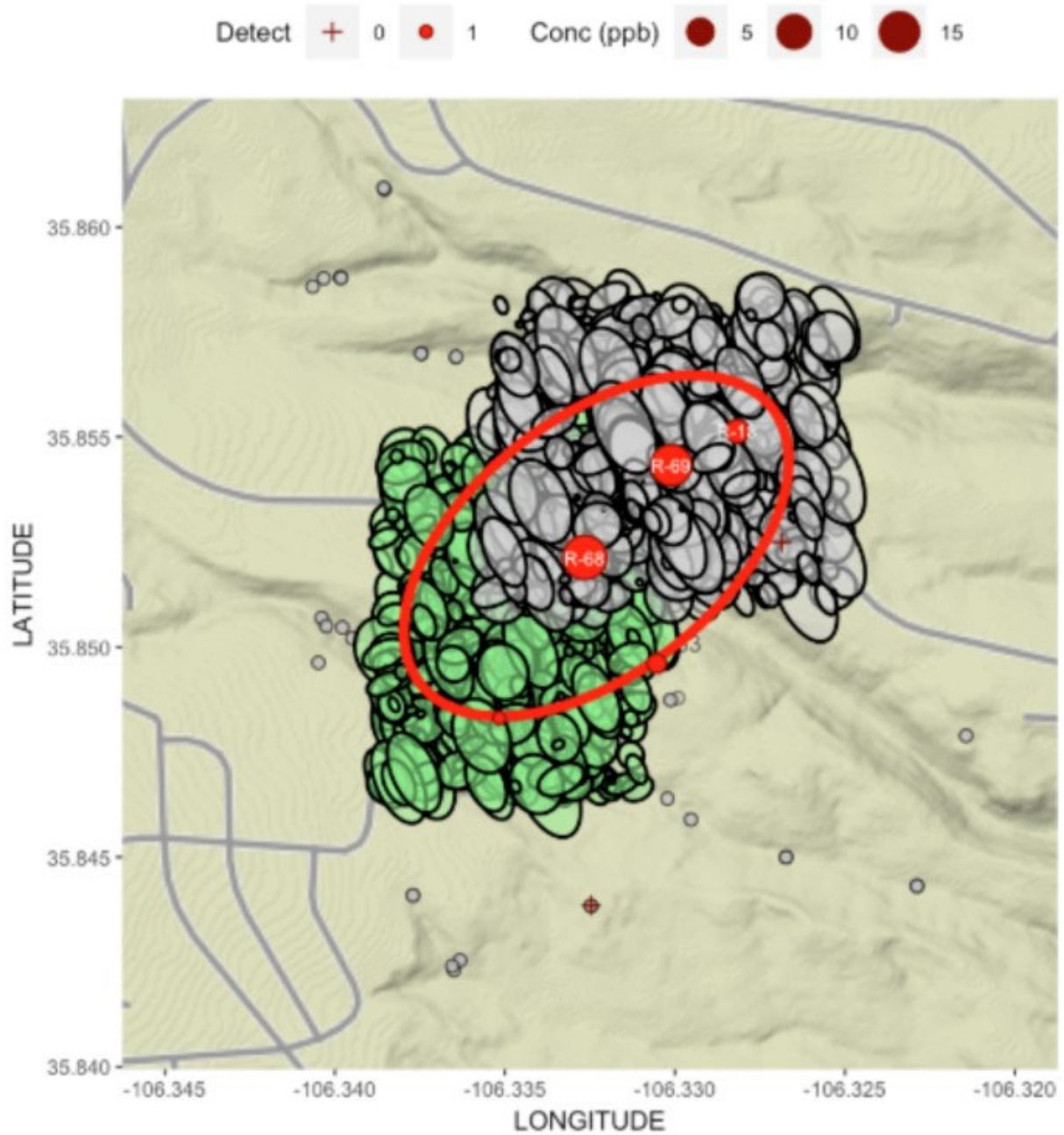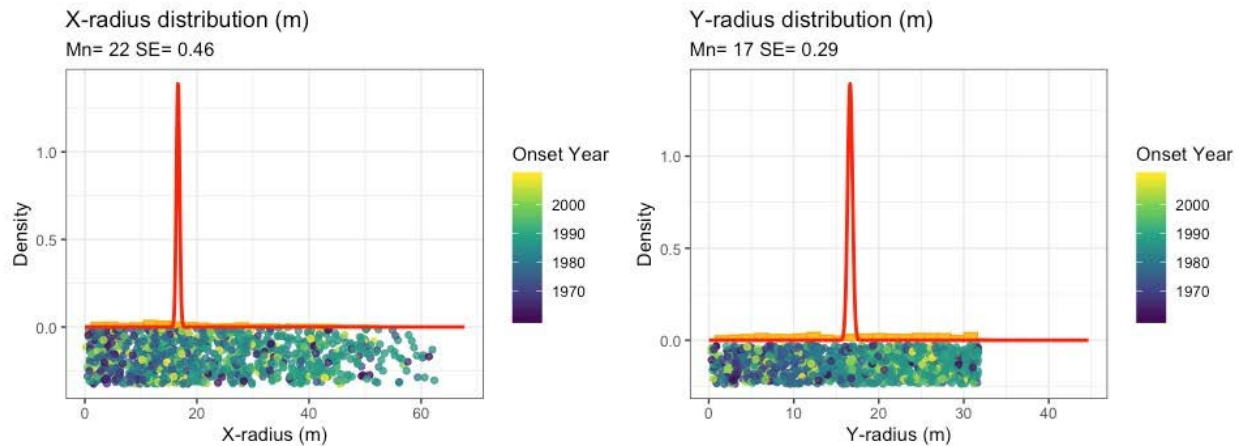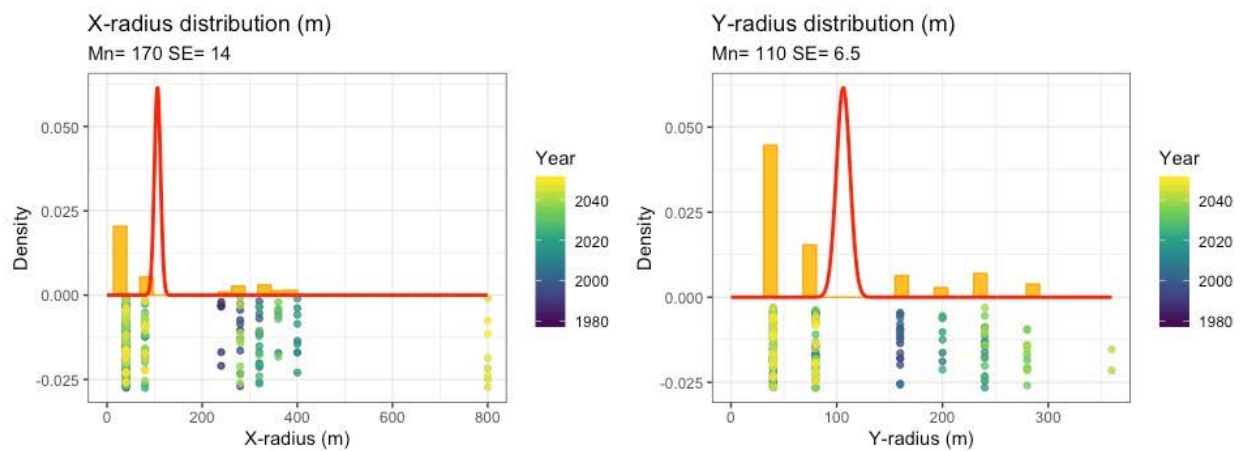**Figure D-4.6-5   Secondary source distribution for source center location**
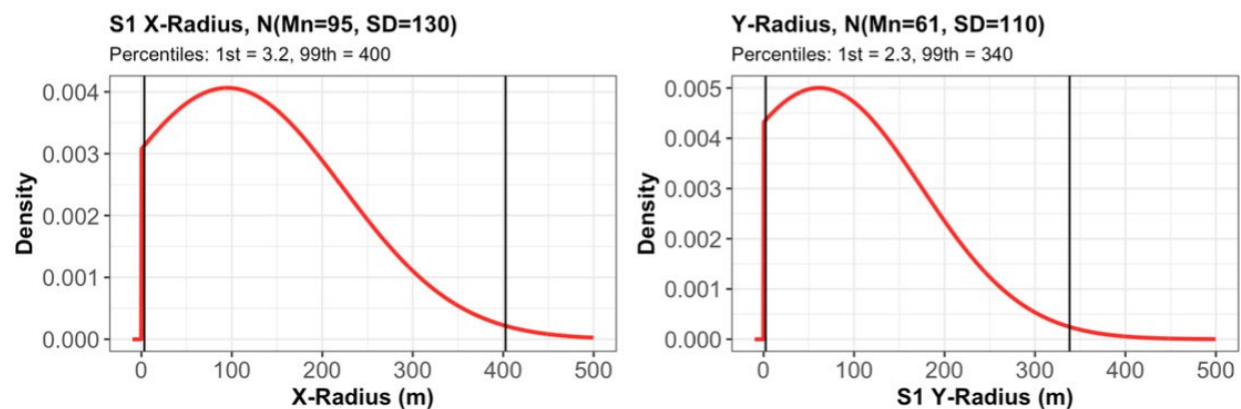
Figure D-4.6-6   Results from the P&D analysis

Figure D-4.6-7   Distributions developed for only the P&D analysis

Figure D-4.6-8   Histogram of source radii from RVZM output and distribution based on only RVZM results

Figure D-4.6-9   Radii distributions for the primary source
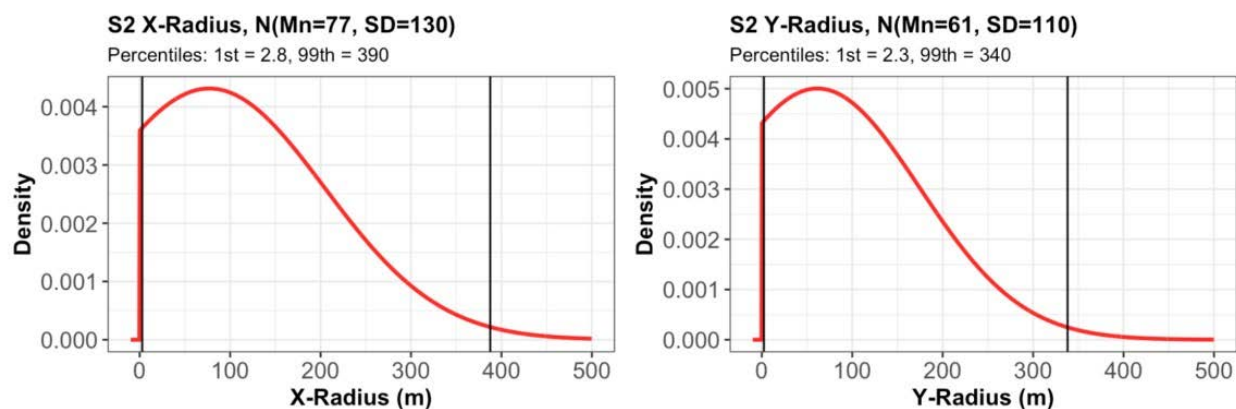
Figure D-4.6-10   Radii distributions for the secondary source
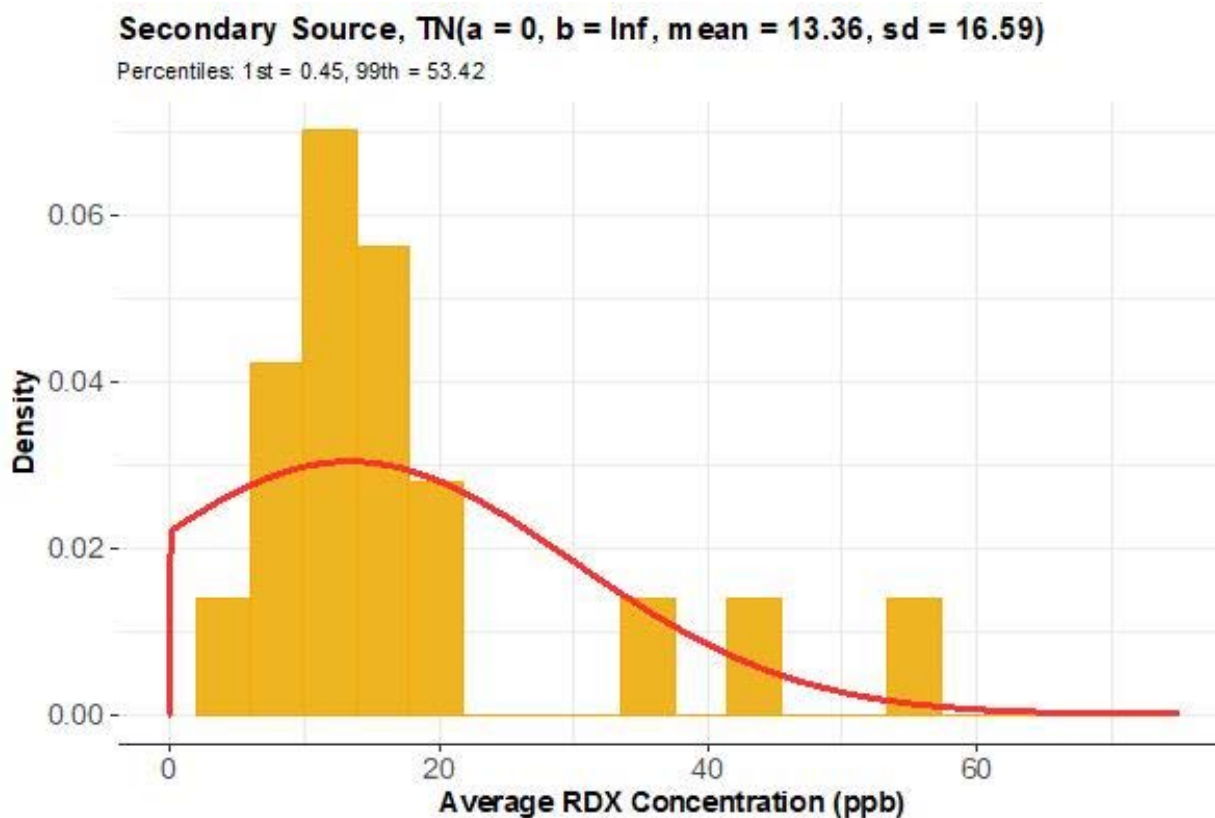

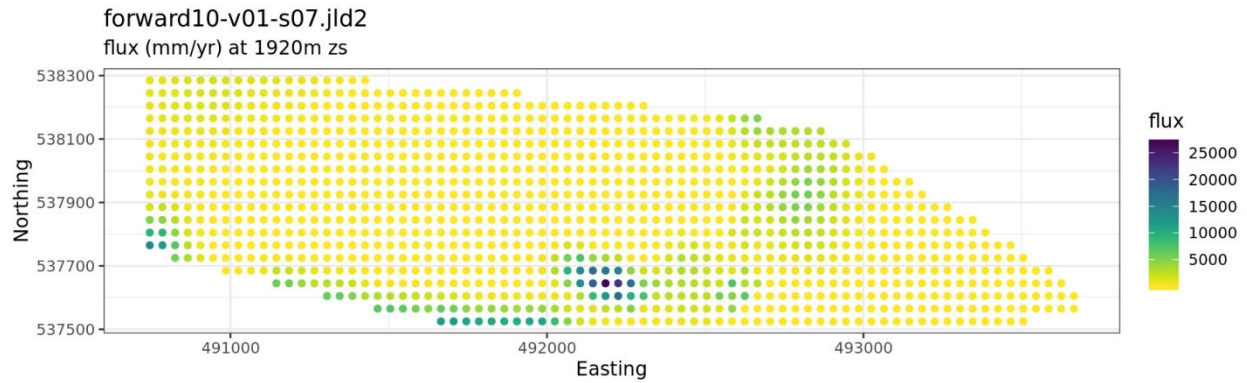**Figure D-4.6-11   Distribution for primary and secondary source concentration at the center of the hydraulic window plotted over histograms of RVZM output used to inform distribution**

Figure D-4.6-12   One of 19 VZ model results for recharge rate at the regional aquifer plotted in space (with boundary nodes removed) demonstrates the predictions of preferential versus background recharge occurring at the regional aquifer.
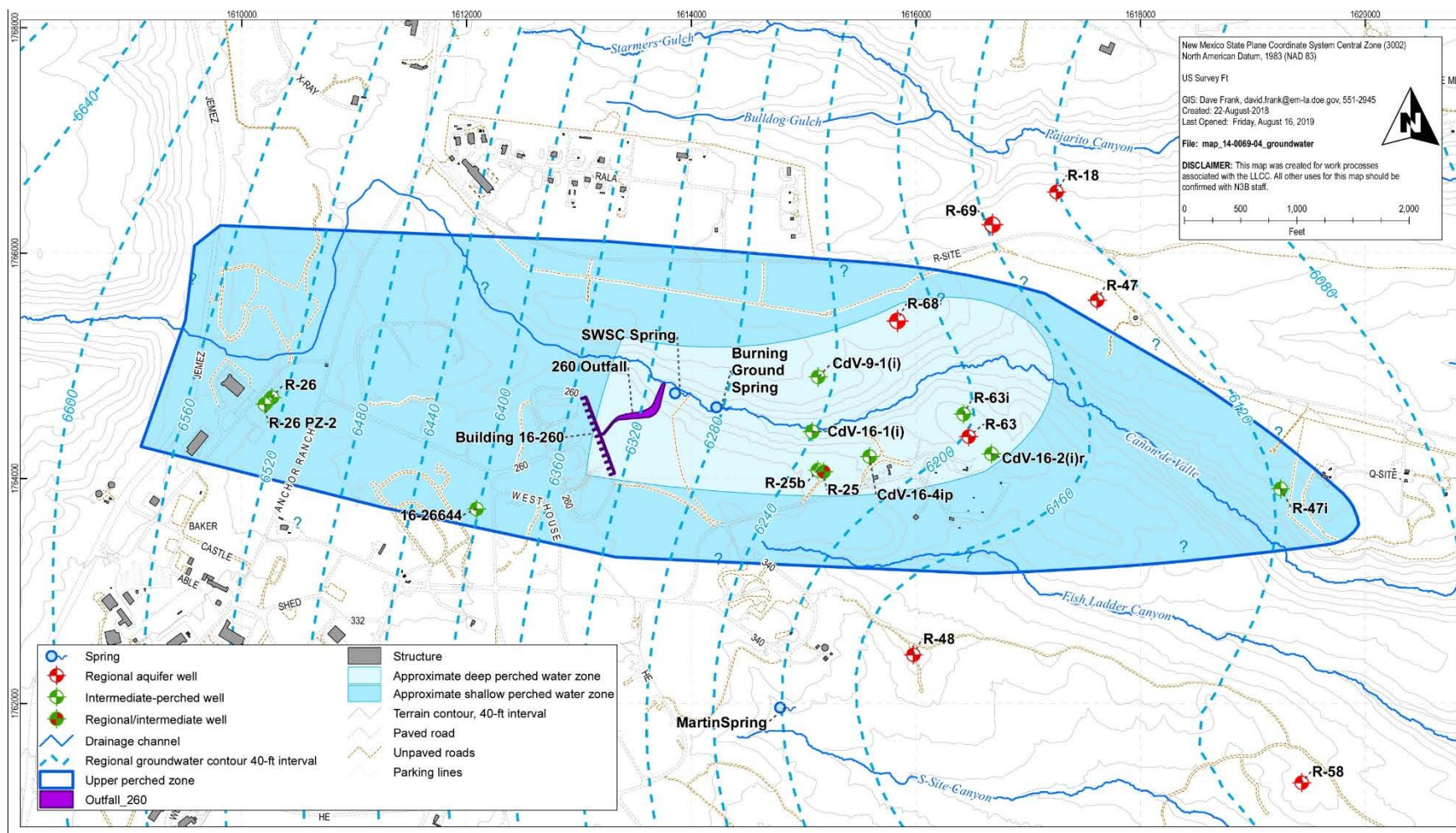
Figure D-4.6-13   Map showing regional water table contours, approximate extents of perched zones in the VZ, Cañon de Valle location, and wells in the vicinity of the regional aquifer RDX plume. The distribution for source 3 center is shown in the dotted lines, and the distribution for the size is between the maximum and minimum x and y radii plotted with the solid lines.
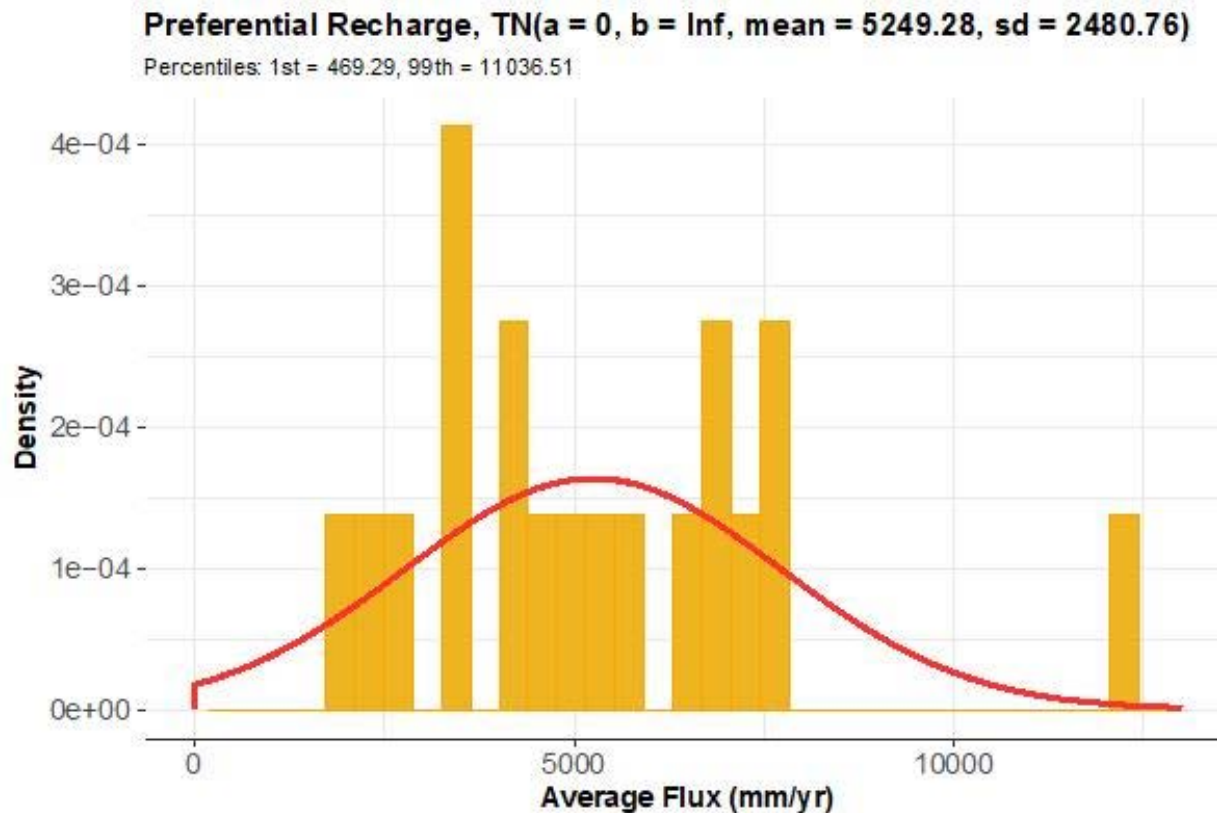
Figure D-4.6-14   Distribution for total recharge (i.e., the sum of preferential recharge, primary recharge, and secondary recharge) from VZ to regional aquifer (mm/yr)
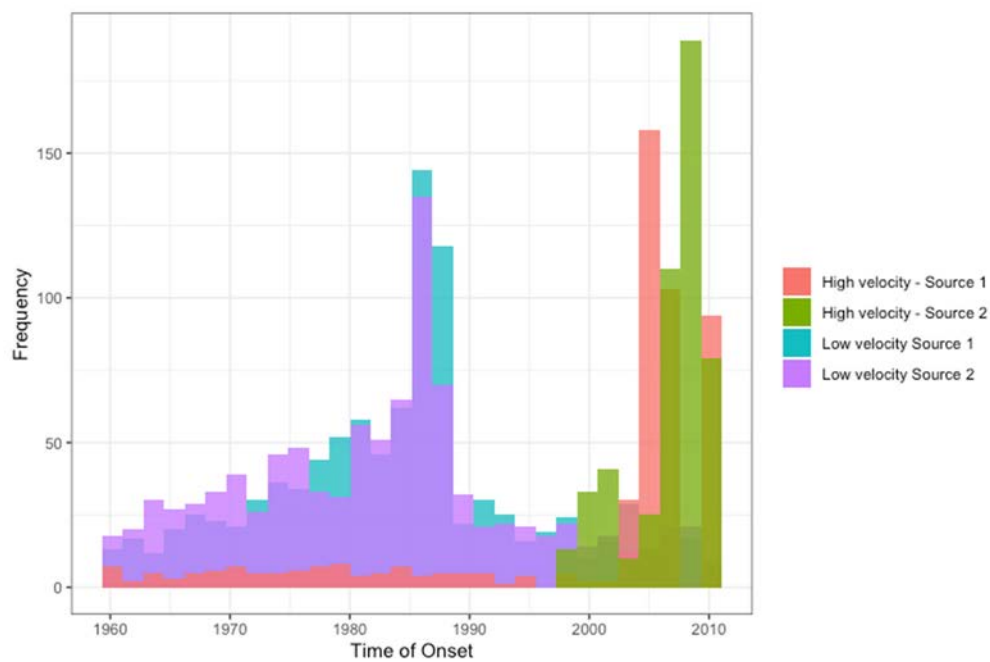
Figure D-4.6-15   Time of onset results for the double-source P&D tool
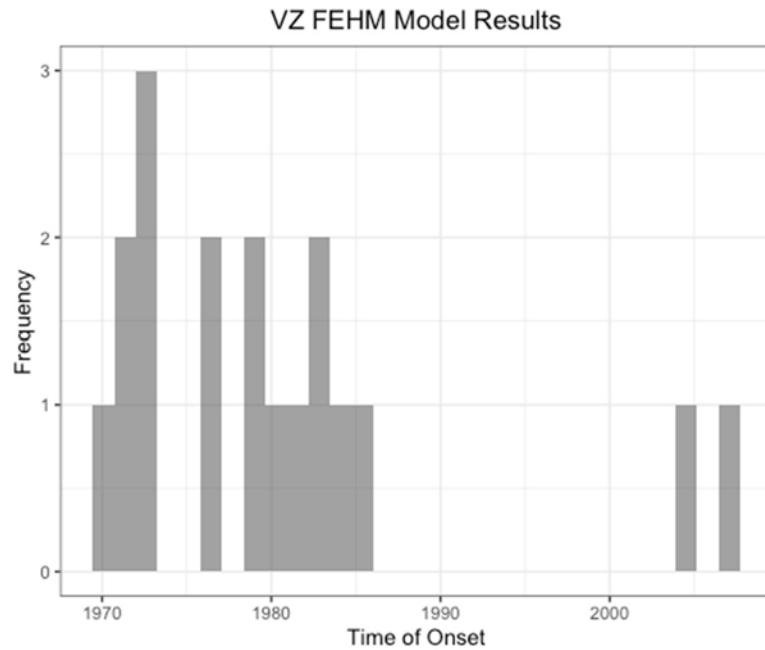
Figure D-4.6-16   Results for time of onset at the regional aquifer from the RVZM
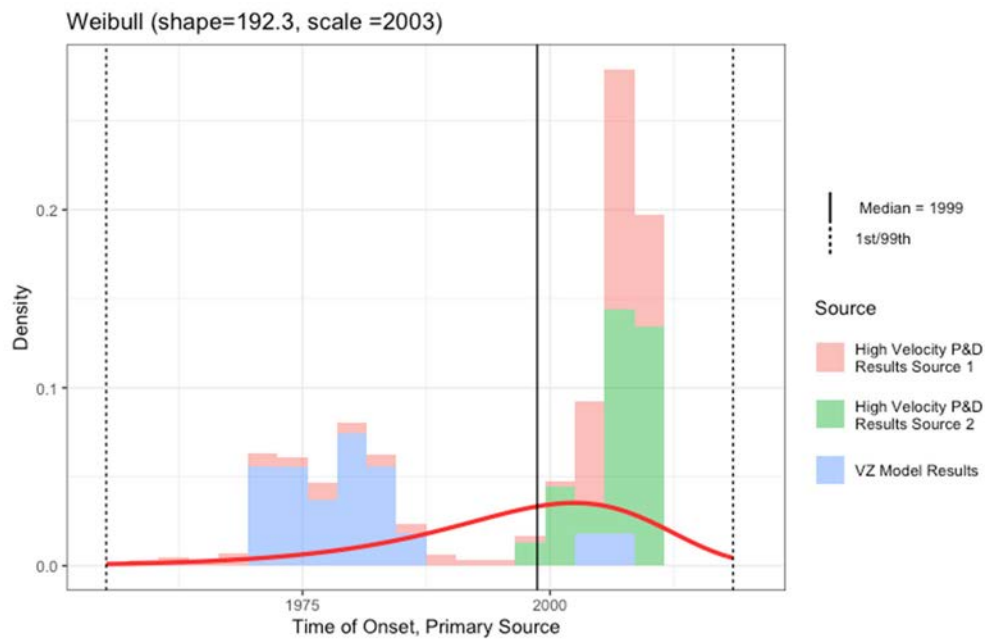
Figure D-4.6-17   Distribution developed for time of onset
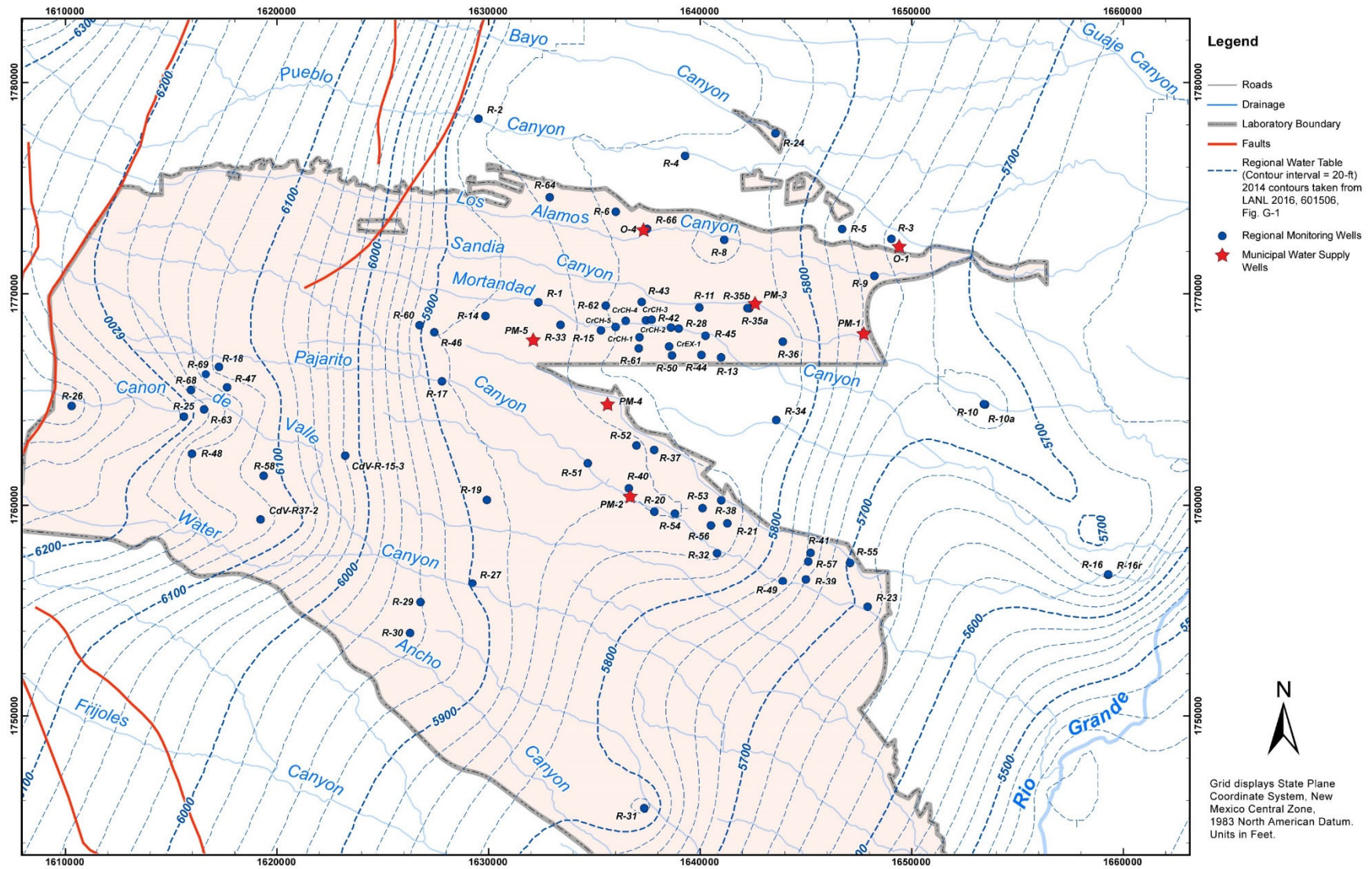
Figure D-4.7-1   Regional water table at LANL
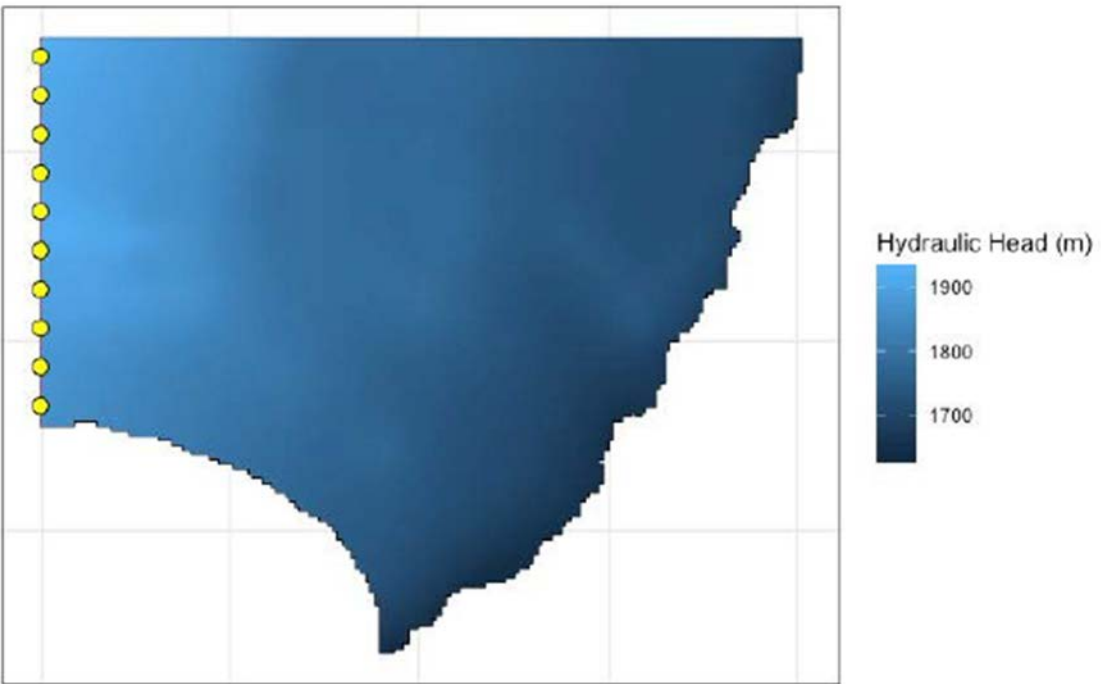
Note: Yellow dots are an example set of 10 points (actual distribution development was based on 100,000 points) selected along the western boundary.

Figure D-4.7-2   Raster data from the 2014 water table map used for distribution development for hydraulic head at the western boundary
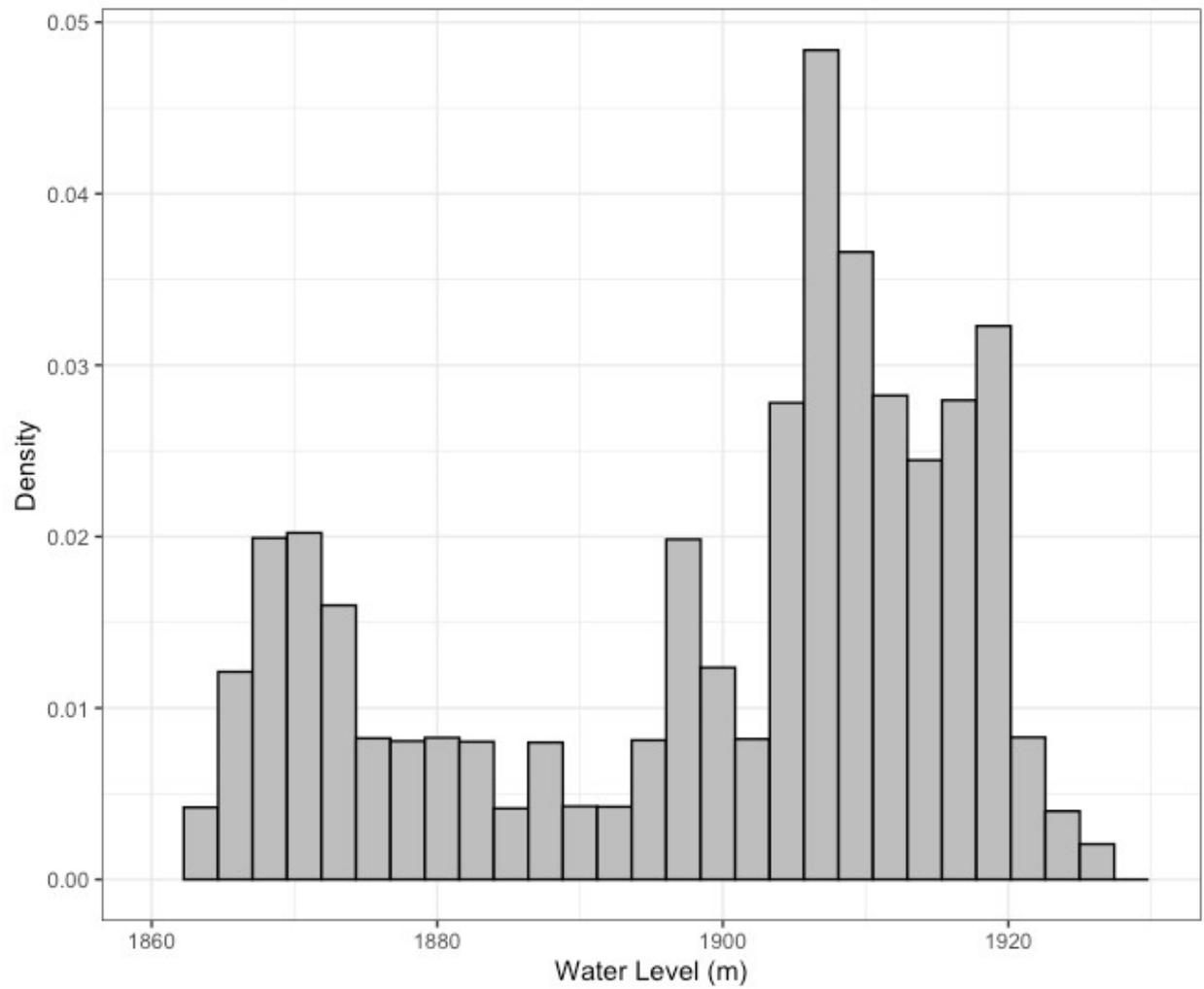
Figure D-4.7-3   Hydraulic head values at the western boundary
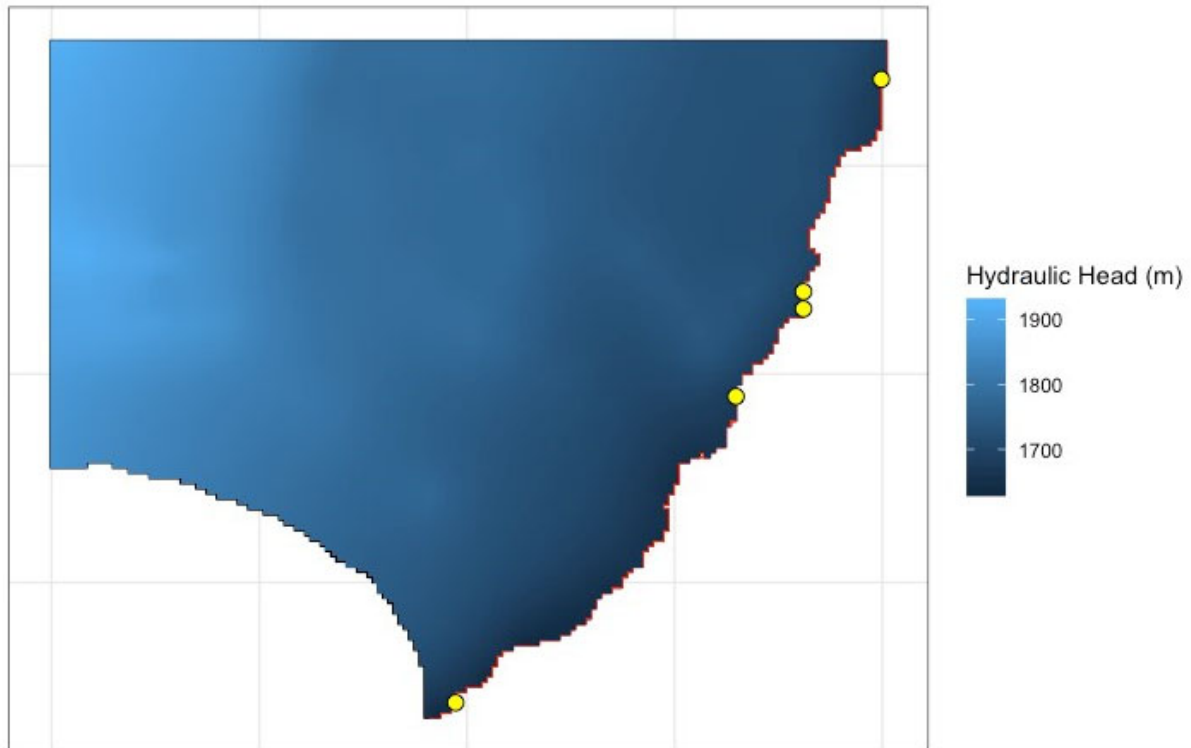
Figure D-4.7-4   Raster data from the 2014 water table map used for distribution development for hydraulic head at the eastern boundary
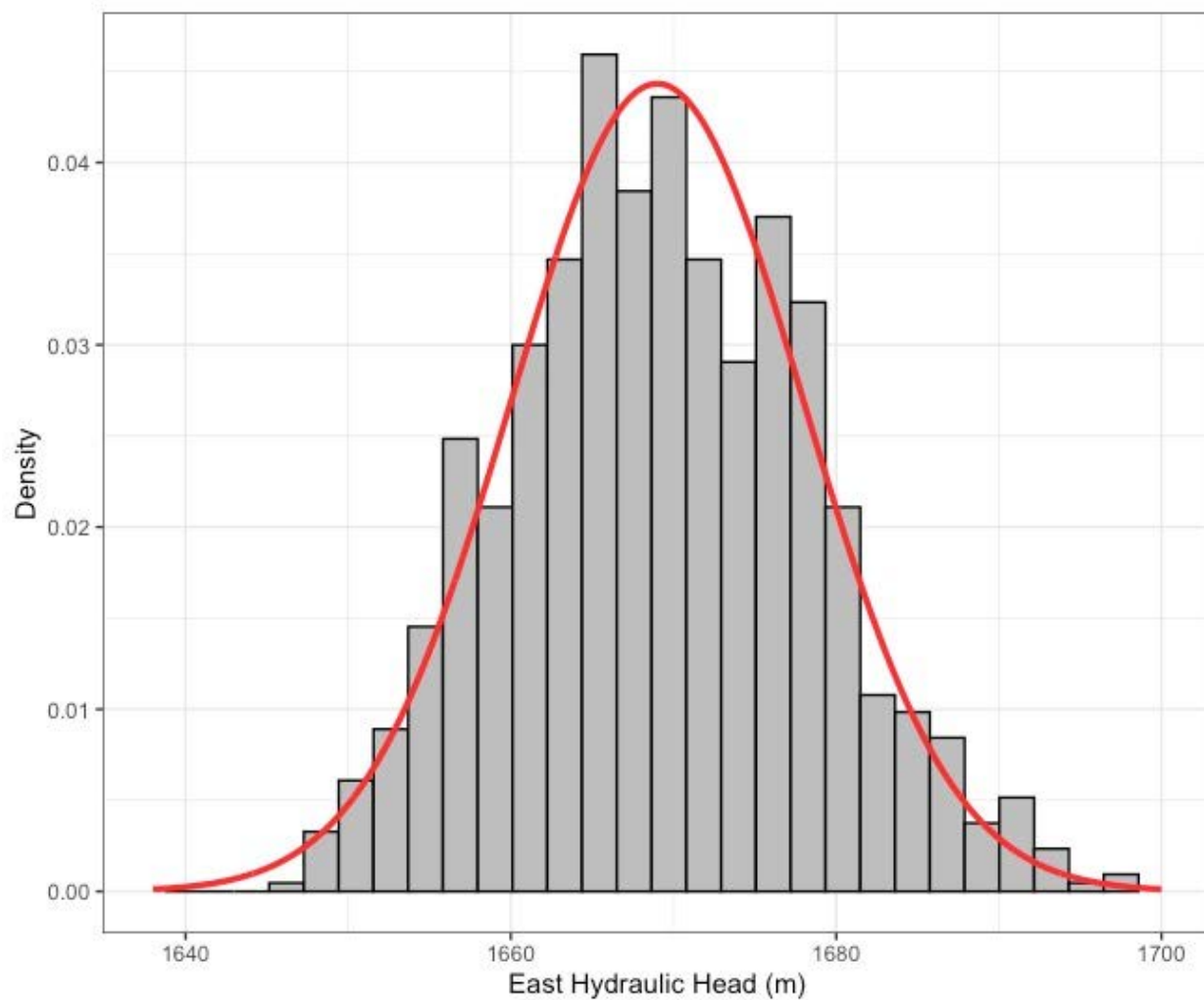
Figure D-4.7-5   Preliminary distribution of values for hydraulic head at the eastern boundary based on the 2014 water level map
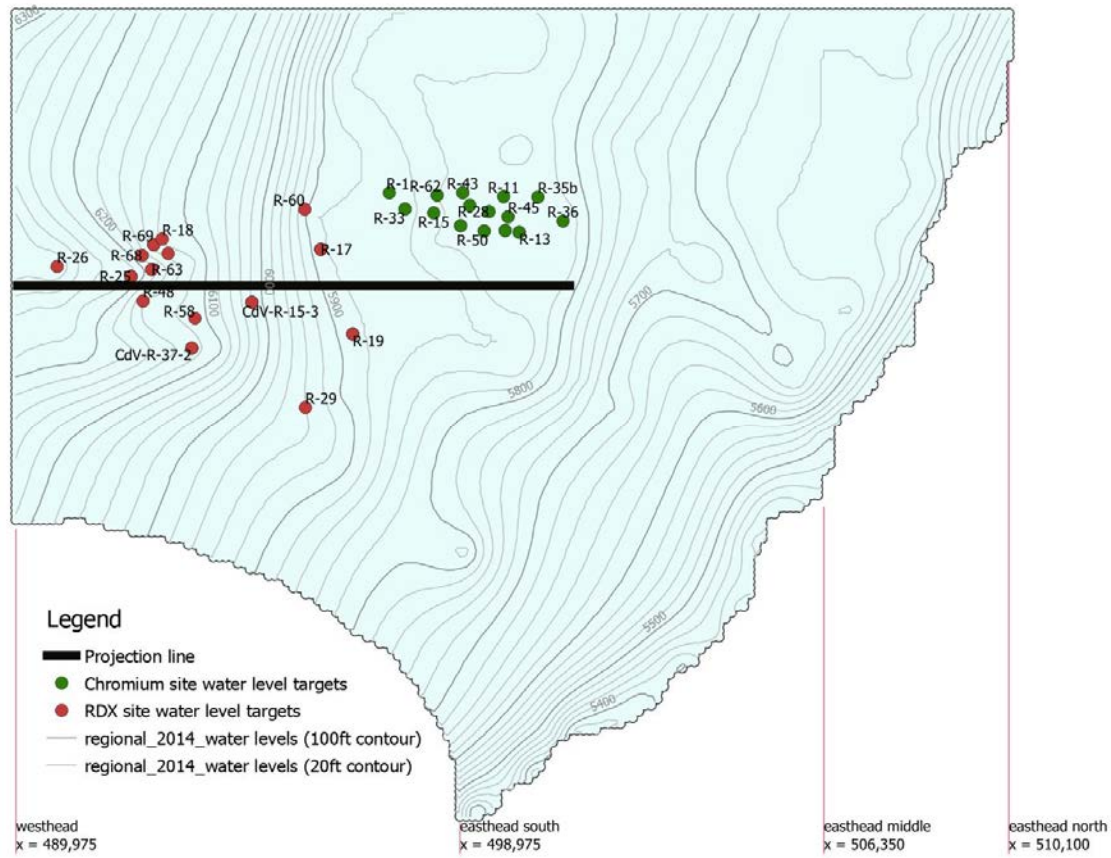
Figure D-4.7-6   Spatial distribution of wells with groundwater level targets at the RDX and chromium sites
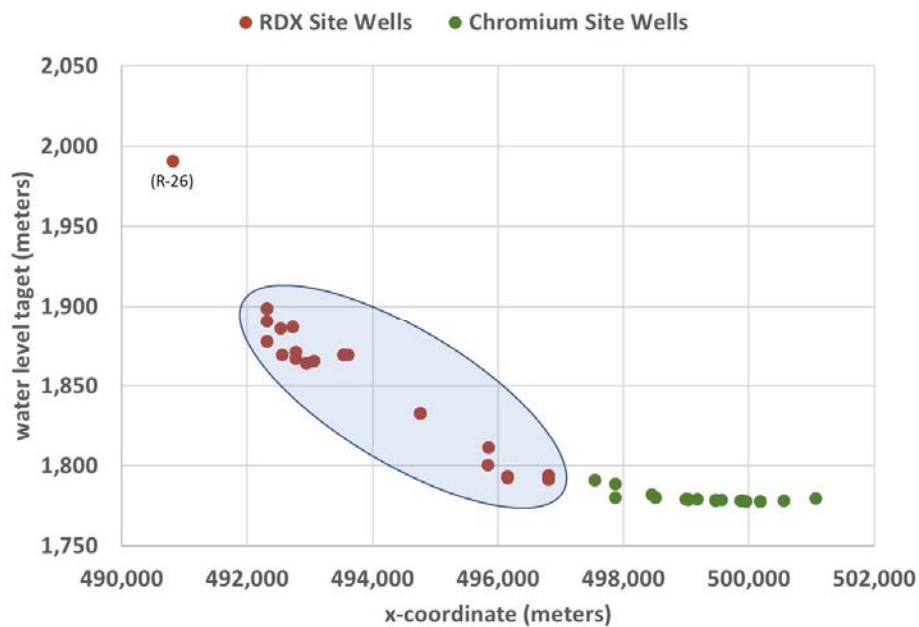
Figure D-4.7-7   Gradient in RDX versus chromium areas
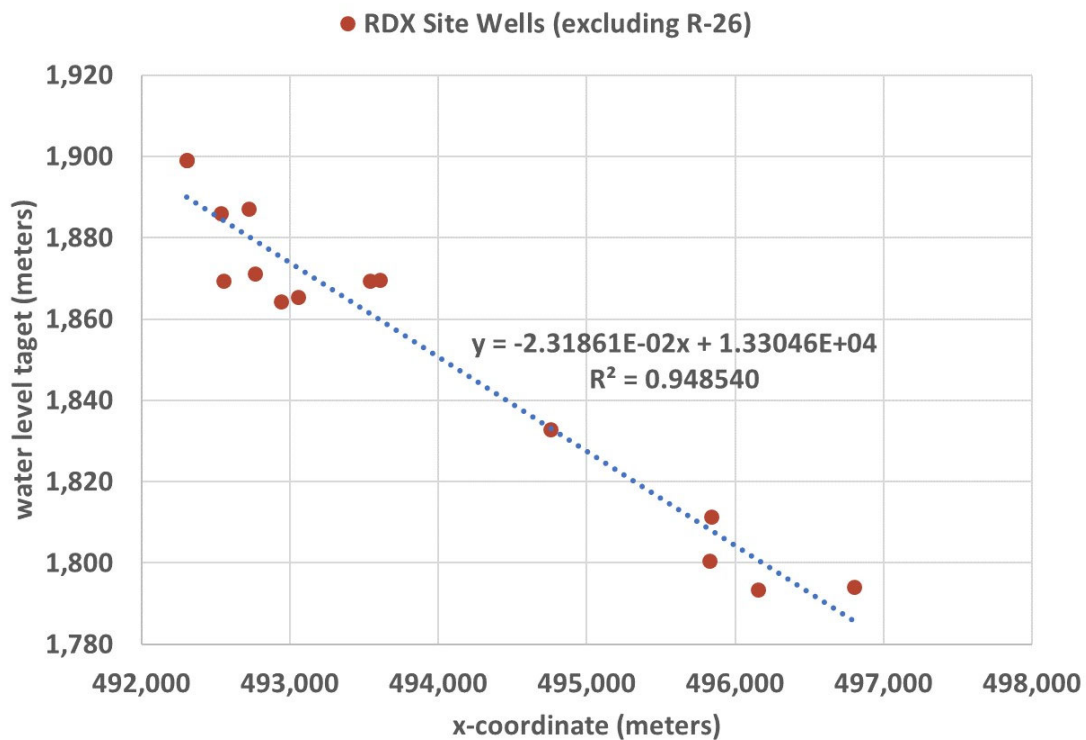
Figure D-4.7-8   Regression of RDX area wells

Observed Coefficients of Adsorption for RDX in Bulk Samples
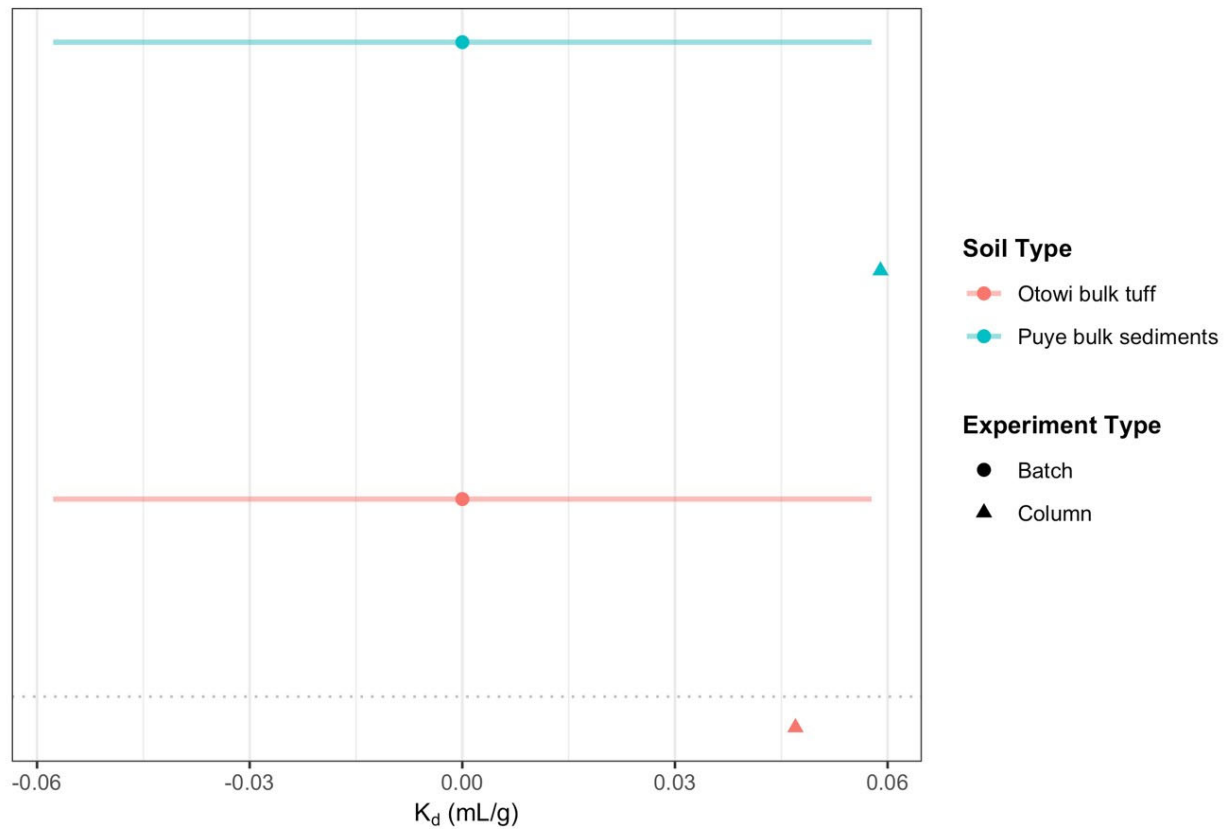
Notes: The solid (colored) horizontal lines represent an approximate 95% confidence interval for the mean K_d. Some records did not have the spread information, and no bars are provided for those records. Horizontal dashed lines are included to help separate the different soil types.

Figure D-4.9-1   Dot and whisker plots of the observed RDX K_d values for bulk samples
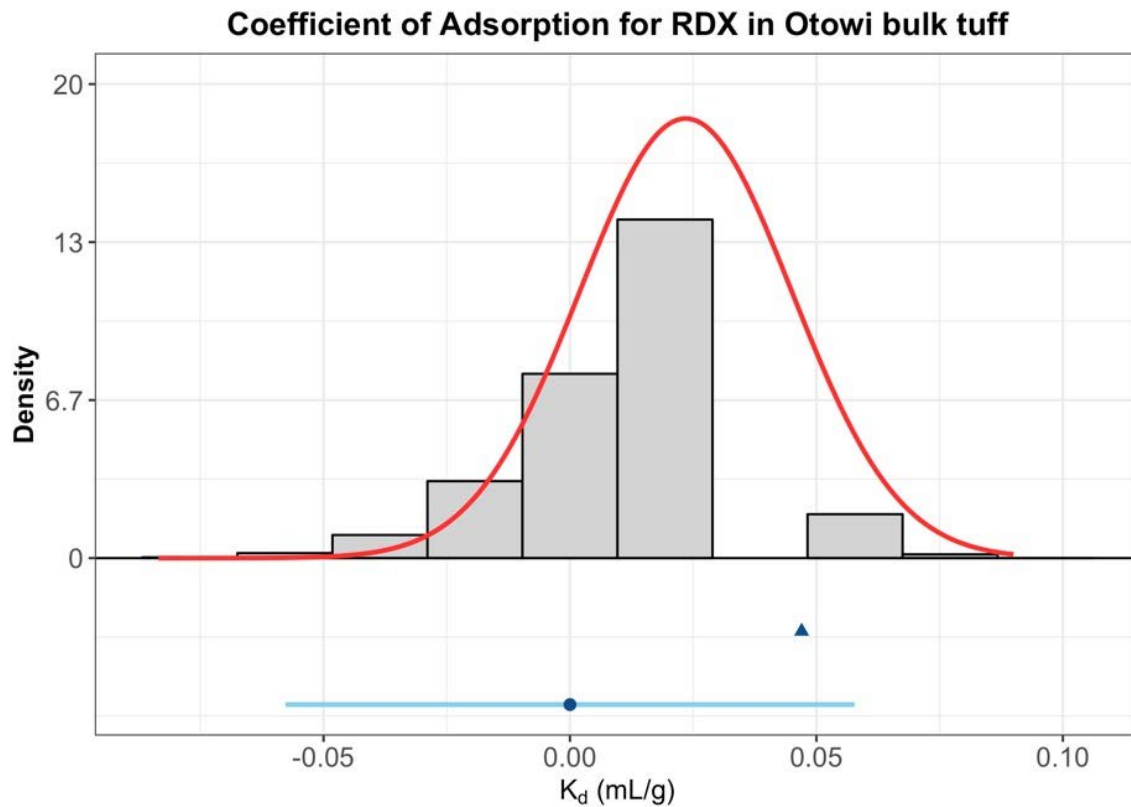
Notes: The observed mean RDX K_d. values for Otowi Formation bulk tuff are included below the plot with horizontal lines showing two standard errors in the mean for the batch experiment records. The experiment type of the record is represented on the plot by triangles (column experiment) and circles (batch experiment).

Figure D-4.9-2   Histogram of mean RDX K_d values obtained from the distribution development procedure for volcanic materials with the corresponding fitted normal distribution (red curve)
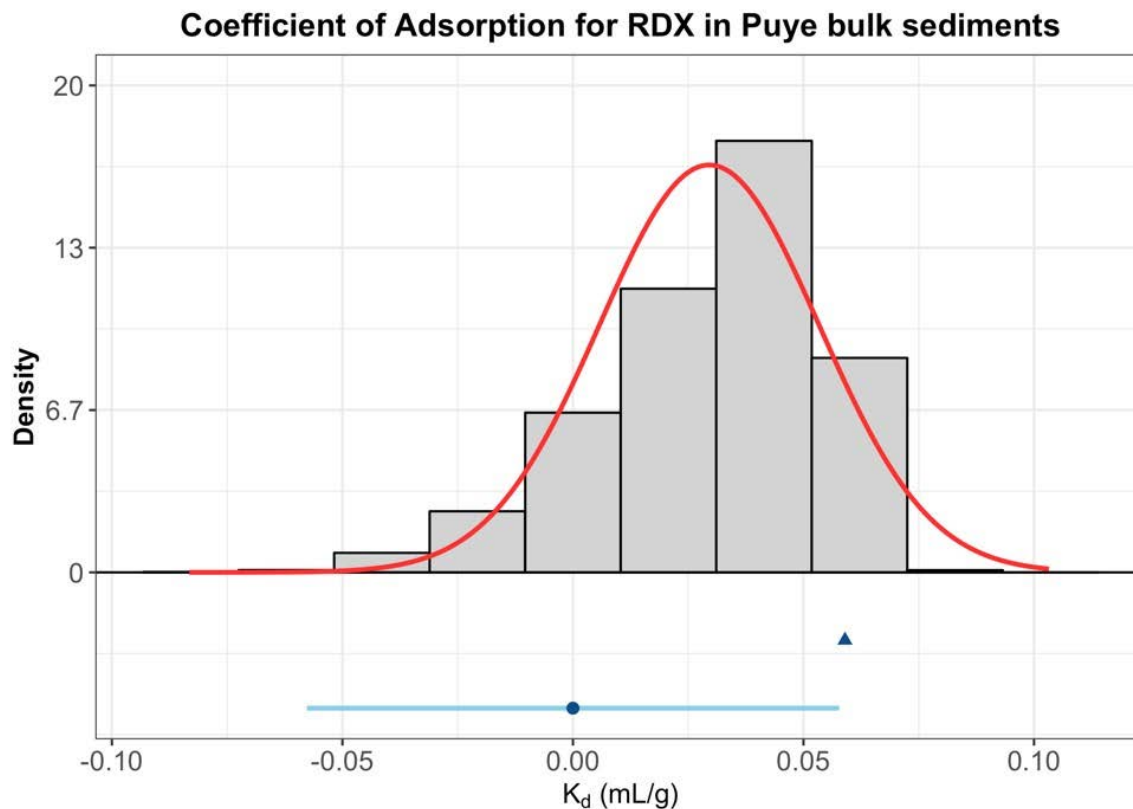
Notes: The observed mean RDX K_d. values for Puye Formation bulk sediments are included below the plot with horizontal lines showing two standard errors in the mean for the batch experiment records. The experiment type of the record is represented on the plot by triangles (column experiment) and circles (batch experiment.)

Figure D-4.9-3   Histogram of mean RDX K_d values obtained from the distribution development procedure for sedimentary materials with the corresponding fitted normal distribution (red curve)
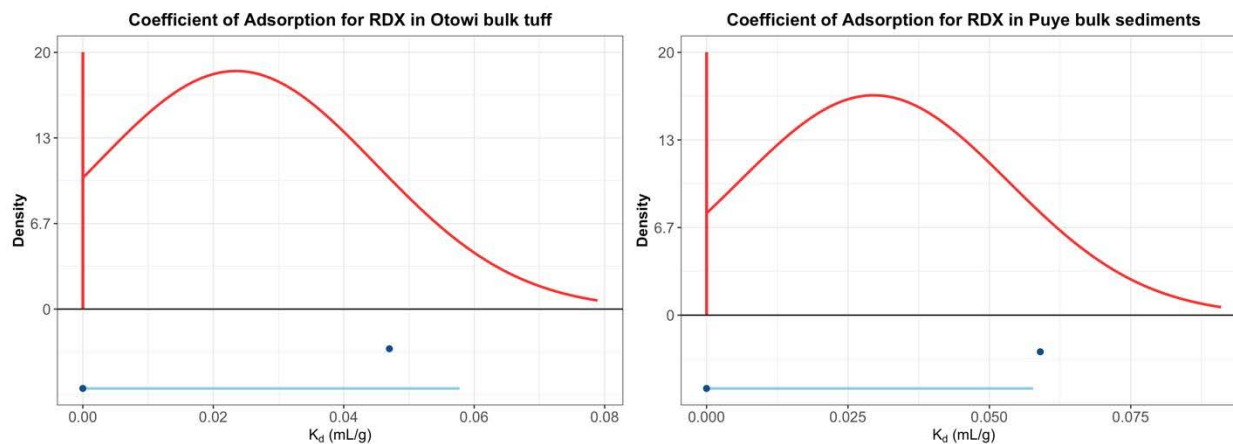
Notes: Information regarding the distributions is found in Table D-4.9-2. The vertical red lines on the left side of each plot illustrate that the distributions are bulldozed at 0 mL/g as opposed to truncated. Observed K_d coefficients are plotted below each distribution as blue points. The horizontal light-blue line extends two standard errors in the positive direction; as the distribution is bulldozed at 0 mL/g, the error bars are not displayed two standard errors in the negative direction.

Figure D-4.9-4   Final "bulldozed" distributions for average K_d coefficients of volcanic materials (left) and sedimentary materials (right)
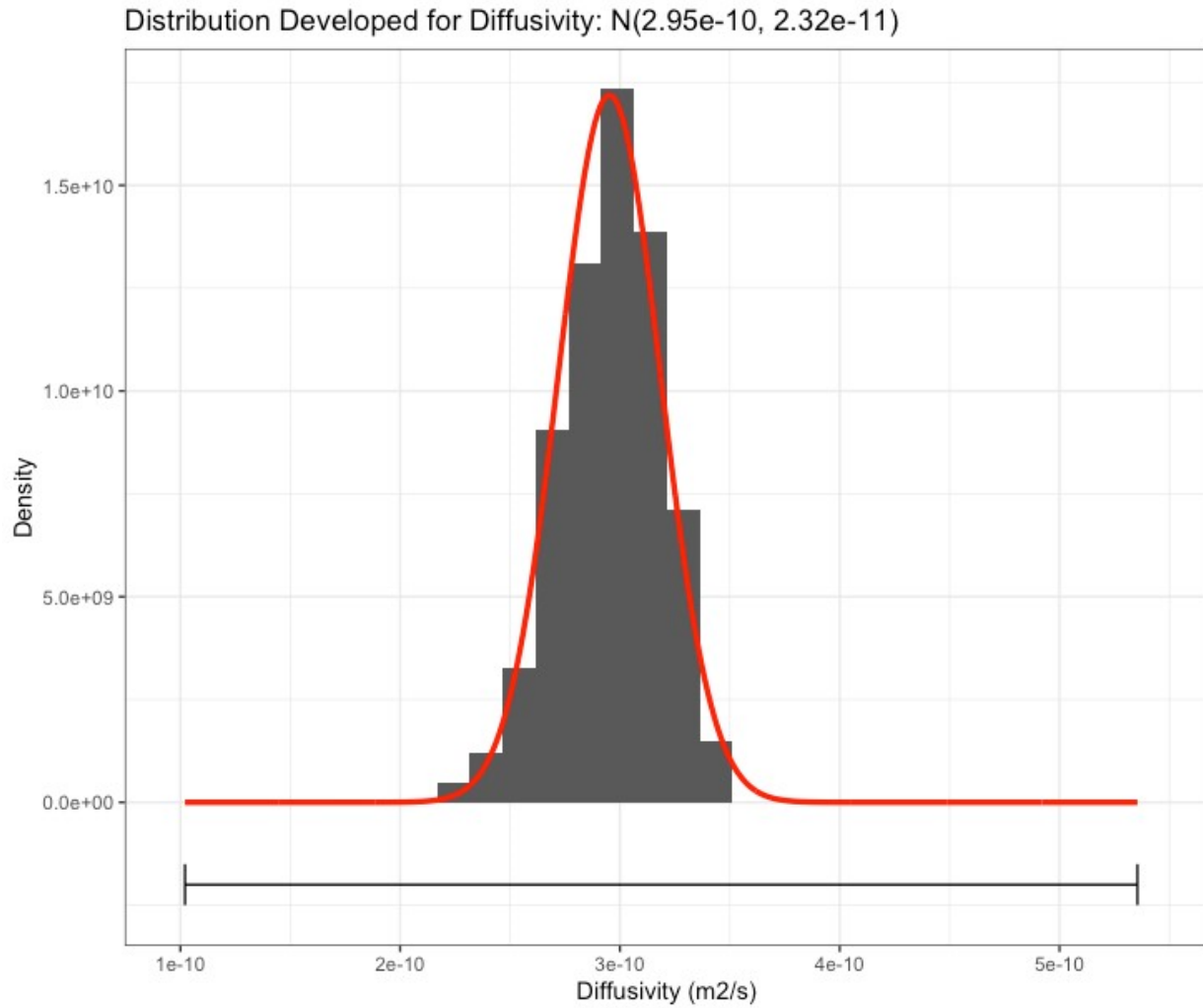
Note: The black line shows the range of possible values from which the distribution was built, using the 1st and 99th percentiles of the distribution for total porosity.

Figure D-4.10-1   Distribution developed for D$_e$
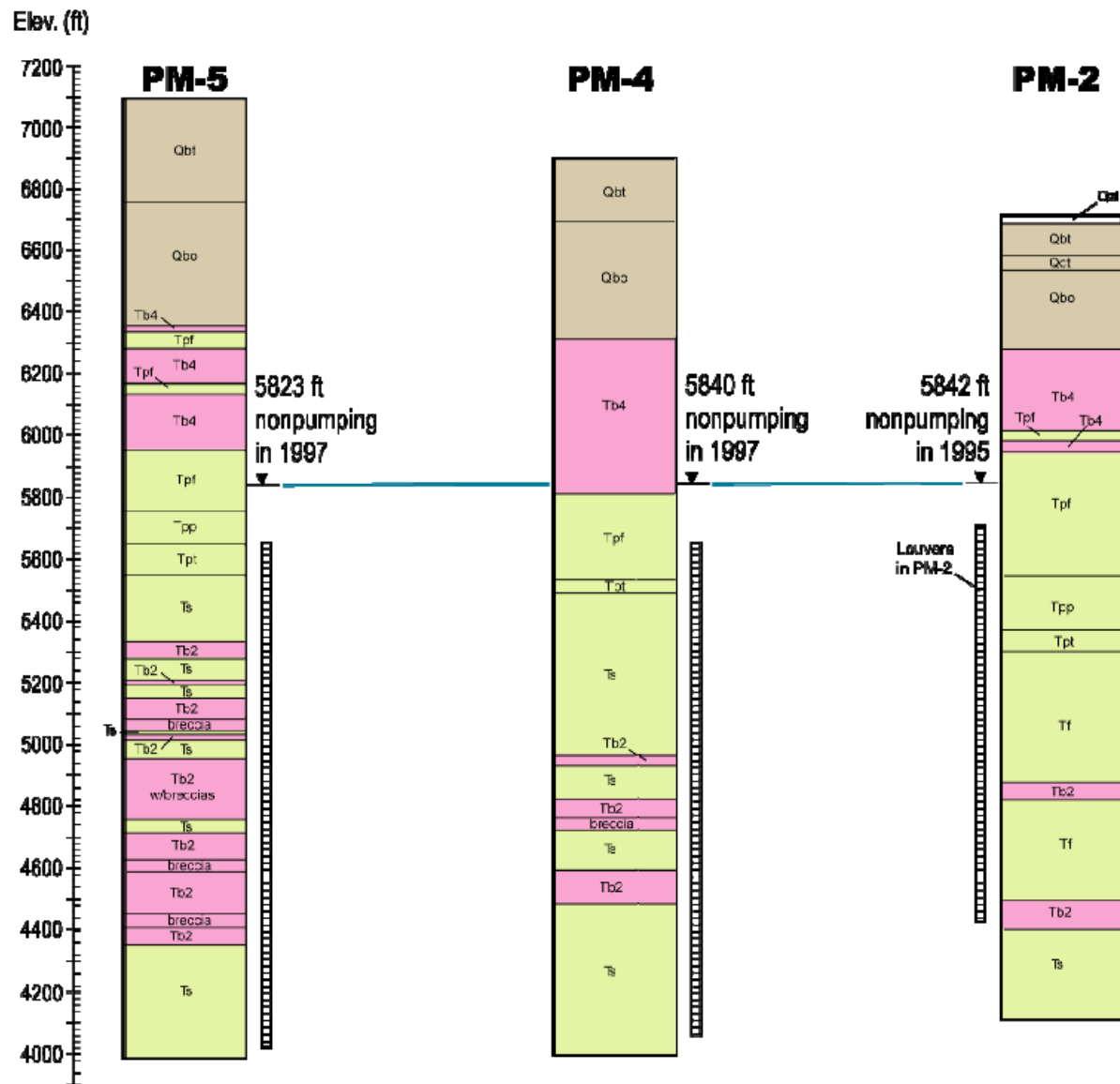
Figure D-4.12-1   Geologic contacts and screens at PM-5, PM-4, and PM-2

Weibull(2,1602.9)

	quantile	value
1	0.001	46.5
2	0.01	151.7
3	0.1	505.9
4	0.3	945.1
5	0.5	1328.4
6	0.7	1762.9
7	0.9	2457.7
8	0.99	3505.8

Show 10 entries   Search:

Showing 1 to 8 of 8 entries   Previous 1 Next
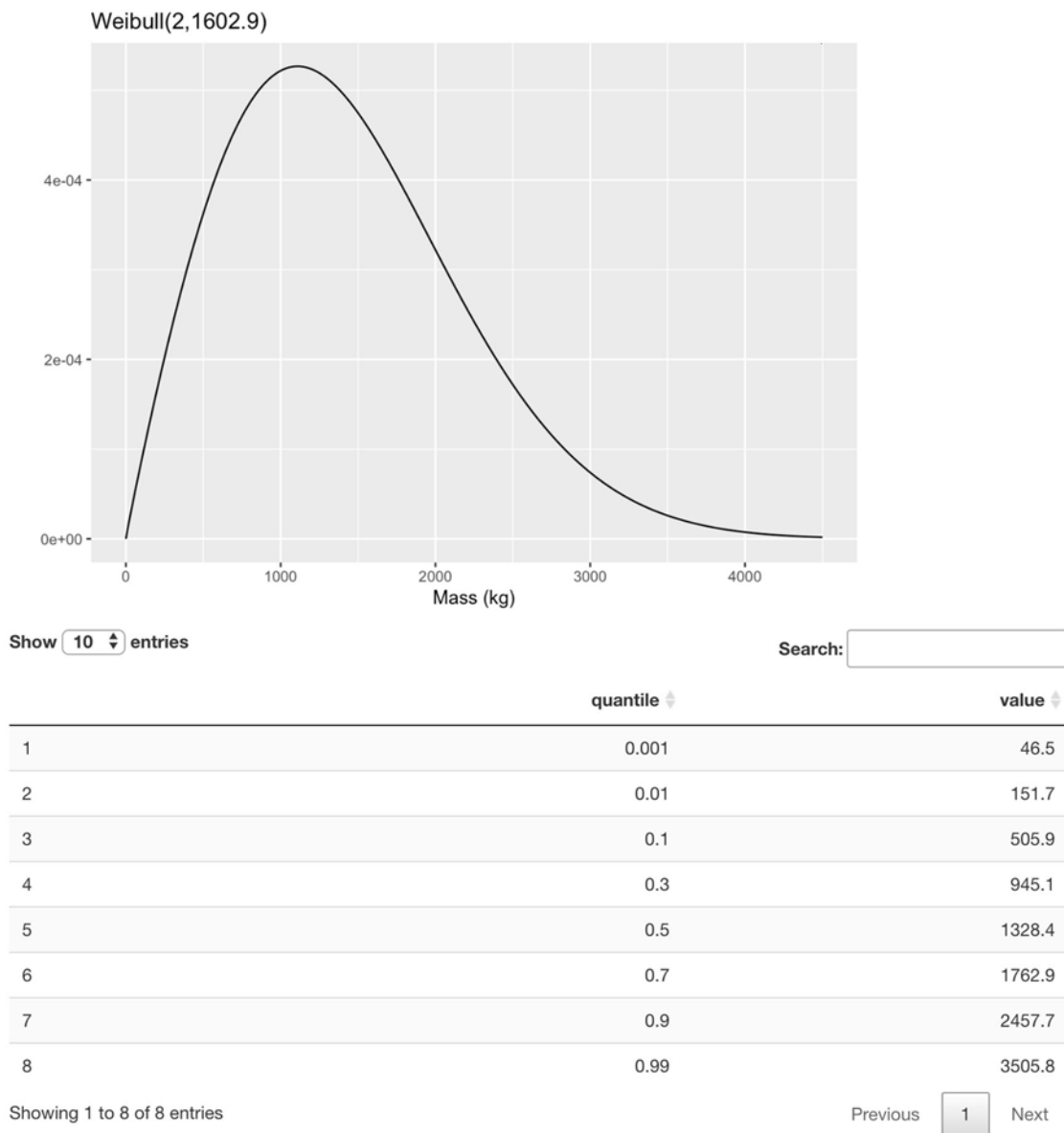
Figure D-4.13-1   Final distribution for total mass and table of quantiles
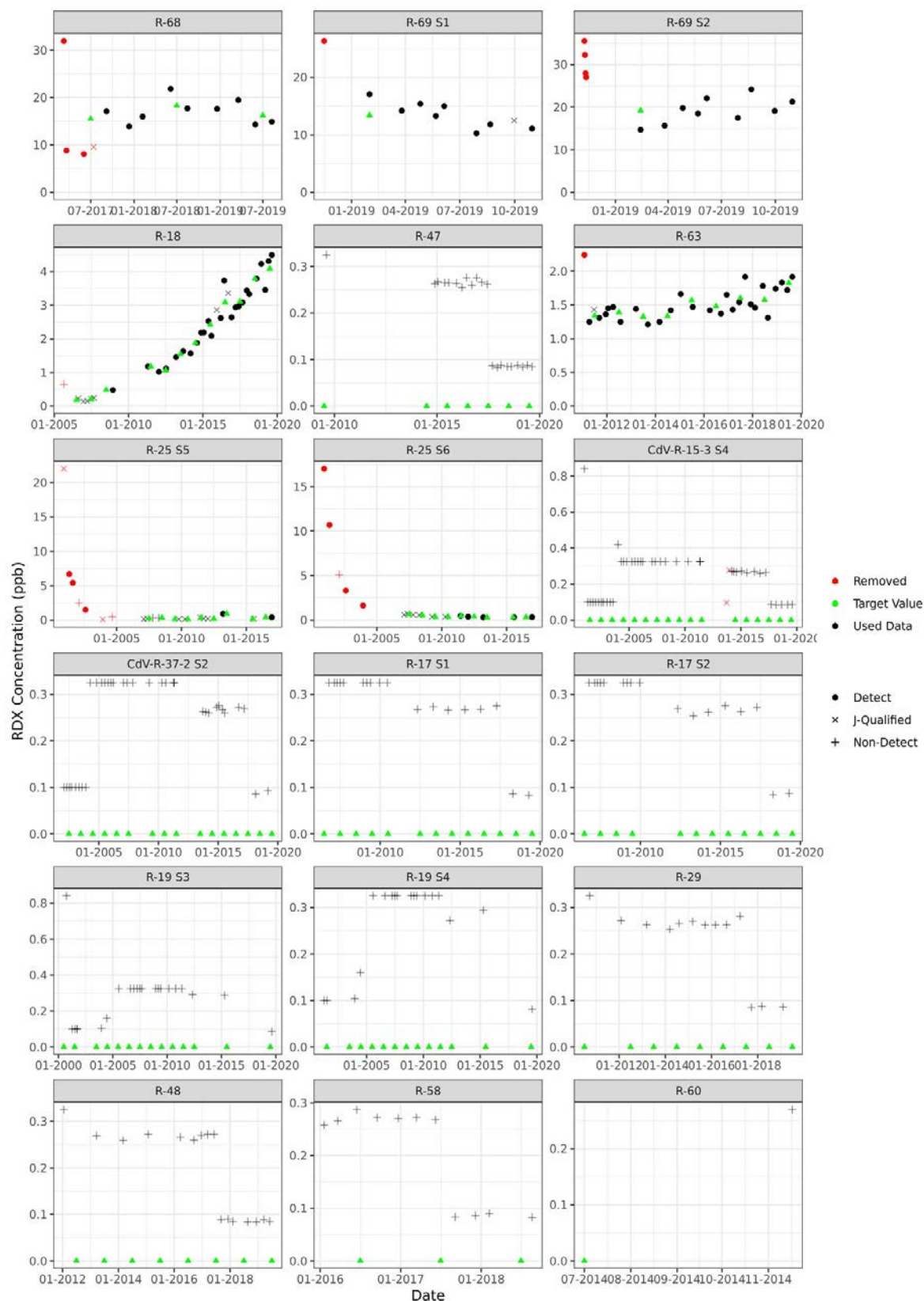
Note: Values shown in red were not included in target development on the basis of expert judgement.

Figure D-5.1-1   Data used to inform yearly target values for RDX concentration in the RRM
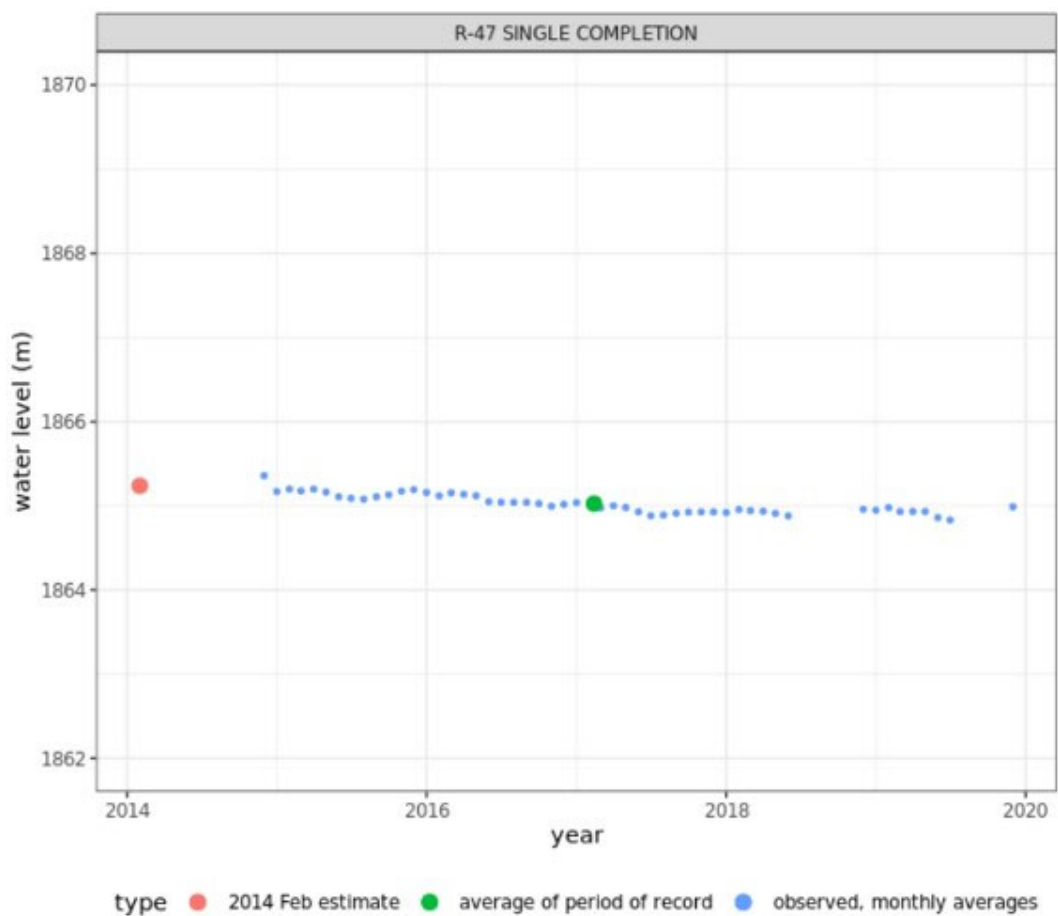
Figure D-5.1-2   R-47 imputed hydraulic head in February 2014
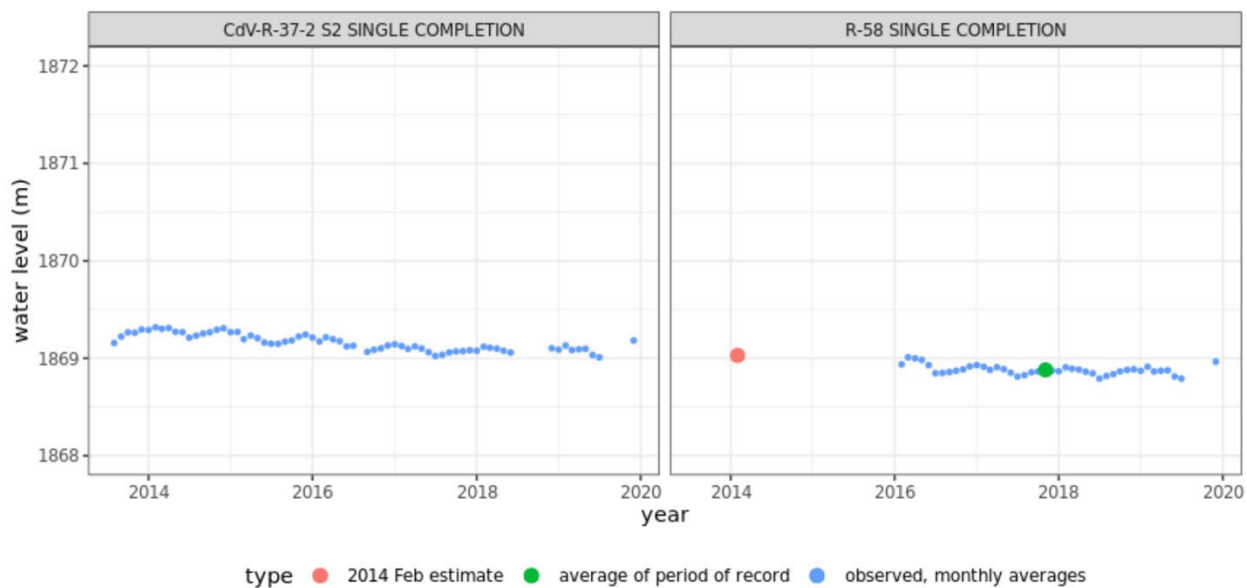
Figure D-5.1-3   CdV-R-37 screen 2 and R-58 imputed hydraulic head in February 2014
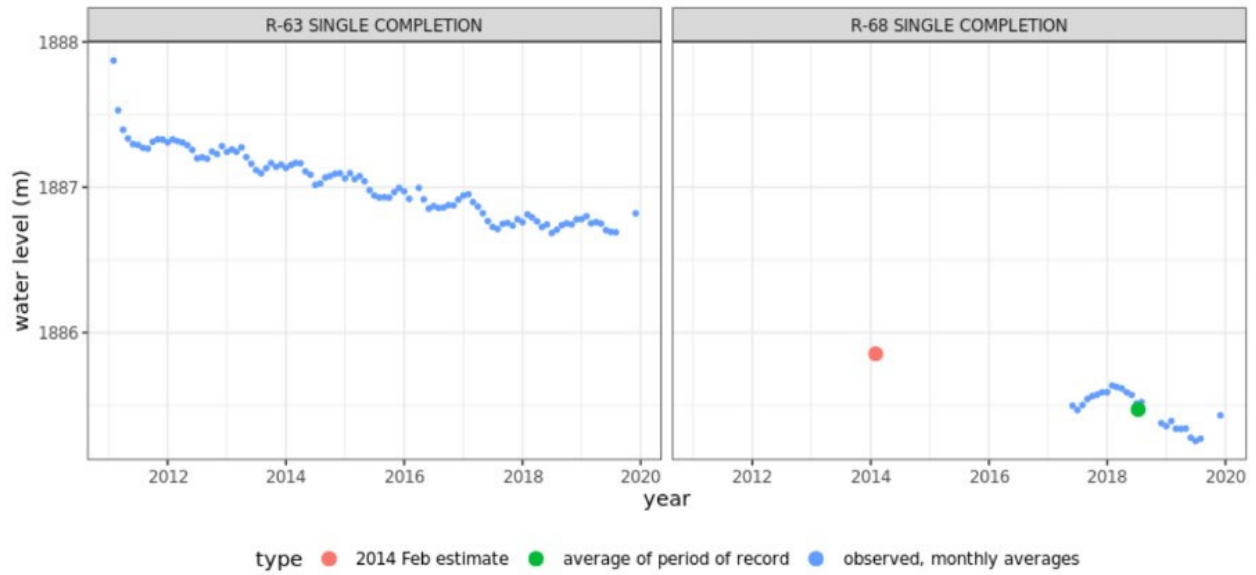
Figure D-5.1-4   R-63 and R-68 imputed hydraulic head in February 2014
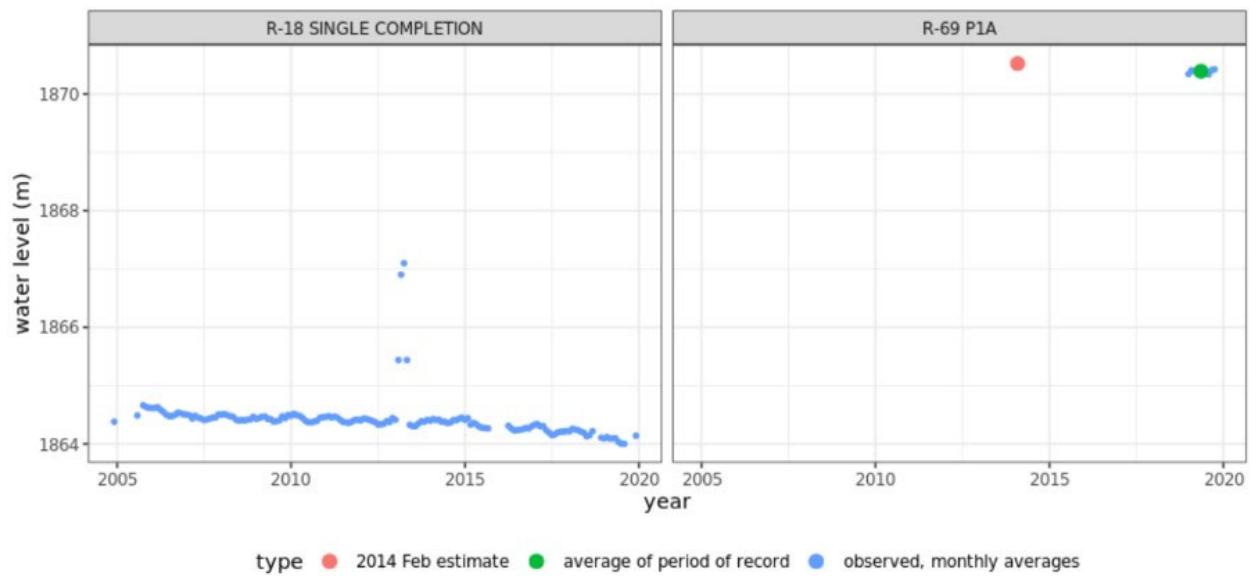
Figure D-5.1-5   R-18 and R-69 screen 1 imputed hydraulic head in February 2014
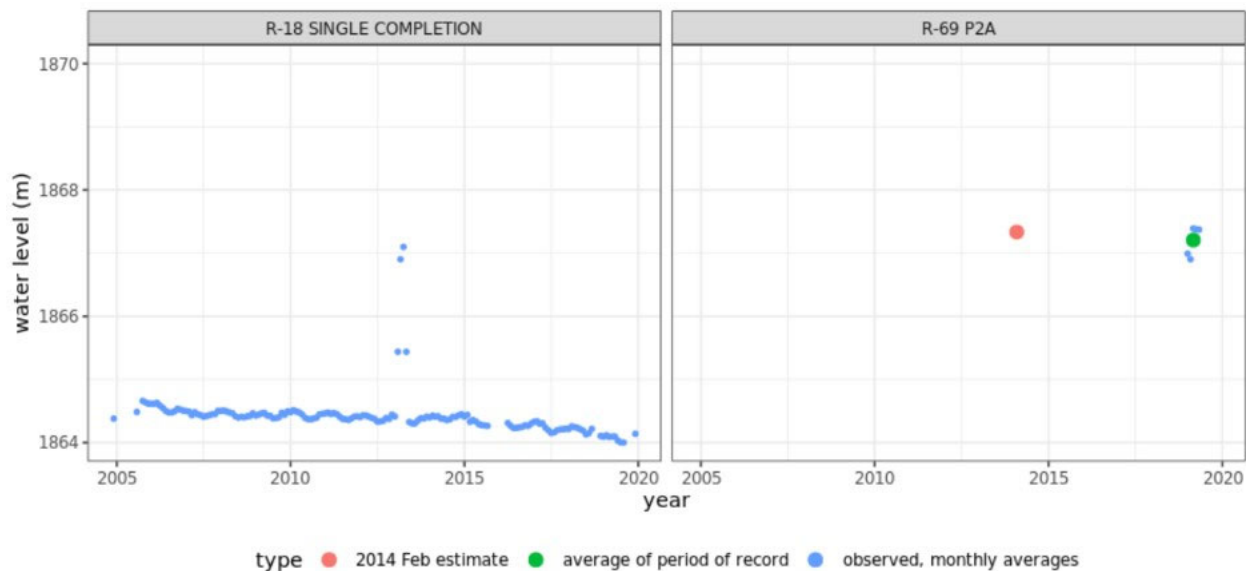
Figure D-5.1-6   R-18 and R-69 screen 2 imputed hydraulic head in February 2014
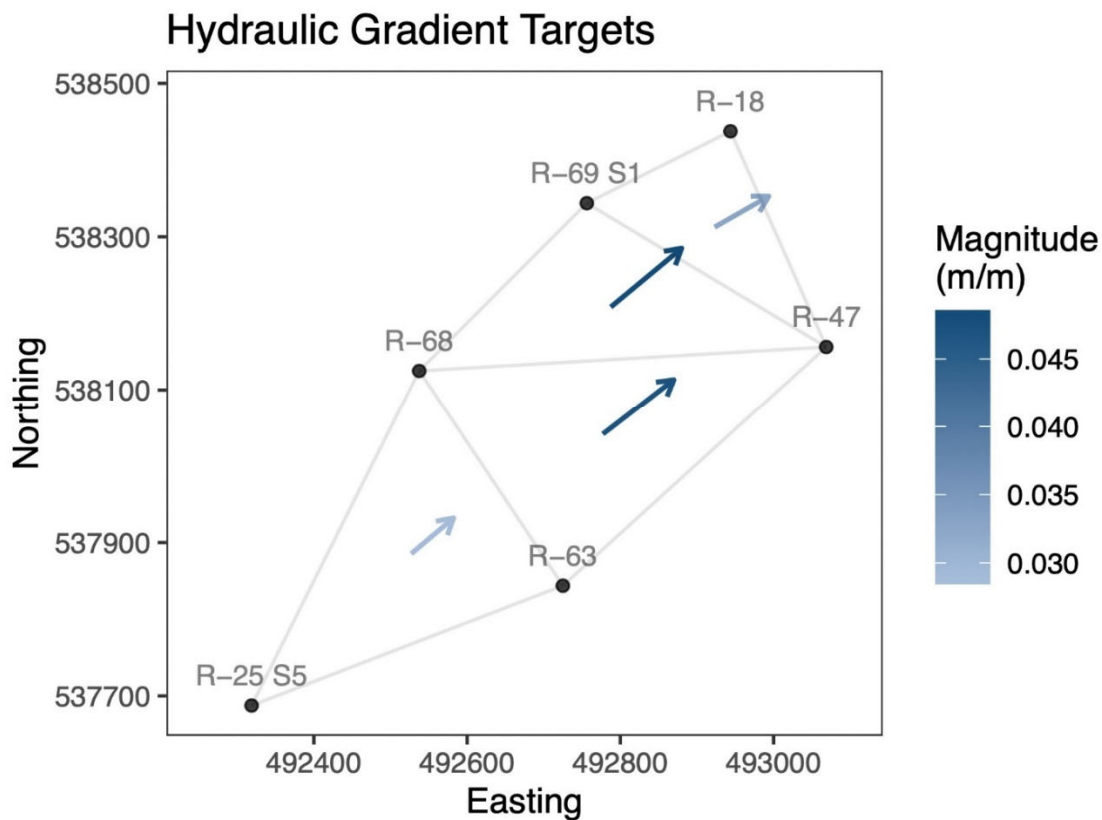
Note: Gradient vectors are anchored to the well triple centroids and relative magnitudes are indicated by a vector's length.

Figure D-5.1-7   Graphical depiction of the hydraulic gradient vectors and subset of wells used to derive them
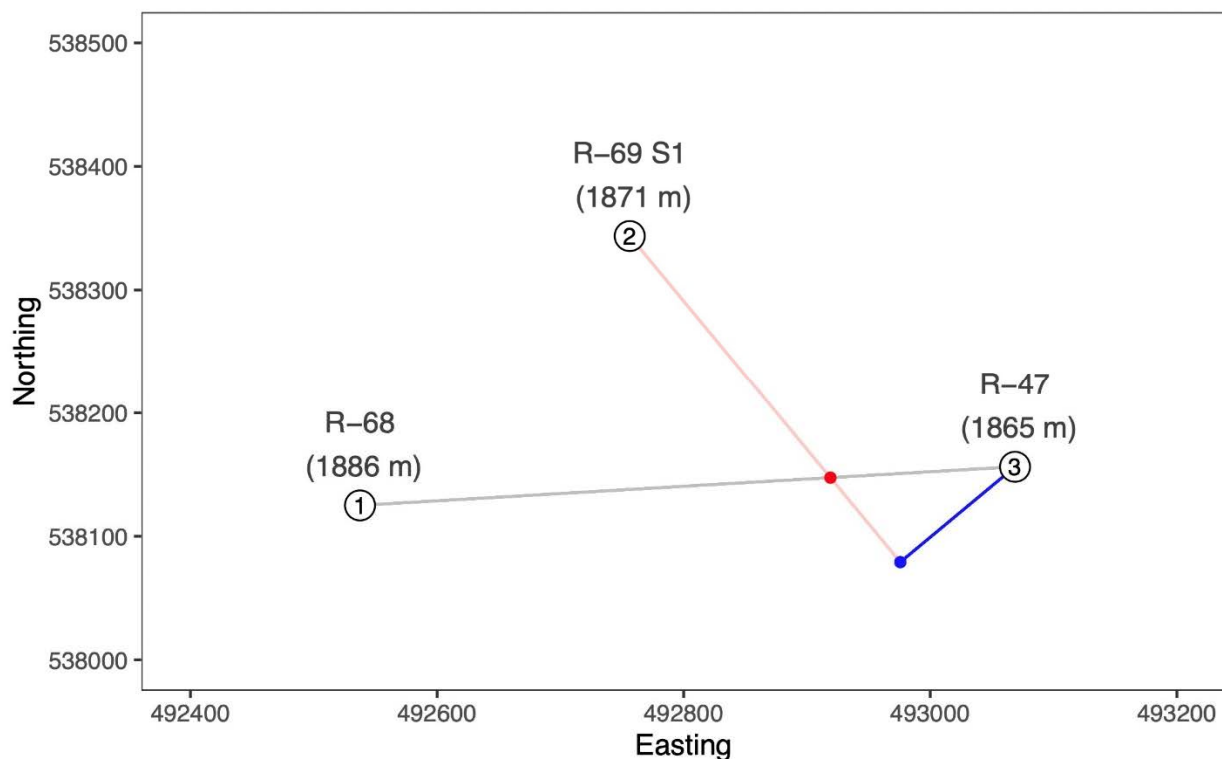
Note: Lines referenced in steps 3 and 4 are plotted in red and blue, respectively.

Figure D-5.1-8   Diagram of gradient computation for wells R-68, R-69 screen 1, and R-47
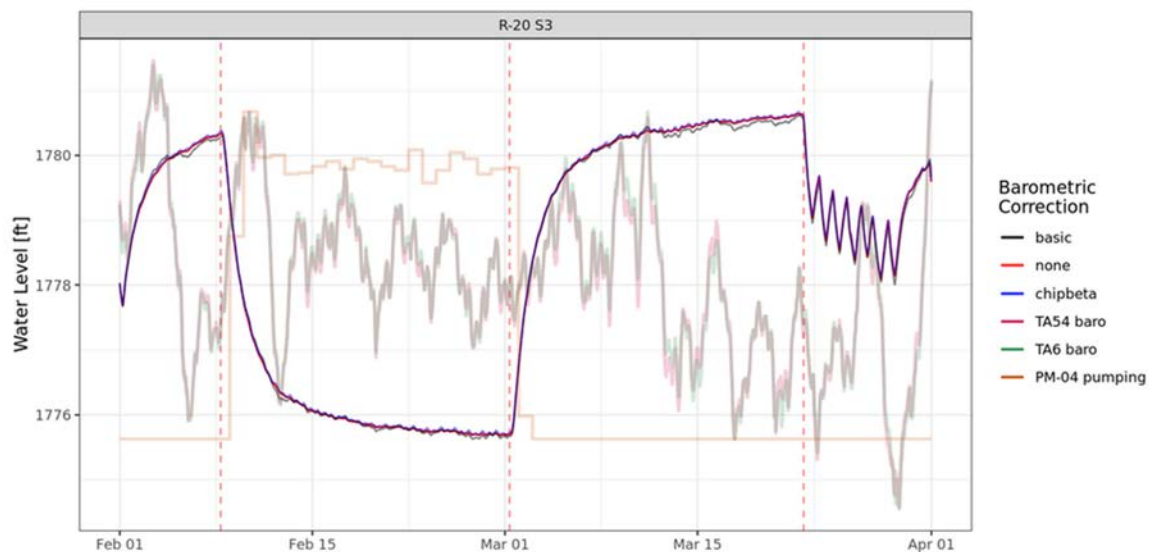
Figure D-5.1-9   Barometric correction of R-20 screen 3 hydraulic head values during the PM-4 pump test event (red vertical dashed lines represent pumping start time, end time, and end of test; orange lines depict relative pump rates). Barometric pressures from LANL's TA-54 and TA-6 weather stations are plotted for reference.
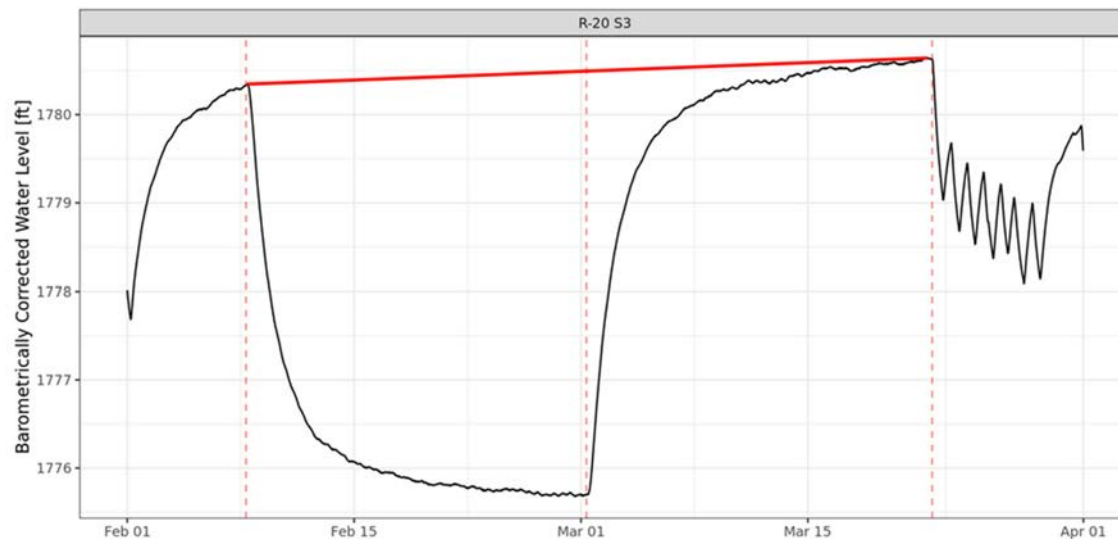
Figure D-5.1-10   Linear regression line (plotted in red) off which drawdowns are computed for R-20 screen 3 during the PM-4 pump test
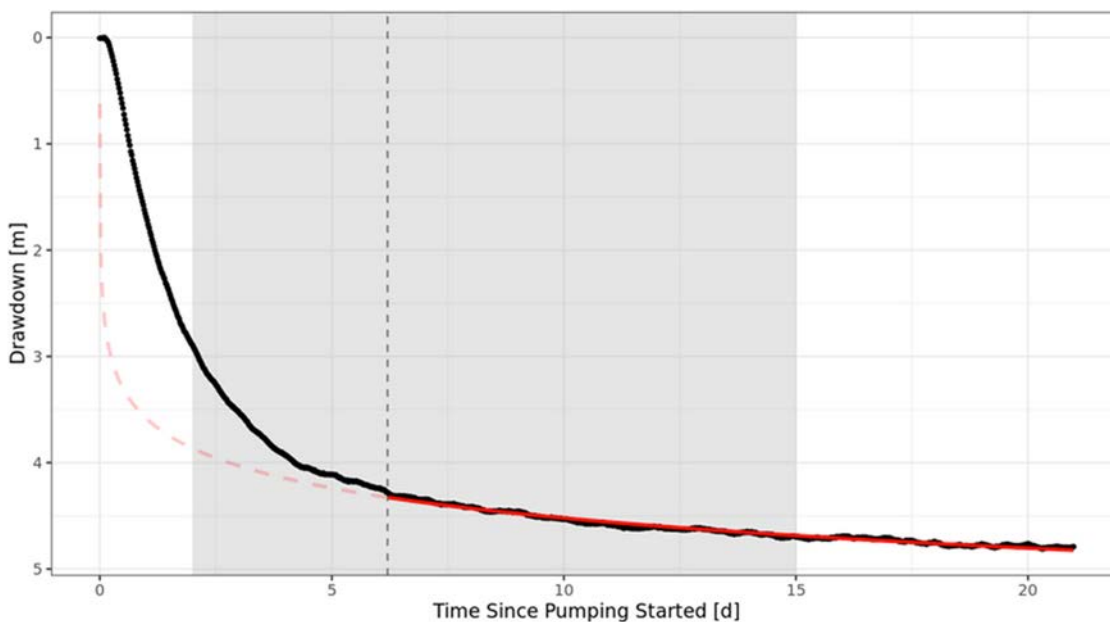
Figure D-5.1-11   Fitted drawdown regression line plotted in red for R-20 screen 3 during the PM-4 pump test. Gray shaded region represents the range of plausible values considered for the beginning of the late-time approximation (vertical dashed line).
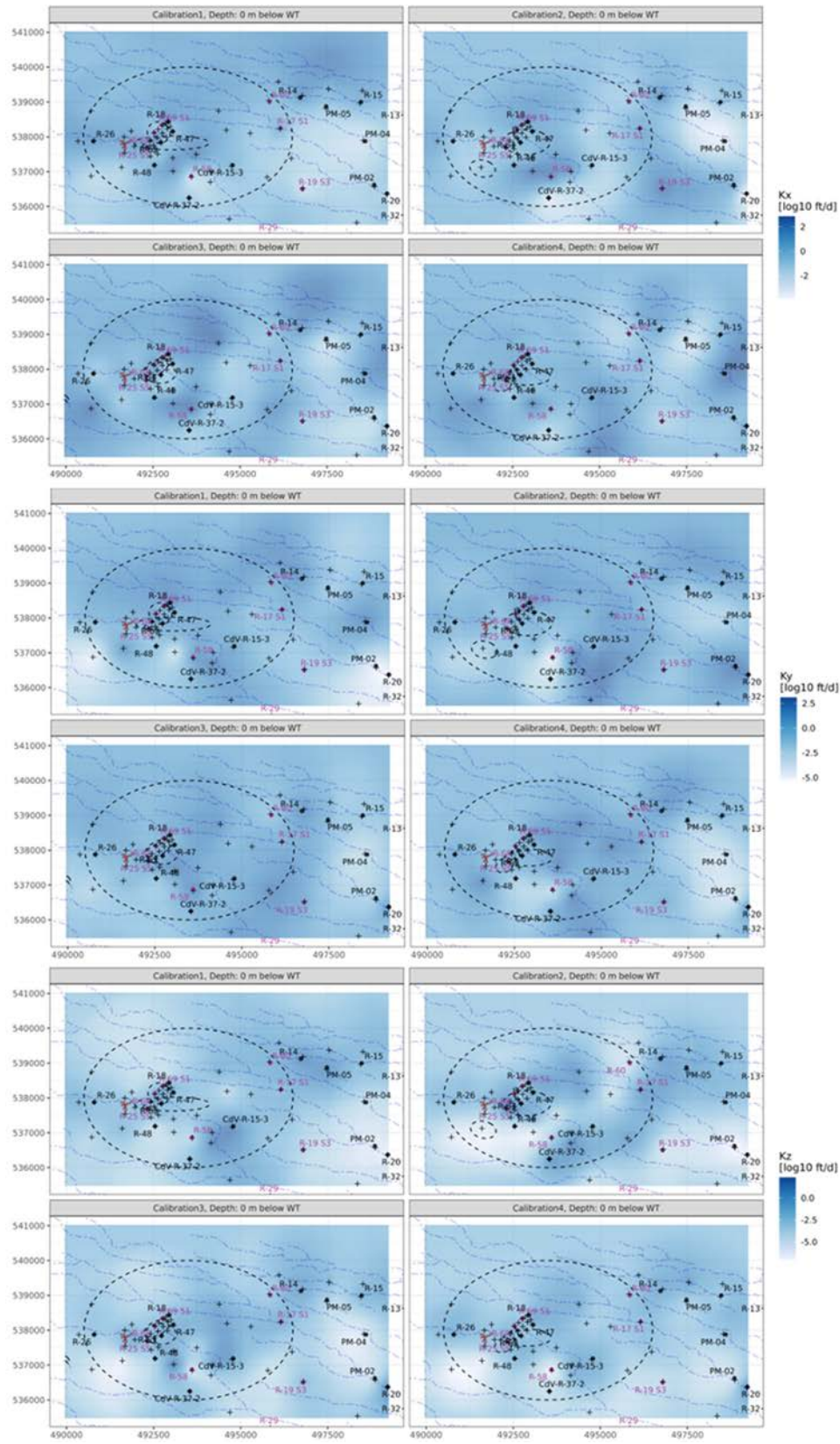
Figure D-6.1-1 K*x*, K*y*, and K*z* for each LM calibration at the water table
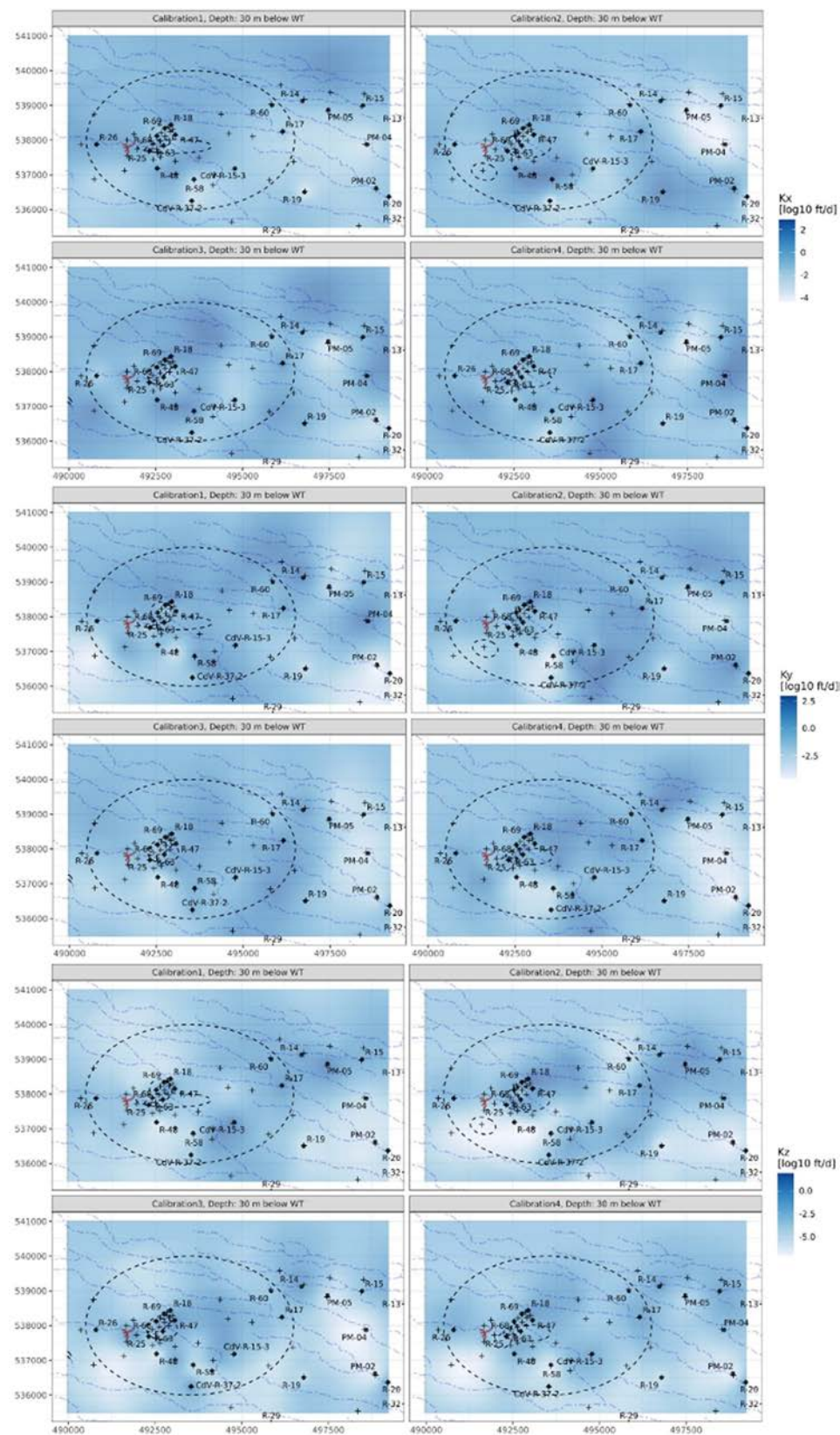
Figure D-6.1-2   K$_x$, K$_y$, and K$_z$ for each LM calibration at 30 m below the water table

Figure D-6.1-3   K$_x$, K$_y$, and K$_z$ for each LM calibration at 68 m below the water table

Figure D-6.1-4   RDX extent across all predictive future runs, plotted as a likelihood of being greater than 0.33 ppb across all depths for all runs (left panels). The depth of the 0.33 contour is plotted next to each map (right panels).
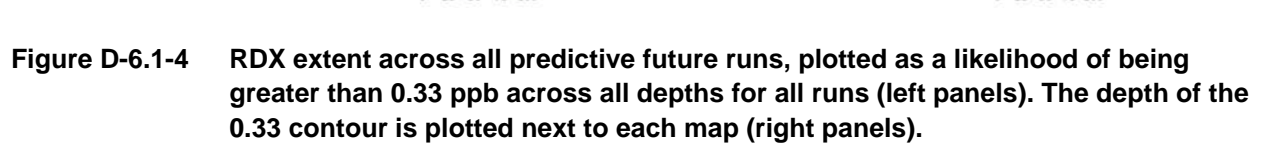
Table D-2.3-1
Weights Calculated Based on
Fraction of Total Annual Pumping

Well	Weight*
O-4	0.283
PM-1	0.14
PM-2	0.247
PM-3	0.145
PM-4	0.128
PM-5	0.057

* Weights based on fraction of total annual pumping.

Table D-2.3-2
Median Computed Hydraulic Gradient Magnitude
and Azimuth Compared with RRM Hydraulic Lateral Gradient Targets

Triplet	Magnitude	Azimuth	Median/Target
R-18, R-47, R-69 screen 1	3.11E-02	6.33E+01	median
R-18, R-47, R-69 screen 1	2.91E-02	6.08E+01	RRM target
R-25 S5, R-63, R-68	2.91E-02	4.84E+01	median
R-25 S5, R-63, R-68	2.91E-02	4.87E+01	RRM target
R-47, R-63, R-68	4.75E-02	5.06E+01	median
R-47, R-63, R-68	4.73E-02	5.16E+01	RRM target
R-47, R-68, R-69 screen 1	4.66E-02	5.23E+01	median
R-47, R-68, R-69 screen 1	4.96E-02	4.80E+01	RRM target

Note: RRM targets reflect estimated water level conditions in February 2014.

Table D-2.3-3
Results of Mann-Kendall Test for Trend, Estimated Linear
Change based on Sen's Method, and Correlation to PM Well Pumping
(PM-2 + PM-4 + PM-5) for Hydraulic Lateral Gradient Magnitude of RRM Gradient Target Triplets

Triple	Mann-Kendall			Sen's Slope			PM Well Pumping	
	Statistic	p-value	n	Estimate	Low	High	Correlation Value	p-value
R-18, R-47, R-69 S1	2.10E+00*	3.55E-02	144	2.32E-06	1.5E-07	3.85E-06	1.02E-01	2.24E-01
R-25 S5, R-63, R-68	−4.92E+00	8.87E-07	48	−9.28E-06	−1.12E-05	−5.98E-06	5.49E-01	5.42E-05
R-47, R-63, R-68	−5.82E+00	5.91E-09	216	−3.89E-07	−5.07E-07	−2.69E-07	−5.93E-02	3.88E-01
R-47, R-68, R-69 S1	−1.52E+01	3.28E-52	144	−3.41E-06	−3.56E-06	−3.28E-06	−5.02E-01	1.53E-10

* Results that are not statistically significant (p >0.001) are highlighted in red.

Table D-2.3-4
Results of Mann-Kendall Test for Trend, Estimated Linear
Change Based on Sen's Method, and Correlation to PM Well Pumping
(PM-2 + PM-4 + PM-5) for Hydraulic Lateral Gradient Azimuth of RRM Gradient Target Triplets

Triple	Mann-Kendall			Sen's Slope			PM Well Pumping	
	Statistic	*p*-value	n	Estimate	Low	High	Correlation Value	*p*-value
R-18, R-47, R-69 S1	1.58E+01	3.52E-56	144	1.12E-02	9.51E-03	1.23E-02	4.46E-01	2.18E-08
R-25 S5, R-63, R-68	7.08E+00	1.40E-12	48	1.32E-02	1.07E-02	1.58E-02	−2.48E-01*	8.91E-02
R-47, R-63, R-68	−1.46E+00	1.45E-01	216	−1.13E-03	−2.24E-03	3.37E-04	2.32E-01	6.16E-04
R-47, R-68, R-69 S1	1.65E+01	1.94E-61	144	8.4E-03	8.04E-03	8.79e-03	4.53E-01	1.21E-08

* Results that are not statistically significant (p >0.001) are highlighted in red.

**Results of Mann-Kendall Test for Trend, Estimated Linear
Change Based on Sen's Method, and Correlation to PM Well Pumping
(PM-2 + PM-4 + PM-5) for Hydraulic Lateral Gradient Magnitude of Water Table Well Screen Triplets**

Triplet	Mann-Kendall			Sen's Slope			PM Well Pumping	
	Statistic	*p*-value	n	Estimate	Low	High	Correlation Value	*p*-value
CdV-R-15-3 S4, CdV-R-37-2 S2, R-19	7.92E+00	2.41E-15	123	4.94E-07	4.23E-07	5.43E-07	−8.11E-02*	3.73E-01
CdV-R-15-3 S4, CdV-R-37-2 S2, R-48	1.18E+01	2.33E-32	382	1.83E-07	1.54E-07	2.10E-07	−1.60E-01	1.66E-03
CdV-R-15-3 S4, R-17 S1, R-19 S3	1.06E+01	4.99E-26	140	2.03E-06	1.57E-06	2.37E-06	1.21E-01	1.53E-01
CdV-R-15-3 S4, R-17 S1, R-48	2.41E+01	7.69E-129	368	9.64E-07	9.35E-07	9.93E-07	−1.74E-01	8.26E-04
R-02, R-01, R-14	−1.90E+01	2.78E-80	671	−2.01E-07	−2.17E-07	−1.85E-07	−3.97E-01	3.30E-26
R-02, R-60, R-14	2.42E+01	6.64E-130	517	9.69E-07	9.20E-07	1.01E-06	3.42E-01	2.99E-15
R-17 S1, R-18, R-48	2.90E+01	7.58E-185	508	5.94E-07	5.79E-07	6.09E-07	1.48E-01	7.91E-04
R-17 S1, R-19 S3, R-51 S1	6.74E+00	1.55E-11	242	3.73E-07	2.71E-07	5.17E-07	2.99E-01	2.09E-06
R-19 S3, CdV-R-37-2 S2, R-27	1.34E+01	9.32E-41	121	7.92E-07	7.20E-07	8.74E-07	1.67E-01	6.64E-02
R-19 S3, R-27, R-51 S1	1.02E+01	2.01E-24	226	3.20E-07	2.40E-07	4.20E-07	3.93E-01	8.71E-10
R-30, CdV-R-37-2 S2, R-27	2.80E+01	3.57E-172	413	4.62E-07	4.50E-07	4.74E-07	5.55E-03	9.11E-01
R-33 S1, R-01, R-14	3.21E+01	2.91E-226	690	2.56E-06	2.50E-06	2.62E-06	2.36E-01	5.29E-10
R-33 S1, R-17 S1, R-14	2.78E+01	1.35E-169	657	5.31E-07	5.08E-07	5.55E-07	3.02E-02	4.45E-01
R-33 S1, R-51 S1, R-17 S1	2.55E+01	1.41E-143	602	3.79E-07	3.68E-07	3.92E-07	1.48E-01	3.05E-04
R-60, R-02, R-18	2.45E+01	1.19E-132	463	4.37E-07	4.21E-07	4.51E-07	1.96E-01	2.50E-05
R-60, R-17 S1, R-14	2.77E+01	3.09E-169	526	1.28E-06	1.24E-06	1.32E-06	2.91E-01	2.00E-11
R-60, R-17 S1, R-18	2.93E+01	8.87E-189	493	6.13E-07	5.93E-07	6.31E-07	2.31E-01	2.64E-07

* Results that are not statistically significant (p >0.001) are highlighted in red.

Table D-2.3-6
Results of Mann-Kendall Test for Trend, Estimated Linear
Change Based on Sen's Method, and Correlation to PM Well Pumping
(PM-2 + PM-4 + PM-5) for Hydraulic Lateral Gradient Azimuth of Water Table Well Screen Triplets

Triplet	Mann-Kendall			Sen's Slope			PM Well Pumping	
	Statistic	*p*-value	n	Estimate	Low	High	Correlation Value	*p*-value
CdV-R-15-3 S4, CdV-R-37-2 S2, R-19 S3	1.42E+01	1.69E-45	123	3.62E-03	3.24E-03	3.93E-03	2.90E-01*	1.15E-03
CdV-R-15-3 S4, CdV-R-37-2 S2, R-48	9.89E+00	4.78E-23	382	2.98E-04	2.46E-04	3.46E-04	−2.53E-02	6.21E-01
CdV-R-15-3 S4, R-17 S1, R-19 S3	4.46E+00	8.10E-06	140	1.28E-03	7.44E-04	1.93E-03	−1.19E-01	1.61E-01
CdV-R-15-3 S4, R-17 S1, R-48	−2.06E+01	4.41E-94	368	−1.57E-03	−1.68E-03	−1.48E-03	1.55E-01	2.90E-03
R-02, R-01, R-14	−1.36E+01	3.89E-42	671	−1.13E-02	−1.47E-02	−7.78E-03	−3.87E-01	6.56E-25
R-02, R-60, R-14	2.24E+01	2.51E-111	517	2.11E-03	2.01E-03	2.23E-03	3.78E-01	1.69E-18
R-17 S1, R-18, R-48	1.07E+01	1.59E-26	508	6.32E-04	4.34E-04	7.50E-04	2.36E-01	7.03E-08
R-17 S1, R-19 S3, R-51 S1	9.93E+00	2.97E-23	242	7.39E-03	6.45E-03	8.30E-03	7.16E-02	2.67E-01
R-19 S3, CdV-R-37-2 S2, R-27	−1.06E+01	2.37E-26	121	−9.04E-04	−1.08E-03	−7.68E-04	−2.86E-01	1.47E-03
R-19 S3, R-27, R-51 S1	1.83E-01	8.55E-01	226	4.57E-04	−3.67E-03	4.94E-03	1.65E-01	1.32E-02
R-30, CdV-R-37-2 S2, R-27	−2.43E+01	1.65E-130	413	−9.77E-04	−1.01E-03	−9.45E-04	−7.72E-02	1.20E-01
R-33 S1, R-01, R-14	2.00E+01	3.94E-89	690	5.99E-03	5.48E-03	6.50E-03	4.30E-01	9.32E-32
R-33 S1, R-17 S1, R-14	8.24E+00	1.70E-16	657	4.64E-03	3.51E-03	5.79E-03	−2.43E-01	4.18E-10
R-33 S1, R-51 S1, R-17 S1	−8.91E+00	5.00E-19	602	−2.73E-03	−3.26E-03	−2.19E-03	2.71E-01	2.17E-11
R-60, R-02, R-18	−5.81E+00	6.38E-09	463	−5.56E-05	−7.22E-05	−3.85E-05	1.76E-01	1.51E-04
R-60, R-17 S1, R-14	1.86E+00	6.35E-02	526	2.13E-04	−1.11E-05	4.64E-04	−2.04E-01	3.31E-06
R-60, R-17 S1, R-18	2.26E+01	7.98E-113	493	2.22E-03	2.12E-03	2.32E-03	1.84E-01	4.54E-05

* Results that are not statistically significant (p >0.001) are highlighted in red.

Table D-2.3-7

**Results of Mann-Kendall Test for Trend, Estimated Linear
Change Based on Sen's Method, and Correlation to PM Well Pumping
(PM-2 + PM-4 + PM-5) for Hydraulic Lateral Gradient Magnitude of Mid-Depth Well Screen Triplets**

Triplet	Mann-Kendall			Sen's Slope			PM Well Pumping	
	Statistic	*p*-value	n	Estimate	Low	High	Correlation Value	*p*-value
CdV-R-37-2 S3, R-19 S4, CdV-R-15-3 S5	−8.60E+00	7.90E-18	220	−3.10E-07	−3.73E-07	−2.48E-07	6.07E-01	1.43E-23
CdV-R-37-2 S3, R-25 S6, CdV-R-15-3 S5	6.55E+00	5.93E-11	224	1.43E-07	1.15E-07	1.70E-07	−2.54E-03*	9.70E-01
R-17 S2, R-19 S4, CdV-R-15-3 S5	−7.32E-01	4.64E-01	125	−1.60E-07	−6.00E-07	2.39E-07	7.67E-01	1.66E-25
R-17 S2, R-19 S4, R-51 S2	5.84E+00	5.30E-09	244	3.64E-07	2.59E-07	4.67E-07	2.44E-01	1.15E-04
R-17 S2, R-25 S6, CdV-R-15-3 S5	−3.87E+00	1.08E-04	153	−3.58E-07	−5.28E-07	−1.87E-07	6.98E-01	1.24E-23
R-17 S2, R-33 S2, R-51 S2	−2.80E+00	5.10E-03	504	−3.94E-07	−6.97E-07	−1.12E-07	6.87E-01	9.86E-72
R-20 S2, R-19 S4, R-51 S2	4.11E+00	3.99E-05	225	4.03E-07	2.14E-07	5.67E-07	8.50E-01	4.38E-64
R-20 S2, R-51 S2, R-52 S2	1.04E+01	3.06E-25	560	4.09E-07	3.42E-07	4.73E-07	2.99E-01	9.42E-13
R-20 S2, R-52 S2, R-53 S2	−9.49E+00	2.36E-21	560	−4.46E-07	−5.36E-07	−3.52E-07	−6.00E-01	1.26E-54
R-33 S2, R-51 S2, R-52 S2	−1.82E-01	8.56E-01	558	−1.82E-08	−2.10E-07	1.64E-07	5.35E-01	1.54E-41
R-69 S2, R-33 S2, R-17 S2	4.14E-01	6.79E-01	85	6.13E-07	−3.23E-06	2.86E-06	−7.20E-01	8.08E-15

* Results that are not statistically significant (p >0.001) are highlighted in red.

Table D-2.3-8
Results of Mann-Kendall Test for Trend, Estimated Linear
Change Based on Sen's Method, and Correlation to PM Well Pumping
(PM-2 + PM-4 + PM-5) for Hydraulic Lateral Gradient Azimuth of Mid-Depth Well Screen Triplets

Triplet	Mann-Kendall			Sen's Slope			PM Well Pumping	
	Statistic	p-value	n	Estimate	Low	High	Correlation Value	p-value
CdV-R-37-2 S3, R-19 S4, CdV-R-15-3 S5	−9.34+00	1.00E-20	220	−3.25E-03	−3.82E-03	−2.72E-03	5.58E-01	2.04E-19
CdV-R-37-2 S3, R-25 S6, CdV-R-15-3 S5	−5.34+00	9.49E-08	224	−3.98E-04	−5.35E-04	−2.47E-04	1.12E-01*	9.53E-02
R-17 S2, R-19 S4, CdV-R-15-3 S5	3.56+01	7.22E-01	125	9.05E-05	−4.48E-04	6.59E-04	1.17E-01	1.94E-01
R-17 S2, R-19 S4, R-51 S2	1.48+01	1.52E-49	244	1.63E-02	1.47E-02	1.78E-02	4.04E-01	5.21E-11
R-17 S2, R-25 S6, CdV-R-15-3 S5	−1.11+00	2.69E-01	153	−4.32E-04	−1.21E-03	3.77E-04	−7.11E-01	7.62E-25
R-17 S2, R-33 S2, R-51 S2	1.06+01	4.89E-26	504	3.89E-03	3.20E-03	4.62E-03	−4.03E-01	4.47E-21
R-20 S2, R-19 S4, R-51 S2	−6.1-01	5.42E-01	225	−2.33E-03	−1.03E-02	4.85E-03	5.22E-01	3.91E-17
R-20 S2, R-51 S2, R-52 S2	8.86+00	7.67E-19	560	8.39E-03	6.62E-03	1.01E-02	5.34E-01	1.67E-41
R-20 S2, R-52 S2, R-53 S2	1.19+01	1.51E-32	560	9.87E-03	8.39E-03	1.14E-02	6.45E-01	1.43E-65
R-33 S2, R-51 S2, R-52 S2	4.43+00	9.58E-06	558	3.08E-03	1.73E-03	4.44E-03	−7.03E-01	2.44E-82
R-69 S2, R-33 S2, R-17 S2	7.17-01	4.73E-01	85	1.36E-03	−3.88E-03	4.20E-03	−7.37E-01	8.70E-16

* Results that are not statistically significant (p >0.001) are highlighted in red.

Table D-2.3-9
Results of Mann-Kendall Test for Trend, Estimated Linear
Change Based on Sen's Method, and Correlation to PM Well Pumping
(PM-2 + PM-4 + PM-5) for Hydraulic Lateral Gradient Magnitude of Deep Well Screen Triplets

Triplet	Mann-Kendall			Sen's Slope			PM Well Pumping	
	Statistic	p-value	n	Estimate	Low	High	Correlation Value	p-value
CdV-R-37-2 S3, R-19 S4, CdV-R-15-3 S5	1.70E+00	8.92E-02	212	−4.74E-08	−1.00E-07	7.30E-09	9.91E-02*	1.50E-01
CdV-R-37-2 S3, R-25 S6, CdV-R-15-3 S5	−1.03E+01	7.84E-25	224	−3.40E-07	−3.89E-07	−2.91E-07	3.04E-01	3.60E-06

* Results that are not statistically significant (p >0.001) are highlighted in red.

Table D-2.3-10

Results of Mann-Kendall Test for Trend, Estimated

Linear Change Based on Sen's Method, and Correlation to

PM Well Pumping (PM-2 + PM-4 + PM-5) for Hydraulic Lateral Gradient Azimuth of Deep Well Screen Triplets

Triplet	Mann-Kendall			Sen's Slope			PM Well Pumping	
	Statistic	p-value	n	Estimate	Low	High	Correlation Value	p-value
CdV-R-37-2 S3, R-19 S4, CdV-R-15-3 S5	−8.09E+00	5.97E-16	212	−1.95E-03	−42E-03	−1.49E-03	6.35E-01	2.36E-25
CdV-R-37-2 S3, R-25 S6, CdV-R-15-3 S5	−1.95E+01	1.63E-84	224	−3.37E-03	−3.47E-03	−3.25E-03	−2.13E-02*	7.51E-01

* Results that are not statistically significant (p >0.001) are highlighted in red.

Table D-2.3-11

Results of Mann-Kendall Test for Trend, Estimated Linear

Change Based on Sen's Method, and Correlation to PM Well Pumping

(PM-2 + PM-4 + PM-5) for Hydraulic Vertical Gradient Azimuth of Water Table Well Screen Pairs

Pair	Mann-Kendall			Sen's Slope			PM Well Pumping	
	Statistic	*p*-value	n	Estimate	Low	High	Correlation Value	*p*-value
CdV-R-15-3 S5-S4	−9.21E+00	3.40E-20	380	−4.41E-06	−5.18E-06	−3.52E-06	2.18E-01	1.82E-05
CdV-R-15-3 S6-S5	9.46E+00	3.07E-21	397	3.99E-06	3.33E-06	4.63E-06	−3.62E-01	9.43E-14
CdV-R-37-2 S3-S2	7.14E+00	9.54E-13	369	1.35E-06	1.06E-06	1.62E-06	−1.32E-01*	1.13E-02
CdV-R-37-2 S4-S3	1.04E+01	1.50E-25	369	1.79E-06	1.52E-06	2.13E-06	−1.61E-01	1.91E-03
R-14 S2-S1	−7.84E+00	4.43E-15	150	−1.27E-05	−1.54E-05	−9.88E-06	−8.59E-02	2.96E-01
R-17 S2-S1	−8.07E+00	6.85E-16	677	−1.29E-05	−1.55E-05	−1.03E-05	−4.73E-01	4.16E-39
R-47/R-18 S1-S1	9.59E+00	8.44E-22	325	5.00E-05	4.26E-05	5.90E-05	1.84E-01	9.89E-04
R-19 S4-S3	−6.87E+00	6.27E-12	488	−7.47E-06	−9.50E-06	−5.49E-06	−5.31E-01	6.47E-37
R-19 S5-S4	7.42E+00	1.18E-13	479	2.45E-06	1.83E-06	3.08E-06	−6.55E-01	5.63E-60
R-19 S6-S5	5.21E-01	6.02E-01	479	6.26E-07	−1.78E-06	2.97E-06	−7.01E-01	4.79E-72
R-19 S7-S6	−3.03E+00	2.45E-03	463	−1.34E-05	−2.01E-05	−4.52E-06	−3.14E-01	4.86E-12
R-20 S2-S1	−1.54E+01	1.53E-53	671	−9.38E-06	−1.04E-05	−8.37E-06	−6.62E-01	3.51E-84

Table D-2.3-11 (continued)

Pair	Mann-Kendall			Sen's Slope			PM Well Pumping	
	Statistic	*p*-value	n	Estimate	Low	High	Correlation Value	*p*-value
R-25 S6-S5	7.74E+00	1.03E-14	583	3.09E-05	2.18E-05	4.04E-05	−9.71E-02	1.90E-02
R-25 S7-S6	−8.91E+00	4.91E-19	590	−9.96E-06	−1.19E-05	−7.60E-06	1.27E-01	1.95E-03
R-25 S8-S7	−6.28E+00	3.31E-10	586	−5.93E-06	−7.34E-06	−4.34E-06	−8.11E-02	4.97E-02
R-31 S3-S2	7.06E+00	1.69E-12	603	6.62E-07	4.85E-07	8.43E-07	−4.36E-02	2.85E-01
R-31 S4-S3	−1.73E+00	8.38E-02	510	−1.06E-06	−2.10E-06	1.55E-07	−4.81E-01	6.59E-31
R-31 S5-S4	−1.15E+01	8.10E-31	613	−4.51E-06	−5.17E-06	−3.85E-06	−5.96E-01	2.75E-60
R-33 S2-S1	2.52E+00	1.18E-02	716	1.27E-05	2.93E-06	2.20E-05	−7.52E-01	7.53E-129
R-51 S2-S1	−5.58E+00	2.43E-08	627	−4.99E-06	−6.77E-06	−3.21E-06	−6.34E-01	2.86E-70
R-52 S2-S1	−6.26E+00	3.76E-10	579	−5.41E-06	−6.93E-06	−3.80E-06	−8.45E-01	3.66E-155
R-53 S2-S1	−9.79E+00	1.29E-22	619	−1.20E-05	−1.44E-05	−9.73E-06	−8.01E-01	1.39E-136
R-54 S2-S1	3.65E+00	2.60E-04	624	7.01E-06	3.28E-06	1.04E-05	−5.75E-01	6.40E-55
R-69 S2-S1	−1.58E+01	4.71E-56	121	−1.14E-04	−1.20E-04	−1.10E-04	−1.07E-01	2.42E-01

* Results that are not statistically significant (p >0.001) are highlighted in red.

Table D-2.5-1
Input Parameter Distributions

Parameter	Model Notation	Median	1st, 99th%	Unit	Source of Information
Material Properties Parameters					
Hydraulic conductivity[1]					
Puye Formation (pilot points)	(kx, ky)(pp#)	12	0.2, 1382	ft/day	Well data, literature
Volcanic formations or Unknown (pilot points)	(kx, ky)(pp#)	10	3E-6, 3000	ft/day	Literature, modeling
Anchor points (all in Puye)	(kx, ky)(ap#)	0.35–153	See Figure C-2.4-2.	ft/day	Well data, literature
Specific Storage					
Shallow (unconfined to semiconfined)[2]	s(pp#)	−3.7	−7.5, −0.7	1/m	Well data, literature
Deep (confined to semiconfined)	s(pp#)	−5.9	−4.2, −7.6	1/m	Well data, literature
Dispersivity[1]					
Longitudinal	disp_long	17.5	5.1, 60.1	m	Literature
Transverse horizontal	disp_trans_hor	4.4	1.1, 17.3	m	Literature
Transverse vertical	disp_trans_vert	0.2	0.1, 0.8	m	Literature
Other					
Hydraulic conductivity krige scale[2]	krige_rangeK	2264	410, 4204	m	Literature, modeling
Specific storage krige scale[2]	krige_rangeS	3985	2093, 6718	m	Literature, modeling
Krige anisotrophy ratio[3]	krige_v(K,S)_semiaxis	0.27	0.01, 0.8	m/s	Literature, modeling
Advective porosity[3]	adv_por	0.15	0.04, 0.35	—	Well data, literature
Diffusivity	diff_w	2.96E-10	2.41E-10, 3.49E-10	m^2/s	literature
RDX sorption coefficient	Kd	0.030	0, 0.085	mL/g	literature

Table D-2.5-1 (continued)

Long Name	Parameter Name	Median	1st, 99th%	Unit	Source of Information
Boundary Condition Parameters					
Primary window centroid coordinates	s1(x,y)0	(492421, 538082)	x(491623, 493220) y(537574, 538592)	State Plane NAD83	Well data, CSM, hydraulic gradient, P&D
Secondary window centroid coordinates	s2(x,y)0	(491956, 537872)	x(489915, 493997) y(536829, 537872)	State Plane NAD83	CSM, surface locations, P&D
Preferential recharge centroid coordinates[4]	s3(x,y)0	(492682, 537810)	x(492306, 493097) y(537686, 537934)	State Plane NAD83	CSM, modeling
Primary window elipse radii	s1r(x,y)	(95,61)	x(3, 403) y(2, 338)	m	RVZM, P&D, CSM
Secondary window elipse radii	s2r(x,y)	(77,61)	x(3, 388) y(2, 338)	m	RVZM, P&D, CSM
Preferential recharge window elipse radii[4]	s3r(x,y)	−760,225	x(309, 1211) y(54, 397)	m	CSM
Primary window Cr concentration[2]	s1c	126	3, 381	ppb	RVZM
Secondary window Cr concentration[2]	s2c	18	0.45, 53	ppb	RVZM
Total rate of preferential recharge[2]	totip	5303	469, 11036	mm/yr	RVZM
Percent of recharge in primary source[4]	s1p	10	1, 19	%	Geochemistry, literature, CSM
Percent of recharge in preferential source[4]	s3p	73	65, 81	%	Geochemistry, literature, CSM
Primary/secondary window arrival time[5]	t0s(1-2)	1999	1956, 2019	yr	RVZM, P&D
Window eccentricity (tilt)	s(1-3)corr	0	−1, 1	—*	RVZM, P&D
Western constant head[4]	wHead(N,S)	1895	1860, 1930	m	Data, literature, modeling
Eastern constant head[4]	eHead(N,S)	1580	1470, 1690	m	Data, literature, modeling
Percent of supply well screen pumped[4]	pm_pct	93	0, 100	%	Data, Literature
Mountain block vertical gradient[4]	wHeavGrad	−0.16	0, −0.3	—	Data, literature, modeling
Total mass of RDX available[5]	totalmass	1327	152, 3506	kg	Literature

Note: Parameter distributions are normal unless marked as follows: (1) lognormal, (2) truncnormal, (3) beta, (4)uniform , (5) Weibull.

* — = Not applicable.

Table D-3.2-1
Fixed Hydraulic Properties for RVZM

Geologic Unit	Density [kg/m³]	Porosity [–]	Residual Saturation [-]	van Genuchten alpha [1/m]	van Genuchten *n* [-]
Tpf 2, Tpf 3	1200	0.35	0.01	5	2.68
Tvt 2	2000	0.05	0.066	0.1	2
Qbof	1200	0.44	0.043	0.59	1.76
Qct	1200	0.45	0.007	1.3	1.5
Qbt 1g	1150	0.46	0.022	0.5	1.75
Qbt 1v-u	1170	0.49	0.006	0.36	1.74
Qbt 2	1400	0.41	0.024	0.47	2.06
Qbt 3	1470	0.469	0.045	0.29	1.884
Qbt 3t	1470	0.466	0	2.57	1.332
Qbt 4	1350	0.478	0.000377	0.667	1.685
Qbof G2, G3	1200	0.44	0	0.081	4.03

Table D-3.2-2
Hydraulic Conductivity Distributions for Geology Groups in the RVZM

Parameter	Geology Group	Geometric Mean [ft/day]	Geometric Standard Deviation [ft/day]	1st % [ft/day]	99th % [ft/day]
K_{xy}	Puye (Tpf 2, Tpf 3)	4.99	1.46	2.05	12.1
	Tschicoma (Tvt 2)	9.58	2.79	0.88	103.8
	Otowi (Qbof, Qbof G2/G3)	0.40	1.62	0.13	1.24
	Cerro Toledo (Qct)	0.26	1.84	0.06	1.08
	Tshirege Bandelier Tuff (Qbt 1g, Qbt 1v-u)	0.60	1.33	0.31	1.15
	Tshirege Bandelier Tuff (Qbt 2)	0.55	1.50	0.22	1.42
	Tshirege Bandelier Tuff (Qbt 3, Qbt 3t)	0.98	2.80	0.09	10.8
	Tshirege Bandelier Tuff (Qbt 4)	0.41	2.41	0.05	3.19
K_z	Puye (Tpf 2, Tpf 3)	0.31	1.92	0.07	1.40
	Tschicoma (Tvt 2)	0.34	8.05	0.00265	43.6
	Otowi (Qbof, Qbof G2/G3)	1.91	3.46	0.11	34.5
	Cerro Toledo (Qct)	775	6.91	8.65	69400
	Tshirege Bandelier Tuff (Qbt 1g, Qbt 1v-u)	0.00112	8.27	0.00000824	0.15
	Tshirege Bandelier Tuff (Qbt 2)	4.65	6.32	0.06	338.68
	Tshirege Bandelier Tuff (Qbt 3, Qbt 3t)	0.03	87.0	0.000000798	845
	Tshirege Bandelier Tuff (Qbt 4)	0.47	7.37	0.00455	49.4

Table D-3.2-3
Calibrated Dispersivity

Unit ID	Formation	Calibration 3			Attachment 8[a]			LANL-EES[b]		
		αx	αy	αz	αx	αy	αz	αx	αy	αz
10	Tpf 2	1.602	4.958	21.531	0.102	0.288	15.000	1.200E-01	0.328	14.644
11	Tvt 2	1.679	2.214	2.539						
14	Tpf 3	1.984	2.202	12.723						
16	Qbof	3.517	1.386	22.053						
17	Qct	1.884	2.141	3.844						
19	Qbt 1g	1.403	1.237	18.218						
21	Qbt1 v-u	4.979	3.589	2.498						
22	Qbt 2	1.363	1.272	23.058						
23	Qbt 3	2.846	2.888	9.021						
24	Qbt 3t	2.695	4.000	7.188						
25	Qbt 4	0.328	2.431	1.456						
27	Qbof	1.438	3.313	2.139						
28	Qbof	2.819	2.655	8.974						
Regional Aquifer	Tpf	177.450	58.920	4.741	—[c]	—	—	—	—	—

Note: Units are meters.

[a] From "Compendium of Technical Reports Related to the Deep Groundwater Investigation for the RDX Project at Los Alamos National Laboratory," Attachment 8 (LANL 2018, 602963).

[b] From "File Transfer Report for Chromium and RDX Project Hydrologic Modeling" (Neptune 2018, 700878).

[c] No data available.

Table D-3.2-4
Calibrated Water Fluxes and Permeability
Reduction Coefficients at the Bottom of Perched Zones

Parameter	Calibration 3	Attachment 8[a]	LANL-EES[b]
Background infiltration	0.0207	0.0332	0.0772
Flux into Cañon de Valle	0.9889	1.75E-05	6.4898
Flux into other canyons	2.9824	5.71001	1.8166
MBR	4.6007	9.99312	1.2062
Permeability reduction coefficient UPZ	4.16E-04	1.13E-05	4.06E-05
Permeability reduction coefficient LPZ	2.32E-04	4.83E-04	9.58E-05
Permeability reduction coefficient UPZ window	5.95E-04	4.49E-05	1.41E-05

Note: Calibrated water fluxes are in kilograms per second.

[a] From "Compendium of Technical Reports Related to the Deep Groundwater Investigation for the RDX Project at Los Alamos National Laboratory," Attachment 8 (LANL 2018, 602963).

[b] From "File Transfer Report for Chromium and RDX Project Hydrologic Modeling" (Neptune 2018, 700878).

Table D-3.2-5
Calibrated Permeability

Unit ID	Formation	Calibration 3		Attachment 8[a]		LANL-EES[b]	
		Kxy	Kz	Kxy	Kz	Kxy	Kz
10	Tpf 2	3.414E-12	1.468E-13	3.105E-12	6.394E-12	3.631E-12	3.631E-12
11	Tvt 2	1.041E-12	1.371E-11	9.164E-12	3.433E-13	2.960E-13	2.943E-13
14	Tpf 3	2.543E-12	1.026E-13	3.107E-12	9.995E-13	3.787E-13	1.055E-13
16	Qbof	1.123E-13	1.262E-12	9.999E-12	9.158E-11	9.030E-13	2.675E-12
17	Qct	3.428E-13	9.254E-09	3.080E-14	9.696E-11	1.716E-14	9.913E-12
19	Qbt 1g	3.458E-13	1.501E-15	6.139E-12	1.515E-15	8.999E-12	1.333E-14
21	Qbt 1v-u	2.272E-13	2.557E-14	2.807E-12	4.295E-14	1.029E-14	4.202E-12
22	Qbt 2	7.951E-14	2.512E-14	6.663E-13	6.031E-12	1.008E-13	1.195E-12
23	Qbt 3	3.970E-12	8.198E-13	4.229E-11	1.582E-14	9.389E-13	1.284E-13
24	Qbt 3t	2.004E-13	1.693E-12	4.350E-12	8.804E-12	2.488E-12	7.688E-12
25	Qbt 4	7.674E-14	2.169E-15	1.771E-12	2.270E-12	2.650E-13	1.415E-14
27	Qbof	5.180E-14	4.103E-12	1.786E-14	7.321E-13	2.409E-14	2.012E-14
28	Qbof	9.858E-14	7.998E-12	2.310E-13	5.860E-12	2.134E-14	2.193E-13
140	Tpf 3	3.905E-12	1.544E-13	7.553E-13	2.595E-13	6.193E-14	4.130E-14
141	Tpf 3	3.826E-12	5.218E-14	9.283E-11	5.386E-14	1.000E-11	3.778E-12
142	Tpf 3	1.254E-12	2.864E-13	8.758E-13	1.556E-13	3.314E-14	3.499E-14

Note: Units are in square meters.

[a] From "Compendium of Technical Reports Related to the Deep Groundwater Investigation for the RDX Project at Los Alamos National Laboratory," Attachment 8 (LANL 2018, 602963).

[b] From "File Transfer Report for Chromium and RDX Project Hydrologic Modeling" (Neptune 2018, 700878).

Table D-3.2-6
Calibrated Matrix Diffusion Coefficient

Calibration 3	Attachment 8[a]	LANL-EES[b]
1.2627E-11	3.88E-10	4.0274E-10

Note: Units are in square meters per second.

[a] From "Compendium of Technical Reports Related to the Deep Groundwater Investigation for the RDX Project at Los Alamos National Laboratory," Attachment 8 (LANL 2018, 602963).

[b] From "File Transfer Report for Chromium and RDX Project Hydrologic Modeling" (Neptune 2018, 700878).

Table D-3.2-7
Calibrated Sorption Coefficient

Unit ID	Formation	Calibration 3	Attachment 8[a]	LANL-EES[b]
10	Tpf 2	0.0997	0.0004	0.00002
11	Tvt 2	0.0276	0.5000	0.5
14	Tpf 3	0.0964	3.9900	0.27993
16	Qbof	0.0791	0.000002	0.00959
17	Qct	0.0416	0.4070	1.99835
19	Qbt 1g	0.0912	1.6360	1.76414
21	Qbt 1v-u	0.0706	0.00001	0.20414
22	Qbt 2	0.052	0.00009	0.00067
23	Qbt 3	0.0505	4.4050	1.97998
24	Qbt 3t	0.0505	4.4050	1.97998
25	Qbt 4	0.0688	0.5670	0.49990
27	Qbof	0.0791	0.000002	0.00959
28	Qbof	0.0791	0.000002	0.00959
Regional Aquifer	—[c]	0.0079	—	—

Note: Units are in milliliters per gram.

[a] From "Compendium of Technical Reports Related to the Deep Groundwater Investigation for the RDX Project at Los Alamos National Laboratory," Attachment 8 (LANL 2018, 602963).

[b] From "File Transfer Report for Chromium and RDX Project Hydrologic Modeling" (Neptune 2018, 700878).

[c] — = Not applicable.

Table D-4.1-1
Geologic Unit Assignment for
Pilot and Anchor Points at the RDX Site

Distribution	Units
Sedimentary	Tpf, Tjfp, Tcar
Volcanics	Tvt, Tb2, Tb4, Tvk

Table D-4.1-2
Anisotropy Information for the Chromium Site

Well	Formation	Anisotropy Estimate
CrEX-3	Tpf	0.1
CrEX-4	Tpf	0.0004
CrIN-1	Tpf	0.22
CrIN-2	Tpf	0.52
CrIN-3	Tpf	0.1
CrIN-4	Tpf	0.34
CrIN-5	Tpf	0.05
R-44 S1	Tpf	0.015
R-28	Tpf/Tpf(p)	0.001
Mean Tpf		**0.15**
Median Tpf		**0.10**
R-50 S2	Tjfp	1.0
R-35a	Tcar	0.01

Table D-4.1-3
Filtering Decisions for the RRM *K* Distributions

Topic	Filtering Decision
Geology	All site data are separated into "sedimentary" or "volcanics" for the purpose of generating a distribution for each.
Spatial distribution	All LANL data are used to inform pilot point distribution; RDX-area data are weighted twice that of data from other areas. Spatial model is used to define initial values using RDX-area data.
Scale	Only Intermediate-scale data (i.e., aquifer tests) are used.
Type of analysis	Only recovery-type analyses are used.

Table D-4.1-4
MLE Fit Distributions With 1st and 99th Percentiles
to Represent Range of Plausible Values for Pilot Points

Distribution	1st Percentile [ft/day]	99th Percentile [ft/day]
Summary Statistics (minimum, maximum)	*0.0020*	*220.0*
Well Location Averages (minimum, maximum)	*0.0022*	*161.0*
Lognormal(5.52, 10.52) [ft/day]*	0.023	1318
Normal(−4.71, 1.02) [log10 m/s]*	−7.08	−2.33
Gamma(0.401, 0.014) [ft/day]	0.0005	213.3

*The lognormal distribution on the log10 scale shifted to m/s is the normal distribution. The distribution is incorporated into the modeling on the log10 m/s scale.

Notes: The sample minimum and maximum and location minimum and maximum are also provided for comparison in italics. The lognormal distribution is selected for the model.

Table D-4.4-1
Distributions Developed for Porosity and Advective Porosity

Parameter	Distribution	Mean	Standard Deviation	Min	Max	d1	d99
Total Porosity	truncnormal	0.26	0.07	0	1	0.10	0.42
Fractional Advective Porosity	truncnormal	0.62	0.20	0	1	0.16	0.97
Advective Porosity	Beta	Shape1 = 4.38, Shape 2 = 23.3		0	1	0.04	0.35

Table D-4.5-1
Distribution Development Weighting and Length Scales Used in References

Reference	VZ Weight	SZ Weight	Length Scale (m)
Neuman 1990, 090184	0.5	0.5	0.1–100,000
Abbaspour et al. 1997, 700896	0.5	0.1	0.4–3
van Genuchten et al. 1987 ("Analysis and Prediction of Water and Solute Transport in a Large Lysimeter" from NRC 1987, 700882)	0.9	0.1	0.36–4.15
Umari et al. 2008, 700899	0.5	0.3	30.4
Waldrop et al. 1985, 700900	0.1	0.8	3500–3500
Reimus et al. 2003, 210315	0.5	0.3	30
Meyer et al. 1981, 700901	0.1	0.3	8
Bromly et al. 2007, 700902	0.05	0.7	0.051–0.3
Bromly et al. 2007, 700902	0.05	0.2	0.1–0.213
Gelhar et al. 1992, 102465	0.5	0.5	<= 115–91
Waldrop et al. 1985, 700900	0.5	0.1	0.23–20
Waldrop et al. 1985, 700900	0.1	0.3	<115–28
Waldrop et al. 1985, 700900	0.1	0.8	0.75–9.3
LANL 2018, 602963	0.3	0.5	3000
Fujinawa 2010, 700903	0.5	0.8	50000
French et al. 2008, 106890	0.1	0	60
Birdsell et al. 1999, 069792	0.1	0	100–250
DOE 2010, 700880	0	0.1	40

Table D-4.5-2
Distribution Values for Longitudinal Dispersivity

Value	RVZM (VZ)	RRM (SZ)
Length scale of application (*L*)	1–500 m	100–10,000 m
$\log_{10}\widehat{\beta_1} = \hat{\gamma}_1$, Equation D-9	−2.68	−0.43
$\widehat{\beta_2} = \hat{\gamma}_2$, Equation D-9	1.88	0.49
$\mathrm{SE}(\widehat{\gamma_1})$, Equation D-10	0.18	0.17
$\mathrm{SE}(\widehat{\gamma_2})$, Equation D-10	0.20	0.08
$\mathrm{Cov}(\widehat{\gamma_1}, \widehat{\gamma_2})$, Equation D-10	−0.03	−0.01

Table D-4.5-3
Distribution Values for the Transverse Dispersivity Directions

Value	Transverse Horizontal	Transverse Vertical
$\log_{10}\widehat{\beta_1} = \hat{\gamma}_1$, Equation D-9	−0.72	−2.02
$\widehat{\beta_2} = \hat{\gamma}_2$, Equation D-9	1.10	1.00
$SE(\hat{\gamma}_1)$, Equation D-10	0.14	0.24
$SE(\hat{\gamma}_2)$, Equation D-10	0.06	0.09
$Cov(\hat{\gamma}_1, \hat{\gamma}_2)$, Equation D-10	−0.007	−0.02

Table D-4.5-4
Distributions for Aqueous Dispersivity Needed for the RDX Area on the log₁₀ Scale

Model, Direction	Distribution	Mean [–]*	Standard Deviation [–]
Regional, Longitudinal	N	$x\begin{bmatrix}-0.43\\0.49\end{bmatrix}$	$\sqrt{\left(x\begin{bmatrix}2.9E\text{-}2 & -1.3E\text{-}2\\-1.3E\text{-}2 & 6.8E\text{-}3\end{bmatrix}x^T\right)}$
Both, Transverse Horizontal	N	$x\begin{bmatrix}-072\\1.10\end{bmatrix}$	$\sqrt{\left(x\begin{bmatrix}1.9E\text{-}2 & -7.1E\text{-}3\\-7.1E\text{-}3 & 3.3E\text{-}3\end{bmatrix}x^T\right)}$
Both, Transverse Vertical	N	$x\begin{bmatrix}-2.02\\1.00\end{bmatrix}$	$\sqrt{\left(x\begin{bmatrix}5.6E\text{-}2 & -2.0E\text{-}2\\-2.0E\text{-}2 & 8.1E\text{-}3\end{bmatrix}x^T\right)}$

* The vector x is a row vector of the form $x = \begin{bmatrix}1 & \log_{10}L\end{bmatrix}$.

Table D-4.7-1
Linear Regression Statistics

Estimate	Coefficient	Standard Error	Confidence Interval	t Statistic	p-value
Intercept	13304.63	739.70	(11706.59, 14902.66)	17.99	<0.001
Slope	-0.023	0.001	(-0.026, -0.020)	-15.48	<0.001

Table D-4.7-2
Extrapolation of Water Levels

Location	x-coordinate	Water Level (m)
Southeast	498975	1735.32
East middle	506350	1564.32
Northeast	510100	1477.37

Table D-4.9-1
RVZM Geologic Unit Groupings

Name	Abbreviation	Unit ID	K_d Group
Puye Formation, Lower	Tpf 2	10	S
Tschicoma Formation, Upper	Tvt 2	11	V
Puye Formation, Upper	Tpf 3	14	S
Otowi Member of the Bandelier Tuff	Qbof	16	V
Cerro Toledo Formation	Qct	17	V
Tshirege Member of the Bandelier Tuff, subunit 1g	Qbt 1g	19	V
Tshirege Member of the Bandelier Tuff, subunit 1vu	Qbt 1v-u	21	V
Tshirege Member of the Bandelier Tuff, subunit 2	Qbt 2	22	V
Tshirege Member of the Bandelier Tuff, subunit 3	Qbt 3	23	V
Tshirege Member of the Bandelier Tuff, subunit 3t (transition zone)	Qbt 3t	24	V
Tshirege Member of the Bandelier Tuff, subunit 4	Qbt 4	25	V
Otowi Member, Ash Flow	Qbof G2	27	V
Otowi Member, Ash Flow	Qbof G3	28	V
Puye Formation, Upper	Tpf 3	140	S
Puye Formation, Upper	Tpf 3	141	S
Puye Formation, Upper	Tpf 3	142	S

Table D-4.9-2
Final K_d Distributions

Material	Dist.	Mean K_d Value (mL/g)	Standard Deviation (mL/g)	1st (mL/g)	99th (mL/g)	Note	Probability (X<0) (%)
(V) Volcanic Materials	Normal	0.0235	0.0215	-0.0266	0.0735	Bulldoze at 0 mL/g	13.7
(S) Sedimentary Materials	Normal	0.0296	0.0238	-0.0259	0.0850	Bulldoze at 0 mL/g	10.8

Table D-4.11-1
Long-Term Equivalent Pumping Rates for PM-2, PM-4, and PM-5

Time Period	PM-2	PM-4	PM-5
[1965,1970)	603.3105	na*	na
[1970,1975)	603.3105	na	na
[1975,1980)	618.1126	na	na
[1980,1985)	618.1126	541.9203	na
[1985,1990)	342.1423	575.8561	229.6613
[1990,1995)	342.1423	575.8561	229.6613
[1995,2000)	543.6931	380.6618	359.3741
[2000,2005)	543.6931	380.6618	359.3741
[2005,2010)	221.6153	278.7443	258.4989
[2010,2015)	221.6153	278.7443	258.4989
[2015,2020)	421.8961	264.2622	153.9748
[2020,2025)	421.8961	264.2622	153.9748

* na = Not available.

Table D-4.13-1
Reproduced from 2018 RDX Compendium

Location	Simple Geometry Minimum (kg)	Simple Geometry Maximum (kg)	Geostatistical Minimum (kg)	Geostatistical Maximum (kg)
260 Outfall former settling pond area, after interim measure	644	644	na*	na
Vadose zone under 260 Outfall former settling pond area	545	940	na	na
SWSC and Burning Ground Springs	33	56	na	na
Cañon de Valle alluvial sediments	5	10	0.16	0.16
Vadose zone under Cañon de Valle alluvial aquifer	8	64	na	na
Intermediate groundwater (228–345 m)	263	1478	650	1581
Regional groundwater (392–439 m)	35	415	1.8	8.5
Total	**1533**	**3608**	**na**	**na**

* na = Not available.

Table D-5.1-1
Summary of the
Concentration Trend Target Values

Well	Slope (ppb/yr)
R-18	5
R-25 S5	0.5
R-25 S6	0.5
R-63	3
R-68	1

Table D-5.1-2
Hydraulic Head Target Data

Well	Method	February 2014 Water Level
CDV-R-15-3 S5	February 2014 monthly mean	1833.12
CDV-R-37-2 S2	February 2014 monthly mean	1869.32
R-13	February 2014 monthly mean	1777.85
R-17 S1	February 2014 monthly mean	1793.51
R-17 S2	February 2014 monthly mean	1792.62
R-18	February 2014 monthly mean	1864.43
R-19 S3	February 2014 monthly mean	1794.06
R-19 S4	February 2014 monthly mean	1791.67
R-25 S5	February 2014 monthly mean	1899.05
R-25 S6	February 2014 monthly mean	1890.69
R-25 S7	February 2014 monthly mean	1877.80
R-48	February 2014 monthly mean	1869.41
R-60	February 2014 monthly mean	1800.55
R-63	February 2014 monthly mean	1887.15
R-29	February 2014 monthly mean	1812.76
R-47	imputed using R-47	1865.24
R-58	imputed using CdV-R-37-2 S2	1869.03
R-68	imputed using R-63	1885.85
R-69 S1	imputed using R-18	1870.52
R-69 S2	imputed using R-18	1867.33

Table D-5.2-1
Mass Balance Information for the Four Calibrations at Calendar Year 2020

	Cal. 1	Cal. 2	Cal. 3	Cal. 4
Total RDX injected (kg)	84.70	104.06	141.19	128.73
Net mass balance (kg)	−0.73	−0.52	−2.47	−1.08
Mass balance error	−0.86%	−0.50%	−1.75%	−0.84%

Appendix E

Perched-Intermediate Groundwater Database Query
(on CD included with this document)